J. Astrophys. Astr. (1982) **3,** 1–4

Spectroscopic Binaries near the North Galactic Pole Paper 3: HD 105341

R. F. Griffin *The Observatories, Madingley Road, Cambridge, England, CB3 OHA*

Received 1981 October 14; accepted 1981 November 13

Abstract. Photoelectric radial-velocity measurements show that HD 105341 is a spectroscopic binary with a near-circular orbit and a period of 194 days.

Key words: radial velocities—spectroscopic binaries—stars, individual

This is the third of a series of papers in this journal (Griffin 1981a, b) describing the orbits of spectroscopic binaries observed during a radial-velocity survey of the North Galactic Pole field.* The survey, which is being undertaken with the Cambridge photoelectric radial-velocity spectrometer (Griffin 1967) embraces all the late-type HD stars at $b > 75°$. It has already brought to light a number of previously unrecognized spectroscopic binaries, as well as confirming the velocity variations of a few that were already known.

The subject of the present paper is HD 105341. Häggkvist and Oja (1973) have given its magnitude and (B — V) colour as 8·39 and 1·52 mag respectively, while Upgren (1962) has published its spectral type as K3 III. The radial-velocity traces show the very deep 'dips' that are characteristic of a late-K giant; the type is probably later than Upgren supposed, as the value of ($B - V$) is between the means for K5 III and M0 III stars and is nearer to the MO III figure (Allen 1973). Since Upgren's classifications were made from objective-prism spectra at a dispersion of 580 Å mm^{-1} at Hγ, a degree of imprecision higher than that achievable by slit spectroscopy at several times higher dispersion is only to be expected.

Table 1 lists the 51 photoelectrically determined radial velocities that are now available for the solution of the orbit of HD 105341. There is no previous determination of the star's radial velocity in the literature. The orbit computed from the data in Table 1 has elements as follows:

*Two other orbits determined in the course of this survey were earlier published elsewhere (Beavers and Griffin 1979, Griffin 1980).

Table 1. Photoelectric radial-velocity measurements of HD 105341.

		Date	MJD	Velocity km s^{-1}	Phase	$(O-C)$ km s^{-1}
1972	Apr	24·94	41431·94	−25·0	0·058	+0·1
1973	June	14·22*	41847·22	−16·9	2·197	−0·6
1975	Apr	30·02	42532·02	−43·0	5·724	−1·8
	May	22·15*	554·15	−41·1	·838	−0·1
	June	20·93	583·93	−30·1	·992	+0·9
1976	Jan	24·19	42801·19	−21·1	7·111	−0·2
	Mar	1·07	838·07	−15·0	·301	+0·6
	Apr	22·94	890·94	−32·4	·573	+0·3
1977	Jan	30·13	43173·13	−29·5	9·026	−1·6
	Feb	4·16	178·16	−25·3	·052	+0·3
		6·16	180·16	−23·5	·063	+1·2
	Mar	15·02	217·02	−14·5	·253	+0·7
		29·06	231·06	−15·3	·325	+0·9
		30·02	232·02	−16·7	·330	−0·3
		31·02	233·02	−17·2	·335	−0·6
	Apr	1·96	234·96	−17·2	·345	−0·3
		5·05	238·05	−17·5	·361	+0·1
		13·99	246·99	−20·4	·407	−0·2
		15·95	248·95	−20·1	·417	+0·7
		18·00	251·00	−22·5	·428	−1·0
		24·97	257·97	−23·4	·463	+0·7
		26·96	259·96	−25·2	·474	−0·3
		28·89	261·89	−24·9	·484	+0·8
		30·92	263·92	−26·3	·494	+0·2
	May	24·91	287·91	−35·8	·618	+0·1
		27·93	290·93	−37·5	·633	−0·6
		28·90	291·90	−36·4	·638	+0·9
		31·90	294·90	−38·7	·654	−0·5
1978	Jan	18·19	43526·19	−41·2	10·845	−0·4
		23·10	531·10	−38·0	·870	+1·7
	May	23·19*	651·19	−26·6	11·489	−0·5
1979	Jan	13·18	43886·18	−39·3	12·699	+1·1
	Feb	23·18	927·18	−37·5	·910	−0·1
		25·10	929·10	−37·0	·920	−0·3
	Mar	1·06	933·06	−36·8	·941	−1·6
		8·06	940·06	−32·3	·977	0·0
	Apr	28·95	991·95	−16·6	13·244	−1·3
	May	14·94	44007·94	−15·8	·326	+0·5
	Dec	4·21	211·21	−18·9	14·373	−0·7
1980	Jan	2·19	44240·19	−29·1	14·523	−0·4
	Feb	23·09	292·09	−41·1	·790	+0·8
	Mar	9·08	307·08	−40·1	·867	−0·2
	May	3·94	362·94	−18·3	15·155	−0·2
		5·94	364·94	−18·0	·165	−0·4
		9·91	368·91	−17·3	·186	−0·6
		11·89	370·89	−15·3	·196	+1·0
		14·90	373·90	−16·2	·211	−0·4
		17·89	376·89	−14·7	·227	+0·8
1981	Feb	2·10	44637·10	−32·3	16·567	−0·1
	Apr	28·93	722·93	−28·8	17·009	+0·6
	May	31·92	755·92	−16·7	·179	+0·3

*Observed, in collaboration with Dr J. E. Gunn, with the 200-inch telescope (Griffin and Gunn 1974).

$P = 194{\cdot}15 \pm 0{\cdot}10$ days	$(T)_{12} = \text{MJD } 43750 \pm 14$
$\gamma = -28{\cdot}54 \pm 0{\cdot}12$ km s^{-1}	$T_0 = \text{MJD } 43608{\cdot}6 \pm 0{\cdot}4$
$K = 13{\cdot}39 \pm 0{\cdot}17$ km s^{-1}	$a_1 \sin i = 35{\cdot}7 \pm 0{\cdot}5$ Gm
$e = 0{\cdot}027 \pm 0{\cdot}012$	$f(m) = 0{\cdot}048 \pm 0{\cdot}002\ M_\odot$
$\omega = 263 \pm 26$ degrees	rms residual $= 0{\cdot}8$ km s^{-1}

It will be noticed that the eccentricity is small, and, indeed, differs from zero by only a little more than two standard deviations. The question arises as to whether the orbit should be regarded as having finite eccentricity, or whether it should be seen as truly circular with the small apparent eccentricity arising simply from the errors of observation. To judge between these possibilities, we use the two statistical tests laid down by Bassett (1978), which depend upon the sums of the squares of the residuals from the orbits computed for the circular and eccentric cases. An orbit calculation in which zero eccentricity was forced on the solution resulted in a sum of squares of 31·81 (km s^{-1})^2, compared with 28·33 (km s^{-1})^2 for the solution in which the eccentricity was allowed as a free parameter. Bassett's two tests agree in showing that the probability that the apparent eccentricity arises by chance, *i.e.* that the orbit is truly circular, is between 5 and 10 per cent. Brownlee (quoted by Griffin, 1979) has pointed out that, despite the preponderance of circular orbits at very short periods, there is no great tendency for orbits to be exactly circular at periods as long as that of HD 105341; so the eccentric solution is adopted in this paper and is illustrated in Fig. 1, but with the reservation that there is a small probability (less than 10 per cent) that the orbit is really circular.

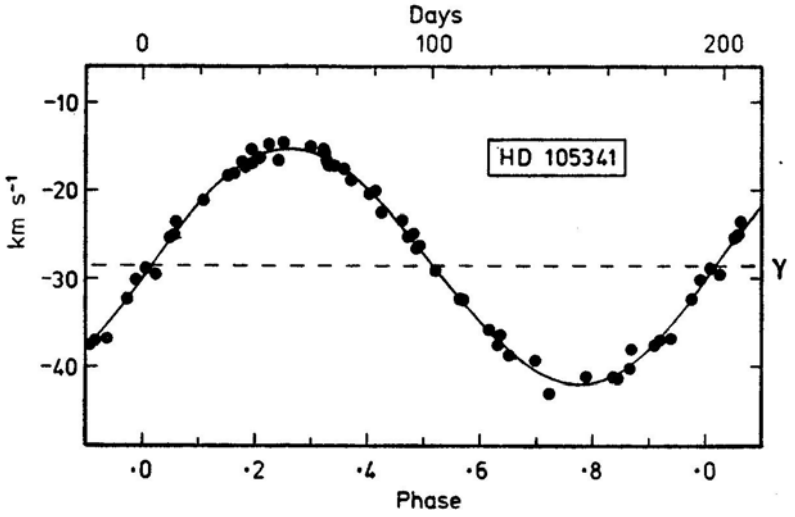

Figure 1. The computed radial-velocity curve for HD 105341, with the measured radial velocities plotted.

References

Allen, C. W. 1973, *Astrophysical Quantities,* 3 edn, Athlone Press, London, p. 206.
Bassett, E. E. 1978, *Observatory,* **98,** 122.
Beavers, W. I., Griffin, R. F. 1979, *Publ. astr. Soc. Pacific,* **91,** 521.

Griffin, R. F. 1967, *Astrophys. J.*, **148,** 465.
Griffin, R. F. 1979, *Observatory*, **99,** 1.
Griffin, R. F. 1980, *Observatory*, **100,** 1.
Griffin, R. F. 1981a, *J. Astrophys. Astr.*, **2,** 115.
Griffin, R. F. 19Slb$_3$ *J. Astrophys. Astr.*, **2,** 309.
Griffin, R. F. Gunn, J. E. 1974, *Astrophys. J.*, **191,** 545.
Häggkvist, L., Oja, T. 1973, *Astr. Astrophys. Suppl Ser.*, **12,** 381.
Upgren, A. R. *1962, Astr. J.,* **67,** 37.

J. Astrophys. Astr. (1982) **3,** 5–11

Braided Rings of Saturn—its Topology

R. Pratap *Physical Research Laboratory, Ahmedabad 380009*

Received 1981 September 23; accepted 1981 November 15

Abstract. The general topology of the braiding in Saturn's F ring is explained by invoking the theory of invariant surfaces to which a plasma would confine itself. This surface, in the framework of self-consistent fields, is indeed generated by two helicoids turning in opposite directions and are braided.

Key words: braided F rings—topology of braiding—plasma helicoids—self-consistent fields

1. Introduction

The formation of thin planetary rings in the solar system attracted a great deal of attention since the discovery of the rings of Uranus. The theory of three-body resonance was invoked by Dermott and Gold (1977) to account for the ring formation. It was argued that the usual three-body resonance between one satellite, the parent body and a ring particle has not much of a dynamical significance, while two satellites and a ring particle will have a profound effect in making the three bodies resonate. The equation for such a condition is

$$qn_1 - (q + p)\, n_2 + pn_3 = 0 \tag{1}$$

where n_1 is the mean period of a ring particle and n_2 and n_3 are the mean periods of the satellites, p and q are integers. In a reference frame rotating with an angular frequency of n_1 the mean motions of the satellites are commensurate in the ratio of p: $(p + q)$.

The discovery of the two satellites 1980 S26 and 1980 S27 have given credence to the theory of 'shepherding' of the ring put forward by Goldreich and Tremaine (1978). This theory however seems to be inadequate to explain the braiding of the two components of the F ring, while the third component is totally inactive. A model based on the continuous distribution of matter in the ring system (Henon 1981) was

Table 1. Energy acquired by a particle of size l00Å in the ring of Saturn.

Magnetic energy at F ring with a surface field of 0·2 G	$2{\cdot}0 \times 10^{-5}$ erg cm^{-3}
Potential energy a grain of 10^{-18} g acquires	$6{\cdot}5 \times 10^{-7}$ erg cm^{-3}
Rotational energy with a Keplerian period of 15 h	$2{\cdot}6 \times 10^{-6}$ erg cm^{-3}

proposed in which only A and B rings were taken and all others were neglected. The recent findings by the Voyager mission have shown that this model cannot be anywhere near the observation of thousands of ringlets and that some are eccentric. This observation incidently also disqualifies the resonance theory of ring formation.

This paper concerns primarily on the formation and topology of the braided F ring. F ring consists of three components each of which is about 20 km wide, and has a Keplerian period of about 15 h. It has been observed that the two outermost ones are braided with five crossovers with a separation of 700 ± 100 km, and a radial separation of about 30 km. The innermost one is very faint and smooth and is totally inactive as far as braiding features are concerned. Besides these five crossovers in the outer rings, they have also observed about nine to ten kinks and knots which are also separated by about 630 ± 150 km. The spacing between the kinks and knots as well as the braiding are almost the same, and this probably would indicate that these kinks and knots are also braiding with a radial separation of $\leqslant 30$ km seen sidewise. It could also be that the radial separation could be less than the resolution of the instruments. We may therefore interpret that the braided rings consist of charged particles or plasma and the innermost one consists of neutral particles and that the braiding is due to the electrical nature of the system (Smith *et al.* 1981). These braidings are observed on the apsidal line.

The study of the brightness at phase angles 140° and 155° has indicated that the particles constituting the F ring are several tenths of a micrometre and that they could be charged due to photoionisation. It has therefore been suggested that the electromagnetic forces could play a dominant role as indicated earlier. Since only two rings have taken part in this interaction phenomenon, one is tempted to suggest that the formation of these rings as well as the braiding as basically due to electromagnetic nature and not gravitational. We propose in this paper a mechanism which explains the formation as well as braiding.

We suggest that the formation of these rings as well as the braiding is essentially due to the self-consistent motion of the charged particles in the presence of the magnetic field and gravitational field. The basic assumption made here is that the 'plasma' which consists of charged grains (of about 100 Å. diameter) move with a velocity distribution which is ellipsoidal in the velocity space (Pratap 1968). It may be seen that the motion is primarily controlled by the charge on the particle rather than its mass. Hence whether the plasma is constituted by an electron-ion gas or an electron -' grain ' gas, the electromagnetic forces are more dominant (Alfven 1981, personal communication). The relative importance of the various fields are discussed in the next paragraph.

The various fields the particle is subjected to are the potential field due to the planet, the rotational field due to the ring around the planet, and the magnetic field. The energy of these fields which a particle of size 100 Å acquires is given in Table 1. The corresponding figures for a particle in the interstellar medium is given in Table 2 (Lin 1970).

Table 2. Energy acquired by a particle in the interstellar medium.

Total radiation (star light)	$0{\cdot}7 \times 10^{-12}$ erg cm^{-3}
Turbulent gas motion	$0{\cdot}5 \times 10^{-12}$ erg cm^{-3}
Total energy of galactic rotation	$1300{\cdot}0 \times 10^{-12}$ erg cm^{-3}
Cosmic rays	$1{\cdot}0 \times 10^{-12}$ erg cm^{-3}
Magnetic field (10^{-5} G)	$4{\cdot}0 \times 10^{-12}$ erg cm^{-3}

It may be realised that a charged particle has always a Debye screening, beyond which the electrical forces are not perceptible, while there are no screening effects as far as the gravitational field is concerned. This is the reason why the gravitational force is three orders of magnitude higher in the case of interstellar particles. In the case of particles in the F ring, the situation is quite different. The magnetic field at 2·33 R_s (position of the F ring) is about $1{\cdot}6 \times 10^{-2}$ G, and hence the magnetic field energy at the F ring is about two orders of magnitude higher than the potential energy and an order higher than the rotational energy as inferred from the Keplerian period of 15 h for the F ring. It can also be realised that these energy estimates are orders of magnitude higher than the effect due to the entire matter distribution at this point. Hence the effect of magnetic field and therefore the effect of electromagnetic field are more dominant, and we can consider this gas of charged grains as a plasma in such a field.

2. Braided topology

Saturn is a peculiar object as compared to the other planets since it has a dipole field almost parallel to the rotation axis and has an equatorial field of 0·2 G (Acuna, Connerney and Ness 1981). It has a magnetosphere of its own and also comes and goes out of Jupiter's magnetospheric tail. Hence the topology of the magnetic field is very complicated in some respects. The spin axis is also inclined to the ecliptic by about 27°. We can therefore consider the plasma as confined to a circular region symmetric about the rotation axis wherein the magnetic field is small due to the interaction between the solar wind and the phenomenon of reconnection. The radius of the ring is about 140,000 km (2·33 R_s). Taking the geometry of the planet into account, we expect the magnetically null region to be an eccentric region confined to the equatorial plane of the planet. In this eccentric, field-free space, if there exists a plasma, one can ask the question as to what are the self-consistent velocity fields, magnetic fields as well as current fields that could exist so that the plasma is in equilibrium? The equation for such an invariant topological surface (rational surface) on which magnetic, current as well as velocity fields would He was first given by Pratap (1968) as

$$\frac{1}{2}(\rho^2 + k^2)\left[\frac{1}{\rho}\frac{d\epsilon}{d\rho} - \nabla^2\,\eta\right] + \rho\frac{\partial\eta}{\partial\rho} - \epsilon + \frac{K}{k_1 + k_2}\left[\frac{k_2}{2k^2}\rho^2 - k_1 \ln\rho\right] = \text{constant} \quad (2)$$

where we have a cylindrical coordinate system with the Z-axis running along the axis of the circular domain and ρ is the radial distance. In the above ϵ is an arbitrary

function of ρ and η is again an arbitrary function of the arguments ρ, $z + k\ \theta$ and η has to satisfy the condition

$$\frac{k}{2\beta}\nabla^2\left(\frac{1}{\rho}\frac{d\epsilon}{d\rho} - \nabla^2\ \eta\right) = 4\pi\ \sigma \tag{3}$$

σ being the density, β, K, k_1 and k_2 are all constants. Equation (3) comes from Poisson's equation, k is the scale length of helicity, as is obvious from the variable $z + k\theta$. Equation (2) defines a one-parametric family of surfaces and since we have done this problem in the framework of the method of characteristics, we have these arbitrary functions such as ε and η which have to be chosen.

If we now make a choice in the linear regime as

$$\nabla^2\ \eta - \frac{1}{\rho}\frac{d\epsilon}{d\rho} = -\frac{2\beta}{\alpha k}\eta \tag{4}$$

and choose ϵ as a polynomial

$$\epsilon = \frac{1}{m+1}\, g_m\, \rho^{m+1} \tag{5}$$

with g_m as constants and m as integer, Equation (4) can be written as

$$\nabla^2\ \eta + \frac{2\beta}{\alpha k}\eta = g_m\, \rho^{m-1} \tag{6}$$

which defines η and hence the density σ as given by Equation (3). The particular solution of Equation (6) is the solution of the differential equation

$$\rho^2\frac{d^2\eta}{d\rho^2} + \rho\frac{d\eta}{d\rho} + \frac{2\beta}{\alpha k}\rho^2\ \eta = g_m\, \rho^{m-1} \tag{7}$$

and this can be obtained (Kamke 1971). We shall take the simplest case $m = 1$ and the general solution of Equation (6) is then written as

$$\eta = \frac{g}{C^2} + \sum_{n=0}^{\infty} J_{nk}\left[\rho\,(C^2 - n^2)^{1/2}\right]\left[A_n \cos n\ \xi + B_n \sin n\ \xi\right] \tag{8}$$

where $\xi = z + k\ \theta$ and $C^2 = 2\beta\ /\alpha k$. J_{kn} are the usual Bessel functions with the argument $[\rho\ (C^2 - n^2)^{1/2}]$. Substituting Equation (8) in (2) and after some manipulations, we get

$$\sum_{n=0}^{\infty} A_n\left[\frac{C^2}{2}\,(\rho^2 + k^2)\,J_{nk}\left[\rho\,(C^2 - n^2)^{1/2}\right] + \rho\ \frac{d}{d\rho}J_{nk}\left[\rho\,(C^2 - n^2)^{1/2}\right]\right]\cos\,(n\ \xi + \phi_n)$$

$$+ \frac{K}{k_1 + k_2}\left[\frac{k_2}{2k^2}\rho^2 - k_1 \ln \rho\right] = \text{constant} \tag{9}$$

where ϕ_n is a phase factor.

As can be seen from Equation (9), with Z-axis in the direction tangential to the equator of the planet, and ρ normal to it, we get for $n = 0$ a torus, which was given by Prendergast (1956). This incidently is the usual configuration that is being used in the design of Tokomak in fusion physics.

If we take the next term $n = 1$ and set $K = 0$, Equation (9) becomes

$$\left[\left\{\frac{C^2}{2}(\rho^2 + k^2) - k\right\} J_k\,[\rho\,(C^2-1)^{1/2}] + \rho\,(C^2-1)^{1/2}\,J_{k-1}\,[\rho\,(C^2-1)^{1/2}]\right]\cos(\xi + \phi_1) = \text{constant.} \tag{10}$$

The choice of $K = 0$ is not quite important as far as the topology is concerned, since it is only a function of ρ. The general structure of the surface is given by Equation (10).

We chose $C^2 = 2$ and $k = 1$ and obtained the isometries. Fig. 1 gives the intersection of the xz-plane with the surface. The radial distance ρ is along the Y-axis and z along the X-axis. The contours are given for the constant = ± 2. These contours give the intersection of two helicoids winding in the clockwise and counter-clockwise directions and hence the two are *braided.* The projection of the axis of the helicoid on the xz-plane, makes an angle of $6/\pi$ and this is the pitch of the helicoid. It may be noted that there are an infinite number of braided helicoids one containing the other. We thus get a series of concentric cylinders and each annular space between two consecutive cylinders contain a braided helicoid. Furthermore, if these braided helicoids contained in a torus are viewed from one point lying along the apsidal line, one would see the crossings on either side of the line as knots and kinks and they would not be discernable as separate helicoids. We feel that this is the explanation for the observed knots and kinks. These braided helicoids constrain the plasma to move along its surface.

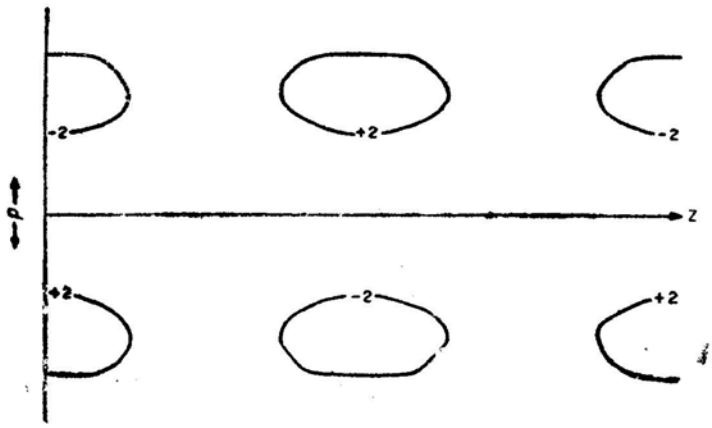

Figure 1. Isometries on the xz-plane intersecting the surface generated by Equation (10) for $C^2 = 2$ and $k = 1$. Two sets of contours with constants + 2 and – 2 form helicoids which have opposite sense of turns and are braided. This is contained in the first torus. A second torus envelops the first one and in the annular space one gets a second set of braided helicoids with a negative number appearing above the positive number indicated in the figure.

3. Conclusions

The basic assumption in this paper is that a plasma confined to an almost field-free space in the equatorial plane of Saturn would confine itself to an equilibrium configuration in a self-consistent manner. The fact that it is in the equatorial plane is because of the parallelism of the rotation and the magnetic dipole axis of the planet. This surface necessarily has to be one of two helicoids which are braided. The eccentricity of this configuration is basically due to the topology of the field-free space imposed by the dipole field of the planet, solar wind and possibly due to ring currents existing in the other rings. One could possibly ascertain this model by the measurement of the polarisation of radiation scattered by this ring. This explains the crossover as well as the kinks and knots as observed by the Voyager mission.

If this model is right, then the system is indeed dynamic and depends on the field-free space configuration. If the magnetosphere of the planet changes either due to solar wind, magnetic field sector structure, or due to Jupiter's magnetospheric tail interacting with Saturn's magnetosphere, then it would affect the eccentricity of this F ring. A polarisation measurement would indeed give credence or otherwise to this model. It is indeed tempting to put forward this model, since such braided structures are observed in the spiral arm magnetic field structures as well (Mathewson and Nicholls 1968).

The topological surfaces generated here have a much wider application than in astrophysics. It could be conjectured that as $n = 0$ gives a torus which is the present configuration for a fusion machine Tokomak, the braided helicoids could possibly be the next generation of fusion machines. As the windings increase from a torus to a helicoid, stability would also increase. The magnetic field lines, velocity-stream lines as well as currents would be helices wound on these helicoids—or will be coiled coils.

References

Acuna, M. H., Connerney, J. E. P., Ness, N. F. 1981, *Nature,* **292,** 721.
Dermott, S. F., Gold, T. 1977, *Nature,* **267,** 590.
Goldreich, P., Tremaine, S. 1978, *Icarus,* **34,** 240.
Henon, M. 1981, *Nature,* **293,** 33.
Kamke, E. 1971, *Differentialgleichungen,* Chelsea, New York.
Lin, C. C. 1970, in *Galactic Astronomy,* Vol. 2, Eds H. Y. Chiu and A. Muriel, Gordon and Breach, New York, p. 1.
Mathewson, D. S., Nicholls, D. C. 1968, *Astrophys. J.,* **154,** L11.
Pratap, R. 1968, *Can. J. Phys.,* **46,** 1257.
Prendergast, K. H. 1956, *Astrophys. J.,* **123,** 498.
Smith, B. A., Soderblom, L., Beebe, R., Boyce, J., Briggs, G., Bunker, A., Collins, S. A., Hansen, C. J., Johnson, T. V., Mitchell, J. L., Terrile, R. J., Carr, M., Cook Π, A. F., Cuzzi, J., Pollack, J. B., Danielson, G. E., Ingersoll, A., Davies, M. E., Hunt, G. E., Masursky, H., Shoemaker, E., Morrison, D., Owen, T., Sagan, C., Veverka, J., Strom, R., Suomi, V. E. 1981, *Science,* **212,** 163.

Note added in proof

Between the two encounters of Voyager I (November 1980) and Voyager II (August 1981) the ring system has materially changed. The three F rings got unbraided; this indicates clearly that the system is very dynamic, and the rings undergo rapid changes in time. Will they get braided again? Any attempt to explain this phenomenon using single-particle theory would be inadequate, since it is a collective phenomenon. A time-dependent theory of the dynamics of these topological surfaces is necessary and this we shall be presenting on a future occasion.

J. Astrophys. Astr. (1982) **3,** 13–25

On Franck-Condon Factors and Intensity Distributions in some Band Systems of I_2, NS and PS Molecules

K. Raghuveer and N. A. Narasimham *spectroscopy Division, Bhabha Atomic Research Centre, Trombay, Bombay 400085*

Received 1981 September 9; accepted 1981 December 16

Abstract. Potential curves for the *B* and *X* states of I_2, NS and PS have been obtained by Rydberg-Klein-Rees (RKR) method. From these RKR potentials, Franck-Condon factors (FCFs) for the above band systems have been calculated using the best available molecular constants, tested for accuracy on the electronic transition moment (ETM)-*r*-centroid curve in the case of I_2 and used in the study of observed abnormal intensity distribution in some bands of NS. A brief outline of the method used in the calculations of the FCFs is given.

Key words: Franck-Condon factors—intensity variations in band systems

1. Introduction

For a proper understanding of the intensity distribution in electronic spectra of molecules and processes like chemi-luminescence resulting from recombination of atoms, it is necessary to obtain accurate values of the potential energies (PE) of the electronic states of the molecules. The potential energies are usually derived either by employing empirical functions like those of Morse (1929) and Lippincott (1953) or by using experimentally obtained rotational and vibrational term values, a method adopted by Rydberg (1931,1933), Klein (1932) and Rees (1947) and widely accepted and known as RKR method. From the potential energies, one can evaluate the Franck-Condon-factors (FCFs) which are the squares of overlap integrals of the vibrational wave functions of the participating electronic states. The FCFs are used in studying the intensity distribution in an electronic band system. The FCFs also lead to the determination of electronic transition moment (ETM). A study of the variation of ETM with *r*-centroids can be made graphically. From such a graph, the accuracy of the FCFs calculated as well as the experimentally measured intensities can be assessed from the scatter of points about a smooth curve over a large range of *r*-centroids.

The RKR potentials were calculated in the present studies for the *B*-*X* system of the I_2 molecule, using the molecular constants recently obtained by Luc (1980) employing fourier transform spectroscopy (FTS). The RKRs so obtained were used to calculate the FCFs. It was found that the ETM deduced from the FCFs, when plotted against *r*-centroids, lie on a smooth curve with little scatter, which demonstrates the correctness of the FCFs and the high precision of the observed intensities.

The calculations of RKR potentials and FCFs discussed above have subsequently been applied in the present work to the *B*–*X* band system of NS primarily to confirm the conclusions drawn regarding the perturbations in the 8–0 band of this system. These calculations have also been carried out for the first time, for the analogous *B*–*X* system of the molecule PS.

The details of the calculations carried out for all the three molecules I_2, NS and PS are presented.

2. Theory

The potential curves for the electronic states of a diatomic molecule are usually calculated using the Morse (1929) function. However, it is known that the Morse potential function is empirically chosen and does not satisfactorily represent all the vibrational levels of an electronic state. Rydberg (1931) used all the observed vibrational levels and obtained the potential curves using the action integral and the integral related to the rotational constant, both of which were evaluated graphically. But in the graphical method, the integrand becomes infinite at the classical turning points. Klein (1932), therefore, modified Rydberg's method, so that the classical turning points r_{min} and r_{max} could be evaluated directly in terms of *f* and *g,* where

$$f = \frac{\partial S}{\partial U} = (r_{max} - r_{min})/2, \tag{1}$$

$$g = -\frac{\partial S}{\partial k} = (r_{min}^{-1} - r_{max}^{-1})/2 \tag{2}$$

and *S* is an auxiliary function which Klein introduced as a mathematically convenient function

$$S(U, k) = (2\pi^2 \mu)^{-1/2} \int_0^{I'} [U - E(I, k)]^{1/2} \, dI. \tag{3}$$

Here $E(I, k)$ is the sum of the vibrational and the rotational energies for any level. $I = h(v + \frac{1}{2})$ is the action variable arising from the quantization of the radial momentum, $k = J(J + 1)\ h^2/8\pi^2\mu$ comes from the quantization of the angular momentum for a molecule of reduced mass μ; $I = I'$ when $E = U$, where *U* is the constant total energy.

Rees (1947) pointed out that *f* and *g* integrals can be evaluated if $E(I, k)$ can be expressed as Quadratic in *I*.

$$E(I, k) = \omega_e (v + \tfrac{1}{2}) - \omega_e x_e (v + \tfrac{1}{2})^2 - \alpha_e (v + \tfrac{1}{2}) J(J + 1)$$
$$+ B_e J(J + 1) - D_e J^2 (J + 1)^2 \quad (4)$$

where ω_e, $\omega_e x_e$, α_e, B_e and D_e are the vibrational and rotational constants.

Usually E (I, k) cannot be represented over the entire range of vibrational levels by such an expression, but it can be expressed as a series of quadratics. The cubic form has been considered by Rees (1947) but the calculations are much more involved.

Vanderslice *et al.* (1959) have improved upon Rees method by using a series of quadratics over the range of potential so that the best least-square choice of the spectroscopic parameters is used for each vibrational level. But this can lead to errors as pointed out by Weissman, Vanderslice and Battino (1963). The main problem is the evaluation of the f and g integrals at the limit of integration. The quadrature method is best suited to solve these integrals by effectively removing the upper limit singularities in the integrands, since this method does not require the evaluation of the integrand at the limits of integration.

In the present calculations, Tellinghuisen's (1974) quadrature method has been used where a proper weight function of the form $(1 - x)^{-\frac{1}{2}}$ has been used, which seems more appropriate for f and g integrals, as both these are of the same type. It may be mentioned that Zare (1963) has earlier used the weight function $W(x) = 1$ which causes the integrand to converge slowly at the limits of integration.

The equations for f and g (1 and 2), on simplifying and changing over from I to v, become (in cm^{-1})

$$f(v) = \frac{1}{2\pi}\left(\frac{2\mu c}{h}\right)^{-1/2} \int_{-\frac{1}{2}}^{v} [G(v) - G(v')]^{-1/2}\, dv', \quad (5)$$

$$g(v) = 2\pi \left(\frac{2\mu c}{h}\right)^{1/2} \int_{-\frac{1}{2}}^{v} B(v')\, [G(v) - G(v')]^{-1/2}\, dv'. \quad (6)$$

In this case we see that the lower limit is $-\frac{1}{2}$ *i.e.* $E(-\frac{1}{2}, 0) = -D_e$. Dunham (1932) has, however, shown by a second order Wentzel-Kramers-Brillouin (WKB) method that at $v = -\frac{1}{2}$,

$$E(-\tfrac{1}{2}, 0) = -D_e + Y_{00}$$

where

$$Y_{00} \simeq \tfrac{1}{4} B_e + \frac{\alpha_e \omega_e}{12 B_e} + \frac{(\alpha_e \omega_e)^2}{144 B_e^2} - \tfrac{1}{4} \omega_e x_e. \quad (7)$$

With the introduction of the Dunham correction Y_{00}, Equations (5) and (6) become

$$f = C_1 \int_{v_{min}}^{v} [G(v) - G(v')]^{-1/2}\, dv', \quad (8)$$

$$g = \frac{1}{C_1} \int_{v_{\min}}^{v} B(v') \, [G(v) - G(v')]^{-1/2} \, dv' \tag{9}$$

where C_1 is the constant including reduced mass μ, and $v_{\min}$ is the value of v where $E(v, J = 0)$ vanishes; in other words $Y_{00} + G(v)$ becomes zero.

After solving the above f and g integrals using the quadrature method of Tellinghuisen (1974), the $r_{\max}$, $r_{\min}$ values were obtained from Equations (1) and (2). From the values of $r_{\min}$ and $r_{\max}$ the potential curves for the electronic states involved were constructed.

For the calculation of FCFs the vibrational wave functions $\psi_{v'}$ and $\psi_{v''}$ for the upper and lower states are obtained by solving the radial part of the second order Schrödinger's equation

$$\frac{\partial^2 \psi_v}{\partial r^2} + [E_v - U(r)] \, \psi_v = 0. \tag{10}$$

The method used is that of Zare and Cashion (1963) in which the one-dimensional second order differential equation is replaced by an equivalent finite difference equation. This equation is iteratively solved for the eigenvalue E_v and the wave function ψ_v by employing Numerov's (1933) method of integration together with a second order iteration-variation procedure due to Löwdin (1963). The molecular constants used in these calculations of FCFs are from Luc (1980) for I_2, Huber and Herzberg (1979) for NS and Jenouvrier and Pascat (1978) for PS.

The Franck Condon factor $q_{v'\,v''}$ associated with (v' - v'') band and defined as the square of the overlap integral is given by

$$q_{v'v''} = \left[\int \psi_{v'} \psi_{v''} \, dr \right]^2. \tag{11}$$

The integrated band intensity in emission is

$$I_{v'v''} = \frac{64}{3} \pi^4 N_{v'} \, c \, \nu^4 \, \bar{R}_e^2 \left[\int \psi_{v'} \psi_{v''} \, dr \right]^2 \tag{12}$$

where $N_{v'}$ is the population of the upper state v', ν is the frequency (band origin) of the band (v' - v''), c is the velocity of light and $\bar{R}_e$ is the average electronic transition moment. For a given electronic transition R_e depends to some extent on the internuclear distance and the wave-mechanical formulation of the Franck-Condon principle rests on the assumption that the variation is slow.

From Equation (12) it is seen that among the terms which control the intensity distribution in an electronic band system, the FCFs play an important part. Equation (12) can be written as

$$\bar{R}_e^2 (\bar{r}_{v'v''}) = I_{\text{obs}}^{v'v''} / (K N_{v'} \nu^4 q_{v'v''}) \tag{13}$$

where

$$\bar{r}_{v'v''} = \frac{\int \psi^{v'} r \psi_{v''} \, dr}{\int \psi_{v'} \psi_{v''} \, dr}. \tag{14}$$

In the above equation $\bar{r}$ is the *r*-centroid which is the average internuclear separation associated with a (v' - v'') transition as defined by Fraser (1954). *K* represents the constant term.

3. Results and discussion

I_2

The system due to $B^3\ \Pi^+_{u0} - X^1\Sigma_g$ transition in I_2 molecule provides a means of testing laser-related phenomena. For such studies it is necessary to have reliable FCFs to correlate the observed intensities. It is seen from Equation (12) that from the observed intensities and the calculated FCFs one may obtain the square of ETMs.

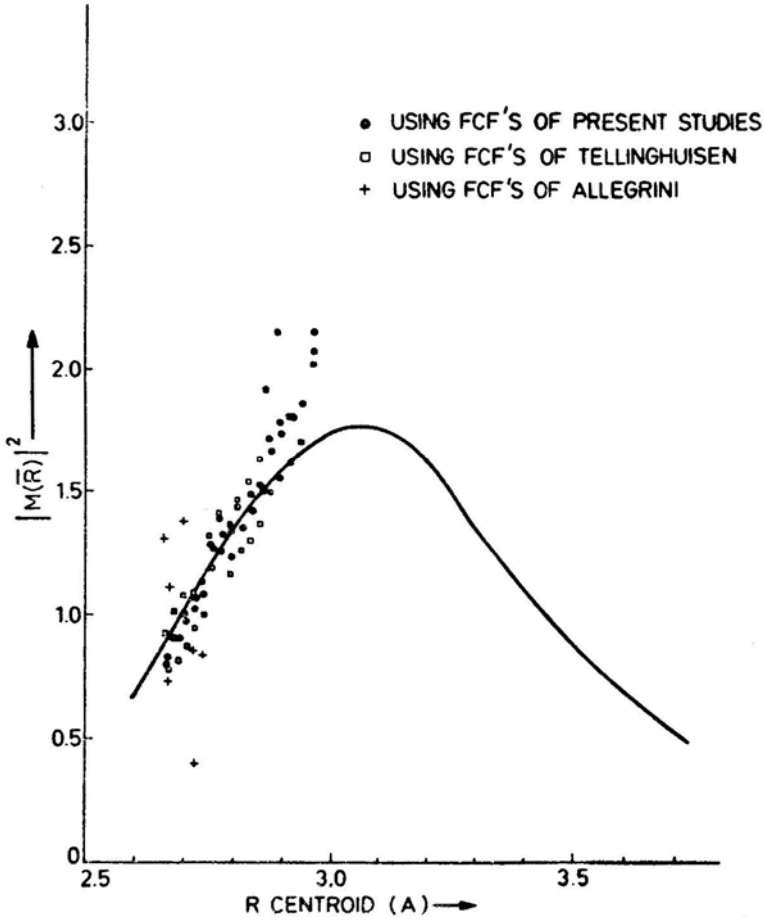

Figure 1. Variation of ETM with *r*-centroids.

On account of the constant K appearing in Equation (12), the ETMs thus obtained must first be multiplied by a suitable scaling factor before meaningful comparisons can be made with ETMs obtained by others. The graph of $(ETM)^2$ against r-centroid provides a check for the accuracies—jointly—of the molecular constants and the FCFs. The solid curve in Fig. 1 represents the approximate variation of the dipole strength in units of (debye)2 as a function of r-centroids for the B–X system of I_2, according to Brewer and Tellinghuisen (1972). If the points representing $(ETM)^2$ obtained from calculated FCFs are plotted against r-centroids the closeness with which they lie on the solid curve is a measure of the simultaneous accuracy of both FCFs and molecular constants, for this band system.

Balasubramanian *et al.* (1981) recently measured the laser-excited fluorescence intensities of the B–X system of I_2. Using these intensities and FCFs calculated by Tellinghuisen (1978) we have plotted the graph of $(ETM)^2$ against r-centroid. These points are designated by squares in Fig. 1. It is seen that these points show an appreci-

Table 1. Franck-Condon factors for the ($B - X$) system of I_2 ($v' = 43$; $J' = J'' = 14$)

v''	Tellinghuisen $\times 10^{-3}$	Present values $\times 10^{-3}$	Allegrini $\times 10^{-3}$
1	3·045	3·551	2·173
2	6·536	6·120	6·999
3	3·909	4·363	3·584
4	3·719	3·369	3·553
5	4·208	4·551	4·701
6	2·472	2·214	1·583
7	4·258	4·502	5·466
8	1·846	1·665	4·465
9	4·134	4·353	5·786
10	1·538	1·411	4·038
11	4·038	4·154	
12	1·422	1·328	
13	3·841	3·925	
14	1·441	1·359	
15	3·595	3·667	
16	1·572	1·482	
17	3·297	3·379	
18	1·804	1·682	
19	2·940	3·057	
20	2·127	1·954	
21	2·524	2·698	
22	2·531	2·291	
23	2·058	2·305	
24	2·995	2·683	
25	1·562	1·886	
26	3·486	3·118	
27	1·071	1·456	
28	3·966	3·574	
29	0·628	1·034	
30	4·390	4·023	
31	0·278	0·648	
32	4·716	4·450	
33	0·061	0·327	
34	4·913	4·812	

able scatter. Again, if FCFs calculated by Allegrini, Alzetta and Civilini (1980)—who used Luc's (1980) more accurate molecular constants—are used to obtain ETMs and use them in the graph, the scatter of points (designated by + in Fig. 1) is found to be larger still. Therefore, in order to determine where exactly the inaccuracy lies, the FCFs (using Luc's molecular constants) were calculated in the manner described above. The FCFs thus obtained are given in Table 1 along with those of Tellinghuisen (1978) and Allegrini, Alzetta and Civilini (1980). In Table 2, we give the present FCFs, *r*-centroids, observed intensities (Balasubramanian *et al.* 1981) and the appropriately scaled ETMs. While these compare well with the values of Tellinghuisen they differ widely from those of Allegrini, Alzetta and Civilini.

Table 2. Measurement of fluorescence intensities in the $B^3\,\Pi_{uo}{}^+ - X^1\Sigma_g^+$ system of I_2; fluorescence excited by 5145 Å line ($v' = 43$; $J' = J'' = 14$).

v''	ν (cm^{-1})	FCF[a] ($\times 10^3$)	*r*-centroid (Å)	intensity[b] (rel. units)	$\mid M(R) \mid^2$ (debye)^2
1	19222	3·551	2·664	208·3	0·79
2	19010	6·12	2·671	358·0	0·82
3	18799	4·363	2·682	268·9	0·90
4	18590	3·369	2·689	195·1	0·90
5	18382	4·551	2·700	281·1	1·00
6	18174	2·214	2·706	127·4	0·97
7	17969	4·502	2·718	260·5	1·02
8	17664	1·665	2·724	94·6	1·06
9	17561	4·353	2·737	243·8	1·08
10	17358	1·411	2·742	75·4	1·08
11	17169	4·154	2·755	251·0	1·28
12	16959	1·328	2·761	75·3	1·26
13	16760	3·925	2·775	231·5	1·38
14	16564	1·359	2·780	73·7	1·32
15	16370	3·667	2·794	191·2	1·33
16	16176	1·482	2·799	67·8	1·23
17	15983	3·379	2·814	171·0	1·43
18	15790	1·682	2·819	76·8	1·35
19	15601	3·057	2·834	146·1	1·48
20	15412	1·954	2·839	84·9	1·41
21	15226	2·698	2·855	120·2	1·53
22	15039	2·291	2·860	96·0	1·50
23	14856	2·305	2·876	104·8	1·71
24	14673	2·683	2·881	112·5	1·67
25	14491	1·886	2·897	80·0	1·78
26	14312	3·118	2·902	123·4	1·73
27	14133	1·456	2·920	57·0	1·80
28	13957	3·574	2·924	132·3	1·80
29	13782	1·034	2·943	62·3	3·39
30	13609	4·028	2·946	139·8	1·86
31	13436	0·648	2·967	23·7	2·07
32	13267	4·450	2·969	160·8	2·15
33	13098	0·327	2·995	12·8	2·45
34	12931	4·812	2·992	216·4	2·91

[a] These FCFs are calculated using Luc's (1980) data.

[b] Intensity of $P(17)$ line of the ($v' = 43$, v'') fluorescence series after correcting for the spectro meter response (in energy units). These intensities have been multiplied by the scaling factor $1{\cdot}84 \times 10^{12}$ before obtaining $\mid M(R) \mid_2$ given in the last column.

Table 3. FCFs (first entry) and *r*-centroids (Å) for the $B^2\Pi - X^2\Pi$ system of NS.

v' \ v''	0	1	2	3	4	5	6	7	8	9
0	2·471–3	1·760–2	5·923–2	7·251–1	1·858–1	2·059–1	1·766–1	1·197–1	6·507–2	2·859–2
	1·590	1·612	1·633	1·655	1·678	1·702	1·726	1·751	1·778	1·805
1	1·246–2	6·162–2	1·287–1	1·385–1	6·750–2	3·056–3	2·757–2	1·089–1	1·585–1	1·416–1
	1·576	1·597	1·618	1·639	1·660	1·673	1·713	1·735	1·760	1·786
2	3·318–2	1·080–1	1·201–1	3.591–2	4·248–3	7·190–2	9·269–2	2·722–2	4·097–3	7·234–2
	1·563	1·583	1·603	1·623	1·656	1·670	1·692	1·712	1·757	1·770
3	6·205–2	1·232–1	5·126–2	2·564–3	6·928–2	6·098–2	8·537–4	4·393–2	8·615–2	3·101–2
	1·550	1·569	1·588	1·621	1·633	1·652	1·650	1·702	1.723	1·743
4	9·165–2	9·820–2	3·114–3	4·860–2	6·039–2	2·459–4	4·983–2	5·715–2	8·622–4	4·399–2
	1.537	1·556	1·569	1·598	1·617	1·597	1·663	1·682	1·674	1·734
5	1·139–1	5·286–2	1·094–2	6·998–2	7·048–3	3·584–2	5·095–2	4·375–6	5·153–2	4·401–2
	1·525	1·543	1·567	1·584	1·598	1·627	1·645	2·056	1·692	1·711
6	1·238–1	1·481–2	4·562–2	3·863–2	9·821–3	5·661–2	1·962–3	4·191–2	3·497–2	4·106–3
	1·513	1·529	1·552	1·569	1·596	1·611	1·617	1·655	1·672	1·712
7	1·211–1	9·054–5	6·541–2	4·527–3	4·485–2	1·958–2	2·086–2	4·239–2	1·053–3	5·091–2
	1·501	1·484	1·539	1·552	1·579	1·594	1·621	1·637	1·685	1·683
8	1·087–1	8·248–3	5·596–2	4·612–3	4·965–2	3·633–4	4·776–2	2·791–3	3·817–2	1·952–2
	1·490	1·512	1·526	1·552	1·565	1·614	1·605	1·612	1·647	1·662
9	9·089–2	2·886–2	3·010–2	2·863–2	2·267–2	2·287–2	2·619–2	1·375–2	3·535–2	4·431–2
	1·479	1·499	1·514	1·536	1·551	1·575	1·589	1·616	1·630	1·666
10	7·159–2	5·024–2	7·641–3	4·762–2	1·357–3	4·300–2	9·498–4	3·982–2	2·763–3	3.572–2
	1·468	1·487	1·500	1·523	1·529	1·560	1·561	1·599	1·606	1·640
11	5·363–2	6·478–2	9·351–6	4·629–2	5·798–3	3·329–2	1·007–2	2·842–2	1·012–2	2·947–2
	1·457	1·476	1·617	1·511	1·535	1·547	1·572	1·584	1·611	1·623
12	3·850–2	6·998–2	7·142–3	2·945–2	2·526–2	1·023–2	3·212–2	3·823–3	3·362–2	2·337–3
	1·447	1·465	1·487	1·499	1·520	1·533	1·556	1·565	1·594	1·598
13	2·666–2	6·705–2	2·226–2	1·075–2	3·939–2	2·595–6	3·529–2	3·674–3	2·841–2	8·104–3
	1·437	1·455	1·474	1·486	1·508	1·800	1·543	1·570	1·579	1·606
14	1·791–2	5·882–2	3·774–2	7·294–4	3·817–2	8·978–3	1·879–2	2·227–2	6·620–3	2·886–2
	1·427	1·445	1·463	1·464	1·496	1·518	1·530	1·552	1·563	1·589
15	1·172–2	4·823–2	4·855–2	2·142–3	2·522–2	2·515–2	2·768–3	3·247–2	8·963–4	2·737–2
	1·418	1·435	1·453	1·478	1·484	1·505	1·513	1·539	1·575	1·574
16	4·723–3	2·789–2	5·153–2	2·408–2	1·270–3	3·175–2	1·260–2	8·128–3	2·766–2	3·519–5
	1·408	1·425	1·443	1·463	1·472	1·493	1·522	1·527	1·549	1·559
17	4·723–3	2·789–2	5·153–2	2·408–2	1·270–3	3·175–2	1·260–2	8·128–3	2·766–2	3·519–5
	1·399	1·416	1·433	1·452	1·453	1·482	1·503	1·513	1·536	1·641
18	9·525–3	2·002–2	4·616–2	3·462–2	8·179–4	2·077–2	2·525–2	8·932–5	2·586–2	9·114–3
	1·391	1·407	1·424	1·442	1·474	1·471	1·491	1·462	1·524	1·546

Table 3. Concluded.

v''	10	11	12	13	14	15	16	17	18
v'									
0	1·019–2	2·942–3	6·845–4	1·271–4	1·854–5	2·097–6	1·799–7	1·018–8	2·270–10
	1·835	1·866	1·900	1·937	1·978	2·024	2·073	2·148	2·402
1	8·923–2	4·196–2	1·513–2	4·222–3	9·120–4	1·512–4	1·883–5	1·703–6	1·065–7
	1·814	1·843	1·875	1·909	1·946	1·988	2·035	2·091	2·160
2	1·411–1	1·398–1	9·006–2	4·119–2	1·387–2	3·489–3	6·541–4	9·012–5	8·820–6
	1·795	1·823	1·852	1·884	1·918	1·956	1·998	2·046	2·103
3	3·074–3	7·183–2	1·397–1	1·318–1	7·836–2	3·217–2	9·455–3	2·007–3	3·039–4
	1·797	1·806	1·832	1·861	1·893	1·928	1·966	2·088	2·058
4	7·900–2	2·001–2	1·032–2	9·147–2	1·441–1	1·160–1	5·892–2	2·033–2	4·880–3
	1·755	1·774	1·824	1·842	1·871	1·902	1·937	1·976	2·019
5	4·808–4	5·783–2	6·584–2	4·679–3	3·304–2	1·209–1	1·409–1	9·041–2	3·687–2
	1·791	1·766	1·787	1·793	1·856	1·881	1·912	1·947	1·986
6	5·901–2	2·277–2	1·127–2	7·313–2	3·932–2	1·709–3	7·558–2	1·443–1	1·206–1
	1·722	1·738	1·782	1·798	1·818	1·904	1·892	1·922	1·956
7	1·335–2	2·167–2	5·572–2	2·664–3	3·988–2	7·002–2	8·185–3	3·061–2	1·258–1
	1·697	1·734	1·750	1·749	1·809	1·830	1·838	1·907	1·932
8	1·600–2	4·575–2	2·647–5	4·760–2	3·055–2	6·483–3	6·963–2	3·700–2	4·140–3
	1·695	1·710	1·495	1·761	1·778	1·832	1·840	1·860	1·947
9	4·431–2	8·086–4	4·061–2	1·948–2	1·534–2	5·383–2	2·262–3	4·321–2	6·348–2
	1·673	1·660	1·720	1·734	1·776	1·790	1·779	1·852	1·872
10	9·232–3	2·666–2	2·380–2	1·104–2	4·361–2	3·925–6	4·789–2	2·326–2	1·372–2
	1·651	1·684	1·698	1·735	1·747		1·801	1·815	1·870
11	6·780–3	3·465–2	1·845–3	4·082–2	5·266–4	4·028–2	1·346–2	2·270–2	4·616–2
	1·654	1·664	1·710	1·709	1·677	1·757	1·768	1·814	1·828
12	3·354–2	3·209–3	3·224–2	7·249–3	2·771–2	1·739–2	1·709–2	3·565–2	2·787–3
	1·633	1·638	1·675	1·683	1·720	1·731	1·771	1·782	1·846
13	2·451–2	1·009–2	2·451–2	9·154–3	2·845–2	5·481–3	3·585–2	8·432–4	4·340–2
	1·616	1·645	1·656	1·688	1·698	1·738	1·743	1·822	1·793
14	1·808–3	1·128–2	4·871–4	3·252–2	3·805–4	3·387–2	1·261–3	3·467–2	5·225–3
	1·591	1·626	1·608	1·666	1·634	1·708	1·693	1·753	1·754
15	6·880–3	2·036–2	1·297–2	1·565–2	1·695–2	1·406–2	1·858–2	1·585–2	1·756–2
	1·601	1·601	1·637	1·647	1·677	1·686	1·719	1·727	1·766
16	2·513–2	1·328–3	2·885–2	5·290–5	2·900–2	1·274–3	2·884–2	2·468–3	3·032–2
	1·584	1·582	1·620	1·751	1·658	1·706	1·697	1·744	1·739
17	2·590–2	6·044–3	1·691–2	1·516–2	8·878–3	2·221–2	4·130–3	2·678–2	2·018–3
	1·570	1·596	1·604	1·630	1·638	1·668	1·670	1·707	1·698
18	1·044–2	2·209–2	9·583–4	2·631–2	9·697–4	2·356–2	6·029–3	1·866–2	1·204–2
	1·555	1·579	1·574	1·614	1·658	1·650	1·682	1·687	1·720

Table 4. FCFs (first entry) and *r*-centroids (A) for the B^2 **II** – X^2 **II** system of PS.

v' \ v''	0	1	2	3	4	5	6	7	8
0	4·670–4 2·007	4·232–3 2·025	1·835–2 2·043	5·069–2 2·062	1·002–1 2·083	1·507–1 2·101	1·793–1 2·121	1·732–1 2·142	1·383–1 2·163
1	3·006–3 1·994	2·061–2 2·012	6·362–2 2·030	1·142–1 2·048	1·261–1 2·067	7·894–2 2·086	1·664–2 2·103	3·292–3 2·136	5·079–2 2·150
2	1·009–2 1·982	5·088–2 2·000	1·048–1 2·017	1·040–1 2·035	3·821–2 2·052	1·431–4 2·110	4·200–2 2·094	8·668–2 2·112	6·017–2 2·131
3	2·358–2 1·970	8·406–2 1·987	1·036–1 2·004	3·730–2 2·021	1·412–3 2·051	5·253–2 2·060	6·844–2 2·078	1·480–2 2·094	8·792–3 2·124
4	4·305–2 1·959	1·029–1 1·975	6·159–2 1.992	1·800–4 1·983	4·365–2 2·029	6·011–2 2·046	5·863–3 2·059	2·244–2 2·087	6·347–2 2·103
5	6·548–2 1·947	9·731–2 1·963	1·605–2 1·978	2·090–2 2·000	6·209–2 2·015	9·981–3 2·029	1·998–2 2·055	5·595–2 2·070	1·074–2 2·084
6	8·635–2 1·936	7·077–2 1·952	7·238–5 2·007	5·374–2 1·987	2·825–2 2·002	7·237–3 2·026	5·215–2 2·039	1·192–2 2·053	1·632–2 2·080
7	1·015–1 1·925	3·704–2 1·940	1·591–2 1·960	5·487–2 1·974	6·126–4 1·976	4·095–2 2·010	2·442–2 2·024	7·527–3 2·050	4·679–2 2·063
8	1·085–1 1·915	1·075–2 1·928	4·123–2 1·948	2·787–2 1·962	1·271–2 1·983	4·330–2 1·997	4·028–9	4·120–2 2·033	1·449–2 2·046
9	1·070–1 1·904	1·441–4 1·898	1·641–2 1·936	3·718–3 1·947	3·854–2 1·970	1·461–2 1·983	1·970–2 2·005	3·100–2 2·019	2·844–3 2·047
10	9·860–2 1·894	5·253–3 1·913	5·088–2 1·925	2·519–3 1·948	4·345–2 1·958	4·658–5 2·033	3·959–2 1·991	2·837–3 2·000	3·052–2 2·027
11	8·567–2 1·884	2·043–2 1·901	3·211–2 1·914	1·969–2 1·933	2·499–2 1·946	1·454–2 1·966	2·699–2 1·978	7·404–3 2·001	3·230–2 2·013
12	7·073–2 1·874	3·835–2 1·891	1·238–2 1·903	3·778–2 1·922	4·861–3 1·932	3·402–2 1·953	4·418–3 1·963	2·974–2 1·986	7·351–3 1·997
13	5·584–2 1·865	5·312–2 1·881	1·204–3 1·887	4·347–2 1·911	8·077–4 1·938	3·504–2 1·942	2·273–3 1·966	3·140–2 1·974	1·868–3 2.001
14	4.240–2 1·855	6·164–2 1·871	1·591–3 1·893	3·504–2 1·900	1·272–2 1·919	1·909–2 1·930	1·875–2 1·950	1·248–2 1·961	2·018–2 1·982
15	3·110–2 1·846	6·341–2 1·862	1·103–2 1·879	1·957–2 1·890	2·840–2 1·907	3·398–3 1·916	3·162–2 1·938	1·229–4 1·917	3·026–2 1·969
16	2·212–2 1·837	5·967–2 1·852	2·444–2 1·868	6·024–3 1·878	3·620–2 1·897	8·408–4 1·923	2·775–2 1·927	7·357–3 1·947	1·877–2 1·957
17	1·531–2 1·829	5·237–2 1·843	3·698–2 1·859	1·152–4 1·843	3·243–2 1·887	1·086–2 1·905	1·305–2 1·915	2·250–2 1·934	3·013–3 1·941
18	1·035–2 1·820	4·342–2 1·834	4·554–2 1·850	2·760–3 1·869	2·099–2 1·877	2·400–2 1·894	1·558–3 1·900	2·848–2 1·923	1·517–3 1·948

Table 4. Concluded.

v' \ v''	9	10	11	12	13	14	15	16	17
0	9·238–2 2·185	5·212–2 2·208	2·499–2 2·231	1·023–2 2·256	3·582–3 2·281	1·074–3 2·308	2·755–4 2·336	6·025–5 2·366	1·118–5 2·397
1	1·124–1 2·170	1·388–1 2·192	1·206–1 2·215	8·036–2 2·238	4·277–2 2·262	1·860–2 2·288	6·698–3 2·315	2·010–3 2·343	5·045–4 2·372
2	7·809–3 2·147	1·106–2 2·182	6·971–2 2·200	1·205–1 2·221	1·232–1 2·245	8·928–2 2·269	4·939–2 2·294	2·163–2 2·321	7·651–3 2·349
3	6·280–2 2·139	6·951–2 2·158	1·870–2 2·176	3·380–3 2·217	5·471–2 2·229	1·114–1 2·252	1·203–1 2·276	8·799–2 2·301	4·778–2 2·328
4	2·507–2 2·120	2·718–3 2·157	5·206–2 2·167	6·743–2 2·186	1·924–2 2·204	3·482–3 2·248	5·630–2 2·260	1·118–1 2·283	1·159–1 2·308
5	1·535–2 2.113	5·795–2 2.129	2·369–2 2.146	3·299–3 2.184	5·287–2 2.194	6·159–2 2·214	1·246–2 2·230	8·534–3 2·274	6·902–2 2·291
6	5·061–2 2·095	7·926–3 2.107	1·845–2 2·139	5·486–2 2.155	1·534–2 2·170	8·748–3 2·207	5·954–2 2·222	5·048–2 2·242	3·500–3 2·249
7	6·835–3 2·075	2·161–2 2.104	4·443–2 2.119	2·129–3 2·124	2·847–2 2·164	4·904–2 2.181	4·834–3 2.190	2·180–2 2·232	6·468–2 2·250
8	1·431–2 2·072	4·087–2 2·086	8·992–4 2·083	3·226–2 2.128	3·293–2 2·143	4.112–4 2·209	4·193–2 2·189	3·527–2 2·206	6·607–5 2·363
9	4·029–2 2·055	3·720–3 2·064	2·646–2 2·095	2·864–2 2·109	1·867–3 2·148	4·198–2 2·152	1·553–2 2·166	1·003–2 2·202	4·975–2 2·215
10	1·492–2 2·039	1·392–2 2·065	3·248–2 2·078	3·932–4 2·132	3·736–2 2·118	1·099–2 2·130	1·521–2 2·162	4·015–2 2·176	1·316–3 2·172
11	1·084–3 2·047	3·552–2 2·048	1·577–3 2·051	2·931–2 2·086	1·499–2 2·099	1·164–2 2·128	3·502–2 2·141	7·928–5 2·061	3·448–2 2·185
12	2·360–2 2·021	1·428–2 2·033	1·423–2 2·058	2·501–2 2·070	3·658–3 2·101	3·424–2 2·108	6·858–4 2·097	3·048–2 2·149	1·620–2 2·162
13	3·110–2 2·007	4·228–4 2·050	3.181–2 2.042	3·791–4 2·028	3·004–2 2·078	5·637–3 2·087	2·177–2 2·117	1·898–2 2·129	7·424–3 2·162
14	1·107–2 1·993	1·856–2 2·015	1·317–2 2·026	1·482–2 2·050	1·850–2 2·062	8·473–3 2·089	2·626–2 2·099	1·757–3 2·138	3·245–2 2·138
15	1·127–4 2·029	2·896–2 2·001	1·730–4 2·059	2·876–2 2·035	6·137–7 1·278	2·890–2 2·070	9·390–4 2·065	2·725–2 2·107	5·671–3 2·115
16	1·278–2 1·978	1·360–2 1·988	1·534–2 2·010	1·189–2 2·020	1·543–2 2·044	1·304–2 2·054	1·324–2 2·080	1·700–2 2·090	8·759–3 2·118
17	2·645–2 1·965	1·978–4 1·947	2·660–2 1·996	7·687–5 2·073	2·614–2 2·029	2·551–4 2·084	2·636–2 2·063	7·582–5 2·159	2·721–2 2·098
18	2·218–2 1·953	7·554–3 1·974	1·516–2 1·983	1·282–2 2·005	1·062–2 2·014	1·589–2 2·037	8·688–3 2·046	1·697–2 2·071	9·017–3 2·080

When the $(ETM)^2$ values obtained from these FCFs are plotted as shown in Fig. 1, the scatter of points (designated by circles) is found to be the least. This proves that the FCFs calculated in this paper and the intensities observed by Balasubramanian *et al.* (1981) are reliable.

NS

Narasimham, Raghuveer and Balasubramanian (1975) discovered the electronic level $B'^2\Sigma^+$ of NS, through the observation of two bands at 2687 Å and 2703 Å. From the studies of spectra of isotopic molecules ^{14}NS and 15NS, Jenouvrier and Daumont (1976) showed that the bands at 2687 Å and 2703 Å were not the sub-bands of 0–0 transition but those belonging to the 1–0 band of the system $B'^2\ \Sigma^+$-$X^2\mathbf{\Pi}_{1/2,\ 3/2}$ of NS. The rotational analysis of the bands showed that the internuclear distances in the two electronic states involved are nearly the same so that the band has a wide open structure. Surprisingly the 0-0 band of such a system was found to be anomalously weak, Later, the rotational analysis of the 8–0 band of the $B^2\mathbf{\Pi}$–$X^2\mathbf{\Pi}$ system of NS exhibited several perturbations in its lower rotational levels. (Raghuveer and Narasimham 1978). These perturbations were traced to some of the rotational levels of the $v = 0$ of the new $B'^2\Sigma^+$ state. Now, the normal intensity distribution in a band system could be obtained by FCFs governing the electronic transition. Hence the FCFs of the system $B^2\ \mathbf{\Pi}$–$X^2\ \mathbf{\Pi}$ were calculated by the method described. These show that the intensity of the band 8–0 is not expected to be high. On the other hand, the intensity of the 00 band of the $\boldsymbol{B'}^2\ \mathbf{\Sigma}^+$– $X^2\ \mathbf{\Pi}$ system which is involved in the observed perturbation is unexpectedly low. It is thus clear that the 8–0 band of $B^2\ \mathbf{\Pi}$ –$X^2\ \mathbf{\Pi}$ borrows intensity from the 0–0 band of $\boldsymbol{B'}^2\mathbf{\Sigma}^+$–$X^2\ \mathbf{\Pi}$. The FCFs and *r*-centroids are given in Table 3.

PS

The diatomic molecule PS is analogous to NS. The electron configurations for the two molecules are similar.

NS: $KKL\ (z\sigma)^2\ (y\sigma)^2\ (x\sigma)^2\ (w\pi)^4\ v\pi\ \ldots\ldots\ldots\ldots X^2\ \mathbf{\Pi}_r$

PS: $KKLL\ (z\sigma)^2\ (y\sigma)^2\ (x\sigma)^2\ (w\pi)^4\ v\pi\ \ldots\ldots\ldots\ldots X^2\ \mathbf{\Pi}_r$

Both these molecules have extensive *B–X* systems. Recently, Jenouvrier and Pascat (1978) have determined accurate vibrational and rotational constants of the two electronic states involved in the *B–X* systems of PS by rotational analysis of a number of bands of the system. Using these vibrational and rotational constants, we have calculated the FCFs which are given in Table 4. It will be seen that the intensity patterns as reflected by their respective FCFs are also very similar for the two molecules.

The present studies show the importance of obtaining accurate FCFs for a better understanding of the observed intensities in the band systems of molecules.

References

Allegrini, M., Alzetta, G., Civilini, M. 1980, *Chem. Phys. Lett.,* **70,** 454.
Balasubramanian, T. K., Bhale, G. L., Dixit, M. N., Narasimham, N. A. 1981, *J. molec. Spectrosc.,* **88,** 259.
Brewer, L., Tellinghuisen, J. 1972, *J. chem. Phys.,* **56,** 3929.
Dunham, J. L. 1932, *Phys. Rev.,* **41,**721.
Fraser, P. A. 1954, *Can. J. Phys.,* **32,** 515.
Huber, K. P., Herzberg, G. 1979, *Constants of Diatomic Molecules,* D. Van Nostrand, New York.
Jenouvrier, A., Daumont, D. 1976, *J. molec. Spectrosc.,* **61,** 313.
Jenouvrier, A., Pascat, B. 1978, *Can. J. Phys.,* **56,** 1088.
Klein, O. 1932, *Z. Phys.,* **76,** 226.
Lippincott, E. R. 1953, *J. chem. Phys.,* **21,** 2070.
Löwdin, P. O. 1963, *J. molec. Spectrosc.,* **10,** 12.
Luc, P. 1980, *J. molec. Spectrosc.,* **80,** 41.
Morse, P. M. 1929, *Phys. Rev,,* **34,** 57.
Narasimham, N. A., Raghuveer, K., Balasubramanian, T. K. 1975, *J. molec. Spectrosc.,* **54,** 160.
Numerov, B. 1933, *Publ. Central Astrophys. Obs., U.S.S.R.,* **2,** 188.
Raghuveer, K., Narasimham, N. A. 1978, *J. molec. Spectrosc.,* **70,** 323.
Rees, A. L. G. 1947, *Proc. phys. Soc.,* **59,** 998.
Rydberg, R. 1931, Z. *Phys.,* **73,** 376.
Rydberg, R. 1933, *Z. Phys.,* **80,** 514.
Tellinghuisen, J. 1974, *Computer Phys. Commun.,* **6,** 221.
Tellinghuisen, J. 1978, *J. quantit. Spectrosc. radiat. Transfer,* **19,** 149.
Vanderslice, J. T., Mason, E. A., Maisch, W. G., Lippincott, E. R. 1959, *J. molec. Spectrosc.,* **3,** 17.
Weissman, S., Vanderslice, J. T., Battino, R. J. 1963, *J. chem. Phys.,* **39,** 2226.
Zare, R. N. 1963, *UCRL,* 10925.
Zare, R. N., Cashion, J. K. 1963, *UCRL,* 10881.

J. Astrophys. Astr. (1982) **3,** 27–38

Spot Activity in the RS CVn Binary HR 1099

M. V. Mekkaden, A. V. Raveendran and S. Mohin
Indian Institute of Astrophysics, Bangalore 560034

Received 1981 November 3; accepted 1982 January 12

Abstract. *UBV* photometry of HR 1099 obtained during the 1979–80 and 1980–81 observing seasons is presented. An analysis of the available data shows that the brightness at the light curve maximum increases as the wave amplitude increases, while the brightness at the light minimum remains almost the same. In terms of the starspot model it implies that there is always a hemisphere of the active component that is nearly 'saturated' with spots and that spots occupy a larger fraction of the stellar surface when the wave amplitude is smaller. The continuous migration attributed to the photometric wave by various authors is far from certain. The amplitude of the wave has a sharp rise followed by slow decay with a period around 5–6 yr. It is found that the two-spot model proposed by Dorren and Guinan (1982) is inadequate to describe all the observed photometric peculiarities of HR 1099.

Key words: UBV photometry—RS CVn variables—spot activity

1. Introduction

HR 1099 (V711 Tau) is one of the brightest members of the RS Canum Venaticorum type systems and its spectral peculiarities were discovered by Bopp and Fekel (1976). Since its recognition as a strong and variable radio source (Owen, Jones and Gibson 1976), HR 1099 has been the subject of intensive spectroscopic and photometric studies by several investigators. It is a double-lined spectroscopic binary with an orbital period around 2·84 day. Bopp and Fekel (1976) have classified both components as G5 V or slightly later, but the spectral types suggested by Popper (1978) for the components are K1 IV and *GS* IV. The most prominent spectral feature of HR 1099 in particular, and RS CVn binaries in general, is the strong and highly variable Ca II H and K and the intermittent H_α emission. In addition to the radio emission, HR 1099 is found to emit both soft and hard X-rays (Walter, Charles and Bowyer 1978; White, Sanford and Weiler 1978). A striking photometric characteristic of

HR 1099 and several other members of its class is the wave-like distortions seen in their light curves.

We observed HR 1099 as part of a photometric programme of RS CVn systems and. related objects. The light curves of most of these close binary systems are variable in shape, mean light level, amplitude and phase. Sometimes, dramatic changes occur in their light curves in a time as short as a few orbital periods. The nature and the timescales of such changes should be known for a comprehensive treatment of any model which would accommodate all the observed peculiarities. In this paper we present new *UBV* photometry of HR 1099 and discuss the aspects of distribution and nature of spots on the surface of the active component.

2. Observations

Observations were made with the 34-cm Cassegrain reflector of the Kavalur Observatory through filters chosen to match the standard *UBV* photometric system. During the 1979–80 season we observed HR 1099 on 38 nights between November and March while during the 1980–81 season observations were made on 24 nights between November and March. The faint visual companion (ADS 2644B, K3 V) was included in all the observations. The measurements were made differentially with respect to the comparison star 10 Tau and were transformed to the Johnson system. Tables 1 and 2 contain the resulting standard differential magnitudes and colours of HR 1099. Each value given in the tables is a mean of three or four independent measurements. The Julian days of observation were converted into orbital phases with the following ephemeris (Landis *et al.* 1978):

$$\mathrm{JD} = 2442766{\cdot}069 + 2^{\mathrm{d}}{\cdot}83782\ E.$$

The observations listed in Tables 1 and 2 are plotted in Figs 1 and 2 respectively.

Fig. 1 which is the plot of the 1979–80 observations reveals a nearly sinusoidal light variation with an amplitude of about 0·15 mag. Both the maximum and minimum of the light curve are clearly defined and occur at phases close to 0·5 and 0·9 respectively. The light curve obtained during the 1980–81 observing run, plotted in Fig. 2, is drastically different from that of the previous season in all details. It is highly asymmetric with two unequal maxima, both of them fiat-topped. The total amplitude of the light variation is only $\sim$ 0·08 mag. On one occasion during the 1980–81 season—namely JD 2444673·092 — the star was brighter by $\sim$ 0·05 mag compared to the expected mean light level. The system was slightly brighter than the expected mean light level on the previous night also.

The $U - B$ and $B - V$ colours do not show any significant correlation with the light variation. They appear scattered about their respective mean values. The typical uncertainty in the differential magnitudes given in Tables 1 and 2 is $\sim$ 0·01 mag; hence the comparatively large scatter seen in Figs 1 and 2 is intrinsic to the star and indicates that fluctuations on a short timescale are present in the brightness of HR 1099.

Table 1. The differential magnitudes and colours of HR 1099 obtained during the 1979–80 season.

JD 2444000+	ΔV	$\Delta (B-V)$	$\Delta (U-B)$
207·260	1·581	0·390	0·441
208·298	1·536	0·371	0·444
209·299	1·506	0·394	0·416
210·287	1·620	0·399	0·414
226·224	1·426	0·358	0·431
229·254	1·430	0·378	0·431
230·275	1·558	0·376	0·444
237·147	1·448	0·366	0·450
238·147	1·499	0·380	0·457
240·229	1·444	0·379	0·452
241·194	1·533	0·376	0·458
244·218	1·546	0·379	0·415
245·161	1·509	0·372	0·469
249·237	1·472	0·384	0·463
251·199	1·480	0·355	0·483
253·227	1·569	0·371	0·458
254·232	1·451	0·371	0·445
255·124	1·514	0·386	0·459
258·152	1·518	0·367	0·443
259·169	1·527	0·381	0·446
261·142	1·570	0·392	
261·172	1·546	0·388	
261·199	1·545	0·367	
261·225	1·542	0·380	
263·209	1·463	0·376	0·456
264·177	1·575	0·377	0·454
266·202	1·472	0·385	0·465
271·222	1·435	0·370	0·435
273·146	1·553	0·393	
274·155	1·450	0·405	0·478
275·157	1·533	0·366	
276·112	1·528	0·397	
278·114	1·594	0·367	0·410
279·109	1·512	0·385	0·444
282·114	1·567	0·347	0·440
290·096	1·575	0·377	0·445
298·105	1·598	0·363	0·435
299·124	1·522	0·385	0·447
303·096	1·492	0·384	0·438
315·098	1·545	0·346	0·451
322·088	1·525	0·372	0·471

Table 2. The differential magnitudes and colours of HR 1099 obtained during the 1980 -81 season.

JD 2444000+	ΔV	$\Delta (B-V)$	$\Delta (U-B)$
571·408	1·582	0·359	0·420
610·195	1·544	0·379	0·417
611·202	1·571	0·366	0·431
616·175	1·552	0·356	0·408
618·165	1·543	0·393	0·419
619·185	1·579	0·367	0·409
632·177	1·581	0·368	0·410
633·214	1·589	0·371	0·386
634·163	1·568	0·351	0·427
635·164	1·574	0·380	0·401
636·126	1·605	0·375	0·394
639·164	1·581	0·383	0·405
645·094	1·593	0·363	0·432
646·084	1·589	0·380	0·409
647·094	1·560	0·376	0·430
660·113	1·617	0·380	0·409
667·094	1·539	0·340	0·405
668·091	1•589	0·378	0·422
670·089	1·559	0·364	0·396
671·095	1·564	0·358	0·435
672·090	1·524	0·369	0·446
673·092	1·525	0·356	0·424
677·080	1·608	0·360	0·418
678·088	1·539	0·356	0·396

3. Discussion

To account for the unusual photometric behaviour of the RS CVn type systems various models have been proposed and the explanation in terms of surface activity in the form of spots has received the strongest support from the observations, mainly from the wide band photometry (Eaton and Hall 1979). According to this model, starspots which are distributed unevenly on the cooler (and generally more massive) component modulate the observed light as the star rotates, causing the ‘ wave-like distortion ’ in the light curve. The changes in the light curve are attributed to the changes in the locations and distribution of spots on the stellar surface. In their spectroscopic study of HR 1099 Ramsey and Nations (1980) found that when the star was at light minimum the TiO *R* branch band-head near 8860 Å dramatically appeared or strengthened while the same was absent in the spectra taken during the light maximum. This means that the hemisphere visible at the light minimum is cooler than the hemisphere visible at the light maximum. Assuming a spectral type K0 for the normal photosphere of the cooler component of HR 1099, Ramsey and Nations found that the spots are cooler than the photosphere by about 1000 K. In what

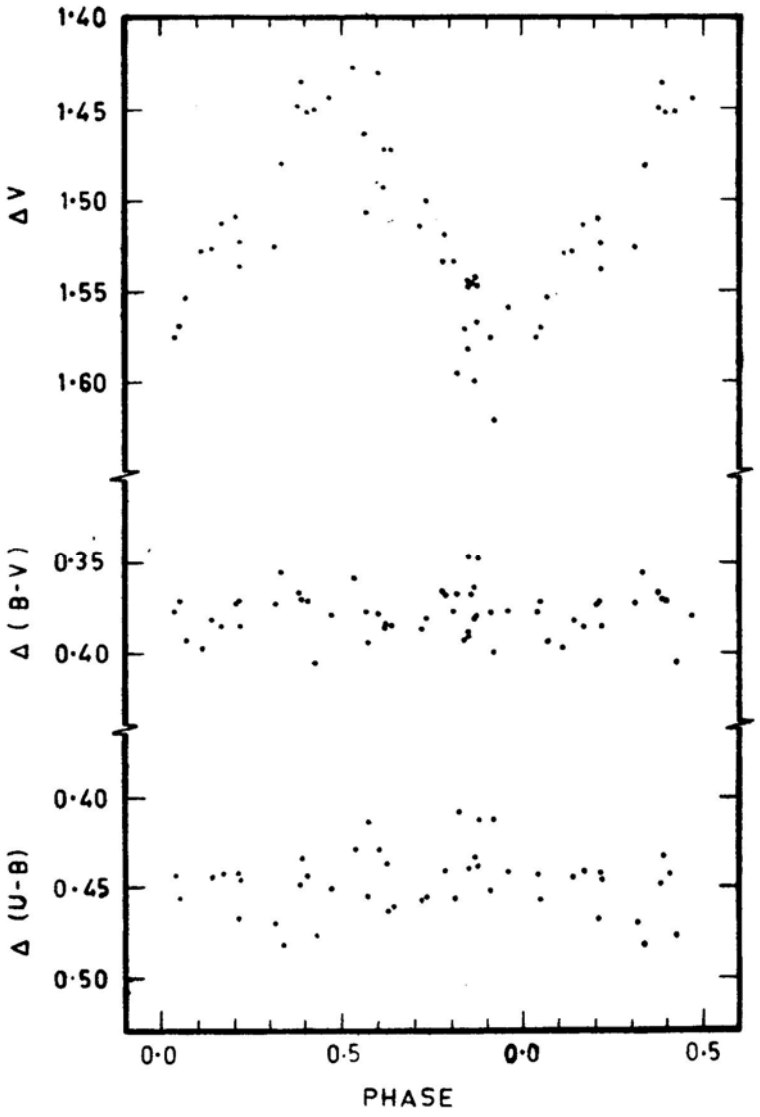

Figure 1. *V, B – V* and *U – B* light curves of HR 1099 obtained during the 1979–80 season.

follows we discuss the implications of the photometric properties of HR 1099 on the nature and the distribution of spots on the surface of the active component.

3.1 *Brightness at the Light Maximum and Minimum*

Several quantities are tabulated in Table 3 for different epochs: the observed maximum and minimum brightness of HR 1099, the amplitude of light variation in the visual band and the phase of light minimum together with its extent over the orbital

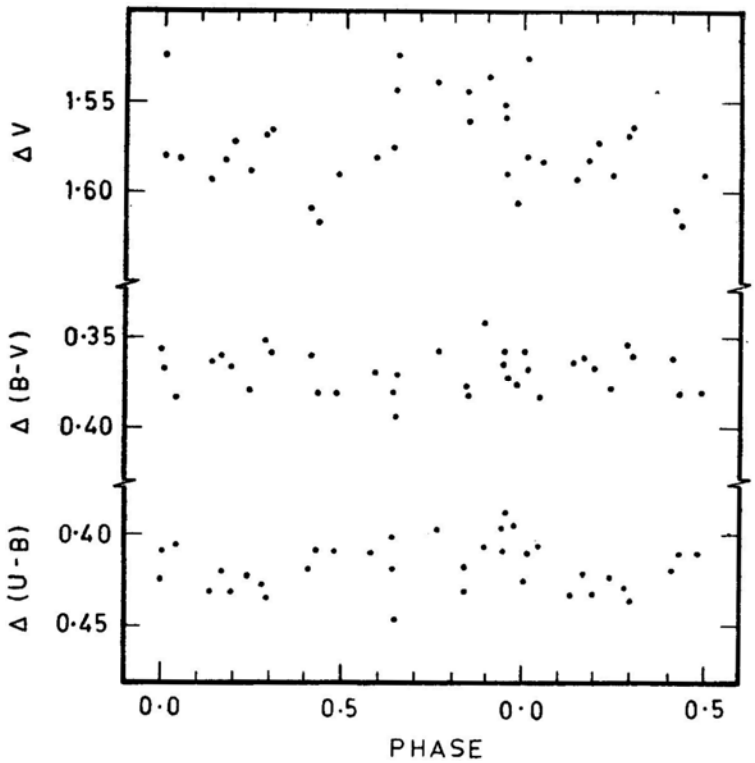

Figure 2. *V, B – V* and *U – B* light curves of HR 1099 obtained during the 1980–81 season.

Table 3. Wave amplitudes, the brightness at light maxima and minima, and the phases of the light minima.

JD 2440000+			ΔV	ΔV	Phase	
Interval	Mean	Amplitude	Maximum	Minimum	Minimum	Reference
2720–2729	2724	0·095	1·525	1·620	0·59 ± 0·15	1
2749–2776	2762	0·115	1·490	1·605	0·63 ± 0·05	1
2780–2809	2794	0·135	1·465	1·595	0·63 ± 0·05	1
2813–2838	2826	0·090	1·495	1·585	0·54 ± 0·07	1
3041–3070	3056	0·115	1·495	1·610	0·57 ± 0·07	2
3081–3131	3106	0·120	1·500	1·620	0·63 ± 0·05	2
3176–3216	3196	0·115	1·495	1·610	0·55 ± 0·11	2, 3
3396–3437	3416	0·110	1·500	1·610	0·60 ± 0·07	4
3485–3537	3506	0·085	1·505	1·590	0·70 ± 0·10	4
3561–3590	3576	0·072	1·520	1·592	0·72 ± 0·08	5
3908–3953	3930	0·210	1·415	1·625	0·91 ± 0·06	6
4207–4258	4232	0·170	1·430	1·600	0·92 ± 0·07	7
4259–4322	4290	0·155	1·440	1·595	0·86 ± 0·07	7
4610–4636	4623	0·053	1·542	1·595	0·02 ± 0·08	7
					0·53 ± 0·07	
4639–4678	4658	0·085	1·530	1·615	0·12 ± 0·08	7
					0·43 ± 0·05	

References:

1. Bopp *et al.* (1977) 2. Landis *et al.* (1978) 3. Parthasarathy, uRaveendran and Mekkaden (1981) 4. Bartolini *et al*. (1978) 5. Chambliss *et al.* (1978) 6. Chambliss and Detterline (1979) 7. Present study

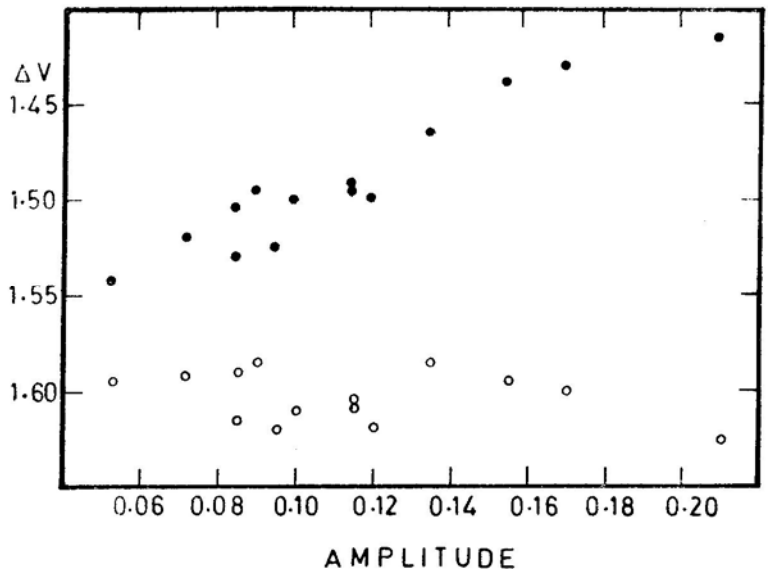

Figure 3. Brightness of HR 1099 at the light maximum (filled circle) and light minimum (open circle) plotted against the wave amplitude.

phase. The only criterion taken into account while subdividing the observations into different groups was that the data contained in each group defined the mean light curve adequately. All the available individual measurements made differentially with respect to the comparison star 10 Tau were considered. The quantities given in Table 3 were evaluated from graphical plots of the observations; the extent of the light minimum refers to the fraction of the orbital phase over which the minimum brightness remains more or less the same, and the amplitude is the difference between the values of ΔV_{max} and ΔV_{min}. Fig. 3 shows the plots of the ΔV_{max} and ΔV_{min} values against the corresponding amplitudes. A part of the scatter seen in the figure is possibly due to the inconsistencies in the transformation from the various instrumental systems to the standard *UBV* system.

If we assume in analogy with sunspots, that the spots responsible for the distortion wave in the light curve are dark, then the spots would be more predominant on the hemisphere visible at the light minimum. An inspection of Fig. 3 shows that the observed brightness of HR 1099 at light minimum is more or less constant within the observational uncertainties; this implies that the hemisphere of the active component which is visible at the light minimum is always nearly ‘ saturated ’ with spots, the fluctuations that might be present being small. We also find in Fig. 3 that the increase in wave amplitude is directly related to an increase in the brightness of HR 1099 at light maximum. It follows that, when the amplitude is small, a substantial fraction of the stellar surface is covered by spots and the increase in the amplitude is a consequence of the disappearance of spots from the stellar surface. The possibility of the spots drifting towards the invisible circumpolar region seems most unlikely. In the case of the sun we know that during maximum activity the fractional area covered by the spots is also a maximum. On the same grounds we find that in the case of

HR 1099 a smaller amplitude for the light variation means that the star is comparatively more active.

3.2 *Wave Amplitude and Phase of the Light Minimum*

In Fig. 4 the amplitude of the light variation in the visual band and the phase of light minimum (ϕ_{min}) are plotted against the mean epoch of observation. In addition to the values given in Table 3 the results of Dean (1979) and Antonopoulou and Williams (1980) are included. The length of the vertical line indicates the extent of the light minimum over the orbital phase. It is interesting to see that there is some correlation between the changes in the amplitude and phase of the light minimum. One of the details usually used to describe the light curve is the ϕ_{min} determined by fitting the light curve with the truncated Fourier series $l = A_0 + A_1 \cos \theta + A_2 \cos 2\theta + B_1 \sin \theta$ (Sarma and Ausekar 1980; Rodonó 1981). In most cases the minimum of the light curve covers an appreciable fraction of the photometric period. Further, the ϕ_{min} derived from the truncated series would be affected by the distribution of observations over the photometric phases, especially when the light curve shows large asymmetry. Hence it is difficult to attach any significant meaning to the ϕ_{min} and the corresponding errors thus determined. If we consider the total extent

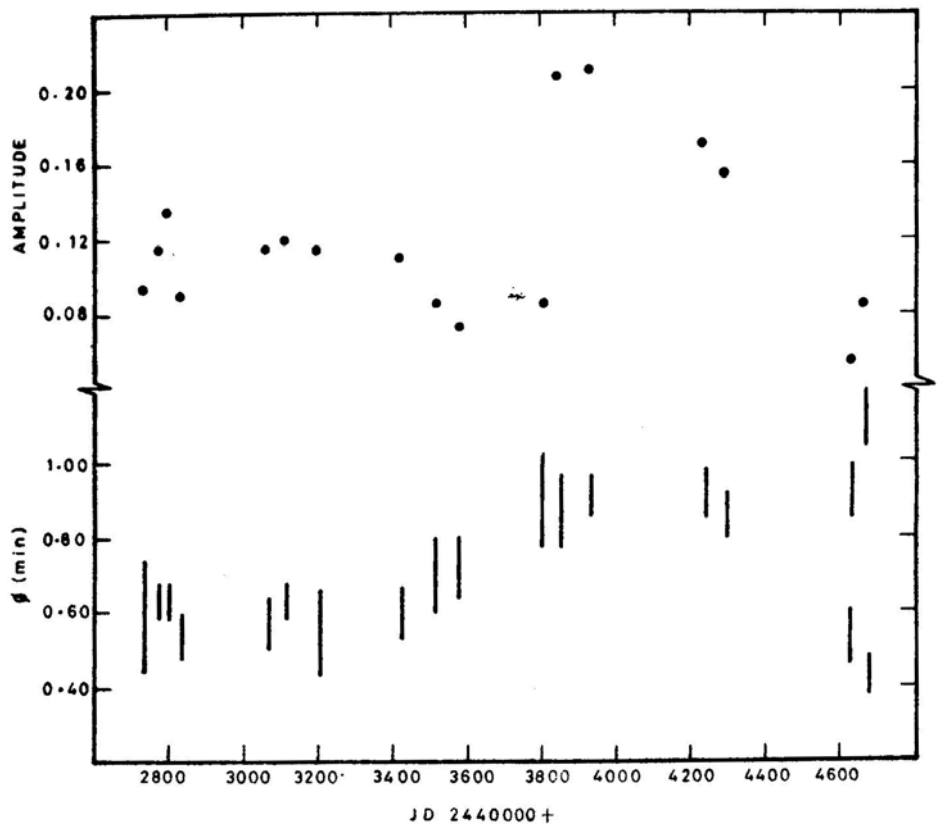

Figure 4. plot of wave amplitude and phase of light minimum against the mean of observation. The length of the vertical line indicates the extent of the light minimum over the orbital phase

of the light minimum, instead of the value of ϕ_{min} alone, the observations till JD 2444600 could be represented by two straight line portions parallel to the JD-axis. This would mean that from JD 2442700 to JD 2443800 spots were predominant more or less on the same hemisphere without any significant migration. But small-scale random fluctuations both in the extent and longitude of the ' centre of activity ' were present. Following the rather sudden increase in the wave amplitude, the longitude of the centre of activity also shifted abruptly and remained nearly the same till JD 2444600 when another region of activity developed around a different longitude as evidenced by the two light minima exhibited by the light curve obtained during the 1980–81 season. This is contrary to the observations of the earlier epochs which always showed only one light minimum. It is evident that the available photometric information on HR 1099 does not give any clear-cut indication regarding the continuous migration of the photometric wave ascribed to it by several investigators (Landis *et al.* 1978; Sarma and Ausekar 1980; Rodonó 1981). In fact what we see is the abrupt change of the location of the activity-centre to some arbitrary longitude rather than its systematic drift over the longitude.

The light curve of HR 1099 exhibits more asymmetry when the amplitude is lower indicating that the distribution of the spots is more uneven when the fractional area covered by the spots is higher. Fig. 4 strongly suggests that when a substantial fraction of the stellar surface is occupied by spots, as evidenced by the low wave amplitude, through some phenomena which occur over comparatively short lengths of time a large fraction of the spots disappear from a hemisphere. Such events seem to have occurred around JD 2443820 causing major changes in the amplitude and phase of the light curve. There is some indication that the variation of the wave amplitude is quasi-periodic with a period around 5–6 yr. From Fig. 4 it is apparent that the wave amplitude rises to a comparatively high value in a time as short as thirty days or still shorter and subsequently falls off at a much slower rate. A similar trend has been observed in the wave amplitude of the well known RS CVn binary system RT Lac (Shore and Hall 1980).

3.3 *Photometric Wave and Chromospheric Activity*

It is well known that active regions on the sun are associated with spots and hence if the starspots invoked to explain the photometric peculiarities of HR 1099 are analogous to sunspots, we should expect chromospheric emission to be correlated with the light variability. In fact spectroscopic studies of HR 1099 by Nations and Ramsey (1980) and Ramsey and Nations (1980) did show that the equivalent width of H_α emission undergoes a modulation over the photometric cycle. But Bopp and Talcott (1978) have reported that their spectroscopic observations of HR 1099 do not indicate any consistent correlation of H_α equivalent width with the light variability. From Fig. 3 it is clear that the available photometry does not provide a 'saturation value' for the brightness at light maximum and hence, it follows that the spots were present nearly all over the stellar surface with the maximum concentration on the hemisphere visible at the light minimum. Sporadic emission from the active regions associated with the starspots might mask the modulation of the equivalent width of H_α over the photometric phase, especially when the amplitude is comparatively low and the observations are spread over a larger number of photometric cycles. Photometric studies of HR 1099 by Parthasarathy, Raveendran and Mekkaden (1981) have shown

that significant changes in the light curve sometimes occur within a couple of orbital periods. Hence it is conceivable that large-scale changes in the distribution of spots could take place in a few photometric cycles. The observations of Nations and Ramsey were confined to only six consecutive nights while those of Bopp and Talcott were spread over more than two years.

3.4 *The Nature of Spots and the Model of Dorren and Guinan*

The photometric study of BY Dra by Oskanyan *et al.* (1977) has shown that the nature of spots —*i.e.* bright or dark—invoked to explain the photometric peculiarities depends on the choice of the brightness of the unspotted photosphere. If we invoke bright spots to explain the unusual photometric behaviour of HR 1099, then from Fig. 3 it follows that the constant brightness observed at the light minimum corresponds to the brightness of the unspotted photosphere and increase in the amplitude is directly related to the increase in the fractional area occupied by the bright spots. The situation when the wave amplitude is high corresponds to the case when the star is at its maximum activity. We know that the strong Ca II H and K and H_α emission indicates the presence of a chromosphere around the cooler component. The bright facular regions could heat the overlying chromosphere producing the observed enhanced emission. In this case one would expect the H_α emission equivalent width to vary in phase with the photometric wave since more bright spots would be facing the observer at the light maximum. However, spectroscopic data of HR 1099 (Nations and Ramsey 1980) show that the variations in the light and equivalent width of H_α emission are anticorrelated. Further, large bright surface inhomogeneities are expected to produce appreciable colour variation (Torres and Ferraz Mello 1973), while in the case of HR 1099 $B - V$ and $U - B$ show no significant correlation with the light variability. These results conclusively rule out the possibility that bright spots cause the observed light variation. We suggest that dark spots similar to sunspots should be preferred; the cooler and darker starspots reduce the continuum emission while the associated plage-like regions give rise to the enhanced emission. The available photometric information does not indicate a saturation value for the brightness at light maximum; this implies that spots did not disappear completely from the field of view. Hence, it is evident that on the assumption that the spots are dark, it is difficult to assign any brightness to the unspotted photosphere from the available photometry.

In the recent analysis of the long-term photometric behaviour of HR 1099, Dorren and Guinan (1982) have tried to interpret the rather complicated changes in the light curves in terms of a simple two-spot model. The spots were assumed to be of circular shape and of equal size and cooler than the photosphere by $\sim$ 1800 K. They found that the assumed two-spot model could reproduce all the diverse light curves of HR 1099. They also found a strong dependence of the amplitude on the spot size. Their results are plotted in Fig. 5. It is clearly seen that, when the wave amplitude tends to zero, their computations predict almost a spot-free component whose brightness should correspond to the maximum observed brightness. Such a conclusion is contrary to the observational results plotted in Fig. 3, where we find that a decrease in the amplitude of the light variation is followed by a decrease in the brightness of the star.

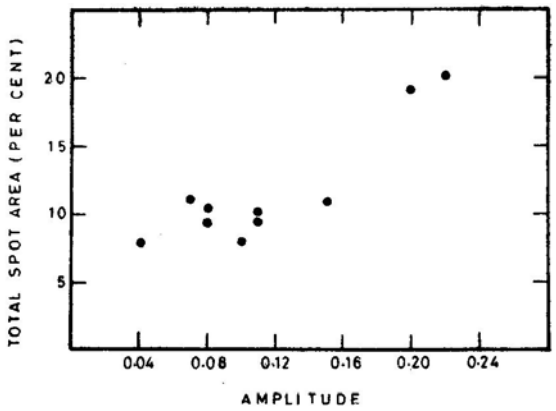

Figure 5. Plot of total spot-area against the wave amplitude (based on Dorren and Guinan 1982).

4. Conclusions

UBV photometry of HR 1099 shows that during the 1979-80 observing season the amplitude of light variation was ~ 0·15 mag whereas during 1980-81 season it was only ~ 0·08 mag. The two light curves are found to differ drastically in all respects.

Depending on the choice of the brightness of the unspotted photosphere either bright or dark spots could be invoked to explain the distortion wave in the light curve of HR 1099. The available spectroscopic information shows that variations in the light and equivalent width of H_α are anticorrelated. In addition, no significant colour variation is seen during the photometric cycle. For these two reasons, we point out, that dark spots analogous to sunspots should be preferred to explain the wave-like distortion in HR 1099.

Because it is found that the brightness of HR 1099 at maximum is linearly dependant on the wave amplitude, while the brightness at the light minimum remains nearly constant, it follows that there is always a hemisphere of the active component which is ‘ saturated ’ with spots.

The light curve of HR 1099 is seen to exhibit more asymmetry when the amplitude is lower. It is seen that a change in the amplitude of light variation from a low to a high value can occur in a time as short as thirty days. The variation of the wave amplitude seems to be quasi-periodic with a period around 5–6 yr. The present study shows that the available photometry does not provide any clear-cut evidence confirming continuous migration of the photometric wave ascribed to it by several different investigators.

The two-spot model proposed by Dorren and Guinan (1982) is found to be inadequate to account for all the observed photometric characteristics. The problems associated with spot modelling have been discussed already in detail by Rodonó (1980). The independent parameters involved in the modelling are locations of the spotted regions, extent of spots in both longitude and latitude, spot temperature and above all the brightness of the unspotted photosphere. In the case of the non-eclipsing systems the orbital inclination appears as yet another independent parameter. In practice it is difficult to obtain a unique set of solutions, even though excellent reproductions of the observed light curves can be obtained by suitably adjusting the

above parameters. Though the spot model is the most promising working hypothesis, all the observational constraints, both spectroscopic and photometric, should be available and well-defined for a comprehensive treatment of the model.

Acknowledgement

We are grateful to Dr M. K. V. Bappu for his valuable suggestions.

References

Antonopoulou, E., Williams, P. M. 1980, *Astrophys. Sp. Sci.,* **67,** 469.

Bartolini, C., Guarnieri, A., Piccioni, A., Catalano, S., Rodono, M., Brooke, A. F., Hall, D. S., Landis, H. J., Sarma, M. B. K., Olson, E. C., Renner, T. R., de Bernardi, C., Scaltriti, F. 1978, *Astr. J.,* **83,** 1510.

Bopp, B. W., Espenak, F., Hall, D. S., Landis, H. J., Lovell, L. P., Reucroft, S. 1977, *Astr. J.,* **82,** 47.

Bopp, B. W., Fekel, F. 1976, *Astr. J*., **81,** 771.

Bopp, B. W., Talcott, J. C. 1978, *Astr. J.,* **83,** 1517.

Chambliss, C. R., Detterline, P. J. 1979, *Inf. Bull. Var. Stars,* No. 1591.

Chambliss, C. R., Hall, D. S., Landis, H. J., Louth, H., Olson, E. C., Renner, T.R., Skillman, D. R. 1978, *Astr. J.,* **83,** 1514.

Dean, J. F. 1979, *Mon. Notes astr. Soc. Sth. Afr.,* **38,** 79.

Dorren, J. D., Guinan, E. F. 1982, *Astrophys. J.,* **252,** 296.

Eaton, J. A., Hall, D. S. 1979, *Astrophys. J*., **227,** 907.

Landis, H. J., Lovell, L. P., Hall, D. S., Henry, G. W., Renner, T. R. 1978, *Astr. J.,* **83,** 176.

Nations, H. L., Ramsey, L. W. 1980, *Astr. J*., **85,** 1086.

Oskanyan, V. S., Evans, D. S., Lacy, C., McMillan, R. S. 1977, *Astrophys. J*., **214,** 430.

Owen, F. N., Jones, T. W., Gibson, D. M. 1976, *Astrophys. J*., **210,** L27.

Parthasarathy, M., Raveendran, A. V., Mekkaden, M. V. 1981, *Astrophys. Sp. Sci.,* **74,** 87.

Popper, D. M. 1978, *Astr. J*., **83,** 1522.

Ramsey, L. W., Nations, H. L. 1980, *Astrophys. J*., **239,** L121.

Rodonó, M. 1980, *Mem. Soc. astr. Ital.,* **51,** 623.

Rodonó, M. 1981, in *Photometric and Spectroscopic Binary Systems,* Eds E. B. Carling, and Z. Kopal, D. Reidel, Dordrecht.

Sarma, M. B. K., Ausekar, B. D. 1980, *Acta Astr.,* **30,** 101.

Shore, S. N., Hall, D. S. 1980, in *IAU Symp. 88*: *Close Binary Stars: Observations and Interpretations,* Eds M. J. Plavec, D. M. Popper and R. K. Ulrich, D. Reidel, Dordrecht, p. 389.

Torres, C. A. O., Ferraz Mello, S. 1973, *Astr. Astrophys.,* **27,** 231.

Walter, F., Charles, P., Bowyer, S. 1978, *Nature,* **274,** 569.

White, N. E., Sanford, P. W., Weiler, E, J. 1978, *Nature,* **274,** 569.

J. Astrophys. Astr. (1982) **3**, 39–61

A Study of the H-AIpha Line in Late G and K Supergiants

Sushma Vasu Mallik *Indian Institute of Astrophysics, Bangalore 560034*

Received 1981 September 24; accepted 1982 February 5

Abstract. A spectroscopic study of H_α has been carried out to investigate the properties of expanding chromospheres of late G and K supergiants. Spectra of 23 stars brighter than V = 6·0 have been obtained at dispersions of 4–10 Å mm^{-1} using the coudé and the coudé-echelle spectrographs at the 102-cm telescope of Kavalur Observatory. The H_α profiles are all asymmetric in the sense that the absorption core is shifted to the blue by amounts ranging between — 4 and — 24 km s^{-1}.

H_α profiles were theoretically computed using radiative transfer in spherically symmetric expanding atmospheres covering a large range of integrated optical depths. These were compared with the characteristics of the observed line in the programme stars. The analysis shows that the H_α line is formed in a region with velocity increasing outward. The computed equivalent widths and line core displacements were matched with those observed to obtain hydrogen column densities and expansion velocities. From these, the rates of mass loss in these stars were determined to be in the range of 10^{-6}–10^{-7} $M_\odot$ yr^{-1}.

Key words: late-type stars—chromospheres—mass loss

1. Introduction

The existence of chromospheres has been well indicated by the presence of Ca II H (λ 3968) and K (λ 3934) emission in late-type stars. The H and K emission components designated as H_2 and K_2, are present in several F stars, in most of the G stars and in all the K and M stars that have been observed (Joy and Wilson 1949; Bidelman 1954; Wilson and Bappu 1957; Warner 1966, 1968, 1969; Wilson 1976). Other spectroscopic features of chromospheric origin include lines of Mg II (h and k), H I (L_α and H_α), He I (λλ 10830, 5876) and O I, Si II and Fe II in the far ultraviolet (Linsky 1980).

The chromospheric emissions in Ca II H and K, particularly in giants and supergiants, show a central absorption reversal. The cores of these absorption components (designated as H_3 and K_3) are displaced to the blue with respect to the ' photospheric ' line centre (Deutsch 1956, 1960; Reimers 1975, 1977; Boesgaard and Hagen 1979) suggesting a net outward motion of the regions of the atmosphere where these lines are formed. Both the chromosphere and the circumstellar envelope contribute to the central absorption reversal. The violetshifted absorption cores along with similar asymmetries detected in many other resonance lines and lines of low excitation potential, have been widely used to determine physical conditions in the circumstellar envelopes of M giants and supergiants in particular, and also to derive the rates of mass loss from their envelopes (Sanner 1976; Bernat 1977; Hagen 1978). At the same time, it has also been found that the emission components K_2 in the same stars are blueshifted with respect to the line centre which indicates that the chromospheres themselves may be expanding (Stencel 1978). Bappu (1981) has studied the relative velocity shifts of Ca II chromospheric emission ΔE and absorption Δa in several stars and has classified the stars according to the chromospheric emission differential velocity. For stars with large negative ΔE ($\Delta E \leqslant -2$ km s^{-1}), he has found that those with $\Delta\alpha - \Delta E \leqslant -2$ km s^{-1} are in the region of large wind outflow which indicates once more that for a fraction of the stars, expansion starts at chromospheric levels.

Unlike the case of M supergiants, the observational data on late G and K supergiants are rather scanty. Reimers (1977) found that the Ca II K_3 and H_3 components in late G and K supergiants showed high time variability in strength as well as in line-core displacement. Therefore, no meaningful mass-loss rates could be derived for these stars. Information from other lines (*e.g.* Ti II λλ 3659, 3383) is not available either (Reimers 1977).

Most of the circumstellar lines in late-type supergiants lie in the violet part of the spectrum, where these stars are quite faint. A survey in the red has the advantage that a much larger sample of them extending to fainter magnitudes can be studied. Weymann (1962) had noticed a distinct asymmetry in the profiles of the Balmer lines of α Ori. Kraft, Preston and Wolff (1964), in their study of H_α core widths in late-type stars, also observed that H_α line cores in most of the K supergiants are shifted to the blue. They also detected in some of the stars small emission components on the blue or on the red side of the absorption profile lying above the level of the continuum. More recently, Cohen (1976) and Mallia and Pagel (1978) have found blueshifted H_α absorption cores and weak emission components in the K giants of some globular clusters. Since the bulk of the H_α absorption is known to occur in the chromospheres (Athay and Thomas 1958), the H_α observations are interpreted as indicative of expanding chromospheres. Goldberg (1979) has recently confirmed Weymann's measurements of the violet displacement of the H_α core in α Ori. His results strengthen further the premise that the bulk of H_α is formed in the innermost layers of the expanding outer atmosphere, *i.e.* the chromosphere itself. A study of H_α is likely to yield information on the layers where the expansion begins and to provide better insight into the mass-loss phenomenon. Boesgaard and Hagen (1979), in their study of the circumstellar shells of M giants, found the H_α line to be asymmetric in many of them. Since H_α is a strong line in G and K supergiants and since the stellar continuum is also bright in the neighbourhood of H_α, the H_α line is a powerful tool for the analysis of expanding chromospheres of these stars.

Moreover, since H_α is the only line in the visual spectrum that has both a large opacity and a large scale-height in the chromosphere (Athay 1976), it can probe the chromosphere over a large extent.

In the present study the H_α line was observed in 23 supergiants brighter than $V = +6{\cdot}0$ ranging in spectral types from G8 to K7. Theoretical H_α profiles were computed and were used to fit the gross characteristics of the observed line, particularly, their equivalent widths and core displacements. Thus the column densities and velocities were determined. Finally, rates of mass loss from the expanding chromospheres of these stars were derived assuming a steady-flow situation.

The observations and the methods of reduction are discussed in Section 2. In Section 3, the theoretical framework for the analysis of the line profiles and also the results are given.

2. Observations

2.1 *The Programme*

Twenty-three stars brighter than $V = +6{\cdot}0$ were sampled in the range of spectral types G7 Ib through K7 Ib from the Bright Star Catalogue (Hoffleit 1964) and the list of supergiants given by Humphreys (1970). Basic data for the programme stars are given in Table 1.

Table 1. Data for programme stars.

Star					
HR	HD	Name	Spectral type	V	M_V
237	4817		K5 Ib	6·07	
834	17506	η Per	K3 Ib	3·76	−3·8
861	17958		K3 Ib	6·51	
2473	48329	ϵ Gem	G8 Ib	3·08	−4·5
2580	50877	o^1 CMa	K3 Iab	3·78	−4·7
2615	52005	41 Gem	K4 Ib	5·62	−3·1
2646	52877	σ CMa	M0 Iab	3·46	−4·2
2764	56577		M0 Ib	4·83	−4·1
2993	62576		K5 Ib	4·58	−4·3
3225	68553		K3 Ib	4·44	
3612	77912		G7 Ib-II	4.60	−2·2
3634	78647	λ Vel	K5 Ib	2·30	−3·8
3692	80108		K3 Ib	5·11	
4050	89388		K5 Ib	3·39	−3·7
4120	91056		K3 Ib	5·26	
5742	137709		K5 Ib	5.25	
6461	157244	β Ara	K3 Ib	2·84	−4·0
7114	174947	33 Sgr	K0 Ib	5·75	
7866	196093	47 Cyg	K5 Ib	4·72	
8079	200905	ξ Cyg	K5 Ib	3·72	−2·0
8308	206778	ϵ Peg	K2 Ib	2·42	−4·1
8465	210745	ζ Cep	K1 Ib	3·35	−4·7
8726	216946		K5 Ib	4·98	−4·4

Fourteen of the twenty-three stars have been observed to have chromospheric Ca II H and K emission. For twelve of these, the absolute magnitudes were taken from Wilson (1976) and for the other two stars, HD 89388 and β Ara, from Warner (1969). The value of M_V *for* HD 62576 was obtained from Luck (1977).

The absolute bolometric magnitudes and hence luminosities for these stars were calculated using the bolometric corrections of Johnson (1966). The effective temperatures are known only for nine of them (Luck 1977, 1979). The radii obtained for these nine using the relation $L = 4\pi R^2 \sigma T_{\text{eff}}^4$ are in the range of (1·0 ± 0·5) $\times 10^{13}$ cm.

2.2 *Coudé Spectrograms*

Spectrograms of λ Vel, η Per and σ^1 CMa were obtained on Kodak 098–02 emulsion at the coudé focus of the 102-cm telescope at Kavalur Observatory using the 112-in camera and a 400 g mm^{-1} grating. The reciprocal dispersion was 4·2 Å mm^{-1} in the second order and the resolution on the plate 0·13 Å. The spectral range covered was from 6200 Å to 6800 Å.

Another set of spectrograms was obtained for all the twenty-three programme stars with an echelle spectrograph at the coudé focus of the same telescope using a 7-in camera and an uncooled single stage Varo image tube. The spectrograph had a 79 g mm^{-1} echelle grating, blazed at 6745 Å in the 34th order which contained the H_α line and the dispersion in that order was 10·5 Å mm^{-1}. The positions of the echelle grating and of the cross-disperser were adjusted such that on each echellogram, the H_α line was in the centre of the field of view. The observed spectrum ranged from 5200 Å to 7800 Å. It was clear from the density tracings obtained of the above spectrograms that the deepest part of the H_α line is shifted shortward of the rest line centre producing a distinct asymmetry.

2.3 *The Reduction Procedure*

It is hard to locate the deepest part of the line on the plate itself because the H_α line is quite broad. So, instead of measuring the position of the line core on the comparator, we have determined it on the density tracing of each star. The dispersion is nonlinear along any single order. An independent measurement showed that a second degree polynomial fits well the relationship between the wavelength and the distance. This scale was determined on each density tracing and the position of the H_α line core located with the aid of the adjacent photospheric Fe I lines, The displacements measured in units of wavelengths are then expressed in units of velocity. The accuracy of the measurements is about 1 km s^{-1} as determined from the error involved in measuring the position of the H_α core. The displacements obtained with respect to the three Fe I lines differ by less than 1 km s^{-1}. Hence the internal accuracy of the measurement is $\leqslant$ 1 km s^{-1}.

A few representative density profiles are shown in Fig. 1. The density profiles were converted into intensity profiles using the calibration spectra. Fig. 2 shows the intensity profiles corresponding to the density profiles in Fig. 1. The equivalent widths

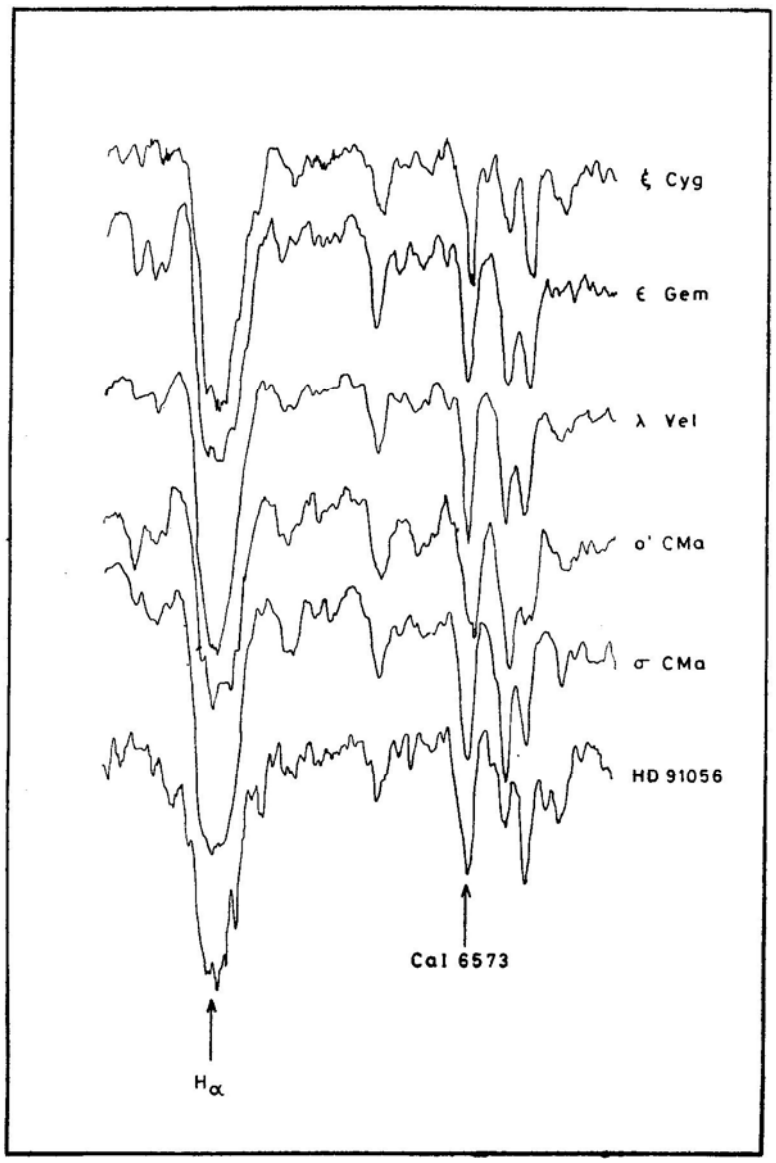

Figure 1. Density profiles of H_α in representative G and K supergiants.

determined from the different intensity profiles of the same star agree to within 10–15 per cent (or ± 0·2 Å). The equivalent widths (EQW) and the line-core displacements (LCD) listed in Table 2(a) are the averages over the number of spectra obtained for each star as given in column (2) of the table. Table 2(b) gives the H_α velocity displacements and the EQWs for the three stars λ Vel, o^1 CMa and η Per observed at the coudé spectrograph. The EQWs and the LCDs obtained in the two cases differ by less than 10 per cent.

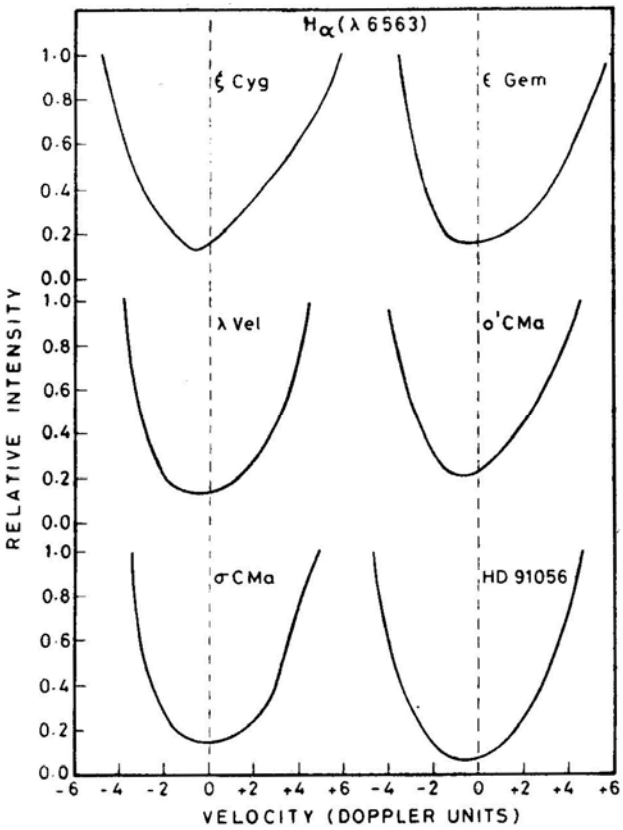

Figure 2. Intensity profiles of H_α corresponding to the density profiles in Fig. 1.

2.4 *Correlations between the Observed Quantities*

Deutsch (1956, 1960), in Ms study of the Ca II circumstellar lines in red giants, found strong correlations between (a) the spectral type and the strength of the H_3 and K_3 lines and (b) the strength and the expansion velocity of H_3 and K_3. According to him, H_3 and K_3 increased in strength and the expansion velocities decreased in the later spectral types. Deutsch attributed these trends to either a decrease in the amount of matter in the envelope and/or an increase in the ioni zation from the observable Ca II to Ca III. Although the ionization of H is insensitive to the range of temperatures involved here, it is worth investigating if similar correlations exist for the H_α line. In Figs 3 and 4, we have plotted the H_α strengths and velocities against the spectral type. It is seen that neither the strength of the H_α line core nor its position is related to the spectral type. The same result was obtained by Boesgaard and Hagen (1979) for the H_α line in M giants.

Table 2. H_α strengths and velocities.

(a) Coudé echelle spectra:

Star	Spectral type	No. of spectrograms n	Shift of the H_α line core (km s^{-1})	EQW of the H_α absorption (Å)
HD 77912	G7 Ib	2	−13·4	1·33
ϵ Gem	G8 Ib	2	− 8·1	1·77
33 Sgr	K1 Ib	1	− 4·9	1·67
ζ Cep	K1 Ib	2	−13·8	1.81
HD 196093	K2 Ib	1	−18·6	1·34
ϵ Peg	K2 Ib	2	− 8·7	1·80
η Per	K3 Ib	3	− 7·5	1·84
HD 17958	K3 Ib	1	−17·2	1·27
σ^1 CMa	K3 Iab	3	− 6·9	1·22
41 Gem	K3 Ib	3	− 9·2	1·36
HD 56577	K3 Ib	4	− 6·1	1·47
HD 62576	K3 Ib	2	−15·4	1·23
HD 68553	K3 Ib	3	−30·1	1·51
HD 80108	K3 Ib	1	−21·4	1·68
HD 91056	K3 Ib	1	− 8·7	1·98
β Ara	K3 Ib	7	−18·3	1·60
HD 4817	K5 Ib	1	−12.0	1·81
λ Vel	K5 Ib	3	−11·8	1·66
HD 89388	K5 Ib	1	−22·9	1·79
HD 137709	K5 Ib	3	− 9·3	1·69
ξ Cyg	K5 Ib	2	− 9·3	1·93
σ CMa	K7 Iab	3	−10·6	1·72
HD 216946	M0 Ib	2	−17·1	1·83
(b) Coudé spectra:				
η Per	K3 Ib		− 5·1	1·76
σ^1 CMa	K3 Iab		− 7·2	1·35
λ Vel	K5 Ib		−10·2	1·72

3. Analysis of the line profiles

3.1 *Theoretical Framework*

Because of their vast extent, the atmospheres of supergiants cannot be properly described by the classical plane-parallel LTE model atmospheres. Therefore, until recently, it was not possible to interpret adequately the observational data relating to the supergiant atmospheres. Only in the last few years, the theory of radiative transfer in extended and spherically symmetric expanding atmospheres has been worked out in some detail and models have become available (Kunasz and Hummer 1974; Mihalas 1978 and the references contained therein). A different formulation of the same problem has been given by Peraiah and Grant (1973) and Peraiah (1979, 1980, 1981) in the framework of the discrete space theory of radiative transfer. With these theoretical advances it is now possible to interpret and model the observations to a much fuller extent.

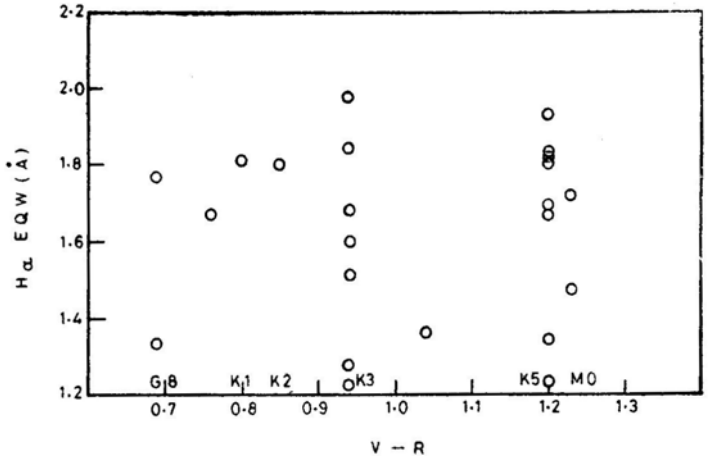

Figure 3. H_α equivalent width versus spectral type. The corresponding *V—R* values are from Johnson (1966).

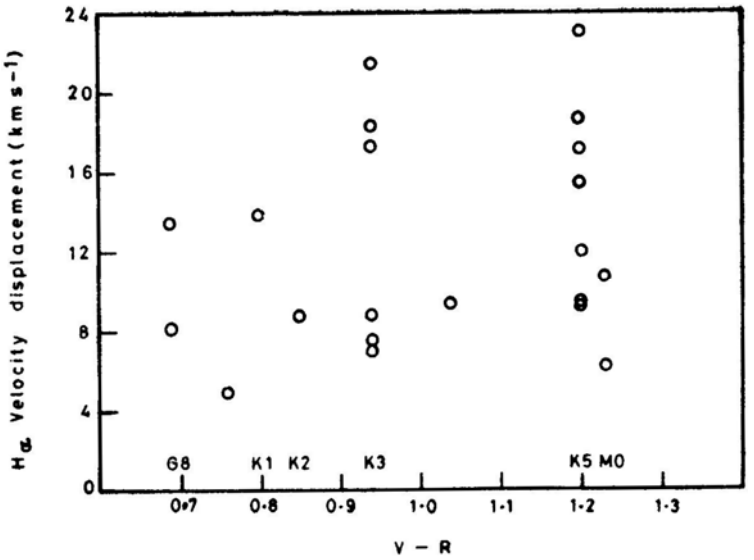

Figure 4. H_α velocity displacement versus spectral type.

The H_α line source function obtained by solving the equation of radiative transfer in the chromosphere can be used to simulate the theoretical line profiles for an observer at infinity. The gross characteristics of the observed line, the equivalent width and the core displacement in particular, are then compared with these theoretical profiles to obtain data on column densities and velocity structure of the line-forming region.

In the present work, the line source function was adopted from the work of Peraiah (1981) where the solution of the equation of radiative transfer has been given for the case of an expanding atmosphere. The line source function, S_l, is written as

$$S_l(x, \pm\mu, r) = (1 - \epsilon) \int_{-\infty}^{\infty} dx' \int_{-1}^{1} \phi(x') I(x', \mu') d\mu' + \epsilon B(r) \quad (1)$$

where $I(x', \mu')$ is the specific intensity of the ray making an angle $\cos^{-1} \mu'$ with the radius vector r and with frequency $x' = (\nu - \nu_0)/\Delta \nu_D$, $\Delta \nu_D$ being the Doppler width; ϵ is the destruction probability of photons via collisions, ϕ is the profile function and $B(r)$ is the continuum intensity which is set equal to the Planck function. The calculation of the source function was based on:

(i) a two level atom without continuum,
(ii) Doppler profile function,
(iii) the density of the absorbing material decreasing linearly with r,
(iv) the velocity increasing linearly with r with V_{max} at the outer radius equal to 10 thermal units, and
(v) ϵ set equal to zero, $\epsilon = 0$ is particularly suited to the case of H_α because it is a photo-ionization dominated line (Jefferies and Thomas 1959). With a non-zero ϵ, the line source function leads to profiles with a prominent central emission (Peraiah 1981), contrary to the observed H_α flux profiles. Further, the ratio of the continuum to line opacity, β, was assumed to be zero.

In the present work, we are dealing with large integrated optical depths in order to obtain the strong absorption profiles, as observed in the programme stars. Since the bulk of the absorption occurs within a narrow region near the inner boundary in the case of a decreasing density distribution, the source function with $\epsilon = \beta = 0$ and large τ is particularly insensitive to either the thickness of the line-forming region (so long as it is not too large) or the assumed density distribution across it.

The boundary conditions on the specific intensities incident on either side of this region are: (a) the radiation incident on the inner boundary is the Planck radiation field of the star $B(r)$ and (b) there is no radiation incident on the outer boundary.

3.2 *Geometry of the Problem*

In previous studies, which have mostly been of circumstellar shells of M giants and supergiants (Weymann 1962; Sanner 1976; Bernat 1977; Hagen 1978; Boesgaard and Hagen 1979), low densities and hence low optical depths were involved. In the case of H_α where the bulk of the absorption takes place in the chromosphere, the inner boundary of the line-forming region is the photosphere itself, in other words, the radius of the star. Consequently, much higher densities and optical depths are encountered. Since the theoretical framework used here could tackle large optical depths, it was possible to treat the H_α line-formation problem satisfactorily. The inner boundary was assumed to be 10^{13} cm for all the stars, based on the calculations for nine of them. At present, there exists no observational clue to the extent of the H_α line

forming region in late-type giants. It is expected, however, that at greater heights in the chromosphere where temperatures are higher than 10,000 K, there is no appreciable neutral hydrogen (Linsky 1980; Athay 1976). In any case, since the radiation field becomes rather dilute at greater heights, it is hard to imagine that the $n = 2$ level of H is populated sufficiently there. This is supported by the recent study of the H_α line in M giants by Boesgaard and Hagen (1979) where they find that H_α formation is confined to a narrow region near the inner boundary. The velocity and density distributions adopted here satisfy the equation of continuity in the plane-parallel limit. Therefore, in the present analysis, the extent of the line-forming region, ΔR, was adopted to be a small fraction of the stellar radius. The line-forming region was divided into a number of shells. The discretised coordinate used in the programme was the shell number which varied from 1 to 90 over the extent of the envelope. The shell number is a linear function of the radial distance from the centre of the star. The frequency was discretised in units of the Doppler width $\Delta\nu_D$ in the same way as the velocity was expressed in thermal units V_{th}. Since the absorbing matter is assumed to expand with a velocity linearly proportional to radius which is discretised in terms of the shell number, the velocity was also assumed to grow in the atmosphere in a discretised fashion in the following way:

$$V_n = V_a + \frac{V_b - V_a}{N}(n - 1 + \tfrac{1}{2}) \tag{2}$$

where V_a is the velocity at the inner edge of the line-forming region and V_b the velocity at its outer edge and N the total number of shells. The source function adopted is displayed in Fig. 5 as a function of the optical depth. It is seen that S (r) drops down by almost four orders of magnitude over the extent of the envelope.

With the velocity v (r), the density n (r) and the source function S (r) specified at each shell, the computation of the line flux as a function of frequency is fairly

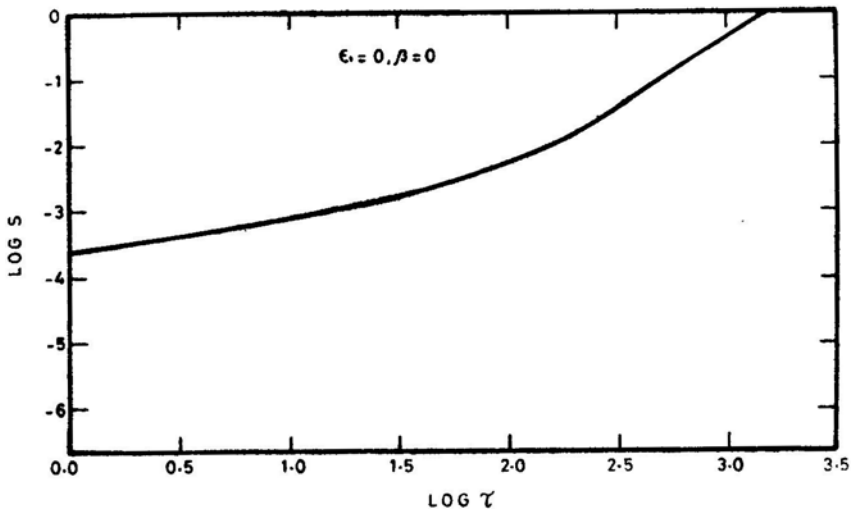

Figure 5. Source function as a function of the optical depth.

straightforward. The material behind the star is hidden from the observer and that in front gives rise to absorption (Fig. 6). The flux F_ν' due to this absorption is calculated at infinity for each frequency by the observer. In the two emission lobes on either side of the absorbing region, velocities in different radial directions contribute differently to the line of sight components of intensities. The intensities of rays for a given frequency, along the line of sight of an observer at infinity are calculated at equally spaced radial points of interval h perpendicular to the line of sight. The flux is calculated by integrating over all such intensities throughout the shell bounded by R_{in} and R_{out}. The flux in each lobe is given by

$$F_\nu = 2\pi \int_{R_{in}}^{R_{out}} I_\nu (h)\, h\, dh. \tag{3}$$

As the two emission lobes are identical the total flux received at infinity is given by

$$f_\nu = F'_\nu + 2\, F_\nu. \tag{4}$$

3.3 *Optical Depth and Column Density*

The optical depth at the centre of the H_α line is

$$\tau_0 = \frac{\sqrt{\pi}\, e^2}{mc} \frac{f}{\Delta\nu_D} N' = \alpha'\, N' \tag{5}$$

where e, m and c are the electronic charge, the electronic mass and the velocity of light respectively and f is the oscillator strength for the H_α transition and is 0·64

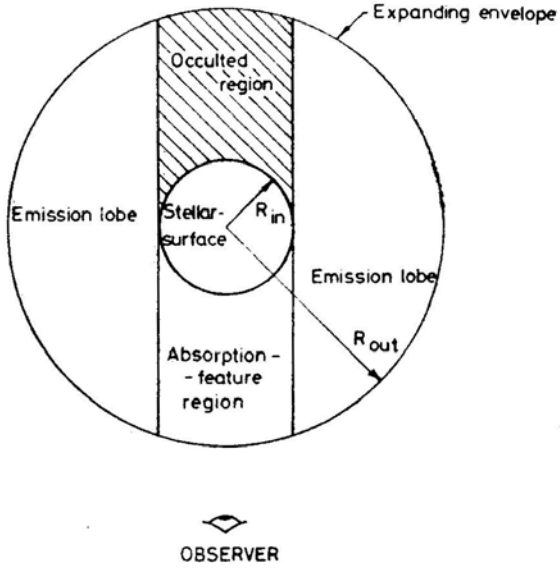

Figure 6. Schematic diagram of the expanding envelope.

(Wiese, Smith and Glennon 1966). N' is the column density of the line-forming atoms and may be written as

$$N' = \int_{R_{in}}^{R_{out}} n_2 dr = \int_{R_{in}}^{R_{out}} \delta n dr \tag{6}$$

where n_2 is the number density of H in the second level and n is the total number density of H. To simulate the overpopulation of the second level of H in the chromosphere, a temperature T was used in calculating δ which was higher than T_{exc} determined by Luck (1977, 1979) for many of the G and K supergiants studied here. According to Mihalas (1978), H_α is formed at depths in the solar chromosphere where T is about 5500 K. In their chromospheric model of α Boo, Ayres and Linsky (1975) find T varying from 4000 to 10,000 K. A temperature of about 5000–5500 K in this model occurs at depths where the number density of hydrogen is in the range 10^{11}–10^{12} cm^{-3}, typical of the middle chromosphere where H_α is likely to be formed. In the present work a temperature of 5500 K was assumed for the H_α forming region of the chromospheres of all the G and K supergiants. Using this value, the fraction δ was calculated. The expression for τ is then

$$\tau = \alpha' \delta N \equiv \alpha N \tag{7}$$

where N *is* the total column density of H. The population of the level $n = 2$ is quite unknown for the programme stars because of a lack of knowledge of the temperatures and the non-LTE factors in the chromosphere. Therefore, τ itself was used as a parameter in the computations.

3.4 *Microturbulence*

In stellar atmospheres the width of an absorption line has contributions from thermal Doppler broadening as well as microturbulence. According to Kuhi (1974), the root-means-quare turbulence ξ_t may be as large as 18 km s^{-1} or higher in supergiants. Boesgaard and Hagen (1979) deduce almost as large a value for microturbulence for late-type supergiants. Ayres and Linsky (1975) find for α Boo, an optimum value of 12·5 km s^{-1} in the chromosphere. Since the width of the line at the continuum level and hence the equivalent width are dependent upon ξ_t it was used as a free parameter in the line profile calculations. No depth dependence of microturbulence was taken into account. A higher ξ_t leads to a lower optical depth in the line for a given density.

3.5 *Computation of Line Fluxes*

With the source function given in Fig. 5 and the adopted density and velocity distributions [$n(r) \propto (1/r)$ and $v(r) \propto r$], theoretical H_α profiles were computed covering a large range of integrated optical depths. Each computer run of a set of theoretical profiles was characterised by a density and a velocity at the inner radius, a turbulent velocity and the extension of the envelope. Each profile in the set was characterised by a particular value of the velocity at the outer radius. The LCD and

the EQW were determined for each profile. The inner velocity was varied to obtain different series of computed profiles. With a higher inner velocity for the same outer velocity, the LCD was higher and the EQW lower. Since most of the observed profiles have high EQW and low LCD, the match with the set of profiles with inner velocity set equal to zero were found to be the best. So the velocity at the inner edge, V_a, was chosen to be zero for the final matching of the observed profiles. The outer velocity was varied from 0 to 9 thermal units. A few representative computed profiles are shown in Fig. 7.

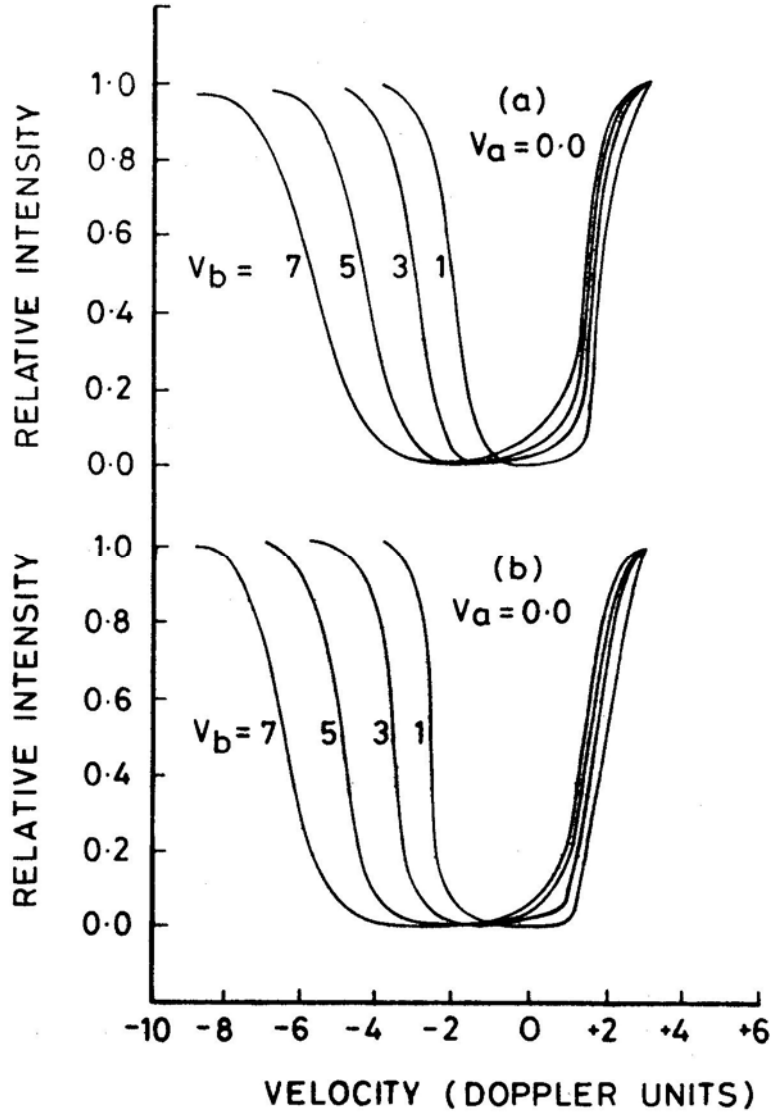

Figure 7. Computed profiles for (a) τ=30 and (b) τ=8 0. V_a and V_b, are the velocities (in Doppler units) at the inner and the outer radius.

3.6 *Results*

Optical depths and velocities

To obtain the optical depth in the H_α line and the velocity structure of the region where the H_α line is formed in these stars, the following procedure was adopted.

The LCD is a function of V_b and τ for a given ξ_t and ΔR (Fig. 8). With increasing V_b the LCD also increases. In general, the LCD increases also with τ, for, a larger optical depth implies that only the outermost layers are seen where the velocities are higher. For the lower optical depths the LCD increases almost linearly with V_b till $V_b \simeq 3{\cdot}0$ beyond which the variation slows down so that the LCD becomes almost independent of V_b. Beyond $\tau = 15$, the LCD – V_b relation is linear over a much larger range of V_b and practically independent of τ.

The EQW is also a function of τ and V_b for a given ξ_t and ΔR (Fig. 9). Increase of V_b stretches the line profile over a larger width in the continuum and a higher EQW is obtained. The EQW increases almost linearly with τ for small values of τ, then there is a change of slope around $\tau = 25$ and for higher values of τ, it is a relatively slowly-varying function. It might be worth noting that this is analogous to the linear and saturated regions of the classical curve of growth.

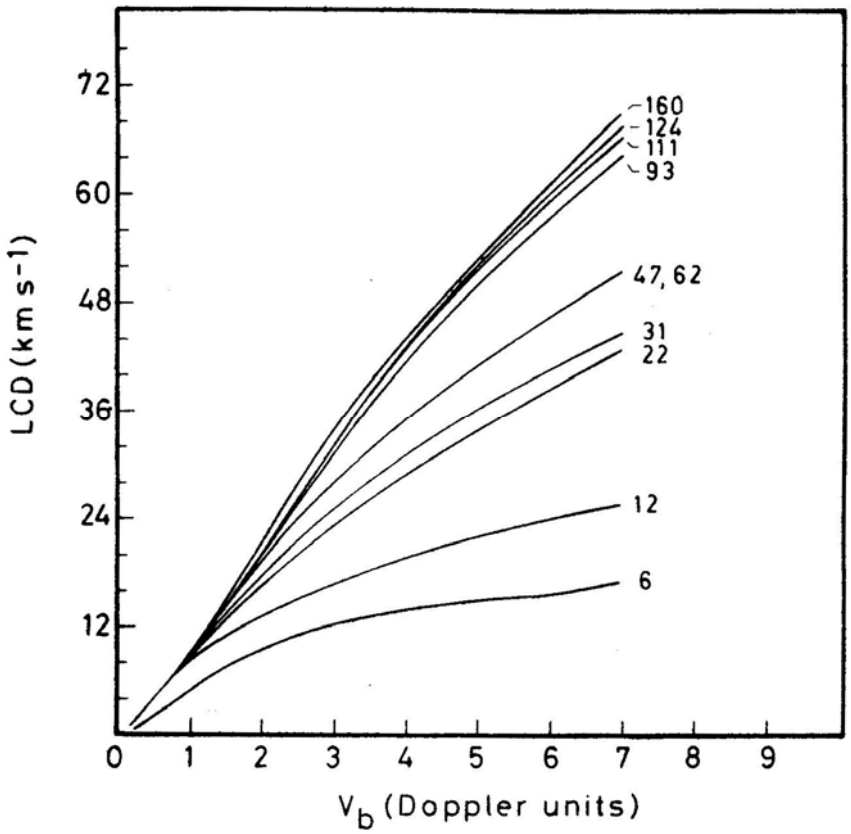

Figure 8. The computed line-core displacement versus outer velocity for $\xi_t = 15$ km s^{-1}, Each curve is labelled by the optical depth, τ.

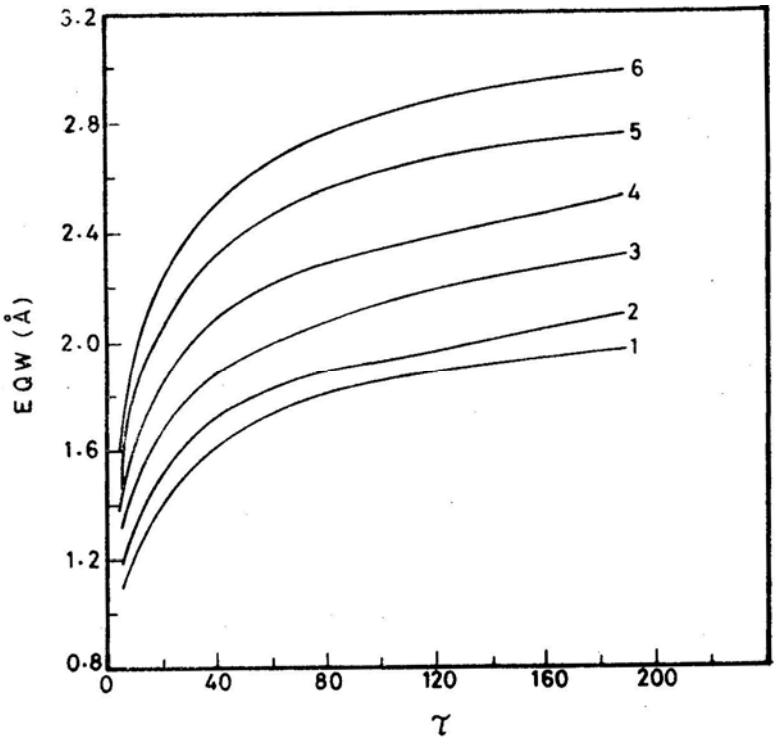

Figure 9. The computed equivalent width versus optical depth for ξ_t = 15 km s^{-1}. Each curve is labelled by the outer velocity V_b.

The final solution of obtaining τ and V_b through a match of the observed and the computed profiles was effected graphically. For a particular star, the observed LCD gives a set of (τ , V_b) solutions on the LCD – V_b graph. The observed EQW also gives a set of (τ , V_b) solutions on the EQW – τ plot. The uniqueness of the solution requires that just one (τ , V_b) combination should be common to both while the rest are discrepant. Such a unique solution was indeed found for sixteen stars which have EQW $\geqslant$ 1·6Å and LCD $\geqslant$ — 12 km s–1. However, for stars with lower EQW and or higher LCD a certain ambiguity crept in. It was seen that more than one (τ , V_b) combination satisfied the observed EQW and LCD. In particular, for these stars, proper matching could be obtained with either a high V_b and low τ or a low V_b and high τ . In order to resolve this ambiguity, some other observed characteristic of the line had to be used. An important parameter used commonly in the Ca II H and K and Mg II h and k studies of late-type stars is the asymmetry of the line profile (Stencel 1978; Stencel and Mullan 1980). In the present work a similar asymmetry parameter for the H_α line was used. If a line is drawn through the displaced line" minimum perpendicular to the direction of dispersion, then the asymmetry γ may be defined as the ratio of the flux to the shortward side of this line to the flux to its longward side, *i.e.* $\gamma = f_-/f_+$. In the observed line profiles, γ is always less than 1·0, ranging from 0·6 to 0·9. In the theoretical profiles, on the other hand, γ varies from 0·5 to 2.2. For the stars for which more than one (τ , V_b) combination was obtained, it was found that the low τ – high V_b set always gave a γ greater than 1, while the other solution fit well with the observed profile. Incidentally, for stars for which unique

Table 3. Optical depths, kinematics and mass-loss rates.

$\Delta R = 1.0 \times 10^{13}$ cm

Star	$\xi_t = 10$ km s^{-1}					$\xi_t = 15$ km s^{-1}				
	V_b km s^{-1}	τ	$\overline{V}$ km s^{-1}	N cm^{-2}	$\dot{M}$ $M_\odot$ yr^{-1}	V_b km s^{-1}	τ	$\overline{V}$ km s^{-1}	N cm^{-2}	$\dot{M}$ $M_\odot$ yr^{-1}
HD 77912	24·5	63	5·0	7·20(+22)	1·61(−6)	25·3	13	5·2	1·98(+22)	4·60(−7)
ϵ Gem	15·9	500	3·3	5·75(+23)	8·35(−6)	15·4	68	3·1	1·04(+23)	1·45(−6)
33 Sgr	11·3	400	2·3	4·60(+23)	4·72(−6)	10·2	49	2·1	7·50(+22)	6·90(−7)
ζ Cep	25·0	375	5·0	4·32(+23)	9·73(−6)	24·4	69	4·9	1·05(+23)	2·29(−6)
HD 196093	36·7	34	7·3	3·90(+22)	1·27(−6)	33·1	12	6·6	1·80(+22)	5·30(−7)
ϵ Peg	16·5	530	3·3	6·10(+23)	9·10(−6)	17·1	75	3·4	1·14(+23)	1·75(−6)
η Per	14·6	570	3·0	6·56(+23)	8·64(−6)	14·5	86	2·7	1·31(+23)	1·60(−7)
HD 17958	36·1	25	7·1	2·90(+22)	9.20(−7)	34·5	9	7·3	1·40(+22)	4·60(−7)
o^1 CMa	13·8	50	2·7	5·80(+22)	6·90(−7)	14·5	10	3·4	1·50(+22)	2·30(−7)
41 Gem	17·1	95	3·4	1·09(+23)	1·67(−6)	17·1	18	3·2	2·70(+22)	3·80(−7)
HD 56577	11·0	203	2·2	2·34(+23)	2·30(−6)	12·5	26	2·6	4·00(+22)	4·60(−7)
HD 62576	32·0	28	6·5	3·20(+22)	9·20(−7)	30·4	10	5·7	1·50(+22)	3·80(−7)
HD 68553	49·6	39	10·0	4·50(+22)	2·02(−6)	53·4	12	10·4	1·80(+22)	8·40(−7)
HD 80108	38·2	165	7·7	1·90(+23)	6·57(−6)	44·4	24	8·8	3·70(+22)	1·45(−6)
HD 91056	16·5	710	3·3	8·17(+23)	1·22(−5)	17·1	198	3·4	3·02(+23)	4·58(−6)
β Ara	30·8	200	6·2	2·30(+23)	6·39(−6)	34·8	27	7·1	4·10(+22)	1·30(−6)
HD 4817	22·0	377	4·5	4·34(+23)	8·64(−6)	21·7	77	4·4	1·17(+23)	2·29(−6)
λ Vel	21·4	269	4·3	3·10(+23)	5·99(−6)	21·5	47	4·3	7·20(+22)	1·37(−6)
HD 89388	40·4	233	8·2	2·68(+23)	9·79(−6)	48·6	30	9·6	4·60(+22)	1·98(−6)
HD 137709	17·1	420	3·5	4·83(+23)	7·49(−6)	17·1	52	3·5	7·90(+22)	1·22(−6)
ξ Cyg	17·1	570	3·5	6·56(+23)	1·02(−5)	17·1	155	3·4	2·36(+23)	3·59(−6)
σ CMa	18·8	365	3·8	4·20(+23)	7·14(−6)	20·1	58	4·1	8·80(+22)	1·60(−6)
HD 216946	29·4	340	6·0	3·91(+23)	1·04(−5)	32·1	61	6·4	9·30(+22)	2·67(−6)

solutions were already obtained without invoking the third parameter, the asymmetry of the matched profile was found to be always close to that of the observed profile. The above analysis was repeated for the other value of ξ_t. The final solutions are tabulated in Table 3.

Mass-loss rates

In a region with a specified density and velocity distribution, an average velocity $\overline{V}$ may be defined as

$$\overline{V} = \int_{R_{in}}^{R_{out}} n(r)\, v(r)\, dr \Big/ \int_{R_{in}}^{R_{out}} n(r)\, dr. \tag{8}$$

If the distribution of matter is uniform throughout the line-forming region, then with $v(r) = 0$ at R_{in} and $v(r) = V_b$ at R_{out}, we have $\overline{V} = V_b/2$. Since in the present case the density goes down linearly, the more general definition of $\overline{V}$ given in Equation (8) has been adopted. The computed values of $\overline{V}$ are displayed in Columns (4) and (9) of Table 3.

The rate of mass outflow from the atmosphere can be calculated from the steady state flow condition where

$$\dot{M} = 4\pi r^2 \rho(r)\, v(r)$$

$$= 4\pi m_H (1 + \eta) r^2 n(r)\, v(r). \tag{9}$$

Here m_H is the mass of the H-atoms and η, the relative abundance by weight of the elements heavier than hydrogen. The value of η was adopted from Bell *et al.* (1976) and is equal to 0·42 for a standard Population I composition. The inner radius of the line-forming region which is taken to be the radius of the star in the present work, enters directly into the mass-loss calculations. An error in R_{in} results in a proportionately large error in the mass-loss rate.

If the above variables are replaced by their average values, then the mass-loss rate in the present model can be written as

$$\dot{M} = 4\pi m_H (1 + \eta) R_{in}^2 \left(1 + \frac{\Delta R}{R_{in}}\right) \frac{N}{\Delta R} \overline{V} \tag{10}$$

where N is the column density and all other quantities have been defined previously. The column densities obtained from Equation (7) are listed in Columns (5) and (10) of Table 3. Using the values of N and $\overline{V}$, the mass-loss rate was evaluated for all the programme stars for each ξ_t. As can be seen, the mass-loss rates lie in the range of 10^{-6} 10^{-7} $M_\odot$ yr^{-1}, higher than the empirical mass-loss relation derived by Reimers (1973). Since the assumption of a particular value of ξ_t affects the value of the column density derived, the mass-loss rates are slightly different, being lower for the higher value of microturbulence by a factor of 5 or so.

In order to produce strong absorption cores, the source function, in general, has to drop rapidly enough (by several orders of magnitude) across the line-forming region. The combination of a constant velocity and a density decreasing as the square of the distance has been widely used in the study of circumstellar envelopes (Weymann 1962; Sanner 1976; Bernat 1977; Hagen 1978). The resultant source function produces profiles with a P Cygni-type appearance. Even in a geometrically thin atmosphere, the red-side emission which is small for low optical depths tends to increase dramatically as the optical depth goes up, resulting in typical P Cygni profiles. This combination of density and velocity will, therefore, never yield profiles to match the observed characteristics of the H_α line.

With a linearly decreasing density and velocity in a pure scattering medium ($\epsilon = \beta = 0$), the line source function drops down by several orders of magnitude over the extent of the line-forming region (Peraiah 1981). A model envelope with these properties could, in principle, be used to generate deep absorption profiles. A preliminary analysis showed that to obtain EQW in the range of the observed values, a large spread in the velocity was generally required. This requirement could only be fulfilled when the inner velocity was chosen to be sufficiently large. Since most of the absorbing material was also located near the inner edge in this model, the LCD became inordinately large. The observed high EQW and low LCD could thus never be matched simultaneously. On the contrary, the model envelope adopted in the present analysis has a linearly decreasing density and a positive velocity gradient. The resulting source function is low enough to produce the strong absorption cores. At the same time, a large velocity spread satisfying the observed high EQW's requires a low velocity at the inner edge and a low LCD is obtained as a result. Therefore, the observed EQW and LCD could be matched simultaneously. In this last case, the equation of continuity is strictly satisfied only in the limit of a plane-parallel geometry. This is not inconsistent since we have also assumed the line-forming region to extend over only a fraction of the stellar radius. With the velocity increasing outward, a model, in strict spherical symmetry, requires a density law $n(r) \propto r^{-3}$. Calculations of the line source function and the H_α line profiles with this density distribution are in progress.

4. Discussion

In the present work, we have tried to model the H_α absorption line in G and K supergiants. The observed asymmetry in H_α has been attributed to the presence of an outward flow in the chromospheres of these stars. A predetermined source function was used to generate the H_α line profiles. The best description of the H_α-forming region is provided by a case of linearly increasing velocity and decreasing density. The theoretical profiles computed with this particular combination of $n(r)$ and $v(r)$ have then been matched with the observed profiles to obtain the column densities and velocities of the H_α -forming regions. Finally, mass-loss rates from the expanding chromospheres have been derived assuming a steady flow.

No other determination of mass-loss rates of G and K supergiants exists except for two of them, namely, η Per and HD 216946. Reimers (1973) calculated on the basis of their Ca II K emission shifts, mass-loss rates on the order of $2 \times 10^{-7}\ M_\odot\ \mathrm{yr}^{-1}$. These are almost one order of magnitude lower than the values quoted in our

Table 3. The situation is different for M giants and supergiants. Following the pioneering work of Deutsch (1956, 1960), a large number of studies has been devoted to the circumstellar envelopes of these stars and a sizable literature on the mass-loss rates exists for these (Weymann 1962; Sanner 1976; Bernat 1977; Hagen 1978). The mass-loss rates determined by all these investigators fall in the range of 10^{-4}–10^{-8} $M_\odot$ yr^{-1}. Since these studies refer specifically to the circumstellar envelopes, the velocities obtained from the blueshifted absorption cores of the lines are treated as true terminal velocities of expansion. The rates obtained by Bernat (1977) are the highest yet calculated, a consequence of the very large inner radii he adopted for the circumstellar envelopes. Very recently, VLA observations of OH maser emission at 1612 MHz in the circumstellar envelopes of twenty very red giants and supergiants have become available (Bowers, Johnston and Spencer 1981). The observed expansion velocities have been used to derive mass-loss rates in the range of 10^{-4}–10^{-6} $M_\odot$ yr^{-1}. The OH emission comes from regions far out in the envelope where the gas has already reached a terminal velocity. Therefore, these observations provide a very accurate way of knowing $V_{\rm exp}$ and hence of determining mass-loss rates. The G, K and early M supergiants do not show any maser emission (Cassinelli 1979). These stars do not show any detectable free-free radio emission either. Therefore, the mass-loss rates derived here cannot be directly compared.

The phenomenon of the stellar wind which is responsible for the loss of mass from stars is not confined only to the very outer layers of the atmosphere. It reaches as deep as the chromosphere as indicated by the blueshifts of Ca II K_2 (Stencel 1978) and the H_α asymmetries (Boesgaard and Hagen 1979). The presence of blueshifted cores of H_α in G and K supergiants studied here also shows that expansion occurs within the chromosphere itself. Mullan (1978) proposed that when the sonic point of a stellar wind lies very close to the chromosphere-corona transition region, the chromospheric gas itself starts participating in the expansion. He derived a supersonic transition locus (STL) on the HR diagram along which the chromospheric expansion is expected to set in. Because of the access of the wind to the chromospheric material, there is a sudden increase in the mass flux as the higher density material starts participating in the expansion and hence stars to the right of the STL are expected to have enhanced mass-loss rates. A number of observations lend support to the idea of the theoretical STL—(a) The STL matches quite well with the observational boundary of the large mass-loss regime determined by Reimers (1977). (b) The Ca II asymmetry dividing line discovered by Stencel (1978) also lies very close to the STL. Stencel and Mullan (1980) have further used the IUE observations of the Mg II resonance lines (λλ 2796, 2803) and located a boundary on the HR diagram where these lines change the sense of their asymmetry in the same way as the Ca II. Since Mg II is formed at greater heights in the chromosphere, the boundary where these lines change the sense of asymmetry lies to the left of the corresponding dividing line for Ca II. (c) Linsky and Haisch (1979) have discovered from the IUE observations of late-type stars, a temperature dividing line which is very close to Mullan's STL. According to them, stars to the left of the dividing line have very hot coronae and hardly lose any mass. On the other hand stars to the right have cool coronae and large expanding chromospheres.

There are indications from the last study that at least two of our programme stars belong to the large mass-loss regime. Both ϵ Gem (G8 Ib) and λ Vel (K5 Ib) have been observed by IUE (Linsky and Haisch 1979; Hartmann, Dupree and Raymond

1980). Their spectra contain chromospheric lines like L_{α}, Si II, C I, O I but no lines arising from the higher stages of ionization, *e.g.* He II, C II–C IV, Si III–Si IV, Nv, usually found in the transition region between the chromosphere and the corona. ϵ Gem and λ Vel fall to the right of the temperature dividing line on the HR diagram. It is hoped that as more UV observations of G and K supergiants become available in future, many more of our programme stars will be found to belong to the class of stars having cool coronae and large mass loss.

The Ca II and the Mg II lines are the most extensively studied features of the chromospheres. Their structures are very similar to each other. First, due to the temperature rise in the chromosphere, the K_2 (or k_2) emission component appears within the main absorption profile and then a further central absorption reversal K_3 (or k_3) occurs in the chromosphere and the circumstellar envelope. In cool supergiants like ϵ Gem (G8 Ib), ϵ Peg (K2 Ib) and ξ Cyg (K5 Ib), the circumstellar absorption completely masks the Ca II and Mg II line asymmetries (Linksy *et al.* 1979; Basri and Linsky 1979). Therefore, it is difficult to disentangle the asymmetric chromospheric line. Also the Mg II k line profile is blended with circumstellar Fe II and Mn I absorption lines (Bernat and Lambert 1976; de Jager *et al.* 1979). The H_{α} line is essentially free of such complications and, therefore, serves as a more efficient indicator of the conditions in the chromosphere itself.

Because of the complex nature of the composite line profiles of Ca II and Mg II, with different parts originating in different regions of the atmosphere, it is very difficult to describe uniquely the velocity patterns with the help of either Ca II or Mg II when differential motions are present. For example downward motions in the K_3–forming region and no detectable motion in the K_2-forming region yield similar line asymmetries as upward motions in the K_2-forming region with no detectable motion in the K_3-forming region. Thus the observed asymmetry does not provide information about the magnitude or the direction of flow in any particular region. On the other hand, H_{α} has the bulk of its absorption in the chromosphere and has no circumstellar contribution. Being a photoionization controlled line in late-type stars, it is a pure absorption profile with no emission reversal. As a result, the observed blueshift of the absorption core can be non-ambiguously interpreted as indicative of an outward flow of the gas.

By using the H_{α} line alone, only the column density is obtained uniquely. Therefore, a definite determination of the extent of the expanding chromosphere is not possible. The derived mass-loss rates are to be treated as approximate in the light of the various uncertainties involved. Most importantly, the mechanism by which the second level of hydrogen is populated is not well understood. A realistic estimate of δ in Equation (7) is thus not possible at present. This alone may lead to an error of $\pm$ 2 orders of magnitude. The mass-loss rate is also crucially dependent upon $R_{\rm in}$, which in this case is the radius of the star. For lack of direct observations of $R_{\rm in}$, we have calculated $R_{\rm in}$ from $L = 4\pi R^2 \sigma T_{\rm eff}^4$, knowing $M_{\rm bol}$ and $T_{\rm eff}$ from observations. This was used in Equation (10) to obtain $\dot{M}$. An error in $R_{\rm in}$ would produce a proportionately large error in $\dot{M}$. However, it seems unlikely that the value of $R_{\rm in}$ used here is off by more than a factor of 2 or 3. Further, since line profile asymmetries are the only means at present of studying chromospheric velocity fields, any discussion of mass outflow from the chromosphere leans heavily on an

average velocity (*e.g.* $\overline{V}$ as in Equation 8). The limitations of using such an average should be kept in mind.

Several improvements on the present analysis are possible which future investigations may incorporate. Since H_α in late-type stars is a photoionization-dominated line, the effect of the continuum together with several levels should be included in a full discussion of the line-formation problem. In using a two-level atom, we have assumed the presence of detailed balance in the Lyman lines. It is now known that in the Sun, detailed balance in L_α may be an erroneous assumption. The formation of L_α itself has to be included in an accurate discussion of the H_α line. The L_α source function sensitively depends upon the redistribution function and since the optical depth in H_α is directly proportional to the population of the $n = 2$ level of H, it is determined by the L_α source function (Athay 1976). In the chromospheres of supergiants, where the densities are much lower, the L_α source function will be greatly affected by partial redistribution of photons and the formation of the H_α line becomes further complicated.

We have used the H_α source function with $\epsilon = 0$ and $\beta = 0$. With $\beta = 0$, the computed line profiles have highly saturated and wide cores. The use of a small but nonzero value of β in the source function would raise the core, resulting in computed profiles that are very similar in appearance to the observed profiles.

It is strongly suspected that there are very small emission components lying above the continuum level either to the left or to the right of the absorption profile in several of the stars studied here. A more widened spectrum of each star with better signal-to-noise ratio would depict such components more easily. While the presence of only red-side emission is a direct consequence of the extended geometry of the situation, both blue and red emission can be explained if one assumes the existence of an extended circumstellar shell—a few stellar radii away—at a higher velocity. The presence of red- and blueshifted emission with respect to the H_α absorption core in bright red giants of several globular clusters has in general been attributed to circumstellar envelopes (Cohen 1976; Reimers 1977; Mallia and Pagel 1978; Cacciari and Freeman 1981). If the reality of these emissions is clearly established for the stars under study, they may be used to probe the very outermost layers of these stars and yield further valuable information on the stellar winds associated with them.

Acknowledgements

This paper is based on a doctoral thesis submitted to the Madurai Kamaraj University. I am most grateful to Professor M. K. V. Bappu for his supervision and wise counsel throughout the course of this work. I am also indebted to him for generous allotment of observing time. I am especially thankful to A. Peraiah for allowing me to use his radiative transfer code and also for his help in the computational aspects of the problem. I have particularly benefited from several stimulating discussions with D. C. V. Mallik. It is also a great pleasure to thank M. H. Gokhale and P. Venkatakrishnan for helpful comments. I also thank an anonymous referee for valuable comments and for clarifying a few conceptual difficulties. This work was supported by the National Council of Educational Research and Training and the Indian Institute of Astrophysics.

References

Athay, R. G. 1976, *The Solar Chromosphere and Corona: Quiet Sun,* D. Reidel, Dordrecht.
Athay, R. G., Thomas, R. N. 1958, *Astrophys. J.*, **127,** 96.
Ayres, T. R., Linsky, J. L. 1975, *Astrophys. J.,* **200,** 660.
Bappu, M. K. V. 1981, *Bok Festschrift,* Ed. R. E. White (in press).
Basri, G. S., Linsky, J. L. 1979, Astrophys. J., **234,** 1023.
Bell, R. A., Eriksson, K., Gustafsson, B., Nordlund, A. 1976, *Astr. Astrophys. Suppl. Ser ,* **23,** 37.
Bernat, A. P. 1977, *Astrophys. J.*, **213,** 756.
Bernat, A. P., Lambert, D. L. 1976, *Astrophys. J.,* **204,** 830.
Bidelman, W. P. 1954, *Astrophys. J. Suppl. Ser.,* **1,** 175.
Boesgaard, A. M., Hagen, W. 1979, *Astrophys. J.*, **231,** 128.
Bowers, P. F., Johnston, K. J., Spencer, J. H. 1981, *Nature,* **291,** 382.
Cacciari, C., Freeman, K. C. 1981, in *Physical Processes in Red Giants,* Eds I. Iben, Jr. and A. Renzini, D. Reidel, Dordrecht, p. 311.
Cassinelli, J. P. 1979, *A. Rev. Astr. Astrophys.,* **17,** 275.
Cohen, J. 1976, *Astrophys. J.,* **203,** L127.
de Jager, C., Kondo, Y., Hoekstra, R., van der Hucht, K. A., Kamperman, T. M., Lamers, H. J. G. L. M., Modisette, J. L., Morgan, T. H. 1979, *Astrophys. J.,* **230,** 534.
Deutsch, A. J. 1956, *Astrophys. J.,* **123,** 210.
Deutsch, A. J. 1960, in *Stellar Atmospheres,* Ed. J. L. Greenstein, University of Chicago Press, p. 543.
Goldberg, L. 1979, *Q. J. R. astr. Soc.,* **20,** 361.
Hagen, W. 1978, *Astrophys. J. Suppl. Ser.,* **38,** 1.
Hartmann, L, Dupree, A. K., Raymond, J. C. 1980, *Astrophys. J.,* **236,** L143.
Hoffleit, D. 1964, *Catalogue of Bright Stars,* Yale University Observatory, New Haven.
Humphreys, R. M. 1970, *Astr. J.,* **75,** 602.
Jefferies, J., Thomas, R. 1959, *Astrophys. J.,* **129,** 401.
Johnson, H. L. 1966, *A. Rev. Astr. Astrophys.,* **4,** 193.
Joy, A. H.., Wilson, R. E. 1949, *Astrophys. J.,* **109,** 231.
Kraft, R. P., Preston, G. W., Wolff, S. C. 1964, *Astrophys. J.,* **140,** 235.
Kuhi, L. V. 1974, in *Highlights of Astronomy,* Vol. 3, Ed. G. Contopoulos, D. Reidel, Dordrecht, p. 121.
Kunasz, P, B., Hummer, D. G. 1974, *Mon. Not. R. astr. Soc.,* **166,** 57.
Linsky, J. L. 1980, *A. Rev. Astr. Astrophys.,* **18,** 439.
Linsky, J. L., Haisch, B. M. 1979, *Astrophys. J.,* **229,** L27.
Linsky, J. L., Worden, S. P., McClintock, W., Robertson, R. M. 1979, *Astrophys. J. Suppl. Ser.,* **41,** 47.
Luck, R. E. 1977, *Astrophys. J.,* **212,** 743.
Luck, R. E. 1979, *Astrophys. J.,* **232,** 797.
Mallia, E. A., Pagel, B. E. J. 1978, *Mon. Not. R. astr. Soc.,* **184,** 55 p.
Mihalas, D. 1978, *Stellar Atmospheres,* 2nd edn, Freeman, San Francisco.
Mullan, D. J. 1978, *Astrophys. J.,* **226,** 151.
Peraiah, A. 1979, *Astrophys. Sp. Sci.,* **63,** 267.
Peraiah, A. 1980, *J. Astrophys. Astr.,* **1,** 101.
Peraiah, A. 1981, *Astrophys. Sp. Sci .,* **77,** 243.
Peraiah, A., Grant, I.1973, *J. Inst. Math. Applics.,* **12,** 75.
Reimers, D.1973, *Astr. Astrophys.,* **24,** 79.
Reimers, D. 1975, in *Problems in Stellar Atmospheres and Envelopes,* Eds B. Baschek, W. H. Kegel and G. Traving, Springer-Verlag, New York, p. 229.
Reimers, D. 1977, *Astr. Astrophys.,* **57,** 395.
Sanner, F. 1976, *Astrophys. J. Suppl. Ser.,* **32,** 115.
Stencel, R. E. 1978, *Astrophys. J.,* **223,** L37.
Stencel, R. E., Mullan, D. J. 1980, *Astrophys. J.,* **238,** 221.
Warner, B.1966, *Observatory,* **86,** 82.
Warner, B.1968, *Observatory,* **88,** 217.
Warner, B. 1969, *Mon. Not. R. astr. Soc.,* **144,** 333.

Weymann, R. 1962, *Astrophys. J.,* **136,** 844.
Wiese, W. L., Smith, M. W., Glennon, B. M. 1966, *Atomic Transition Probabilities,* Vol. 1, Nat. Bur. Stand., (U.S.).
Wilson, O. C. 1976, *Astrophys. J.,* **205,** 823.
Wilson, O. C., Bappu, M. K. V. 1957, *Astrophys. J.,* **125,** 661.

J. Astrophys. Astr. (1982) 3, 63–67

Kerr – Newman Metric in Cosmological Background

L. K. Patel and Hiren B. Trivedi *Department of Mathematics, Gujarat University, Ahmedabad 380009*

Received 1981 November 21; accepted 1982 February 5

Abstract. A new solution of Einstein-Maxwell field equations is presented. The material content of the field described by this solution is a perfect fluid plus sourceless electromagnetic fields. The metric of the solution is explicitly written. This metric is examined as a possible representation of Kerr-Newman metric embedded in Einstein static universe. The Kerr-Newman metric in the background of Robertson-Walker universe is also briefly described.

Key words: Kerr-Newman metric—cosmology—Einstein universe—Robertson-Walker universe

1. Introduction

The Schwarzschild exterior metric and the well-known Kerr (1963) metric go over asymptotically to a flat space. Therefore these solutions can be interpreted as gravitational fields due to isolated bodies (without and with angular momentum respectively). The charged versions of these two solutions are described by the well-known Nordstrom metric and the Kerr-Newman (1965) metric respectively. These charged versions are also described under flat background. These solutions have been proved of great interest in the gravitational theory and its applications to astrophysics. The Kerr metric in the cosmological background has been discussed by Vaidya (1977). Because of the potential use of Kerr-Newman black holes in relativity, it would be worthwhile to obtain the Kerr-Newman metric in the cosmological background.

The geometry of Einstein universe is described by the metric

$$ds^2 = dt^2 - dx^2 - dy^2 - dz^2 - \frac{(xdx + ydy + zdz)^2}{R^2 - (x^2 + y^2 + z^2)} \tag{1}$$

where R is a constant. Vaidya (1977) has given a transformation from (x, y, z) to (r, α, β) which transforms the metric (1) into the form

$$ds^2 = 2\,(du + a\sin^2\alpha\, d\beta)\, dt - (du + a\sin^2\alpha\, d\beta)^2$$

$$- M^2\left[\left(1 - \frac{a^2}{R^2}\sin^2\alpha\right)^{-1} d\alpha^2 + \sin^2\alpha\, d\beta^2\right] \tag{2}$$

where $u = t - r$, a is a constant and

$$M^2 = (R^2 - a^2)\sin^2(r/R) + a^2\cos^2\alpha.$$

The Kerr-Newman metric can be expressed in the form

$$ds^2 = 2\,(du + \sin^2\alpha\, d\beta)\, dt$$

$$-\left[1 + \frac{2mr - 4\pi e^2}{r^2 + a^2\cos^2\alpha}\right](du + a\sin^2\alpha\, d\beta)^2$$

$$-(r^2 + a^2\cos^2\alpha)\,(d\alpha^2 + \sin^2\alpha\, d\beta^2). \tag{3}$$

The constants m, e and a appearing in the metric (3) are interpreted as the mass, the charge and the angular momentum per unit mass respectively. When $e = 0$, the metric (3) reduces to Kerr metric in the form given by Vaidya (1974).

In the next section we shall discuss the metric (3) in the background of Einstein static universe. The last section is devoted to a brief discussion of the Kerr-Newman metric in the background of Robertson-Walker universe.

2. Kerr-Newman metric in the background of Einstein universe

In this section we shall use the following field equations corresponding to the perfect fluid distribution plus source-free electromagnetic fields

$$R_{ik} = -8\pi\,[(p + \rho)\, v_i v_k + \tfrac{1}{2}(\rho - p)\, g_{ik} + E_{ik}] + \lambda\, g_{ik}, \quad v_i\, v^i = 1 \tag{4}$$

$$E_{ik} = -g^{lm} F_{il} F_{km} + \tfrac{1}{4} g_{ik} F_{lm} F^{lm} \tag{5}$$

$$F_{ik} = A_{i,k} - A_{k,i} \tag{6}$$

$$F^{ik};_k = 0. \tag{7}$$

The symbols occurring in the above equations have their usual meanings.

We now give in a nutshell the Kerr-Newman metric in the background of Einstein universe. The detailed calculations are lengthy but straightforward. For the sake of brevity, these calculations are not given here.

The metric obtained by us can be expressed in the form

$$ds^2 = 2\,(du + a\sin^2\alpha\, d\beta)\,dt$$

$$- M^2\left[\left(1 - \frac{a^2}{R^2}\sin^2\alpha\right)^{-1} d^2\alpha + \sin^2\alpha\, d\beta^2\right]$$

$$- (1 + 2m\mu - 4\pi e^2\gamma)\,(du + a\sin^2\alpha\, d\beta)^2 \tag{8}$$

where m, a and e are constants and M^2, μ and γ are given by

$$M^2 = (R^2 - a^2)\sin^2\frac{r}{R} + a^2\cos^2\alpha, \tag{9}$$

$$\mu M^2 = R\sin\frac{r}{R}\cos\frac{r}{R}, \tag{10}$$

$$(R^2 - a^2)\,M^2\gamma = R^2\left(1 - 2\sin^2\frac{r}{R}\right). \tag{11}$$

Here R is a constant.

After lengthy computations, we have verified that the metric (8) alongwith (9), (10) and (11) satisfies the field equations (4), (5), (6) and (7).

The final expressions for the pressure p, the density ρ and the electromagnetic four-potential A_t are given by

$$8\pi p = \lambda - \frac{2}{R^2}(1 - L), \tag{12}$$

$$8\pi\rho = -\lambda + \frac{6}{R^2}(1 - L), \tag{13}$$

$$A_t = (A, 0, A\,a\sin^2\alpha, 0) \tag{14}$$

where

$A = (eR/M^2)\sin(r/R)\cos(r/R)$

and

$$2L = 1 + 2m\mu - 4\pi e^2\gamma. \tag{16}$$

The functions M^2, μ and γ are given by Equations (9), (10) and (11) respectively. Here we have denoted the coordinates as

$$x^1 = u,\ x^2 = \alpha,\ x^3 = \beta,\ x^4 = t.$$

When $m = e = 0$, the metric (8) reduces to the metric (2) of Einstein universe. When R tends to infinity the metric (8) reduces to the metric (3). Therefore in the vicinity of the source the metric (8) reduces to Kerr-Newman metric. Thus the metric (8) describes the Kerr-Newman metric in the cosmological background of the Einstein Universe.

3. Kerr-Newman metric in the background of Robertson-Walker universe

The present section is devoted to a very brief discussion of the metric describing the field of a charged rotating source in the background of Robertson-Walker universe. The Kerr-Newman metric in the background of Robertson-Walker universe turns out to be

$$ds^2 = e^{2F}\Big[2\,(du + a\sin^2\alpha\, d\beta)\,dt - M^2\left\{(1-\frac{a^2}{R^2}\sin^2\alpha)^{-1}\,d\alpha^2 + \sin^2\alpha\, d\beta^2\right\} - \{1 + (2m\mu - 4\pi e^2\gamma)\,e^{-2F}\}\,(du + a\sin^2\alpha\, d\beta)^2\Big] \tag{17}$$

where M, μ and γ are given by Equations (9), (10) and (11) respectively. Here F is an arbitrary function of time t.

The detailed calculations are lengthy and tedious and so they are not given here. If we put $m = e = 0$ in metric (17) we recover the Robertson-Walker metric representing the closed universe. If we put $F = 0$ in metric (17), we obtain the Einstein-Kerr-Newman metric (8). Thus the metric (17) represents the Kerr-Newman metric in the background of Robertson-Walker universe. There is one qualitative difference between the solution (17) and the solution discussed in the previous section. The resultant effect of the isotropic expansion of the cosmic fluid and the presence of the rotating charged Kerr source is that the cosmic fluid in the vicinity of the source exhibits anisotropy in pressure (see Vaidya 1977).

At the point in the 3-space, if we choose three mutually orthogonal infinitesimal vectors θ^1, θ^2, θ^3 defined by

$$\theta^1 = e^F\,(du + a\sin^2\alpha\, d\beta),$$

$$\theta^2 = e^F\,M\,[1 - (a^2/R^2)\sin^2\alpha]^{-1/2}\,d\alpha,$$

$$\theta^3 = e^F\,M\sin\alpha\, d\beta, \tag{18}$$

then the pressure in θ^2 and θ^3 directions are equal(say p) and the pressure in θ^1 direction is $q \neq p$. This is an unpalatable feature of this solution. However in the case $F = 0$ we have $p = q$. The expressions for p and q are lengthy and therefore not reported here.

Here it should be noted that when $e = 0$, the electromagnetic field disappears and our results reduce to those obtained by Vaidya (1977).

We shall now study the event horizon of the Kerr-Newman black hole embedded in an expanding universe. Adopting the method described by Vaidya (1977), we get the event horizon of the Kerr-Newman black hole immersed in an expanding universe as the spheroid with r parameter given by

$$R^2 \tan^2 (r/R) - 2m\, R \tan (r/R)\, e^{-2F} + a^2 + \frac{4\pi\, e^2\, e^{-2F}}{1 - (a^2/R^2)} = 0$$

i. e.

$$R \tan (r/R) = me^{-2F} + \left[m^2\, e^{-4F} - a^2 - \frac{4\pi\, e^2\, e^{-2F}}{1 - (a^2/R^2)} \right]^{1/2}. \tag{19}$$

This event horizon exists if the restriction

$$m^2 \geqslant \left[a^2\, e^{2F} + \frac{4\pi\, e^2}{1 - (a^2/R^2)} \right] e^{2F}$$

is satisfied.

The substitution $e = 0$ in the above discussion gives us the event horizon of the Kerr black hole immersed in an expanding universe.

When $R \to \infty$ and $F = 0$, we recover the usual horizon

$$r = r_+ = m + (m^2 - 4\pi e^2 - a^2)^{1/2} \tag{20}$$

of Kerr-Newman black hole. In a similar way, the modifications of other electromagnetic effects of the Kerr-Newman black hole in an expanding universe can be studied.

Acknowledgements

The authors are highly indebted to Professor P. C. Vaidya for many helpful discussions and are also thankful to the referee for his constructive comments.

References

Kerr, R. P. 1963, *Phys. Rev. Lett.,* **11,** 237.

Newman, E. T., Couch, E., Chinnapared, K., Exton, A., Prakash, A., Torrence, R. 1965, *Phys. Rev. Lett.,* **15,** 231.

Vaidya, P. C. 1974, *Proc. Camb. phil. Soc. math. phys. Sci.*, **75,** 383.

Vaidya, P. C. 1977, *Pramana,* **8,** 512.

J. Astrophys. Astr. (1982) **3,** 69–77

Doppler Shift Measurements on the Green Coronal Line—Evidence for Largescale Macroscopic Mass Motion

J. N. Desai and T. Chandrasekhar *Physical Research Laboratory, Ahmedabad 380009*
P. D. Angreji *The Vedhshala, Ahmedabad 380013*

Received 1981 August 24; accepted 1982 February 22

Abstract. Fabry-Perot interferometric observations on the green coronal line (λ 5303 Å) carried out during the total solar eclipse of 1980 February 16 have yielded relative Doppler shift velocities with an accuracy of ± 7 km s^{-1}. The values show a peak in the 30–50 km s^{-1} range indicating largescale macroscopic mass motion in the solar maximum corona.

Key words: total solar eclipse—green coronal line—Doppler shifts

1. Introduction

Doppler shift measurements provide significant observational data on the macroscopic mass motion in the corona. However, coronal-line observations are inherently difficult to make. The data available till recently was limited to a few spectrograms taken sporadically at mountain top coronagraphs and during the brief moments of totality of a few eclipses. These observations—Dollfus (1957) and Billings (1963)—sample only a small portion of the corona as defined by the slit of the spectrograph. Further coronagraphic observations of this type are constrained by scattering effects in the terrestrial atmosphere and rarely go up to 1·2 $R_{\odot}$. The analyses of the spectro grams have not yielded any significant Doppler shift in the coronal lines.

More recently, Fabry-Perot interferometric observations in the green coronal line (λ 5303 Å) and the red coronal line (λ 6374 Å) have been attempted from which it is possible in principle to determine Doppler shifts at many different points in the corona simultaneously (Liebenberg 1975; Delone and Makarova 1969; Hirschberg, Wouters and Hazelton 1971). Liebenberg (1975), discussing the results of the eclipse of 1965 May 30, finds Doppler shifts in the green line to be < 5 km s^{-1}. Delone and Makarova (1969), after a study of 170 profiles of the red line and 20 profiles of the green line, however find significant Doppler velocities in the range 10–40 km s^{-1}

during the same eclipse. In some active regions their values go up to 70 km s^{-1}. Hirschberg, Wouters and Hazelton (1971) have reported a complex vortex structure with green-line Doppler-shift velocities of ∼ 6 km s^{-1} from their observations of the 1970 eclipse. Harvey and Livingston (1981) reporting the observations taken with a multi-slit high-dispersion spectrograph during the 1980 eclipse find in 30 per cent of their samples inward flow velocities in the range 3–15 km s^{-1}

We present in this paper results indicating significant Doppler shifts in the green line in the velocity range 30–50 km s^{-1} from the interferometric observations made during the total solar eclipse of February 16, 1980 at Gadag, India (15° 25′ N, 75° 37′ E).

2. Instrumentation

Fig. 1 is a schematic sketch of the experimental set up used during the eclipse. Coronal light, after reflection from the coelostat mirror M, was collected by an achromatic lens O (focal length 2280 mm; f/15 system) to form the image at focal position A. An interference pre-filter centred at λ 5303 Å with a bandwidth of 7 Å F isolated the green line. After 'A' the light was recollimated by the lens L_1 (focal length 80 mm; f/1·2 system), allowed to pass through the Fabry-Perot etalon E and finally imaged by a camera lens L_2 (focal length 55 mm; f/1·2 system) on the 35 mm film format C. Precalibrated (step wedge calibration supplied by Kodak) Kodak (400 ASA) 35 mm film was used.

The Fabry-Perot etalon E was an optically-contacted one which ensured complete freedom from misalignment problems which usually plague Fabry-Perot systems. The etalon had an air-spacing of 307 μm, a coating of 88 per cent reflectivity at λ 5303 Å and a free spectral range of 4·7 Å at λ 5303 Å. The finesse value was ∼ 20.

In order to evaluate the system performance, immediately after totality the interferometer was calibrated using a spectral lamp in the green line of mercury (λ 5460·74 Å). Microdensitometry of this calibration frame yielded an instrumental profile of full width at half-maximum (FWHM) ∼ 0·23 Å. The shape of this profile is shown along with the theoretical Airy and Gaussian profiles of the same FWHM (Fig. 2). The instrumental line shape is seen to follow the Airy profile closely indicating that the Fabry-Perot etalon had been in excellent alignment during the period of totality.

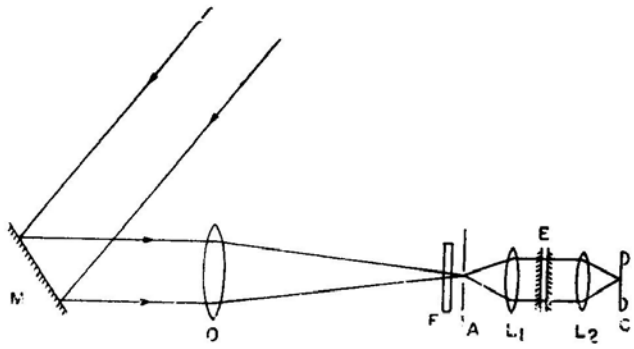

Figure 1. Experimental set up.

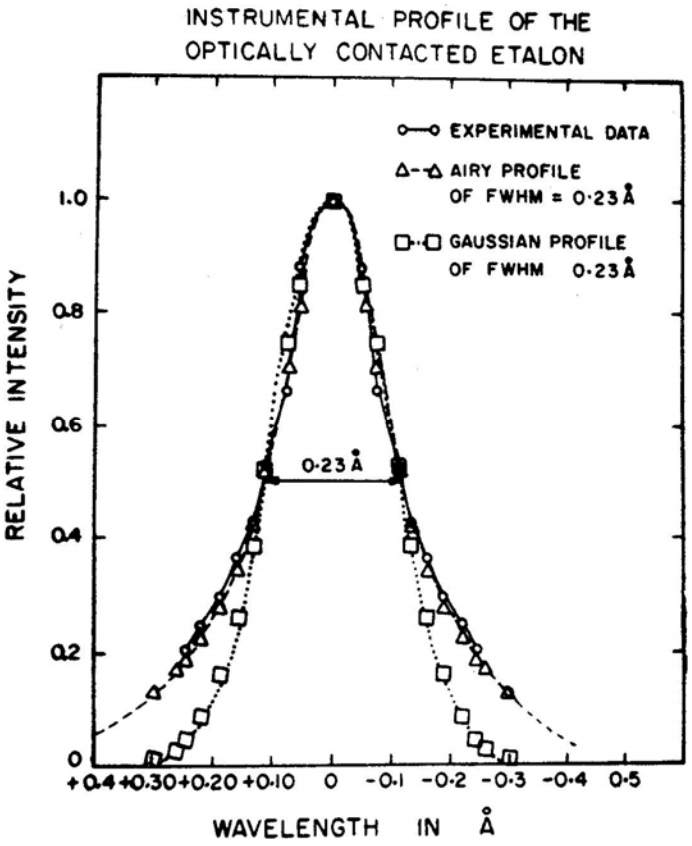

Figure 2. Instrumental profile.

3. Observations and redaction procedure

Four photographs were taken under perfect sky conditions during the 2 min 46 s of totality with exposure times 4, 10, 30 and 90s. All exposures recorded the interferogram successfully. The 90s frame is shown in Fig. 3.

The centre of the Fabry-Perot system was kept off-centred with respect to the centre of the solar disk by $\sim$ 20 arcmin. This was done to ensure continuous measurements of FWHM along a few position angles. However, about 1/3 of the azimuthal coverage had to be sacrificed to gain this advantage. Hence no fringes are seen between position angles 95° and 220°. The order of interference ranges from 1130 to 1150.

The eclipse frames along with the mercury line calibration frames were simultaneously developed strictly according to the specifications of the manufacturer. All the frames were then scanned on a Carl Zeiss microdensitometer with a slit area corresponding to 13 arcsec × 6 arcsec in the plane of the sky. From the densitometry of the wedge calibration, the photographic curve was constructed, digitised and used in the calculation of relative intensities. On the eclipse frames microdensitometric scans were made radially outwards from the fringe centre, Since the green

line during this eclipse was much stronger than the continuum in the 7 Å bandwidth filter used, $\left(\frac{E_{\text{line}}}{E_{\text{continuum}}} > 10\right)$ the fringes had a high contrast and there was no ambiguity in locating the fringe peaks. Fringes are observed from 0·03 $R_\odot$ above the solar limb upto 0·5 $R_\odot$. Typically, fringe peaks could be located with an accuracy of ± 0·05 mm on the film as measured from the fringe centre. The fringe peaks could however be located with respect to each other with a much greater accuracy of < ± 0·005 mm. This value translates to a relative line of sight velocity of ± 6 km s^{-1}. Any shift in the centre of the fringe pattern between the eclipse frame and the calibration frame can significantly affect absolute Doppler velocity determination. Since relative fringe peak positions can be determined better (< ± 0·005 mm) than their absolute position from the fringe centre (~ ± 0·05 mm) we have considered only the relative Doppler shifts and their standard deviation for each scan. For each scan we calculate the standard deviation of the Doppler shift velocities of the fringes in that scan. Thus, from an examination of 659 fringes spread over 59 scans made radially outwards from fringe centre in the 90 s and 30 s frames we get 59 velocity dispersion values which should be accurate to ± 6 km s^{-1}. In order to verify this expectation we have rescanned the calibration frame treating it as a hypothetical eclipse frame in λ 5461 Å. The dispersion value of ± 7 km s^{-1} obtained agrees very well with calculated error and justifies the method for detecting relative Doppler shifts greater than 7 km s^{-1}. Since each scan is made radially outwards from the fringe centre which has been kept displaced from the solar centre, the dispersion velocity is necessarily averaged over the few degrees of position angle and also over the entire radial extent of the scan. Hence, from this reduction it is not possible to draw any conclusion regarding the radial variation of the dispersion velocity.

The spatial resolution as determined by fringe separation is variable, improving with increasing distance from fringe centre. A typical fringe separation of ~ 0·2 mm on film gives a spatial resolution of 0·03 $R_\odot$ at the corona.

The spacer value (μt) of the interferometer required in the calculations for Doppler shifts was experimentally determined from a careful study of the calibration frame. For this purpose a special projection technique was developed and used by which the frame could be magnified by ~ 200 times. Measurements on the calibration fringes yielded a spacer value of 307 μm with an estimated error of < 1 per cent.

4. Calculation of Doppler shifts

The basic Fabry-Perot equation is

$$2\ \mu t \cos\theta = n\lambda \tag{1}$$

where μt = air-spacer = 307 μm, n = order of interference, λ = wavelength of light and θ is given by

$$\tan\theta = R / F.$$

R refers to the fringe radius (measured from the fringe centre and *not* the solar centre).

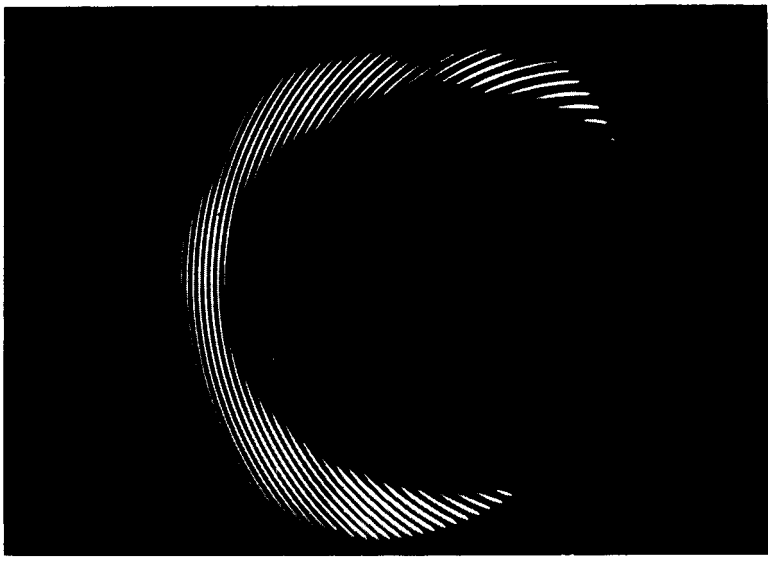

Figure 3. Coronal Interferogram (90s exposure).

F is the focal length of the camera lens used. In our case, F = 55 mm. We have taken the ' rest ' wavelength of the green line to be λ_0 = 5302·86 Å (Unsöld 1977). For the rest wavelength, fringe peak positions are given by

$$2\ \mu t \cos\theta_0 = n\lambda_0. \tag{2}$$

θ_0 can be calculated for the different orders of interference expected in the fringe pattern. Hence

$$2\ \mu t\ (\cos\theta - \cos\theta_0) = n\ (\lambda - \lambda_0)$$

and

$$\frac{\cos\theta - \cos\theta_0}{\cos\theta_0} = \frac{\lambda - \lambda_0}{\lambda_0} = \frac{V}{c}. \tag{3}$$

Measuring R and using calculated θ_0, the line of sight Doppler shift velocity V can be calculated. The standard deviation in V in each densitometric scan is the value actually used in drawing our conclusions.

5. Results

Our results are shown in Figs 4 and 5. Fig. 4 shows standard deviation of the Doppler shift velocities in km s^{-1}—indicated by numbers—plotted for each of the 59 scans in the different portions of the corona. The radial extent of each scan is also marked by a radial line at the mean position angle for the scan. Fig. 5 is a histogram plot of the dispersion velocities deduced from both 90 s and 30 s frames.

6. Discussion

The histogram plotted to bring out the distribution of relative line of sight velocities shows a peak in the velocity range 30–50 km s^{-1}. There is a smaller peak in the histogram in the velocity range 11–20 km s^{-1}.

As seen in Fig. 4 the large dispersion velocities are not confined to a small portion of the corona but apply over a wide range of azimuth and radial extent. Our measurements, further, are not directly measured Doppler shifts but statistically inferred dispersion velocities. They also, by the very nature of their deduction, have the disadvantage of not showing any radial variation in their values. However, as the dispersion velocities measured are significantly above the error limits that we can ascribe to them (~ 7 km s^{-1}), we feel justified in presenting the results.

While linewidth measurements are a measure of thermal and statistically random motion, the dispersion velocities represent the net nonrandom motion directed towards or away from the observer.

There is a considerable body of evidence showing largescale relative motion in the corona above the western limb during this eclipse. Liebenberg and Keller (1980)

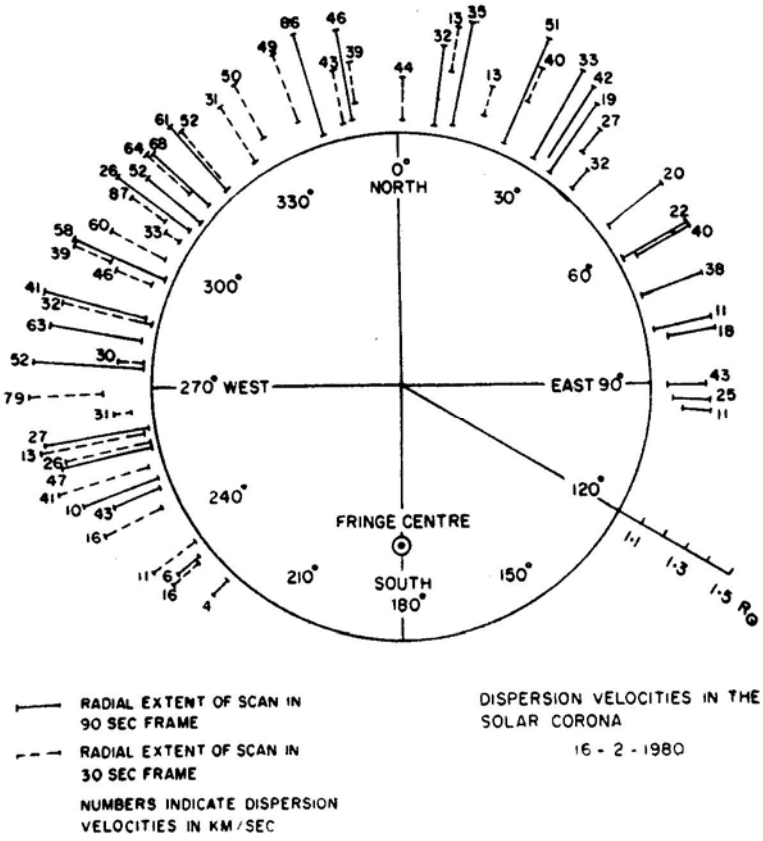

Figure 4. Doppler shift dispersion velocity distribution in the corona.

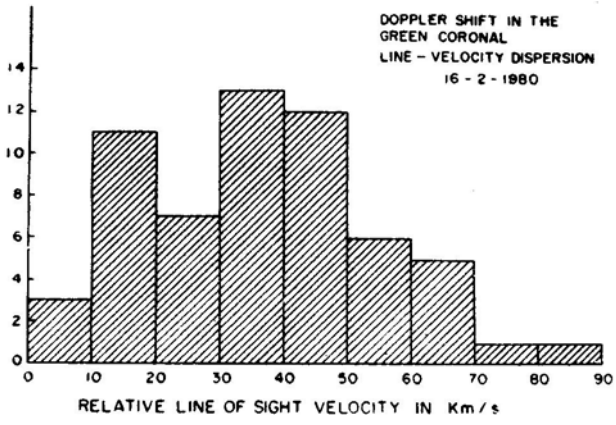

Figure 5. Doppler shift dispersion velocity histogram.

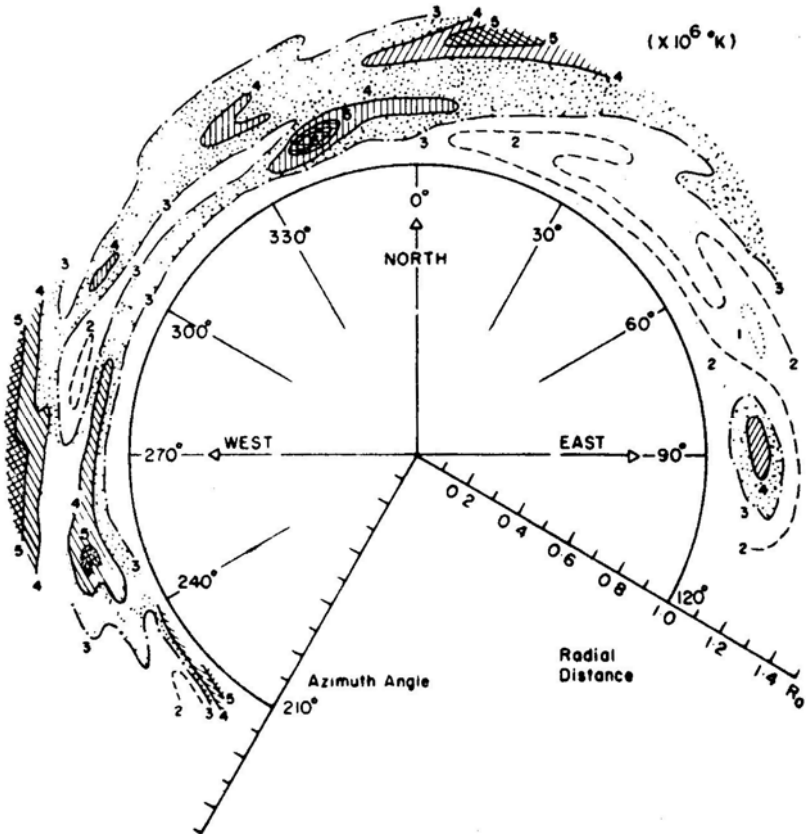

Figure 6. Temperature distribution in the corona.

report a largescale eruptive disturbance in this limb from their aircraft observations. It is also seen in white light pictures taken from Kenya but not in those taken from India 90 min later. Their preliminary results show large streaming velocities in this region. White light coronagraph pictures taken from PS 78–1 satellite a few hours before totality over India, also show mass ejection a few degrees north of west above the solar limb (Koomen 1981, personal communication). In our 30 s interferogram frame, fringe splitting is clearly evident at position angle 256°. The splitting corresponds to a differential mass motion with velocity of $\sim 70 \pm 5$ km s_{-1} (Chandrasekhar, Desai and Angreji 1981).

Figs 6 and 7 which show the Doppler line-width temperature distribution and the relative intensity distribution of the corona as deduced from the 90 s frame are included mainly for the sake of comparison. It is however difficult to establish one-to-one correspondence between the intensity, temperature and velocity maps. There is a spot of high temperature at position angle 255° and the relative intensity values are also high in the same region. However, Fig. 4 shows nothing unusual in this region. On the other hand, though temperature and intensity show no peculiarities near 315°, the dispersion velocities (Fig. 4) show a consistently high value > 60 km s^{-1} in this portion of the corona. While the fringe-split region may not be linked with the eruptive disturbance, this high value could well be due to the same eruptive distur-

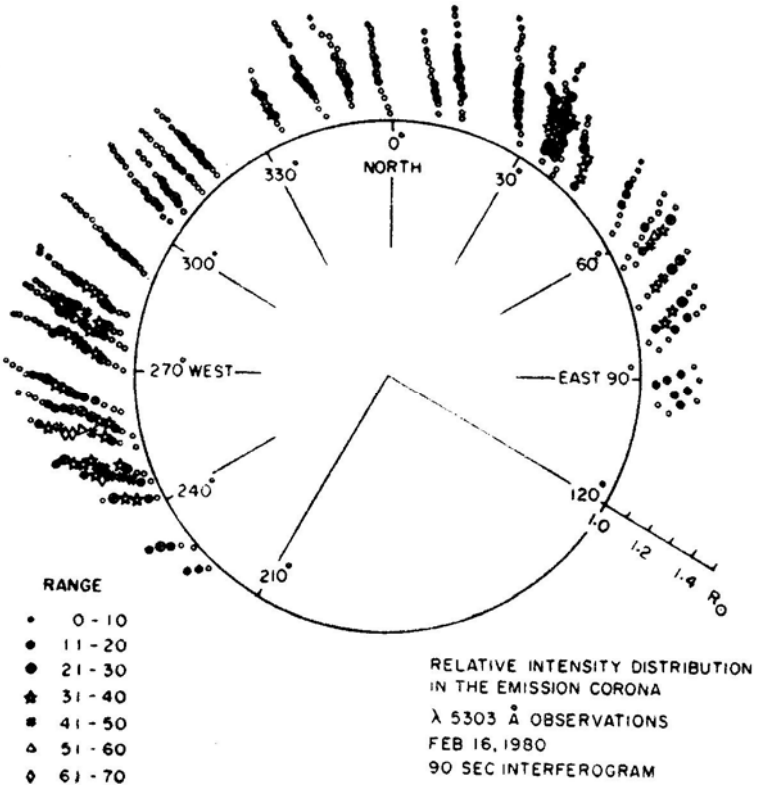

Figure 7. Relative intensity distribution in the corona.

bance mentioned earlier. Dispersion velocities are not low in other parts of the corona too suggesting largescale relative motion in the solar maximum corona.

7. Conclusion

Relative Doppler shift measurements in the green coronal line have yielded values mainly in the range 30–50 km s^{-1}. The measurements spread over a large portion of the corona in azimuth and upto 1·5 $R_\odot$ in radial extent indicate largescale macroscopic mass motion in the solar maximum corona.

Acknowledgements

The authors wish to thank J. Pasachoff of Hopkins Observatory, Massachusetts for a timely supply of precalibrated films. The authors are also grateful to M. J. Koomen of Naval Research Laboratory, Washington, D. C. for the preliminary unpublished white light coronagraphic data obtained by PS 78–1 satellite. The work was financially supported by Department of Space, Government of India.

References

Billings, D. E. 1963, *Astrophys. J.,* **137,** 592.
Chandrasekhar, T., Desai, J. N., Angreji, P. D. 1981, *Appl. Opt.,* **20,** 2172.
Delone, A. B., Makarova, E. A. 1969, *Solar Phys.,* **9,** 116.
Dollfus, A. 1957, *C.r. hebd. Seanc. Acad. Sci. Paris,* **244,** 1880.
Harvey, J., Livingston, W. 1981, in *Proc. International Symposium on Solar Eclipse,* INSA, New Delhi.
Hirschberg, J. G., Wouters, A., Hazelton, L., Jr. 1971, *Solar Phys.,* **21,** 448.
Liebenberg, D. H. 1975, *Solar Phys.,* **44,** 331.
Liebenberg, D. H., Keller, C. F. 1980, *Los Alamos Science,* p. 1.
Unsold, A. 1977, *The New Cosmos,* 2 edn, Springer-Verlag, New York, p. 191.

J. Astrophys. Astr. (1982) **3,** 79–92

Ultraviolet Observations of the Hydrogen-Deficient Variable Star MV Sagittarii†

N. Kameswara Rao *Indian Institute of Astrophysics, Bangalore 560034*
K. Nandy *Royal Observatory, Edinburgh, UK*

Received 1981 October 13; accepted 1982 March 2

Abstract. IUE observations of the hydrogen-deficient irregular variable star MV Sgr obtained in 1980 June-October and also in 1979 November are discussed. These observations show a prominent λ 2200 absorption feature. A value of $E(B - V) = 0{\cdot}55$ is deduced from the strength of λ 2200 band assuming that this absorption is caused by interstellar medium. The dereddened continuum obtained at different times can be fitted to a theoretical energy distribution of a helium star model with $T_{\rm eff}$ = 18000 K and log $g = 2{\cdot}5$, similar to that of BD + 10° 2179. This theoretical energy distribution, after applying interstellar extinction, gives $V = 12{\cdot}7$ mag, agreeing with the observed visual magnitude of $\simeq$ 13 in 1979 November and 1980 June-October. Even though there was no change in the continuum flux, the ultraviolet line-spectrum shows variations. The IUE spectra of 1980 October show enhanced (circumstellar) absorption lines of Fe II, Si II, O I, C I and others along with the absorption lines of a B star. In view of the similarity of the spectroscopic phenomena of MV Sgr with that of α Sco system, a model is proposed in which a cool companion star, surrounded by dust, occasionally blows gas towards the hotter hydrogen-poor B star. This model explains the irregular light variations and the spectroscopic phenomena.

Key words: variable stars—ultraviolet spectra—circumstellar dust

1. Introduction

MV Sagittarii is probably the only known ‘ hot ’ R CrB-type star. The R CrB-type

† Based on observations obtained with IUE satellite at the Villafranca Satellite Tracking Station of the European Space Agency.

stars are hydrogen-poor carbon-rich irregular variables. They seem to be spread out across the HR diagram from early B through F to late R-type stars. A majority of them are later than F. Only two stars—V348 Sgr and MV Sgr—have been classified as hot members of this class with spectral types O–B and B2 respectively. Some of the important questions regarding the evolutionary state of R CrB stars relate to the causes and stage of evolution when the hydrogen-deficiency characteristic occurs and also their future course of evolution in the HR diagram. There seem to be principally two possibilities for the stars to lose the hydrogen envelope: (1) Mass loss from the star in a steady way either as super-winds (Schönberner 1975; Renzini 1981) or explosive ejection of the whole hydrogen rich envelope (Sackmann, Smith and Despain 1974; (2) the hydrogen is consumed by the star itself in the course of its evolution (Paczynski 1971). In such a happening it is very essential to see evidence for extensive mass loss in these stars and further, to estimate the rate of such mass loss. According to Schönberner (1975) R CrB stars are supposed to be progenitors of hot helium-rich carbon stars like BD + 10°2179. Thus MV Sgr, which resembles BD + 10°2179 in the spectrum is a good candidate to look for an evidence for extensive mass loss.

The spectrum of MV Sgr in the blue and red regions has been investigated by Herbig (1964, 1975) when it was slightly below maximum light. At 100 Å mm^{-1} dispersion in the blue, the spectrum of the star resembles very much the carbon-rich BD + 10°2179 ($T_{\rm eff}$ = 18000 K log g = 2·5) with He I and C II absorption lines and very weak or non-existent hydrogen lines. However, in the visual and red region the spectrum is dominated by the emission lines of Fe II, [Fe II], Si II, He I and also H_α. Apparently the emission spectrum is very similar to that seen in ν Sgr, which is a known hydrogen-deficient single-lined spectroscopic binary. In addition, the infrared colours obtained by Feast and Glass (1973) and Glass (1978) show that MV Sgr has infrared excesses which can be characterized by a blackbody of about 1500–2000 K, very much unlike the other R CrB stars and also V348 Sgr. It has been suggested by Humphreys and Ney (1974) that the infrared excess in R CrB could be due to the presence of a cool companion. Such a possibility in MV Sgr has already been indicated by Herbig (1975). The radial velocity measurements of Herbig are inconclusive about the variations. Although the presence of emission lines and infrared excess might be the consequence of mass loss, there is no direct observational evidence for such a phenomenon. Thus it is important to investigate the ultraviolet (UV) spectral region, where resonance lines of many elements occur. Moreover, if the irregular light variations are caused by the obscuration by a cloud or shell of circumstellar dust (the traditional explanation for R CrB type of light variations) around the B star, the effects of this extinction would be more pronounced in the UV than in the visible region. With these characteristics in mind, we obtained spectra with the IUE satellite and also used the images of MV Sgr obtained by other observers.

2. Observations and data reduction

All the observations discussed here have been obtained with the IUE satellite (Boggess *et al.* 1978) in the low resolution mode using the large aperture. Table 1 summarises the image number, exposure times, dates of observation and the visual magnitude at

Table 1. Observations.

Image no.	Date	Exposure time m s	$m_v^{\ddagger}$
LWR 4816	1979 June 20	99 59	13·09
LWR 6052*	1979 November 9	99 59	12·85
SWP 7120	1979 November 9	230 00	12·90
LWR 7972†	1980 June 7	32 00	12·97
SWP 10302	1980 October 7	100 00	12·94

*The header and the IUE log shows this as image no. 6053 with the same exposure and observing time.
†$\lambda < 2450$ Å underexposed.
‡Calculated from FES counts using the relation given by Holm and Crabb (1979).

the time of these IUE observations. The images LWR 4816, LWR 6052 and SWP 7120 have been obtained from the VILSPA data bank.

The visual magnitude for the images are obtained from the FES counts obtained at the time of observation, with the aid of the relation given by Holm and Crabb (1979). This V magnitude is supposed to be accurate to ± 0·1 mag. It should be pointed out that the visual magnitude estimates given in the IUE logs of MV Sgr are not correct for the images discussed here. A few days before the IUE observations of 1979 November (LWR 6052, SWP 7120), the star seems to have gone through a light minimum. Landolt (1979) measured the *UBV* colours of 1979 October 23 as $V = 15{\cdot}18$, $B - V = 0{\cdot}87$ and $U - B = 0{\cdot}17$.

All the data (except LWR 7972) have been processed at Royal Observatory Edinburgh using the standard procedures. These have been briefly described by Nandy and Morgan (1980).

To improve the photometric accuracy of the absolute fluxes, fluxes averaged over 50 Å band have been computed. These broad-band fluxes with estimated errors are given in Table 2. The image LWR 7972 was underexposed below λ 2450 and was not used, but the fluxes agree with those obtained from the other two images.

3. λ 2200 feature, reddening and distance

The fluxes given in Table 2 show that they agree with each other within the standard deviation. These fluxes are plotted in Fig. 1, along with an ANS observation. MV Sgr was observed on 1975 April 1 by ANS. The observation with higher count-rate is shown in the figure. These observations show the prominent broad depression at 2200 Å, that is characteristic of the interstellar extinction curves. Assuming that this band is of interstellar origin, the reddening is estimated as follows.

Because of the crowding of the lines in the spectrum, only the high points of the 50 Å band fluxes are considered for the representative energy distribution to be corrected for interstellar reddening. This correction is accomplished by assuming that the mean reddening curve obtained by Seaton (1979) is applicable. This curve was tried with different values of $E(B - V)$ to get a smooth stellar energy distribution. A value of 0·55 mag is derived for $E(B - V)$ with an uncertainty of ± 0·05 mag.

Herbig (1964) had previously estimated the reddening of MV Sgr as $E(B - V) = 0{\cdot}44$ by assuming that the intrinsic *UBV* colours of BD + 10°2179 and MV Sgr

Table 2. Observed flux with 50Å bandpass and its standard deviation, in units of 10^{-14} erg cm^{-2} s^{-1} Å^{-1}.

	SWP 7120		SWP 10302			LWR 6052		LWR 4816	
λ	F_λ	σ	F_λ	σ	λ	F_λ	σ	F_λ	σ
1275·68	1·56	0·23	1·13	0·44	2029·20	1·30	0.29	1·33	0·27
1326·22	1·67	0·29	1·53	0·56	2080·72	1·26	0·20	1·16	0·22
1376·22	2·54	0·32	2·73	0·44	2132·24	1·02	0·28	0·94	0·24
1427·30	2·57	0·45	2·58	0·47	2183·76	1·19	0·76	0·98	0·70
1477·84	3·10	0·36	3·01	0·39	2235·28	0·81	0·36	0·94	0·32
1528·38	2·94	0·41	3·07	0·51	2286·80	0·91	0·21	1·12	0·34
1578·92	2·88	0·50	2·84	0·49	2338·32	1·50	0·27	1·43	0·28
1629·46	3·13	0·36	2·98	0·43	2389·84	1·56	0·27	1·60	0·17
1680·00	3·44	0·31	3·59	0·41	2441·36	2·12	0·29	2·17	0·32
1730·54	3·00	0·30	3·12	0·48	2492·88	2·37	0·30	2·26	0·21
1781·08	2·79	0·61	2·74	0·62	2544·40	2·40	0·19	2·43	0·20
1831·62	2·82	0·23	3·01	0·30	2595·92	2·27	0·37	2·33	0·29
1882·16	2·20	0·24	2·22	0·29	2647·44	2·73	0·27	2·81	0·20
					2698·96	3·02	0·25	3·10	0·19
					2750·48	3·39	0·19	3·43	0·22
					2802·00	3·48	0·48	3·45	0·45
					2853·52	3·88	0·36	3·85	0·38
					2905·04	3·93	0·37	3·85	0·30
					2956·56	3·91	0·21	3·90	0·15
					3008·07	3·76	0·42	3·77	0·39
					3059·59	3·38	0·28	3·19	0·30
					3111·11	3·69	0·37	3·53	0·26
					3162·63	4·03	0·54	4·11	0·61

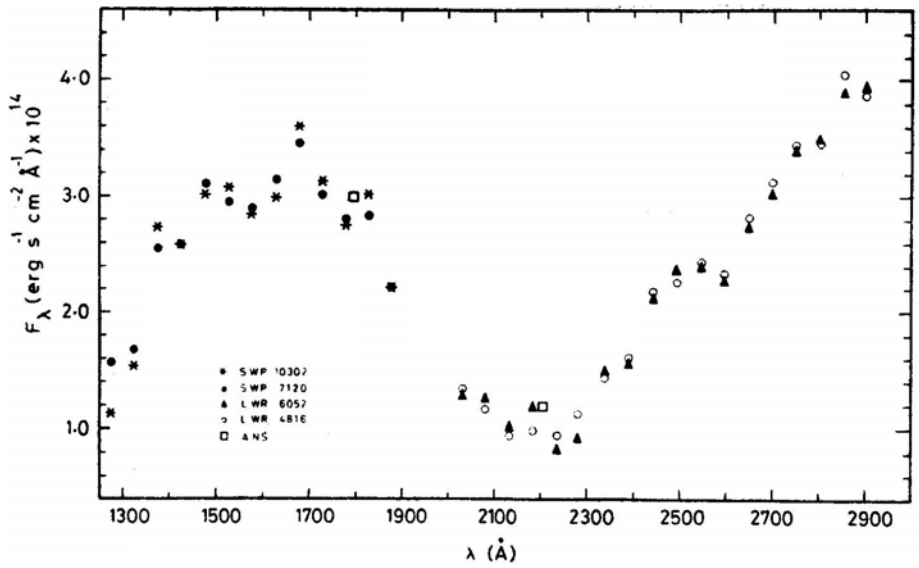

Figure 1. Observed energy distribution in the UV with 50 Å passband.

are the same. He used the *UBV* colours obtained by Paczynski, when the star was at $V = 12{\cdot}70$.

The assumption that the reddening is entirely due to the interstellar medium seems to be justified for the following reason. The distribution of $E(B - V)$ in the galactic plane is given by FitzGerald (1968) and Lucke (1976). For distances greater than 1·5 kpc in the region 2° north of the position of MV Sgr ($l = 13°.4$, $b = -7°.9$), the mean $E(B - V)$ is between 0·6 and 0·9 (Fig. 7 of FitzGerald 1968). A minimum distance of 1·5 kpc thus leads to an absolute magnitude M_V of 0·06, which agrees with the estimated lower limit of MV Sgr (Herbig 1964). From the data obtained with the sky survey telescope (S2/68) in the TD-1 satellite, Nandy *et al.* (1978) mapped the strength of the 2200 Å feature and mean $E(B - V)$ as a function of distance in the galactic plane for all galactic longitudes. In the longitude zone of MV Sgr, the mean $E(B - V)$ per kpc is $\simeq 0{\cdot}22$, which gives a distance of 2·5 kpc for MV Sgr, if the estimated $E(B - V)$ is entirely due to the interstellar medium. This distance, in turn, leads to an absolute magnitude M_V of — 1·05. This is in the range of M_V (— 1 to —2) preferred by Herbig (1964) for MV Sgr on the grounds that M should be same for MV Sgr as for the rest of R CrB stars. The above estimate of — 1·05 for MV Sgr is also close to the estimated $M_V = 1{\cdot}6$ of BD + 10°2179 (Klemola 1961). Although there is some uncertainty in the estimated M_V of MV Sgr as discussed by Herbig (1964), the above estimates indicate that the reddening as determined from 2200 Å band is all due to the interstellar medium.

4. UV continuum

The reddening-corrected energy distribution of MV Sgr is compared with the energy distributions computed by Heber and Schönberner (1980), with abundances of

Table 3. Published *UBV* photometry of MV Sgr.

Date	*V*	*B*−*V*	*U*−*B*	Observer
1963 July 26, August 10	12·70	0·26	−0·60	Paczynski (Herbig 1964)
1979 October 23	15·18	0·87	0·17	Landolt (1979)

n_H = 0·0, n_{He} = 0.99 and n_C = 0·01 for different temperatures. As can be seen from Fig. 2, UV energy distribution of MV Sgr fits well with the theoretical energy distribution for a model of T_{eff} = 18000 K and log g = 2·5—same as that which fits BD + 10°2179—showing further similarities between these two stars. The uncertainty in fitting model energy distribution, with respect to changes of carbon abundance in particular, is not known. The visual magnitude obtained from the computed model energy distribution is V_0 — 10·96 and after applying the interstellar extinction of 1·76 mag, the visual magnitude is 12·72. The estimate of the visual magnitude at the time of 1979 and 1980 IUE observations (Table 1: $m_v \simeq$ 13·0) is slightly fainter or agrees with the above estimate.

Fig. 3 shows all the published *UBV* (Herbig 1964; Landolt 1979), infrared (Glass 1978) and IUE observations—all corrected for interstellar extinction—plotted along with the theoretical energy distribution (T_{eff} = 18000 K, log g = 2·5) of the helium star. The value of total-to-selective extinction ratio R is taken to be 3·2. The energy distribution longward of 0·55 μm (V band) is an extrapolation of the black body (T = 18000 K) line. The *UBV* observations of Paczynski (Herbig 1964) follow the theoretical energy distribution of the helium star. Landolt's *UBV* observations

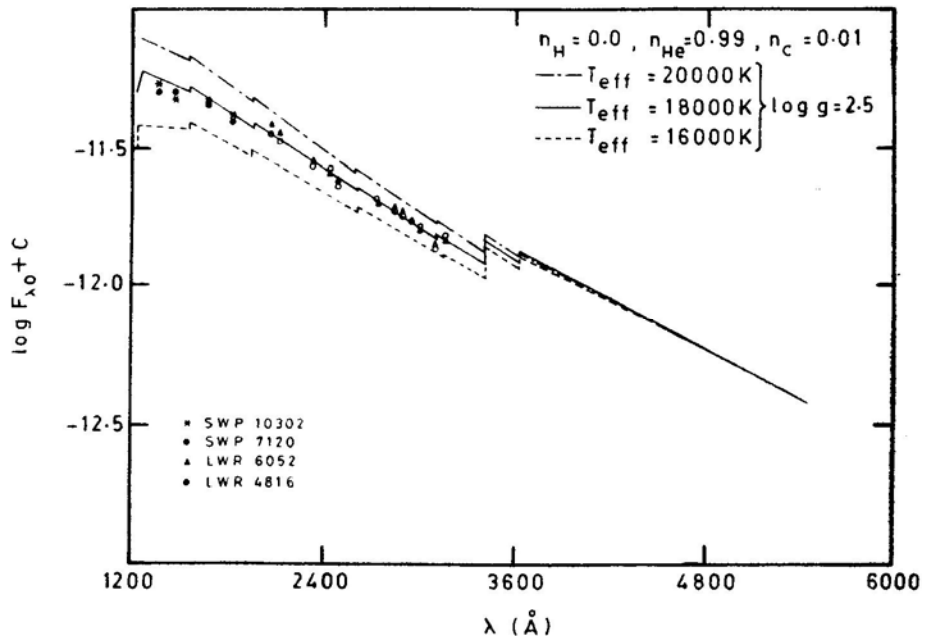

Figure 2. Reddening-corrected energy distribution of MV Sgr superposed on the theoretical energy distributions computed by Heber and Schönberner (1980). The ordinate is log F_λ + ·396.

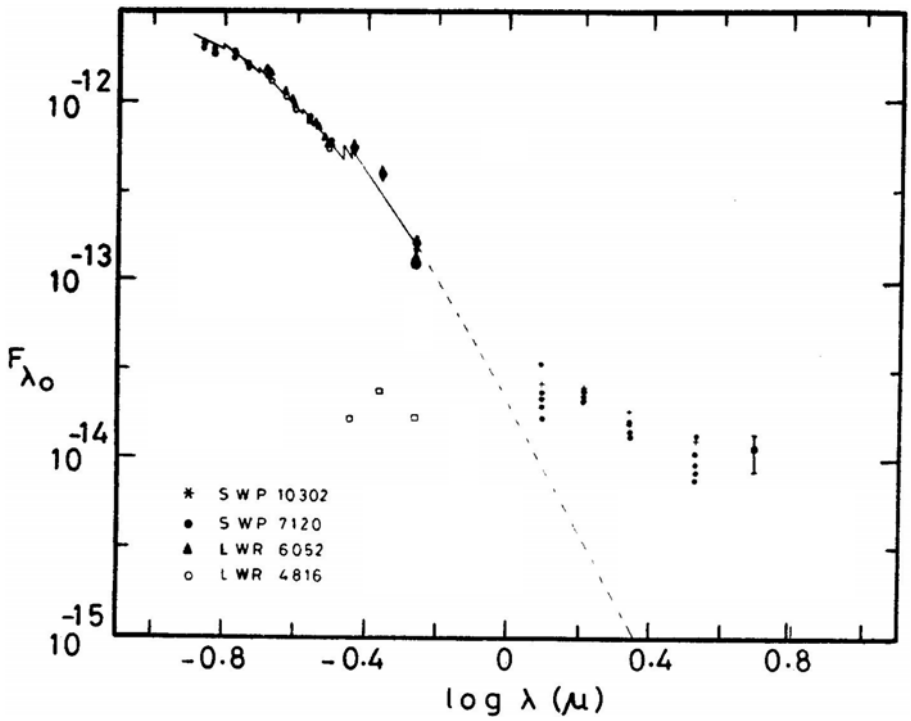

Figure 3. Reddening corrected fluxes of all the UV, *UBV* and infrared observations discussed in this paper plotted with the theoretical energy distribution of Heber and Schönberner for T_{eff} = 18000 K black body longward of 0·55 μm. (*V* filter).

♦ *UBV* observations of Paczynski (1971).
□ *UBV* observations of Landolt (1979).
× *V* magnitude estimated from FES counts for SWP 10302 and LWR 7972.
⊙ *V* magnitude estimated from FES counts for SWP 7120 and LWR 6052.
●, + Infrared observations of Glass (1978).

were obtained when the star was quite faint, and show that the colours become redder.

5. Line spectrum

The observed low-resolution short-wavelength spectra SWP 7120 (dashed line) and SWP 10302 (full line) obtained in 1979 and 1980 are shown in Fig. 4. The line spectrum shows many absorption lines and there does not seem to be any prominent emission line in both the spectra (although there are a few spikes which might not be spurious). Moreover because of high interstellar extinction the spectrum is expected to show many interstellar lines. The line spectrum in absorption is characterized by two types of features: (1) those that do not change in strength between the two spectra (SWP 7120, SWP 10302) within about 5–10 per cent and (2) the lines which change their strength and are particularly enhanced in SWP 10302.

The line identification has been done with the help of the line list for BD + 10°2179

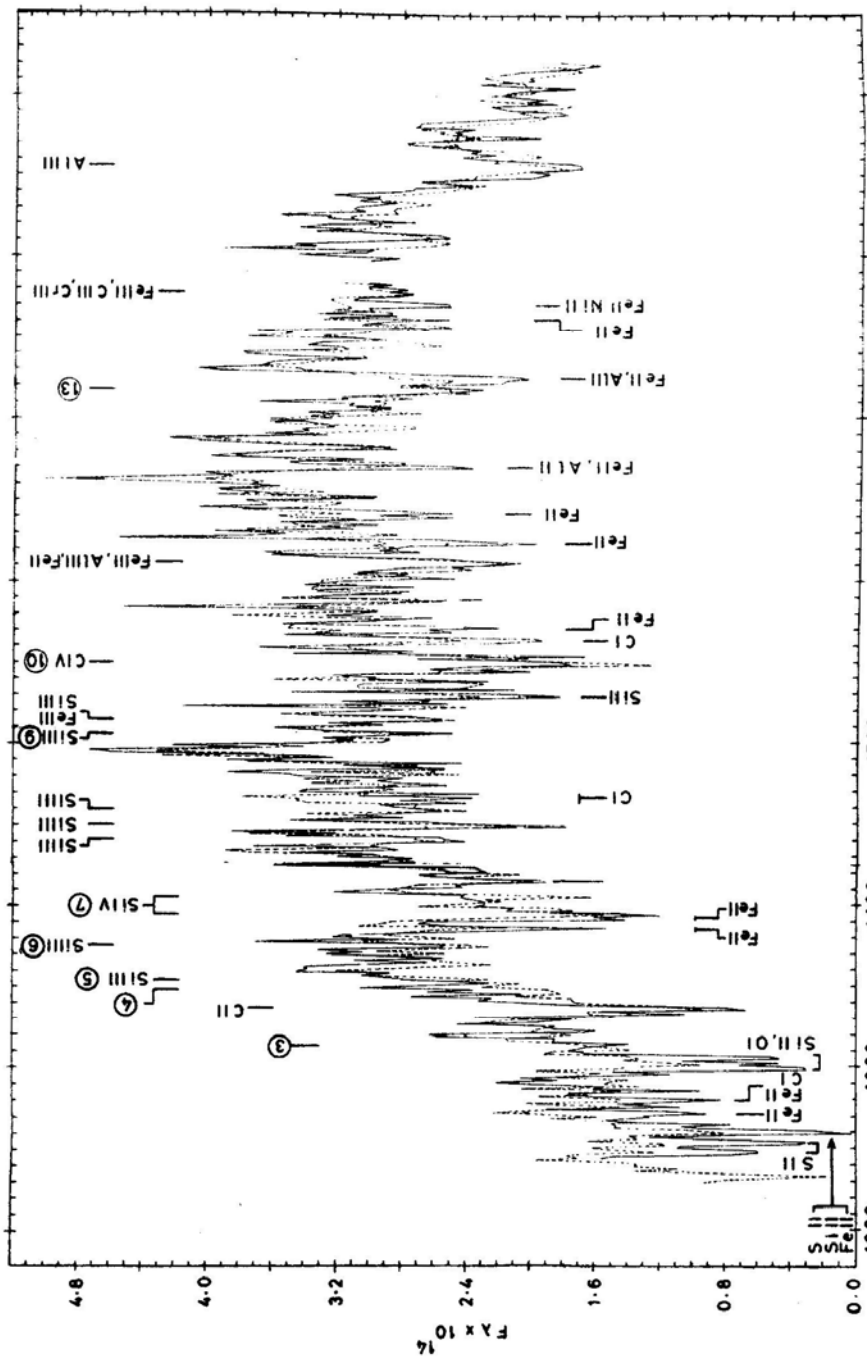

Figure 4. Low-resolution IUE spectra of MV Sgr at two different occasions: SWP 10302 (continuous line) obtained in 1980 October when the star was at $m_v \simeq 11{\cdot}4$ and SWP 7120 (dashed line) obtained in 1979 November when the star was at $m_v \simeq 13$. The gap near λλ1780–1790 is the place where the reseaux mark occurs (not plotted).

(Schönberner and Hunger 1978) and line identification lists of B stars by Stalio and Selvelli (1975), Kelly and Palumbo (1973), Moore (1950) and Johansson (1978).

Many of the lines which do not change in strength are those that are seen (and expected) in a star of spectral type ~ B2. Some of these identifications are shown on the top of Fig. 4. The identification of the numbered lines is given by Nandy and Morgan (1980). There might be some enhancement in some of these lines in the spectrum of SWP 7120. The other variety of features which are strong in SWP 10302 and are either weak or absent in SWP 7120 are mostly due to Fe II, C I, Si II, Al II, O I and perhaps S I. These lines are not expected to be strong in a B2 star. Some of these are shown below the spectrum in Fig. 4. Particularly, the region between 1560–1720 Å shows the presence of strong Fe II lines in absorption in SWP 10302 relative to SWP 7120. A list of some of these lines are given in Table 4. This trend also seems to be true with Fe II lines in the long wavelength range (*e.g.* multiplets 62 and 63). These lines are denoted as circumstellar shell lines for further discussion.

As mentioned in the introduction, Herbig (1975) had identified several lines in emission, mainly due to Fe II, [Fe II], Si II *etc.* It is of interest to see whether any Fe II line emission occurred in the UV, when the star was slightly fainter ($m_v \simeq 13{\cdot}0$: same visual magnitude as in SWP 7120). It is hard to detect incipient emission in the absorption lines on this low-resolution spectra, but none of the Fe II emissions rise above the level of the continuum in SWP 7120. The upper levels of the Fe II emissions seen in the red are connected to the strong UV lines; particularly multiplet numbers 34, 38, 40, 73 and 74 are connected to UV 1, UV 62, UV 63 *etc.* Even these multiplets do not seem to get strengthened in absorption in LWR 6052 ($m_v \simeq 13$) compared with LWR 7972 and 4816. Moreover, they seem to be weak. This probably indicates that resonance fluorescence might not be a dominant process for the excitation of the Fe II emissions seen in the blue and red regions of the spectrum.

The Si II lines λλ 6347, 6371 have also been seen in emission by Herbig. The lower levels of these transitions are the upper levels for the resonance lines λλ 1533, 1526. Although there is some weakening at λ 1526 in SWP 7120, it is not clear whether it is because of the emission. Moreover, this line might have been blended with an interstellar component.

Changes in the emission-line strengths also seem to occur in the blue region of the spectrum. Westin (1980) has published a tracing of the spectrum of MV Sgr in the wavelength range λλ 3700–4200 and 4380–4925. The visual brightness of the star at the time of this observation is not known but it could be around maximum light. The only discernable emission line in this spectrum is λ 4584 of Fe II. This is in contrast to the description of the 1963 blue spectrograms by Herbig (1975) where he could certainly see emission at λλ 4549, 4555, 4583, 4731 and possibly at λλ 4258, 4314, 4385.

The line spectrum of BD + 10°2179 in the IUE wavelength range has been analysed by Schönberner and Hunger (1978) and Heber and Schönberner (1980). The strongest feature in the whole UV spectrum is that of the C II resonance lines λλ 1334–35. They use these lines to calculate the carbon abundance for the reason that it falls on the damping part of curve of growth and hence is independent of microturbulence. In MV Sgr which is very similar to BD + 10°2179, the λλ 1334–35 feature is not as strong, even though it might have a blended interstellar component (The central depth ≃ 0·7 in MV Sgr whereas it is 0·99 in BD + 10°2179). Herbig (1964) has already commented about the weakness of C II lines in MV Sgr

Table 4. Identifications for some enhanced (circumstellar) lines in SWP 10302.

λ_{obs}(Å)	λ(Å)	Identification (multiplet no.)
1247	1246·7	Si II (8)
	48·4	
1252	1250·5	S II (1)
	53·8	
	1251·2	Si II (8)
1260	1260·5	Fe II (9)
	59·5	S II (1)
	60·7	Si II (4)
1272	1271·2	Fe II (9)
	72·0	
	72·6	
1275–77	1275·1	Fe II (9)
	75·8	
	1277·1	C I (7)
	77·3	
	77·6	
	77·8	
1298–1304	1302·1	O I (2)
	04·8	
	06·0	
	1304·4	Si II (3)
	1298·9	Si III (4)
1385	1385·5	Fe II
	85·0	S I (7)?
1465-68	1463·3	C I (37)
	1467·4	C I (36)
	67·8	
	68·4	
1526	1526·7	Si II (2)
	1525	Fe III
1562	1561·3	C I (3)
	61·4	
	1562·4	Si II (11)
	62·8	
	1563·7	Fe II (45)
1567-70	1570·2	Fe II (45)
	74·9	
	1566·8	Fe II (44)
	1569·6	Fe II (44)
	74·9	
1622	1621·3	Fe II (8)
	25·9	
	1625·5	Fe II (43)
1631-41		Fe II (8) Fe II (43) Fe II (42) Fe II (68) V II (18)?
1670	1670·7	Al II (2)
	1670·7	Fe II (40)
1722-25	1719·4	Al II (6)
	21·2	
	25·0	
	1720·0	Fe II (64)
	20·6	Fe II (38)
	26·3	
	24·8	Fe II (39)
	25·0	Fe II (37)
1760	1761·3	Fe II (100)
	60·4	Fe II (101)
	1761·9	Al II (5)
	60·1	
1771	1772·5	Fe II (99)
	1773·9	Ni II (3)?

in the blue region. Thus carbon might not be as abundant in MV Sgr as it is in BD + 10°2179.

We also note that no blueshifted components of the P Cygni type have been seen in the UV spectrum of MV Sgr.

6. Discussion

The main aspects to be considered for an explanation in terms of a model for MV Sgr are the following:

The spectrum in the blue shows absorption lines mainly due to a hydrogen-poor helium star of approximate spectral type B2.

The UV continuum can be well matched by a helium star model of $T_{\rm eff}$ = 18000 K, log g = 2·5 consistent with the approximate spectral type of B2. Even the UV absorption-line spectrum, when the star is $m_v \simeq 13$ (SWP 7120) is consistent with this spectral type.

The optical emission line spectrum seen at $m_v \simeq 13$ is mainly due to Fe II, Si II, [Fe II], H_α, He I, O I, N I, and Ca II. No emission lines are clearly detectable in the UV.

Even at maximum light, on certain occasions (SWP 10302) there appeared circumstellar shell (absorption) lines due to Fe II, C I, O I, Si II, Al II *etc.* Those of Fe II were however, the strongest.

Infrared excess in *JHKL* bands can be characterized by a blackbody temperature of 1500–2000 K (Glass 1978). Infrared photometric variations occur with a range in magnitudes of $\Delta J = 0.76$, $\Delta H = 0.36$, $\Delta K = 0.33$, $\Delta L = 0.63$, $\Delta(K - L) = 0.56$.

Finally, irregular light variation in the range 11·71–15·6 m_{pg} has been reported by Hoffleit (1959).

The colours $B - V$ and $U - B$ are redder at the light minimum as seen when the star was at V = 15·15 (Landolt 1979).

The traditional picture of an R CrB star is that the light minima are supposed to be caused by a cloud (or shell) of dust grains (formed presumably from the ejected gas) obscuring the star light. In such a case, the presence of circumstellar shell lines in 1980 IUE spectra without any accompanying changes in the visual light is puzzling, particularly since, these shell lines were absent or very weak just after the light minimum in 1979. This situation is in contrast to the case with R CrB or RY Sgr, where the shell lines in the optical region (*e.g.* Ca II H and K, He I λ 3889, Na I D) are seen during the late recovery phase of the light curve (Gaposchkin 1963; Rao 1974; Alexander *et al.* 1972). Unless there is another ejection of gas in the line of sight in 1980 and this ejection is not accompanied by the formation of dust which causes visual extinction, the explanation for the presence of cooler circumstellar lines becomes difficult in a single star model for MV Sgr. On the other hand, as mentioned in the introduction, in the binary star model with a cool companion the circumstellar shell lines find a natural explanation in the gas ejected from the cooler star towards the hotter B star.

MV Sgr also shows infrared excess in *JHKL* wavelength bands which can be fitted to a blackbody temperature of 1500–2000 K (which also varies). Any stellar object of temperature 2000 K or slightly hotter would be able to satisfy the above condition. But the luminosity should be $L/L_\odot > 10^3$. It is hard to specify the nature of the

companion with the uncertainty in the M_v for the B star and in the estimation of $T_{\rm eff}$ for the cool star. But normally such a star would be easily recognisable in the spectrum and also from infrared photometry. The spectra obtained by Herbig (1975) in the red do not show the presence of any such companion. The spectrum is smooth with many emission lines and few absorptions. One of the possibilities to overcome the above difficulty is that this late-type companion itself is covered up with circumstellar dust which absorbs the visible and near infrared flux and re-radiates it in the far infrared wavelengths beyond 3·5 μm (L band). Some support to this possibility comes from the 5 μm observation by Glass (1978) which shows more flux than could be fitted by a blackbody at 1500–2000 K, to which the J, H, K and to some extent L fluxes can be fitted to. Thus the model might be like that of the α Sco system with a B2 star (hydrogen-poor in case of MV Sgr) and a late-type giant (a supergiant in the case of α Sco). There seem to be several similarities between the two systems.

The emission spectrum of MV Sgr described by Herbig is very similar to that of the emission nebula around α Sco B described by Swings and Preston (1978) except that the red star dominates in the long wavelength range so that emissions are seen in the blue. In the case of MV Sgr the B star dominates the blue region and hence the emission lines are seen in the red. Both systems show emission lines of Fe II, [Fe II], Si II, H_α (no other hydrogen line in emission), He I (λλ 6678, 5876, 7065, in the case of MV Sgr and probably λ 4471 in α Sco). However, in α Sco the [Fe II] lines are stronger whereas in MV Sgr the Fe II lines are stronger. This may indicate a higher electron density in the gas around MV Sgr. The similarities between these two systems also extend to the circumstellar (shell) absorption lines seen in the B star spectrum, α Sco B shows shell lines of Fe II, Mn II, Cr II, Zn II and also Ti II *etc.* in the spectrum studied longward of λ 2000 (van der Hucht, Bernat and Kondo 1980). MV Sgr at maximum light shows lines of Fe II, C I, O I, Si II, Al II and others in the wavelength range λλ 1240–1900 (SWP 10302). The degree of ionization in the circumstellar gas also seems to be roughly the same in both the stars.

With this analogy of α Sco system the following scenario is suggested for MV Sgr. The system is a binary with a B2, hydrogen-poor, helium star and a cool companion. The companion is normally covered by its own circumstellar dust and might also be a variable as seen from the variations in infrared flux. On certain occasions, enhanced cool stellar wind is blown towards the B star giving rise to the circumstellar shell lines due to Fe II, C I, O I *etc.* without diminishing the continuum of the B star. There is also the possibility that there might be a steady wind all the time. However, when some dust is also blown towards the B2 star, a deeper visual minimum occurs and the colours of the B star get redder as observed by Landolt (1979) when the star was at V = 15·18; presumably such blow-up of gas and dust occurs irregularly since the visual minima are irregular. The emission lines of Fe II *etc.* observed by Herbig could come from a nebula around the B star fed from the stellar wind of the cool star. Good radial velocity measurements of the emission lines would be helpful regarding this point.

It is of interest to see how the extinction properties of the circumstellar dust around the hot star like MV Sgr differ relative to other R CrB stars if the visual minima of MV Sgr are caused by the dust. The *UBV* colors observed by Paczynski and Landolt at maximum and minimum (Table 3) give the following reddening relations

$\Delta V/\Delta(B - V)$ = 4·1 and $\Delta(U - B)/\Delta(B - V)$ = 1·26 for the ratio of total-to-selective absorption and for the two-colour relation respectively. These values are similar to the reddening relations observed for RY Sgr (*i.e.* 4·3 and 1·3, Alexander *et al.* 1972) and SU Tau (4·3 and 1·47, Rao 1980) during the recovery phase of the light curve.

Obviously more observations in the UV, visible and infrared regions are needed to study the system more exhaustively.

7. Conclusion

The UV and visual continuum of MV Sgr can be fitted to the theoretical energy distribution of a hydrogen-deficient carbon-rich helium star of $T_{\rm eff}$ = 18000 K and log g = 2·5, after correcting for interstellar reddening of E (B — V) = 0·55. The IR excess and the spectroscopic phenomenon of the transient shell absorption lines could be caused by a cool companion blowing gas and dust towards the hot star in a system similar to the $_{\alpha}$ Sco system. Thus if the binary model is correct, MV Sgr might have had a different scheme of evolution for the loss of its hydrogen (envelope) than other single stars like R CrB.

Acknowledgements

We are grateful to IUE Data Center at VILSPA for providing the IUE images obtained by other observers. We would also like to express our appreciation to Mrs. Cranston for processing the IUE data at ROE. We are grateful to Drs. G. Herbig, A. Cassatella, A. Holm and M. K. V. Bappu for their help and comments on the earlier version of this paper.

References

Acker, A. 1976, *Publ. Obs. astr. Strasbourg,* **4,** No. 1.

Alexander, J. B., Andrews, P. J., Catchpole, R. M., Feast, M. W., Lloyd Evans, T., Menzies, J. W., Wisse, P. N. J., Wisse, M. 1972, *Mon. Not. R. astr. Soc.,* **158,** 305.

Boggess, A., Carr, F. A., Evans, D. C., Fischel, D., Freeman, H. R., Fuechsel, C. F., Klinglesmith, D. A. Krueger, V. L., Longanecker, G. W., Moore, J. V., Pyle, E. J., Rebar, F., Sizemore, K. O., Sparks, W., Underhill, A. B., Vitagliano, H. D., West, D. K., Macchetto, F. Fitton, B., Barker, P. J., Dunford, E., Gondhalekar, P. M., Hall, J. E., Harrison, V. A. W., Oliver, M. B., Sandford, M. C. W., Vaughan, P. A., Ward, A. K., Anderson, B. E., Boksenberg, A., Coleman, C. I., Snijders, M. A. J., Wilson, R. 1978, *Nature,* **275,** 372.

Feast, M. W., Glass, I. S. 1973, *Mon. Not. R. astr. Soc.,* **161,** 293.

FitzGerald, M. P. 1968, *Astr. J.*, **73,** 983.

Gaposchkin, C. P. 1963, *Astrophys. J.,* **138,** 320.

Glass, I. S. 1978, *Mon. Not. R. astr. Soc.,* **185,** 23.

Heber, U., Schönberner, D. 1980 in *Proc. Second European IUE Conf.,* ESA, Paris, p. 327.

Herbig, G. H. 1964, *Astrophys. J.*, **140,** 1317.

Herbig, G. H. 1975, *Astrophys. J.,* **199,** 702.

Holm, A. V., Crabb, W. 1979, NASA. *IUE Newsletter No. 7.*

Hoffleit, D. 1959, *Astr. J.,* **64,** 241.

Humphreys, R. M., Ney, E. P. 1974, *Astrophys. J.,* **190,** 339.

Johansson, S. 1978, *Phys. Scripta,* **18,** 217.

Kelly, R., Palumbo, L. J. 1973, *Naval Research Laboratory Report 7599.*
Klemola, A. R. 1961, *Astrophys. J*., **134,** 130.
Landolt, A. R. 1979, *IAU Circ. No. 3419.*
Moore, C. E. 1950, *An Ultraviolet Multiplet Table:* NBS Circ. No. 488.
Nandy, K., Morgan, D. H. 1980, *Mon. Not. R. astr. Soc.,* **192,** 905.
Nandy, K., Thompson, G. I., Carnochan, D. J., Wilson, R. 1978, *Mon. Not. R. astr. Soc.,* **184,** 733.
Paczynski, B. 1971, *Acta Astr.,* **21,** 1.
Rao, N. K. 1974, *Ph D thesis,* University of California, Santa Cruz.
Rao, N. K. 1980, *Astrophys. Sp. Sci.,* **70,** 480.
Renzini, A. 1981, in *1AU Coll. 59*: *The Effects of Mass-loss on Stellar Evolution,* Eds C. Chiosi and R. Stalio, D. Reidel, Dordrecht, p. 319.
Sackmann, I. J., Smith, R. L., Despain, K. H. 1974, *Astrophys. J*., **187,** 555.
Schönberner, D. 1975, *Astr. Astrophys.,* **44,** 383.
Schönberner, D., Hunger, K. 1978, *Astr. Astrophys.,* **70,** L57.
Seaton, M. J. 1979, *Mon. Not. R. astr. Soc.,* **187,** 73p.
Swings, J. P., Preston, G. W. 1978, *Astrophys. J*., **220,** 883.
Stalio, R., Selvelli, P. L. 1975, *Astr. Astrophys. Suppl. Ser.,* **21,** 241.
van der Hucht, K. A., Bernat, A. P., Kondo, Y. 1980, *Astr. Astrophys.,* **82,** 14.
Westin, B. A. M. 1980, *Astr. Astrophys.,* **81,** 74.

J. Astrophys. Astr. (1982) **3**, 93–99

Analysis of the *U B V* Light Curves of TT Hydrae by Kopal's Frequency Domain Method

Jawahar Koul and K. D. Abhyankar *centre of Advanced study in Astronomy, Osmania University, Hyderabad 500007*

Received 1982 February 12; accepted 1982 March 5

Abstract. The light curves of the totally eclipsing system TT Hya in *UBV* colours observed by Kulkarni and Abhyankar during 1973–77 have been analysed by Kopal's frequency domain method with slight modification. We find r_s (primary) = 0·104 ± 0·005, r_g (secondary) = 0·215 ± 0·008 and i = 89° ± 1°. The value of r_g obtained in this study is smaller than that determined earlier by Kulkarni and Abhyankar by the method of Russell and Merrill; this confirms the undersized nature of the secondary component. The ultraviolet colour excess of the secondary is also confirmed.

Key words: close binaries—absolute dimensions

1. Introduction

The Algol type eclipsing binary TT Hya shows a deep total eclipse and an almost inconspicuous secondary eclipse. From an analysis of the *UBV* light curves obtained at Japal Rangapur Observatory, Kulkarni and Abhyankar (1978, 1980) have derived the eclipse elements of the system by the Russell-Merrill method. On combining with Popper's radial–velocity data they (Kulkarni and Abhyankar 1981) have obtained the absolute dimensions of the components and a model of the system in which the secondary is found to be undersized and the ultraviolet (UV) excess during secondary eclipse is attributed to circumstellar matter around the primary. Since the evolutionary status of undersized secondaries is controversial (Hall 1974) we have re-analysed the same data by Kopal's frequency domain technique which gives the solution in closed form. The general method outlined by Kopal (1979) for occultation eclipses is modified to some extent for convenience of numerical calculations.

2. Evaluation of generalised moments

The first step is to evaluate the generalised moments $\bar{A}_{2m}$ defined by

$$\bar{A}_{2m} = \int_0^{\pi/2} \{l(\pi/2) - l(\psi)\}\, d(\sin^{2m}\psi), \tag{1}$$

m = 1, 2, 3 *etc.* As the light curve usually shows some asymmetry we reflect the observed points for negatives ψ's on to the positive side and obtain a symmetric curve for ψ=0° to 180°. If the observed (or normal) points are numerous the integrals of Equation (1) can be evaluated numerically by trapezoidal rule. But since the observations of Kulkarni and Abhyankar (1978) did not cover all the phases at quadrature the estimation of the generalised moments by this procedure becomes erroneous especially for higher order moments that depend largely on the intensities near ψ= 90°. We have, therefore, followed a slightly different procedure as described below.

The $\bar{A}_{2m}$ s actually consist of three parts:

$$\bar{A}_{2m} = A_{2m} + A_{2m}^{\text{prox}} + \mathfrak{P}_{2m} \tag{2}$$

where A_{2m} are the moments for spherical stars, A_{2m}^{prox} include the proximity effects such as reflection and rotational-tidal distortion, and $\mathfrak{P}_{2m}$ are photometric perturbations within eclipses due to differential limb-darkening and gravity brightening caused by the distortions of both components. At first we neglect the photometric perturbations and write

$$A'_{2m} = \bar{A}_{2m} - A_{2m}^{\text{prox}}, \tag{3}$$

where A'_{2m} are the rectified moments. Now representing the light outside eclipse by

$$l(\psi) = 1 + c_0 + \sum_{j=1}^{n} c_j \cos^j \psi, \tag{4}$$

we can evaluate the rectification coefficients c_j by

$$c_j = \int_{-a}^{+a} \{l(\pi/2) - l(\psi)\}\, \mathcal{P}_j^{(a,n)}(x)\, dx \tag{5}$$

where χ= cos ψ and a = cos ψ_e, ψ_e being the angle of external tangency; n is usually taken to be 4. The functions $\mathcal{P}_j$ will be discussed in the next section. Then, A_{2m}^{prox} are given by

$$A_{2m}^{\text{prox}} = -\int_0^{\pi/2} \left\{\sum_{j=1}^{n} c_j \cos^j \psi\right\} d(\sin^{2m}\psi), \tag{6}$$

and the rectified moments A'_{2m}, by Equation (3). However,as explained above, A'_{2m} obtained in this way would be inaccurate due to the errors in $\bar{A}_{2m}$ caused by the paucity of observed points near $\psi = 90°$. But since

$$l(\pi/2) = 1 + c_0 = l(\psi) - \sum_{j=1}^{n} c_j \cos^j \psi, \tag{7}$$

we can evaluate l $(\pi/2) = 1 + c_0$ by averaging the right-hand side of Equation (7) over all points outside the eclipse. We then have

$$A'_{2m} = \int_0^{\psi_e} \left\{1 + c_0 - l(\psi) + \sum_{j=1}^{n} c_j \cos^j \psi\right\} d(\sin^{2m} \psi) \tag{8}$$

because the integrand can be equated to zero for $\psi > \psi_e$. This amounts to rectifying the light curve before evaluating the moments. Thus, we are able to avoid the use of points near $\psi = 90°$ for evaluating the moments. Further, we also obtain $A_0 = L_1 = 1 + c_0 - \langle l(\text{totality})\rangle$

3. General expressions for $\mathscr{P}_j^{(a,n)}(x)$

Kopal (1979) has given expressions for $\mathscr{P}_j^{(a,\,4)}(x)$for three values of $\psi_e = 30°$, 45° and 60°. However, in order to enhance the accuracy of c_j's it is desirable to keep $a = \cos \psi_e$ as a free parameter to be chosen appropriately for any particular case. Then we obtain the following expressions for $\mathscr{P}_j$'s:

$$\mathscr{P}_1^{(a,\,4)}\left(\frac{x}{a}\right) = \frac{15}{8}\left(\frac{7x^3}{a^5} - \frac{5x}{a^3}\right),$$

$$\mathscr{P}_2^{(a,\,4)}\left(\frac{x}{a}\right) = \frac{105}{32}\left(\frac{45x^4}{2a^7} - \frac{21x^2}{a^5} + \frac{5}{2a^3}\right),$$

$$\mathscr{P}_3^{(a,\,4)}\left(\frac{x}{a}\right) = -\frac{35}{8}\left(\frac{5x^3}{a^7} - \frac{3x}{a^5}\right),$$

$$\mathscr{P}_4^{(a,\,4)}\left(\frac{x}{a}\right) = -\frac{315}{64}\left(\frac{35x^4}{2a^9} - \frac{15x^2}{a^7} + \frac{3}{2a^5}\right). \tag{9}$$

In the case of TT Hya we have taken $\psi_e = 19°$ which is close to its value of 18·55 found by Kulkarni and Abhyankar (1980) as well as the final value obtained in this study. The c_j 's and the rectified moments for *UBV* light curves obtained from the normal points tabulated by Kulkarni (1979) are given in Table 1.

Table 1. c_j's and rectified moments for TT Hya.

Parameter	*V*	*B*	*U*
c_1	−0·0081985	−0·0073175	−0·0136457
c_2	−0·0212155	+0·0010891	+0·0365864
c_3	−0·0073379	−0·0065493	−0·0022387
c_4	−0·0510867	−0·0331143	−0·0482243
A_0	0·7131	0·8561	0·8952
A'_2	0·0325181	0·0395723	0·0418011
A'_4	0·0017927	0·0022144	0·0023926
A'_6	0·0001127	0·0001412	0·0001575
A'_8	0·0000078	0·0000098	0·0000114

4. Preliminary elements

Taking $A_{2m} = A'_{2m}$ we can derive the preliminary elements by the following standard method. From

$$A_2 = L_1 \bar{C}_3,$$

$$A_4 = L_1 (\bar{C}_3^2 + \bar{C}_2^2),$$

$$A_6 = L_1 (\bar{C}_3^3 + 3\,\bar{C}_2^2\,\bar{C}_3 + \bar{C}_1\,\bar{C}_2^2), \tag{10}$$

we get $\bar{C}_3$, $\bar{C}_2$ and $\bar{C}_1$, and from

$$A_8 = L_1 (\bar{C}_3^4 + 4\,\bar{C}_1\,\bar{C}_2^2\,\bar{C}_3 + 6\,\bar{C}_2^2\,\bar{C}_3^2 + a\,\bar{C}_2^4 + b\,\bar{C}_1^2\,\bar{C}_2^2),$$

where

$$a = \frac{30\,(3 - u_1)\,(35 - 19u_1)}{7(15 - 7u_1)^2}$$

and

$$b = \frac{7\,(15 - 7u_1)\,(315 - 187u_1)}{27\,(35 - 19u_1)}, \tag{11}$$

we can find u_1. The inaccuracy of A_8 did not allow us to determine a unique value for u_1 Hence we have adopted u_1 = 0·520, 0·680 and 0·420 for *V, B* and *U* respectively, as given by Kulkarni and Abhyankar (1980), Then

$$C_3 = \bar{C}_3,$$

$$C_2 = \sqrt{\frac{5\,(3 - u_1)}{(15 - 7u_1)}}\,\bar{C}_2,$$

$$C_1 = \frac{7\,(15 - 7u_1)}{3\,(35 - 19u_1)}\,\bar{C}_1, \tag{12}$$

give C_1, C_2, C_3 from which we get the elements by

$$r_{1,2}^2 = \frac{C_{1,2}^2}{(1 - C_3)\, C_2 + C_2^2}$$

and

$$\sin^2 i = \frac{C_1}{(1 - C_3)\, C_1 + C_2^2}. \tag{13}$$

The various constants and preliminary elements obtained in this way are given in Table 2.

5. Photometric perturbations and improvement of elements

The preliminary elements are derived by neglecting the photometric perturbations. We can now improve the elements by allowing for the photometric perturbations evaluated on the basis of the preliminary elements. The complete formulae are given by Livaniou (1977). They involve two additional quantities: the mass ratio m_2/m_1 for which we have taken a value of 0·269 found from Popper's radial velocity data, and the gravity-brightening coefficient τ_1 which is taken as unity. We then obtain

$$A_{2m} = A'_{2m} - \mathfrak{P}_{2m} \tag{14}$$

and follow the procedure of Section 4 to derive a set of improved elements. The iterative procedure can be repeated until convergence is achieved. We required 6 iterations for *V,* 11 for *B* and 9 for *U* light curves. The starting, intermediate and final values for various parameters are given in Tables 3, 4 and 5 for *V, B* and *U,* respectively. The final definitive elements obtained by averaging the results for the three colours are given in Table 6 which also gives for comparison the elements obtained by Kulkarni and Abhyankar.

Table 2. Preliminary elements for TT Hya.

Parameter	*V*	*B*	*U*
$\bar{C}_1$	0·0086911	0·0083840	0·0104844
$\bar{C}_2$	0·0208446	0·0212124	0·0221879
$\bar{C}_3$	0·0456010	0·0462239	0·0466947
u_1	0·520	0·680	0·420
C_1	0·0091709	0·0090725	0·0109190
C_2	0·0217779	0·0225771	0·0229476
C_3	0·0456010	0·0462239	0·0466947
r_1	0·0954735	0·0947791	0·1044142
r_2	0·2267179	0·2358583	0·2194387
i	85°·528	84°·301	87°·760

Table 3. Corrected moments, elements and photometric perturbations for *V* light curve of TT Hya.

	Initial value	Third iteration	Final (mean of two)
r_s	0·0954735	0·1014171	0·1008162
r_g	0·2267179	0·2135840	0·2148870
i	85°·5	90°·0	90°·0
$\mathfrak{P}_2$	−0·0010592	−0·0008109	−0·0008326
$\mathfrak{P}_4$	−0·0000849	−0·0000714	−0·0000742
$\mathfrak{P}_6$	−0·0000068	−0·0000061	−0·0000063
A_2	0·0335773	0·0333290	0·0333507
A_4	0·0018776	0·0018641	0·0018669
A_6	0·0001195	0·0001188	0·0001190

Table 4. Corrected moments, elements and photometric perturbations for *B* light curve of TT Hya.

	Initial value	Third iteration	Final (mean of two)
r_s	0·0947791	0·1001969	0·1002206
r_g	0·2358583	0·2218484	0·2232298
i	84°·3	87°·8	87°·3
$\mathfrak{P}_2$	−0·0015010	−0·0011347	−0·0011688
$\mathfrak{P}_4$	−0·0001170	−0·0001038	−0·0001057
$\mathfrak{P}_6$	−0·0000088	−0·0000089	−0·0000091
A_2	0·0410733	0·0407070	0·0407411
A_4	0·0023314	0·0023183	0·0023201
A_6	0·0001500	0·0001501	0·0001503

Table 5. Corrected moments, elements and photometric perturbations for *U* light curve of TT Hya.

	Initial value	Fifth iteration	Final (mean of two)
r_s	0·1044142	0·1097163	0·1097275
r_g	0·2194387	0·2076176	0·2076721
i	87°·8	90°·0	90°·0
$\mathfrak{P}_2$	−0·0011813	−0·0009304	−0·0009316
$\mathfrak{P}_4$	−0·0001033	−0·0000777	−0·0000779
$\mathfrak{P}_6$	−0·0000090	−0·0000065	−0·0000066
A_2	0·0429824	0·0427315	0·0427327
A_4	0·0024958	0·0024703	0·0024705
A_6	0·0001665	0·0001640	0·0001641

Table 6. Final eclipse elements for TT Hya.

	Shapley (1927)	Kulkarni and Abhyankar (1981) (Russell and Merrill method)	Koul and Abhyankar (Kopal's frequency domain method)
r_s	0·072	0·0929	0·104 ± 0·005
r_g	0·240	0·2438	0·215 ± 0·008
i	82°·6	83°·64	89°·0 ± 1°
L_s (*V*)		0·7682	0·7131
L_g (*V*)		0·2318	0·2869
L_s (*B*)		0·8858	0·8561
L_g (*B*)		0·1142	0·1439
L_s (*U*)		0·9100	0·8952
L_g (*U*)		0·0900	0·1048

Table 7. Colours and spectral types for components of TT Hya.

	Kulkarni and Abhyankar (1981) (Russell and Merrill method)	Koul and Abhyankar (Kopal's frequency domain method)
(*V*) Primary	7·526	7·624
(*V*) Secondary	8·903	8·612
(*B*−*V*) Primary	+0·027	−0·023
(*B*−*V*) Secondary	+0·970	+0·925
(*U*−*B*) Primary	−0·019	−0·040
(*U*−*B*) Secondary	+0·283	+0·353
(Sp) Primary	Al V	A0 V
(Sp) Secondary	Kl III	G8 III
UV colour excess of secondary	0·5–0·6 mag	0·35 mag

6. Conclusions

From Table 6 we note that the radius of the primary is 12 per cent larger and that of the secondary 12 per cent smaller as compared to the values obtained by Kulkarni and Abhyankar (1981). In particular the radius of the secondary has now turned out to be 0·215 ± 0·008 which is much smaller than the Roche lobe radius of 0·264 for m_2/m_1 = 0·269 according to Plavec and Kratochvil (1964). We thus confirm the undersized nature of the secondary in TT Hya.

In Table 7 we give the colours and spectral types of the two components obtained from the present study. The UV excess is present in secondary, but its value is reduced from 0·60 to 0·35 magnitude because the spectral type of that star is found to be G8 III instead of Kl III.

Acknowledgement

J.K. is thankful to University Grants Commission, New Delhi for the award of a Junior Research Fellowship.

References

Hall, D. S. 1974, *Acta Astr.,* **24**, 215.
Kopal, Z. 1979, *Language of the Stars,* D. Reidel, Dordrecht.
Kulkarni, A. G. 1979, *Ph D Thesis,* Osmania University, Hyderabad.
Kulkarni, A. G., Abhyankar, K. D. 1978, *Contr. Nizamiah Japal-Rangapur Obs.,* No. 9.
Kulkarni, A. G., Abhyankar, K. D. 1980, *Astrophys. Sp. Sci.,* **67,** 205.
Kulkarni, A. G., Abhyankar, K. D. 1981, *J. Astrophys. Astr.,* **2,** 119.
Livaniou, H. J. 1977, *Astrophys. Sp. Sci.,* **51,** 77.
Plavec, M., Kratochvil, P. 1964, *Bull. astr. Inst. Czl.,* **15**, 165.
Shapley, M. B. 1927, *Harvard Coll. Obs. Bull.,* No. 847**,** 12.

J. Atrophy's. Astr. (1982) **3**, 101–105

Spectroscopic Binaries near the North Galactic Pole Paper 4: HD120803

R. F. Griffin *The Observatories, Madingley Road, Cambridge, England, CB3OHA*

Received 1982 January 25; accepted 1982 February 20

Abstract. Photoelectric radial-velocity measurements show that HD 120803 is a spectroscopic binary with a rather eccentric orbit and a period of 700 days. Early DDO photographic observations, published individually here for the first time, fit the orbit well.

*Key words:*radial velocities—spectroscopic binaries—stars, individual

HD 120803 is a late-type giant star, about 7° north-preceding Arcturus in the sky. Photometry by Häggkvist and Oja (1973) shows its magnitude and colours to be V = 7·61, $(B - V)$= 1·16, and $(U - B)$ = 1·09; Eggen (1976) gives V = 7·58, $(B - V)$= 1·17 and $(U - B)$ = 1·035, and deduces from an estimate of its space motion that it is an old-disk object and probably a member of the "Arcturus group".

About thirty years ago, the David Dunlap Observatory made a radial-velocity survey (Heard 1956) of more than a thousand stars in the + 25° to + 30° zone of declination; HD 120803 was one of them. In its entry in the published catalogue, a velocity of — 47·4 km s^{-1} is quoted as the mean of six plates, whose results are not given individually. The statistical test used by Heard to assess radial-velocity variability showed that the DDO measurements did not demonstrate variability of HD 120803 at the 5 per cent significance level. The DDO survey included MK spectral classifications as well as radial velocities; HD 120803 is given as type K1 III, which accords well with its colours.

Radial-velocity variations of HD 120803 were discovered with the Cambridge photoelectric spectrometer (Griffin 1967) in 1974, and the 73 observations shown in Table 1 have now been accumulated. The period is close to two years, a circumstance which has made it difficult to obtain uniform phase coverage of the orbit and accounts for the efforts made to maximize the length of the observing season—October is the only calendar month not represented in Table 1.

Table 1 lists not only the photoelectric measurements but also the photographic ones, which were kindly made available by the DDO. There are eight photographic

Table 1. Radial-velocity measurements of HD 120803.

	Date	MJD	Velocity km s^{-1}	Phase	$(O-C)$ km s^{-1}
1947 Apr	15·25*	32290·25	−41·0	0·139	−4·7
1948 Feb	5·45*	32586·45	−53·9	0·563	+0·2
1950 May	14·19*	33415·19	−64·2	1·748	−1·9
1951 Apr	20·28*	33756·28	−27·3	2·236	+12·3
	27·27*	763·27	−34·7	·246	+5·3
1952 June	5·16*	34168·16	−64·6	2·825	+0·6
July	11·17*	204·17	−62·2	·876	+3·8
1953 July	28·08*	34586·08	−43·3	3·422	+4·6
1973 Apr	25·07	41797·07	−60·6	13·735	+1·1
1974 Apr	15·05	42152·05	−39·3	14·242	+0·5
May	8·12†	175·12	−42·1	·275	−0·8
	30·21	197·21	−42·2	·307	+0·6
July	28·88	256·88	−45·6	·392	+1·0
Dec	30·25	411·25	−56·7	·613	−0·4
1975 Jan	13·21	42425·21	−57·3	14·633	−0·1
Feb	28·10	471·10	−59·6	·699	+0·5
Mar	7·14	478·14	−59·2	·709	+1·4
Apr	8·01	510·01	−61·5	·754	+1·0
	20·04	522·04	−63·2	·771	+0·1
	28·99	530·99	−65·4	·784	−1·6
May	30·96	562·96	−65·9	·830	−0·5
June	5·91	568·91	−65·8	·839	−0·2
	20·91	583·91	−64·3	·860	+1·7
July	2·90	595·90	−65·2	·877	+0·8
Aug	3·87	627·87	−64·6	·923	−0·3
	25·85	649·85	−59·3	·954	+1·3
1976 Jan	24·21	42801·21	−37·0	15·171	0·0
Mar	1·12	838·12	−40·5	·223	−1·5
Apr	4·05	872·05	−41·2	·272	0·0
	22·99	890·99	−41·9	·299	+0·5
May	4·02	902·02	−42·9	·315	+0·2
June	7·93	936·93	−45·1	·365	+0·3
July	9·15‡	968·15	−47·6	·409	−0·2
	31·88	990·88	−47·1	·442	+1·7
Aug	15·85	43005·85	−50·2	·463	−0·5
1977 Jan	30·20	43173·20	−62·0	15·703	−1·7
Mar	28·10	230·10	−64·2	·784	−0.4
Apr	16·00	249·00	−64·9	·811	−0·1
	26·99	259·99	−64·7	·827	+0·6
May	24·94	287·94	−67·2	·867	−1·2
June	1·94	295·94	−65·5	·878	+0·5
	10·95	304·95	−66·3	·891	−0·4
July	15·90	339·90	−62·7	·941	−0·2
	29·92	353·92	−58·8	·961	+0·6
Sept	3·82	389·82	−47·9	16·012	0·0
Nov	25·28	472·28	−35·9	·130	+0·3

Table 1. Concluded.

	Date	MJD	Velocity km s^{-1}	Phase	$(O-C)$ kms^{-1}
1978 Jan	18·24	43526·24	−39·7	16·208	−1·3
	23·20	531·20	−38·1	·215	+0·6
Mar	24·11	591·11	−43·0	·300	−0·5
Apr	13·01	611·01	−43·9	·329	−0·1
May	23·23‡	651·23	−47·3	·386	−1·0
June	12·02	671·02	−46·0	·415	+1·6
July	26·90	715·90	−51·2	·479	−0·8
Aug	18·86	738·86	−50·8	·512	+1·1
Nov	16·26	828·26	−58·3	·639	−0·8
1979 Jan	3·28	43876·28	−60·0	16·708	+0·5
	13·22	886·22	−61·2	·722	0·0
Feb	25·19	929·19	−63·8	·784	0·0
Mar	12·11	944·11	−64·6	·805	0·0
Apr	25·09	988·09	−65·9	·868	+0·1
May	18·96	44011·96	−65·7	·902	−0·2
	23·96	016·96	−65·8	·909	−0·6
June	22·97	046·97	−60·8	·952	+0·1
July	11·92	065·92	−57·6	·979	−1·9
Aug	27·83	112·83	−41·0	17·046	+0·2
1980 Jan	2·27	44240·27	−39·2	17·229	+0·1
May	9·97	368·97	−49·1	·413	−1·6
July	21·90	441·90	−52·3	·517	−0·2
Aug	20·85	471·85	−53·6	·560	+0·4
	31·82	482·82	−55·0	·576	−0·3
1981 Mar	13·13	44676·13	−67·2	17·852	−1·3
May	2·99	726·99	−63·6	·925	+0·6
	31·97	755·97	−58·4	·966	+0·1
June	28·90	783·90	−47·5	18·006	+1·9
July	4·92	789·92	−47·5	·015	−0·1
	16·89	801·89	−45·0	·032	−1·3
	18·90	803·90	−45·0	·035	−1·8
	26·89	811·89	−41·6	·046	−0·4
Aug	2·88	818·88	−39·5	·056	+0·3
	10·87	826·87	−36·8	·068	+1·7
	16·85	832·85	−37·2	·076	+0·6

*DDO photographic observation, not used in orbital solution.
†Observed by Dr G. A. Radford with the Cambridge spectrometer.
‡Observed, in collaboration with Dr J. E. Gunn, with the 200-inch telescope (Griffin and Gunn 1974).

measures, although only six were included in the published mean: Heard rejected the two plates taken in 1951, not only because they were weakly exposed but also because he felt some doubt (since dispelled) as to whether the plates were of the correct star. The first plate in Table 1 was obtained with the 25-inch camera, which gave a dispersion of 33 **Å** mm^{-1} at Hγ; all the others were taken with the 12y-inch camera (66 **Å** mm^{-1}). A systematic correction of — 5·0 km s^{-1}, which has been found desirable for observations of late-type stars at the lower dispersion (Griffin 1980), has been applied to the 66 **Å** mm^{-1} velocities in Table 1.

The orbital solution is based only on the photoelectric measures. It is illustrated in Fig. 1 and has elements as follows:

$P = 699{\cdot}3 \pm 0{\cdot}9$ days	$(T)_{16}$	$=$ MJD 43381 $\pm$ 3
$\gamma = -51{\cdot}21 \pm 0{\cdot}13$ km s^{-1}	$a_1 \sin i$	$= 131{\cdot}4 \pm 1{\cdot}8$ Gm
$K = 14{\cdot}93 \pm 0{\cdot}19$ km s^{-1}	$f(m)$	$= 0{\cdot}185 \pm 0{\cdot}007\ M_\odot$
$e = 0{\cdot}402 \pm 0{\cdot}009$		
$\omega = 270{\cdot}9 \pm 1{\cdot}9$ degrees	rms residual $= 0{\cdot}9$ km s^{-1}	

It is apparent from Fig. I that the DDO photographically-determined velocities fall satisfactorily close to the computed velocity curve, especially if the two under-exposed plates (the two highest velocities) are disregarded. However, it was not thought appropriate to include the DDO velocities in the orbital solution, because (a) they are considerably less accurate than the photoelectric observations, (b) there is none on the rising branch of the velocity curve, so a zero-point error will mimic a phase shift (Griffin 1981) and introduce an error in the period, and (c) because the original author (Heard 1956) considered that they did not demonstrate any velocity variation at all.

The mass function of HD 120803 is quite large, and implies a secondary mass running from 0.74 to 1.85 $M_\odot$ as the assumed primary mass ranges from 0.74 to 4.0 $M_\odot$. However, no secondary dip has been seen in the radial-velocity traces, and the photometric colours are entirely normal for the spectral type; so it seems safe to deduce that the secondary star, though of considerable mass, is substantially fainter than the primary.

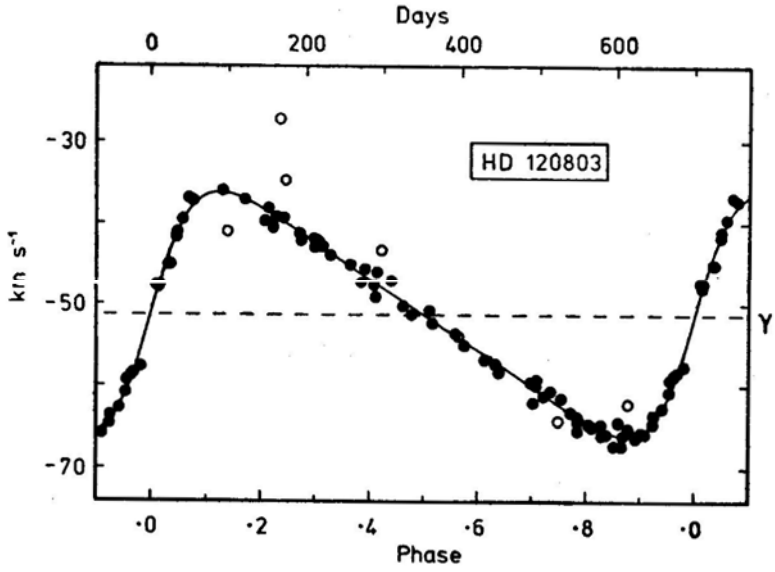

Figure 1. The computed radial-velocity curve for HD 120803, with the measured radial velocities plotted. The filled circles represent the photoelectric measures; the open circles show the early DDO photographic observations, which were not used in the orbital solution.

Acknowledgements

It is a pleasure to thank Drs C. T. Bolton, J. D. Fernie and D. A. MacRae for supplying the individual DDO plate velocities.

Reference

Eggen, O. J. 1976, *Publ. astr. Soc. Pacific*, **88,** 426.
Griffin, R. F. 1967, *Astrophys. J.*,**148,** 465.
Griffin, R. F. 1980, *J. R. astr. Soc. Can*., **74,** 348.
Griffin, R. F. 1981, *J. Astrophys. Astr*., **2,** 115.
Griffin, R. F., Gunn, J. E. 1974, Astrophys. J., **191,** 545.
Haggkvist, L., Oja, T. 1973, *Astrophys. Suppl. Ser*., **12,** 381.
Heard, J. F. 1956, *Publ. Dunlap Obs*., **2,** 105.

J. Astrophys. Astr. (1982) **3**, 107-109

Spectroscopic Binaries near the North Galactic Pole
Paper 5: HD 117064

R. F. Griffin *The Observatories, Madingley Road, Cambridge, England, CB3 OHA*

Received 1982 April 21; accepted 1982 May 6

Abstract. Photoelectric radial-velocity measurements, which, in 1971 showed HD 117064 to be a spectroscopic binary, have been continued and now permit the derivation of an eccentric orbit with a period of 6·08 years.

Key words: radial velocities—spectroscopic binaries—stars, individual

HD 117064 was first observed for radial velocity in the course of the Cambridge work on the 15° Selected Areas (Griffin 1971). Velocity variations were definitely established by that work, so the star has remained under systematic observation with the photoelectric spectrometer (Griffin 1967) at the Cambridge 36-inch telescope. A total of 62 observations, extending over an interval of more than 16 years, is now available for discussion. Those measurements are set out in Table 1 and yield the orbit shown in Fig. 1 having the following elements:

$P = 2222 \pm 9$ days	$(T)_2$	$=$ MJD 42495 $\pm$ 19
$\gamma = -7{\cdot}81 \pm 0{\cdot}16$ km s^{-1}	$a_1 \sin i$	$= 151 \pm 8$ Gm
$K = 5{\cdot}70 \pm 0{\cdot}26$ km s^{-1}	$f(m)$	$= 0{\cdot}028 \pm 0{\cdot}004\ M_\odot$
$e = 0{\cdot}50 \pm 0{\cdot}03$		
$\omega = 231 \pm 5$ degrees	rms residual $= 1{\cdot}1$ km s^{-1}	

Nicolet (1978) lists the magnitude and colours of HD 117064 as $V = 9{\cdot}10$, $(B - V) = 0{\cdot}97$, and $(U - B) = 0{\cdot}77$. Unpublished photometry in the Copenhagen system, obtained at Palomar Observatory by G. A. Radford and the author and reduced by L. Hansen, shows the star to be a giant, as indeed the smallness of its proper motion (Barney 1947, Heckmann and Dieckvoss 1975) would lead one to expect. Its colours would be consistent with a spectral type of about G8 III; the only actual classification available is, however, the HD type of K0 (Cannon and Pickering 1920).

Table 1. Photoelectric radial-velocity measurements of HD 117064.

Date		MJD	Velocity km s^{-1}	Phase	$(O-C)$ km s^{-1}
1966 Feb	27·08	39183·08	−8·2	0·509	−2·1
	28·09	184·09	−4·3	·510	+1·8
1969 Apr	18·06	40329·06	−10·6	1·025	−0·2
	28·98	339·98	−10·3	·030	−0·4
1970 Mar	19·14	40664·14	−3·0	1·176	+0·9
July	12·91	779·91	−3·9	·228	0·0
1971 Feb	14·10	40996·10	−5·6	1·325	−1·2
	21·17	41003·17	−5·5	·329	−1·0
1972 Mar	28·04	41404·04	−9·0	1·509	−2·9
Apr	8·06	415·06	−6·7	·514	−0·5
1973 Feb	24·21	41737·21	−6·8	1·659	+1·3
June	12·21*	845·21	−8·3	·707	+0·6
Dec	17·59*	42033·59	−9·9	·792	+0·8
1974 Apr	15·03	42152·03	−14·2	1·846	−2·1
May	30·20*	197·20	−11·7	·866	+1·1
Dec	30·23	411·23	−16·9	·962	−1·7
1975 Jan	13·20	42425·20	−14·2	1·968	+0·9
Feb	28·08	471·08	−12·9	·989	+1·2
Apr	3·07	505·07	−13·9	2·004	−1·2
	20·02	522·02	−12·6	·012	−0·7
May	4·98	536·98	−8·7	·019	+2·4
	30·94	562·94	−10·0	·030	−0·2
June	21·92	584·92	−9·4	·040	−0·6
1976 Jan	24·23	42801·23	−4·6	2·138	−0·4
Mar	1·11	838·11	−3·1	·154	+1·0
Apr	4·05	872·05	−2·1	·170	+1·9
	22·98	890·98	−5·4	·178	−1·5
1977 Jan	30·19	43173·19	−3·5	2·305	+0·8
Mar	28·10	230·10	−4·6	·331	−0·1
Apr	15·99	248·99	−5·0	·339	−0·5
	30·99	263·99	−3·9	·346	+0·7
May	27·95	290·95	−3·3	·358	+1·4
July	5·91	329·91	−4·31	·376	+0·5
1978 Jan	18·23	43526·23	−7·0	2·464	−1·4
Mar	24·10	591·10	−6·4	·493	−0·4
May	23·22*	651·22	−6·0	·520	+0·2
June	18·94	677·94	−5·1	·532	+1·3
Nov	20·26	832·26	−6·7	·602	+0·5
1979 Jan	3·27	43876·27	−7·5	2·621	0·0
Feb	25·18	929·18	−8·6	·645	−0·7
Mar	8·12	940·12	−8·3	·650	−0·4
	22·01	954·01	−8·4	·656	−0·4
Apr	29·04	992·04	−6·3	·674	+2·0
May	14·00	44007·00	−8·3	·680	+0·1
	23·96	016·96	−7·5	·685	+1·0
Dec	25·26	232·26	−10·4	·782	0·0

Table 1. Concluded.

Date		MJD	Velocity km s^{-1}	Phase	$(O-C)$ km s^{-1}
1980 Jan	13·26	44251·26	−11·3	2·790	−0·7
Feb	23·17	292·17	−11·1	·809	0·0
May	3·97	362·97	−11·5	·840	+0·5
	15·94	374·94	−11·9	·846	+0·3
July	22·90	442·90	−14·7	·876	−1·6
Dec	7·25	580·25	−14·8	·938	+0·3
1981 Jan	17·26	44621·26	−15·2	2·957	+0·1
Mar	1·10	664·10	−13·7	·976	+1·1
Apr	18·02	712·02	−12·8	·998	+0·6
	28·02	722·02	−14·6	3·002	−1·7
May	31·95	755·95	−11·9	·017	−0·6
June	21·95	776·95	−11·2	·027	−1·0
	28·92	783·92	−8·9	·030	+1·0
July	16·90	801·90	−8·0	·038	+1·0
1982 Jan	10·25	44979·25	−4·9	3·118	−0·3
Mar	5·15	45033·15	−5·0	·142	−0·8

*Observed, in collaboration with Dr J.E.Gunn, the 200-inch telescope (Griffin and Gunn 1974).

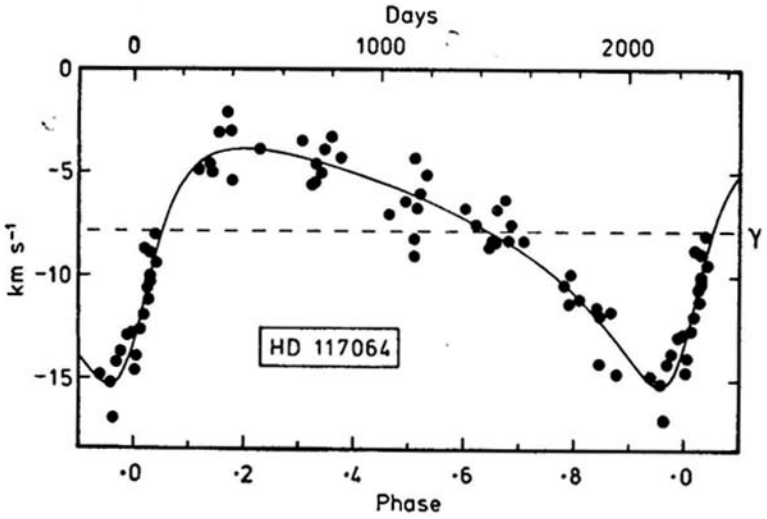

Figure 1. The computed radial-velocity curve for HD 117064, with the measured radial velocities plotted.

References

Barney, I. 1947, *Trans, astr. Obs. Yale University,* **18,** 95.
Cannon, A. J., Pickering, E. C. 1920, *Ann. Han. Coll. Obs.,* **95,** 137.
Griffin, R. F. 1967, *Astrophys. J.,* **148,** 465.
Griffin, R. F. 1971, *Mon. Not. R. astr. Soc.,* **155,** 1.
Griffin, R. F., Gunn, J. E. 1974, *Astrophys. J.*, **191,** 545.
Heckmann, O., Dieckvoss, W. 1975, *AGK3,* Hamburger Sternwarte, Hamburg-Bergedorf, **6,** 137.
Nicolet, B. 1978, *Astr. Astrophys. Suppl. Ser.,* 3**4,** 1.

J. Astrophys. Astr. (1982) **3,** 111–123

The Jeans Problem for a Thin Galaxy in Steady State

Robert Whitley *University of California, Irvine, California 92717, USA*

Received 1981 November 25; accepted 1982 March 12

Abstract. Given the potential, the equation of continuity and Poisson's equation are solved for the variation perpendicular to the Galactic plane for a thin galaxy in a steady state. Simple expressions are obtained for the joint density function for the mass density and velocity, and for the distribution function for the velocity and its moments.

These results are applied using a potential suggested by Woolley and Stewart (1967) and Whitley (1977), which is Camm's potential due to an isothermal gas stratified in parallel layers, *plus* the potential due to the Galactic centre. The resulting velocity distribution is quite close to the normal distribution usually assumed and cannot be distinguished from it by the data. The mass density distribution fits the log (relative density) curves better than the Camm solution, especially at large distances from the Galactic plane.

A formula, valid under conditions more general than usual, is found for the total mass density in the neighbourhood of the Sun.

Key words: Jeans problem—disk galaxies—local mass density

1. Introduction

In order to introduce notation, we begin with well-known equations and results: the equation of continuity

$$\frac{\omega^* \, \partial\psi^* \, (z^*, \ldots^*)}{\partial z^*} - \frac{\partial V^* \, (z^*)}{\partial z^*} \frac{\partial\psi^* \, (x^*, \omega^*)}{\partial\omega^*} = 0, \tag{1}$$

Poisson's equation

$$\frac{d^2 \, V^*}{d(z^*)^2} = 4\pi G\rho^*(z^*), \qquad V^*(0) = \frac{dV^*}{dz^*}(0) = 0, \tag{2}$$

and the density integral

$$\rho^*(z^*) = m^* \int \psi^* (z^*, \omega^*)\, d\omega^* \tag{3}$$

for the steady state problem of variations perpendicular to the galactic plane in a thin galaxy (Lindblad 1959; Lin and Segel 1974).

The asterisks denote unscaled variables which will be scaled in the next paragraph; ψ^* is the density function for the number of stars (all of which are assumed to have mass m^*), ω^* the velocity, z^* the height above the galactic plane, V^* the potential, ρ^* the mass density of the stars, and G the gravitational constant. The general solution of Equation (1) is

$$\psi^*(z^*, \omega^*) = f^* [\tfrac{1}{2}(\omega^*)^2 + V^*(z^*)] \tag{4}$$

with $\frac{1}{2}(\omega^*)^2 + V^*(z^*)$ the energy per unit mass integral.

The scaling parameters β and z_0 are used to define

$$\omega = \sqrt{\beta}\omega^*, \quad V = \beta V^*, \quad z = z^*/z_0 \quad \text{and} \quad z_0^2 = [2\pi G\beta\rho^*(0)]^{-1}. \tag{5}$$

The scaled mass density and density functions are

$$\rho = \rho^*/\rho^*(0) \quad \text{and} \quad f(E) = f^* (E/\beta). \tag{6}$$

In terms of this scaling

$$\frac{d^2V(z)}{dz^2} = 2\rho(z), \qquad V(0) = \frac{dV}{dt}(0) = 0, \tag{7}$$

and

$$\rho(z) = \frac{1}{A_0\sqrt{2\pi}} \int f [\tfrac{1}{2}\omega^2 + V(z)]\, d\omega, \tag{8}$$

where

$$A_0 = \left[\frac{m^*}{\rho^*(0)} \sqrt{2\pi/\beta}\right]^{-1}.$$

Camm's (1950) important solution to Equations (7) and (8), corresponding to an isothermal gas stratified in parallel layers is

$$V_0(z) = 2 \ln \cosh (z), \qquad \rho_0(z) = \operatorname{sech}^2 (z),$$

$$\ln f_0(E) = \ln A_0 - E, \quad E = \tfrac{1}{2}\omega^2 + V_0(z). \tag{9}$$

For stars of type A or A0, it is found that the Camm solution (9) gives a reasonably good fit to the observed density and velocity distributions, except that the empirical log (relative density) curves show an upward curvature at large distances from the Galactic plane (Woolley 1957; Wolley and Stewart 1967), which is not present in Equations (9). In Whitley (1977) it was shown that a possible explanation for this curvature is, qualitatively, that while for a star near the Galactic plane the local Galactic potential does indeed resemble that given by an isothermal gas stratified in parallel layers, a higher star sees a less homogeneous mass, namely the plane layers plus the concentrated mass of the Galactic centre. To quote Hill, Hilditch and Barnes (1979), 'Camm's formulation does not take account of the high concentration of matter towards the Galactic centre, a factor which becomes increasingly important as we proceed to larger distances from the plane.' The potential due to the mass of the Galactic centre adds to Camm potential; after scaling, the effect is that of taking a given (say unit) mass which is distributed in parallel planes and redistributing it, putting more at the Galactic centre, and less in the planes. This leads to an upward curvature in the log (relative density) curves for large z. Quantitatively, this effect was calculated by perturbing In f_0 of Equations (9) by a truncated quadratic term, using perturbation methods to solve the resulting equations, and then choosing the two parameters occuring in the perturbed ρ so as to obtain a curve fitting the data

Several problems remain after this perturbation treatment: The perturbation approximation to ρ gives a good fit out to about 400 pc, but then breaks down and ln ρ begins to curve up far too sharply (see Fig. 4 in Whitley 1977). The perturbed f^* is defined by In f^* $(E) = \alpha - \beta E + \epsilon E^2$, $\epsilon > 0$ for $E \leqslant E_0$, and ln f^* $(E) = \alpha - \beta E$ for $E > E_0$. This truncation at E_0 was necessary to make the integrals converge. Because the accuracy of the perturbation solution depends on E_0 in a complex way, E_0 must be chosen carefully even though it is so large that $f^*(E)$ is quadratic over all physically realisable energies (see Table 2 of Whitley 1977).

The mass density in the neighbourhood of the sun can be calculated from three parameters. Two of these three parameters, z_0 and ϵ, ϵ being 0 in Equations (9), were determined from density data in a way which takes into account the effect of the perturbation by the Galactic centre. The third parameter β, which is obtained from the velocity data, was not adjusted for this perturbation effect, mainly because of the difficulty of obtaining the perturbed form of the velocity distribution. And because of this difficulty in obtaining the perturbed velocity distribution, it could not be shown that it was close to normal and hence consistent with the data.

The problem of obtaining an accurate formula for the total mass density in the neighbourhood of Sun is more subtle than supposed in Whitley (1977)—see Section 4 below.

It turns out that all these problems can be solved if we begin with the potential suggested by the final results of Woolley and Stewart (1967) and Whitley (1977). To do this we must solve the 'Jeans problem' (Freeman 1975), *i.e.* assuming that V is given, obtain f and useful information about the velocity distribution. [Prendergast (1954) solves the inverse Jeans problem; assuming f given, he obtains V.] Then we can apply a generalized form of Oort's assumptions and these solutions for a hypothetical system of stars of equal mass can be used to determine the local Galactic mass density.

2. The Jeans problem

Assume that we are given the potential V. Prendergast (1954) shows that V is symmetric about the plane which divides the system into equal masses. We will suppose this plane to be the Galactic plane and therefore suppose that the given V is even in z.

The density ρ can be directly obtained from Equation (7), so knowing V we know ρ. Our first problem will be to obtain f from Equation (8). Since $f\,[\frac{1}{2}\omega^2 + V(z)]$ is even in both ω and z it will suffice to consider ρ for $z \geq 0$ given by

$$\rho(z) = \frac{2}{A_0\sqrt{2\pi}} \int_0^\infty f[\tfrac{1}{2}\omega^2 + V(z)]\, d\omega. \tag{10}$$

In Section 4 we will need the solution of the more general equation where no relation holds between ρ and V. To emphasize this generality we will put $\rho = \rho_1$ in Equation (10). Substitute $t = \frac{1}{2}\omega^2 + V(z)$ and, noting that Equation (7) shows that V is increasing, introduce the function g, defined for $z \geq 0$ by

$$g(z) = A_0\sqrt{\pi}\,\rho_1\,[V^{-1}(z)]. \tag{11}$$

Then Equation (10) becomes

$$g(z) = \int_z^\infty f(t)\,(t - z)^{-1/2}\, dt,$$

an equation which can be put into the form of Abel's integral equation by the change of variables $u = 1/t$ and $x = 1/z$ (also see Morse and Feshbach 1953):

$$g(1/x)x^{-1/2} = \int_0^x f(1/u)u^{-3/2}\,(x - u)^{-1/2}\, du,$$

which has the solution (Hochstadt 1973),

$$f(1/t)t^{-3/2} = \frac{1}{\pi}\frac{d}{dt}\int_0^t g(1/u)u^{-1/2}\,(t - u)^{-1/2}\, du.$$

Let $s = 1/t$ and $y = 1/u$, then let $u^2/2 = y/s - 1$, and then set $t^2 = su^2/2$ to obtain

$$f(s) = -(2/\pi)\int_0^\infty g'\,(t^2 + s)dt. \tag{12}$$

Substituting for g from Equation (11) and letting $y = V^{-1}(t^2 + s)$ for $s \geq 0$, Equation (12) can be written as

$$f(s) = \frac{-A_0}{\sqrt{\pi}} \int_{V^{-1}(s)}^{\infty} \rho_1'(y)\,[V(y) - s]^{1/2}\,dy. \tag{13}$$

Numerical calculations using Equation (13) are simplified by removing the singularity with an integration by parts.

For the rest of this section we will take $\rho_1 = \rho$ and suppose that $V'' = 2\rho$.

The two random variables, the velocity W, and the height Z, have a joint probability density function $cf\,[\frac{1}{2}\omega^2 + V(z)]$, the constant c being determined by the condition

$$1 = \int\int cf[\tfrac{1}{2}\omega^2 + V(z)]\,d\omega dz = A_0 c\sqrt{2\pi}\int \rho(z)\,dz = cA_0\sqrt{2\pi}\,V'(\infty).$$

So

$$c = [A_0\,V'(\infty)\,\sqrt{2\pi}]^{-1}. \tag{14}$$

(Note that from a probabilistic point of view, Camm's solution (9) corresponds to the case where Z and W are independent; this simple probabilistic relationship is reflected by the simple form of the solution.)

To obtain the distribution function F_W for the velocity W, defined by $F_W(t)$ = prob ($W \le t$), we need to evaluate

$$F_W(t) = c\int_{-\infty}^{t}\int_{-\infty}^{\infty} f[\tfrac{1}{2}\omega^2 + V(z)]\,dzd\omega$$

$$= \tfrac{1}{2} + 2c\int_{0}^{t}\int_{0}^{\infty} f[\tfrac{1}{2}\omega^2 + V(z)]\,dzd\omega$$

which, using Equations (13) and (14) becomes

$$F_W(t) = \tfrac{1}{2} - \frac{\sqrt{2}}{\pi V'(\infty)}\int_0^t\int_0^\infty\int_{V^{-1}[\frac{1}{2}\omega^2 + V(z)]}^{\infty} \rho'(y)\left[V(y) - \frac{\omega^2}{2} - V(z)\right]^{-1/2} dydzd\omega. \tag{15}$$

It is most helpful that Equation (15) can be substantially simplified by interchanging the order of integration:

$$F_W(t) = \tfrac{1}{2} - \frac{\sqrt{2}}{\pi V'(\infty)}\int_0^\infty\int_0^y\int_0^{\min(t,\,\sqrt{2}[V(y)-V(z)]^{1/2})} \rho'(y)\left[V(y) - \frac{\omega^2}{2} - V(z)\right]^{-1/2} d\omega dzdy$$

$$F_W(t) = \tfrac{1}{2} - \frac{\sqrt{2}}{\pi V'(\infty)}\int_0^\infty \rho'(y)\int_0^y \sin^{-1}\left(\min\left\{1,\,\frac{t}{\sqrt{2}}[V(y) - V(z)]^{-1/2}\right\}\right)dzdy. \tag{16}$$

The moments of W can be computed in the same way. The odd moments of W are zero, by symmetry, so we will compute the absolute moments $E(|W|^k) = M_k$. By definition

$$M_k = \int_{-\infty}^{\infty} |\omega|^k \int_{-\infty}^{\infty} cf[\tfrac{1}{2}\omega^2 + V(z)]\, dzd\omega.$$

Substitute from Equations (13) and (14) and interchange the order of integration, as above, to obtain

$$M_k = \frac{2^{k/2+1}}{V'(\infty)\sqrt{\pi}} \frac{\Gamma\left(\frac{k+1}{2}\right)}{\Gamma\left(\frac{k+2}{2}\right)} \int_0^{\infty} [-\rho'(y)] \int_0^{y} [V(y) - V(z)]^{k/2}\, dzdy. \tag{17}$$

Similar expressions for the expectation of simple functions of Z and W can be computed analogously.

3. Camm's potential plus the potential due to the Galactic centre

Suppose that our hypothetical system of stars of the same mass has a substantial concentration near the Galactic centre, which we will regard as a point of mass M at a distance R from the place in the Galactic plane from which we measure z^*. The corresponding force F per unit mass at a height z^* has as its component in the z^*-direction

$$-\frac{MG}{R^2}(z^*/R)\,[1 + (z^*/R)^2]^{-3/2}.$$

Temporarily treat R as a variable. Then

$$-MG[(z^*)^2 + R^2]^{-1/2}$$

is a potential with gradient — F. Because the basic equations (1) to (3) for a thin galaxy are in terms of only the variable z^*, we fix R and regard this potential $V_c^*(z^*)$ as a function of z^* alone. As long as z^* is much less than R, $V_c^*(z^*)$—as a function only of z^* —is 'almost a potential' in the sense that $dV_c^*(z^*)/dz^*$ is the one component of a force which accounts for nearly all of the force. Add a constant to V_c^* so that

$$V_c^*(0) = \frac{d}{dz^*} V_c^*(0) = 0,$$

to obtain

$$V_c^*(z^*) = \frac{MG}{R}\left\{1 - \frac{1}{[1 + (z^*/R)^2]^{1/2}}\right\}.$$

Camm's potential V_0^* plus V_c^* is:

$$\frac{2}{\beta_0}\ln\cosh(z^*/z_0) + \frac{2a}{\beta_0 b^2}\{1 - [1 + (bz^*/z_0)^2]^{-1/2}\}$$

where β_0 is the scale factor for V_0^*, $b = z_0/R$, and a is the constant $MG\beta_0 b^2/2R$. Using Poisson's equation

$$4\pi G\rho^*(z^*) = \frac{2}{\beta_0 z_0^2}\{\operatorname{sech}^2(z^*/z_0) + a[1 - 2(bz^*/z_0)^2][1 + (bz^*/z_0)^2]^{-5/2}\}.$$

Evaluate at $z^* = 0$ to see that with z_0 given by Equation (5) we must have $\beta = \beta_0/(1 + a)$. The scaled version of $V_0^* + V_c^*$ is

$$V(z) = \frac{1}{1+a}[2\ln\cosh z + \frac{2a}{b^2}\{1 - [1 + (bz)^2]^{-1/2}\} \tag{18}$$

and

$$\rho(z) = \frac{1}{1+a}\{\operatorname{sech}^2(z) + a[1 - 2(zb)^2][1 + (zb)^2]^{-5/2}\}. \tag{19}$$

One consequence of the fact that V_c^*, and hence V, differs from a true potential, is that $\rho(z)$, given by Equation (19) is not a true density and can be negative for $z > (b\sqrt{2})^{-1}$When we apply this model to A-type stars in our Galaxy, z_0 turns out to be about 200 pc and b about 0·02, and so ρ is negative for $z^* > 7000$ pc and therefore there is not much cause for concern about this anomaly. In fact, for $z = 3$, corresponding to about 600 pc, the factor multiplying a in Equation (19) is 0·98. Thus for all z of interest

$$\rho(z) = \frac{1}{1+a}[\operatorname{sech}^2(z) + a]. \tag{20}$$

In what follows we will use Equation (20) and the corresponding

$$V(z) = \frac{1}{1+a}[2\ln\cosh(z) + az^2]. \tag{21}$$

This potential has the same form as that adopted by Hill, Hilditch and Barnes (1979, p. 816). They evaluate a via the rotation of the Galaxy, as we discuss at the end of Section 4.

As will be discussed in Section 4, a fundamental assumption is that the form of ρ for a suitably chosen class of stars is that given by Equation (20). This equation was applied to A-type stars by doing a least-squares fit of ln ρ to data taken from the log (relative density) graph of Woolley (1957, p. 209), for $z = 0(25)500$. The same procedure was followed for the data on A0 stars from Woolley and Stewart (1967, p. 336), for $z = 0(25)550$. Fig. 1 shows both the results. The parameter values are:

A stars (Woolley 1957) $a = 0{\cdot}20$ $z_0 = 185$ pc,

A0 stars (Woolley and Stewart 1967) $a = 0{\cdot}18$ $z_0 = 200$ pc. (22)

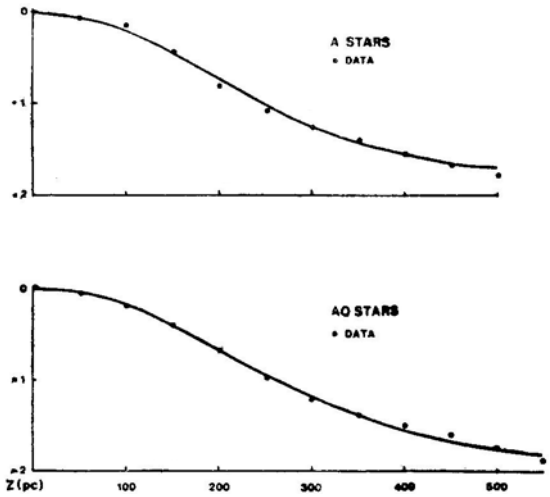

Figure 1. Theoretical fit to the data on A stars (top) from Woolley (1957) and the data on A0 stars (bottom) from Woolley and Stewart (1967). The ordinates are log (relative density) and abscissae the height z(pc) above the galactic plane.

In comparison, the fit obtained using the Camm solution (9) is about the same for $z \leq z_0$, but is a straight line for larger z.

A possible alternative is to find a and z_0 by using moments of ρ. This method of Nation's is discussed in Lindblad (1959 pp. 50-51). (Note that even in the case of $a = 0$, the height out to which ρ is observed must be taken into account; see Whitley 1977, p. 331), Since a good test of the parameter values is how well the curve fits the data, leasts-quares is a good criterion to use in determining them; except in the case $a = 0$ where the poor fit for large values of z will distort the value obtained for z_0.

The value of a controls the amount of upward curvature in In ρ and, since this curvature is mostly in evidence for large z, will depend on the densities at these hard-to-observe heights. To get an idea of the size of this effect we can compute a and z_0 using smaller values of z only. For example, Table 5 in Woolley and Stewart (1967) contains their A0 density data for z out to 350 pc; for larger values of z they use the data of van Rhijn, which is given as a straight line in the range 350 to 500 pc Using the data of Table 5 gives a = 0155 (*versus* 0·179) and z_0 = 199(*versus* 200). The same calculation for the A stars for z = 0(25)350 gives a = 0·211 (*versus* 0·196) and z_0 = 181 (*versus* 185).

The function In $f(E)$ can be calculated from Equation (13) using Equations (20) and (21). A realistic range of energy *is* $E \leq 10$. At $z = 3$, corresponding to about 600 pc, $V(3) \leq 5{\cdot}5$ for $a \leq 0{\cdot}2$. The velocities are approximately normally distributed (see below), exactly so for $a = 0$, and so $W^2/2 \leq 3^2/2$ with high probability. Thus $W^2/2 + V(z) \leq 10$ for nearly all observable stars. For $E \leq 10$ and $a \leq 0{\cdot}2$, In $f(E)$ has the form studied in Whitley (1977) as a perturbation. For example, calculations show that for $E \leq 10$, to within three per cent ln $f(E)$ is given by $-E + \epsilon E_2$, where $\epsilon = 0{\cdot}013$ for $a = 0{\cdot}1$ or $\epsilon = 0{\cdot}019$ for $a = 0{\cdot}2$.

Equation (16) can be used to compare the distribution of the velocity W with that of a normal distribution $N = N(0, 1)$ (in the determination of the constant c by Equation (14), recall that $\frac{d}{dz^*} V_c^*(\infty) = 0$). The result of this calculation is that for

$a \leq 0{\cdot}2$, the distribution function F_W differs from F_N by less than 0·01. To detect such a small difference by using, say, the Kolmogorov-Smirnov test, would require more than 4000 velocity observations to achieve a modest 0·1 significance level (Breiman 1973). (As an example of what can be done, Perry (1969) gives the z-velocities for 105 A0–A2 stars). So F_W and F_N are empirically indistinguishable.

The second moment M_2 will be required in Section 4. Numerical calculations using Equations (17), (20) and (21) show that, for $a \leq 0{\cdot}2$, within an accuracy of two decimal places

$$M_2 \simeq 1 + a\,(0{\cdot}556). \tag{23}$$

Another comparison of W with a normal distribution, less discriminating than the Kolmogorov-Smirnov test, can be made by computing the kurtosis statistic $\gamma_2 = M_4/M_2^2 - 3$, which is commonly used to measure deviation from normality (Kendall and Stuart 1977, p. 88). The result of the calculations is that, for $a \leq 0{\cdot}2$,

$$\gamma_2 \simeq a\,(1{\cdot}126).$$

If the velocity distribution were truly normal, then to distinguish $\gamma_2 = 0{\cdot}23$ corresponding to $a = 0{\cdot}2$, from $\gamma_2 = 0$ corresponding to $a = 0$, would require more than 450 observations at one-sigma level and more than 1800 observations at two-sigma level (Kendall and Stuart 1977, p. 258).

4. The local mass density

We will generalize Oort's important ideas, as discussed, for example, in Oort (1965) and Woolley (1965), and apply them to the results of Section 3 to compute the mass density in the solar neighbourhood.

The succeeding development will be easier to follow if we first discuss briefly the case $a = 0$. First suppose that a class of stars can be singled out, which in our case will be A or A0 stars, whose motions are independent of the other stars and dust, in the sense that the density function ψ_1^* for this class satisfied Equation (1), which is equivalent to saying that $\psi_1^*(z^*, \omega^*) = f_1^*[\frac{1}{2}(\omega^*)^2 + V^*(z^*)]$, where $V^*(z^*)$ is the potential for the entire Galaxy. Secondly assume that the function f_1^* has the same form as the function obtained in Section 3 for a system of stars—all of the same mass; in the case of $a = 0$, $f_1^*(E) = A_0 \exp(-\beta E)$. By integrating with respect to ω^* we find

$$\rho_1^*(z^*)/\rho_1^*(0) = \exp(-\beta V^*)(z^*). \tag{24}$$

Differentiate twice and set $z^* = 0$ to get

$$(\rho_1^*)''(0)/\rho_1^*(0) = -\beta\,(V^*)''(0). \tag{25}$$

There are two further assumptions which are supported by empirical evidence: First, that $\rho_1^*/\rho_1^*(0)$ has the form $\operatorname{sech}^2(z/z_0)$, where z_0 can be found from the fit to the

empirical log (relative density) curves, and so the left-hand side of Equation (25) can be evaluated as $-2/z_0^2$ Second, that the velocity distribution likewise has the form found for the hypothetical galaxy of stars all of the same mass, normally distributed for $a = 0$. Integrating out z^*, we see that $1/\beta$ is the standard deviation of the velocity distribution. Then Equation (25) gives the density m_0 of the entire Galaxy by

$$m_0 = \frac{1}{2\pi G z_0^2 \beta}.$$

Note that in this derivation there is no need to assume that the entire Galaxy can be divided into a finite number of classes, each of which has a density function of the form above. Our treatment is thereby an improvement of the standard one (Oort 1965; Woolley 1965), even when Camm's $a = 0$ solutions are used.

The above outline will be our guide for the case $a \neq 0$. In what follows we will use unsealed variables and functions, but omit asterisks for simplicity.

First suppose that we can find a class of stars, say A or A0, whose independence from the rest of the Galaxy gives a joint density function $\psi_1(z, \omega) = f_2[\frac{1}{2}\omega^2 + V(z)]$, where V is the potential for the entire Galaxy. Integrate out ω, to obtain

$$\frac{\rho_1(z)}{\rho_1(0)} = \frac{\int_0^\infty f_2[\frac{1}{2}\omega^2 + V(z)]\,d\omega}{\int_0^\infty f_2(\frac{1}{2}\omega^2)\,d\omega}. \tag{26}$$

Differentiate twice and set $z = 0$ to obtain

$$\frac{\rho_1''(0)}{\rho_1(0)} = V''(0)\frac{\int_0^\infty f_2'(\frac{1}{2}\omega^2)\,d\omega}{\int_0^\infty f_2(\frac{1}{2}\omega^2)\,d\omega}. \tag{27}$$

From Poisson's equation, $V''(0) = 4\pi G m_0$ Assuming that $\rho_1(z)/\rho_1(0)$ has the form given by Equation(20),the value of the left-hand side of Equation (27)can be empirically determined from

$$\frac{\rho_1(z)}{\rho_1(0)} = \frac{\operatorname{sech}^2(z/z_1) + a_1}{1 + a_1}$$

as $\dfrac{-2}{(1 + a_1) z_1^2}$. It remains to evaluate

$$K_1 = \frac{\int_0^\infty f_2'(\frac{1}{2}\omega^2)\,d\omega}{\int_0^\infty f_2(\frac{1}{2}\omega^2\,d\omega)}.$$

Apply the second hypothesis that the function f_2 has the form given in Section 3. What this means is that there is a function V_2 of the form

$$V_2(z) = \frac{1}{\beta_2 (1 + a_2)} [2 \ln \cosh (z/z_2) + a_2 (z/z_2)^2],$$

where ρ_2 is defined by $V''_2 = 4\pi G\rho_2$, and

$$\frac{\rho_2(z)}{\rho_2(0)} = \frac{\int f_2 [\frac{1}{2} \omega^2 + V_2(z)] \, d\omega}{\int f_2 (\frac{1}{2} \omega^2) \, d\omega} \tag{28}$$

implicitly defining f_2, via Equation (13) with $\rho_1 = \rho_2$ and $V = V_2$. That f_2 is implicitly defined is a source of difficulty not encountered in case $a = 0$.

Proceed as in the derivation of Equation (27) to find

$$\rho''_2(0)/\rho_2(0) = V''_2(0) K_1$$

and so

$$K_1 = \frac{-\beta_2}{1 + a_2}.$$

To determine m_0 we must relate a_2 and β_2 to empirically measurable parameters. To do this we use the general solution (13) of Equation (28) in (26); integrate with respect to ω and interchange the order of integration to obtain:

$$\frac{\rho_1(z)}{\rho_1(0)} = \frac{\rho_2 \{V_2^{-1} [V(z)]\}}{\rho_2(0)}. \tag{29}$$

Up to this point our arguments have been quite general. Now we must use a special property which depends upon the exact form of ρ_1 and ρ_2. If Equation (29) holds for small z, and if V is analytic in a neighbourhood of the positive real axis, then Equation (29) holds for large real z from which we can see that $a_1 = a_2$. The point here being that we only know the form (20) for ρ_1 and ρ_2 for moderatesized z. (A more informative argument is possible, which shows that if V has four derivatives for small z and Equation (29) is an approximate equality for small z, then it can be shown that $a_1 \simeq a_2$, but this requires lengthy calculations.)
Once we have $a_1 = a_2$, it follows that

$$V(z) = V_2 (\lambda z) \tag{30}$$

with $\lambda = z_2/z_1$. Thus, as in the case $a = 0$ under Oort's assumptions, one can derive the form of the total Galactic potential.

The second moment of the velocity W_1 of our class of stars is $E(W_1^2) = (1/\beta_1)M_2$, where M_2 is given by Equation (23) with $a = a_1 = a_2$. But, also

$$E(W_1^2) = \int_0^\infty \int_0^\infty \omega^2 f_2 [\tfrac{1}{2}\omega^2 + V(z)]\, dz d\omega \Big/ \int_0^\infty \int_0^\infty f_2 [\tfrac{1}{2}\omega^2 + V(z)]\, dz d\omega. \tag{31}$$

Substitute $V_2(\lambda z)$ for $V(z)$ and let $t = \lambda z$ to obtain $E(W_2^2) = (1/\beta_2)M_2$. Thus $\beta_1 = \beta_2$ and the final formula for the total mass density m_0 in the solar neighbourhood becomes

$$m_0 = \frac{1}{2\pi G z_1^2 \beta_1}. \tag{32}$$

To complete the estimation of m_0 we will use the empirical estimates of the second moment of the velocity distribution given in Whitley (1977); for A stars, $(9{\cdot}9 \text{ km s}^{-1})^2$; for A0 stars, $(10{\cdot}7 \text{ km s}^{-1})^2$. These non-parametric estimates are effectively the same as those obtained by removing the high-velocity stars from the class and then using the usual sum-of-squares estimate. From these estimates, the value of β_1 can be found using (returning to the *-notation) $M_2 = E(W_1^2) = \beta_1 E(W_1^*)^2$ and Equation (23). The end result, using the A and the A0 figures, is

$$m_0 = 0{\cdot}095 - 0{\cdot}096\ M_\odot\ (\text{pc})^{-3}.$$

The value of m_0 is not excessively sensitive to the values of a and z_0; for example, using the data discussed in Section 3 for A or A0 stars and $z = 0(25)350$ will increase the value of m_0 to 0·0980 – 099.

It is interesting to compare these numbers with those obtained from the data given in Hill, Hilditch and Barnes (1979). From the log (relative density) curve for F stars (their Table 7) we get $a = 0{\cdot}22$, $z_0 = 230$. Using their choice for $h = \sqrt{(E(W_1^*)}$ of 10·4 km s^{-1} gives $m_0 = 0{\cdot}07\ M_\odot$ pc^{-3}, while the larger value of 11·1 km s^{-1} (their Table 6) gives $m_0 = 0{\cdot}08$. From the log (relative density) curve for A-stars (their Table 8) we obtain $a = 0{\cdot}18$, $z_0 = 155$. There is more variability in the estimate for m_0 using A-stars because of the variability in the reported velocity data. Using their choice for h of 7·3 km s^{-1} leads to $m_0 = 0{\cdot}075$, while combining (their Table 6) the Clegg and Bell velocity data gives 10·8 km s^{-1} and reducing this by 0·2 km s^{-1} leads to $m_0 = 0{\cdot}16$.

We can now estimate the total Galactic potential V to within the scalar λ, since we can estimate a_1 and β_1. *If* the second term of V given by Equation (18) can be interpreted, as in Section 3, as the potential due to the Galactic centre, then λ can be estimated. Consider the z^* component of the force per unit mass due to the Galactic centre on a star at height z^* from the Galactic plane and distance R from the centre, with circular velocity S; it is, for small z*, $z^* S^2/R^2$. Compare with the second term of Equation (21) to obtain

$$\frac{1}{\lambda^2 \beta_1 z_1^2} \frac{a_1}{1 + a_1} = \frac{S^2}{2R^2}.$$

The standard choice $R = 10^4$ pc and $S = 250$ km s^{-1} gives $\lambda = 1{\cdot}17$ for A stars or $\lambda = 1{\cdot}13$ for A0 stars, with the values of the parameters a_1, β_1 and z_1 as obtained above. These values of λ are reduced somewhat by using the smaller values for R and S which are given in several papers in (Burton 1979); *e.g.* using $R = 8{\cdot}5$ kpc and $S = 225$ km s^{-1} (Einasto 1979) gives values for λ of 1·10 and 1·07.

Acknowledgements

I thank M. E. Mayer for his advice, here and in Whitley (1977), and I thank both the referees for their helpful comments.

References

Breiman, L. 1973, *Statistics with a View towards Applications,* Houghton Mifflin, Boston, p. 213.
Burton, W. B. 1979, Ed., IAU Symp. 84: The Large-Scale Characteristics of the Galaxy, D. Reidel Dordrecht.
Camm, G. L. 1950, *Mon. Not. R. astr. Soc.,* **110,** 305.
Einasto, J. 1979, in *IAU Symp. 84: The Large-Scale Characteristics of the Galaxy,* Ed. W. B. Burton, D. Reidel, Dordrecht, p. 451.
Freeman, K. 1975, *Galaxies and the Universe,* Eds A. Sandage and J. Kristian, University of Chicago Press, p. 409.
Hill, G., Hilditch, R. W., Barnes, J. V. 1979, *Mon. Not. R. astr. Soc.,* **186,** 813.
Hochstadt, H. 1973, *Integral Equations,* Wiley, New York, p.42.
Kendall, M., Stuart, A. 1977, *The Advanced Theory of Statistics,* Vol. 1, Hafner, New York.
Lin, C. C., Segel, L. A. 1974, *Mathematics Applied to Deterministic Problems in the Natural Sciences,* Macmillan, New York, p. 17.
Lindblad, B. 1959, in *Handbuch der Physik,* Vol. 53, Ed. S. Flugge, Sprin ger-Verlag, Berlin, p. 2.
Morse, P., Feshbach, H. 1953, *Methods of Theoretical Physics,* Vol. 1, McGraw-Hill, New York, p. 974.
Oort, J. 1965, in *Galactic Structure,* Eds A. Blaauw and M. Schmidt, University of Chicago Press, p. 455.
Perry, C. L. 1969, *Astr. J.,* **74,** 139.
Prendergast, K. H. 1954, *Astr. J.,* **59,** 260.
Whitley, R. 1977, *Astr. Astrophys.,* **59,** 329.
Woolley, R. 1957, *Mon. Not. R. astr. Soc.,* **117,** 198.
Woolley, R. 1965, in *Galactic Structure,* Eds A. Blaauw and M. Schmidt, University of Chicago Press, p. 85.
Woolley, R., Stewart, J. M. 1967, *Mon. Not. R. astr. Soc.,* **136,** 329.

J. Astrophys. Astr. (1982) **3,** 125–144

Global Stability of Disk-Bulge Systems: Spiral Structure of Disk Galaxies

Ashok Ambastha and Ram K. Varma *Physical Research Laboratory, Navrangpura, Ahmedabad 380009*

Received 1982 January 21; accepted 1982 March 22

Abstract. The spiral arms of disk galaxies are very sensitive to various morphological properties, such as, the gas content, the disk-to-bulge ratio *etc.* Here, the stability of self-gravitating annular disks surrounding the central rigid bulge component has been studied in order to explain the transition from the tight spiral arms in Sa galaxies to rather open patterns in Sc galaxies as the central amorphous component diminishes. Smooth spiral patterns are found associated with the dominant (or the fastest growing) modes of the system. When the disk-to-bulge mass ratio is small, a tight pattern results restricted to the inner regions of the disk. This pattern opens up and occupies larger disk areas as the disk component becomes comparable to the bulge. It is found here that the ‘ explosive ‘ instabilities of the global density waves do not occur in the presence of a massive bulge. The growth-rates of the eigen-modes decrease as the disk-to-bulge mass ratio decreases. It is also found that unstable modes of the annular disk can be suppressed by increasing the thermal pressure sufficiently.

Key words: global density waves—spiral galaxies—disk-bulge systems

1. Introduction

The density-wave theory has been the most successful approach in explaining the spiral structure of disk galaxies (Lin and Shu 1964, 1966; Lin, Yuan and Shu 1969). However, these ‘local’ density-wave theories are based on asymptotic approximations and face severe theoretical difficulties, *viz.* the anti-spirality (Lynden-Bell and Ostriker 1967; Shu 1970) and the problem of radial propagation of these waves (Toomre 1969). These problems can be removed to some extent by invoking certain excitation mechanisms for the density waves (Kato 1970; Mark 1977; Ambastha

and Varma 1978; Bertin and Mark 1978) and, alternatively, by considering the non-linear effects on the local density waves (Norman 1978).

Such asymptotic theories, which are essentially based on the assumption of tightly wrapped spiral waves, are obviously inappropriate for the study of galactic systems having rather open spiral structures. In fact, even the origin of the spiral structure remains unclear, as these theories assume, *a priori,* the existence of a quasi-stationary spiral structure (QSSS) and then proceed to study its consequences through a dispersion relation. However, there have been some attempts to relax the assumption of tight winding by including the terms of higher order in the asymptotic studies (see the review by Bertin 1980). But, for a complete understanding of the large-scale stability of the disks, a global approach with suitable boundary conditions has to be undertaken (lye 1978; Aoki, Noguchi and Iye 1979; Pannatoni and Lau 1979). Ambastha (1981) has studied the global stability of a large number of flat disk models in the form of an eigen-value problem with increasing central density and thermal energy of the disk. A large number of unstable modes are allowed in cold disks, the fastest-growing mode exhibiting the tightest patterns. As the central condensation increases, modes with smaller growth rates are stabilized. On the other hand, an increase in the thermal energy affects the tight spiral modes more appreciably and stabilizes them. In almost all cold disks, with no thermal or internal energy, there exists a number of 'explosive' modes with large growth-rates as compared to their pattern-frequencies. However, some computer simulations (Hohl 1976), as well as studies of global modes (Takahara 1978) have found that the ' explosive ' instabilities could be suppressed to some extent if extensive halos existed around the flat disk. We find here that a massive central bulge may also have a pronounced effect on the density waves sustained by the annular disk surrounding it.

The central bulge or the spheroidal subsystem of the disk galaxies may vary from a very massive and prominent one as in NGC 4594 to extremely small sizes as in NGC 4565. Also, there are galaxies with essentially no bulge, for instance, NGC 598 and NGC 5204. Though the spiral patterns are the characteristic features of the flat disk component, their physical appearance seems to be governed by the size and the massiveness of the bulge which itself does not exhibit any such features. Sandage, Freeman and Stokes (1970) and Freeman (1970) have discussed the role of the disk-to-bulge ratio in the classification of normal spiral galaxies. The bulges, in fact, comprise of old stars with large random velocities and hence they have a spheroidal spread. They do not possess any significant circular rotation and can be assumed to be rigid and stationary. On the other hand, the disk consists of massive young stars, gas and dust clouds and other population I objects apart from a background distribution of intermediate class of population II stars. The grand spiral arms are delineated by these young objects and appear to originate symmetrically from the edge of the central bulge. These spiral tracers are distributed in a ring within 2 kpc $< r <$ 16 kpc with a peak in density at $r \sim$ 4–6 kpc in our Galaxy. (Gordon and Burton 1976; Stecker 1976; Hart and Pedlar 1976; Kodaira 1974).

Considering such a picture of the disk galaxies we have divided the model under investigation here into two subsystems-*viz*. the fixed, central spherical bulge and the flat disk surrounding it–in order to carry out the stability analysis and to understand the effect of the bulge-to-disk ratio on. the density waves sustained by the annular disk. The problem has been posed as an eigen–value problem and the allowed modes

of oscillation in the plane of disk are obtained under the combined influence of the self-consistent potential of the disk and the external potential contributed by the bulge.

We have considered a wide range of values of the ratio of disk mass to the mass of the bulge and also the ratio of the bulge radius to the radius of the disk. Various components of the disk, like gas, dust and young objects have been assumed to constitute a single averaged smeared-out distribution and hence one-component hydrodynamic equations have been used to describe the dynamics of the material constituting the disk. The surface-density profile considered for the annular disk is of a similar form as that of the radial distribution of the spiral tracers in disk galaxies.

In a mathematically similar attempt, Yabushita (1969) has studied the stability of Saturnian rings against axisymmetric ($m = 0$) perturbations under the potential of the massive planet and determined the ratio of the mass of the rings to the mass of the planet in order that the rings may be stable. However, in the galactic context of the spiral structures, one is interested in the non-axisymmetric ($m \neq 0$) modes in pressureless as well as warm disks.

We consider the basic equations describing the dynamics of the disk in Section 2; the equilibrium of disk-bulge system is defined in Section 3. The stability of the equilibrium state against small amplitude perturbations is formulated in Section 4. Section 5 discusses the results in detail and some conclusions are derived in Section 6.

2. Basic equations

In this Section we consider the hydrodynamic equations governing the dynamics of the flat disk around the fixed central bulge. The disk is rotating about an axis perpendicular to its plane and passing through the centre of the bulge. In what follows, we have used the cylindrical coordinates.

The continuity equation of the disk is given by

$$\frac{\partial \sigma}{\partial t} + \frac{1}{r}\frac{\partial}{\partial r}(r\sigma u) + \frac{1}{r}\frac{\partial}{\partial \theta}(\sigma v) = 0 \tag{1.1}$$

where $\sigma(r, \theta, t)$ is the surface-density at a point on the annular disk; $u(r, \theta, t)$ and $v(r, \theta, t)$ are the radial and the azimuthal velocities, which are given by the momentum conservation equations as

$$\frac{\partial u}{\partial t} + u\frac{\partial u}{\partial r} + \frac{v}{r}\frac{\partial u}{\partial \theta} - \frac{v^2}{r} = -\frac{1}{\sigma}\frac{\partial p}{\partial r} + \frac{\partial \Psi_d}{\partial r} + \frac{\partial \Psi_b}{\partial r}, \tag{1.2}$$

$$\frac{\partial v}{\partial t} + u\frac{\partial v}{\partial r} + \frac{v}{r}\frac{\partial v}{\partial \theta} + \frac{uv}{r} = -\frac{1}{r\sigma}\frac{\partial p}{\partial \theta} + \frac{1}{r}\frac{\partial \Psi_d}{\partial \theta}. \tag{1.3}$$

Here, ψ_d (r, θ, t), ψ_b (r), $p(r, \theta, t)$ represent the self-consistent potential of the disk, the fixed potential exerted by the central bulge and the pressure, respectively.

The gravitational potential of the disk ψ_d (r, θ, t), corresponding to the surface-density $\sigma(r, \theta, t)$, is given by Poisson's equation

$$\nabla^2 \Psi_d = -4\pi G \delta(z) \sigma(r, \theta, t). \tag{1.4}$$

The term $\partial\psi_b/\partial r$ representing the gravitational force at a point on the disk due to the bulge has been defined in Section 3.

Finally, we assume a polytropic relation for pressure in the form

$$p = c\sigma^{\gamma} \tag{1.5}$$

for the closure of the set of Equations (1.1) – (1.4). Here, c represents a measure of the ' warmness ' of the disk and γ is the polytropic index.

3. Equilibrium of the disk-bulge system

Let us now consider a general axisymmetric surface-density distribution in a flat annular disk

$$\sigma_0(r) = \sum_{j=0}^{\infty} a_j F_0(\lambda_j^{(0)} r); \quad a \leqslant r \leqslant b$$
$$= 0 \quad ; \quad r > b \text{ and } r < a \tag{2.1}$$

where

$$F_0(\lambda_j^{(0)} r) \equiv J_0(\lambda_j^{(0)} r) + G_j^{(0)} Y_0(\lambda_j^{(0)} r). \tag{2.2}$$

Here, $J_0(x)$ and $Y_0(x)$ are Bessel functions of order zero and $\lambda_j^{(0)}$ denote the roots of the transcendental equation

$$J_0(\lambda a) Y_0(\lambda b) - J_0(\lambda b) Y_0(\lambda a) = 0. \tag{2.3}$$

Also, $G_j^{(0)}$ in Equation (2.2) are defined as

$$G_j^{(0)} = -\frac{J_0(\lambda_j^{(0)} a)}{Y_0(\lambda_j^{(0)} a)} = -\frac{J_0(\lambda_j^{(0)} b)}{Y_0(\lambda_j^{(0)} b)}, \tag{2.4}$$

in order to ensure the vanishing of the surface-density at both the edges of the annular disk, *i.e.* at the inner radius $r = a$, and the outer edge $r = b$.

The roots of Equation (2.3), $\lambda_j^{(0)}$, would depend on the specification of the disk boundary. We have listed the zeros $\lambda_j^{(m)}$ of $F_m(\lambda_j^{(m)} r) = 0$ at $r = a$ in Table 1 for a/b $(\equiv a) = 0{\cdot}25$, $0{\cdot}5$ and $0{\cdot}75$ and $m = 0$ and 2. The functions $F_m(x)$; as constructed according to Equation (2.2), are orthogonal.

Now, any density distribution can be constructed in the form (2.1) by choosing appropriate coefficients of expansion, a_j, which can be found by using the orthogo-

Table 1. Roots of $F_{jr}^{m} = 0$ at $r = a$ and $r = b$.

	$m = 0$			$m = 2$		
a/b	0·25	0·50	0·75	0·25	0·5	0·75
j						
1	4·097686	6·246062	12·553266	5·319868	6·813843	12·761297
2	8·323774	12·546871	25·126130	9·144361	12·855532	25·231701
3	12·528667	18·836415	37·694697	13·121498	19·045705	37·765274
4	16·726277	25·122846	50·262169	17·184754	25·280762	50·315154
5	20·920591	31·407996	62·829202	21·292746	31·534683	62·871609
6	25·113152	37·692496	75·396014	25·425757	37·798231	75·431362
7	29·304675	43·976623	87·962700	29·573912	44·067336	87·993003
8	33·495534	50·260516	100·52931	33·731852	50·339937	100·55582
9	37·685943	56·544251	113·09586	37·896453	56·614877	113·11943
10	41·876034	62·827878	125·66238	42·065783	62·891460	125·68360
11	46·065893	69·111424	138·22887	46·238587	69·169238	138·24816
12	50·255576	75·394910	150·79534	50·414014	75·447915	150·81302
13	54·445122	81·678350	163·36180	54·591471	81·727284	163·37812
14	58·634562	87·961753	175·92824	58·770530	88·007197	175·94340
15	62·823916	94·245128	188·49468	62·950873	94·287546	188·50882

nality of the functions, $F_0\ (\lambda_j^{(0)}\, r)$. Thus, it should suffice here if we consider a particular distribution of the form

$$\sigma_0(r) = a_0\left[J_0(\lambda_0 r) - \frac{J_0(\lambda_0 a)}{Y_0(\lambda_0 a)}\, Y_0(\lambda_0 r)\right]; \quad a \leqslant r \leqslant b$$
$$= \qquad 0 \qquad ; \quad r < a \text{ or } r > b \tag{2.5}$$

where λ_0 is the smallest root of the Equation (2.3).

The gravitational potential in the plane of the axisymmetric flat disk corresponding to a given surface-density distribution is obtained by using the Hankel transform $A\ (\tilde{\omega})$ of $\sigma_0(r)$ such that

$$A_0(\tilde{\omega}) = \int_0^\infty J_0(\tilde{\omega} r)\, \sigma_0(r)\, r\, dr. \tag{2.6}$$

This can be inverted to obtain

$$\sigma_0(r) = \int_0^\infty J_0(\tilde{\omega} r)\, A_0(\tilde{\omega})\, \tilde{\omega}\, d\tilde{\omega}$$

(*cf.* Clutton-Brock 1972). Correspondingly, the potential is given by

$$\Psi_0(r, z) = 2\pi G \int_0^\infty J_0(\tilde{\omega} r)\, A_0(\tilde{\omega}) \exp(-\tilde{\omega}\,|z|)\, d\tilde{\omega}. \tag{2.7}$$

On substituting for $\sigma_0\ (r)$ from Equation (2.5) in Equation (2.6), one gets

$$A_0(\tilde{\omega}) = \frac{2a_0}{\pi(\tilde{\omega}^2 - \lambda_0^2)}\left[\frac{J_0(\tilde{\omega} a)}{Y_0(\lambda_0 a)} - \frac{J_0(\tilde{\omega} b)}{Y_0(\lambda_0 b)}\right]. \tag{2.8}$$

On substituting for A_0 ($\tilde{\omega}$) from Equation (2.8), the gravitational potential in the plane of the disk can be obtained, following Yabushita (1969), as

$$\Psi_0(r) = 2\pi G a_0 \left[\frac{F_0(\lambda_0 r)}{\lambda_0 b} + \frac{4}{\pi^2} \int_0^\infty \left\{ \frac{I_0(zr) K_0(zb)}{Y_0(\lambda_0 b)} - \frac{I_0(za) K_0(zr)}{Y_0(\lambda_0 a)} \right\} \frac{dz}{(\lambda_0^2 + z^2)} \right] \quad (2.9)$$

where $I_0(x)$ and $K_0(x)$ are modified Bessel functions of first and second kind and order zero.

The equation of continuity (1.1) and the azimuthal component of the momentum conservation equation (1.3) are satisfied identically for the axisymmetric equilibrium disk, while the radial component of the momentum conservation equation (1.2) yields the rotational velocity of the disk as

$$-r\Omega_0^2 \equiv -\frac{V_0^2}{r} = -\frac{1}{\sigma_0}\frac{dP_0}{dr} - \frac{GM_b}{r^2} + \frac{d\Psi_d}{dr}, \quad (2.10)$$

where M_b denotes the mass of the central spherical bulge. Here, GM_b/r^2 is the external gravitational force exerted by the fixed bulge and $d\psi_d/dr$ represents the self-consistent potential of the disk component. The azimuthal velocity, $V_0(r)$, can thus be obtained by Equation (2.10) once the nature of the pressure force is specified.

Now, we define the non-dimensional quantities $\hat{\sigma}(\xi)$, $\hat{\psi}(\xi)$ *etc.* such that

$$\Psi(r) = (\pi GM/b)\,\hat{\Psi}(\xi),$$

$$\sigma(r) = (M/2\pi b^2)\,\hat{\sigma}(\xi),$$

$$P(r) = (GM^2/2b^3)\,\hat{P}(\xi)$$

and

$$V_0(r) = (\pi GM/b)^{1/2}\,\hat{V}_0(\xi), \quad (2.11)$$

where $\xi = r/b$.

Thus, using the definitions (2.11) in Equation (2.10), we get the non-dimensional radial equation of motion

$$\frac{\hat{V}_0^2(\xi)}{\xi} = \frac{1}{\hat{\sigma}_0(\xi)}\frac{d\hat{P}_0(\xi)}{\partial\xi} + \frac{1}{\pi(1+\beta)}\cdot\frac{1}{\xi^2} - \frac{d\hat{\Psi}_d(\xi)}{d\xi} \quad (2.12)$$

where the net mass of the system is

$$M = M_d + M_b$$

and $\beta = M_d/M_b$.

The surface-density profiles for various values of the disk-to-bulge mass ratio ($\equiv \beta$) are shown in Fig. 1. As the mass of the bulge decreases, the mass of the disk increases so as to keep the net mass M fixed. In all these cases, the ratio of the inner and the outer radii is kept constant at $\alpha = 0{\cdot}25$. The circular-velocity profile is only slightly altered if β is varied. Fig. 2 exhibits the surface-density and rotational profiles for $\beta = 0{\cdot}2$ and various values of α.

It should be noted here that, for a physical and realistic disk, the following criteria should be satisfied throughout the disk

$$\Omega_0^2(\xi) \geqslant 0, \tag{2.13a}$$

$$K_0^2(\xi) \equiv 2\Omega_0\left[2\Omega_0 + \xi\frac{d\Omega_0}{d\xi}\right] \geqslant 0 \tag{2.13b}$$

and

$$\frac{d\Omega_0(\xi)}{d\xi} \leqslant 0, \tag{2.13c}$$

Ω_0 and K_0 being the angular and epicyclic frequencies, respectively.

Here, the disks do not satisfy the condition (2.13a) when $\alpha \geqslant 0{\cdot}75$ and $\beta > 0{\cdot}5$. The condition (2.13c) also does not hold good for disks with $\alpha \geqslant 0{\cdot}75$. Table 2 shows the azimuthal velocities at the inner and the outer edges of the disk for some values of the parameters α and β.

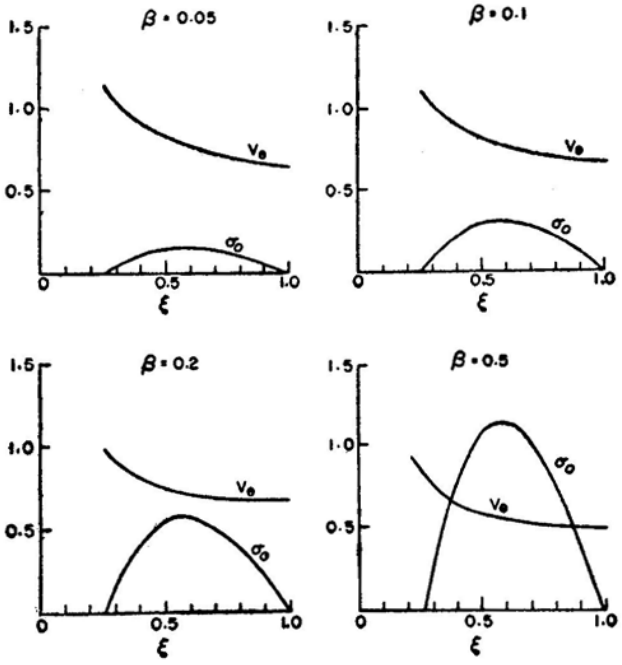

Figure 1. The radial profiles of surface density and circular velocity for various values of M_d/M_b and $a/b = 0{\cdot}25$.

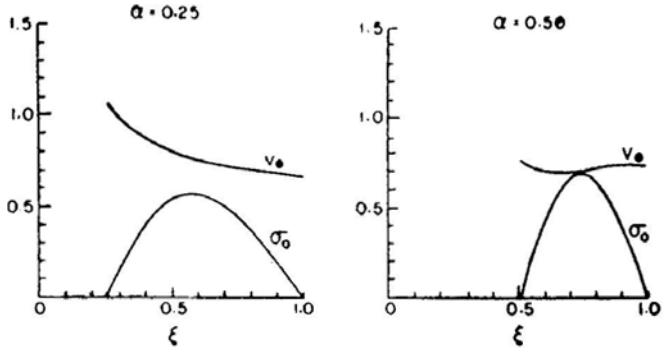

Figure 2. The radial profiles of surface density and circular velocity for two values of inner-to-outer radii of the disk and $M_d/M_b = 0{\cdot}20$.

4. Normal mode analysis of the perturbed disk

We consider an infinitesimally small perturbation in the gravitational potential of the annular disk, which in turn perturbs the surface density, velocity *etc.* of the equilibrium disk (as defined in Section 3). Since the boundaries of the disk are free to move, we now have

$$a(\tau) = a + \epsilon_a(\tau)$$

and

$$b(\tau) = b + \epsilon_b(\tau), \tag{3.1}$$

for the inner and the outer radii of the perturbed disk. Here, ε_a and ε_b are some small quantities of first order in the perturbation. One can linearize the basic hydrodynamic equations (1.1)—(1.5) governing the system and obtain the following set of equations for the perturbed quantities:

$$\left(\frac{\partial}{\partial\tau} + \frac{V_0}{\xi}\frac{\partial}{\partial\theta}\right)\tilde{\sigma} + \frac{1}{\xi}\left[\frac{\partial}{\partial\xi}(\xi\,\sigma_0\,\tilde{u}) + \frac{\partial}{\partial\theta}(\sigma_0\,\tilde{v})\right] = 0, \tag{3.2}$$

Table 2. Circular velocities for disk-bulge systems at inner and outer edges of the disk.

α	0·25		0·50		0·75	
β	$V(a)$	$V(b)$	$V(a)$	$V(b)$	$V(a)$	$V(b)$
0·40	1·045	0·737	0·748	0·843	0·318	1·000
0·50	1·030	0·762	0·740	0·881	0·217	1·000
0·75	1·000	0·810	0·722	0·952		
1·00	0·977	0·843	0·709	1·002		
1·50	0·944	0·889	0·690	1·068		
2·00	0·921	0·918	0·677	1·111		
2·50	0·905	0·938	0·667	1·39		
3·00	0·892	0·953	0·660	1·61		

Unphysical disk

Note:

The condition $\dfrac{d\Omega_0(\xi)}{d\xi} < 0$ does not hold inside the box.

$$\left(\frac{\partial}{\partial \tau}+\frac{V_0}{\xi}\frac{\partial}{\partial \theta}\right)\tilde{u}-\frac{2V_0}{\xi}\tilde{v}=-\frac{1}{\sigma_0}\frac{\partial \tilde{p}}{\partial \xi}+\frac{\tilde{\sigma}}{\sigma_0^2}\frac{dP_0}{d\xi}+\frac{\partial \tilde{\psi}_d}{\partial \xi}, \tag{3.3}$$

$$\left(\frac{\partial}{\partial \tau}+\frac{V_0}{\xi}\frac{\partial}{\partial \theta}\right)\tilde{v}+\left(\frac{V_0}{\xi}+\frac{dV_0}{d\xi}\right)\tilde{u}=\frac{1}{\xi}\left[-\frac{1}{\sigma_0}\frac{\partial \tilde{p}}{\partial \theta}+\frac{\partial \tilde{\psi}_d}{\partial \theta}\right], \tag{3.4}$$

where $\tilde{\sigma}\,(\xi,\ \theta,\ \tau)$, $\tilde{u}\ (\xi,\ \theta,\ \tau)$, $\tilde{v}\ (\xi,\ \theta,\ \tau\ )$, $\tilde{P}\ (\xi,\ \theta,\ \tau)$, $\tilde{\psi}_d\ (\xi,\ \theta,\ \tau)$ are perturbed density, velocities, pressure and potential, respectively and τ is a non-dimensional time, given by

$$\tau = (\pi\, G\, M/R^3)^{1/2}\, t.$$

The bulge being rigid and stationary, the perturbations of the bulge density *etc.* have been neglected and hence it does not contribute to the perturbed equations apart from influencing the rotational profile of the system.

Since the equilibrium density distribution, $\sigma_0\ (\xi)$, is redistributed due to a perturbation in the gravitational potential, which itself corresponds to a small density perturbation, $\sigma_1(\xi,\ \theta,\ \tau)$, the net surface density of the annular disk can be written as

$$\sigma\,(\xi,\ \theta,\ \tau) = a_0\, F_0\,(\Lambda_0\ \xi) + \sigma_1\,(\xi,\ \theta,\ \tau) \tag{3.5}$$

where Λ_0 is the smallest root of the transcendental equation

$$F_0\,(\Lambda_0\ \xi) \equiv J_0\,(\Lambda_0\ \xi) + G^{(0)}\ Y_0\,(\Lambda_0\ \xi) = 0 \tag{3.6}$$

at $\xi = a(\tau)$ and $\xi = b(\tau)$. Let us write

$$a_0\, F_0\,(\Lambda_0\ \xi) - a_0\, F_0\,(\lambda_0\ \xi) = \epsilon \sum_{k=0}^{\infty} D_k\, F_m\,(\lambda_k^{(m)}\ \xi), \tag{3.7}$$

where $\lambda_k^{(m)}$ are the roots of the equation

$$J_m\,(\lambda)\ Y_m\,(\lambda\alpha) - J_m\,(\lambda\alpha)\ Y_m\,(\lambda) = 0$$

and where

$$F_m\,(\lambda_k^{(m)}\ \xi) \equiv J_m\,(\lambda_k^{(m)}\ \xi) + G_k^{(m)}\ Y_m\,(\lambda_k^{(m)}\ \xi)$$

with $\quad G_k^{(m)} = -\,J_m\,(\lambda_k^{(m)}\ \alpha)/Y_m\,(\lambda_k^{(m)}\ \alpha).$

Similarly, one can also expand the perturbed density, $\sigma_1\,(\xi,\ \theta,\ \tau)$ as

$$\sigma_1\,(\xi,\ \theta,\ \tau) = \epsilon \sum_{k=0}^{\infty} E_k\, F_m\,(\lambda_k^{(m)}\ \xi). \tag{3.8}$$

Here,

$$\epsilon(\theta, \tau) = \epsilon_0 \exp[i(\omega\tau + m\theta)].$$

Thus the net surface density in the disk is

$$\sigma(\xi, \theta, \tau) = a_0 F_0(\lambda_0 \xi) + \epsilon \sum_{k=0}^{\infty} C_k F_m(\lambda_k^{(m)} \xi) \equiv \sigma_0(\xi) + \tilde{\sigma}(\xi, \theta, \tau) \tag{3.9}$$

where we have defined $C_k = E_k + D_k$ which is to be determined later. Now, the potential $\hat{\psi}_{\kappa}^{(m)}(\xi)$ corresponding to the surface-density distribution $F_m(\lambda_{\kappa}^{(m)} \xi)$ can be written in a non-dimensional form as

$$\hat{\psi}_k^{(m)}(\xi) = \frac{1}{\pi}\left[\frac{F_m(\lambda_k^{(m)} \xi)}{\lambda_k^{(m)}} + \frac{4}{\pi^2}\int_0^{\infty}\left\{\frac{I_m(z\xi) K_m(z)}{Y_m(\lambda_k^{(m)})} - \frac{I_m(za) K_m(z\xi)}{Y_m(\lambda_k^{(m)} a)}\right\}\frac{dz}{z^2 + \lambda_k^{(m)2}}\right] \tag{3.10}$$

as in Equation (2.9). The net potential is hence

$$\Psi(\xi, \theta, \tau) = \Psi_0(\xi) + \tilde{\Psi}(\xi, \theta, \tau) \tag{3.11}$$

$$\text{with} \qquad \tilde{\Psi}(\xi, \theta, \tau) = \epsilon \sum_{k=0}^{\infty} C_k \hat{\psi}_k^{(m)}(\xi).$$

Considering the azimuthal and the time dependence of the form

$$\tilde{A}(\xi, \theta, \tau) = \hat{A}(\xi) \exp[i(\omega\tau + m\theta)] \tag{3.12}$$

for all the perturbed quantities, and by adding to and subtracting from Equation (3.3) i times Equation (3.4), one obtains

$$i\omega(\hat{u} - i\hat{v}) + i(m-1)\frac{V_0}{\xi}(\hat{u} - i\hat{v}) - \frac{V_0}{\xi}\hat{v} - i\hat{u}\frac{dV_0}{d\xi}$$

$$= -\frac{1}{\sigma_0}\left\{\frac{d\hat{p}}{d\xi} + \frac{m}{\xi}\hat{p}\right\} + \frac{\hat{\sigma}}{\sigma_0^2}\frac{dP_0}{d\xi} + \left\{\frac{d\hat{\psi}}{d\xi} + \frac{m}{\xi}\hat{\psi}\right\}, \tag{3.13}$$

$$i\omega(\hat{u} + i\hat{v}) + i(m+1)\frac{V_0}{\xi}(\hat{u} + i\hat{v}) - \frac{V_0}{\xi}\hat{v} + i\hat{u}\frac{dV_0}{d\xi}$$

$$= -\frac{1}{\sigma_0}\left\{\frac{d\hat{p}}{d\xi} - \frac{m}{\xi}\hat{p}\right\} + \frac{\hat{\sigma}}{\sigma_0^2}\frac{dP_0}{d\xi} + \left\{\frac{d\hat{\psi}}{d\xi} - \frac{m}{\xi}\hat{\psi}\right\} \tag{3.14}$$

and

$$i\left(\omega+\frac{m}{\xi}V_0\right)\hat{\sigma}+\frac{1}{\xi}\frac{d}{d\xi}(\xi\,\sigma_0\,\hat{u})+i\frac{m}{\xi}\sigma_0\,\hat{v}=0. \tag{3.15}$$

And the perturbed pressure $\hat{p}\,(\xi)$ in Equations (3.13) and (3.14) is given by

$$\hat{p}(\xi)=\frac{\gamma P_0(\xi)}{\sigma_0(\xi)}\hat{\sigma}(\xi), \tag{3.16}$$

using Equation (1.5).

We expand the perturbed quantities $\hat{u}-i\hat{v}$ and $\hat{u}+i\hat{v}$ as

$$\hat{u}-i\hat{v}=i\sum_{k=0}^{\infty}A_k\,F_{m-1}\,(\lambda_k^{(m)}\,\xi) \tag{3.17}$$

and

$$\hat{u}+i\hat{v}=i\sum_{k=0}^{\infty}B_k\,F_{m+1}\,(\lambda_k^{(m)}\,\xi) \tag{3.18}$$

where the coefficients of expansion A_k, B_k are to be determined. Substituting the expansions for the perturbed quantities from the Equations (3.9), (3.11), (3.16)–(3.18) in the set of Equations (3.13)–(3.15) and carrying out the necessary simplifications, one obtains the following equations:

$$\sum_{k=0}^{\infty}\Big[A_k\cdot\tfrac{1}{2}\{F_{m-1}\,(\lambda_k\,\xi)\,\sigma_0'-\lambda_k\,F_m\,(\lambda_k\,\xi)\,\sigma_0\}+B_k\cdot\tfrac{1}{2}\{F_{m+1}\,(\lambda_k\,\xi)\,\sigma_0'$$
$$+\lambda_k\,F_m\,(\lambda_k\,\xi)\,\sigma_0\}+C_k\left\{\omega+\frac{m}{\xi}V_0\right\}F_m\,(\lambda_k\,\xi)\Big]=0, \tag{3.13a}$$

$$\sum_{k=0}^{\infty}\left[A_k\left\{-\left(\omega-\frac{m-1}{\xi}V_0\right)+\frac{1}{2}\left(\frac{V_0}{\xi}+V_0'\right)\right\}F_{m-1}\,(\lambda_k\,\xi)+B_k\left\{\frac{1}{2}\left(V_0'-\frac{V_0}{\xi}\right)\right\}\right.$$
$$\times F_{m+1}\,(\lambda_k\,\xi)+C_k\left\{-\left(\frac{\gamma P_0}{\sigma_0^2}\lambda_k+\frac{1}{\pi}\right)F_{m-1}\,(\lambda_k\,\xi)-\frac{\gamma\,(\gamma-2)}{\sigma_0^3}P_0\,\sigma_0'\,F_m\,(\lambda_k\,\xi)\right.$$
$$\left.\left.-\frac{4}{\pi^3}\mathbf{L}_k^{(m-1)}\,(\xi)\right\}\right]=0 \tag{3.14a}$$

and

$$\sum_{k=0}^{\infty}\left[A_k\left\{\frac{1}{2}\left(\frac{V_0}{\xi}-V_0\right)\right\}F_{m-1}\,(\lambda_k\,\xi)+B_k\left\{-\left(\omega+\frac{m+1}{\xi}V_0\right)\right.\right.$$
$$-\frac{1}{2}\left(\frac{V_0}{\xi}+V_0'\right)\Big\}F_{m+1}\,(\lambda_k\,\xi)+C_k\left\{-\left(\frac{\gamma\,P_0}{\sigma_0^2}\lambda_k-\frac{1}{\pi}\right)F_{m+1}\,(\lambda_k\,\xi)\right.$$
$$\left.\left.+\frac{\gamma\,(\gamma-2)\,P_0\,\sigma_0'}{\sigma_0^3}F_m\,(\lambda_k\,\xi)-\frac{4}{\pi^3}\mathbf{L}_k^{m+1}\,(\xi)\right\}\right]=0 \tag{3.15a}$$

where we have defined

$$\mathbf{L}_k^{(m-1)}(\xi) = \int_0^\infty \frac{z\,dz}{\lambda_k^2 + z^2} \left\{ \frac{I_{m-1}(z\xi)\, K_m(z)}{Y_m(\lambda_k)} + \frac{I_m(z\alpha)\, K_{m-1}(z\xi)}{Y_m(\lambda_k\, \alpha)} \right\} \tag{3.19}$$

and

$$\mathbf{L}_k^{(m+1)}(\xi) = \int_0^\infty \frac{z\,dz}{\lambda_k^2 + z^2} \left\{ \frac{I_{m+1}(z\xi)\, K_m(z)}{Y_m(\lambda_k)} + \frac{I_m(z\alpha)\, K_{m+1}(z\xi)}{Y_m(\lambda_k\, \alpha)} \right\}. \tag{3.20}$$

In all the above equations, we have dropped the superscript m from the roots $\lambda_k^{(m)}$ for brevity.

Now, we multiply the Equations (3.13a)–(3.15a) by $\xi F_m(\lambda_j\, \xi)$, $\xi F_{m\text{-}1}(\lambda_j \xi)$ and $\xi F_{m+1}(\lambda_j, \xi)$, respectively and integrate the resulting equations over the annular disk in the interval $(\alpha, 1)$ to get an infinite s et of algebraic equations:

$$\sum_{k=0}^{\infty} [A_k\, P_{kj} + B_k\, Q_{kj} + C_k\, R_{kj}] = \omega\, A_j, \tag{3.13b}$$

$$\sum_{k=0}^{\infty} [A_k\, S_{kj} + B_k\, T_{kj} + C_k\, U_{kj}] = \omega\, B_j, \tag{3.14b}$$

$$\sum_{k=0}^{\infty} [A_k\, V_{kj} + B_k\, W_{kj} + C_k\, X_{kj}] = \omega\, C_j, \tag{3.15b}$$

with the coefficients P_{kj}, Q_{kj} *etc*. as defined in Appendix. Equations (3.13b)–(3.15b) can conveniently be written in a matrix from as an eigen-value problem

$$\begin{bmatrix} P & Q & R \\ S & T & U \\ V & W & X \end{bmatrix} \begin{bmatrix} A \\ B \\ C \end{bmatrix} = \omega \begin{bmatrix} A \\ B \\ C \end{bmatrix} \tag{3.21}$$

or $\quad MZ = \omega Z$

where P, Q, R, .. represent infinite-dimensional matrices and M, consequently, is a $3\infty \times 3\infty$ matrix. Equation (3.21) is an eigen-value value problem for the perturbations $\tilde{\sigma}(\xi, \theta, \tau)$, $\tilde{\psi}(\xi, \theta, \tau)$ *etc*. in the plane of the disk with the ω as the eigen-values and Z $\{\equiv (A, B, C)^{\dagger}\}$ representing corresponding eigen-functions.

The matrix M is real and, in general, is non-symmetric. Hence, the eigen-value problem would permit real and/or complex conjugate pairs of eigen-values. The complex eigen-modes will be associated with complex eigen-functions, contributing radial phase shifts in the location of the maxima of the perturbations. Thus, the complex eigen-modes may naturally allow spiral patterns in the disk. This result—

that only complex modes admit spiral patterns—confirms the 'antispiral' theorem according to which no spiral waves are allowed to be associated with the neutral (or, purely oscillatory) modes

It is impossible to solve the eigen-value problem given by Equation (3.21) as it stands, with infinite-dimensional matrices, and suitable truncated forms of M and Z have to be employed. Of course, the convergence of the resulting modes of oscillations is to be ensured.

In order to study the eigen-patterns associated with the perturbations in a satisfactory way, we have plotted here the amplitudes of the perturbation, say, the surface density perturbation, at a large number of points, in-and out-side the annular disk boundaries. The results have been presented in a three-dimensional form.

5. Results and discussion

In this Section, we discuss the results of the eigen-value problem for the stability of the annular disk under the combined influence of the external field of the central bulge and the collective field of the disk. The surface density adopted vanishes at both the boundaries. In fact, such a density distribution represents the young objects, *viz.* the spiral tracers in galactic disks, which are only a small fraction of the total mass of the disk. Thus, we have ignored the background population of the intermediately old population II stars which have an exponential distribution in the disk. However, we have already investigated the problem of the stability of disks where the collective effects of the entire system has been considered (Ambastha 1981). Here, our interest lies mainly in the study of the effects of a fixed bulge component on the density waves sustained by the gaseous disk. For this reason, and also to avoid the presence of the singularities at the edges, we have considered that the density vanishes at the boundaries. In a separate paper, we would consider the effect—on the density waves in the disk—of the field generated by a static distribution of the old population II stars in the disk besides that due to the central bulge.

Here, all the eigenvalues, real as well as complex, corresponding to a truncated $N \times N$ matrix are obtained by using similarity transformation method for the evaluation of the eigen-value problem. The real modes exhibit spoke-like features because of the fact that the neutral modes do not yield radial phase shifts, which would otherwise be contributed by the imaginary part of the eigen-functions in the case of the complex modes. Thus, only the complex modes may provide spirals, and only those which are associated with unstable modes would survive in the disk. For this reason, we have considered here only the growing modes in detail. Since the matrix M is nonsymmetric, with no regular or well-defined variations in the magnitude of the matrix elements away from the diagonal, it is not possible to evaluate, exactly, all the eigen-values and the associated eigen-functions of the truncated matrix. As the dimension of the truncated matrix is increased, one expects to refine the eigen-modes; however, the numerical errors start becoming significant for larger matrices and hence one cannot increase the dimension of the matrix without limit. We have considered here in most cases, matrices of the order of 45×45. Only those modes have been discussed which exhibit a reasonable convergence and the rest of them are ignored while discussing the spiral patterns.

Table 3. The principal mode for various disk-bulge models (cold disk).

α	0·25		0·5		0·75	
β	ω_r	$-\omega_i$	ω_r	$-\omega_i$	ω_r	$-\omega_i$
0·02	1·9844	0·2278	No unstable mode exists		No unstable mode exists	
0·10	1·8188	0·2278				
0·25	1·6954	0·2604				
0·40	1·5659	0·2931	1·3427	0·0160	0·8287	0·0333
0·50	1·5231	0·2950	1·3343	0·0366	0·7215	0·0521
0·75	1·4386	0·2881	1·3212	0.0601	Unphysical disks	
1·00	1·3650	0·2820	1·3166	0·0697		
1·50	1·2909	0·3027	1·3116	0·0680		
2·00	1·2670	0·3026	1·3042	0·0496		
2·50	1·2564	0·2948	1·2755	0·0424		
3·00	1·2516	0·2859	1·2685	0·0413		

The convergence of the eigen-frequency of the fastest-growing (or the principal) mode as the dimension of the matrix M is increased, is shown in Table 3 for $m = 2$ (bisymmetric) perturbation in cold disk with $\alpha = 0{\cdot}25$ and $\beta = 1{\cdot}0$. It can be seen that the relative variations in the real and the imaginary parts of the eigen-value, ω defined by

$$\Delta\,\omega_r^{(i,j)} = \left|\frac{\omega_r^{(i)} - \omega_r^{(j)}}{\omega_r^{(i)}}\right|, \quad \Delta\,\omega_i^{(i,j)} = \left|\frac{\omega_i^{(i)} - \omega_i^{(j)}}{\omega_i^{(i)}}\right|$$

are fairly small. Here the superscripts denote the dimension of the matrices used. For instance, considering $i = 45$ and $j = 39$, one obtains $\Delta\,\omega_r = 1{\cdot}4 \times 10^{-4}$ and $\Delta\,\omega_i = 7 \times 10^{-2}$.

Fig. 3 compares the eigen-patterns for the principal mode with $m = 2$ as obtained from a 27 × 27 matrix and a 45 × 45 matrix. It can be noticed here that the patterns remain essentially unaltered by an increase in the size of the matrix considered, confirming thereby the proper convergence of the frequency, as well as the eigen-functions of the principal mode.

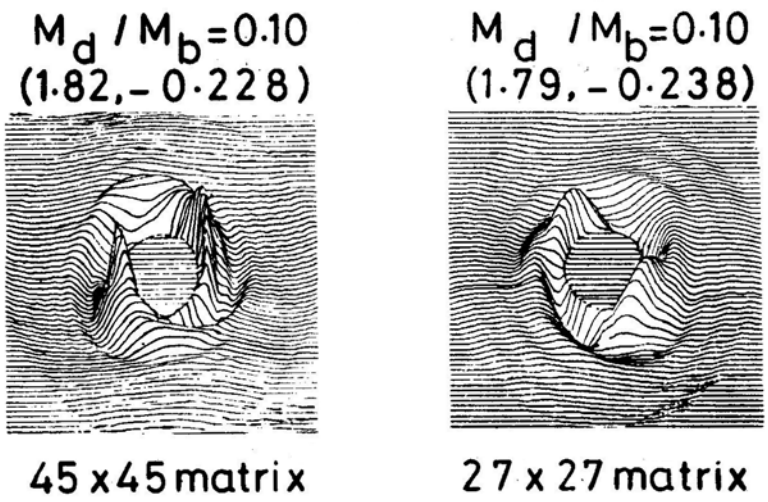

Figure 3. The bi-symmetnc ($m = 2$) principal (fastest-growing) eigen-mode as obtained by 27×27 and 45×45 matrices. Notice that the patterns are unaltered apart from a small rotational shift in resulting patterns.

Table 4. The convergence of various eigen-frequencies of the annular disk with the increase in the number of segments in the interval (a, b). $m = 2$, $a/b = 0{\cdot}25$, $M_d/M_b = 0{\cdot}5$, $c = 0$ (cold disk).

No. of segments	1		2		3	
Eigen-mode	ω_r	$-\omega_i$	ω_r	$-\omega_i$	ω_r	$-\omega_i$
I	1·5231	0·2952	1·5229	0·2948	1·5231	0·2950
II	1·4748	0·0542	1·4743	0·0563	1·4745	0·0567
III	0·5820	0·0098	0·5801	0·0064	0·5800	0·0044
IV	1·0723	0·0161	1·0753	0·0052		

Now, the matrix elements such as P_{kj}, Q_{kj}, which are certain integrated quantities over the disk, are obtained by using a 32-point Gaussian quadrature. To check the accuracy of the matrix elements themselves, we divide the interval (α, 1) in more segments and then use the quadrature in each segment. The net quantities are obtained by summing up the contributions from each segment. Table 4 shows the allowed modes with $n_d = 1$, 2 and 3, where n_d is the number of divisions in the interval (α, 1). The relative errors for the first two modes are fairly small, while the two lower modes do not appear to be valid unstable modes of the system since the errors are large for them. We notice that as one adopts more accurate quadratures, these unstable modes disappear (*i.e.* stabilized) and do not yield spiral patterns. In our calculations, we have used $n_d = 3$.

In almost all the cases, we find that the principal mode shows a fairly smooth spiral pattern. We do not find any 'explosive' modes, with $\omega_i > \omega_r$, in our calculations. Also, there are no unstable modes in the disks with $\alpha = 0{\cdot}5$, $0{\cdot}75$ when $\beta < 0{\cdot}25$. Thus, massive bulge appears to suppress the unstable modes completely. A similar result is obtained by Hohl (1976) and Berman, Brownrigg and Hockney (1979) that bar instabilities are completely quenched in the presence of massive halo around the flat disk. We find here that the central spherical bulge also acts in a similar fashion. However, for the disks with $\alpha = 0{\cdot}25$ this is not the case even with the bulges as massive as 50 M_d (*i.e.* $\beta \sim 0{\cdot}02$). Thus the suppression of the unstable modes is not efficient if the central bulge is confined to a smaller region. The pattern velocity ($\equiv -\omega_i/m$) and the amplification rates ($\equiv \omega_i$) for the principal mode, with $m = 2$, are listed in Table 5. As the bulge decreases, the pattern velocity also decreases, which implies that the dominant pattern rotates slower in systems with smaller bulge content. On the other hand, the amplification rate decreases as the bulge increases (or β decreases). However, in the disks with $0{\cdot}4 < \beta < 3{\cdot}0$ and $\alpha = 0{\cdot}25$, ω_i remains essentially constant.

Table 5. Convergence of eigenmodes with the increase in the dimension of the matrix M. $m = 2$, $c = 0$ (cold disk), $a/b = 0{\cdot}25$, $M_d/M_b = 1{\cdot}0$.

Dimension of the truncated eigenmatrix	Principal mode	
	ω_r	$-\omega_i$
9 × 9	1·2727	0·2654
15 × 15	1·3481	0·3508
21 × 21	1·3591	0·3640
27 × 27	1·3617	0·3473
33 × 33	1·3625	0·3229
39 × 39	1·3631	0·2999
45 × 45	1·3650	0·2800

Fig. 4 shows the two armed patterns associated with the principal mode in the cold disks with α = 0·25 and with gradually increasing β. The spirals are smooth and tightly wrapped in the systems with massive bulge component (small β). It is noticed that the resulting patterns are strongly wrapped towards the central inner edge of the disk. However, as β increases (or the bulge diminishes) the patterns open up and spread over the entire disk. Thus, we find here that the spiral patterns tend to be more open in the systems with smaller central bulge. Such a feature would, probably in a more rigorous study with the background population II stars in the disk, help the understanding of the transition of Sa $\rightarrow$ Sc galaxies.

Takahara (1978), Aoki, Noguchi and Iye (1979) and Ambastha and Varma (1981) pointed out that the global density waves in self-gravitating disks can be suppressed if the thermal energy (or pressure) is increased. In moderately warm disks, the snort wavelength (or the tightly wound) modes are significantly affected by the pressure. We obtain a similar result here in the case of disk-bulge systems also. Table 6

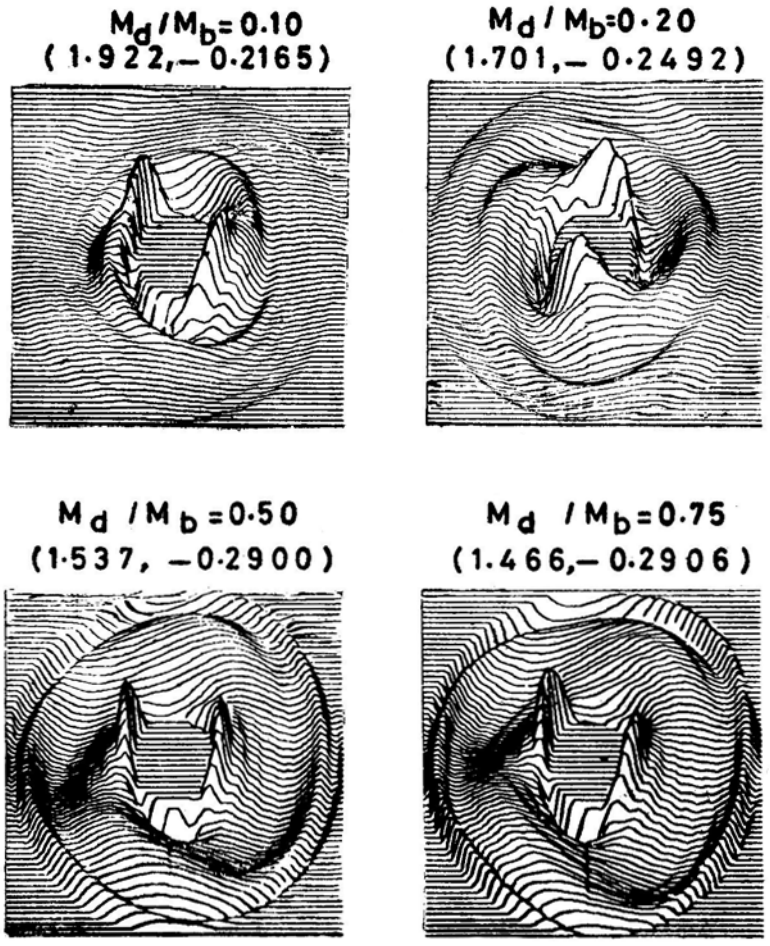

Figure 4. The bisymmetric (m = 2) surface-density perturbation Patterns associated with the principal mode.The sequence exhibits the patterns in the disks with decreasing bulge mass.

Table 6. Effect of thermal pressure on unstable modes, (m = 2), M_d/M_b = 1·0, a/b = 0·25.

	I		II	
c	ω_r	$-\omega_i$	ω_r	$-\omega_i$
0·000	1·3650	0·2820	1·3150	0·0774
0·001	1·3472	0·2633	1·3341	0·0813
0·002	1·3264	0·2457	1·3474	0·0848
0·003	1·3040	0·2321	1·3823	0·0853
0·004	1·2838	0·2223	1·4046	0·0819
0·005	1·2672	0·2140	1·4232	0·0766
0·006	1·2536	0·2057	1·4390	0·0706
0·007	1·2425	0·1968	1·4527	0·0643
0·008	1·2337	0·1873	1·4649	0·0580
0·009	1·2269	0·1772	1·4760	0·0516
0·010	1·2212	0·1667	1·4862	0·0450
0·015	1·2208	0·1152		
0·020	1·2393	0·0741		
0·025	1·2620	0·0327		
0·030				

shows the frequencies in. 'hot' disks for β = 1·0, α = 0·25 and m = 2. As the pressure (measured by the parameter c) increases, the amplification rate of the principal mode decreases and finally vanishes completely at c = 0·03. The second unstable mode follows this trend at $c \gtrsim 0{\cdot}015$. Fig. 5 shows the pattern of oscillation associated with the density perturbations for the principal mode when β = 1·0. α = 0·25 and c = 0·002. We find that the peaks near the inner edge remain unchanged, whereas, the amplitude near the outer edge exhibits an abrupt jump.

In all cases, the eigen-patterns rotate in a clock-wise sense.

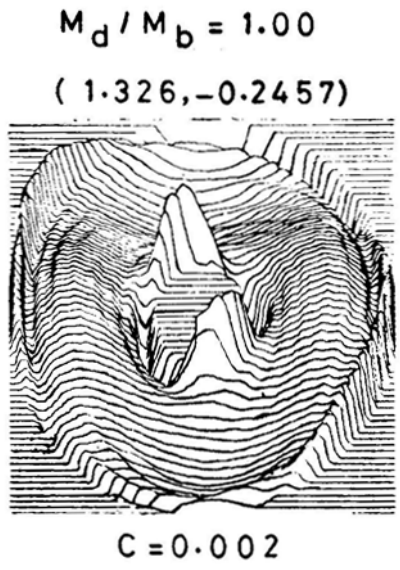

Figure 5. The principal bisymmetric mode in a hot disk, with the measure of 'hotness', c = 0·002.

6. Conclusions

In all cold disks, there exist modes with large growth rates, which represent the 'explosive' or violent instabilities of the system. Such modes, however, cannot grow indefinitely, since the energy content of the disk is not infinite. Their growth would be affected by nonlinear effects and also by large halo enveloping the disk. We show here that such instabilities may not occur in the presence of massive central bulge of the galactic systems.

We find here some indications that the nature of the spiral patterns would depend on the disk-to-bulge ratio. The dominant mode shows a regular and smooth spiral pattern, which opens up and covers entire disk as the central bulge diminishes. This may, in some sense, explain the transition from Sa to Sc type as the amorphous bulge decreases in the galactic systems. There exist some modes with $\omega_i \ll \omega_r$ growing very slowly compared to the principal mode and show broken and ill-defined patterns, suggesting that the principal mode may dominate the system ultimately. However, only a nonlinear analysis governing the evolution of the system would resolve this problem.

It may be interesting to consider the possibility of the disk continuing inside the bulge. However, the bulge has been considered here as fixed and spherical in shape such that the potential contributed by it at a point, external to its surface, can simply be assumed as the potential of a point mass placed at the centre of the system. If the disk continues inside the bulge, the potential of the bulge has to be modified accordingly.

A study of the effect of various fixed population II distributions on the stability of the annular disks is being carried out.

Acknowledgements

The computational work has been carried out on IBM 360/44 at the computer centre, Physical Research Laboratory.

Appendix

We list here the expressions for the matrix elements constituting the infinite sub-matrices, P, Q, R ... of the eigen-matrix, M:

$$M_j P_{kj} = \tfrac{1}{2}\,{}^{(m-1)}\mathbf{F}_{kj}^{(m-1)} + \tfrac{1}{2}\int_a^1 \xi\, V_0(\xi)\,(\lambda_j F_{j\xi}^m F_{k\xi}^{m-1} + \lambda_k F_{j\xi}^{m-1} F_{k\xi}^m)\, d\xi$$

$$- 2(m-1)\int_a^1 V_0(\xi)\, F_{j\xi}^{m-1} F_{k\xi}^{m-1}\, d\xi$$

$$M_j Q_{kj} = \tfrac{1}{2}\,{}^{(m-1)}\mathbf{F}_{kj}^{(m+1)} - \tfrac{1}{2}\int_a^1 \xi\, V_0(\xi)\,(\lambda_k F_{j\xi}^{m-1} F_{k\xi}^m - \lambda_j F_{j\xi}^m F_{k\xi}^{m-1})\, d\xi$$

$$M_j\, R_{kj} = c\,\gamma \int_\alpha^1 \xi\, \sigma_0^{\gamma-2}\,(\xi)\,\lambda_j\, F_{j\xi}^m\, F_{k\xi}^m\, d\xi - \frac{1}{\pi}\left(M_k\,\delta_{kj} + \frac{4}{\pi^2}\mathbf{I}_{kj}^{(1)}\right)$$

$$M'\, S_{kj} = -\tfrac{1}{2}\,{}^{(m+1)}\mathbf{F}_{kj}^{(m-1)} + \tfrac{1}{2}\int_\alpha^1 \xi\, V_0\,(\xi)\,(\lambda_j\, F_{j\xi}^m\, F_{k\xi}^{m-1} - \lambda_k\, F_{k\xi}^m\, F_{j\xi}^{m+1})\, d\xi$$

$$M_j'\, T_{kj} = -\tfrac{1}{2}\,{}^{(m+1)}\mathbf{F}_{kj}^{(m+1)} - 2\,(m+1)\int_\alpha^1 F_{j\xi}^{m+1}\, F_{k\xi}^{m+1}\, V_0\,(\xi)\, d\xi$$

$$+ \tfrac{1}{2}\int_\alpha^1 \xi\, V_0\,(\xi)\,(\lambda_j\, F_{j\xi}^m\, F_{k\xi}^{m+1} + \lambda_k\, F_{j\xi}^{m+1}\, F_{k\xi}^m)\, d\xi$$

$$M_j'\, U_{kj} = -\,c\,\gamma \int_\alpha^1 \xi\, \sigma_0^{\gamma-2}\,(\xi)\,\lambda_j\, F_{j\xi}^m\, F_{k\xi}^m\, d\xi + \frac{1}{\pi}\left(M_k'\,\delta_{kj} - \frac{4}{\pi^2}\mathbf{I}_{kj}^{(2)}\right)$$

$$M_j''\, V_{kj} = \tfrac{1}{2}\int_\alpha^1 \xi\, \sigma_0\,(\xi)\,\lambda_j\, F_{j\xi}^{m-1}\, F_{k\xi}^{m-1}\, d\xi$$

$$M_j''\, W_{kj} = -\tfrac{1}{2}\int_\alpha^1 \xi\sigma_0\,(\xi)\,\lambda_j\, F_{j\xi}^{m+1}\, F_{k\xi}^{m+1}\, d\xi$$

$$M_j''\, X_{kj} = -\,m\int_\alpha^1 V_0\,(\xi)\, F_{j\xi}^m\, F_{k\xi}^n\, d\xi$$

where, we have defined

$${}^{(m-1)}\mathbf{F}_{kj}^{(m-1)} = V_0\,(1)\, F_k^{m-1}\, F_j^{m-1} - V_0\,(\alpha)\, F_{k\alpha}^{m-1}\, F_{j\alpha}^{m-1}$$

$${}^{(m-1)}\mathbf{F}_{kj}^{(m+1)} = V_0\,(1)\, F_k^{m-1}\, F_{jk}^{m+1} - V_0\,(\alpha)\, F_{k\alpha}^{m-1}\, F_{j\alpha}^{m+1}$$

$${}^{(m+1)}\mathbf{F}_{kj}^{(m-1)} = V_0\,(1)\, F_k^{m+1}\, F_j^{m-1} - V_0\,(\alpha)\, F_{k\alpha}^{m+1}\, F_{j\alpha}^{m-1}$$

$${}^{(m+1)}\mathbf{F}_{kj}^{(m+1)} = V_0\,(1)\, F_k^{m+1}\, F_j^{m+1} - V_0\,(\alpha)\, F_{k\alpha}^{m+1}\, F_{j\alpha}^{m+1}$$

and

$$\mathbf{I}_{kj}^{(1)} = \int_0^\infty \frac{z^2 dz}{(\lambda_k^2+z^2)\,(\lambda_j^2+z^2)}\left[\frac{K_z^m}{Y_j^m}\left\{ zF_k^{m-1}\, I_z^m - z\alpha\, F_{k\alpha}^{m-1}\, I_{z\alpha}^m \right.\right.$$

$$\left.\left. - \frac{I_{z\alpha}^m}{Y_{j\alpha}^m}\left\{ zF_k^{m-1}\, K_z^m - z\alpha\, F_{k\alpha}^{m-1}\, K_{z\alpha}^m \right\} \right]\right.$$

$$\mathbf{I}_{kj}^{(2)} = \int_0^\infty \frac{z^2\,dz}{(\lambda_k^2+z^2)\,(\lambda_j^2+z^2)}\left[\frac{K_z^m}{Y_j^m}\left\{zF_k^{m+1}\,I_z^m - za\,F_{k_a}^{m+1}\,I_{z_a}^m\right\}\right.$$
$$\left. + \frac{I_{z_a}^m}{Y_{j_a}^m}\left\{zF_k^{m+1}\,K_z^m - za\,F_{z_a}^{m+1}\,K_{z_a}^m\right\}\right].$$

Also, M_j, M'_j and M''_j are defined as

$$M_j = -\tfrac{1}{2}\,[F_j^{m-1}\,F_j^{m-1} - F_{j_a}^{m-1}\,F_{j_a}^{m-1}]$$

$$M'_j = -\tfrac{1}{2}\,[F_j^{m+1}\,F_j^{m+1} - F_{j_a}^{m+1}\,F_{j_a}^{m+1}]$$

$$M''_j = -\tfrac{1}{2}\,[F_j^{m+1}\,F_j^{m-1} - F_{j_a}^{m+1}\,F_{j_a}^{m-1}].$$

In all the above expressions, we have represented Bessel's functions, for brevity, as

$F_{j_a}^m \rightarrow F_m\,(\lambda_j\,a)$, *etc.*

References

Ambastha, A. 1981, *Ph D thesis*, Physical Research Laboratory, Ahmedabad.
Ambastha, A., Varma, R. K. 1978, *Astrophys. Sp. Sci*., **55,** 459.
Ambastha, A., Varma, R. K. 1981, Preprint.
Aoki, S., Noguchi, M., Iye, M. 1979, *Publ. astr. Soc. Japan*, 31, 737.
Berman, R. H., Brownrigg, D. R. K., Hockney, R. W. 1978, *Mon. Not. R. astr. Soc*, **185,** 861.
Bertin, G. 1980, *Phys. Rep*., **61,** 1.
Bertin, G., Mark, J. W.-K. 1978, *Astr. Astrophys*., **64,** 389.
Clutton-Brock, M. 1972, *Astrophys. Sp. Sci.*, **16,** 101.
Freeman, K. C. 1970, *Astrophys. J*., **160,** 811.
Gordon, M. A., Burton, W. B. 1976, *Astrophys. J*., **208**, 346.
Hart, L., Pedlar, A. 1976, *Mon. Not. R. astr. Soc.*, **176,** 547.
Hohl, F. 1976, *Astr. J*., **81,** 30.
Iye, M. 1978, *Publ, astr. Soc. Japan*, **30**, 223.
Kato, S. 1970, *Publ. astr. Soc. Japan*, **22,** 285.
Kodaira, K. 1974, *Publ. astr. Soc. Japan*, **26,** 255.
Lin, C. C., Shu, F. H. 1964, *Astrophys. J*., **140,** 646.
Lin, C. C., Shu, F. H. 1966, *Proc nat. Acad. Sci. Am*., 55, 229.
Lin, C. C, Yuan, C, Shu, F. H. 1969, *Astrophys. J*., **155,** 721.
Lynden-Bell, D., Ostriker, J. P. 1967, *Mon. Not. R. astr. Soc.*, **136,** 293.
Mark, J. W.K. 1977, *Astrophys. J.*, **212**, 645.
Norman, C. A. 1978, *Mon. Not. R. astr. Soc.*, **182,** 457.
Pannatoni, R. F., Lau, Y. Y. 1979, *Proc nat. Acad. Sci. Am*., **76,** 4.
Sandage, A., Freeman, K. C., Stokes, N. R. 1970, *Astrophys. J*., **160,** 831.
Shu, F. H. 1970, *Astrophys. J.,* **160,** 89.
Stecker, F. W. 1976, GSFC Report X-662-76-154, 357.
Takahara F. 1978, *Publ. astr. Soc. Japan,* **30**, 253.
Toomre, A. 1969, *Astrophys. J*., **158,** 899.
Yabushita, S. 1969, *Mon. Not. R. astr. Soc*., **142,** 201.

J. Astrophys. Astr. (1982) **3**, 145–150

Spectrophotometric Observations of a Peculiar Nitrogen-Rich Planetary Nebula NGC 2440*

R. Louise *Observatoire de Marseille, 2 Place Le Verrier, 13248 Marseille Cedex 4, France*

Received 1981 February 22; accepted 1982 March 24

Abstract. By using the Boller and Chivens spectrograph with a moderate dispersion (59 Å mm^{-1}) in the red spectral region, we obtained 65 spectra covering the whole surface of the planetary nebula NGC 2440. Intensities of Hα, [N II] λλ 6548–6584 and [S II] λλ 6717–6731 lines are derived using the IDS system available at the ESO in La Silva (Chile). The nebula is known to be a nitrogen-rich nebula (Peimbert 1978) surrounded by secondary structures (Minkowski 1964). The unusual high value of the [N II]/Hα in the central core (~ 3·0) is certainly due to the nitrogen overabundance occurring in that part of the nebula. Its variations from the centre to the outer regions are interpreted as a consequence of small-scale ionization structure (Capriotti, Cromwell and Williams 1971). The observations show clearly an outward increase of both [NII]/Hα and I(6717)/I(6713) ratios.

Key words: planetary nebulae—line intensities

1. Introduction

Long exposure plates taken in the Hα + [N II] light reveal faint nebulosities surrounding some planetary nebulae (Duncan 1937; Minkowski and Osterbrock 1960; Minkowski 1964). They generally show filamentary structure emitting strong [N II] line relative to Hα (Louise 1981a). In order to study these 'secondary structures' —following the terminology of Louise (1981b)—the planetary nebula NGC 2440 is a good sample for spectrophotometric investigations. Indeed, this nebula emits an unusually strong [N II] line and shows a complex filamentary structure. In photographs taken by Minkowski (1964) with increasing exposure, it shows a hierarchy of structures. It appears at first as a chaotic central core surrounded by filaments

*All observations were made at the ESO in Chile.

and condensations, then as a butterfly resembling the structure of NGC 650-1 (Louise 1981b) and finally as a broken hour-glass. In the classification of Greig (1971, 1972) it belongs to the B class which is defined as having strong forbidden lines of elements in very different degrees of ionization. It is also a member of the subgroup of lielium- and nitrogen-rich planetary nebulae defined by Peimbert (1978). These nebulae, with galactic distribution and kinematical properties corresponding to Population I, are thought to be products of stars with masses towards the higher end of the progenitor mass range (Kaler 1979).

Isophotal contour maps are given in various emission lines by Aller (1956) and Phillips, Reay and Worswick (1980). Radio contours are obtained at 8085 and 2695 MHz by Terzian, Balick and Bignell (1974). Both optical and radio observations show clearly a strong north-south bipolarity.

2. Observations and results

By using the Boller-and-Chivens spectrograph mounted at the Cassegrain focus of the 1·52-m telescope of the ESO in La Silla (Chile), we obtained 65 spectra covering the whole surface of NGC 2440. The Image Dissector Scanner (IDS) system was used throughout, and Feige 110 was adopted as a standard star (Stone 1972). The spectral dispersion and slit aperture were respectively 59 Å mm^{-1} and 4 arcsec ×4 arcsec.

Fig. 1 gives a sample of spectra obtained with the IDS system. Intensities are given with respect to the standard star intensity for each wavelength. The strength of the [N II] line relative to Hα is really striking. The mean value of the [N II]/Hα is equal to 3 in the central core of the nebula. This ratio is unusually high compared with the other planetary nebulae and H II regions. This is easy to understand in the light of the high nitrogen abundance in NGC 2440 (Peimbert 1978).

Intensities of the [S II] λλ 6717–6731 lines are measurable in spite of their relative weakness. Their ratio leads to the determination of electron density (Pradhan 1978; Cantó *et al.* 1980; Czyzak and Aller 1979).

Table 1 gives, for each position of the slit with respect to the centre of the nebula, the measured intensities of various lines. They are expressed in 10^{-2} of the corresponding intensity of the standard star, Feige 110. The ratios of [NII]/Hα and

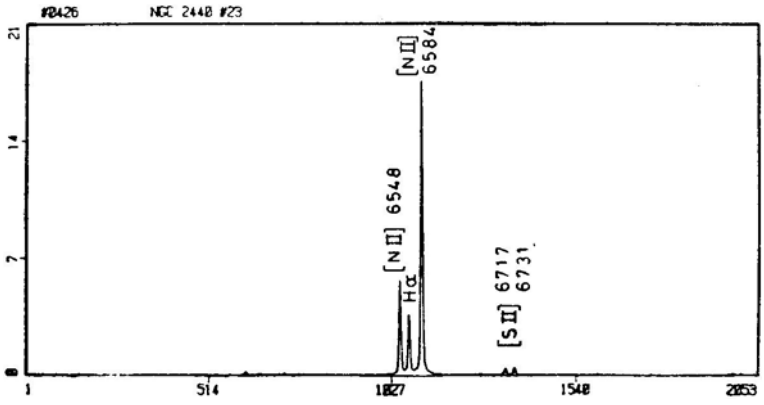

Figure 1. A sample of spectra obtained with the IDS system. Intensities are given with respect to the standard star Feige 110 for every wavelength.

Table 1. Measured intensities of various emission lines expressed in 10^{-2} of the corresponding intensity of the standard star, Feige 110.

$\Delta\alpha$ (arcsec)	$\Delta\delta$ (arcsec)	$I(6548)$ $(10^{-2}I_*)$	$I(\mathrm{H}\alpha)$ $(10^{-2}I_*)$	$I(6584)$ $(10^{-2}I_*)$	$I(6717)$ $(10^{-2}I_*)$	$I(6731)$ $(10^{-2}I_*)$	$\frac{I(6584)}{\mathrm{H}\alpha}$	$\frac{I(6717)}{I(6731)}$
0	0	9667	13933	26268	267	400	1·9	0·7
−4	0	6067	7467	17967	233	420	2·4	0·6
−8	0	2133	2098	6711	124	160	3·2	0·8
−12	0	607	622	2053	29·6	53·3	3·3	0·6
−16	0	84	126·4	281	10	7·9	2·2	1·3
−20	0	32·7	52·3	99·5	3·3	3·9	1·9	0·8
−24	0	21·9	32·7	61·1	4·1	4·8	1·9	0·9
−28	0	44·1	31·6	111·5	5·8	5·8	3·5	1·0
−32	0	35·1	24·9	96·6	5·3	3·8	3·9	1·4
−36	0	9·5	11·1	17·9			1·6	
+4	0	9022	11600	25133	322	387	2·2	0·8
+8	0	2400	2600	7700	120	190	3·0	0·6
+20	0	77·4	98·2	208·4	11·9	7·4	2·1	1·6
+24	0	116·9	109·4	373	17·4	14·9	3·4	1·2
+28	0	111·4	79·6	392·7	17·5	15·9	4·9	1·1
+32	0	47·3	30·9	125·5	9·7	8·7	4·1	1·1
+36	0	7·2	10·3	14·6			1·4	
+40	0	6·7	8·6	12·1			1·4	
0	−4	10491	12207	29756	458	572	2·4	0·8
0	−8	2176	1667	6667	167	185	4·0	0·9
0	−12	570	376	1763	52	52	4·7	1·0
0	−16	46·2	41	114·8	4·5	4·9	2·8	0·9
0	−20	38·7	31·8	96·7	5	3·9	3·0	1·3
0	−24	36·8	21·8	83·9	3·4	4·6	3·8	0·8
0	−28	9·8	15·9	15·1			1·0	
0	+4	8815	8343	23296	346	409	2·8	0·9
0	+8	1067	613	3093	102	107	5·0	1·0
0	+12	622	320	1970	65	65	6·2	1·0
0	+16	16·5	10·5	47·5	1·4	1·2	4·5	1·2
0	+20	5·4	4·3	9·9	1	1	2·3	1·0
−8	+20	6·8	5·7	20·7	1	1·2	3·6	0·8
−8	+12	63·7	69·2	215·9	7·8	6·9	3·1	1·1
−8	+4	16·1	19·9	48·1	3·4	3·4	2·4	1·0
−8	−12	55·1	27·1	179·6	7·7	6·7	6·6	1·1
−8	−20	5	5·2	13·8			2·7	
−16	−20	3·2	3·4	6·3			1·9	
−16	−12	52·6	28·5	171	6·8	8·3	6·0	0·8
−16	−4	16·7	19·6	57·3	1·5	1·9	2·9	0·8
−16	+4	85·1	52·7	309·9	8·1	9·3	5·9	0·9
−16	+12	64·5	39·3	218·7	5·6	5·6	5·6	1·0
−16	+20	5·4	3·9	18·1			4·7	
−24	+20	1·9	3·3	4·4			1·4	
−24	+12	15·2	8·7	47	2·2	2·2	5·4	1·0
−24	+4	8·8	7·2	26·8			3·7	
−24	−4	6·2	6·2	18·4			3·0	
−24	−12	6·2	6·2	18·4			3·0	
−24	−20	1·5	2·4	3·7			1·6	
+8	−20	12·4	6·9	38·3	1·1	1·1	5·6	1·0
+8	−12	184·6	110·8	615·4	17·2	20·5	5·6	0·8
+8	−4	753	710	2533	33·3	40	3·6	0·8
+8	+4	467	367	1489	22·2	22·2	4·1	1·0
+8	+12	28·4	15	101·6	5·4	4·7	6.8	1·1
+8	+20	3·6	3·8	7·2			1·9	
+16	+20	3·4	2·8	5			1·8	
+16	+12	25·5	14·8	87·6	4·1	3	5·9	1·4

Table 1. Concluded.

Δα (arcsec)	Δδ (arcsec)	I(6548) ($10^{-2}I_*$)	I(Hα) ($10^{-2}I_*$)	I(6584) ($10^{-2}I_*$)	I(6717) ($10^{-2}I_*$)	I(6731) ($10^{-2}I_*$)	$\frac{I(6584)}{H\alpha}$	$\frac{I(6717)}{I(6731)}$
+16	+4	30·7	25·2	90·8	2·5	2·5	3·6	1·0
+16	−4	116	66	354	12·6	12·6	5·4	1·0
+16	−12	109	55	356	9·5	9·5	6·5	1·0
+16	−20	596	207	1582	39	26	7·6	1·5
+24	−20	3	2·8	7·9			2·9	
+24	−12	27·3	15·4	87·9	2·4	4·8	5·7	0·5
+24	−4	59·9	34·9	169·7	7·5	10	4·9	0·8
+24	+4	21·1	17·8	72	3·8	3·2	4·1	1·2
+24	+12	10	7·2	33·2	1·8	1·3	4·6	1·3
+24	+20	2	2·6	3·7			1·5	

I(6717)/I(6731) can be directly calculated without any correction for interstellar reddening.

It is noted that [N II] /Hα ratio covers a large range of values from 1 to 7·6 , with a mean value equal to 3 in the central core. Certainly the nebula is overabundant in nitrogen, but variations of [N II] /Hα from one point to another must be explained in terms of small-scale ionization structure and/or temperature effect (see Section 3). The ratio of the two lines of [S II] varies slowly outwards. The mean value is equal to 1 in the central region, indicating a typical electron density (10^3 cm^{-3}) occurring in planetary nebulae.

In Fig. 2 contours of [N II] /Hα are drawn. The underlined numbers indicate mean values of the corresponding contours. It may be noted that they increase outwards, particularly in the southwest direction, indicating the typical feature of secondary structures in planetary nebulae (Louise 1981a).

Fig. 3 gives contours of I(6717)/I(6731). This ratio also increases outwards, but slower than [N II]/Hα. This means that the density variations within the nebula

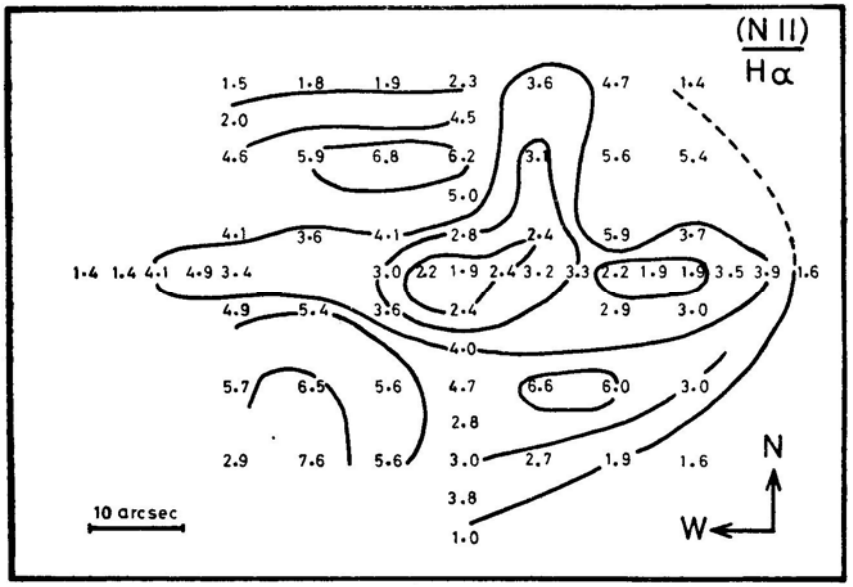

Figure 2. Contours of the intensity ratio I(6584)/Hα. Underlined numbers indicate mean values of the corresponding contours.

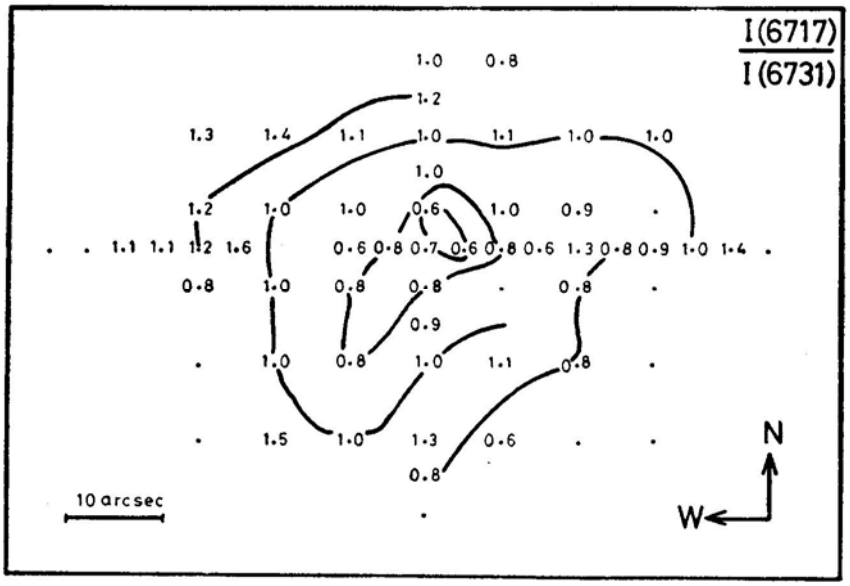

Figure 3. Contours of the intensity ratio *I*(6717)/*I*(6731).

are small. Again, filaments and globules occuring in outer parts of nebula can account for these variations.

3. Discussions

Elevated temperature is usually invoked to account for the enhancement of [N II] line with respect to Hα (Louise 1981a). In fact, the presence of filaments and/or globules introduces small-scale ionization structure. Capriotti, Cromwell and Williams (1971) show that, unlike optically thin condensations (Harrington 1969; Flower 1969; Kirkpatrick 1970; Williams 1970), optically thick condensations as small as 10^5 cm in diameter could survive for the lifetime of a planetary nebula. It is demonstrated that small-scale ionization structure enhances the emission by low excitation ions such as N+, O° and O^+. This is supported by direct photography (Louise 1981a; Capriotti, Cromwell and Williams 1971). In addition, following the study of van Blerkom and Arny (1972), filaments extending radially outward from the condensations are considered to be shadows. The shadowed regions are expected to contain low excitation ions, because only diffuse radiation of low temperature could reach them.

High density is expected to occur in filaments and condensations. Because of the effects mentioned above, only their surface layer emits [S II] lines. Therefore, our measures of *I*(6717)/*I*(6731) do not reflect the inside densities of filaments and condensations. Hence the increase of that ratio outwards, as indicated by Fig. 3, must be interpreted as an increase of 'skin density' of secondary structures occurring in NGC 2440.

4. Conclusion

Spectrophotometry with modern instruments such as the IDS system permits detailed observations of the secondary structures in planetary nebulae. Line ratios, such as [N II] /Hα and 7(6717)/ (6731), are directly measurable. They lead to a more critical study of the physical properties of these structures, the origin of which is not yet clear.

NGC 2440 is certainly a nitrogen-rich planetary nebula for it presents high values of [N II]/Hα over its whole surface. However, because of the presence of secondary structures, the outward enhancement of [N II] line relative to Hα must be understood by means of the small-scale ionization structure. Furthermore, measures of *I*(6717)/ *I*(6731) must be interpreted as reflecting the 'skin density' of filaments and condensations within the nebula. From the observational point of view, it is clearly shown that both [N II]/Hα and *I*(6717)/*I*(6731) ratios increase outwards. This is a typical feature of secondary structures in planetary nebulae.

References

Aller, L. H. 1956, *Gaseous Nebulae*, Vol. 3, Chapman and Hall, London, p. 262.
Canto, J., Elliott, K. H., Meaburn, J., Theokas, A. C. 1980, *Mon. Not. R. astr. Soc.,* **193**, 911.
Capriotti, E. R., Cromwell, R. H., Williams, R. E. 1971, *Astrophys. Lett.,* **7,** 241.
Czyzak, S. J., Aller, L. H. 1979, *Mon. Not. R. astr. Soc.,* **188,** 229.
Duncan, J. C. 1937, *Astrophys. J.,* **86**, 496
Flower, D. R. 1969, *Mon. Not. R. astr. Soc.,* **146**, 243.
Greig, W. E. 1971, *Astr. Astrophys.,* **10,** 161.
Greig, W. E. 1972, *Astr. Astrophys.,* **18,** 70.
Harrington, J. P. 1969, *Astrophys. J.,* **156,** 903.
Kaler, J. B. 1979, *Astrophys. J.,* **228**, 163.
Kirkpatrick, R. C. 1970, *Astrophys. J.,* **162,** 33.
Louise, R. 1981a, *Astr. Astrophys.,* **98**, 81.
Louise, R. 1981b, *Astr. Astrophys.,* **102,** 303.
Minkowski, R. 1964, *Publ. astr. Soc. Pacific,* **76,** 197.
Minkowski, R., Osterbrock, D. 1960, *Astrophys. J.,* **131,** 537.
Peimbert, M. 1978, in *IAU Symp. 76: Planetary Nebulae: Observations and Theory,* Ed. Y. Terzian, D. Reidel, Dordrecht, p. **215.**
Phillips, J. P., Reay, N. K., Worswick, S. P. 1980, *Mon. Not. R. astr. Soc.,* **193**, 231.
Pradhan, A. K. 1978, *Mon. Not. R. astr. Soc.,* **183,** 89p.
Stone, R. P. S. 1972, *Astrophys. J.,* **218,** 767.
Terzian, Y., Balick, B., Bignell, C. 1974, *Astrophys. J.,* **188,** 257.
Van Blerkom. D., Arnyy, T. T. 1972, *Mon. Not. R. astr. Soc.,* **156,** 91.
Williams, R. E. 1970, *Astrophys. J.,* **159,** 829.

J. Astrophys. Astr. (1982) **3,** 151–159

Time Structure of Solar Decametre Type III Radio Bursts

G. Thejappa and Ch. V. Sastry *Indian Institute of Astrophysics, Bangalore 560034*and *Raman Research Institute, Bangalore 560080*

Received 1981 December 30; accepted 1982 March 26

Abstract. The time structure of solar radio decametre Type III bursts occurring during the periods of enhanced emission is investigated. It is found that the time profiles can take a variety of forms of which three distinct types are the following: (1) profiles where the intensity rises to a small but steady value before the onset of the main burst, (2) the intensity of the main burst reduces to a finite level and remains steady before it decays to the base level, (3) the steady state is present during the rise as well as the decay phase of the main burst.

It is shown that these profiles are not due to random superposition of bursts with varying amplitudes. They are also probably not manifestations of fundamental-harmonic pairs. Some of the observed time profiles can be due to superposition of bursts caused by ordered electron beams ejected with a constant time delay at the base of the corona.

Key words: Sun–Type III bursts—time profiles

1. Introduction

The time structure of Type III radio bursts was investigated in detail by several authors. These bursts are believed to be caused by electron streams moving outwards through the corona and exciting plasma waves which are transformed into electromagnetic waves. The usual time profile of a Type III burst is characterized by a sharp rise followed by an exponential type of decay. If the decay is due to collisional damping then one can calculate the kinetic temperature of the corona where the bursts originate. It was pointed out by Aubier and Boischot (1972) that it is possible to estimate the duration of the exciter (the time taken for the electron streams to cross a particular plasma level) and the decay constant from the observed time profiles. They also showed that the exciter duration and decay constants are positively correlated and questioned the collisional damping hypothesis. During the

course of our observations of storm Type III bursts, we found that the time profile of these bursts can take a variety of forms of which three distinct profiles are presented here. They are (1) profiles where the intensity rises to a small but steady value before the onset of the main burst, (2) the intensity of the main burst reduces to a finite level and remains steady before it decays to the base level, (3) the steady state is present during the rise as well as the decay phase of the main burst.

2. Equipment and observations

2.1 *Equipment*

The observations were made with the Gauribidanur radio telescope (latitude 13° 36′ 12″ N and longitude 77° 26′ 07″ E). We have used the NS array of the telescope in conjunction with a multi-channel receiver. The effective area of the NS array exceeds 10,000 m^2. The central frequency of the receiving system is 34·5 MHz. The pre-detection bandwidth and the post-detection time constants were 15 KHz and 10 ms respectively. The separation between channels is 50 KHz and the present number of channels is sixteen covering a total bandwidth of 800 KHz. The minimum detectable flux with the above parameters is about 1 solar flux unit (SFU). The data are recorded in analog form using oscillographic recorders and also digitally on magnetic tape units. The equipment was operated for about an hour around the local noon during periods of enhanced emission from the sun.

2.2 *Observations*

We have already reported some of our observations on storm bursts which are mainly Of short duration (≈ 1s)and narrow band (Sastry 1969, 1971, 1972, 1973). In the present study we have considered time profiles of bursts whose total duration lies between 10–20 s. It is well known that the decametric noise storms consist of a succession of many Type III bursts. The duration of a Type IΠ burst at frequencies around 30 MHz lies in the above range (*e.g.* Krishan, Subramanian and Sastry 1980; Subramanian, Krishan and Sastry 1981). The frequency drift of a Type III burst at these frequencies is of the order of 30 MHz s^{-1}. Since the duration is in the expected range and also there is no measurable frequency drift in our records we believe that the events we discuss here are Type III bursts. Also, all the other types of known solar bursts have completely different characteristics in this frequency range.

Fig. 1 shows typical examples of bursts which were studied. In Fig. la, one can see that the intensity rises to about 20 per cent of the level of the main peak and remains reasonably steady for a period of about 4 s before the onset of the main burst, and we designate this as Type A profile. Another type of burst in which the intensity decays to about 30 per cent of the main peak level and remains steady for a period of 2 s before it decays to the base level is shown in Fig. lb, and is designated as Type B profile. In Fig. lc, there is a small but steady rise in intensity for a period of 3 s before the onset of the main burst, and also the main burst decays to a constant level of about 20 per cent of the main peak and remains steady for a period of 3 s, which we call a Type C profile. Out of the total number of 165 bursts studied, 34 per cent belong to Type A, 45 per cent to Type B and 21 per cent to Type C profiles. We have

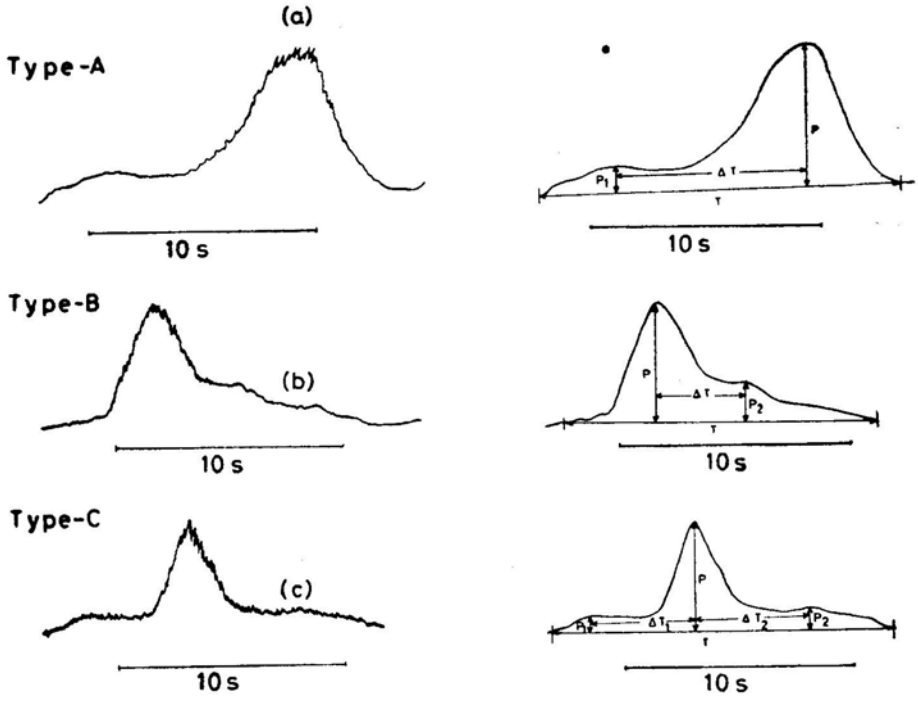

Figure 1. Typical examples of Type III burst profiles and the definition of burst parameters.

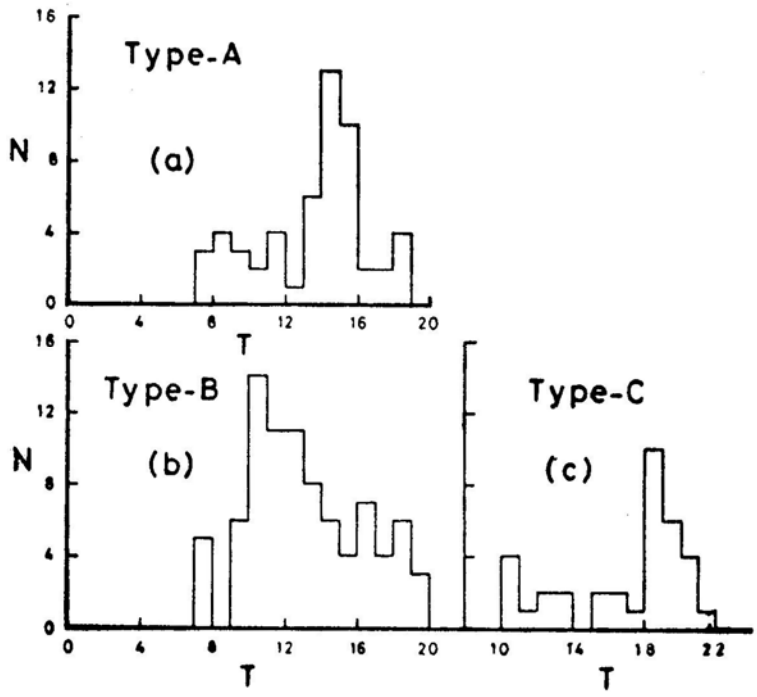

Figure 2. Histograms showing the number of bursts (*N*) versus total duration (*T*).

measured the various characteristics of these bursts illustrated in Fig. 1, which are of interest to us in the following discussion.

Histograms depicting the variation of the number of bursts versus duration are given in Fig. 2 for the three types of profiles. It can be seen that in the case of Type A profiles the duration lies in the range 14–16 s and that for Type B lies in the range 10–15 s. The duration of Type C profiles is larger (≥18 s).

In Fig. 3 the distribution of ΔT,the time interval between the peak of the main burst and the onset time of steady level in the case of Type A and the start of decay of the steady level in the case of Type B is shown. For Type A profiles, ΔT is about 5–6 s, whereas it lies between 3–6 s for Type B profiles. In the case of Type C profiles, ΔT_1 (interval between the main peak and the onset of steady level) ranges from 5–7 s and ΔT_2 (time interval between the main peak and the start of decay of the steady level) is ≤ 8 s.

The distribution of the following amplitude ratios are shown in Fig. 4: (1) the level of the pre-rise to that of the main peak P_1/P, (2) the level to which the main burst

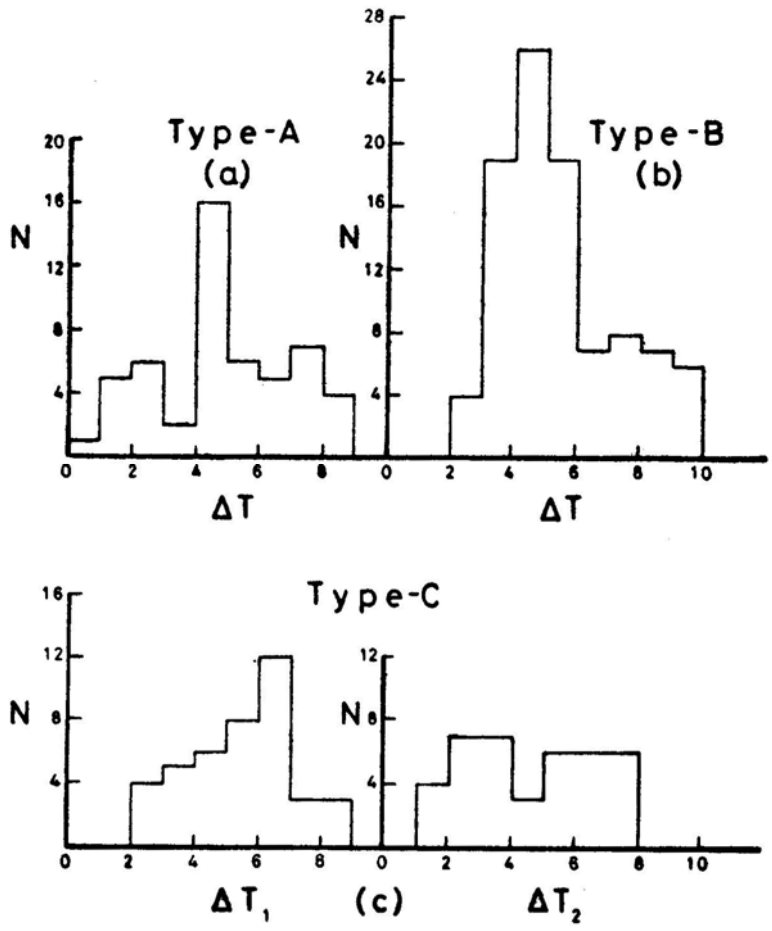

Figure 3 Histogarms showing the distributions of time intervals (ΔT). See Fig. 1 for the defintion of ΔT_1 and ΔT_2 in Type C profiles.

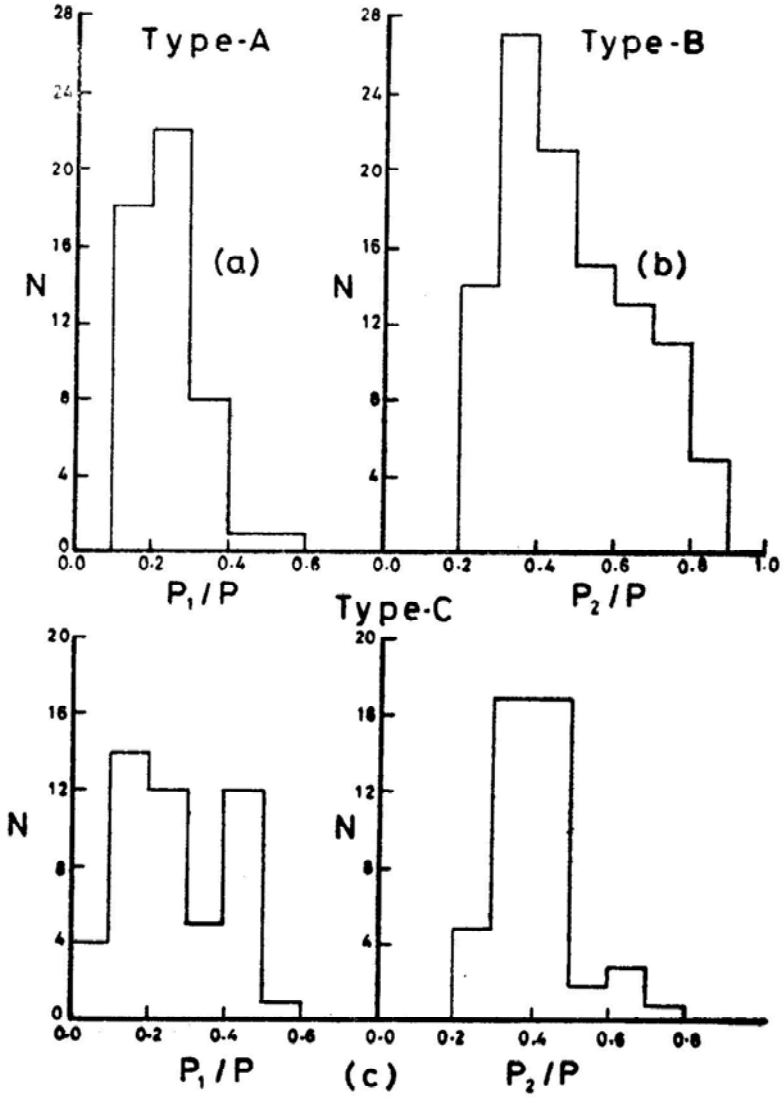

Figure 4. Histograms depicting the distribution of amplitude ratios P_1/P and P_2/P.

decays and remains steady to the level of the main peak P_2/P. It can be seen that the ratios P_1/P and P_2/P lie in the range 0·1 to 0·3 in all the profiles.

Following the procedure of Aubier and Boischot (1972) we have measured the decay constants of the main burst (τ_1)and also that of the final decay of the steady level (τ_2). Note that in the case of Type A profiles only τ_1 is present. From the histograms given in Fig. 5 it can be seen that the decay constants τ_1 and τ_2 lie in the range 1–4 s for all the three types of profiles. We did not find any strong correlation between the decay constant τ_1 and the duration of the exciter. Also τ_1 and the total duration T are uncorrelated.

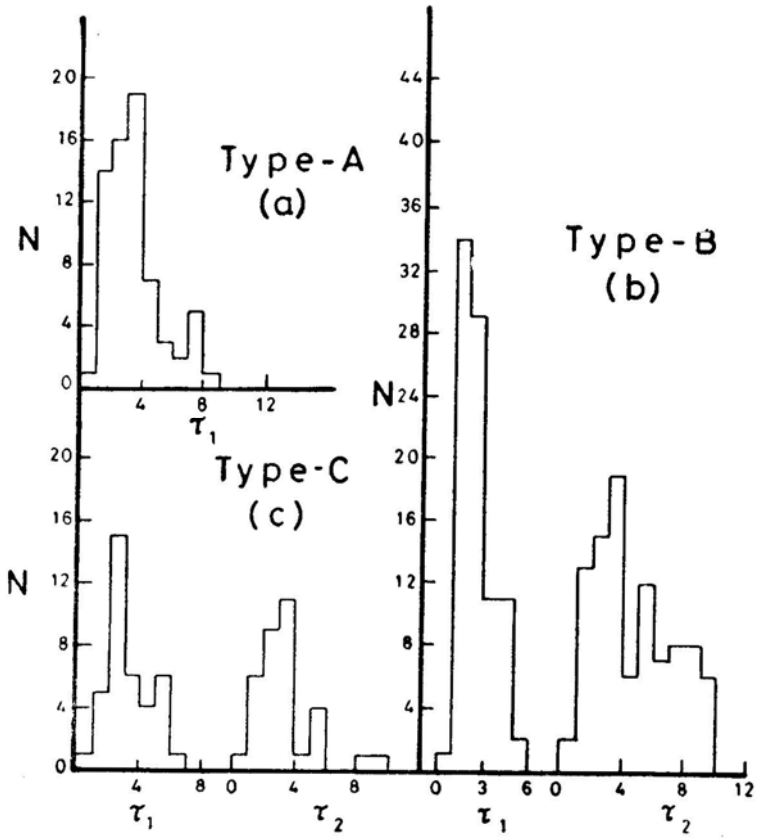

Figure 5. Histograms showing the distribution of decay constants τ_1 and τ_2.

3. Discussion

During the periods of enhanced emission at decametre wavelengths we have observed that there can be single or groups of bursts occurring at random intervals. Therefore, the simplest possible explanation for the three types of profiles presented here can be that they are due to superposition of bursts occurring randomly in time. But it is found that the occurrence of the three types of profiles presented here is maximum only on particular days although the period of enhanced emission may last for a much longer time. The fact that the time interval, ΔT as defined above tends to lie in a rather narrow range irrespective of the total duration of the burst, indicates that the profiles are not produced by entirely random superposition of independent events. Also the measured ratio of the amplitudes shows that the amplitudes of the initial and final phases are always a fraction of the main peak, and this ratio lies between 0·1–0·3. This need not be the case in case of bursts of various amplitudes occurring randomly In time.

The second possibility is that these profiles are the manifestations of fundamental-harmonic(f-h)pairs. From the work of Daigne and Møller-Pedersen (1974) and Rosenberg (1975), it is clear that the time separation between the peaks of the fundamental

and harmonic emissions is, in general, constant and is equal to about 4 s. It was also found that the amplitudes in f-h pairs are comparable (Rosenberg 1975). In the present case it is difficult to rule out the f-h pair hypothesis on the basis of the time intervals ΔT which are about the same as found by above authors. But the fact that the intensity ratios P_1/P and P_2/P observed by us are much less than unity does not lend support to this hypothesis. Also, according to Caroubalos, Poquerusse and Steinberg (1974) the ratio τ_F/τ_H of the decay constants of the fundamental and harmonic should be of the order of two if one assumes that the intensity of the fundamental $I_F \propto W$ (the energy density of plasma waves), the intensity of the harmonic $I_H \propto W^2$ and the temperatures in the regions of both fundamental and harmonic emissions are the same. Our observations show that τ_1 and τ_2 are in general same and in some cases τ_2 can be greater than τ_2 Even if our Type A and Type B profiles are possible manifestations of f-h pairs, it is difficult to interpret Type C profile on this basis. In the case of f-h pairs studied by Caroubalos, Poquerusse and Steinberg there are two clear-cut peaks in emission whereas in the profiles presented here no prominent subsidiary peak exists. Therefore, we believe that the profiles are probably not due to fundamental and harmonic emission. Zaitsev, Mityakov and Rapo port (1972) have calculated the Type III burst profiles by solving the one-dimensional relativistic quasi-linear equations on a timescale $t \gg \tau$ where τ is the characteristic time for the development of two-stream instability (time taken for the plateau formation $= \omega_{Pe}\, n/n_S$ where ω_{P_e} is the plasma frequency,*tnt*is the density of the background plasma and n_s is the density of electrons in the stream) and for the spatial scales $x \gg L$ where L is the initial thickness of the cloud under the initial conditions of a local explosion type. They have shown that at decametre and longer wavelengths—where the characteristic time of the absorption associated with collisions of electrons with ions in a 'cold' plasma, ν_{eff}^{-1} is much greater than the characteristic time of absorption due to Landau damping in the back of the stream $\Delta x/V_s$ (where Δx and V_s are the extent of the stream in the corona and its mean speed respectively) is satisfied—collisions can be neglected and only Landau damping in the tail of the stream determines the dissipation of plasma wave energy. Their theoretical profiles agree well with the experimental data in the hectometre range under the assumption that electromagnetic wave generation takes place at the second harmonic of the plasma frequency. Zaitsev *et al.* (1974) extended the same in the case where the injection time of hot electrons from the region of the flare is considerably greater than the time of existence of the burst at a given fixed frequency. The dissipation mechanism is the same Landau damping on tail of the beam even at the decametre and metre wavelengths. The results of Zaitsev *et al.* (1974) have been confirmed by the extensive numerical work done by many authors (Takakura and Shibahashi 1976; Magelssen and Smith 1977; Grognard 1980). The energy density of plasma waves is given by

$$W_L(\xi) = \frac{n_s\, \epsilon_0}{3\sqrt{2\pi}} \frac{(\epsilon_0/m)^{1/2}}{\nu_{eff}\, x} \left(\frac{2m\, \xi^2}{\epsilon_0}\right)^3 \exp\left(\frac{-2m\, \xi^2}{\epsilon_0}\right)$$

for the initial momentum distribution of the stream

$$f_0(p) = p \frac{n_s}{(2\pi m \epsilon_0)^{1/2}} \exp(-p^2/2m\epsilon_0).$$

The mean velocity of the beam

$$V_s = (\epsilon_0/m)^{1/2}$$

where n_s is the electron density in the beam, ε_0 is the initial energy of the beam, $\xi = x/t$, x is the distance between the photosphere and the respective plasma layer, m is the mass of an electron and ν_{eff} is the effective number of collisions.
The energy density reaches its maximum when

$$t = t_{max} = x\left(\frac{3}{2}\frac{\epsilon_0}{m}\right)^{-1/2}.$$

It is possible that the profiles presented here are due to the superposition of two or three bursts caused by ordered electron beams ejected with a constant time difference. In the case of Type A profiles, the electron beam responsible for the main burst should reach the appropriate plasma level soon after the electron beam causing the pre-rise leaves the same level. Then the time interval 'ΔT' is equal to the time at which W_L (plasma wave energy density) causing the main burst reaches its maximum. Since we know ΔT from observations, we can find the initial energy of the beam causing the main burst. From the observed ratio P_1/P, we can find the initial energy of the first beam. If we take $x = 1{\cdot}1 \times 10^{11}$ cm and $\Delta T = 4$ s, then $V_2 = 1{\cdot}856 \times 10^{10}$ cm s^{-1} and $V_1 = 0{\cdot}37 \times 10^{10}$ cm s^{-1}, where V_1 and V_2 are the mean velocities of the first and second beams respectively. By computing the resultant time profile with the above initial energies of the beams, we are able to reproduce approximate profiles of Type A and the rise part of Type C. It is not possible to reproduce the steady decay of Type B and Type C profiles in this manner. Note that the superposition of W_L is possible since we have used a combination of two beams which follow independent paths. It may be possible to construct all the time profiles by a combination of more than two beams. But it is not clear how the electron beams are accelerated to the above energies and ejected with constant time difference.

The other possible explanation for the observed profiles is that the conversion mechanism of plasma waves into electromagnetic waves and their decay show such a peculiar character.

4. Conclusion

We have investigated three distinct time profiles of Type III bursts occurring during the periods of enhanced emission. These are: (1) profiles where the intensity rises to a small but steady value before the onset of the main burst, (2) the intensity of the main burst reduces to a finite level and remains steady before it decays to the base level, and (3) the steady state is present during the rise as well as the decay phase of the main burst.

It was shown that these profiles are not due to random superposition of bursts with varying amplitudes. They are also probably not manifestations of f-h pairs. Some of the observed time profiles can be due to superposition of bursts caused by ordered electron beams ejected with a constant time delay at the base of the corona.

Acknowledgements

We are grateful to M. K. V. Bappu and V. Radhakrishnan for their continued interest and support of the low-frequency Radio Astronomy Project at Gauribidanur. Our thanks are also due to K. R. Subramanian for his help in collecting the data and for useful discussions.

References

Aubier, M., Boischot, A. 1972, *Astr. Astrophys*., **19,** 343.
Caroubalos, C., Poquerusse, M., Steinberg, J. L. 1974, *Astr. Astrophys*., **32,** 255.
Daigne, G., Møller-Pedersen, B. 1974, *Astr. Astrophys*., **37,** 355.
Grognard, R. J.M. 1980, in *IAU Symp. 86: Radio Physics of the Sun,* Eds M. R. Kundu and T. E. Gergely, D. Reidel, Dordrecht, p. 303.
Krishan, V., Subramanian, K. R., Sastry, Ch. V. 1980, *Solar Phys*., **66,** 347.
Magelsson, G. R., Smith, D. F. 1977, *Solar Phys*., **55,** 211.
Rosenberg, H. 1975, *Solar Phys*., **42,** 247.
Sastry, Ch. V. 1969, *Solar Phys*., **10,** 429.
Sastry, Ch. V. 1971, *Astrophys. Lett.,* **8,** 115.
Sastry, Ch. V. 1972, *Astrophys. Lett.,* **11,** 47.
Sastry, Ch. V. 1973, *Solar Phys*., **28,**197.
Subramanian, K. R., Krishan, V., Sastry, Ch. V. 1981, *Solar Phys*., **70,** 375.
Takakura, T., Shibahashi, H. 1976, *Solar Phys.,* **46,** 323.
Zaitsev, V. V., Kunilov, M. V., Mityakov, N. A., Rapoport, V. O. 1974, *Soviet Astr.,* **18,** 147.
Zaitsev, V. V., Mityakov, N. A., Rapoport, V. 0.1972, *Solar Phys.,* **24,** 444.

J. Astrophys. Astr. (1982) **3**, 161171

Compact Radio Cores and the Relation between the Radio and Optical Axes of Elliptical Galaxies

V. K. Kapahi and D. J. Saikia, *Radio Astronomy Centre, Tata Institute of Fundamental Research, P O Box 1234, Bangalore 560012*

Received 1982 March 9; accepted 1982 May 4.

Abstract. We have reinvestigated the reported tendency for the extended radio structures associated with bright elliptical galaxies to be oriented preferentially along the optical minor axes. It is found that such a tendency exists only for those galaxies in which the compact radio cores coincident with their nuclei are quite prominent. If the galaxies are divided into two groups according to whether their cores account for less than or greater than 10 per cent of the total flux density at 2·7 GHz, the angle ϕ (between the radio axis and the optical minor axis) appears to be uniformly distributed between 0° and 90° for the former, but is nearly always < 30° for the latter group. One possible explanation is that the radio emission from compact cores suffers thermal absorption by ionized gas that is distributed differently in the two groups.

Key words: radio galaxies—elliptical galaxies—extended radio sources

1. Introduction

The relative orientation of the radio axes of extended radio sources and their associated elliptical galaxies can in principle be used as a test for models of formation of radio galaxies. Although there are many practical problems in applying such a test (see *e.g.* Palimaka *et al.* 1979), it has been found that in carefully selected samples of well-collimated radio structures the radio axes appear to be oriented preferentially but not exclusively towards the minor axes of the parent elliptical galaxies (Guthrie 1979; Palimaka *et al.* 1979, henceforth referred to as PBFB). The interpretation of this trend is however not straight-forward, mainly because the relation between the distribution of light and rotation of elliptical galaxies is unclear (*e.g.* Binney 1978; Jenkins and Scheuer 1980).

From the sample of 78 galaxies used by them, it was also noted by PBFB that the

trend towards minor-axis alignment of radio orientations was stronger for the larger radio sources (with a projected size > 250 kpc). More recently, however, Guthrie (1980) has examined several other large sources in addition to those in the PBFB sample and found that the minor-axis trend is not significantly stronger for the large radio sources. A similar result has been reported also by Wilkerson and Romanishin (1981) who find that the radio axes of several large sources from the southern hemisphere are not aligned with their optical minor axes.

Noticing that some of the aligned large sources are known to have prominent compact radio components coincident with their optical nuclei (*e.g.* NGC 315 and 6251) we have investigated the relation between the strength of the nuclear radio component and the optical—radio orientation. We find, somewhat to our surprise, that the minor-axis trend noted earlier arises primarily due to galaxies with prominent radio cores (cores that account for > 10 per cent of the total flux density at 2·7 GHz). In galaxies that have only a weak or no detected core component, there is no evidence for the radio axis to show a preferred orientation.

In Section 2, we describe the sample of galaxies used by us and in Section 3 the results obtained. A brief discussion of the results is given in Section 4.

2. The sample

Although the orientation of the radio axis can usually be measured quite reliably, it is often difficult to determine the position angle (PA) of the optical image of the galaxy. Guthrie (1980) has independently attempted to measure on the glass plates of the Palomar Sky Survey (PSS), the optical orientations of all the 78 galaxies used by PBFB. He found that the optical PA of 31 galaxies could not be measured reliably because the galaxies either have very small ellipticities, or they appear too faint or asymmetric, or their images are confused with those of nearby objects. To ensure that the PAs of the galaxies are reliable, the basic sample used by us consists of the 47 PBFB galaxies measured also by Guthrie and the 14 additional well-collimated radio galaxies measured by him (listed in Table 5 of Guthrie 1980). We do not include the 18 galaxies measured by Wilkerson and Romanishin (1981) because few of them have been mapped in the radio with high angular resolution.

A careful examination of the available optical and radio data for the basic sample of 61 sources has led us to discard 7 of these for the following reasons. The optical PAs for four galaxies (*viz.* 0124 + 189, 1250 – 102, 1940 + 504 and 2354 + 471) measured from the red copies of the PSS by PBFB and by Guthrie differ by large amounts (in the range of 22° to 58°; the root-mean-square (rms) difference of the two sets of measurements for the other 43 galaxies is only about 7°). The source 1452 + 165 was excluded because its optical identification is uncertain (Bridle and Fomalont 1978). Two other sources *viz.* 1514 + 072 and 0034 + 254 were excluded because their radio axes cannot be determined reliably; the former is very poorly collimated (Fomalont, Palimaka and Bridle 1980) and the latter appears to have a wide-angle tailed structure with an opening angle of $\sim 90°$ (Ekers *et al.* 1981). Our final sample therefore consists of the 54 sources listed in Table 1.

High - (few arcsec) resolution radio structures and information on the flux densities of core components for most of the sources in Table 1 are available in the literature from observations made either at 2·7 and 8·1 GHz, with the NRAQ interferometer,

or at 4·9 GHz with the Very Large Array (Bridle and Fomalont 1978; Fomalont and Bridle 1978; Fomalont, Palimaka and Bridle 1980). A few sources have been mapped at 5 GHz with the Cambridge 5-km telescope or the Westerbork synthesis telescope. In a couple of cases maps with poorer resolution are available only at 1·4 GHz but the flux densities of their core components have been determined at higher frequencies using either the VLA or the NRAO interferometer.

For each source, where information on core flux density is available, we have evaluated the ratio, f_c, of the core flux density to the total source flux density at 2·7 GHz. The frequency of 2·7 GHz was chosen because measurements are available for a majority of the sources at this frequency. Where measurements do not exist at 2·7 GHz we have estimated f_c from measurements at a higher frequency using the spectral indices for the core and extended emission if known, or otherwise assuming values of $\alpha_{core} = 0$ and $\alpha_{ext} = 0{\cdot}8$, (spectral index defined as $S \propto \nu^{-\alpha}$), the typical values for well-observed sources. Since nearly all the galaxies in the sample have a redshift < 0·1 no attempt was made to transform f_e to the frame of reference of each galaxy.

For most of the sources without detected core components, upper limits of a few per cent can be placed on the values of f_c from the published maps. We have adopted a generally conservative upper limit of 0·1 in such cases.For 9 sources, however, the measurements are not of adequate resolution or sensitivity to place a reliable upper limit at $f_c = 0{\cdot}1$. These sources are considered separately.

The observed and estimated parameters are given in Table 1. The source name in coordinate designation and an alternative name or catalogue by which the source is generally known are listed in Columns 1 and 2 respectively. The redshift (generally taken from the compilation by Burbidge and Crowne 1979) is entered in Column 3. The PA of the optical minor axis is given in Column 4. If the PA has been measured both by PBFB and Guthrie, the average value from their measurements on the red copies of the PSS is entered. Column 5 gives the PA of the radio axis determined from the best available maps, references to which are given in Column 8 with the code given at the end of the Table. The magnitude of the difference between the optical and radio PAs is listed in Column 6 and an estimate of the largest linear size of the radio structure (for $H_0 = 50$ km s^{-1} Mpc^{-1}) is given in Column 7. Column 9 gives an estimate of f_c. A blank in Column 9 implies that the source has not been adequately mapped to determine f_c reliably. The total source luminosity at 2·7 GHz in W Hz^{-1} sr^{-1} is given in Column 10. The linear size and luminosity for sources without measured redshift have been computed by estimating the redshift from the apparent magnitudes as in PBFB. An indication of additional notes on some sources is given by an asterisk in Column 9.

3. The relation between f_c and ϕ

There are 45 galaxies in Table 1 for which fairly reliable values of (or upper limits to) the fractional flux density in the core component at 2·7 GHz, f_c, could be determined from observations reported in the literature. The values of f_c are plotted in Fig. 1 against the angle, ϕ , between the radio axis and the optical minor axis. A clear tendency can be seen for galaxies with relatively strong radio cores to have their

Table 1. The sample of radio galaxies.

Source	Other name	Redshift	PA_{opt}	PA_{rad}	ϕ $\lvert PA_{opt} - PA_{rad} \rvert$	Linear size	Reference to radio structure	f_c	Log P_t 2·7 GHz
			deg	deg	deg	kpc			
(1)	(2)	(3)	(4)	(5)	(6)	(7)	(8)	(9)	(10)
0018 − 194	PKS		104	111	7	1100	SM		24·8
0043 − 424	PKS	0·0526	69	136	67	150	E69		24·7
0043 + 201	3C 21	0·1028	165	172	7	900	ORP, BF	0·06	24·1
0055 + 300	B2, N 315	0·0167	131	129	2	1400	B79, BF	0·34	23·1
0153 + 053	4C 05·10, N 741	0·0185	170	84	86	45	FPB	<0·05	22·8
0300 + 162	3C 76·1	0·0324	54	110	56	40	JPR, MKN	<0·01	23·8
0305 + 039	3C 78	0·0288	53	56	3	78	FPB	0·19	24·1
0325 + 023	3C 88	0·0302	64	63	1	200	FPB	0·05	24·0
0331 + 391	4C 39·12	0·0209	10	0	10	15	BF, F77	0·34	23·0
0356 + 102	3C 98	0·0306	164	25	41	249	JPR, FB	<0·01	24·2
0518 − 458	PKS, Pictor A	0·0350	2	102	80	414	C77	0·02	25·1
0652 + 426	4C 42·22		33	50	17	69	BF	0·33	23·8
0714 + 286	4C 28·18	0·083	158	133	25	105	BF	<0·05	24·1
0744 + 559	DA 240	0·0350	160	63	83	1955	WSW, SBW	0·06	24·1
0924 + 302	B2	0·0266	139	55	84	488	E81	<0·02	22·5
0938 + 399	3C 223·1	0·1075	136	15	59	199	RP, FB	<0·01	24·7
1003 + 351	3C 236	0·0989	137	123	14	5700	WSW, BF	0·60	25·1
1005 + 282	B2	0·1476	95	150	55	587	F78	*	23·5
1033 + 003	4C 00·37		46	8	38	300	FPB	<0·1*	23·7
1102 + 304	B2	0·072	57	70	13	260	F77	0·10	23·6
1113 + 295	4C 29·41	0·0481	50	71	21	105	R75, BF	0·02	24·0
1122 + 390	B2, N 3665	0·0067	124	118	6	60	K79	0·16*	21·2
1127 + 012	PKS		11	12	1	140	FPB	<0·1	24·4
1137 + 123	PKS		46	12	34	140	FPB	<0·1	24·0
1154 − 038	PKS		134	122	12	400	FPB	0·18	23·3
1216 + 061	3C 270, N 4261	0·0073	63	83	20	104	FPB	0·02	23·3
1222 + 131	3C 272·1, N 4374	0·0031	27	167	40	11	JPR	0·09	22·1
1249 + 035	PKS		118	146	28	150	FPB	<0·1	24·0
1254 + 277	B2, N 4839	0·0249	150	11	41	23	F77		21·9
1317 + 258	4C 25·42		165	54	69	65	BO	<0·05	24·1
1318 − 434	PKS, N 5090	0·011	6	24	18	550	SM, S76	0·20*	23·8
1321 + 318	B2, N 5127	0·0161	159	111	48	320	E 81		22·9
1322 + 366	4C 36·24, N 5141	0·0174	166	7	21	23	BF	0·10	22·8
1323 + 370	4C 37·38		2	154	28	25	RA	<0·1	23·7
1333 − 337	PKS, IC 4296	0·0129	141	125	16	780	G77	0·01	23·5

1358 − 113	PKS	0·025	135	125	10	205	SM		23·3
1407 + 177	4C 17·57		94	73	21	250	FPB	<0·1	23·0
1414 + 110	3C 296	0·0237	55	65	10	200	FPB	0·02	23·7
1422 + 268	B2	0·037	30	96	66	121	FPB, F77	<0·02	23·4
1514 + 004	4C 00·56	0·053	147	135	12	500	FPB	0·26	24·2
1553 + 245	4C 24·35	0·0426	107	129	22	23	BF, F77	0·35	23·0
1559 + 021	3C 327	0·1039	48	99	51	762	FPB	<0·02	25·3
1610 + 296	B2, N 6068	0·0313	91	66	25	55	F77		22·4
1637 − 771	PKS	0·0431	179	165	14	182	E 69		24·4
1640 + 826	N 6251	0·0234	114	124	10	2800	WWB	0·51	23·4
1710 + 156	MLO		96	169	73	19	FPB	<0·11	24·0
1744 + 557	4CT 55·33·1	0·0304	100	77	23	223	BF	0·35	23·3
1759 + 211	4C 21·51		145	50	85	179	BF	0·07	24·1
1833 + 326	3C 382	0·0578	166	48	62	416	RB, BF	0·06	24·6
2103 + 124	PKS		155	138	17	260	FPB	0·13	24·4
2116 + 262	B2, N 7052	0·0164	154	22	48	23	F77, CD	0·41	22·1
2117 + 605	3C 430	0·0549	18	35	17	140	RP	<0·01	24·7
2229 + 391	3C 449	0·0171	98	9	89	168	BF, F77	0·02	23·2
2356 − 611	PKS	0·0963	93	134	41	900	C77		25·5

References to radio structure:

B79 Bridle *et al.* (1979)
BF Bridle and Fomalont (1978)
BO Burns and Owen (1979)
C77 Christiansen *et al.* (1977)
CD Condon and Dressel (1978)
E69 Ekers (1969)
E81 Ekers *et al.* (1981)
F77 Fanti *et al.* (1977)
F78 Fanti *et al.* (1978)
FB Fomalont and Bridle (1978)
FPB Fomalont, Palimaka and Bridle (1980)
G77 Goss *et al.* (1977)
JPR Jenkins, Pooley and Riley (1977)
K79 Kotanyi (1979)
MKN Macdonald, Kenderdine and Neville (1968)
ORP Owen, Rudnick and Peterson (1977)
R75 Riley (1975)
RA Rudnick and Adams (1979)
RB Riley and Branson (1973)
RP Riley and Pooley (1975)
S76 Schilizzi (1976)
SBW Strom, Baker and Willis (1981)
SM Schilizzi and McAdam (1975)
WSW Willis, Strom and Wilson (1974)
WWB Waggett, Warner and Baldwin (1977)

Additional notes:

1005 + 282: Map at 1415 MHz (Fanti *et al.* 1978) shows a possible central component. But as the total measured flux density is only ∼ 60 mJy, it is not possible to estimate f_c (2·7 GHz) reliably.

1033 + 003: Fomalont, Palimaka and Bridle (1980) note that the central component ($\alpha_c \sim 0{\cdot}45$) has a size of ∼ 5 arcsec at 2·7 GHz and is probably an equal double at 8·1 GHz. The core could therefore be of the 'extended' type. If one of the two components coincides with the nucleus the value of f_c is likely to be < 0·1.

1122 + 390: The value of $f_c = 0{\cdot}16$ is based on the measured flux density of 15 mJy at 5 GHz (Kotanyi 1979). In a VLBI experiment at this frequency, van Breugel *et al.* (1981), however, find a correlated flux density of 30 ± 7 mJy.

1318 − 434: Schilizzi (1976) reports a correlated flux density of 630 mJy at 8·1 GHz in a VLBI experiment. The value of f_c (2·7 GHz) = 0·20 assuming $\alpha = 0$ for the VLBI component.

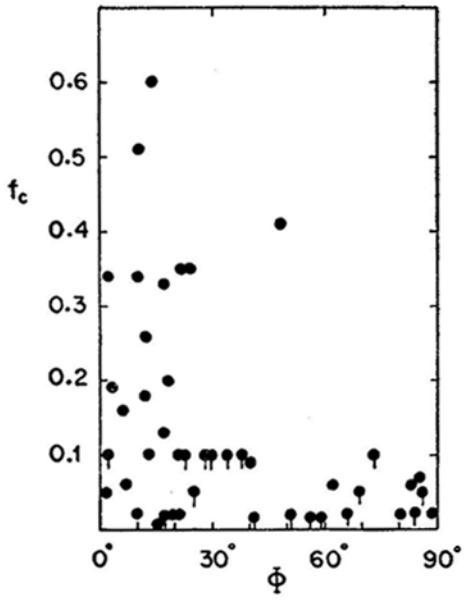

Figure 1. Relation between the fractional flux density in the core (f_c) , and the angle between the radio axis and the optical minor axis (ϕ). Points with short vertical lines are upper limits to f_c.

radio axes aligned preferentially towards their optical minor axes. Of the 16 galaxies in which the core component accounts for at least 10 per cent of the total flux density, only one is seen to have its radio axis misaligned by more than 30° with respect to the optical minor axis. Even in the case of this single exception (2116 + 262), the radio contours (Fanti *et al.* 1977) show a considerable bending of the radio axis away from the nucleus. The radio PA listed in Table 1 for this galaxy is based on the shape of the outermost contours, whereas contours close to the nucleus suggest an orientation within 30° of the optical minor axis. Fig. 1 also suggests that the range of φ-values may increase fairly abruptly for $f_c \lesssim 0{\cdot}1$. A larger sample of galaxies and better estimates of f_c for those with upper limits are needed to assess the significance of any such trend.

The distributions of ϕ in the two subsamples comprising of 29 galaxies with $f_c < 0{\cdot}1$ and 16 galaxies with $f_c \geqslant 0{\cdot}1$ are shown as histograms in Fig. 2 which also shows separately the distributions of ϕ for the 9 galaxies for which f_c is unknown and for all the 54 galaxies taken together. It may be seen that the radio axes of galaxies with weak cores ($f_c < 0{\cdot}1$) seem to bear no relation with their optical appearance A χ^2 test for this sample shows no significant departure from a uniform distribution of f between 0° and 90°. But the ϕ - distribution for galaxies with prominent cores ($f_c \geqslant 0{\cdot}1$) appears to depart strongly from a uniform distribution, with 12 of the 16 galaxies having $\phi < 20°$. The χ^2 test in this case rejects the uniform distribution with a confidence level of 99·9 per cent. It is also interesting to note that the distribution of ϕ for the 9 galaxies with unknown values of f_c lies closer to that for galaxies with $f_c < 0{\cdot}1$, which is consistent with the above trend since most galaxies in Table 1 have weak cores.

When all the galaxies in Table 1 are considered together there is a significant tendency towards minor axis alignment as noted earlier by Palimaka *et al.* (1979) and

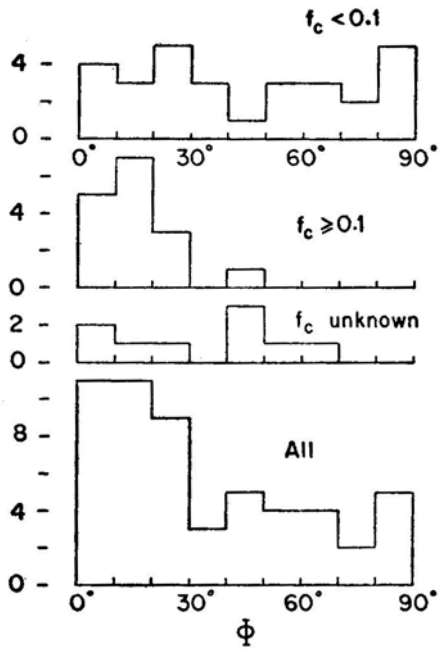

Figure 2. Distributions of the alignment-angle ϕ

Guthrie (1980). But it now seems clear from Fig. 2 that this tendency arises almost entirely from the galaxies with prominent cores. The reported alignment between the radio and optical axes appears to be true only for this class of galaxies.

Given that the strength of the radio core is somehow related to the relative radio-optical orientation of radio galaxies it is worth enquiring if this relation depends on the nature of the core component. It has been shown by Bridle and Fomalont (1978) that the core components in galaxies can be of two kinds depending on their size and radio spectrum. Most cores are of the 'compact' kind with sizes much smaller than 1 kpc (VLBI observations often indicate sizes of $\lesssim 1$ pc) and flat or inverted radio spectra characteristic of regions showing synchrotron self0-absorption. A significant minority of cores are however of the 'extended' kind with steep spectra ($\alpha > 0{\cdot}5$) and sizes up to few kpc. In the present sample of galaxies with $f_c \geqslant 0{\cdot}1$, only one source (*viz.* $1003 + 351 \equiv 3C\ 236$) appears to have an extended steep-spectrum core, all others having $\alpha_{core} < 0{\cdot}5$ at high frequencies. Galaxies in the $f_c < 0{\cdot}1$ group for which spectral information is available, also appear to have $\alpha_{core} < 0{\cdot}5$. The relation between f_c and ϕ therefore appears to apply to the compact cores. Little can however be said about such a relation for the extended cores alone from the present sample.

Apart from the correlation with f_c, we have also attempted to see if the angle ϕ correlates with other known properties of the radio galaxies. In Figs 3 and 4 we show plots of ϕ against the total radio luminosity, P_t (2·7 GHz), and the core luminosity, P_c (2·7 GHz), respectively. Within the range of luminosities covered by the sample, ϕ shows no significant correlation with P_t . Although there appears to be a possible weak anticorrelation between ϕ and P_c , such a relation is only to be expected in view of the f_c–ϕ relationship.

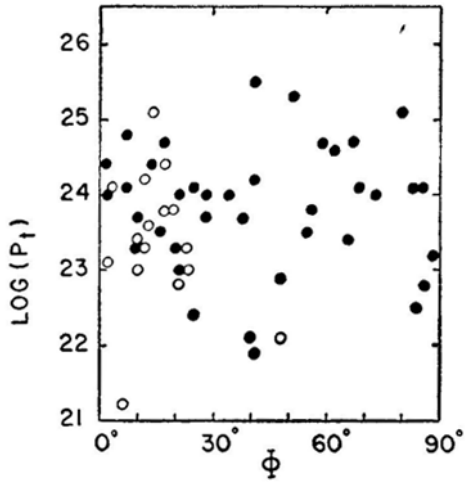

Figure 3. The total radio luminosity, P_t (2·7 GHz), plotted against the alignment angle ϕ. Unfilled circles here and in subsequent figures refer to galaxies with $f_c \geqslant 0{\cdot}1$

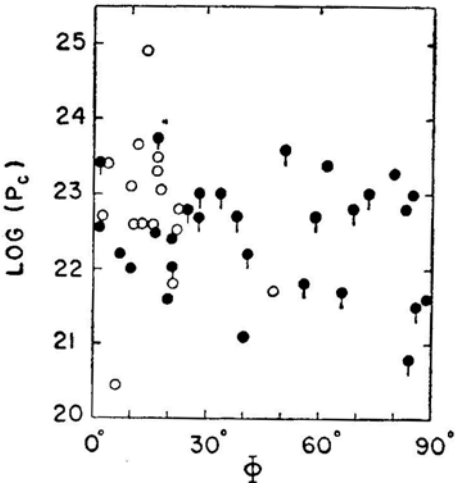

Figure 4. The core luminosity, P_c (2·7 GHz), versus the alignment angle ϕ.

A plot of the total linear extent of the radio galaxies versus ϕ, shown in Fig. 5, does not indicate any significant correlation, contrary to such a suggestion in the data of PBFB.

4. Discussion

Although the galaxies used in the present investigation do not form a complete sample in any well-defined way, we can think of no observational or selection bias that could have led to the distributions shown in Fig. 2. If elliptical galaxies are generally oblate spheroids, the fact that the radio axes appear to lie preferentially towards the minor axes of their light distribution appears to be consistent with the beam model of radio sources (*e.g.* Blandford and Rees 1974) in which the beams are collimated

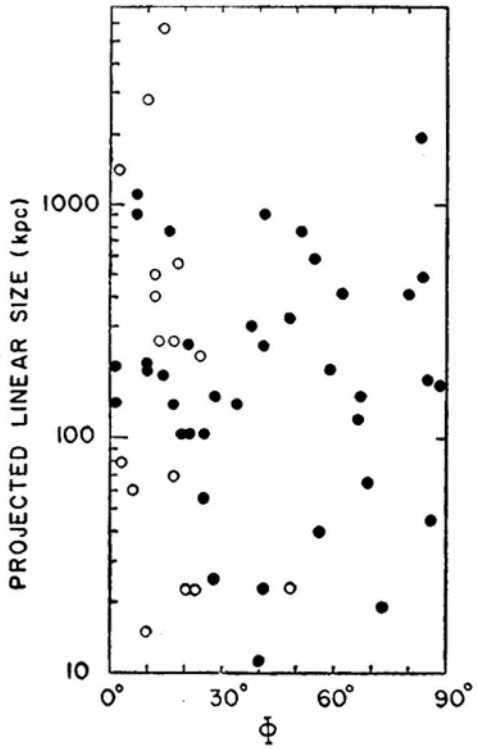

Figure 5. Plot of the maximum projected linear size of radio emission versus the alignment angle ϕ.

by a flattened mass distribution in the galactic nucleus and emerge along the rotation axis of the nuclear engine. An alignment that is not perfect and universal can be caused by one or both of the two main possibilities: the apparent ellipticity of galaxies not being due to rotation and a misalignment of the nuclear collimator with respect to the stellar distribution.

If the present finding that the relative strength of the radio core component is a good filter for the minor-axis trend is indeed true and not just the result of an extreme statistical fluctuation, then it must tell us something important about the processes taking place in the nuclei of extended radio sources.

The fact that the galaxies showing the best minor-axis alignment (those with prominent radio cores) have the same range of radio luminosities and projected linear sizes as the galaxies that show no preferential alignment, suggests that the difference in the relative core intensities of the two sets of galaxies is more likely to arise from different geometrical and/or absorption effects rather than from a difference in the strength of the nuclear activity itself.

If relativistic beaming effects are important in the cores of these radio galaxies, as suggested for the cores of the much more luminous quasars (Scheuer and Readhead 1979; Blandford and Konigl 1979), the relative core strength would be expected to be a function of the orientation of the radio axis with respect to the observer's line of sight. This does not however explain the alignment of the radio and optical axes. Furthermore, if the beams in strong-cored galaxies are oriented closer to our lines of sight, the image of such galaxies should appear more circular than those of the

Weak-cored ones. No significant difference in the apparent ellipticities of the two types of galaxies can, however, be noticed in the present sample. Another argument against strong relativistic beaming is that some of the largest known radio galaxies in the sample (*e.g.* NGC 6251 and NGC 315) have very prominent cores, so that their true sizes would then have to be even larger.

If absorption effects are invoked to explain the observations, the cut-off frequency (below which absorption is important) would have to be significantly higher in the misaligned galaxies (with weak cores at 2·7 GHz) than in the well-aligned galaxies (large f_c). There is marginal evidence in support of this in the data. The two-point spectral index of the core component between 2·7 and 8·1 GHz, $\alpha_{2.7}^{8.1}$, is known for 10 galaxies with $f_c < 0{\cdot}1$ and 10 with $f_c \gtrsim 0{\cdot}1$ (excluding 3C 236). Although all these have $\alpha_{2.7}^{8.1} < 0{\cdot}5$, four galaxies in the former group have an inverted spectrum with $\alpha_{2.7}^{8.1} < -0{\cdot}2$ while none in the latter group have $\alpha_{2.7}^{8.1} < -0{\cdot}2$. High resolution observations at a number of frequencies are clearly necessary to determine the spectra of the core components more accurately.

The absorption could be either synchrotron self-absorption within the core or free-free absorption in an ionized medium on the line of sight to the core. In the case of synchrotron self-absorption it is not clear why the cutoff frequency should be different in the two groups of galaxies. An interesting possibility that deserves further investigation can however be suggested to explain the f_c–ϕ relation in terms of thermal absorption of the core components if the absorbing material is distributed differently in the two groups. In the aligned galaxies, the rotation axes of the inner nuclear engine and of the rest of the galaxy presumably coincide, and if the ionized gas (possibly that responsible for the narrow emission lines) is distributed in a thin accretion disk, the radio emission from the core would traverse very little gas from most directions of view. In the case of the misaligned galaxies, on the other hand, the two rotation axes could be very different and the ionized gas distributed more or less spherically around the nucleus. Free-free absorption would then be important from all directions of view.

For an electron temperature $T_e \sim 10^4$ K, the cutoff frequency ν_c (in MHz) for thermal absorption is given approximately by the relation

$$\nu_c \sim \tfrac{1}{2}\, n_e\, l^{1/2}$$

where n_e is the electron density (cm^{-3}) and / the l pathlength (pc). Since the narrow-line regions of radio galaxies have generally been inferred to have electron densities of 10^2–10^5 cm^{-3} and sizes of ~ 10–10^3 pc, free-free absorption can indeed be important at frequencies near 2·7 GHz even for fairly small filling factors.

If absorption is indeed important, one might expect the cores of galaxies with low values of f_c to have on an average lower brightness temperatures than those with large values of f_c . It is, however, not yet possible to test this with the available data since there is little information on the angular sizes of the cores.

From a search of the literature, we find that the stellar rotation axes have been determined (Simkin 1979; Jenkins and Scheuer 1980; Jenkins 1981) for only 5 galaxies in the present sample. Four of these (*viz.* 3C 98, 3C 270, 0153 + 053 and 1330-337) have $f_c < 0{\cdot}1$ and show no tendency for their rotation axes to align either with their radio axes or with their isophotal minor axes. The other galaxy (NGC 3665) with $f_c > 0{\cdot}1$ has a rotation axis of 105° ± 5° (Jenkins 1981), within 20° of its optical

minor axis and the radio axis. It would be extremely valuable to study the stellar kinematics of many more radio galaxies particularly those with relatively strong central components.

References

Binney, J. J. 1978, *Comm. Astrophys.,* **8,** 27.
Blandford, R. D., Konigl, A. 1979, *Astrophys. J.,* **232,** 34.
Blandford, R. D., Rees, M. J. 1974, *Mon. Not. R. astr. Soc.,* **169,** 395.
Bridle, A. H., Davis, M. M., Fomalont, E. B., Willis, A. G., Strom, R. G. 1979, *Astrophys. J.,* **228,** L9.
Bridle, A. H., Fomalont, E. B. 1978, *Astr. J.,* **83,** 704.
Burbidge, G., Crowne, A. H. 1979, *Astrophys. J. Suppl. Ser.,* **40,** 583.
Burns, J. O., Owen, F. N. 1979, *Astr. J.,* **84,** 1478.
Christiansen, W. N., Frater, R. H., Watkinson, A., O'Sullivan, J. D,, Lockhart, I. A., Goss, W. M. 1977, *Mon. Not. R. astr. Soc.,* **181,** 183.
Condon, J. J.$_s$ Dressel, L. L. 1978, *Astrophys. J.*, **221,** 456.
Ekers, R. D. 1969, *Austr. J. Phys., Astrophys. Suppl.,* No. 6.
Ekers, R. D., Fanti, R., Lad, C, Parma, P. 1981, *Astr. Astrophys.,* **101,** 194.
Fanti, C, Fanti, R., Gioia, I. M., Lad, C, Parma, P., Ulrich, M. H. 1977, *Astr. Astrophys. Suppl. Ser.,* **29,** 279.
Fanti, R., Gioia, I., Lad, C., Ulrich, M. H. 1978, *Astr. Astrophys. Suppl. Ser.,* **34,** 341.
Fomalont, E. B., Bridle, A. H. 1978, *Astr. J.,* **83,** 725.
Fomalont, E. B., Palimaka, J. J., Bridle, A. H. 1980, *Astr. J.,* **85,** 981.
Goss, W. M., Wellington, K. J., Christiansen, W. N., Lockhart, I. A., Watkinson, A., Frater, R.H., Little, A. G. 1977, *Mon. Not. R. astr. Soc.,* **178,** 525.
Guthrie, B. N. G. 1979, *Mon. Not. R. astr. Soc.,* **187,** 581.
Guthrie, B. N. G. 1980, *Astrophys. Sp. Sci.,* **70,** 211.
Jenkins, C. J., Pooley, G. G., Riley, J. M. 1977, *Mem. R. astr. Soc.,* **84,** 61.
Jenkins, C. R. 1981, *Mon. Not. R. astr. Soc.,* **196,** 987.
Jenkins, C. R., Scheuer, P. A. G. 1980, *Mon. Not. R. astr. Soc.,* **192,** 595.
Kotanyi, C. G. 1979, *Astr. strophys.,* **74,** 156.
Macdonald, G. H., Kenderdine, S., Neville, A. C. 1968, *Mon. Not. R. astr. Soc.,* **138,** 259.
Owen, F. N., Rudnick, L., Peterson, B. M. 1977, *Astr. J.*, **82,** 677.
Palimaka, J. J., Bridle, A. H., Fomalont, E. B., Brandie, G. W. 1979, *Astrophys. J.,* **231,** L7 (PBFB).
Riley, J. M. 1975, *Mon. Not. R. astr. Soc.,* **170,** 53.
Riley, J. M., Branson, N. J. B. A. 1973, *Mon. Not. R. astr. Soc.,* **164,** 271.
Riley, J. M., Pooley, G. G. 1975, *Mem. R. astr. Soc.,* **80,** 105.
Rudnick, L., Adams, M. T. 1979, *Astr. J.,* **84,** 437.
Scheuer, P. A. G., Readhead, A. C. S. 1979, *Nature,* **277,**182.
Schilizzi, R. T. 1976, *Astr. J.,* **81,** 946.
Schilizzi, R. T., McAdam, W. B. 1975, *Mem. R. astr. Soc.,* **79,** 1.
Simkin, S. M. 1979, *Astrophys. J.,* **234,** 56.
Strom, R. G., Baker, J. R., Willis, A. G. 1981, *Astr. Astrophys.,* **100,** 220.
Van Breugel, W. J. M., Schilizzi, R. T., Hummel, E., Kapahi, V. K. 1981, *Astr. Astrophys.,* **96,** 310.
Waggett, P. C., Warner, P. J., Baldwin, J. E. 1977, *Mon. Not. R. astr. Soc.,* **181,** 465.
Wilkerson, M. S., Romanishin, W. 1981, *Astrophys. J.,* **243,** 427.
Willis, A. G., Strom, R. G., Wilson, A. S. 1974, *Nature,* **250,** 625.

J. Astrophys. Astr. (1982) **3,**173–187

VLA Observations of Hot Spots in High Luminosity Radio Sources

R. T. Schillzzi *Netherlands Foundation for Radio Astronomy, Dwingeloo, The Netherlands*
V. K. Kapahi *Radio Astronomy Centre, Tata Institute of Fundamental Research, P O Box 1234, Bangalore 560012*
S. Gr. Neff* *Astronomy Program, University of Virginia,Charlottesville, Virginia, USA* and *National Radio Astronomy Observatory, Charlottesville, Virginia, USA*

Received 1982 March 16; accepted 1982 May 6

Abstract. VLA observations at 6 cm have been made of 16 distant luminous 3C sources that appeared to be unresolved or slightly resolved in Cambridge maps but which were known from VLBI observations to contain significant fine structure on the scale of about 1 kpc in their lobes. The general morphology of these sources is very similar to that of their nearby powerful counterparts; most of the lobes contain low brightness tails which are often directed from the hot spots towards the associated optical object. The hot spots are generally unresolved by the VLA observations; in 3C 254, 3C 268.4 and 3C 352, one of the lobes contains two hot spots.

Key words: hot spots—radio galaxies—quasars

1. Introduction

Most of the powerful extragalactic radio sources are known to contain regions of enhanced brightness near the outer edges of their double radio lobes. Such ‘hot spots’ are believed to represent the ends of beams that supply energy from the nucleus of the associated galaxy or quasar to the outer lobes. The sizes and morphologies of hot spots can therefore provide valuable information on the formation of double sources and on the interaction of beams with the intergalactic medium. Due to the limited angular resolution of aperture-synthesis instruments, hot spots have generally been well mapped only in the relatively nearby sources, in which they appear to have

*Present address: Netherlands Foundation for Radio Astronomy, Dwingeloo, The Netherlands

sizes of up to a few kpc. In the more distant (and hence more powerful) sources where the outer lobes themselves are often of the order of ten kpc (or smaller) in size, it has not generally been possible to map any finer-scale structure in the lobes. Single-baseline interferometric observations (*e.g.* Wilkinson 1972) have however suggested such structure on a scale of $\lesssim 0{\cdot}5$ arcsec. More recently, VLBI observations (Kapahi and Schilizzi 1979a, b) have indicated the presence of significant structures on a scale of $< 0{\cdot}1$ arcsec (corresponding to linear sizes of < 1 kpc) in several distant sources selected from the 3CR catalogue. These results suggest that the statistical properties of hot spots derived from observations *with a fixed angular resolution,* of sources covering a large range in redshift, such as the reported strong correlation between the total source luminosity and the fractional flux density in hot spots (Jenkins and McEllin 1977), could be seriously contaminated by resolution effects (see *e.g.* Kapahi 1978; Neff and Rudnick 1980).

In this paper we present synthesis maps, made at 6 cm with the partially completed N.R.A.O.* Very Large Array (VLA), of several 3CR sources that appeared from the VLBI observations to contain significant fine structure in their lobes. The aims of the observations were twofold: firstly to check that the fine structure indicated by the limited VLBI data had been correctly identified with features in the outer lobes and secondly to map the structure of the hot spots when possible. The angular resolution of the present observations is typically in the range of about 0·5 to 1 arcsec, significantly better than was previously available for most of these sources. Our results show the presence of bright regions towards the outer edges of most of the sources and indicate the need for much higher angular resolution to map the hot spots adequately.

2. Observations and results

Measurements of 16 sources were made at 4·885 GHz on 1979 June 29–30 with the partially completed VLA. A maximum of sixteen antennas were in operation, with typically thirteen available for any particular observation. The baselines ranged from 0·1 to 18·25 km. Each source was observed at two to seven different hour angles (see Table 1); individual scans were typically 3 minutes in length, Observations of 17 calibrator sources were interleaved with those of the programme objects to allow a reasonable understanding of the amplitude and phase behaviour of the array during that time.

Table 1. Number of hour angles at which each source was observed.

Source	No. of scans	Source	No. of scans
3C 13	7	3C 263	7
3C 22	5	3C 268·4	6
3C 55	4	3C 270·1	6
3C 186	6	3C 280	6
3C 196	6	3C 330	4
3C 216	7	3C 334	4
3C 220·2	7	3C 352	2
3C 254	6	3C 455	3

*Operated by Associated Universities, Inc., under contract with the U.S. National Science Foundation.

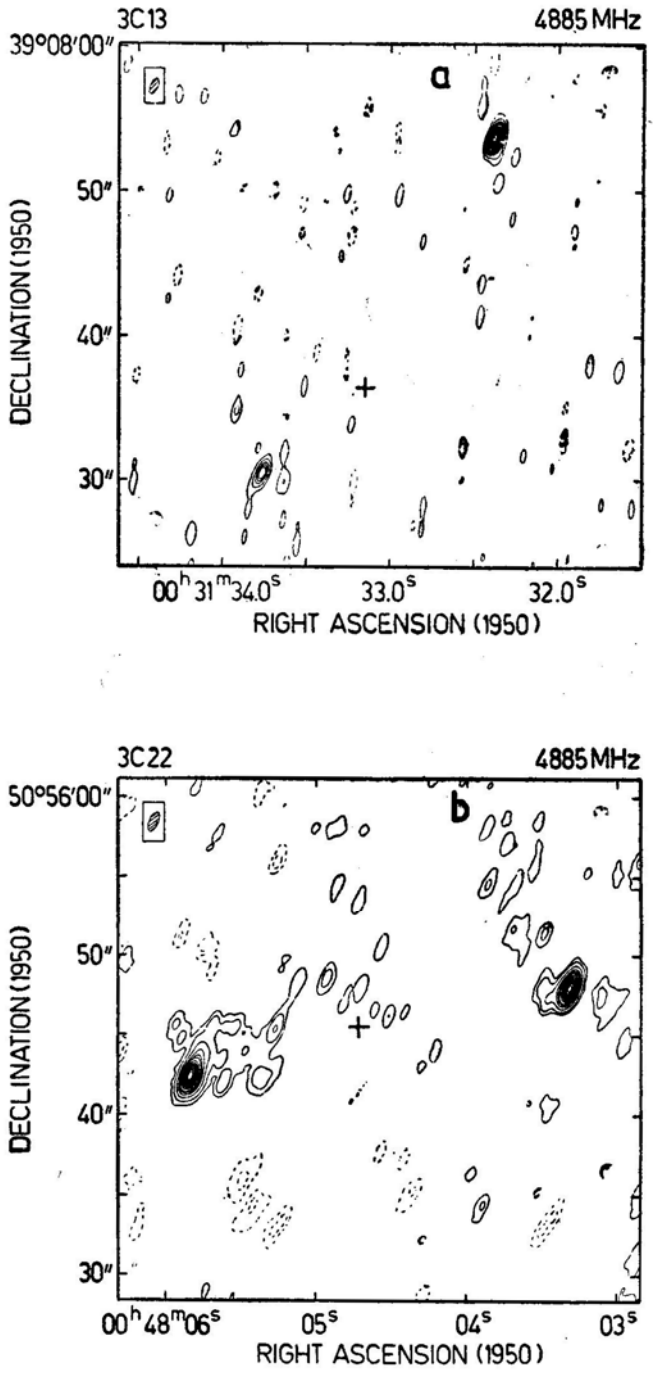

Figure 1. (a) 3C 13: peak flux is 191 mJy. (b) 3C 22: peak flux is 182 mJy. The optical position is from Riley, Longair and Gunn (1980).

Following a point-by-point editing, the data were self-calibrated using an early version of the self-calibration technique of Schwab (1980). The self-calibrated data were then used to produce CLEANed maps of the brightness distribution of the sources. Contour representations of these maps are shown in Fig. 1–9. Maps with a restoring beam of half the dimensions of the main lobe of the dirty beam were also generated to give an indication of the presence of more compact structures in the sources (even though it is known that such 'super-resolution' does not give unique information on source structure). The results of this analysis are mentioned in the following notes.

2.1 *Notes on the Individual Source Structure*

Here we give comments on the source structure, making reference to the VLBI data of Kapahi and Schilizzi (1979a, b), hereafter KS, and to other maps of the sources. The KS data allowed only a rough estimate of angular size, < 0·15 arcsec, to be made. Linear sizes are determined using $q_0 = 0{\cdot}5$ and $H_0 = 50$ km s^{-1} Mpc^{-1}, and redshifts obtained from Smith and Spinrad (1980) and references therein. In the following, N and S refer to 'north' and 'south' ,*p* and *f* to 'preceding' and' following', when referring to the relative positions of components.

Figs 19 show contour maps of the sixteen sources. Contour levels are —5, —2, − 1, 1, 2, 5, 10, 15, 20, 30, 40, 50, 60, 70, 80 and 90 per cent of the peak values in the maps for 3C13, 55, 220·2, 254, 334, 352 and 455. In all of the other maps the lowest contours are at the 2 per cent level except for 3C 270·1, where the 5 per cent contour is the lowest one shown. Beamsizes and orientations are indicated in boxes on each map. The best available optical positions (generally accurate to better than 1 arc-sec unless noted otherwise) are also marked on the contour maps.

3C 13 (Fig. 1a): There is some evidence of extended structure in the 2 and 5 per cent contours of the northern component. This is confirmed by Laing (personal communication) using the complete VLA; his map shows inward extensions in both components at levels below our lowest contour. The point-like components in our map presumably contain the (< 1·3 kpc, $z = 1{\cdot}05$) structures observed by KS in both lobes.

3C 22 (Fig. lb): Both components show evidence of unresolved hot spots at the outer edges of the lobes which are probably associated with the compact components (< 0·08 arcsec) found in both lobes by Schilizzi and Seielstad (unpublished observa tion) at 13 cm.

3C 55 (Fig. 2): Fig. 2 is in broad agreement with the maps of Jenkins, Pooley and Riley (1977) at 5 GHz and of Laing (1981) at 2·7 GHz. The map shows that the western lobe has a hot spot at the outer edge, with an inward extension at position angle (PA) ~ 80°; the eastern lobe has a central hot spot with extensions to east and west. The eastern extension, which appears real, was not detected in the Cambridge observation. The VLBI data of KS show that there is compact structure < 0·7 kpc in the western lobe only. Laing (1981) did not detect the hot spots at 15 GHz which implies < 20 mJy in structure < 0·5 arcsec at this frequency. The spectrum of the western hot spot must therefore be steep.

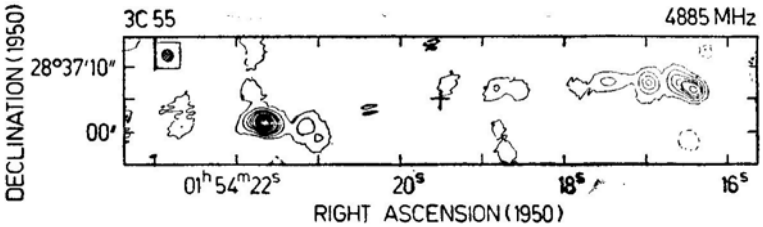

Figure 2. 3C 55: peak flux is 174 mJy.

3C 186 (Fig. 3a): Both components are extended and there is no evidence of a link between the N*p* and S*f* components. Fig. 3b shows the N*p* component to be a double separated by 1·2 arcsec in PA 137° with extensions to the north and south (note that Fig. 3a does not have the same scale north-south as east-west). The optical object (17·6 mag quasar, z = 1·0630) lies close to the northern component of the double, which is the weaker of the two. The errors in the radio and optical scales do not, however, preclude the optical object lying between the two lobes, which is the more likely location in view of the steep radio spectrum. The VLBI structure of KS (< 1·3 kpc) is associated with the close double.

3C196 (Fig. 4a): The weak structure seen to the south-east of the N*f* component in the maps by Pooley and Henbest (1974) at 5 GHz and by Lonsdale and Morison (1980) at 408 MHz, is almost completely resolved out by the VLA. Laing (1981) has shown that this component has a steep spectrum. Similarly, the structure to the north-west of the S*p* component seen in the Lonsdale and Morison (1980) map is resolved out here, or its spectrum is too steep for the present dynamic range to retrieve. Laing (1982) gives a recent VLA map in which the extended regions are seen well at 5 GHz. The data of KS indicate substantial resolution on scales of 0·15 arcsec (<1·3 kpc), probably in the southern lobe.

3C 216 (Fig. 4b): The structure appears triple with a central bright component presumably coincident with the optical object (18·48 mag quasar, z = 0·668). Porcas and Pauliny-Toth (personal communication) have detected a 1 milli-arcsec component at 6 cm in 3C 216 with ~ 30 per cent of the flux density; this must surely be associated with the nucleus of the quasar. The variation in flux density observed by KS could well be due to compact structure <0·15 arcsec (< l·2 kpc) in one or both of the lobes on either side of the core. The weak component to the south-west is probably real.

3 C 220·2 (Fig. 5a): Each of the lobes shows a hot spot at the outer edge of the structure. The inward extensions of both lobes curve towards the central component. The VLBI measurements of KS were unable to distinguish which of the three components contained compact structure (<l·3 kpc). It is quite likely that the hot spots in the outer lobes do contain compact structure since there is not sufficient flux density in the core component to account for all the observed 21-cm flux density of KS unless the core has a steep spectrum.

3C 254 (Fig. 5b): Several authors (*e.g.* Pooley and Henbest 1974; Laing 1981) have remarked on the unusual position of the quasar associated with this source which

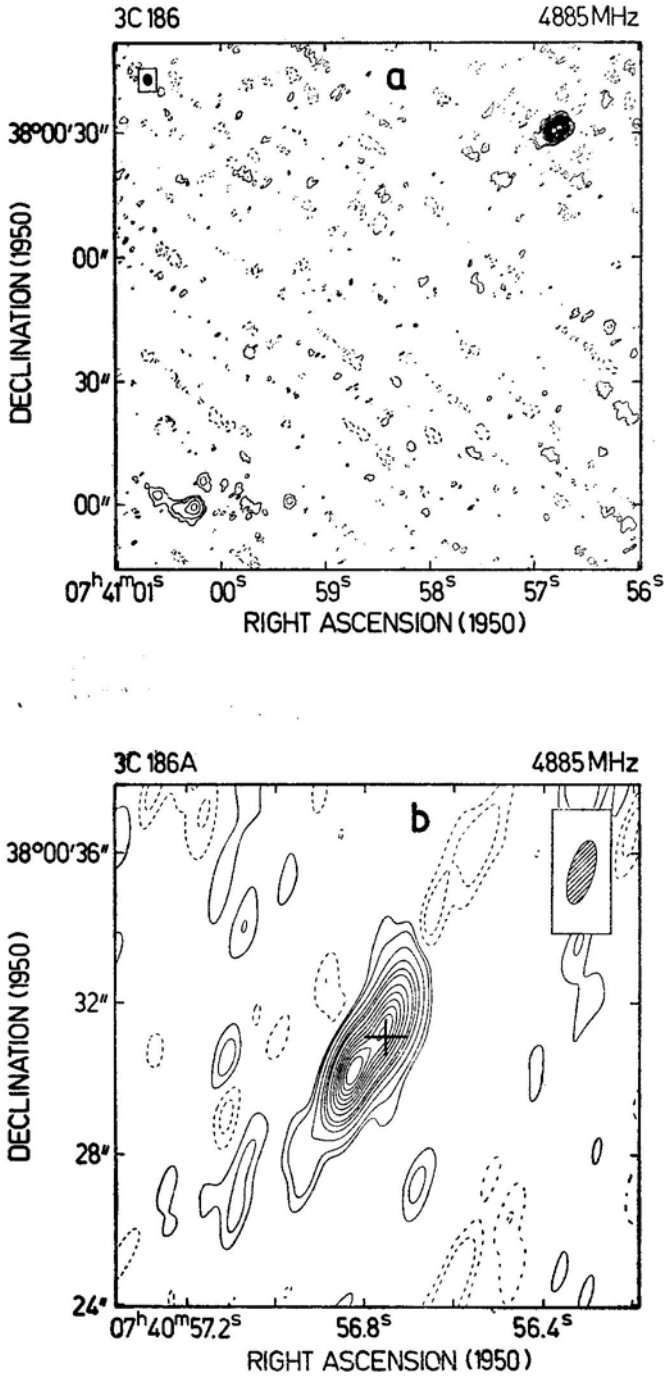

Figure 3. 3C186: peak flux is 128 mJy. The optical position is from Argue and Kenworthy (1972).

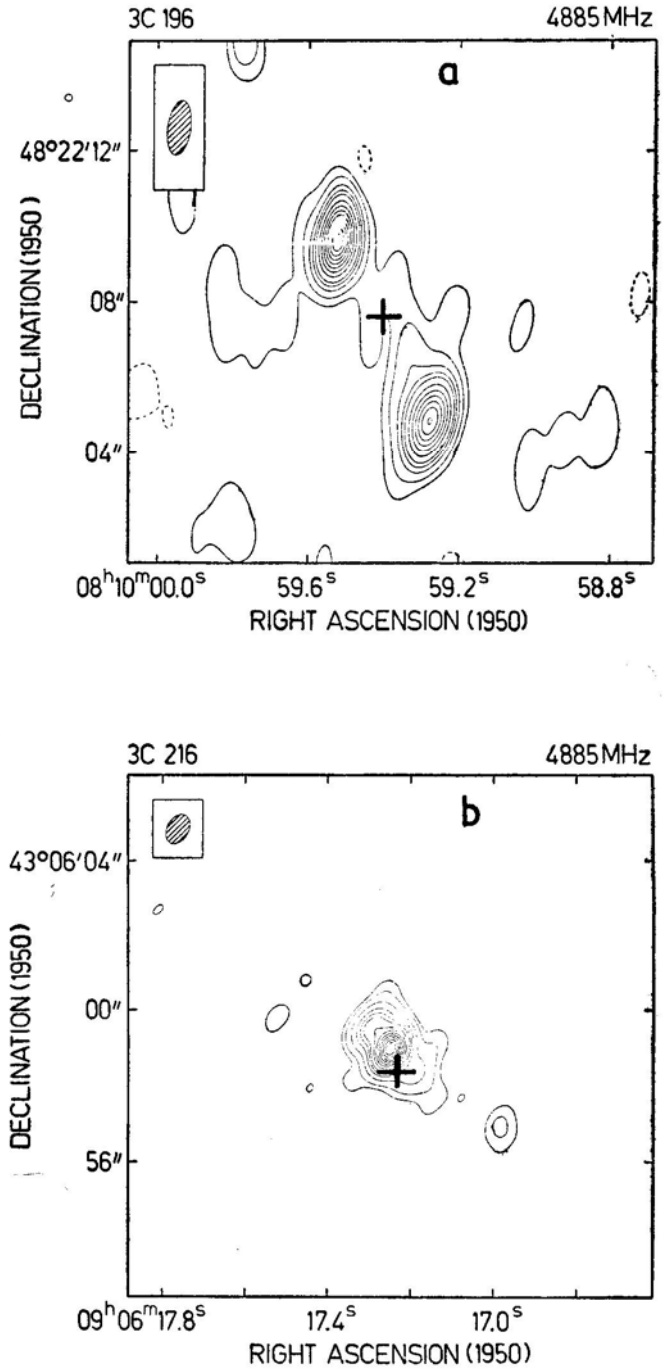

Figure 4. (a) 3C196: peak flux is 1289 mJy. (b) 3C216: peak flux is 1156 mJy. The optical position is from Cohen *et al.* (1977).

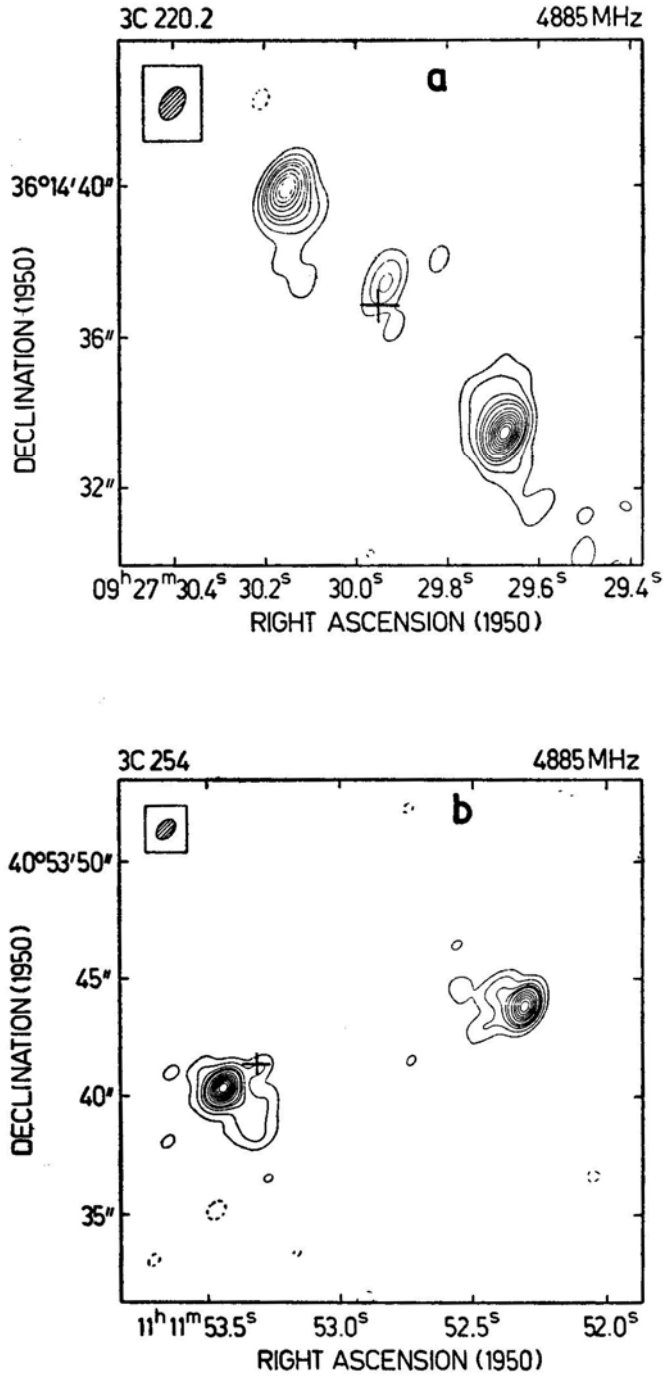

Figure 5. (a) 3C 220.2: peak flux is 212 mJy. (b) 3C 254: peak flux is 216 mJy. The optical position is from Riley, Longair and Gunn (1980).

lies to the northwest of the S*f* component. It clearly has a weak radio emission associated with the nucleus seen here in the lowest two contours. Each lobe is extended, being composed of a hot spot and a low brightness tail pointing approximately at right angles to the source axis. Laing (personal communication) has made a more recent VLA map which shows the N*p* lobe to be double in PA ~ 2° (also indicated by restoration of the present data with a smaller beam). KS found structure < 1·2 kpc in both lobes. There is not sufficient flux in the nuclear component to have been detected by KS if the core spectrum is flat.

3C263 B (Fig. 6a): This is the eastern part of the source only. The N*p* component in this map is unresolved and coincident with a 16 mag quasar (z = 0·6463). The S*f* component is composed of a hot spot and a low brightness extension back towards the nucleus. Both components contain structure on the scale of 1·2 kpc (KS).

3C268·4 (Fig. 6b): Both outer lobes are extended; the *Sp* component appears to have a double structure (separation 0·94 arcsec in PA 122°) as seen in a map restored with a smaller beam. The alignment of the *Sp* double is approximately perpendicular to the overall source axis. At 15 GHz, Laing (1981) detected only a single component in the Sp lobe whose position coincides with the stronger (north-west) component of the double seen by us. It is therefore likely that the weaker component of the double has a steep spectrum. The VLBI data of KS indicate that the *Sp* lobe contains compact structure on the scale of < 1·3 kpc.

3C 270·1 (Fig. 7a): The southernmost component is slightly extended to the west (see Stocke, Christiansen and Burns 1982, for a more recent VLA map). KS could not distinguish between the core component and the southern component for the location of their observed compact structure (<1·3 kpc).

3C280 (Fig. 7b): The structure is quite similar to 3C254 in having a compact, low-brightness component located close to one of the two main lobes. This component does not, however, coincide with the proposed identification (Gunn *et al.* 1981) in contrast to 3C 254. The western component appears extended to the north-west, away from the hot spot. A more recent VLA map by Laing (personal communicaiton) shows this extension in more detail as well as the compact component referred to above. The eastern component in our map appears slightly resolved; again in Laing's map greater detail is seen, the component having a low-level inward extension. The evidence from KS points to the western lobe as containing compact structure on the scale of 0·15 arcsec; though compact, the low-surface-brightness component near the western lobe is not strong enough to contribute all of the flux density seen by KS.

3C330 (Fig. 8a): The overall structure is in broad agreement with that of Jenkins, Pooley and Riley (1977) and Laing (1981). Both components are extended towards each other but there is no central component. The low-brightness inward extension of the N*f* component is more clearly seen in the present map than in the earlier maps. From very limited data KS suggested that the *Sp* component was the more likely candidate for the observed compact structure (< 1 kpc). From our map, the N*f*

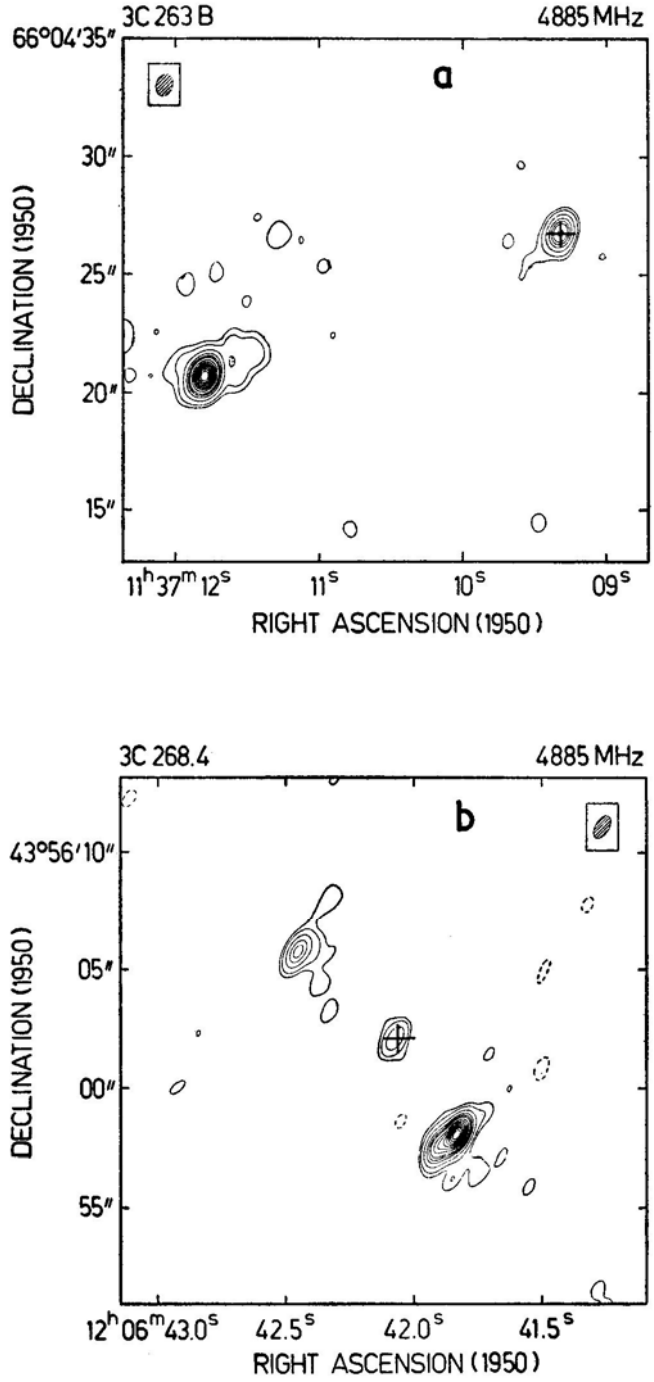

Figure 6. (a) Eastern part of 3C 263: peak flux is 485 mJy. There is little compact structure in the western lobe (Pooley and Henbest 1974). (b) 3C 268·4: peak flux is 302 mJy.

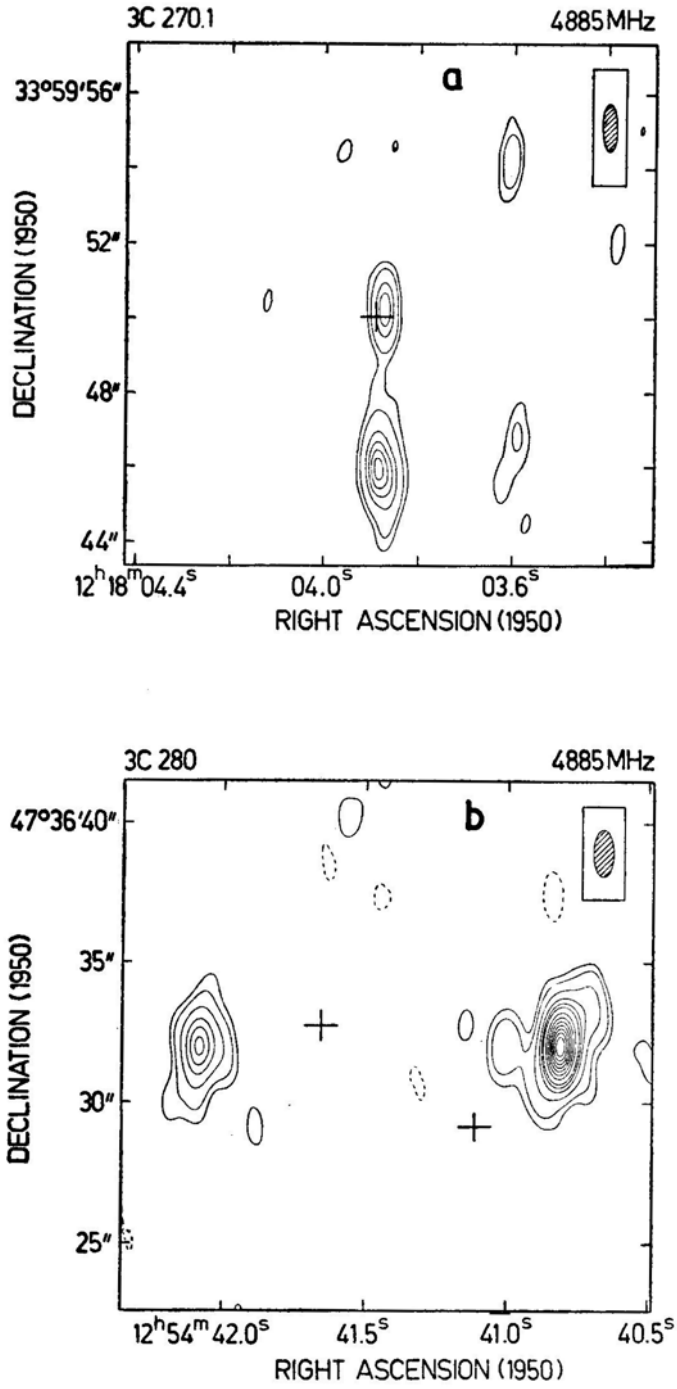

Figure 7. (a) 3C 270·1: peak flux is 247 mJy. (b) 3C 280: peak flux is 904 mJy. The optical positions are from Gunn *et al.* (1981).

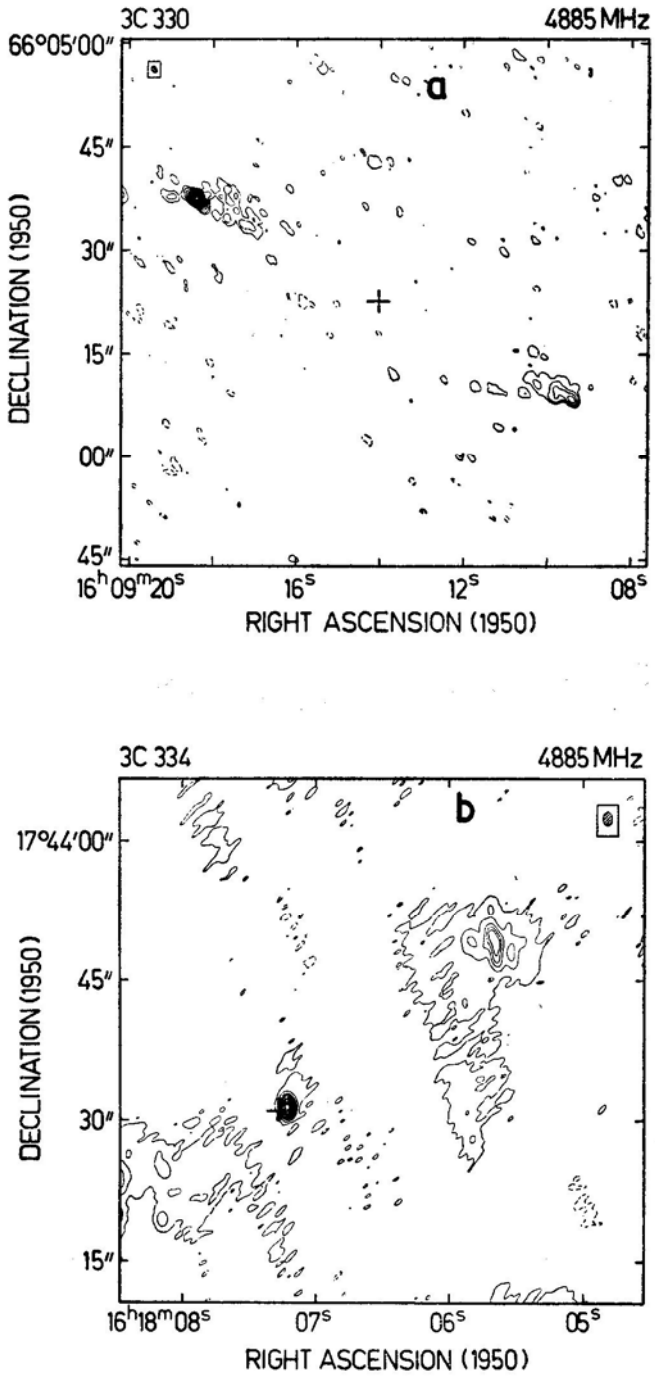

Figure 8. (a) 3C 330: peak flux is 679 mJy. (b) 3C 334: peak flux is 135 mJy. There is no compact structure in the eastern lobe (Jenkins, Pooley and Riley 1977).

component looks more likely than the *Sp* because it is far stronger, although the *Sp* is also edge-brightened. Laing (1981) notes that the N*f* component has a significantly steeper spectral index than the *Sp* between 5 and 15 GHz, but not between 2·7 and 5 GHz. This can be understood from a comparison of the present map with Laing's. The weak extension seen in our map to the north-east of the hot spot in the N*p* lobe is not present in the 15 GHz map, implying a steep spectrum for this feature.

3C334 (Fig. 8b): The structure is similar to the map of Jenkins, Pooley and Riley (1977) except that the northern component here is very much more resolved. The compact component (< 1·1 kpc) detected by KS is clearly associated with the central quasar. The KS structure shows considerable effects of resolution which might be arising from the narrow jet near the core seen in a recent VLA map by Wardle and Potash (1982).

3C352 (Fig. 9a): The Np component is a close double separated by 1·5 arcsec in PA – 22° with extensions to the south-west and north-east seen in the 2, 5 and 10 per cent contours. The strongest feature appears unresolved in this component. The S*f* component has one unresolved feature with extensions towards east and west up to the10 per cent level. There is some evidence of these extension in both components in the map by Jenkins, Pooley and Riley (1977). No emission can be seen at the position of the associated galaxy. KS could not unambiguously determine the location of their detected compact structure (< 1·2 kpc).

3C455 (Fig. 9b): The S*p* component is extended towards the N*f* component. The optical object (quasar, $z = 0{\cdot}543$) is associated with the unresolved N*f* component; the structure may therefore be of the D2 class, and the compact structure (< 1·1 kpc) of KS would then most likely be in this component.

3. Conclusion

The outer lobes of most of the high-luminosity sources reported here were previously known from maps made with the Cambridge 5-km telescopes (with a resolution of $2 \times \text{cosec}\ \delta$ arcsec at 5 GHz) to be unresolved or only slightly resolved, therefore usually appearing to consist of 'naked' hot spots without any associated regions of extended emission. The present VLA observations show that most of the lobes actually have extended emission in the form of low brightness 'tails' which often, though not always, point back towards the associated galaxy or quasar. The hot spots appear in general to be unresolved (<0·3 arcsec). In at least 3 of the sources discussed in this paper, (3C 254, 268·4, and 352) there is evidence for one of the lobes containing two hot spots. Such multiple-hot-spot structure has also been found to be fairly common by Laing (1981) from observations with the Cambridge 5-km telescope at 15 GHz.

From VLA observations at 15 GHz of several powerful but relatively nearby ($z < 0{\cdot}2$) radio galaxies, Dreher (1981) has recently noted that the hot spots often have sharp outer edges (< 300 pc wide) oriented perpendicular to the source axis. Because such small features would subtend angles < 0·04 arcsec at high redshifts, it is not surprising that the present observations show little fine structure in the hot

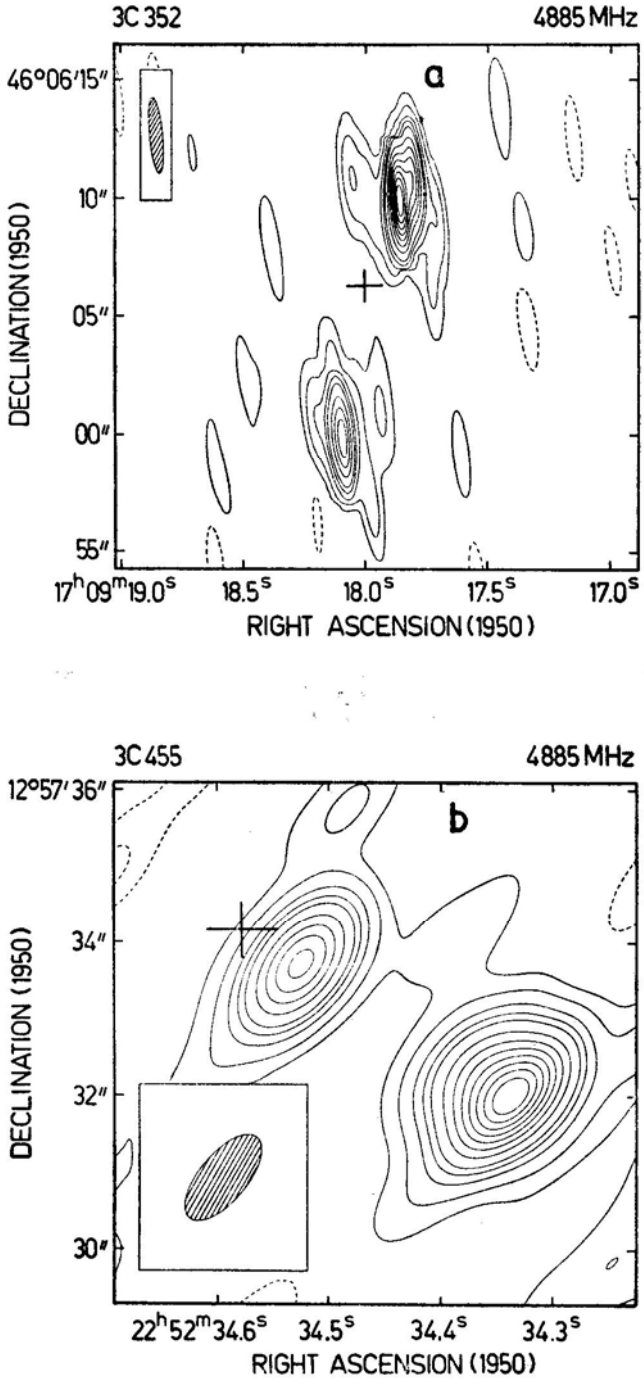

Figure 9. (a) 3C 352: peak flux is 175 mJy. (b) 3C 455: peak flux is 253 mJy.

spots. We plan to look for such fine structure with multi-station observations in the European VLBI network. We expect multiple hot spots to be as common in the powerful, distant sources as they are in the more nearby luminous radio galaxies. If this proves not to be the case, it will have interesting implications for theories of radio-source evolution.

The current observations indicate that the distant, luminous radio sources are morphologically very similar to their nearby, radio-powerful counterparts. Most of the observed structural differences appear to result from observing the distant sources with limited resolution, or limited dynamic range, or both.

Acknowledgements

We wish to thank Dr. R. A. Sramek for advice and assistance during the observations, and Dr. R. A. Laing for communicating his results before publication, and for discussions.

References

Argue, A. N., Kenworthy, C. M. 1972, *Mon. Not. R. astr. Soc.*, **160,** 197.
Cohen, A. M., Porcas, R. W., Browne, I. W. A., Daintree, E. J., Walsh, D. 1977, *Mem. R. astr. Soc.*, **84,** 1.
Dreher, J. W. 1981, *Astr. J.*, **86,** 833.
Gunn, J. E., Hoessel, J. G., Westphal, J. A., Perryman, M. A. C., Longair, M. S. 1981, *Mon. Not R. astr. Soc.*, **194,** 111.
Jenkins, C. J., McEllin, M. 1977, *Mon. Not. R. astr. Soc.,* **180,** 219.
Jenkins, C. J., Pooley, G. G., Riley, J. M. 1977, *Mem. R. astr. Soc.,* **84,** 61.
Kapahi, V. K. 1978, *Astr. Astrophys.,* **67,** 157.
Kapahi, V. K., Schilizzi, R. T. 1979a, *Nature.,* **277,** 610(KS).
Kapahi, V. K., Schilizzi, R. T. 1979b, *Astr. Astrophys. Suppl. Ser.,* **38,** 11(KS).
Laing, R. A. 1981, *Mon. Not. R. astr. Soc.,* **195,** 261.
Laing, R. A. 1982, in *IAU Symp. 97: Extragalactic Radio Sources,* Eds D. S. Heeschen and C. M. Wade, D. Reidel, Dordrecht, p. 161.
Lonsdale, C. J., Morison, I. 1980, *Nature,* **288,** 66.
Neff, S. G., Rudnick, L. 1980, *Mon. Not. R. astr. Soc.,* **192,** 531.
Pooley, G. G., Henbest, S. N. 1974, *Mon. Not. R. astr. Soc.,* **169,** 477.
Riley, J. M., Longair, M. S., Gunn, J. E. 1980, *Mon. Not. R. astr. Soc.,* **192,** 233.
Schwab, F. R. 1980, *International Computing Conference: Proc. Soc. Photo-Opt. Instrum. Eng.* **231,** 18.
Smith, H. E., Spinrad, H. 1980, *Publ. astr. Soc. Pacific,* **92,** 553.
Stocke, J., Christiansen, W., Burns, J. 1982, in *IAU Symp. 97: Extragalactic Radio Sources,* Eds D. S. Heeschen and C. M. Wade, D. Reidel, Dordrecht, p. 39.
Wardle, J. F. C., Potash, R. I. 1982, in *IAU Symp. 97: Extragalactic Radio Sources,* Eds D. S. Heeschen and C. M. Wade, D. Reidel, Dordrecht, p. 129.
Wilkinson P. N. 1972, *Mon. Not. R. astr. Soc.,* **160,** 305.

J. Astrophys. Astr. (1982) **3,**189–192

The Identification of CTA 21

David A. Allen *Anglo-Australian Observatory, PO Box 296, Epping NSW 2121, Australia*
Alan E. Wright and Jon G.Ables *CSIRO Division of Radiophysics, PO Box 76, Epping NSW 2121, Australia*

Received 1982 April 21 ; accepted 1982 May 10

Abstract. CTA 21 has long been the outstanding example of a strong, compact radio source lacking an optical identification. We report the discovery at infrared wavelengths of the counterpart of CTA 21, and show that its spectral shape is unusual.

Key words: radio sources—infrared sources

1. Introduction

It has long been an embarrassment to those working in the field that no optical counterparts can be found to some prominent extragalactic radio sources. Of late, however, the search for 'optical' identifications has migrated to infrared wavelengths, with considerable success (Rieke, Lebofsky and Kinman 1979; Lilly and Longair 1982). At a wavelength of 2.2 μm the completeness of identifications approaches 100 per cent. This is especially so for sources with flat radio spectra, which are invariably compact radio objects whose coordinates can be determined accurately. This is of relevance because sensitive imaging devices are not available for 2.2 μ.m.

Probably the outstanding example of a strong, compact source with no optical counterpart is CTA 21 (= Pks 0316 + 16). The 1950 position of CTA 21 is given by Wade (1970), and its compact nature (<0·4 arcsec) was demonstrated by Anderson *et al.* (1965). The ~ 1400 MHz radio flux density from this object is around 8 Jy, while Kristian and Sandage (1970) published a photographic magnitude limit of 22 (~ 7 μJy). We report here our observations and detection of an infrared counterpart to CTA 21.

2. Observations

Our measurements were made in the *J*, *H* and *K* bandpasses (1.20,1.64 and 2.19 μm) using the infrared photometer-spectrometer on the 3.9m Anglo-Australian Tele-

Table 1. Photometry of CTA 21 and object M.

Date	Magnitudes			Flux μJy		
	J	*H*	*K*	*J*	*H*	*K*
1980 October 25	18·29 ± 0·19	17·72 ± 0·21	16·73 ± 0·18	74 ± 13	84 ± 17	132 ± 22
November 14	18·89 0·20	18·23 0·26		43 8	53 12	
1981 February 27	18·03 0·22			95 20		
	(17·19 0·15)*					
October 13†	18·80 0·15		17·07 0·13	47 6		97 12

* object M
† centred

scope (AAT). For the first three observations we offset in position from a nearby star (SAO 093393) and found a detectable signal at all three wavelengths. A 7-arcsec circular focal-plane aperture was used, with sky references being taken 11 arcsec to north and south. The data are given in Table 1.

Of concern in these measurements was the presence of an adjacent object, probably nonstellar, designated M by Kristian and Sandage. Object M lies 6 arcsec east and 8 arcsec north of the radio position of CTA 21, and we ascertained (Table 1, February 27) that it is considerably brighter than CTA 21 itself at *J*.

Fearing contamination by this object, we made a partial map of the region, and so confirmed that a distinct infrared source lies at the position (relative to object M) appropriate to CTA 21 to within an uncertainty of about 1.5 arcsec. CTA 21 has thus been identified. Our map showed, however, that our early measurements had been centred 2 ± 1.5 arcsec N of CTA 21. This error, presumed due to an inadequately accurate position for SAO 093393, does introduce some uncertainty into the early data on CTA 21, due to possible contamination from object M. However, consideration of the beamsize, optical seeing disk and positional error satisfies us that the contamination from object M was small. We therefore consider the data in Table 1 to offer some evidence that CTA 21 is an infrared variable. Amongst flat-spectrum radio sources infrared variability is common in the BL Lac objects, but not normally seen in quasars or galaxies. Further measurements are desirable.

A magnitude of about 18–19 at *J* together with the optical magnitude limit would make CTA 21 a very red object. However, the possibility of infrared variability questions whether the optical counterpart has brightened in the decade since observation by Kristian and Sandage. To check this we obtained more optical data on CTA 21. A IV-N plate taken at our request by the U.K. Schmidt Telescope Unit, shows no object brighter than the plate limit of ∼ 19 mag at ∼ 7000 Å. A 10-minute exposure with unfiltered RCA CCD chip (∼ 40009000 Å) at the prime focus of the AAT likewise showed no image at the radio position. No calibration of the latter was possible, though it appears to go significantly deeper than the plate of Kristian and Sandage. Nevertheless, we estimate conservatively a *V* magnitude fainter than 22.

3. Discussion

The photometric data and upper limits are presented together in Fig. 1. Here we have shown only the last set of *J* and *K* data when the object was well-centred in the aperture. The radio data are from the compilation of Kühr *et al.* (1981). CTA 21 is unusual in having a strongly curved radio spectrum. The data appear to require at least three spectral regimes: $F_\nu \propto \nu^{0.2}$ in the low frequency radio, $F_\nu \propto \nu^{-1.0}$ in the radio-infrared; and $F_\nu \propto \nu^{-3}$ in the infrared–optical.

This radio–infrared spectral index is steeper than that of any other extragalactic object known. Likewise, the infrared–optical spectral index is steeper than any quasar except 3C 68.1 (Neugebauer *et al.* 1979). Ignoring the slender possibility that CTA 21 is a galactic object, we propose that it is most plausibly a radio galaxy or BL Lacertae object. An elliptical galaxy at a redshift $0.6 \lesssim z \lesssim 2$ can fit the existing data. Alternatively the *J*—*K* colour, the steepening optical spectral index and the shallower radio spectral index are typical of BL Lac objects (Allen, Ward and Hyland 1982). However, this interpretation is opposed by the striking and extensive history of radio non-variability (unpublished data drawn from work at Parkes at 2700 and 5000 MHz over the period 1968 to 1980). Furthermore, the linear polarization of CTA 21 is quite small (Gardner, Whiteoak and Morris 1975), and more typical of compact quasars than BL Lac objects. If indeed CTA 21 is a BL Lac object, then it is also unusual in having two spectral breaks in accessible parts of the electromagnetic spectrum.

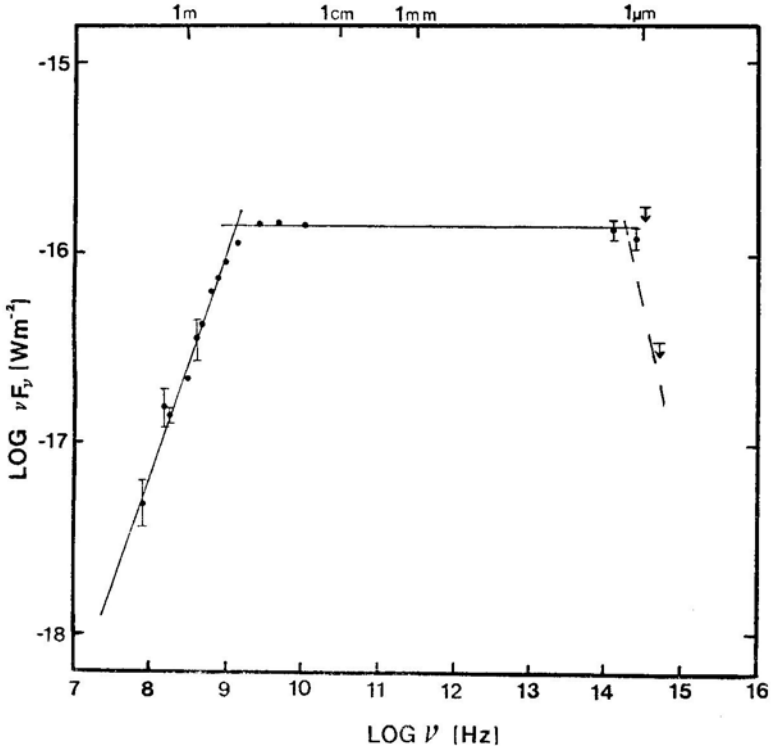

Figure 1. Energy distribution for CTA 21 showing the three regimes of spectral index.

In addition to the further infrared measurements needed, millimetre wavelength data would be valuable to determine better whether the radio spectrum does show an abrupt break.

Acknowledgements

We thank the U.K. Schmidt Telescope Unit for securing a plate of CTA 21, and J. Gordon Robertson for making the observations on 1981 February 27.

References

Allen, D. A., Ward, M. J., Hyland, A. R. 1982, *Mon. Not. R. astr. Soc.,* **199,** 969.
Anderson, B., Donaldson, W., Palmer, H. P., Rowson, B. 1965, *Nature,* **205,** 375.
Gardner, F. F., Whiteoak, J. B., Morris, D. 1975, *Austr. J. Phys. Astrophys. Suppl.,* No. 35.
Kristian, J., Sandage, A. R. 1970, *Astrophys. J.* **162,** 391.
Kühr, H., Witzel, A., Pauliny-Toth, I.I. K., Nauber, U. 1981, *Astr. Astrophys. Suppl. Ser.,* **45,** 367
Lilly, S. J., Longair, M. S. 1982, *Mon. Not. R. astr. Soc.,* **199,** 1053.
Neugebauer, G., Oke, J. B., Becklin, E. E., Matthews, K. 1979, *Astrophys. J.,* **230,** 79.
Rieke, G. H., Lebofsky, M. J., Kinman, T. D. 1979, *Astrophys. J.,* **232,** L151.
Wade, C. M. 1970, *Astrophys. J.,* **162,** 381.

J. Astrophys. Astr. (1982) **3**, 193–206

Structure and Stability of Rotating Fluid Disks around Massive Objects. II. General Relativistic Formulation

D. K. Chakraborty* and A. R. Prasanna *physical Research Laboratory, Navrangpura, Ahmedabad 380009*

Received 1982 January 4; accepted 1982 May 24

Abstract. In this paper we have considered the structure of a thick perfect fluid disk of constant density rotating around a Schwarzschild black hole and its stability under axisymmetric perturbation. The inner edge of such disk cannot lie within $4m$. The critical γ_c for neutral stability is found to be much less than 4/3 indicating that the disks are generally stable.

Key words: fluid disks—general relativity—stability

1. Introduction

Recent developments in the study of high energy emission from cosmic sources has emphasised quite frequently the importance of the study of structure and stability of accretion disks around compact objects. After the early analysis of Pringle and Rees (1972), Novikov and Thorne (1973), Shakura and Sunyaev (1976), the subject has been treated in a more detailed way by many authors with the analysis of both thin and thick disks. Subsequent to the review of Lightman, Shapiro and Rees (1978), the Polish school has considered several aspects of accretion disk models, a reference to which may be seen in Paczynski (1980). It is now well known that if the accretion rate exceeds the critical limit the inner regions of the disk render a thick structure as first pointed out by Shakura and Sunyaev (1973), and thus it is very relevant to consider the detailed analysis of the structure and stability of thick disks in the same spirit as has been done earlier for thin disks. However almost all these analyses restricted themselves to the study of disks under equilibria with respect to the gravitational, centrifugal and pressure gradient forces only. Prasanna and Chakraborty (1981; hereafter referred to as Paper I) emphasised the necessity of considering the analysis including the self-generated electromagnetic fields also and they showed that

*Permanent Address: Government College, Jagdalpur 494001

pressureless thin disks of charged perfect fluid are indeed generally stable under radial pulsations. However an analysis of the thick disks under the action of all the four forces (gravitational, electromagnetic, centrifugal and pressure gradient) has been quite formidable and as such we consider the detailed structure and stability of thick disks around Schwarzschild black hole without the electromagnetic field. The analysis of such disks in Newtonian formulation showed that both under radial as well as axisymmetric perturbation there are large regions of stability (Chakraborty and Prasanna 1981, hereafter referred to as Paper II). We present in this paper the analysis of similar disks with a fully relativistic treatment.

2. Steady state solutions

The general set of equations governing the dynamics of a non-self-gravitating perfect fluid disk can be obtained from the general momentum equations (Paper I, Equations 2.15 – 2.17) and are given by

$$\left(\rho+\frac{p}{c^2}\right)\left\{\frac{DV^{(r)}}{Dt}+\frac{mc^2}{r^2}\left(1-\frac{V^{(r)2}}{c^2}\right)-\left(1-\frac{2m}{r}\right)\left(\frac{V^{(\theta)2}+V^{(\phi)2}}{r}\right)\right\}$$
$$=-\left(1-\frac{V^2}{c^2}\right)\left\{\left(1-\frac{2m}{r}\right)\frac{\partial p}{\partial r}+\frac{V^{(r)}}{c^2}\frac{\partial p}{\partial t}\right\}, \tag{2.1}$$

$$\left(\rho+\frac{p}{c^2}\right)\left\{\frac{DV^{(\theta)}}{Dt}+\left(1-\frac{3m}{r}\right)\frac{V^{(r)}V^{(\theta)}}{r}-\left(1-\frac{2m}{r}\right)^{1/2}\frac{\cot\theta\,V^{(\phi)2}}{r}\right\}$$
$$=-\left(1-\frac{V^2}{c^2}\right)\left\{\left(1-\frac{2m}{r}\right)^{1/2}\frac{1}{r}\frac{\partial p}{\partial\theta}+\frac{V^{(\theta)}}{c^2}\frac{\partial p}{\partial r}\right\}, \tag{2.2}$$

$$\left(\rho+\frac{p}{c^2}\right)\left\{\frac{DV^{(\phi)}}{Dt}+\left(1-\frac{3m}{r}\right)\frac{V^{(r)}V^{(\theta)}}{r}+\left(1-\frac{2m}{r}\right)^{1/2}\frac{\cot\theta\,V^{(\theta)}V^{(\phi)}}{r}\right\}$$
$$=-\left(1-\frac{V^2}{c^2}\right)\left\{\left(1-\frac{2m}{r}\right)^{1/2}\frac{1}{r\sin\theta}\frac{\partial p}{\partial\phi}+\frac{V^{(\phi)}}{c^2}\frac{\partial p}{\partial t}\right\}, \tag{2.3}$$

the continuity equation (Paper I, Equation 2.6) is given by

$$\frac{D}{Dt}\left(\rho-\frac{p}{c^2}\right)+\left(\rho+\frac{p}{c^2}\right)\left\{\left(1-\frac{2m}{r}\right)^{1/2}\left[\frac{1}{r^2}\frac{\partial}{\partial r}(r^2V^{(r)})\right.\right.$$
$$\left.\left.+\frac{1}{r\sin\theta}\left(\frac{\partial}{\partial\theta}(\sin\theta\,V^{(\theta)})+\frac{\partial V^{(\phi)}}{\partial\phi}\right)\right]\right\}+\frac{1}{c^2}\left(1-\frac{V^2}{c^2}\right)\frac{\partial p}{\partial t}=0, \tag{2.4}$$

the equation of baryon conservation $(nu^i)_{;\,i}=0$, as given by

$$n\left(1-\frac{2m}{r}\right)^{1/2}\left\{\left(1-\frac{2m}{r}\right)^{1/2}\frac{1}{r^2}\frac{\partial}{\partial r}(r^2V^{(r)})+\frac{1}{r\sin\theta}\left(\frac{\partial}{\partial\theta}(\sin\theta\,V^{(\theta)})+\frac{\partial V^{(\phi)}}{\partial\phi}\right)\right\}$$
$$+\frac{Dn}{Dt}-\frac{n}{c^2}\left(\rho+\frac{p}{c^2}\right)^{-1}\left\{\frac{Dp}{Dt}+\left(1-\frac{V^2}{c^2}\right)\frac{\partial p}{\partial t}\right\}=0 \tag{2.5}$$

and the equation for the adiabatic flow

$$\frac{D}{Dt}(p\, n^{-\gamma}) = 0 \tag{2.6}$$

where p, ρ, n and $V^{(\alpha)}$ are the pressure, density, baryon number density and the components of 3-velocity in the local Lorentz frame and

$$\frac{D}{Dt} = \frac{\partial}{\partial t} + \left(1 - \frac{2m}{r}\right)^{1/2} \left\{ \left(1 - \frac{2m}{r}\right)^{1/2} V^{(r)} \frac{\partial}{\partial r} + \frac{1}{r} V^{(\theta)} \frac{\partial}{\partial \theta} + \frac{1}{r \sin\theta} V^{(\phi)} \frac{\partial}{\partial \phi} \right\},$$

$$V^2 = V^{(r)2} + V^{(\theta)2} + V^{(\phi)2},$$

$$m = MG/c^2. \tag{2.7}$$

Restricting ourselves to the case of an axisymmetric disk in pure rotational flow as expressed by $V_0^{(r)} = 0$, $V_0^{(\theta)} = 0$, $V_0^{(\phi)} = V_0$, the equations governing the steady state reduce to

$$\left(\rho_0 + \frac{p_0}{c^2}\right)\left[\frac{mc^2}{r^2} - \left(1 - \frac{2m}{r}\right)\frac{V_0^2}{r}\right] = -\left(1 - \frac{2m}{r}\right)\left(1 - \frac{V_0^2}{c^2}\right)\frac{\partial p_0}{\partial r}, \tag{2.8}$$

$$\left(\rho_0 + \frac{p_0}{c^2}\right)\cot\theta\, V_0^2 = \left(1 - \frac{V_0^2}{c^2}\right)\frac{\partial p_0}{\partial \theta}, \tag{2.9}$$

the remaining equations being identically satisfied. The above two equations can be solved exactly for the special case, ρ_0 = constant. Using this in Equations (2.8) and (2.9), we obtain

$$\cot\theta \frac{\partial}{\partial r} V_0^2 - \frac{1}{r}\frac{\partial}{\partial \theta} V_0^2 + \frac{m}{r^2}\left(1 - \frac{2m}{r}\right)^{-1} \frac{\partial}{\partial \theta} V_0^2 = 0 \tag{2.10}$$

whose solution is given by

$$V_0^2 = Ac^2 (1 - 2m/r) \,/\, r^2 \sin^2\theta, \tag{2.11}$$

A being a constant. Substituting this in Equations (2.8) and (2.9), we get

$$\left(\rho_0 + \frac{p_0}{c^2}\right)\left[\frac{mc^2}{r^2} - Ac^2\left(1 - \frac{2m}{r}\right)^2 \Big/ r^3 \sin^2\theta\right]$$

$$= -\left[1 - A\left(1 - \frac{2m}{r}\right)\Big/ r^2 \sin^2\theta\right]\left(1 - \frac{2m}{r}\right)\frac{\partial p_0}{\partial r}, \tag{2.12}$$

$$\left(\rho_0 + \frac{p_0}{c^2}\right) Ac^2 \cot\theta \left(1 - \frac{2m}{r}\right)\Big/ r^2 \sin^2\theta = \left[1 - A\left(1 - \frac{2m}{r}\right)\Big/ r^2 \sin^2\theta\right]\frac{\partial p_0}{\partial \theta} \tag{2.13}$$

whose solution may be obtained as

$$p_0/c^2 = B\left[\left(1-\frac{2m}{r}\right)^{-1} - A/r^2\sin^2\theta\right]^{1/2} - \rho_0, \tag{2.14}$$

where B is another constant. Using the boundary condition $p_0 = 0$ at r_a and r_b, the inner and outer edges at the plane $\theta = \pi/2$ we obtain the solutions of steady state as

$$\rho_0 = \text{constant}, \tag{2.15}$$

$$\frac{V_0^2}{c^2} = A\left(1-\frac{2}{R}\right)\Big/ R^2\sin^2\theta, \tag{2.16}$$

$$\frac{p_0}{c^2} = \rho_0\left[B\left\{\left(1-\frac{2}{R}\right)^{-1} - \frac{A}{R^2\sin^2\theta}\right\}^{1/2} - 1\right], \tag{2.17}$$

wherein

$$A = 2a^2b^2 / (a+b)(a-2)(b-2),$$

$$B = \left[\frac{(b^2-a^2)(b-2)(a-2)}{b^3(a-2) - a^3(b-2)}\right]^{1/2},$$

$$R = \frac{r}{m}, \quad a = \frac{r_a}{m}, \quad b = \frac{r_b}{m}. \tag{2.18}$$

The solutions obtained above are physically acceptable if $p_0 > 0$ throughout the interior of the disk and it goes over to zero at the boundary. The former condition leads us to the constraint that the inner edge cannot lie within $4m$ and further

$$b > 2a/(a-4), \quad \text{if} \quad 4 < a < 6. \tag{2.19}$$

There is no restriction on outer edge if $a \geqslant 6$. The latter condition $(p_0)_b = 0$ gives the edge of the disk θ_e (and $\pi - \theta_e$) on the meridional plane as given by

$$\sin^2\theta_e = AB^2 / R^2\,[B^2(1-2/R)^{-1} - 1]. \tag{2.20}$$

Fig. 1 shows the profiles of velocity and pressure as the functions of equatorial distance while Fig. 2 shows the meridional section of the disk.

3. Stability analysis

We consider the axisymmetric perturbations of the disk as described above and use the normal mode analysis restricting the perturbations to linear terms only; the general procedure of the analysis remains the same as used in Paper II which is based on

the technique developed by Chandrasekhar and Friedman (1972a, b). The set of equations governing the perturbations are obtained from Paper I, Equations (3.1)–(3.4) as given by

$$\left(\rho_0+\frac{p_0}{c^2}\right)\left[\frac{\partial}{\partial t}\delta V^{(r)}-\frac{2}{r}\left(1-\frac{2m}{r}\right)V_0\delta V^{(\phi)}\right]+\left(\delta\rho+\frac{\delta p}{c^2}\right)\left[\frac{mc^2}{r^2}-\frac{1}{r}\left(1-\frac{2m}{r}\right)V_0^2\right]$$

$$=-\left(1-\frac{2m}{r}\right)\left[\left(1-\frac{V_0^2}{c^2}\right)\frac{\partial}{\partial r}\delta p-\frac{2V_0\delta V^{(\phi)}}{c^2}\frac{\partial p_0}{\partial r}\right], \tag{3.1}$$

$$\left(\rho_0+\frac{p_0}{c^2}\right)\left[\frac{\partial}{\partial t}\delta V^{(\theta)}-\frac{2}{r}\left(1-\frac{2m}{r}\right)^{1/2}V_0\,\delta V^{(\phi)}\cot\theta\right]-\left(\delta\rho+\frac{\delta p}{c^2}\right)\frac{V_0^2}{r}$$

$$\times\left(1-\frac{2m}{r}\right)^{1/2}\cot\theta=-\left(1-\frac{2m}{r}\right)^{1/2}\left[\left(1-\frac{V_0^2}{c^2}\right)\frac{1}{r}\frac{\partial}{\partial\theta}\delta p-\frac{2V_0\,\delta V^{(\phi)}}{rc^2}\frac{\partial p_0}{\partial\theta}\right] \tag{3.2}$$

and

$$\left(\rho_0+\frac{p_0}{c^2}\right)\left[\frac{\partial}{\partial t}\delta V^{(\phi)}+\frac{1}{r}\left(1-\frac{2m}{r}\right)^{1/2}\left\{\frac{\partial V_0}{\partial\theta}+V_0\cot\theta\right\}\delta V^{(\theta)}\right.$$

$$\left.+\left\{\left(1-\frac{2m}{r}\right)\frac{\partial V_0}{\partial r}+\frac{1}{r}\left(1-\frac{3m}{r}\right)V_0\right\}\delta V^{(r)}\right]=-\left(1-\frac{V_0^2}{c^2}\right)\frac{V_0}{c^2}\frac{\partial}{\partial t}\delta p \tag{3.3}$$

while Equations (2.4) – (2.6) yield

$$\left(\rho_0+\frac{p_0}{c^2}\right)\left(1-\frac{2m}{r}\right)^{1/2}\left\{\left(1-\frac{2m}{r}\right)^{1/2}\frac{1}{r^2}\frac{\partial}{\partial r}(r^2\delta V^{(r)})+\frac{1}{r\sin\theta}\frac{\partial}{\partial\theta}(\sin\theta\;\delta V^{(\theta)})\right\}$$

$$+\frac{\partial}{\partial t}\left(\delta\rho-\frac{\delta p}{c^2}\right)+\left(1-\frac{2m}{r}\right)^{1/2}\left\{\left(1-\frac{2m}{r}\right)^{1/2}\delta V^{(r)}\frac{\partial}{\partial r}+\frac{\delta V^{(\theta)}}{r}\frac{\partial}{\partial\theta}\right\}\left(\rho_0-\frac{p_0}{c^2}\right)$$

$$+\frac{1}{c^2}\left(1-\frac{V_0^2}{c^2}\right)\frac{\partial}{\partial t}\delta p=0, \tag{3.4}$$

$$\left(\rho_0+\frac{p_0}{c^2}\right)n_0\left(1-\frac{2m}{r}\right)^{1/2}\left\{\left(1-\frac{2m}{r}\right)^{1/2}\frac{1}{r^2}\frac{\partial}{\partial r}(r^2\,\delta V^{(r)})+\frac{1}{r\sin\theta}\frac{\partial}{\partial\theta}(\sin\theta\,\delta V^{(\theta)})\right\}$$

$$+\left(\rho_0+\frac{p_0}{c^2}\right)\left\{\frac{\partial}{\partial t}\delta n+\left(1-\frac{2m}{r}\right)^{1/2}\left[\left(1-\frac{2m}{r}\right)^{1/2}\delta V^{(r)}\frac{\partial}{\partial r}+\frac{\delta V^{(\theta)}}{r}\frac{\partial}{\partial\theta}\right]n_0\right\}$$

$$-\frac{n_0}{c^2}\left\{\frac{\partial}{\partial t}\delta p+\left(1-\frac{2m}{r}\right)^{1/2}\left[\left(1-\frac{2m}{r}\right)^{1/2}\delta V^{(r)}\frac{\partial}{\partial r}+\frac{\delta V^{(\theta)}}{r}\frac{\partial}{\partial\theta}\right](p_0)\right.$$

$$\left.-\left(1-\frac{V_0^2}{c^2}\right)\frac{\partial}{\partial t}\delta p\right\}=0, \tag{3.5}$$

$$\frac{\partial}{\partial t}\left(n_0^{-\gamma}\,\delta p - \gamma\, p_0\, n_0^{-\gamma-1}\,\delta n\right)$$

$$+\left(1-\frac{2m}{r}\right)^{1/2}\left\{\left(1-\frac{2m}{r}\right)^{1/2}\delta V^{(r)}\,\frac{\partial}{\partial r}+\frac{\delta V^{(\theta)}}{r}\,\frac{\partial}{\partial\theta}\right\}\left(p_0\,n_0^{-\gamma}\right)=0. \tag{3.6}$$

Defining the Lagrangian displacement ξ^{α}, ($\alpha = r,\ \theta$) through

$$\delta V^{\alpha}=\frac{\partial \xi^{\alpha}}{\partial t}, \qquad \xi^{\alpha}(r,\theta,t)=\xi^{\alpha}(r,\theta)\exp(i\sigma t), \tag{3.7}$$

we obtain from Equations (3.1) – (3.6)

$$\left(\rho_0+\frac{p_0}{c^2}\right)\delta V^{(\phi)}=-\,S_2 V_0\,\delta p/c^2, \tag{3.8}$$

$$\delta\rho=-\left(\rho_0+\frac{p_0}{c^2}\right)\sqrt{S_1}\left[\frac{\sqrt{S_1}}{r^2}\,\frac{\partial}{\partial r}(r^2\,\xi^r)+\frac{1}{r\sin\theta}\,\frac{\partial}{\partial\theta}(\sin\theta\,\xi^{\theta})\right]$$

$$+\frac{V_0^2}{c^4}\delta p+\sqrt{S_1}\left\{\sqrt{S_1}\,\xi^r\frac{\partial}{\partial r}+\frac{\xi^{\theta}}{r}\,\frac{\partial}{\partial\theta}\right\}(p_0/c^2), \tag{3.9}$$

$$\delta n=-\,n_0\sqrt{S_1}\left[\frac{\sqrt{S_1}}{r^2}\,\frac{\partial}{\partial r}(r^2\,\xi^r)+\frac{1}{r\sin\theta}\,\frac{\partial}{\partial\theta}(\sin\theta\,\xi^{\theta})\right]$$

$$-\sqrt{S_1}\left[\sqrt{S_1}\,\xi^r\frac{\partial n_0}{\partial r}+\frac{\xi^{\theta}}{r}\,\frac{\partial n_0}{\partial\theta}\right]+\left(\rho_0+\frac{p_0}{c^2}\right)^{-1}\frac{n_0}{c^2}\left[\delta p+\sqrt{S_1}\left\{\sqrt{S_1}\,\xi^r\frac{\partial p_0}{\partial r}\right.\right.$$

$$\left.\left.+\frac{\xi^{\theta}}{r}\,\frac{\partial p_0}{\partial\theta}\right\}-S_2\,\delta p\right], \tag{3.10}$$

$$\delta p=\frac{\gamma p_0}{n_0}\,\delta n-\sqrt{S_1}\left\{\sqrt{S_1}\,\xi^r\frac{\partial p_0}{\partial r}+\frac{\xi^{\theta}}{r}\,\frac{\partial p_0}{\partial\theta}\right\}+\frac{\gamma p_0}{n_0}\sqrt{S_1}\left\{\sqrt{S_1}\,\xi^r\frac{\partial n_0}{\partial r}+\frac{\xi^{\theta}}{r}\,\frac{\partial n_0}{\partial\theta}\right\}, \tag{3.11}$$

$$-\left(\rho_0+\frac{p_0}{c^2}\right)\sigma^2\,\xi^r=\left(\rho_0+\frac{p_0}{c^2}\right)\frac{2}{r}\,S_1\,V_0\,\delta V^{(\phi)}-S_1\,S_2\,\frac{\partial}{\partial r}\delta p$$

$$-\left(\delta\rho+\frac{\delta p}{c^2}\right)\left[\frac{mc^2}{r^2}-\frac{S_1}{r}\,V_0^2\right]+2S_1\,\frac{V_0}{c^2}\,\frac{\partial p_0}{\partial r}\,\delta V^{(\phi)}, \tag{3.12}$$

$$-\left(\rho_0+\frac{p_0}{c^2}\right)\sigma^2\,\xi^{\theta}=\left(\rho_0+\frac{p_0}{c^2}\right)\frac{2}{r}\sqrt{S_1}\cot\theta\,V_0\,\delta V^{(\phi)}-\sqrt{S_1}\,S_2\,\frac{1}{r}\,\frac{\partial}{\partial\theta}\delta p$$

$$+\left(\delta\rho+\frac{\delta p}{c^2}\right)\frac{V_0^2}{r}\sqrt{S_1}\cot\theta+2\sqrt{S_1}\,\frac{V_0}{c^2}\,\frac{1}{r}\,\frac{\partial p_0}{\partial\theta}\,\delta V^{(\phi)}, \tag{3.13}$$

wherein

$$S_1 = \left(1 - \frac{2m}{r}\right), \; S_2 = \left(1 - \frac{V_0^2}{c^2}\right) \tag{3.14}$$

and all the perturbed variables represent only the spatial parts. Equations (3.8)–(3.11) are the initial value equations while (3.12) and (3.13) are the pulsation equations. In the above treatment, we have dropped out those terms which become zero because of the steady-state solutions and also we have integrated the initial-value equations with respect to time. Equation (3.9) together with (3.10) yields

$$\frac{\Delta\rho}{(\rho_0 + p_0/c^2)} = \frac{\Delta n}{n_0}, \tag{3.15}$$

while Equation (3.11) can be rewritten as

$$\frac{\Delta p}{p_0} = \gamma \frac{\Delta n}{n_0} \tag{3.16}$$

in terms of Lagrangian perturbations. From Equations (3.9)–(3.11), we obtain

$$\begin{aligned}
&\delta p \left[1 - (\rho + p_0/c^2)^{-1} \frac{\gamma p_0}{c^2} \frac{V_0^2}{c^2}\right] \\
&\quad = -\left[1 - \left(\rho_0 + \frac{p_0}{c^2}\right)^{-1} \frac{\gamma p_0}{c^2}\right]\left(S_1 \xi^r \frac{\partial p_0}{\partial r} + \sqrt{S_1}\, \frac{\xi^\theta}{r} \frac{\partial p_0}{\partial \theta}\right) \\
&\qquad - \gamma p_0 \left[\frac{S_1}{r^2} \frac{\partial}{\partial r}(r^2 \xi^r) + \frac{\sqrt{S_1}}{r \sin\theta} \frac{\partial}{\partial \theta}(\sin\theta\, \xi^\theta)\right],
\end{aligned} \tag{3.17}$$

$$\begin{aligned}
&\delta\rho \left[1 - \left(\rho_0 + \frac{p_0}{c^2}\right)^{-1} \frac{\gamma p_0}{c^2} \frac{V_0^2}{c^2}\right] \\
&\quad = -\left(\rho_0 + \frac{p_0}{c^2}\right)\left[\frac{S_1}{r^2} \frac{\partial}{\partial r}(r^3 \xi^r) + \frac{\sqrt{S_1}}{r \sin\theta} \frac{\partial}{\partial \theta}(\sin\theta\, \xi^\theta)\right] \\
&\qquad + \frac{S_2}{c^2}\left(S_1 \xi^r \frac{\partial p_0}{\partial r} + \sqrt{S_1} \frac{\xi^\theta}{r} \frac{\partial p_0}{\delta\theta}\right).
\end{aligned} \tag{3.18}$$

The problem is then to solve Equations (3.12) and (3.13) as the eigen-value equations, consistently with the initial value equation (3.17) and (3.18) and the appropriate boundary conditions.

As we did in Paper II, we define ‘ trial displacements’ $\overline{\xi^r}$ and $\overline{\xi^\theta}$, multiply Equation (3.12) by $\overline{\xi^r}$ and Equation (3.13) by $\overline{\xi^\theta}$, add and integrate over the range of r and θ. In order to bring the resultant expression in a symmetrical form in barred

and unbarred variables, we limit ourselves to the class of perturbations such that $\delta p = 0$ at the boundary of the disk. This in turn requires that both ξ^r and ξ^θ be zero at the boundary. Performing several integrations by parts and using Equation (3.8) and the steady state equations we finally obtain

$$\sigma^2 \int\int \frac{1}{S_2}\left(\rho_0 + \frac{p_0}{c^2}\right)(\bar{\xi}^r \xi^r + \bar{\xi}^\theta \xi^\theta)\, r^2 \sin\theta \, dr\, d\theta$$

$$= \int\int \left[S_1 \left(\bar{\xi}^r \frac{\partial}{\partial r}\delta p + \xi^r \frac{\partial}{\partial r}\bar{\delta p}\right) + \frac{\sqrt{S_1}}{r}\left(\bar{\xi}^\theta \frac{\partial}{\partial \theta}\delta p + \xi^\theta \frac{\partial}{\partial \theta}\bar{\delta p}\right)\right.$$

$$+ \frac{2m}{r^2}(\bar{\xi}^r \delta p + \xi^r \overline{\delta p})$$

$$+ \frac{V_0^2}{c^4}\left(\rho_0 + \frac{p_0}{c^2}\right)^{-2}\left(S_1 \xi^r \frac{\partial p_0}{\partial r} + \sqrt{S_1}\frac{\xi^\theta}{r}\frac{\partial p_0}{\partial \theta}\right)\left((S_1 \bar{\xi}^r \frac{\partial p_0}{\partial r} + \sqrt{S_1}\frac{\bar{\xi}^\theta}{r}\frac{\partial p_0}{\partial \theta}\right)$$

$$+ \frac{\gamma p_0 S_2}{c^2}\left(\rho_0 + \frac{p_0}{c^2}\right)^{-2}\left\{\delta\rho\left(S_1 \bar{\xi}^r \frac{\partial p_0}{\partial r} + \frac{\sqrt{S_1}\,\bar{\xi}^\theta}{r}\frac{\partial p_0}{\partial \theta}\right)\right.$$

$$\left.\left. + \overline{\delta\rho}\left(S_1 \xi^r \frac{\partial p_0}{\partial r} + \frac{\sqrt{S_1}\,\xi^\theta}{r}\frac{\partial p_0}{\partial \theta}\right)\right\}\right.$$

$$\left. - \frac{\gamma p_0}{(\rho_0 + p_0/c^2)^2}\left\{1 - \frac{\gamma p_0/c^2}{(\rho_0 + p_0/c^2)}\frac{V_0^2}{c^2}\right\}\delta\rho\,\overline{\delta\rho}\right] r^2 \sin\theta\, dr\, d\theta, \tag{3.19}$$

where $\overline{\delta\rho}$ and $\overline{\delta p}$ are variations in perturbed density and pressure obtained by using the trial displacements in initial-value equations. As it was shown in Paper II the symmetrical expression of σ^2 implies a variational principle: identifying barred variables with the unbarred ones in Equation (3.19), we write the expression for σ^2 and calculate σ^2 by using two trial displacements ξ^α and $\xi^\alpha + \delta\,\xi^\alpha$. If we now demand that the resultant variation $\delta\sigma^2$ in σ^2 is zero, then it amounts to solving the original eigenvalue equations (3.12) and (3.13). To calculate the critical value of adiabatic index for neutral stability we limit ourselves to the situations where $(\gamma p_0/c^2)(V_0^2/c^2) \times (\rho_0 + p_0/c^2)^{-1}$ is very small compared to unity so that we can write Equations (3.17) and (3.18) in the form

$$\delta p = -\left[\left\{1 - \frac{\gamma p_0/c^2}{(\rho_0 + p_0/c^2)}\right\}\left\{S_1 \xi^r \frac{\partial p_0}{\partial r} + \sqrt{S_1}\frac{\xi^\theta}{r}\frac{\partial p_0}{\partial \theta}\right\}\right.$$

$$\left. + \gamma p_0 \left\{\frac{S_1}{r^2}\frac{\partial}{\partial r}(r^2 \xi^r) + \frac{\sqrt{S_1}}{r \sin\theta}\frac{\partial}{\partial \theta}(\sin\theta\, \xi^\theta)\right\}\right]\left[1 + \frac{\gamma p_0/c^2}{(\rho_0 + p_0/c^2)}\frac{V_0^2}{c^2}\right] \tag{3.20}$$

and

$$\delta\rho = -\left[\left(\rho_0 + \frac{p_0}{c^2}\right)\left\{\frac{S_1}{r^2}\frac{\partial}{\partial r}(r^2\,\xi^r) + \frac{\sqrt{S_1}}{r\sin\theta}\frac{\partial}{\partial\theta}(\sin\theta\,\xi^\theta)\right\}\right.$$
$$\left. - \frac{S_2}{c^2}\left(S_1\,\xi^r\frac{\partial p_0}{\partial r} + \sqrt{S_1}\,\frac{\xi^\theta}{r}\frac{\partial p_0}{\partial\theta}\right)\right]\left[1 + \frac{\gamma p_0/c^2}{(\rho_0 + p_0/c^2)}\,\frac{V_0^2}{c^2}\right], \tag{3.21}$$

and using these we obtain

$$\frac{m^2\sigma^2}{c^2}\int\int\frac{1}{S_2}(\rho_0 + p_0/c^2)\,(\xi^{r2} + \xi^{\theta 2})\,R^2\sin\theta\,\mathrm{d}R\,\mathrm{d}\theta$$
$$= \int\int\left[\frac{V_0^2/c^2}{(\rho_0 + p_0/c^2)}T_2^2 - 2S_1\,\xi^r\frac{\partial T_2}{\partial R} - \frac{2\sqrt{S_1}}{R}\,\xi^\theta\frac{\partial T_2}{\partial\theta} - \frac{4}{R^2}\,\xi^r\,T_2\right]R^2\sin\theta\,\mathrm{d}R\,\mathrm{d}\theta$$
$$+ \gamma\int\int\left[\left(\frac{2\sqrt{S_1}}{R}\right)\left(R\sqrt{S_1}\,\xi^r\frac{\partial}{\partial R} + \xi^\theta\frac{\partial}{\partial\theta}\right)\left(-T_1\frac{p_0}{c^2} + S_2\,S_3\,T_2\right)\right.$$
$$- \frac{4}{R^2}\,\xi^r\left(\frac{p_0}{c^2}T_1 - S_2\,S_3\,T_2\right) - 2S_2\,S_3\,[T_1\,T_2 - S_2\,T_2^2\,(\rho_0 + p_0/c^2)^{-1}]$$
$$\left. - S_3\left\{\left(\rho_0 + \frac{p_0}{c^2}\right)T_1^2 + S_2^2\,T_2^2\,(\rho_0 + p_0/c^2)^{-1} - 2S_2\,T_1\,T_2\right\}\right]R^2\sin\theta\,\mathrm{d}R\,\mathrm{d}\theta$$
$$+ \gamma^2\int\int\left[\left[-2S_1\xi^r\frac{\partial}{\partial R}(S_5T_1\,p_0/c^2) + 2S_1\xi^r\frac{\partial}{\partial R}(S_4^2T_2)\right.\right.$$
$$- \frac{2\sqrt{S_1}\xi^\theta}{R}\frac{\partial}{\partial\theta}(S_5\,T_1\,p_0/c^2) + \frac{2\sqrt{S_1}\,\xi^\theta}{R}\frac{\partial}{\partial\theta}(S_4^2\,T_2) + \frac{4}{R^2}\,\xi^r\left[\left(S_4^2\,T_2 - \frac{p_0}{c^2}\,T_1\,S_5\right)\right]$$
$$- 2\,S_1\,S_3\left\{S_5\,T_1\,T_2 - S_2\,S_5\,T_2^2\left(\rho_0 + \frac{p_0}{c^2}\right)^{-1}\right\}$$
$$+ S_3\,S_5\left\{\left(\rho_0 + \frac{p_0}{c^2}\right)T_1^2 + \left(\rho_0 + \frac{p_0}{c^2}\right)^{-1}S_2^2\,T_2^2 - 2\,S_2\,T_1\,T_2\right\}$$
$$\left. - S_3\left\{2\left(\rho_0 + \frac{p_0}{c^2}\right)S_5\,T_1^2 + \left(\rho_0 + \frac{p_0}{c^2}\right)^{-1}2\,S_2^2\,S_5\,T_2^2 - 4\,S_5\,S_2\,T_1\,T_2\right\}\right]$$
$$+ \gamma^3\left[-S_3\left\{\left(\rho_0 + \frac{p_0}{c^2}\right)S_5^2\,T_1^2 + \left(\rho_0 + \frac{p_0}{c^2}\right)^{-1}S_5^2\,S_2^2\,T_2^2 - 2\,S_5^2\,T_1\,T_2\,S_2\right\}\right.$$
$$\left. + S_3\,S_5\left\{2\left(\rho_0 + \frac{p_0}{c^2}\right)S_5\,T_1^2 + \left(\rho_0 + \frac{p_0}{c^2}\right)^{-1}2\,S_2^2\,S_5\,T_2^2 - 4\,S_5\,S_2\,T_1\,T_2\right\}\right]$$
$$+ \gamma^4\left[S_3\,S_5\left\{\left(\rho_0 + \frac{p_0}{c^2}\right)S_5^2\,T_1^2 + \left(\rho_0 + \frac{p_0}{c^2}\right)^{-1}S_5^2\,S_2^2\,T_2^2 - 2\,S_2\,S_5^2\,T_1\,T_2\right\}\right]\Bigg]$$
$$\times\,R^2\sin\theta\,\mathrm{d}R\,\mathrm{d}\theta, \tag{3.22}$$

wherein

$$S_3 = \frac{p_0}{c^2} \Big/ \left(\rho_0 + \frac{p_0}{c^2}\right), \quad S_5 = \frac{V_0}{c} S_4 = \frac{V_0^2}{c^2} S_3,$$

$$T_1 = \frac{S_1}{R^2} \frac{\partial}{\partial R} (R^2\ \xi^r) + \frac{\sqrt{S_1}}{R \sin\theta} \frac{\partial}{\partial \theta} (\sin\theta\ \xi^\theta),$$

$$T_2 = S_1\, \xi^r \frac{\partial p_0}{\partial R} + \sqrt{S_1}\, \frac{\xi^\theta}{R}\, \frac{\partial}{\partial \theta} \left(\frac{p_0}{c^2}\right). \tag{3.23}$$

We chosse a function q as

$$q = \frac{1}{\sin^2\theta} - \frac{R^2\,[B^2\,(1 - 2/R)^{-1} - 1]}{AB^2} \tag{3.24}$$

Which is zero at the boundary of the disk and the take

$$\xi^r = q + \alpha\, q^2, \quad \xi^\theta = q + \beta\, q^2\,, \tag{3.25}$$

wherein α and β are constants determined by extremising σ^2 as calculated by using these trial displacements in Equation (3.22). For such choice of ξ^r and ξ^θ we calculate critical value γ_c of the adiabatic index for the neutral stability.

Table 1 shows the values of γ_c for the onset of instability ($\gamma < \gamma_c$ for instability) for different values of 'a' and 'b' for general-relativistic as well as for the Newtonian case. It turns out that the coefficients of γ^2, γ^3 and γ^4 on the right-hand side of Equation (3.22) are very small as compared to the first two terms and therefore in the calculation of γ_c we can drop them out. The critical g for the Newtonian case is calculated by taking the limit $c \to \infty$, of Equations (3.17), (3.18) and (3.19). In this case we obtain

$$m^2\sigma^2 \int\int \rho_0\, [(\xi^r)^2 + (\xi^\theta)^2]\ R^2 \sin\theta\ \mathrm{d}R\ \mathrm{d}\theta$$

$$= -\int\int \left\{2\left(\xi^r \frac{\partial T_2}{\partial R} + \frac{\xi^\theta}{R}\, \frac{\partial T_2}{\partial \theta}\right) + \gamma\left[2\left(\xi^r \frac{\partial}{\partial R} + \frac{\xi^\theta}{R}\, \frac{\partial}{\partial \theta}\right)\left(\frac{p_0 T_1}{c^2}\right)\right.\right.$$

$$\left.\left. + \frac{p_0}{c_2}\, T_1^2\right]\right\} R^2 \sin\theta\ \mathrm{d}R\ \mathrm{d}\theta, \tag{3.26}$$

Table 1. Values of γ_c and $\theta_{e\,(\min)}$ for different choices of a and b.

		General relativistic		Newtonian	
a	b	γ_c	$\theta_{e\,(\min)}$	γ_c	$\theta_{e\,(\min)}$
8·1	100	0·7488	0·63	0·7107	0·55
7·1	100	0·7758	0·61	0·7420	0·52
6·1	100	0·8007	0·56	0·7732	0·48
5·1	100	0·8214	0·56	0·8043	0·44
4·1	100	0·8320	0·55	0·8356	0·40
4·1	140	0·8850	0·47	0·8726	0·33
4·1	180	0·9155	0·42	0·8936	0·30
4·05	180	0·9155	0·42	0·8948	0·30

where

$$T_1 = \frac{1}{R^2}\frac{\partial}{\partial R}(R^2\,\xi^r) + \frac{1}{R\sin\theta}\frac{\partial}{\partial\theta}(\sin\theta\,\xi^\theta)$$

$$T_2 = \left(\xi^r\frac{\partial}{\partial R} + \frac{\xi^\theta}{R}\frac{\partial}{\partial\theta}\right)(p_0/c^2), \tag{3.27}$$

with the steady state solutions as

$$\frac{V_0^2}{c^2} = \frac{A}{R^2\sin^2\theta} \quad ; \quad A = \frac{2ab}{(a+b)},$$

$$\frac{p_0}{c^2} = \rho_0\left[\frac{1}{R} - \frac{A}{2R^2\sin^2\theta} + B\right]; \quad B = -\frac{1}{(a+b)}. \tag{3.28}$$

We note that the σ^2 equation obtained here for the Newtonian case has a different form than that reported in Paper I. This is because of the different boundary conditions used for ξ^r and ξ^θ in the two sets of calculations.

As a special case we find that in case $p_0 = 0$, the disk collapses to $\theta = \frac{\pi}{2}$ plane, rotating with velocity

$$V_0 = \left[\frac{mc^2}{r}\left(1 - \frac{2m}{r}\right)^{-1}\right]^{1/2} \tag{3.29}$$

as may be seen from Equations (2.8) and (2.9) . Considering further the radial oscillations of such disk $\xi^\theta = 0$, $\xi^r \neq 0$ with $\delta p = 0$, we have

$$\delta V(\phi) = -\left[\left(1 - \frac{2m}{r}\right)\frac{\partial V_0}{\partial r} + \frac{1}{r}\left(1 - \frac{3m}{r}\right)V_0\right]\xi^r \tag{3.30}$$

$$\sigma^2\,\xi^r = \frac{2}{r}\left(1 - \frac{2m}{r}\right)V_0\,\delta V(\phi) \tag{3.31}$$

as the equations governing the radial perturbations appropriate to this case. Combining these, we get

$$\sigma^2 = \frac{mc^2}{r^4}(r - 6m) \tag{3.32}$$

which shows that such disks are stable for $r > 6m$.

4. Results and discussion

The steady-state parameters of velocity and pressure as a function of radial distance along the equatorial plane for a constant-density thick disk rotating around a Schwarzschild black hole is presented in Fig. 1 while Fig. 2 shows the meridional

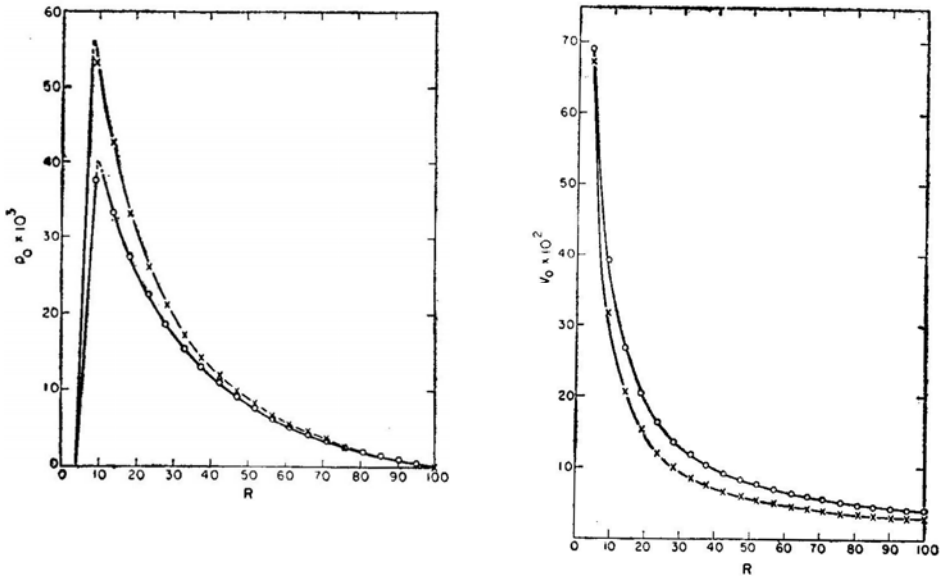

Figure 1. Profiles of pressure (left) and velocity (right) for relativistic (circles) and for Newtonian (crosses) disks along the equatorial plane α=4·1, b=100.

section of such a disk. The corresponding plots in the Newtonian formulation for the same values of inner and outer radii a and b (and for a constant density mode) are also shown in these figures. We find that for the same a and b the Newtonian disk occupies more volume than the relativistic one. It seems that the relativistic disks show a formation of cusp at the inner edge specially when it is near 4. For a Newtonian disk the pressure at any point is higher while the velocity at any point is lower at the equatorial plane, than in the case of a relativistic disk.

For the case of a relativistic disk we find a constraint that the inner edge cannot be less than 4*. Further, if $4 < a < 6$, then $b = 2a/(a - 4)$. For $a \geqslant 6$, any $b > a$ gives rise to a plausible disk. No such restriction appeared in the Newtonian formulation indicating a pure general-relativistic origin of the present constraint.

From the values of γ_c as tabulated in Table 1 we find that the disks considered here represent stable configurations ($\gamma_c < 4/3$). In calculating γ_c through Equation (3.22) we have used the approximation that $(V_0^2/c^2)\ (p_0/c^2)\ (\rho_0 + \rho_0/c^2)^{-1} \ll 1$, which is quite justified from the values of V_0/c and p_0/c as we obtained. There is a qualitative agreement between the γ_c calculated for relativistic and the corresponding Newtonian disks. In these two cases, although the inner and outer radii a and b are the same, the regions occupied by the disk in the two cases are not the same. In general, Newtonian disks are thicker [minimum angular elevation= $\pi - 2\theta_e$ (min)]. We also find from the numbers that γ_c depends upon the size of the disk. In the calculation of γ_c, the effects due to general relativistic convections and that due to the difference in sizes contribute simultaneously and therefore the agreement between the general relativistic γ_c and the Newtonian γ_c is no better than a qualitative one.

* The fact that the inner edge r_α of the disk should always be greater than $4m$ is consistent with the general proof given by Kozlowsky, Jaroszynski and Abramowicz (1978) that $R_i \geqslant R_{mb}$ for the marginally bound orbit.

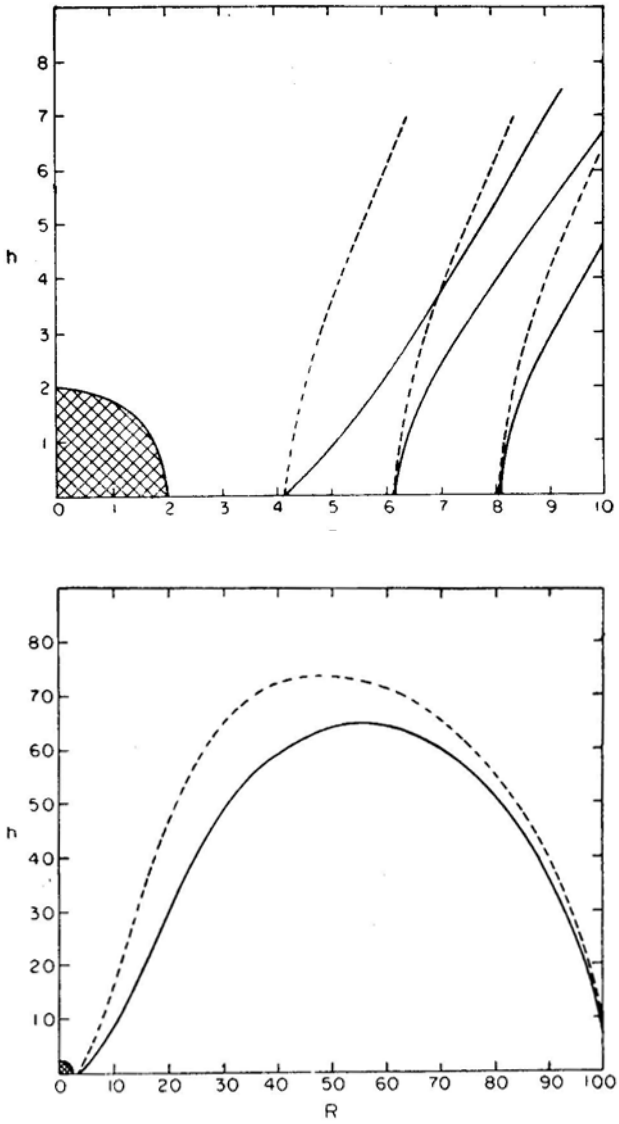

Figure 2. Meridional section of the disk in general relativistic (solid curves) and of corresponding Newtonian case (dashed curves). Top: Various choices of a, b = 100; inner portion of the disk Bottom: $a = 4{\cdot}1$, $b = 100$.

It does not seem to be possible to identify separately the contributions from general relativity, in the present formulation.

Starting from the general equations, if we take $p_0 = 0$, we found that the disk collapses on to $\theta = \pi/2$ plane and is stable under radial perturbation only if the inner edge is beyond $6m$ as its local frequency is $[mc^2 (r - 6m)/r^4]^{1/2}$. Now, since a pressureless fluid is essentially an aggregate of non-interacting particles, the above conclusion can be regarded as an alternative derivation of the well-known result that the last stable circular orbit for Schwarzschild geometry is at $6m$.

The general conclusion that the perfect-fluid thick disk rotating around Schwarzschild black hole is generally stable under axisymmetric perturbation, at least when the density is constant (or a function of r when considered in Newtonian framework) may have important significance in the study of the models of accretion disks developed for explaining the radiation from high-energy sources.

Acknowledgement

One of us (DKC) would like to thank UGC for the award of Teacher Fellowship and Director, PRL, for the hospitality during his stay at Ahmedabad.

References

Chakraborty, D. K., Prasanna, A. R. 1981, *J. Astrophys. Astr.*, **2,** 421 (Paper II).
Chandrasekhar, S., Friedman, J. L. 1972a, *Astrophys. J.*, **175,** 379.
Chandrasekhar, S., Friedman, J. L. 1972b, *Astrophys. J.*, **176,** 745.
Kozlowsky, M., Jaroszynski, M., Abramowicz, M.A. 1978, *Astr. Astrophys.*, **63,** 209.
Lightman, A. P., Shapiro, S. L., Rees, M. J. 1978, in *Physics and Astrophysics of Neutron Stars and Black Holes*, Eds R. Giacconi and R. Ruffini, North Holland, Amsterdam, p. 786.
Novikov, I. D., Thorne, K. S. 1973, in *Les Houches: Black Holes*, Eds C. DeWitt and B. S. DeWitt, Gordon and Breach, New York.
Paczynski, B. 1980, *Acta Astr.*, **30.4,** 347.
Prasanna, A. R., Chakraborty, D. K. 1981, *J. Astrophys. Astr.*, **2,** 1 (Paper I).
Pringle, J. E., Rees, M. J. 1972, *Astr. Astrophys.*, **21,** 1.
Shakura, N. I., Sunyaev, R. A. 1973, *Astr. Astrophys.*, **24,** 337.
Shakura, N. I., Sunyaev, R. A. 1976, *Mon. Not. R. astr. Soc.*, **175,** 613.

J. Astrophys. Astr. (1982) **3,** 207–216

Observations of the Supernova Remnants HB 9 and 1C 443 at 34·5MHz

K. S. Dwarakanath, R. K. Shevgaonkar and Ch. V. Sastry
Raman Research Institute, Bangalore 560080 and Indian Institute of Astrophysics, Bangalore 560034

Received 1982 February 1; accepted 1982 June 30

Abstract. We have observed the extended supernova remnants HB 9 (G 160·5 + 2·8) and IC 443 (G 189·1 + 2·9) at 34·5 MHz with a resolution of 26 arcmin × 40 arcmin. A map of HB 9 is presented. The integrated flux density of HB 9 at 34·5 MHz is 750 ± 150 Jy. The spectral index in the frequency range from 34·5 MHz to 2700 MHz is found to be constant (– 0·58 ± 0·06) without any spectral break such as was reported earlier by Willis (1973). There is no significant variation of the spectral index across the remnant. The integrated flux density of IC 443 at 34·5 MHz is 440 ± 88 Jy. The spectral index in the frequency range from 20 MHz to 10700 MHz is – 0·36 ± 0·04. The reduction in flux at very low frequencies (10 MHz) is attributable to free-free absorption in the interstellar medium and/or in the H II region S 249.

Key words: supernova remnants—spectral break—free-free absorption

1. Introduction

Extensive observations of supernova remnants (SNRs) exist at high radio frequencies, and have provided significant information on the origin of the radio emission and the evolution of SNRs. It is important to extend these observations of SNRs to low frequencies from several points of view. Low-frequency observations will give information not only on the structure of the sources themselves, but also on the intervening medium. One can investigate the changes in the continuum spectrum caused by the effects that are intrinsic to the SNRs such as changes in the relativistic electron spectrum, while turnovers in the low-frequency spectra can also give information about physical conditions in the medium causing the absorption. It may also be possible to derive information about the interaction of the SNRs with their immediate surroundings.

We have recently initiated a programme of observations of extended SNRs at 34·5 MHz. Our observations of the Cygnus Loop have already been published (Sastry, Dwarakanath and Shevgaonkar 1981). The present paper deals with the results of

observations of the two SNRs HB 9 (G 160·5 + 2·8) and IC 443 (G 189·1 + 2·9). The SNR HB 9 is believed to be at a distance of 1·8 kpc (Caswell and Lerche 1979) and its angular extent is about 2°·5 (Kallas and Reich 1980). Its optical counterpart is a faint nebulosity marking the periphery of the remnant. Soft X-ray observations of the nebula by Tuohy, Clark and Garmire (1979) indicate an age of nearly 15,000 yr

IC 443 is a shell-type SNR with the optical counterpart similar to the radio shell. It is thought to be at a distance of 1·5 kpc (Duin and van der Laan 1975). X-ray observations by Parkes *et al.* (1977) indicate an age of approximately 12,700 yr for this remnant.

2. Equipment and observations

The observations reported here were made with the low-frequency radio telescope at Gauribidanur (Longitude 77° 26′ 07″ E and Latitude 13° 36′ 12″ N). The telescope can be operated in the frequency range 25 to 35 MHz. The antenna system of the telescope consists of two broadband arrays arranged in the form of a 'T'. The half-power beamwidths at 34·5 MHz are 26 arcmin and 40 sec(δ – 14·1) arcmin. in the east-west and north-south directions respectively. The collecting area is approximately 250 λ^2. The telescope is of the transit type and using remotely-controlled diode phase shifters, the beam can be pointed anywhere along the meridian in the zenith angle range ± 45°. A time-multiplexing system is used to cycle the beam through eight different declinations sequentially, the beam being changed from one direction to another in a few milliseconds. The receiving system extracts the in-phase (cos) and the quadrature (sin) correlations between the two arms for each one of the eight beam positions. Pre-detection bandwidths of 30 and 200 kHz and post-detection time constants ranging from 1 to 30 s are available. The output of the receiving system is recorded in both analog and digital forms. Full details of the telescope will be published elsewhere.

The observations of HB 9 were made with a 200 kHz bandwidth and a 10 s time constant. Drift scans were taken in R. A. from $4^h\ 20^m$ to $5^h\ 20^m$, in the declination range from + 43° to + 49° in steps of 24 arcmin. Thus the region of HB 9 could be covered once in two days. Each scan was calibrated using the apparent source due to the combined emission from 3C 129 and 3C 129·1. To minimise ionospheric effects such as refraction, absorption and scintillation, and also interference due to terrestrial broadcasts, repeated scans were taken over many days and checked for consistency. Using the calibrated scans, a raw map of HB 9 was constructed. The map thus obtained was CLEANed to eliminate sidelobe effects and the 'CLEAN' components were convolved with a gaussian beam to obtain the final map.

In the case of IC 443 drift scans were taken in R.A. from 6^h to $6^h\ 30^m$, in the declination range + 21° to + 23°. The rest of the procedure was as described above excepting that 3C 192 was used as the calibration source.

3. Results and discussion

HB 9

The map of HB 9 at 34·5 MHz is presented in Fig. 1. The notable features of the map are: (1) the elongation in the northern direction around 5^h R. A. and (2) the

strong region in the centre of the map at 4^h 54^m R.A. and 46° 06' in Dec. (The double source 3C 129 + 3C 129·1 is seen towards the south-west of HB 9). The only other low-frequency map of this nebula is that due to Williams, Kenderdine and Baldwin (1966) at 38 MHz with a resolution of 45 arcmin. The peak of emission seen on the 38 MHz map coincides with the intense peak of HB 9 in our map. In the

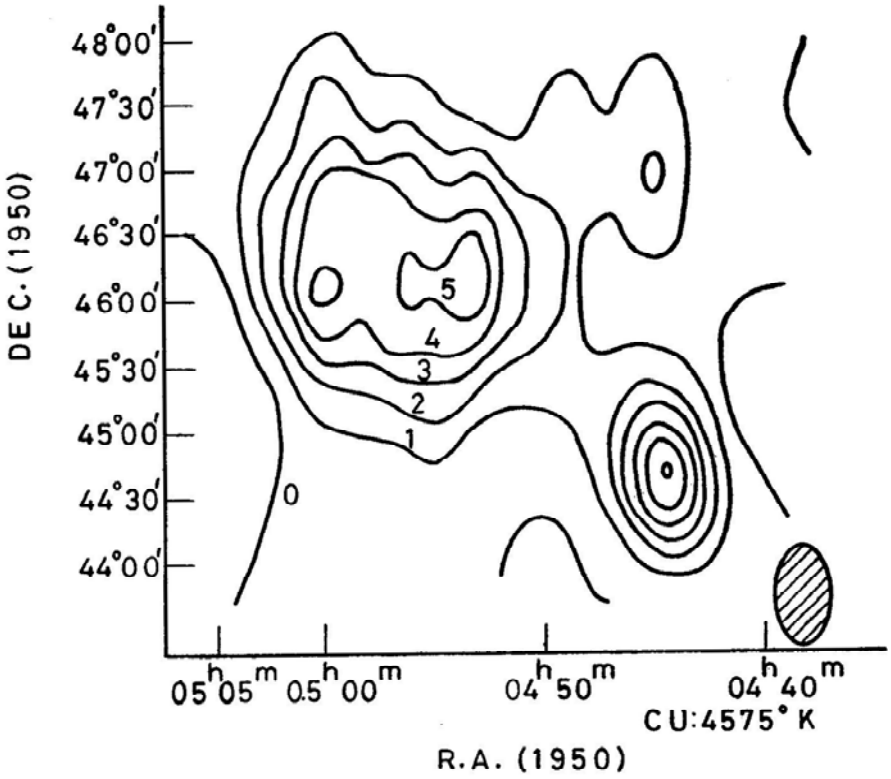

Figure 1. HB 9 at 34.5 MHz. The half-power beam is shown at the bottom right-hand corner.

map of Dickel and McKinley (1969) at 610 MHz, observed with 16 arcmin resolution, there are intense emission features extended in R.A. which are not present in our map. These features are also not present in the 2·7 GHz map of Willis (1973) which has a resolution of 10 arcmin. We believe the ridge of emission extending in the northerly direction to be real since it also appears in the 1·4 GHz map of Felli and Churchwell (1972), Willis (1973), and Kallas and Reich (1980). We have convolved the 21-cm Effelsberg map of Kallas and Reich (1980) to our beam and found that the convolved map agrees quite well in appearance and position with our map within the errors of observation. It therefore appears that the structure of the source remains similar over the frequency range from 34·5 MHz to 1·4 GHz. We have integrated over our map from 4^h 48^m to 5^h 04^m in R.A. and 44° 54' to 47° 54' in Dec. to obtain the integrated flux density. The double source (3C 129 + 3C 129·1) which is very near to HB 9 both in R.A. and Dec. was used as a calibrator. The flux density of (3C 129 + 3C 129·1) at 34·5 MHz is 190 Jy according to Kellerman, Pauliny-Toth and Williams (1969). The correction to the above flux density to bring it to the

absolute scale of Baars *et al.* (1977) is only two per cent. Willis (1973) listed four point sources at 2·7 GHz, all presumably extragalactic, in the field of HB 9. Their total contribution at 34·5 MHz is 60 Jy if the spectral index ($S \propto \nu^{\alpha}$) is – 0·8 between 34·5 MHz and 2·7 GHz. The integrated flux density of HB 9 at 34·5 MHz, after correcting for the contribution of the point sources mentioned above, is 750 ± 150 Jy.

The spectrum of the integrated flux density of HB 9 was investigated previously by Bazelyan, Braude and Meg' (1967) and by Willis (1973). Bazelyan, Braude and Meg' conclude that the spectral index in the frequency range from 40 to 160 MHz is – 1·3 while for frequencies above 160 MHz it is – 0·44. Willis used all the available data in the frequency range from 10 MHz to 2·7 GHz, except the values of Bazelyan, Braude and Meg'. According to Willis, the spectrum shows a break around 1000 MHz with the values of spectral index being — 0·44 below, and – 1·1 above, 1000 MHz. The flux densities measured by Bazelyan, Braude and Meg' are very high compared to the general trend, and further they did not map the region. We therefore omit all their values in further analysis. The values of flux densities, at various frequencies, used by Willis (1973) do not conform to any common scale and we have made an attempt to bring all values to the scale defined by Baars *et al.* (1977). Table 1 shows

Table 1. Spectrum of HB 9.

Frequency (MHz)	Flux* (Jy)	Flux† (Jy)	Reference
10·03[1]	600[4]		Caswell (1976)
13[1]	810 ± 140		Andrew (1967)
34·5[6]		750 ± 150	present value
38[2]	550 ± 110	700 ± 70	Williams, Kenderdine and Baldwin (1966) Haslam and Salter (1971)
92[1]	395 ± 150		Hazard and Walsh (1960) Haslam and Salter (1971)
158·5[1]	80		Brown and Hazard (1953)
178	250 ± 50	300 ± 60	Bennett (1964); 19 per cent correction‡
408	190 ± 40	202 ± 43	Haslam and Salter (1971); 6·5 per cent correction‡
610·5	157 ± 26	164 ± 27	Dickel and McKinley (1969); 5 per cent correction‡
960	160 ± 30	165 ± 31	Harris (1962); 3 per cent correction‡
1420[3]	84 ± 6	84 ± 6	Reich (personal communication)
1660	80 ± 20	82 ± 21	Willis (1973); 3 per cent correction‡
2700	47 ± 9	48 ± 9	Willis (1973); 1·1 per cent correction‡
5000[5]	36 ± 8		DeNoyer (1974)

* Flux quoted in the reference cited.

† Flux (on the scale defined by Baars *et al.* 1977) used to obtain the spectrum of HB 9 (Fig. 2).

‡Percentage corrections indicate the amounts by which the quoted flux values were increased to bring them to the scale defined by Baars *et al.* (1977).

[1] Large beam ($\gtrsim 2$). Region of HB 9 not well defined. Confusion from 3C 129 + 3C 129·1.

[2]Integration of the 38 MHz map of Williams, Kenderdine and Baldwin (1966) over the region of our 34·5 MHz map. The 18th contour (= 15,066K) in the map published by Williams, Kenderdine and Baldwin (1966) has been taken as the baseline level.

[3]See Kallas and Reich (1980) for a map of HB 9 at 1420 MHz.

[4]Bridle and Purton (1968) quote 800 ± 200 Jy for HB 9 at 10·03 MHz. Their value also suffers from the drawbacks mentionedin Note (1). Hoewever, it is tobenoted thatthey quote 270±55Jy for 3C 129 while the value expected on the basis of constant spectral index is 574 Jy (Kellermann, Pauliny-Toth and Williams (1969). Incorporating this factor, flux of HB 9 would be 1700 Jy which is very close to the value expected from the spectrum indicated in this paper.

[5]Calibration scale used by these authors is not clear..

[6]Since the observations were made in the correlation mode of the telescope, there is no ambiguity of the baseline here; The telescope does not respond to zero-order spatial frequency.

the values after renormalization, together with those quoted in the original papers. The reasons for discarding some values are indicated at the end of the table. Original references are cited against each frequency. Using the values given in Table 1 the spectral index of HB 9 has been computed. The spectrum is consistent with a power law over the whole frequency range from 34·5 MHz to 2·7 GHz and the spectral index is — 0·58 ± 0·06. The spectrum is shown in Fig. 2.

A spectral index map of HB 9 was made by comparing our 34·5 MHz map and the 1·4 GHz Effelsberg map of Kallas and Reich (1980) convolved to the same beam. This spectral index map is shown in Fig. 3. It can be seen that the spectral index is constant over the major portion of the source within the limits defined by the 1·4 GHz map.

The poor resolution of our map precludes a detailed comparison of the optical and radio emission from HB 9. Nevertheless, it should be pointed out that an optical feature extends northwards (Willis 1973), at the position where the radio contours also show elongation in the same direction as seen in our map. The optical surface brightness is greater in the southern parts of the nebula where the radio emission is also comparatively strong as, for example, seen in the 21-cm Effelsberg map. As already pointed out, the radio structure and the spectral index remain relatively constant throughout the nebula in the frequency range from 34·5 MHz to 1400 MHz. This implies that there is no significant thermal emission from any part of the nebula. Also, the relativistic electron energy spectrum appears not to change in different parts of the remnant.

1C 443

The shell structure of this SNR is unresolved by our beam. Our map shows peak emission at the position of $6^h\ 14^m\ 30^s$ in R.A. and 22° 36’ in Dec. The observed

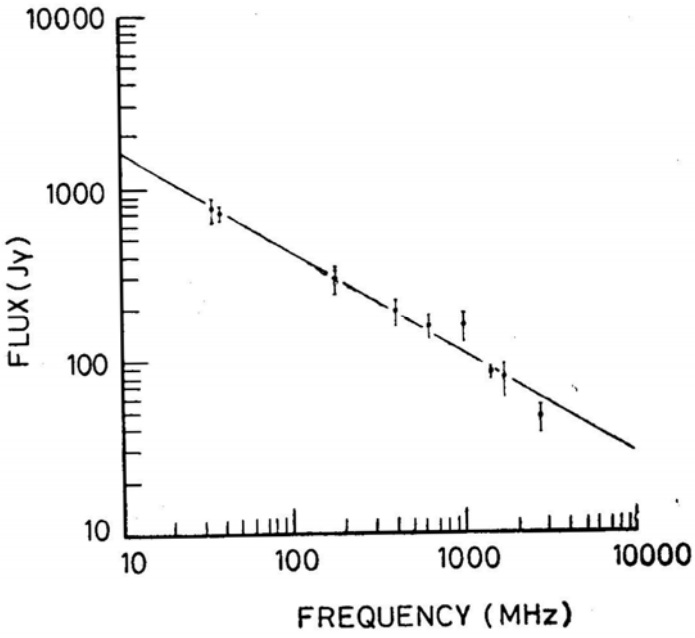

Figure 2. Integrated flux-density spectrum of HB 9.

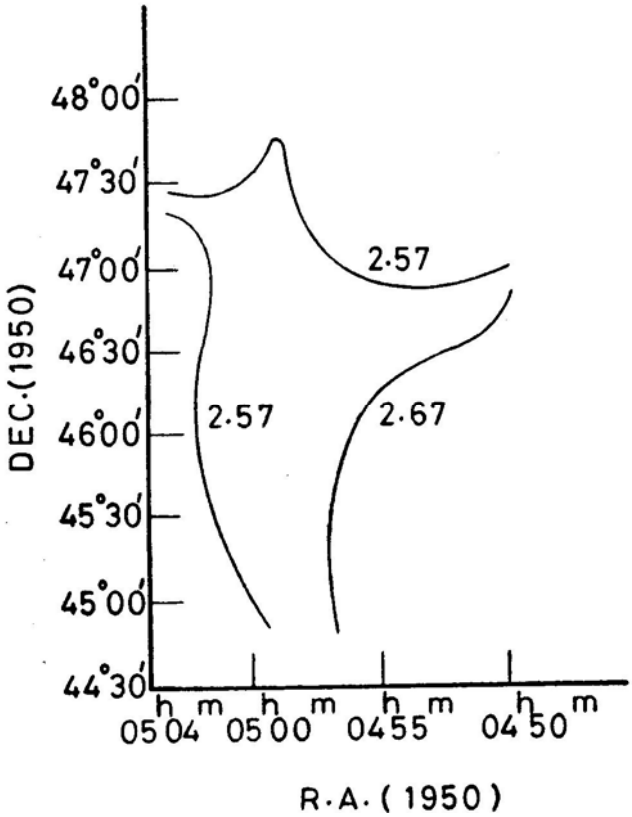

Figure 3. Spectral-index map of HB 9. Only significant contours are plotted. Numbers ($-\beta$) near each contour indicate temperature spectral indices ($T \propto \nu^{+\beta}$, where $\beta = \alpha - 2$).

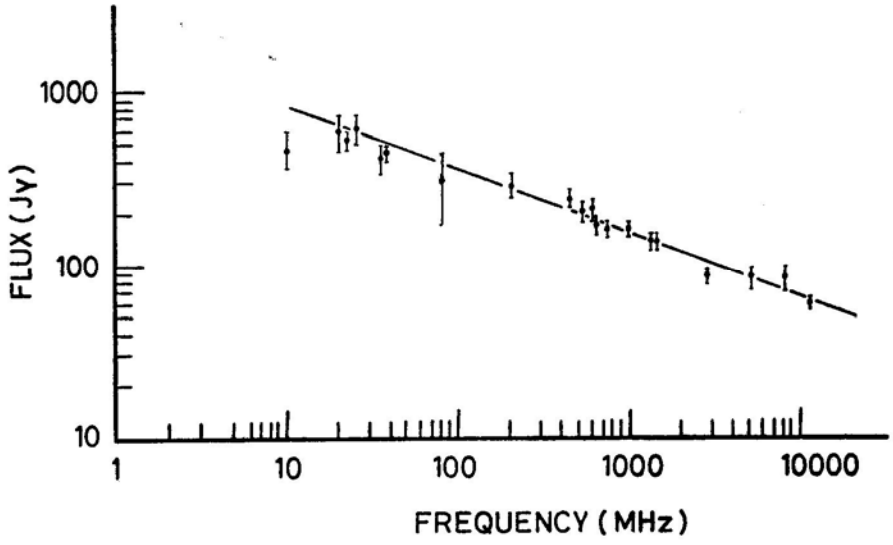

Figure 4. Integrated flux-density spectrum of IC 443.

half-power widths of the source in R.A. and Dec. are 29 arcmin and 43 arcmin respectively. We have convolved the 21-cm map of Duin and van der Laan (1975) to our beam and found that the position of the peak emission and the widths are approximately the same as those observed by us. The integrated flux density of IC 443 has been estimated using 3C 192 as a calibrator. The flux density of 3C 192 at 34·5 MHz is assumed to be 85 Jy on the KPW scale (Kellermann, Pauliny-Toth and Williams 1969). The measured integrated flux density of IC 443 at 34·5 MHz is 440 ± 88 Jy. In Table 2 we have listed all the flux densities of IC 443 used for the purpose of obtaining the spectral index in the frequency range from 10 MHz to 10·7 GHz, along with the references. Some of these values were however discarded for the reasons indicated (see notes under Table 2). The spectral index computed between 20 MHz and 10700 MHz is – 0·36 ± 0·04.

Table 2. Spectrum of IC 443.

Frequency (MHz)	Flux† (Jy)	Reference
10·03	480 ± 120	Bridle and Purton (1968); Caswell (1976)
20	600* ± 144	Braude *et al.* (1969)
22·25	535* ± 65	Roger, Costain and Lacey (1969)
25	630* ± 132	Braude *et al.* (1969)
26·3[2]	263 ± 23	Viner and Erickson (1975)
34·5	440* ± 88	present value
38	460* ± 46	Williams, Kenderdine and Baldwin (1966)
80	315* ± 150	Dickel (1973)
195	290 ± 45	Kundu and Velusamy (1968)
430	245 ± 30	Kundu and Velusamy (1968)
513	205 ± 27	Bondar *et al.* (1965)
610	215 ± 32	Dickel and McKinley (1969)
635	173* ± 17	Milne and Hill (1969)
740	164 ± 15	Bondar *et al.* (1965)
750[1]	190 ± 25	Hogg (1964)
960	165 ± 10	Bondar *et al.* (1965)
1400[1]	170 ± 20	Hogg (1964)
1410	131* ± 13	Milne and Hill (1969)
1420	138 ± 15	Hill (1972)
2700	88* ± 9	Milne and Hill (1969)
3000[1]	100^{+5}_{-15}	Hogg (1964)
5000	85 ± 13	Kundu and Velusamy (1969)
8000	85 ± 17	Howard and Dickel (1963)
9400[2]	16 ± 4	Yamashita and Watanabe (1968)
10700	60 ± 5	Kundu and Velusamy (1972)

† Since most of the authors have not explicitly stated the flux value(s) assumed for the calibrator(s) used, all flux values are quoted here as stated by the respective authors. However, the spectral index obtained between 20 MHz and 2700 MHz using only those flux values (marked with an asterisk) which could be brought to the scale of Baars *et al.* (1977) agrees within the error limits with the spectral index obtained using all the values.

[1] The value of flux quoted by Hogg appear to be consistently higher. Since it is not clear what calibration is adopted by Hogg, these values have not been considered in obtaining the spectrum.

[2] These values are lower than those indicated by the general trend by factors of about 2·5 and 4. They have not been used in obtaining the spectrum.

Note, however, that flux measurements of IC 443 made around 1960 and earlier have not been considered in preference to recent well-calibrated measurements made near the corresponding frequencies. See, Milne and Hill (1969) and references therein.

The expected flux density at 10 MHz on the basis of this spectrum is 820 Jy whereas the flux density observed by Bridle and Purton (1968) is 480 ± 120 Jy. (The flux density quoted by these authors is 400 ± 100 Jy. A 20 per cent increase in flux density to bring it to the KPW scale has been adopted as suggested by Roger, Bridle and Costain 1973). This reduction in flux is probably not due to absorption by regions within the source since in this case the turnover in the spectrum would be more gradual. The optical depth required to reduce the 10 MHz flux from 820 Jy to 480 Jy is about 0·5 if the absorption is external to the source. In this case it could be due to (1) the interstellar medium (ISM) and/or (2) one or more ionized hydrogen regions (H II regions) along the line of sight.

Assuming the picture of the ISM put forward by McKee and Ostriker (1977) it is easy to see that almost the entire free-free absorption in the ISM will be caused by the cold neutral medium (electron density, n_e = 0.042, electron temperature, T_e = 80 K, filling factor, f = 0·024) and the warm ionized medium (n_e = 0·17, T_e = 8000 K, f= 0·23). Assuming the distance to IC 443 to be 1·5 kpc, we obtain an optical depth of 0·3 at 10 MHz for the values of n_e, T_e and f assumed above. With the uncertainties inherent in these parameters the difference in the observed and calculated optical depths is not really significant.

We now explore the second possibility that H II regions are responsible for the observed absorption. For a kinetic temperature of 10^4 K, the necessary emission measure of an H II region to produce the required optical depth has to be about 100 pc cm^{-6}. Close to IC 443, in the north-eastern direction, lies the faint H II region S 249. Churchwell and Walmsley (1973) derived an emission measure of 750 pc cm^{-6} for it, assuming a kinetic temperature of 10^4 K. Therefore the absorption along the central line of sight to S 249 should be 6–7 times more than required. However, as the optical position of S 249 is about a degree away from IC 443, it is possible that the line of sight to IC 443 passes only through the outer layers of this H_{II} region. This would be consistent with the derived smaller optical depth. Churchwell and Walmsley (1973) also mention the possibility that S 249 may be a 'fossil Strömgren sphere' with a very low kinetic temperature of 100 K and an emsision measure of 150 pc cm^{-6}. If so, the expected absorption due to this object would be about 100 times more than if it were a normal H II region. The observed absorption would then put an upper limit to the extension of this 'fossil Strömgren sphere'. Assuming the position of the centre of the sphere as that of the quoted optical position (α = 6^h 17^m 54^s, δ = 23° 06', Churchwell and Walmsley 1973), the diameter of the 'fossil Strömgren sphere' is unlikely to be more than about 80 arcmin (note that the major portion of the flux from IC 443 comes from the north-eastern region of the remnant).

It is worth mentioning here, that Georgelin, Georgelin and Roux (1973) suggest an 09 V star (distance 1·9 kpc) to be the exciting star of S 249 and if this is the case the nebula need not be a ' fossil Strömgren sphere'.

4. Conclusions

HB 9

1. The structure of the supernova remnant is essentially the same in the frequency

range from 34·5 MHz to 1420 MHz and there is no significant variation of spectral index across the remnant.

2. The spectrum is straight between 34·5 MHz and 2700 MHz with an index of – 0·58 ± 0·06. No evidence is found for the spectral break suggested by Willis (1973).

1C 443

1. The spectrum is straight with an index of — 0·36 ± 0·04 in the frequency range from 20 MHz to 10700 MHz. At very low frequencies (10 MHz) there is a reduction in the flux which is believed to be due to absorption in the interstellar medium and/or in the H II region S 249.
2. If S 249 were to be a 'fossil Strömgren sphere' its diameter is unlikely to be more than 80 arcmin.

Acknowledgements

We are grateful to M.K.V. Bappu for his interest and continued support of the low frequency radio astronomy project at Gauribidanur, and to V. Radhakrishnan for useful discussions. We thank C. J. Salter for his valuable suggestions and help during the analysis, and R. Narayan and R. Nityananda for discussions and advice regarding the application of CLEAN to our data. W. Reich is thanked for communication of his 1420 MHz flux density.

References

Andrew, B. H. 1967, *Astrophys. J.,* **147,** 423.
Baars, J. W. M., Genzel, R., Pauliny-Toth, I. I. K., Witzel, A. 1977, *Astr. Astrophys.,* **61,**99.
Bazelyan, L. L., Braude, S. Ya., Meg', A. V. 1967, *Sov. Astr.,* **10,** 588.
Bennett, A. S. 1964, *Mon. Not. R. astr. Soc.,* **127,** 3.
Bondar, L. N., Krotikov, V. D., Stankevich, K. S., Tseitlin, N. M. 1965, *Izv. Vuz Radiofiz.* **8,** 437
Braude, S. Ya., Lebedeva, O. M., Megn, A. V., Ryabov, B. P., Zhouck, I. N. 1969, *Mon. Not. R. astr. Soc.,* **143,**289.
Bridle, A. H., Purton, C. R. 1968, *Astr. J.,* **73,** 717.
Brown, R. H., Hazard, C. 1953, *Mon. Not. R. astr. Soc.,* **113,** 123.
Caswell, J. L. 1976, *Mon. Not. R. astr. Soc.,* **177,** 601.
Caswell, J. L., Lerche, I. 1979, *Mon. Not. R. astr. Soc.,* **187,** 201.
Churchwell, E., Walmsley, C. M. 1973, *Astr. Astrophys.,* **23,** 117.
DeNoyer, L. K. 1974, *Astr. J.,* **79**, 1253.
Dickel, J. R. 1973, *Aust. J. Phys.,* **26,** 369.
Dickel, J. R., McKinley, R. R. 1969, *Astrophys. J.,* **155,** 67.
Duin, R. M., van der Laan, H. 1975, *Astr. Astrophys.,* **40,** 111.
Felli, M., Churchwell, E. 1972, *Astr. Astrophys. Suppl. Ser.,* **5,** 369.
Georgelin, Y. M., Georgelin, Y. P., Roux, S. 1973, *Astr. Astrophys.,* **25,** 337.
Harris, D. E. 1962, *Astrophys. J.,* **135,** 661.
Haslam, C. G. T., Salter, C. J. 1971, *Mon. Not. R. astr. Soc.,* **151,** 385.
Hazard, C., Walsh, D. 1960, *Jodrell Bank Ann.,* **1,** 338.
Hill, I. E. 1972, *Mon. Not. R. astr. Soc.,* **157,** 419.
Hogg, D. E. 1964, *Astrophys. J.,* **140,** 992.

Howard, W. E. III, Dickel, H. R. 1963, *Publ. astr. Soc. Pacific,* **75,** 149.
Kallas, E., Reich, W. 1980, *Astr. Astrophys. Suppl. Ser.,* **42,** 227.
Kellermann, K. L, PaulinyToth, I. I. K., Williams, P. J. S. 1969, *Astrophys. J.*, **157,** 1.
Kundu, M. R., Velusamy, T. 1968, *Mon. Not. R. astr. Soc*., **140,** 173.
Kundu, M. R., Velusamy, T. 1969, *Astrophys. J.,* **155,** 807.
Kundu, M. R., Velusamy, T. 1972, *Astr. Astrophys.,* **20,** 237.
McKee, C. F., Ostriker, J. P. 1977, *Astrophys. J.,* **218,** 148.
Milne, D. K., Hill, E. R. 1969, *Aust. J. Phys.,* **22,** 211.
Parkes, G. E., Charles, P. A., Culhane, J. L., Ives, J. C. 1977, *Mon. Not. R. astr. Soc*., **179,** 55.
Roger, R. S., Bridle, A. H., Costain, C. H. 1973, *Astr. J.,* **78,** 1030.
Roger, R. S., Costain, C. H., Lacey, J. D. 1969, *Astr. J.,* **74,** 366.
Sastry, Ch. V., Dwarakanath, K. S., Shevgaonkar, R. K., 1981, *J. Astrophys. Astr.,* **2,** 339.
Tuohy, I. R., Clark D. H., Garmire, G. P. 1979, *Mon. Not. R. astr. So*c., **189,** 59p.
Viner, M. R., Erickson, W. C. 1975, *Astr. J.,* **80,** 931.
Williams, P. J. S., Kenderdine, S., Baldwin, J. E. 1966, *Mem. R. astr. So*c., **70,** 53.
Willis, A. G. 1973, *Astr. Astrophys.,* **16,** 237.
Yamashita, T., Watanabe, T. 1968, *Proc. Res. Inst. Atmos. Nagoya Univ.,* **15,** 75.

M. K. Vainu Bappu
(1927–1982)

It was with profound sorrow that the news of the sudden demise of Professor Vainu Bappu on August 19, 1982 was received by the astronomical world and by all others who knew him. Professor Bappu, President of the International Astronomical Union, Director of the Indian Institute of Astrophysics and Chairman of the Editorial Board of the *Journal of Astrophysics and Astronomy* passed away due to complications following heart surgery while on an assignment at the European Southern Observatory in Munich. In the brief span of fifty-five years, he made enormous contributions to the furtherance of astrophysics not only in India, but internationally as well.

Manali Kallat Vainu Bappu was born on August 10, 1927, the only son of M. K. Bappu, who was employed at the Nizamia Observatory, Hyderabad. He graduated from Nizamia College, Hyderabad in 1946, from where he also obtained his Master's degree in physics in 1949. His research contributions started right during this period, and his first papers on visual observations of variable stars were published in 1946 in Volume 15 of *Current Science.* He also obtained at this young age of nineteen, spectra of the night sky requiring exposures of several nights, using a spectrograph of his own design.

After obtaining his Master's degree, Vainu Bappu earned a state scholarship for higher studies in astrophysics at Harvard University. Harvard was at its prime then, Harlow Shapley at its helm, and stalwarts like Donald Menzel, Bart Bok, Cecilia Payne-Gaposchkin and Fred Whipple among its staff. Within months of joining Harvard, Bappu discovered a comet on one of the celestial photographs he had obtained. More than the discovery itself, his achievement was in computing its orbit immediately, ahead of more experienced professionals. The Bappu-Bok-Newkirk comet earned him the Donohoe comet medal of the Astronomical Society of the Pacific in 1949. Bappu continued to observe variable stars and also studied the influence of solar activity on the night sky, while he was working for his Master's degree in astronomy.

Vainu Bappu submitted his thesis on spectroscopic studies of Wolf-Rayet stars under the supervision of Bart Bok and obtained his doctoral degree in 1952. He then spent a year at Mount Wilson and Palomar Observatories as a Carnegie Post-Doctoral Fellow. This gave him an opportunity to obtain high-resolution coudé spectra of Wolf-Rayet and late-type stars with the 100-inch telescope. The Wilson-Bappu effect, published in detail in 1957, was based on these excellent spectra. Apart from serving as a new luminosity indicator, the Wilson-Bappu effect gave an impetus to the study of stellar chromospheres. Bappu continued to enrich the understanding of this field, and one of his last contributions, a collaborative effort with Y. Uchida, appears in this issue of the Journal.

The 1950s were the times when astrophysics was fast developing in the United States. But Bappu's ambition however was to foster astronomy in his own country and to create facilities for astrophysical research for future generations. He returned to India and pursued laboratory spectroscopy waiting for a suitable opportunity which presented itself in 1954, when he was appointed the Director of the U.P. State Observatory, Benares. He found soon that the dusty plains of Benares were ill-suited for astronomical observations, and a few months later, he shifted the observatory to Naini Tal at the foot of the Himalayas, where the clearest skies prevailed in winter. For the next few years, he instrumented the small telescopes available at

the Observatory and utilized them in developing H-gamma photometry for an absolute magnitude calibration of early-type stars, in addition to making observations of Mars, the polarization of comets and continuing his favourite study of Wolf-Rayet stars. He also led an expedition to observe the total solar eclipse of 1955 in Sri Lanka, to be followed by several other such expeditions over the years.

In 1960, Vainu Bappu was offered the directorship of the solar observatory of Kodaikanal, an institution which had a history dating back to the Madras Observatory founded in 1792. Its list of past directors included the illustrious names of N. R. Pogson and J. Evershed. It was at Kodaikanal that Bappu's dream of a full-fledged astrophysical institute and observatory began to take shape. He constructed a 40-cm reflector telescope at the workshop of the Observatory. Realising that the skies of Kodaikanal were not suitable for prolonged stellar exposures over a substantial portion of the year, he looked for and found a more appropriate site. Thus the Kavalur Observatory came into existence in the semi-arid region of Javadi Hills in Tamil Nadu. The 1-m Carl Zeiss telescope was commissioned here in early 1972, within a year of the creation of the Indian Institute of Astrophysics.

Subsequent years were spent in equipping the Kavalur Observatory with instruments mainly designed by him and constructed at the laboratories of the Institute, collaborating with the Raman Research Institute in setting up the low-frequency radio array at Gauribidanur, creating computing facilities for theoretical astrophysics, constructing a 75-cm telescope at the workshops of the Institute, and finally in planning and launching the construction of a 2·34-m telescope scheduled for operation by 1983. It was in this period that Bappu's organizational ability and vision in planning were demonstrated best. Professor S. Chandrasekhar, who visited the Indian Institute of Astrophysics recently, and who had also visited Kodaikanal Observatory at the beginning of Bappu's era, exclaimed that it was an example of what one dedicated individual can accomplish in a mere twenty years.

Although the recipient of numerous awards and honours, Bappu always remained a courteous and charming personality. He also retained a simplicity of thought and a dedication to his work which included a high degree of commitment to society. He took a keen interest in the affairs of the International Astronomical Union, and served it as a Commission President (1976–1979), as a Vice-President (1967–1973) and finally as its President (1979–1982). He was a great teacher and an outstanding lecturer to audiences of all levels, and his non-technical writings instantly reveal an aesthete who was deeply sensitive to the beauties of Nature.

Bappu was not only the author of numerous scientific publications, but had also served as a member of the editorial boards of several international scientific journals. However, he had always felt the need for a new international journal for astrophysics and astronomy which would help in the dissemination of new results and findings of the fast-expanding world of astronomical research. Hence it was with enthusiasm that he assumed chairmanship of the editorial board of the *Journal of Astrophysics and Astronomy*, when the Indian Academy of Sciences launched this new endeavour and requested him to guide its course. He nurtured the journal over its first two years, and took great pains to improve every aspect of its quality. It was Bappu's efforts that have brought the Journal to its present status and that will ensure its progress in the future.

V. Radhakrishnan
for the Editorial Board

J. Astrophys. Astr. (1982) **3,** 219–231

The Eclipsing Binary V 836 Cygni: Photometric Evidence for an Early Evolutionary Status

R. A. Breinhorst* *Sternwarte der Universität Bonn, 5300 Bonn, F R Germany*
H. W. Duerbeck *Observatorium Hoher List der Universitäts-Sternwarte Bonn, 5568 Daun, F R Germany*

Received 1982 March 24; accepted 1982 May 20

Abstract. Three *UBV* light curves of the short-period EB-type eclipsing binary V 836 Cyg, observed in 1971, 1976 and 1980, are presented. The instability of the light curve found by previous authors is confirmed. However, the activity was not very strong between 1971 and 1980. From the observed period variation, previous light-curve analysis data and spectroscopic data it is concluded that V 836 Cyg consists of two main-sequence stars, and will undergo rapid mass exchange before terminating the main sequence (case A evolution).

Key words: eclipsing binaries—period variations—mass exchange

1. Introduction

V 836 Cyg is an eclipsing binary of EB-type light-curve variability with a relatively short orbital period of 0·653 d. Since its discovery on Bamberg plates (Strohmeier, Kippenhahn and Geyer 1956), and a subsequent photometric investigation by Deinzer and Geyer (1959) in 1957–58, pronounced variations of the light curve have drawn attention to this system which in turn led to an almost regular observational control. In contrast to the earlier results of Deinzer and Geyer depicting a strongly disturbed secondary maximum, the observations of Cester (1963) fit to a more regular light curve with only a modest asymmetry. Cester's orbital solution, based on the classical Russell-Merrill method, yields a contact system. Harris (1968) collected his observations over a relatively long period (1963–1965) which obviously coincided with a phase of irregular brightness variations, and therefore resulted in a strong obser-

*Visiting astronomer, Kitt Peak National Observatory, operated by the Association of Universities for Research in Astronomy, Inc., under contract with the National Science Foundation

vational scatter. The more recent observations of Wester (1977) again led to a light curve contaminated by short-term variations. By applying synthetic light-curve techniques, he determined from his orbital solution a state of marginal undercontact. No spectroscopic data have been published hitherto, except for a spectral classification by Hill *et al.* (1975). Thus the solutions for the essential parameters of the system are vague. It may be surmised, however, that the binary consists of two main-sequence components proceeding in an early evolutionary stage prior to the rapid mass exchange. The present observations were aimed therefore at obtaining complete *BV* light curves over short time intervals ($\Delta t \leqslant 10^2\ P$) in order to minimize the influence of superimposed secular brightness variations (see *e.g.* Bergeat *et al.* 1981), and to improve the precision of photometric element determination.

2. Observations

A first set of two observing runs was obtained in 1971 and 1976 at the Hoher List Observatory with a single-channel *UBV* photometer (unrefrigerated 1P21 photomultiplier) attached to the 35-cm Cassegrain telescope. Each of these series covers an almost complete, almost instantaneous light curve, the data of both samples being confined to an interval of roughly 100 cycles (or two months). It should be mentioned that—while the mechanical photometer construction has been replaced by an improved design in between—the identical photomultiplier and filter combination has been retained throughout. A third observing run was performed at Kitt Peak National Observatory in 1980 July, using the No. 3 0·4-m telescope, equipped with a single-channel standard *UBV* photometer. Here, an essentially complete light curve was sampled over a period of only 10 cycles. The Hoher List observations were measured against BD + 35°4461 and BD + 35°4460 as comparison and check star, respectively. For the KPNO data set, BD + 35°4497 was chosen as comparison star, occasionally checked against BD + 35°4461. Its small angular distance from the variable improved the measuring speed fairly well, however, at the expense of introducing second-order extinction coefficients because of its widely differing spectral type. All necessary data on variable, comparison and check stars are given in Table 1. Figs 1–3 show

Table 1. Catalogue data of variable and comparison stars.

Star	BD HD SAO	RA (1950) h m s	Dec. ° ′ ″	Sp. type	m_v
V 836 Cyg	+35°4496 203470 71239	21 19 20	+35 31 23	A0	8·7
Comparison (HL) Check (KPNO)	+35°4461 202768 71153	21 15 04	+35 33 35	A2	8·2
Comparison (KPNO)	+35°4497 ... 71246	21 19 48	+35 34 45	K0	8·6
Check (HL)	+35°4460	21 15 02	+35 35 42	A0*	9·2

*photometric classification by Harris (1968)

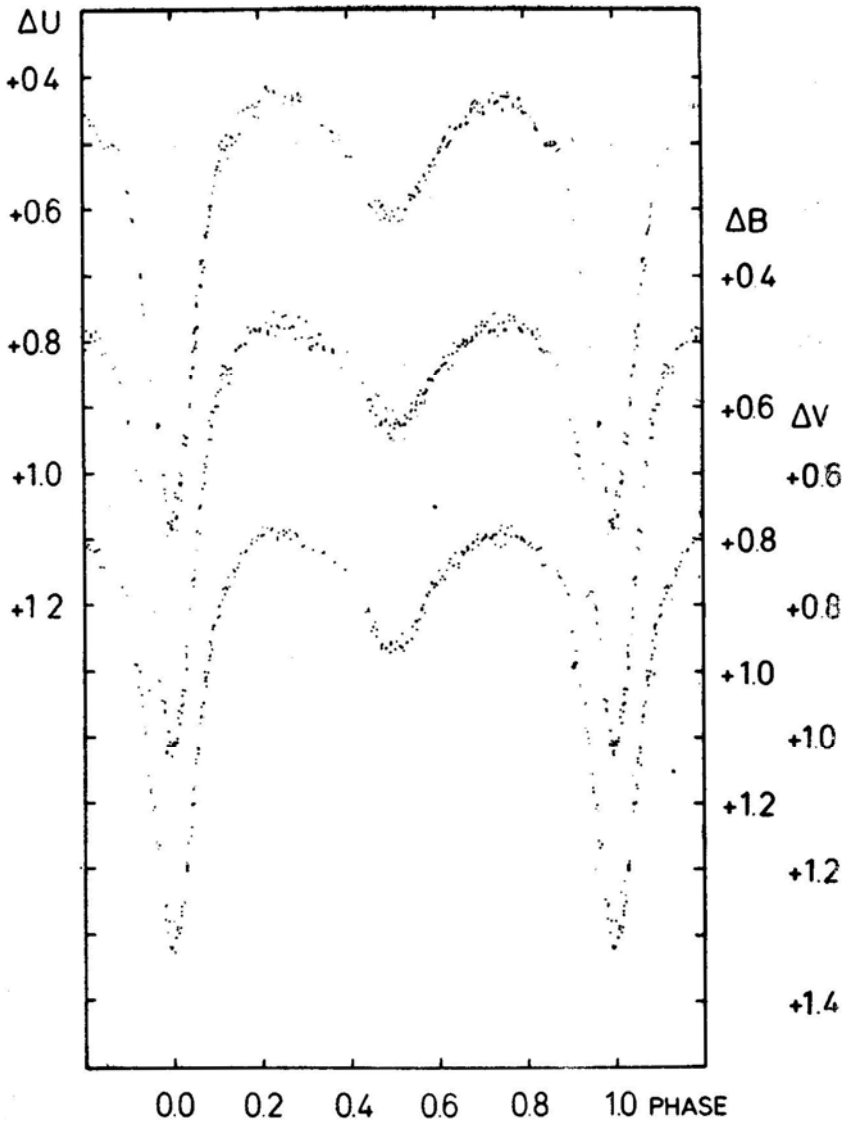

Figure 1. *UBV* light curves of V 836 Cyg in 1971, relative to BD + 35°446L.

the light curves observed in 1971, 1976 and 1980. The individual observations will be published separately (Breinhorst and Duerbeck 1983).

3. The light curves

Some of the previously reported light-curve anomalies (in particular those mentioned by Deinzer and Geyer) are confirmed by the present observations. In the Hoher List observations of 1976 as well as in the Kitt Peak data of 1980, there is a clearly-visible brightness deficiency over a short phase interval on the ascending branch of minimum II, around phase 0·55. The effect is strongly pronounced in the *U* curves, and is

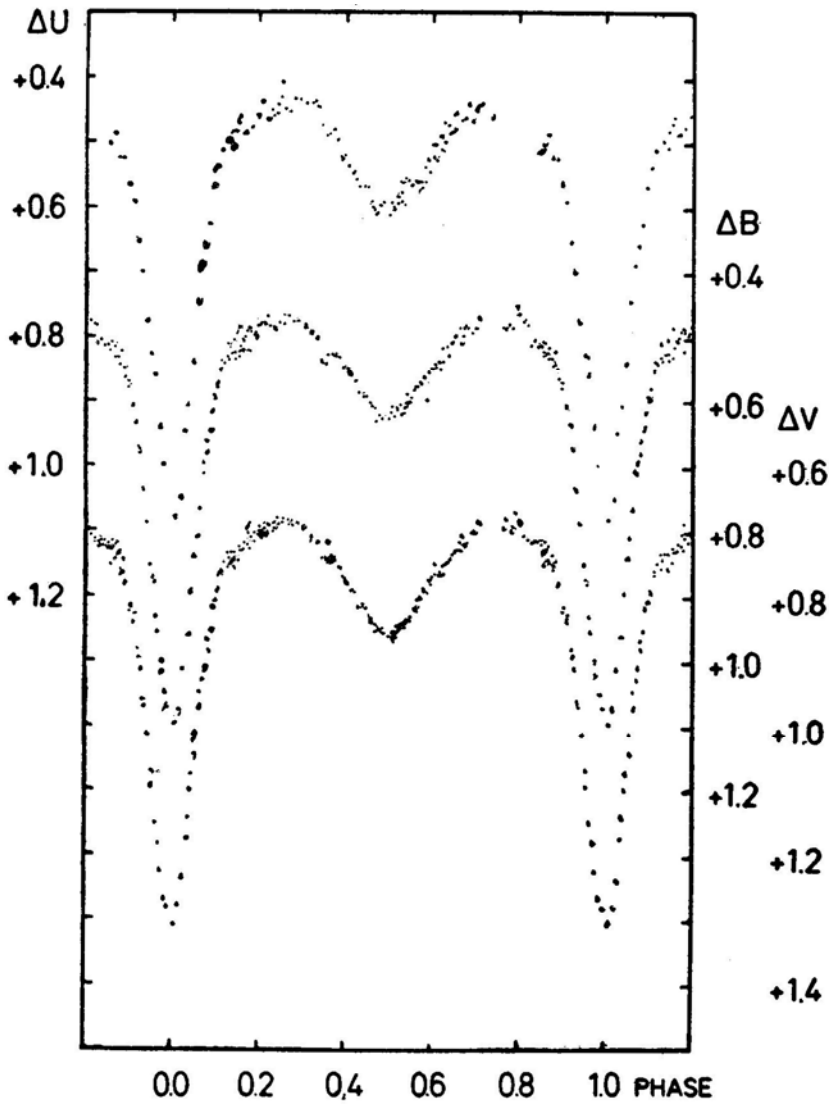

Figure 2. *UBV* ligit curves of V 836 Cyg in 1976, relative to BD + 35°4461.

almost invisible in the *V* observations. We further note a light curve asymmetry in the sense Δm (maximum I – maximum II) < 0. Only the Hoher List data of 1971 show an almost regular, nearly symmetric EB-type light curve. However, a pronounced disturbance of maximum II, as observed by Deinzer and Geyer in 1957–58, was never observed in the time interval 1960–1980.

Fourier coefficients up to the second harmonics have been calculated for all *B* light curves to specify the out-of-eclipse variations. They are normalized by division by $(A_0 - A_2)$, and are listed in Table 2. They outline possible light curve changes from secular variations of reflection (A_1, A_2), ellipticity (A_2), and asymmetry (B_1, B_2). No dramatic changes are obvious. Mean differences between different light curves are always below 0.01 mag.

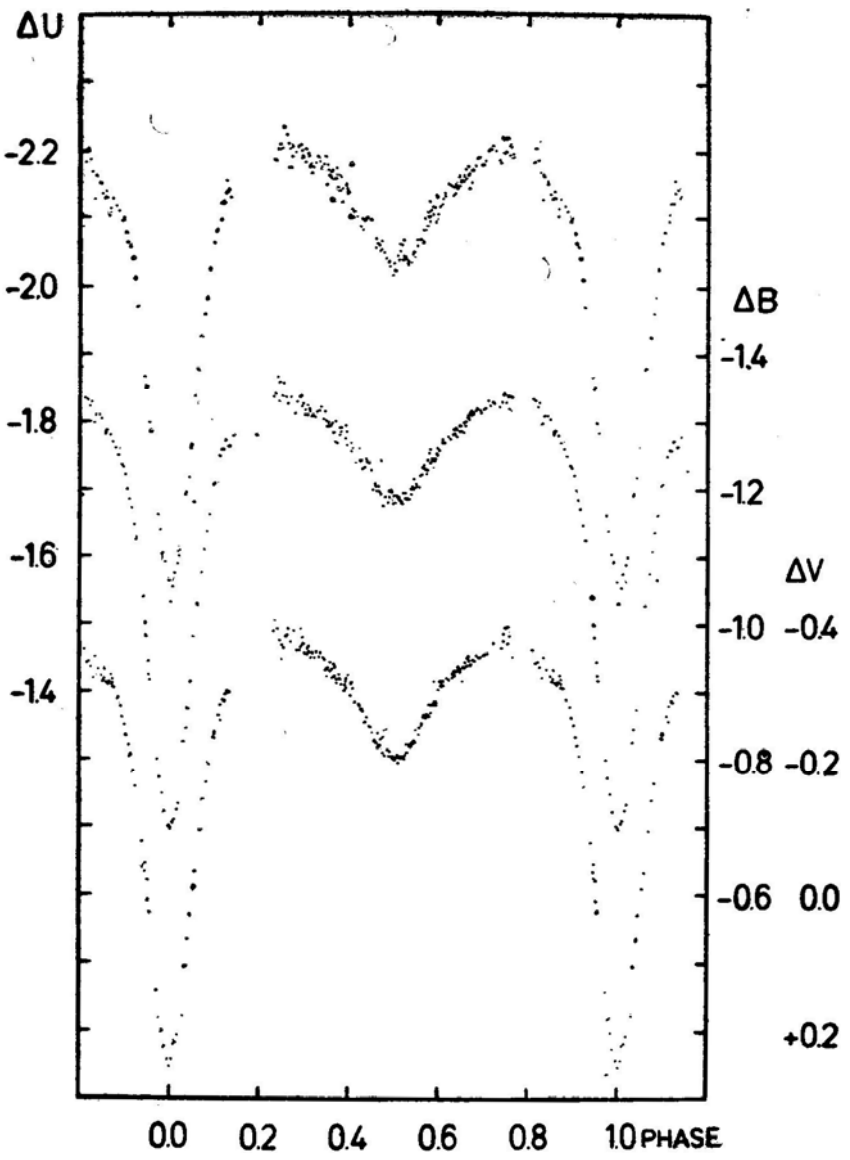

Figure 3. *UBV* light curves of V 836 Cyg in 1980, relative to BD + 35°4497.

From the *B* and. *V* observations of all new data sets, there are clear indications for a flat-bottomed minimum II, *i.e.* for a short phase of totality during the secondary eclipse. As judged from these observations, the interval of constant light extends over almost 0·05 in phase.

Cester (1963), Harris (1968) and Wester (1977) have attempted to solve the light curve. Cester's and Harris' solutions are based on the Russell-Merrill method, while Wester tried the Wood and the Hutchings-Hill synthetic light-curve techniques. A summary of the solutions is given in Table 3. While the solutions of Cester, Harris and Wester (Wood model) result in partial eclipses, Wester's Hutchings-Hill solution yields total eclipses, resulting in an occultation during secondary and a transit during

Table 2. Fourier coefficients of the *B* light curves of V 836 Cyg.

Author(s)	Year(s)	A_0	A_1	A_2	B_1	B_2
Deinzer and Geyer (1959)	1957–58	+0·963?		−0·037?		
Cester (1963)	1960–62	+0·9608 ±·0016	+0·0135 ±·0015	−0·0392 ±·0023	+0·0038 ±·0008	+0·0066 ±·0009
Harris (1968)	1963–65	+0·9486 ±·0039	−0·0006 ±·0042	−0·0514 ±·0058	+0·0010 ±·0021	+0·0018 ±·0025
Duerbeck (present study)	1971	+0·9570 ±·0005	+0·0089 ±·0003	−0·0430 ±·0006	+0·0008 ±·0001	+0·0025 ±·0002
Duerbeck (present study)	1976	+0·9550 ±·0012	+0·0007 ±·0007	−0·0450 ±·0016	−0·0016 ±·0003	+0·0017 ±·0004
Wester (1977)	1975–77	+0·9432 ±·0041	+0·0084 ±·0026	−0·0568 ±·0052	−0·0013 ±·0008	+0·0001 ±·0015
Breinhorst (present study)	1980	+0·9511 ±·0006	+0·0089 ±·0004	−0·0489 ±·0008	+0·0016 ±·0002	+0·0017 ±·0002

Table 3. Geometric and photometric elements of V 836 Cyg.

	Cester I	Cester II	Harris	Wester I	Wester II	Wester III
Method*	RM	RM	RM	Wood	Wood	HH
k	0·63	0·72	0·7	0·68	0·75	0·61
a_g	0·47	0·45	0·412	0·45	0·43	0·40
b_g	0·45	0·43	0·399	0·43	0·41	
a_s	0·30	0·32	0·288	0·32	0·33	0·245
b_s	0·29	0·31	0·279	0·29	0·30	
i	77°	74°	77°·3	76°·8	74°·8	82°·3
ϵ	0·043	0·044	0·031			
$L_g(B)$	0·934	0·916	0·952	0·969	0·970	
$L_s(B)$	0·066	0·084	0·048	0·031	0·030	
I_g/I_s	5·62	5·65	4·78			
x	0·6	0·6	0·6	0·6–0·75	0·6–0·75	
a_0^{oc}	0·96	0·76	0·85			
a_0^{tr}	0·90	0·70	0·79			
$1-l^{oc}$	0·064	0·064	0·041			
$1-l^{tr}$	0·364	0·365	0·405			
q				0·40	0·50	0·48
T_A				10800	10800	10800
T_B				5800	5600	6080

*RM: Russell-Merrill; HH: Hutchings-Hill.

primary minimum. However, the primary minimum of V 836 Cyg does not exhibit a gently curved 'transit-like' shape, as, for example, the similar system TX Cet (Duerbeck and Ammann 1978), but appears to be very 'acute', indicating a partial eclipse.

4. Period study

A large amount of fairly precise photoelectrically-observed minimum times has been published in the last two decades. All hitherto published minimum-time determinations are compiled in Table 4. This table also includes five primary and two secondary minima, derived from the present observations, which were averaged from individual determinations independently evaluated in each colour.

Some of the minima of Deinzer and Geyer, and of Harris differ from the results given in this compilation. Here, the original observations (kindly put at our disposal by Professor Geyer) have been used to re-determine uniformly (by an iterated Kwee-van Woerden method), and to possibly confirm the earlier results. With these modifications, all photoelectric minimum times (except for a few results of lower precision, labelled '0' in the table and shown with smaller circles in Fig. 4) were used to determine the improved linear light elements

$$JD_{\odot}\,(\text{minimum I}) = 2441\,239{\cdot}4687 + 0{\cdot}65341146\,E.$$
$$\pm\ {\cdot}0005\ \pm\ {\cdot}00000012$$

The resulting values of (O — C) are plotted in Fig. 4. The normal points in this diagram, averaged from adequately grouped individual (O — C) data, depict a strictly parabolic distribution of all photoelectrically determined values. A quadratic fit yields

$$JD_{\odot}\,(\text{minimum I}) = 2441\,239{\cdot}4671 + 0{\cdot}65341169\,E + 1{\cdot}00 \times 10^{-10}\,E^2.$$
$$\pm\ {\cdot}0003\ \pm\ {\cdot}00000008\qquad \pm\,{\cdot}17$$

The period increase $\dot{P}/P$ is about $4{\cdot}7 \times 10^{-10}$, with an uncertainty $\Delta P/P$ of $\pm\ 8{\cdot}0 \times 10^{-11}$.

Evidently the earlier photographic minimum determinations do not fit the accurate parabolic (O — C) curve. Gross errors, resulting from misidentifications of the epochs of early minimum times can almost safely be excluded. This obvious complication in the (O — C) structure prevents any definite conclusion to be drawn on the nature of period variations from the data available at present.

A considerable increase in the precision and number of future observations of minimum times is needed to test the following hypotheses.

1. The (O — C) pattern is sinusoidal (*i.e.* periodic) and results from the light-time effect due to the motion of the binary in the orbit of a triple system(Apsidal motion in the binary system is excluded because of the constant phase lag of 0·5 P between primary and secondary minimum). Since no complete cycle has yet been covered, the period of the light-time orbit is very uncertain. A rough estimate yields P_1 = 40000 P= 71·5 yr, K_1 = 0·0050 ± 0·0008 d (corresponding to a_1 = 0·86 ± 0·14 AU). If this orbit is coplanar to that of the eclipsing system whose mass is assumed to be 4 $M_{\odot}$, a third body with m_3 = 0·12 $M_{\odot}$, a_2 = 26·6 AU is derived, which would be unnoticeable in the spectrum and in the photometric solution. Thus, a third body in an orbit which is not strongly inclined to that of the eclipsing binary is compatible with the (O — C) diagram. However, more

Table 4. Minimum times of V 836 Cyg.

Minimum time ($JD_\odot$—2400000)	Epoch	$O-C$	Comments	Reference
25 742·517	−23717	+0·008	pg	Schmidt (1956)
26 295·317	−22871	+0·022	pg	,,
26 331·236	−22816	+0·003	pg	,,
26 547·533	−22485	+0·021	pg	,,
26 589·340	−22421	+0·010	pg	,,
26 600·428	−22404	−0·010	pg	,,
26 619·402	−22375	+0·015	pg	,,
26 915·381	−21922	−0·002	pg	,,
26 915·408	−21922	+0·025	pg	,,
27 000·328	−21792	+0·002	pg	,,
27 993·526	−20272	+0·014	pg	,,
28 391·454	−19663	+0·015	pg	,,
29 187·304	−18445	+0·010	pg	,,
29 581·309	−17842	+0·008	pg	,,
36 073·6008	−7906	+0·0031	pe, nr	Deinzer and Geyer (1959)
36 113·4581	−7845	+0·0023	pe, nr	,,
36 132·4080	−7816	+0·0033	pe, nr	,,
36 305·5606	−7551	+0·0018	pe, nr	,,
36 343·4634	−7493	+0·0068	pe, nr, 0	,,
37 116·4425	−6310	+0·0001	pe	Cester (1963)
37 129·5110	−6290	+0·0004	pe	,,
37 148·4605	−6261	+0·0010	pe	,,
37 188·3200	−6200	+0·0024	pe	,,
37 587·552	−5589	−0·000	pe	Fürtig (1963)
37 885·5095	−5133	+0·0018	pe	Cester (1963)
38 309·5695	−4484	−0·0022	pe	Harris (1968)
38 326·5573	−4458	−0·0031	pe	,,
38 623·8586	−4003	−0·0040	pe	,,
38 625·8195	−4000	−0·0034	pe	,,
38 627·7831	−3997	±0·0000	pe	,,
38 635·6212	−3985	−0·0028	pe	,,
38 644·7700	−3971	−0·0006	pe, nr	,,
38 937·475	−3523	−0·025	vis, 0	Braune and Hübscher (1967)
38 937·502	−3523	+0·002	vis, 0	,,
38 976·7037	−3464	+0·0014	pe, nr	Harris (1968)
38 993·6922	−3437	−0·0015	pe, nr	,,
38 997·6147	−3431	+0·0007	pe	,,
39 008·7195	−3414	+0·0011	pe, nr	,,
39 403·384:	−2810	+0·001	vis, 0	Braune, Hübscher and Mundry (1970)
39 403·386:	−2810	+0·003	vis, 0	,,
39 405·335	−2807	−0·008	vis, 0	,,
39 405·348	−2807	+0·005	vis, 0	,,
39 716·369	−2331	+0·002	pe	Kizilirmak and Pohl (1969)
39 729·436	−2311	+0·001	pe	,,
39 769·2886	−2250	−0·0043	pe	Popovici (1968)
39 782·3588	−2230	−0·0023	pe	,,
40 057·444	−1809	−0·003	pe	Pohl and Kizilirmak (1970)
40 142·395	−1679	+0·004	vis, 0	Diethelm and Locher (1969)
40 157·412	−1656	−0·007	vis, 0	,,
40 180·292	−1621	+0·003	vis, 0	,,
40 353·429	−1356	−0·014	vis, 0	Locher and Diethelm (1969)
40 406·369:	−1275	−0·000	pe	Pohl and Kizilirmak (1970)

Table 4. Concluded.

Minimum time ($JD_\odot$—2400000)	Epoch	$O-C$	Comments	Reference
40 455·3740	−1200	−0·0010	pe	Popovici (1970)*
40 830·435	− 626	+0·002	vis, 0	Diethelm and Locher (1970)
40 832·396	− 623	+0·003	vis, 0	,,
40 836·3129	− 617	−0·0009	pe	Popovici (1970)*
40 851·344	− 594	+0·002	vis, 0	Diethelm and Locher (1970)
40 866·368	− 571	−0·003	vis, 0	Diethelm and Locher (1971)
40 887·277	− 539	−0·003	vis, 0	,,
41 126·423	− 173	−0·006	vis, 0	Diethelm, Isles and Locher (1971a)
41 154·522	− 130	−0·003	vis, 0	,,
41 213·324	− 40	−0·008	vis, 0	Diethelm, Isles and Locher (1971b)
41 230·3200	− 14	−0·0009	pe	Duerbeck (present study)
41 239·4663	0	−0·0024	pe	,,
41 260·3751	+ 32	−0·0028	pe	,,
41 492·3348	+ 387	−0·0018	pe	Kizilirmak and Pohl (1974)
41 521·408:	+ 431·5	−0·008	pe, 0	,,
41 525·321:	+ 437·5	−0·015	pe, 0	,,
41 854·327:	+ 941	−0·002	pe, 0	,,
41 881·446	+ 982·5	+0·001	pe, 0	,,
41 901·381	+1013	+0·006	vis, 0	BBSAG 11 (1973)
42 414·290	+1798	−0·013	vis, 0	BBSAG 20 (1975)
42 570·450	+2037	−0·018	vis, 0	BBSAG 23 (1975)
42 606·392	+2092	−0·013	vis, 0	,,
42 623·392	+2118	−0·002	vis, 0	,,
42 653·4508	+2164	−0·0003	pe	Brancewicz and Kreiner (1976)
42 740·3534	+2297	−0·0014	pe	Wester (1977)
42 742·3168	+2300	+0·0017	pe	,,
43 013·4786	+2715	−0·0022	pe	,,
43 013·4812	+2715	+0·0004	pe	Duerbeck (present study)
43 015·4405	+2718	−0·0006	pe	Wester (1977)
43 043·5369	+2761	−0·0008	pe	,,
43 401·6059	+3309	−0·0013	pe	,,
43 434·275	+3359	−0·003	vis, 0	BBSAG 35 (1977)
43 777·318	+3884	−0·001	vis, 0	BBSAG 39 (1978)
44 082·463	+4351	+0·001	pe	BBSAG 44 (1979)
44 129·5100	+4423	+0·0024	pe	Patkos (1980)
44 423·8721	+4873·5	+0·0027	pe	Breinhorst (present study)
44 424·8516	+4875	+0·0020	pe	,,
44 425·8318	+4876·5	+0·0021	pe	,,
44 461·430	+4931	−0·011	vis, 0	BBSAG 49 (1980)
44 929·265	+5647	−0·018	vis, 0	BBSAG 57 (1981)

*See correction in Popovici (1971).

Abbreviations:

pg = photographic observations
pe = photoelectric observations
vis = visual observations
0 = zero weight
nr = new reduction

BBSAG = Bedeckungsveränderlichen-Beobachter der Schweizerischen Astronomischen Gesellschaft-Bulletin (edited by K. Locher)

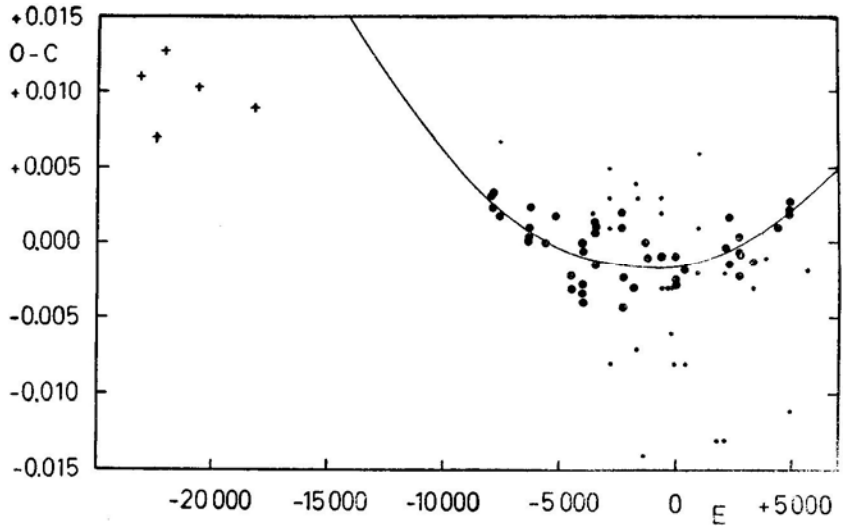

Figure 4. The (*O* — *C*) diagram of V 836 Cyg. Crosses, means form two or three photographic minima; large dots, photoelectric minima; small dots, visual minima or photoelectric minima having zero weight. The quadratic (parabolic) ephemeris curve shown in the diagram is a fit to the normal points which were omitted for reasons of clarity.

minimum times over a much longer time interval are necessary to prove or to disprove the reality of the light-time orbit.

2. The (*O* — C) data are uniformly represented as a sequence of parabolic segments, as proposed in the theory of Biermann and Hall (1973); see also Hall (1975). This theory has primarily been developed to explain the (*O* — *C*) pattern of Algol systems which proceed in an evolutionary state posterior to the phase of rapid mass exchange; it requires, via short-term processes of sudden mass transfer from the cooler to the hotter component, the temporary storage of (orbital) angular momentum as rotation of the mass-accreting layers around the primary star, and its subsequent feedback to the orbit. Since the matter is released from the evolved (*i.e.* less massive) component, the secular period increases, *i.e.* the series of upward-curved parabolic sections (each resulting from a short-time period increase due to the feedback of angular momentum to the orbit) is also enveloped by an upward-curving parabola. Application of this model to an unevolved system requires a downward curvature for the parabolic envelope common to all single parabolic sections, since in the pre-mass-exchange phase the mass-losing component has the larger mass.

5. The evolutionary status of V 836 Cyg

The determination of suitable combinations of parameters (luminosity–temperature; radius–mass) which are subject to sensible changes on the evolutionary track of the star off the main sequence is limited to systems with reliable observational results (see, *e.g.* Kreiner and Ziolkowski 1978). For binaries actually being in contact, Leung and Schneider (1978) compare the observed orbital period with the corresponding critical period adjusting such a distance *A*—through Kepler's 3rd law—that the

Primary component with its actual (ZAMS, main-sequence or TAMS) radius just fills its critical Roche volume. The corresponding relations, tabulations and references are given in detail by Plavec (1968). Because of the Roche geometry involved, the dependence on the mass ratio q is weak: $R_1/R_2=(M_1/M_2)^{0.46}$. Therefore a rough estimate of the primary mass, based on spectral classification, may suffice to decide at which evolutionary state the system (actually in contact) is.

Since V 836 Cyg is an out-of-contact system with poorly determined elements, none of these methods is applicable. However, from a number of single-lined spectra, the mass function could be derived (Duerbeck and Schumann 1982). The result, $f(m)=0{\cdot}050 \pm 0{\cdot}005$, agrees well with the Hutchings-Hill model solution of Wester, where main-sequence stars are assumed. Then, by adopting $i=80^{o}$ (weighted mean of photometric results),both the individual masses and the separation of the components can immediately be evaluated as a function of the (unknown) mass ratio q (*cf.* Plavec 1970). A plot of these relationships is given in Fig. 5. It also contains, as a function of q, the fractional radius Y_1 of component 1, constituting an upper limit to the radial extent of the primary, and in addition the radii R_1 of normal ZAMS, main sequence and TAMS stars with corresponding masses. The TAMS and Y_1 lines intersect at $q \simeq 0{\cdot}39$, or $m_1 \simeq 1{\cdot}7\ m_{\odot}$, *i.e.* for primary masses exceeding this limit (corresponding to spectral types earlier than A9) the radius of component 1 expands beyond the Roche limit and initiates the rapid mass exchange before terminating the main-sequence stage

A few conclusions can be drawn. The mass ratio $q_0=0{\cdot}31$, being at variance with the photometric result (Table 3), uniquely determines $m_1=3{\cdot}3\ m_{\odot}$ (which is compatible with the MK classification A0 by Hill *et al.* (1975), and with Wester's value $T_{\rm eff}$ = 10800 K), and $m_2=1{\cdot}02 m_{\odot}$ (in agreement with Wester's value $T_{\rm eff} \simeq 6000$ K, *i.e.* G1 V; Koch (1973) also derives, from the surface intensity ratio $J_2/J_1=0{\cdot}006(B)$, a spectral type G1 for the secondary component). We note that the combination of spectroscopic and photometric results yields a secondary radius $R_2=a_s \times A=0{\cdot}87 \times 10^6$ km $=1{\cdot}25\ R_{\odot}$, which is only modestly in excess of the corresponding G1 V radius. Thus we are safe to state that the system consists of two unevolved main-sequence stars prior to the phase of rapid mass exchange, and is likely to proceed through case A evolution.

Since component 1 is almost filling the corresponding Roche lobe, light curve and period variations may be considered as the result of small-scale transient mass flow from the primary component. It is obvious that either case—conservative mass transfer onto component 2 and/or mass loss from the system—leads to a secular decrease of the systemic angular momentum, and therefore to a shortening of the period. The period increase, as deduced from the parabolic section of the (O — C) diagram (Fig. 4), is under due consideration of the earlier photographic minima only a transient phenolmenon and (when interpreted in terms of the Biermann-Hall model as resulting from the restoration of angular momentum on a short dynamical time scale) not in contradiction to an overall secular decrease of the period.

Since the available minimum-time observations are too scanty to test any secular period changes, the interpretation of the (O — C) diagram by a modified Biermann-Hall theory (involving mass loss from the primary component of an unevolved binary system) remains hypothetical. Future photometric and minimum-time observations supplying more accurate data for an extended (O — C) diagram should, however, be supported by spectroscopic observations with advanced detectors to prove the

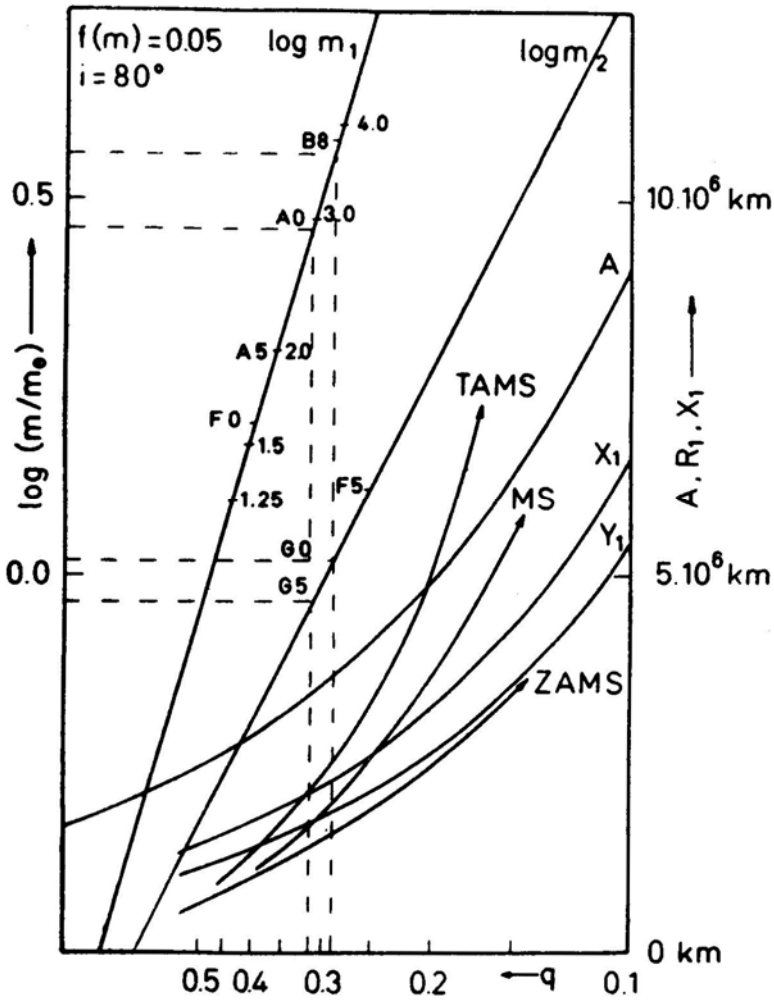

Figure 5. The individual masses m_1 and m_2 of V 836 Cyg versus mass ratio q for the mass function $f(m) = 0{\cdot}050$ and $i = 80°$ in units of solar mass (left side, logarithmic scale). The log m_1 curve is labelled in units of $m_\odot$. Note that the definition of m_1 or a corresponding effective temperature (or spectral type) determines q and m_2. The separation A of the components and the distances X_1 and Y_1 of L_1 from the centre of m_1 as functions of q are given in absolute units of 10^6 km (right ordinate, linear scale). Drawn to scale are the corresponding radii R_1 of normal stars on the ZAMS, TAMS, and standard main sequence (MS). The intersection of the TAMS and the Y_1 curves at $q \approx 0{\cdot}39$, $m_1 \approx 1{\cdot}7\ m_\odot$ defines a lower limit for primary masses undergoing rapid mass loss before terminating the main sequence (case A evolution). As derived from spectroscopic and photometric results, V836 Cyg is found in the interval marked by dashed lines.

presence of circumstellar matter and to determine the physical and kinematical properties of mass flow.

Acknowledgement

It is a pleasure to thank the director and community of Kitt Peak National Observatory for their generous assistance and hospitality, and the referee for his helpful

criticism of the earlier version of the text. Financial support from a travel grant (Br 752/1) of the Deutsche Forschungsgemeinschaft for R. A. B. is gratefully acknowledged. Part of the data reduction has been performed on the Cyber 172 of the Max-Planck-Institut für Radioastronomie, Bonn.

References

Bergeat, J., van't Veer, F., Lunel, M., Gamier, R., Sibille, F., Roux, S. 1981, *Astr. Astrophys.*, **94,** 350.
Biermann, P., Hall, D. S. 1973, *Astr. Astrophys.*, **27,** 249.
Brancewicz, H., Kreiner, J. M. 1976, *Inf. Bull. Var. Stars*, No. 1119.
Braune, W., Hübscher, J. 1967, *Astr. Nachr.*, **290,** 105.
Braune, W., Hübscher, J., Mundry, E. 1970, *Astr. Nachr.*, **292,** 185.
Breinhorst, R. A., Duerbeck, H. W. 1983, *Veröff. astr. Inst. Univ. Bonn*, No. 96.
Cester, B. 1963, *Pubbl. Oss. astr. Trieste*, No.317.
Deinzer, W., Geyer, E. 1959, *Z. Astrophys.*, **47,** 211.
Diethelm, R., Isles, J., Locher, K. 1971a, *Orion*, **29 ,**142.
Diethelm, R., Isles, J., Locher, K. 1971b, *Orion*, **29,** 182.
Diethelm, R., Locher, K. 1969, *Orion*, **14,** 23.
Diethelm, R., Locher, K. 1970, *Orion*, **28,** 191.
Diethelm, R., Locher, K. 1971, *Orion*, **29,** 21.
Duerbeck, H. W., Ammann, M. 1978, *Astr. Astrophys.*, **70,** 355.
Duerbeck, H. W., Schumann, J. D. 1982, *J. Astrophys. Astr.* **3,** 233.
Fürtig, W. 1963, *Mitt. veränderl. Sterne*, **2,** 9.
Hall, D. S. 1975, *Acta astr.*, **25,** 1.
Harris, A. J. 1968, *Astr. J.*, **73,** 164.
Hill, G., Hilditch, R. W., Younger, F., Fisher, W. A. 1975, *Mem. R. astr. Soc.*, **79,** 131.
Kizilirmak, A., Pohl, E. 1969, *Astr. Nachr.*, **291,** 111.
Kizilirmak, A., Pohl, E. 1974, *Inf. Bull. Var. Stars*, No. 937.
Koch, R. H. 1973, *Astr. J.* **78,** 410.
Kreiner, J. M., Zio1kowski, J. 1978, *Acta astr.*, **28,** 497.
Leung, K. C., Schneider, D. P. 1978, *Astrophys. J.*, **222,** 917.
Locher, K. 1973, *BBSAG Bull.*, No. 11, 20, 23, 35, 39, 44, 49, 57.
Locher, K., Diethelm, R. 1969, *Orion*, **14,** 109.
Patkos, L. 1980, *Inf. Bull. Var. Stars*, No. 1751.
Plavec, M.1968, *Adv. Astr. Astrophys.*, **6,** 201.
Plavec, M.1970, *Publ. astr. Soc. Pacific*, **82,** 957.
Pohl, E., Kizilirmak, A. 1970, *Inf. Bull. Var. Stars*, No. 456.
Popovici, C. 1968, *Inf. Bull. Var. Stars*, No. 322.
Popovici, C. 1970, *Inf. Bull. Var. Stars*, No. 419.
Popovici, C. 1971, *Inf. Bull. Var. Stars*, No. 508.
Schmidt, H.1956, *Kleine Veröff. Remeis-Sternw.*, No.16.
Strohmeier, W., Kippenhahn, R., Geyer, E. 1956, *Kleine Veröff. Remeis-Sternw.*, No. 15.
Wester, J.1977, M.A. *Thesis*, *University of Tübingen*, *Germany.*

J. Astrophys. Astr. (1982) **3,** 233–235

The Spectroscopic Orbit of the Short Period Eclipsing Binary V 836 Cygni

H. W. Duerbeck and J. D. Schumann *Observatorium Hoher List der Universitäts-Sternwarte Bonn,* 5568 *Daun, F. R. Germany*

Received 1982 May 19; accepted 1982 June 2

Abstract. Spectroscopic elements of the single-lined spectroscopic binary V 836 Cyg are presented.

Key words: radial velocities—spectroscopic binaries—stars, individual

1. Introduction

V836 Cyg (BD + 35°4496, HD 203470, A0), an EB-type eclipsing binary with a period of 0·6534 d, is remarkable because its light curve is subject to marked secular disturbances. The star has been the object of several photometric studies (Breinhorst and Duerbeck 1982 and references therein), but no spectroscopic orbit has been published until now. Spectroscopic elements are presented here; the implications of this analysis are found in the paper by Breinhorst and Duerbeck (1982).

2. Observations

Twenty-six spectrograms (dispersion 30 Å mm^{-1}, emulsion IIa-O) were obtained with the UAGS grating spectrograph attached to the 1·06-m Cassegrain telescope of the Hoher List Observatory. The plates were sensitized by nitrogen soaking (Schumann 1979) and exposure times were of the order of 1 hr. The spectrograms were measured with the modified Grant oscilloscope measuring machine of the European Southern Observatory (Melnick 1980).

The spectra are single-lined; the lines Hγ, Hδ, H8, Mg II 4481 and Ca II 3933 could be measured; due to the large rotational broadening, the weaker lines in Batten's (1976) list could not be seen. Due to the line broadening and the small number of useful lines, the internal errors of the spectrograms are large, they amount to ± 13·0 km s^{-1} on the average.

3. Results

The resulting radial velocities, with applied heliocentric corrections, are given in Table 1. The phases were calculated with the light elements (including the quadratic term) given by Breinhorst and Duerbeck (1982). The solution for an elliptical orbit yields e=0·083 ± 0·094 and the application of Lucy and Sweeney's (1971) criterion shows that a circular orbit can be assumed. The elements of the circular orbit, which is shown in Fig. 1, are:

$T = 2\,444\,647{\cdot}6662\ \mathrm{JD}_{\odot}$ $\quad P = 0{\cdot}65341221$ d
$K = 90{\cdot}3 \pm 4{\cdot}1$ km s^{-1} $\quad V_0 = -43{\cdot}3 \pm 3{\cdot}0$ km s^{-1}
$f(m) = 0{\cdot}050 \pm 0{\cdot}005$

The time T given above is that of the V_0 crossing point (motion towards the observer), which is equal to the time of primary minimum and which is derived from photoelectric observations. The system has a variable period, the period P is valid for the mean epoch of the spectroscopic observations.

Table 1. Radial velocities of V 836 Cyg.

No.	JD⊙ (2444000+)	Phase	Radial velocity
5405	379·5237	0·6292	+ 56·0
5408	381·4883	0·6359	+ 30·7
5409	381·5334	0·7049	+ 34·3
5412	382·4959	0·1779	−126·2
5413	382·5463	0·2551	−133·6
5416	426·4469	0·4446	− 88·9
5578	477·3411	0·3315	− 92·9
5579	477·3849	0·3986	− 99·4
5580	477·4289	0·4659	− 50·7
5581	477·4747	0·5360	− 39·3
5582	477·5188	0·6035	+ 9·4
5583	477·5629	0·6710	+ 42·7
5584	477·6070	0·7385	+ 39·0
5587	480·3331	0·9106	− 10·2
5726	518·3559	0·1017	− 73·8
5727	518·4018	0·1714	−128·1
5729	526·3183	0·2875	−139·4
5730	526·3610	0·3529	−108·4
5731	526·4090	0·4263	− 78·1
6276	829·4881	0·2665	−151·2
6277	829·5457	0·3547	−114·7
6358	859·4166	0·0699	−102·2
6406	916·2406	0·0348	− 75·0
6407	916·2974	0·1217	− 88·1
6408	916·3599	0·2174	−134·1
6409	916·4280	0·3216	−128·6

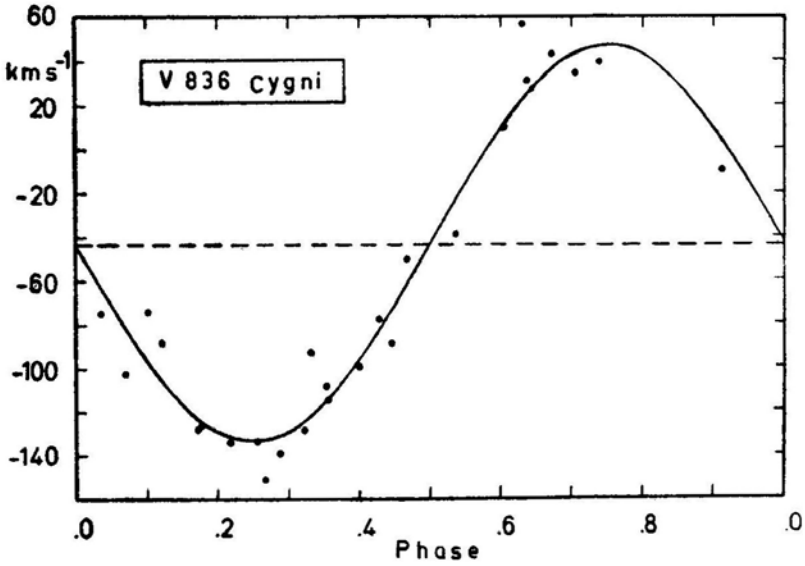

Figure 1. The computed radial-velocity curve for V 836 Cyg, with the measured radial velocities plotted.

References

Batten, A. H. 1976, *Publ. Dom. astrophys. Obs.*, *Victoria*, **14,** No. 17.

Breinhorst, R. A., Duerbeck, H. W. 1982, *J. Astrophys. Astr.*, **3,** 219.

Lucy, L. B., Sweeney, M. A. 1971, *Astr. J.*, **76,** 544.

Melnick, J. 1980, in *Proc. ESO Workshop on Two Dimensional Photometry*, Eds P. Crane and K. Kjär, p.53.

Schumann, J.-D. 1979, *Veröff. astr. Inst. Univ. Bonn,* No. 91.

J, Astrophys. Astr. (1982) **3,** 237–247

On Selection Effects in Pulsar Searches

M. Vivekanand, R. Narayan and V. Radhakrishnan
Raman Research Institute, Bangalore 560080

Received 1982 February 25; accepted 1982 May 31

Abstract. Selection effects are a major source of error in statistical studies of pulsar data since the observed sample is a biased subset of the full galactic pulsar population. It is important to identify all selection effects and make a reasonable model before attempting to determine pulsar properties. Here we discuss a hitherto neglected selection effect which is a function of the period P of the pulsar. We find that short-P pulsars are more difficult to detect, particularly if their dispersion measures are high. We also discuss a declination-dependent selection effect in the II Molonglo Survey (II MS), and find some evidence for the existence of both selection effects in the pulsar data from this survey. We discuss the implications of these additional selection effects for the recently proposed 'injection' of pulsars whereby pulsars seem to switch on only at longer P. Using the II MS data we calculate that the observability of pulsars with P between 0·0 s and 0·5 s is about 18 per cent less with the new selection effects than hitherto believed; the mean correction is 6 per cent for P between 0·5 s and 1·0 s. We conclude that injection is not qualitatively affected by these corrections.

Key words: pulsar searches—selection effects

1. Introduction

Vivekanand and Narayan (1981; henceforth VN) have shown that there is apparently a physical deficit of pulsars with periods $P < 0{\cdot}5$ s. Before seeking an explanation for this so-called 'injection' of pulsars at long periods, it is important to verify that it is a genuine pulsar phenomenon and not an artifact arising from some period-dependent selection effect in pulsar searches.

It is currently believed that a satisfactory representation of the minimum detectable flux $S_{\min}$ of a pulsar survey is that given by Taylor and Manchester (1977)

$$S_{\min} = S_0 \beta (1 + T_{\rm sky}/T_{\rm r}) (1 + D/D_0)^{1/2} \text{ mJy} \quad (1)$$

where T_{sky} and T_r are the sky and receiver noise temperatures, D is the dispersion measure of the pulsar, D_0 is a constant, S_0 is the minimum sensitivity of the survey and β is a factor (greater than 1) representing the reduction in sensitivity resulting from displacement of the source from the beam centre. In Equation (1), S_{min} does not depend upon P; indeed, Taylor and Manchester (1977) only refer to a limiting period (of the order of tens of milliseconds) above which the sensitivity of the survey is believed to be uniform, and below which the sensitivity decreases rapidly. However, much earlier, Large and Vaughan (1971) had demonstrated the presence of a selection effect, dependent both on P and D, in the I Molonglo Survey (I MS). Because the I MS used a different method for pulsar search than that currently employed, their results are not directly relevant today.

In this paper we argue that two modifications to Equation (1) are necessary. Firstly, S_{min} depends not on the dispersion measure D alone (as in Equation 1) but on D/P (this is related to the effect discussed by Large and Vaughan 1971). Hence, short period pulsars are more difficult to detect than Equation (1) would suggest. Huguenin (1976) has mentioned the period-dependent selection effect and has pointed out that short-period, high-dispersion pulsars are very difficult to observe. This could have implications when analysing period-dependent effects such as injection. Secondly, high-declination (δ) pulsars are somewhat easier to detect because some surveys (*e.g.* II Molonglo Survey, hereafter II MS; Manchester *et al.* 1978) spend longer observing times at higher δ. Since δ is correlated with height above the galactic plane (z), particularly for nearby pulsars, this could have consequences for z-dependent studies of pulsars. Equation (6) gives a new formula for S_{min} incurporating these new effects.

Table 1 shows that both the above effects are indeed present in the II MS. Table l(a) considers the II MS pulsars in three period bins. In each bin we have tabulated (i) the number of pulsars (n_0) detected below the quoted minimum detectable flux, *i.e.* pulsars with $S_{pulsar}/S_{min} < 1$ where S_{min} is given by Equation (1), (ii) the total number of pulsars detected ($n_0 + m_0$), (iii) the expected number of pulsars (n_e) with $S_{pulsar}/S_{min} < 1$, based on the total n_0 in all the bins, $n_e = (n_0+m_0)(\Sigma\ n_0)/(\Sigma n_0 + \Sigma m_0)$, *i.e.* $n_e \propto (n_0 + m_0)$, (iv) the difference $n_0 - n_e$ and (v) the expected standard deviation (σ) on (n_0 — n_e). It is reasonable to expect that n_0 should differ from n_e in each bin by a quantity of the order of σ. Table 1 (a) shows that this is clearly not so. We obtain a χ^2 (computed as $\Sigma\{(n_0 - n_e)^2/\sigma^2\}$;

Table 1. Each column shows (i) observed number of pulsars (n_0) with $S_{pulsar}/S_{min} < 1{\cdot}0$, (ii) all pulsars in that bin ($n_0 + m_0$), (iii) expected number (n_e) with $S < S_{min}$ in the bin, (iv) the difference ($n_0 - n_e$), and (v) standard deviation (σ) on $n_0 - n_e$. S_{min} was derived using Equation (1).

(a) Pulsars in bins of period (in seconds):

(b) Pulsars in bins of declination:

	$0{\cdot}0 \leqslant P < 0{\cdot}5$	$0{\cdot}5 \leqslant P < 1{\cdot}0$	$1{\cdot}0 \leqslant P < 1{\cdot}5$	$0° \leqslant \delta < 30°$	$30° \leqslant \delta < 60°$	$60° \leqslant \delta < 90°$
n_0	11	21	19	18	26	16
$n_0 + m_0$	76	89	40	97	89	38
n_e	18·9	22·1	10·0	26	23·8	10·2
$n_0 - n_e$	−7·9	−1·1	9·0	−8·0	2·2	5·8
σ	3·0	2·9	2·45	3·3	3·24	2·5

see Section 3 for details) of 20·6 against the expected value 3·0, implying that S_{min} probably has some P-dependence in addition to the factors written down in Equation (1). In Table 1 (b), which considers the declination dependence, we similarly obtain a χ^2 of 11·8 against 3. These results appear to suggest that Equation (1) may not be an adequate description of the selection effects in pulsar surveys.

In Section 2 we present the theory of the new selection effects. Our results for the dependence of S_{min} on D/P differ quantitatively from those of Large and Vaughan (1971); we offer a possible explanation for this. In Section 3 we present some evidence to show that our modified formula for S_{min}. which for practical purposes can be simplified to Equation (8), is a better representation of the selection effects in the II MS than Equation (1). In particular, it is shown that arguments similar to those used in Table 1 but with the new S_{min} (Equation 8) give results significantly more consistent with the observations. We demonstrate in Section 4 that these extra selection effects we have discussed are unimportant as far as the recently derived pulsar injection properties are concerned. There continues to be strong evidence for the sudden appearance of many pulsars at long periods. Another possible selection effect due to the period derivative $\dot{P}$, which might have a P dependence, is briefly discussed. It is conlcuded that this is not likely to be of importance.

2. Theory of the selection effects

In Fig. 1, we have schematically plotted the signal as a function of time in the de-dispersed folded output from a pulsar survey. The plot is for the duration of one period, and signal strength is measured in units of temperature. Due to the ionized interstellar medium, the intrinsic pulse width w is broadened to. $w + t$, where t is the dispersion broadening in a single frequency channel. In what follows we assume that (a) the signal is folded at the correct P of the pulsar, (b) the time resolution of the

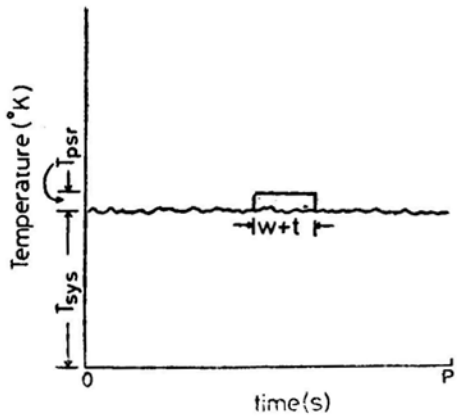

Figure 1. A schematic folded output from a pulsar survey. T_{sys} is the system noise level, and T_{psr} is the mean pulsar level for the pulse duration. The pulse of intrinsic width w is broadened by t because of dispersion in the interstellar medium. For convenience in presentation the fluctuations in T_{sys} have been scaled down.

data is $1/B$ where B is the bandwidth, (c) the signals in the various channels have been de-dispersed with the correct delay, and (d) the position of the pulse and its width ($w + t$) have been properly identified in the integrated profile. We later show that (b) is not a necessary requirement.

Let the mean system temperature without the pulsar be $T_{\rm sys}$. This is the receiver temperature T_r plus the background sky contribution; so

$$T_{\rm sys} = T_{\rm r}\,(1 + T_{\rm sky}/T_{\rm r}). \tag{2}$$

Let the pulsar under consideration, with mean signal strength $T_{\rm psr}$ within the pulse window, be just at the threshold of detectability. For detection, the difference between the mean level ($T_{\rm psr}$ + $T_{\rm sys}$) *on-pulse* and the mean level $T_{\rm sys}$ *off pulse* should be some factor n (typically 5) times the noise $\sigma_{\rm diff}$ on the difference. Now

$$\sigma_{\rm diff} = (\sigma_{\rm on}^2 + \sigma_{\rm off}^2)^{\frac{1}{2}}$$

$$= \left\{\frac{T_{\rm sys}^2}{(\tau/P)\,(w+t)\,B} + \frac{T_{\rm sys}^2}{(\tau/P)\,(P-w-t)\,B}\right\}^{\frac{1}{2}} \tag{3}$$

where τ is the total observation time per sky position. Hence at the threshold of detection

$$T_{\rm psr} = \frac{n\,T_{\rm r}}{(\tau\,B)^{\frac{1}{2}}}\,(1 + T_{\rm sky}/T_{\rm r})\left[\frac{1}{(w+t)/P}\right]^{\frac{1}{2}}\left[1 + \frac{w+t}{P-w-t}\right]^{\frac{1}{2}}. \tag{4}$$

$T_{\rm psr}$ can be written in terms of the mean pulsar flux density S (energy per pulse divided by period) as

$$T_{\rm psr} = \frac{1}{\beta}\,S\left[\frac{P}{w+t}\right]\frac{A}{k_{\rm B}} \tag{5}$$

where β has been defined in Equation (1), A is the effective collecting area of the telescope and $k_{\rm B}$ is Boltzmann's constant. Let us use the symbol d for the pulsar duty cycle (w/P), and write the dispersion broadening explicitly as $t = K_1\,D$ where K_1 is a constant proportional to B. Further, the total observation time $\tau = \tau_0/\cos\,\delta$ for transit observations such as II MS, where τ_0 is assumed to be a constant for a given survey. We then obtain

$$S_{\rm min} = \beta\,S_0\,(1 + T_{\rm sky}/T_{\rm r})\,(d/d_0)^{\frac{1}{2}}\left[1 + \frac{K_1\,D}{Pd}\right]^{\frac{1}{2}}\left[1 + \frac{Pd + K_1\,D}{P - Pd - K_1\,D}\right]^{\frac{1}{2}}(\cos\,\delta)^{\frac{1}{2}} \tag{6}$$

where d_0 is a reference value of the duty cycle for all pulsars (taken to be 0·04) and S_0 is defined by

$$S_0 = \frac{n\,T_{\rm r}\,k_{\rm B}\,d_0^{\frac{1}{2}}}{A\,(\tau_0\,B)^{\frac{1}{2}}} \tag{7}$$

which is a constant for a given survey (assuming A is independent of δ as is true for the II MS). For convenience, we will refer to the term $(d/d_0)^{\frac{1}{2}}$ as term A, the terms in the first and second square brackets in Equation (6) as terms B and C respectively and the term $(\cos\delta)^{\frac{1}{2}}$ as term D.

In Equation (6) the term C is not prominent until the pulse width $(w+t)$ becomes a significant fraction of P. Since this is rare, except when the effects of multipath propagation become overwhelming, C can usually be taken as 1. The term D essentially represents the increased integration time at higher declinations for surveys such as the II MS*. The term B has a non-trivial period dependence (actually D/P dependence) which we wish to highlight in this paper. In the light of this term, we see that Equation (1) is valid only at one value of period, P_0, which can be obtained by equating $P_0\ d_0/K_1$ in Equation (6) to D_0 in Equation (1). If P_0 turns out to be the average period ($\approx$ 0·7 s) for pulsars, one might argue that Equation (1) is valid in an average sense. However, the values of P_0 which we obtain for the three major surveys, *viz.* Jodrell Bank Survey, Arecibo Survey and II MS are 3 s, 0·8 s and 1·6 s respectively. We thus conclude that Equation (1) does not properly represent the selection effects at low periods, where significant fractions of the Galaxy might be relatively inaccessible to the surveys. As an illustration, for $P < 0{\cdot}4$ s, the sensitivity of II MS is reduced by more than $\sqrt{2}$ over more than 90 per cent of the volume of the Galaxy. The term A in Equation (6) shows the variation of $S_{\min}$ with duty cycle d. This term is important if $t < w$, when the term B collapses to ≈ 1. If $t \gg w$, the $d^{\frac{1}{2}}$ in A is approximately cancelled by $d^{-\frac{1}{2}}$ in B.

What happens when the pulse width $w+t$ is not resolved in the integrated profile? This occurs for nearly 20 per cent of the pulsars detected by the II MS where the minimum time resolution was not $1/B$ but a much larger quantity t_0 = 20 ms. In the case when $w+t<t_0$, $w+t$ is to be replaced by t_0 in both Equations (4) and (5), and Equation (6) implies $S_{\min} \propto P^{-\frac{1}{2}}$. In the intermediate situation when w and t are both $< t_0$ but $w + t > t_0$, Equation (6) continues to be valid. Thus, in all cases, the period dependence of $S_{\min}$ remains and cannot be neglected.

To summarize, we believe that Equation (6) is a better formula to be used in describing selection effects in pulsar searches (such as the II MS). Equation (1) is inadequate particularly at short periods, and is not appropriate for studies such as injection (VN) which seek to determine pulsar properties as a function of period.

We should mention here that Large and Vaughan (1971) experimentally demonstrated the variation of $S_{\min}$ with both P and D for the I MS. We have verified that their $S_{\min}$ (Fig. 4 in their paper) depends approximately upon the specific combination (D/P) as in our formula (term B). To make a more detailed comparison with our theory, we have estimated the function $F = -\ d\ (\log S_{\min})/d\ (\log P)$ from their published curves of $S_{\min}$ for the three systems they have studied, *viz.* single channel, double channel and 20 channel systems (Figs 4, 5 and 6 respectively in their paper). In all cases we find that their results imply values of F greater than 0·5. On the other hand, our formula (Equation 6) shows that F should asymptotically tend to a maximum value of 0·5 at small periods (assuming that P is not so small that term C

*This term would be absent for the Jodrell Bank survey (Davies, Lyne and Seiradakis 1972, 1973) which tracked the search regions and would be more complicated for the Arecibo Survey (Hulse and Taylor 1974, 1975) where the effective area of the telescope is highly zenith-angle dependent,

becomes important). It thus appears that the I MS had a stronger dependence of $S_{\min}$ on D/P than we expect from our theory.

The discrepancy between the results of Large and Vaughan and our theory, is puzzling, since both refer to the same effect. We feel that it probably arises from the visual pulse-search method used in I MS to detect pulsars from chart records. Considering the complex pattern-recognition powers of the human eye it is quite possible that sensitivity falls off rapidly as the pulses are broadened. Our formula on the other hand refers to a computer search on digitized data, which could have totally different sensitivity characteristics. We show in the next section that the data from the II MS (which used a computer search technique) are in good agreement, with our theory.

3. Evidence from pulsar data

We have carried out some simple tests on pulsar observational data to confirm that the new selection effects discussed in the previous section really exist. The calculations have been done on the sample of pulsars detected by the II MS. This is the most recent as well as the most extensive of all the pulsar surveys, and yielded a total of 224 pulsars. In what follows, we assume that all pulsars have the same duty cycle d_0, for the following reasons. Firstly, we feel that duty cycles which are derived from pulse equivalent widths (W_e) may not be appropriate in Equation (6). Some calculations we have done using Equation (6) do indeed suggest that W_e is an unreliable parameter for our purposes here. Secondly, d is found to be almost independent of P; so this approximation will not introduce any *systematic* period-dependent effects into our results. Thirdly, the discussion in the previous section shows that the d-dependence in Equation (6) is likely to be weak in the majority of cases. We therefore replace d by d_0 in Equation (6) to obtain

$$S_{\min} = \beta S_0 (1 + T_{sky}/T_r) (1 + K_2 D/P)^{1/2} (\cos \delta)^{1/2} \tag{8}$$

where K_2 ($=K_1 / d_0$) is a constant.

Figs 2 and 3 show the results of some tests we have carried out on the II MS data using the old (Equation 1) and new (Equation 8) formulae for the selection effects. In Fig. 2(a) we have plotted the number of pulsars detected (N_0) against a normalized flux X (derived from Equation 1).

$$X = S/\{\beta (1 + T_{sky}/T_r) (1 + D/D_0)^{1/2}\}. \tag{9}$$

The pulsars have been sorted into bins of width 0·2 in $\log_{10} X$. Fig. 3(a) shows results using a similar definition of X based on Equation (8). In both Figs 2(a) and 3(a) N_0 decreases at high X because the pulsar number density itself decreases at higher luminosities. N_0 also decreases for low values of X (below S_0) because of the reduced sensitivity of the survey. Under ideal conditions, this transition should be quite sharp, around $X = S_0$. However, in actual practice it is broadened. Firstly, there is a statistical broadening caused among other things by the variability of pulsar luminosities (*cf.* Krishnamohan 1981). Secondly any unaccounted selection effect

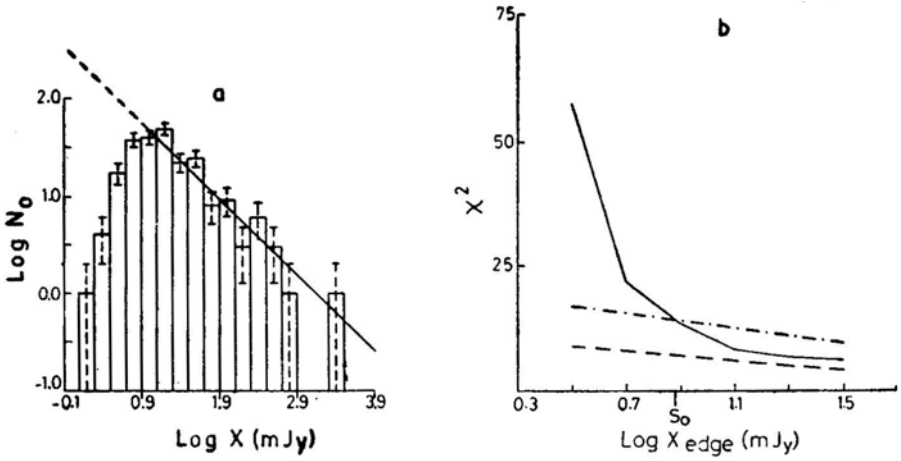

Figure 2. (a) Histogram of observed number of pulsars (N_0) against normalized flux $X = S/\{\beta\ (1 + T_{sky}/T_r)\ (1+ D/D_0)^{1/2}\}$.. The error bars represent variance at the level of one Standard deviation ($= \sqrt{N_0}$). The solid line is the least-squares fit of a straight line to the data in the descending limb of the histogram and gives the expected number of pulsars (N_e). The dashed line is its extrapolation, (b) Plot of x^2 obtained by fitting the curve $N_e = {}_\alpha X^{-\beta}$ to the descending limb in Fig. 2(a) (solid line), along with the expected value (dashed line) and its 95 per cent confidence upper bound (chained line). X_{edge} is the lowest X value used in the curve fitting. The x^2 increases rather abruptly from its normal value around $X_{edge} = S_0$, showing that the curve fitting has broken down.

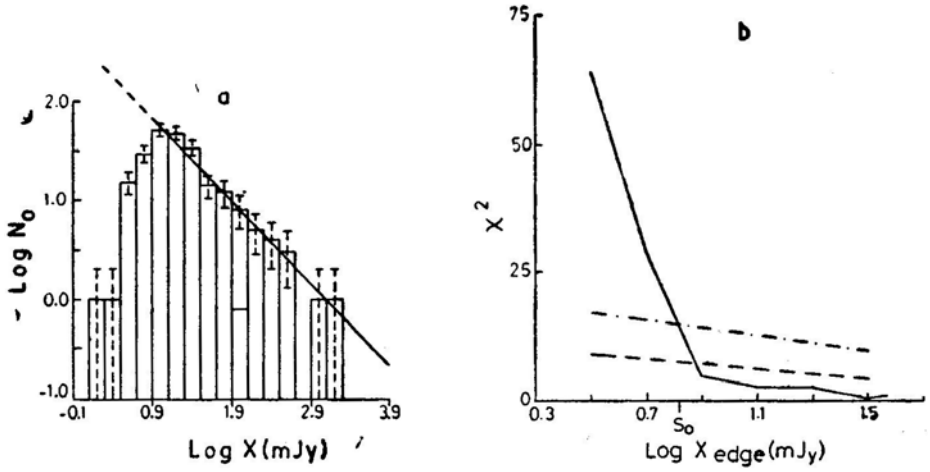

Figure 3. Same as in Fig. 2, with $X = S/\{\beta(1 + T_{sky}/T_r)\ (1 + K_2D/P)^{1/2}\ (\cos\ \delta)^{1/2}\}$.

would broaden the transition. The width of the transition region σ_{tr} can therefore be used to decide which of Equations (1) and (8) fits the II MS data better.

Another test is the number of pulsars below $X = S_0$, As mentioned before, under ideal conditions the transition region is very sharp and there will be no pulsars below S_0. Any selection effect tends to smear out S_0 so that there are now pulsars below it.

To carry out the above tests we had first to determine S_0 for Equations (1) and (8). This was done as follows. Starting with Fig. 2(a), we initially assumed a certain value of X on the descending limb of N_0 *vs* X to be S_0. We took all bins above this

value of X (we shall call it X_{edge}) and fitted a curve of the form $N_e = {}_{\alpha} X^{-\beta}$ (suggested by the actual data) by least squares. This curve gives the expected number of pulsars N_e at each X. We computed a X^2 as

$$\chi^2 = \sum \{(N_0 - N_e)^2/N_e\} \tag{10}$$

where the summation is over all bins above X_{edge}, and used it as a measure of the goodness of the curve fit. We repeated this exercise for successively lower values of X_{edge} where the fit becomes progressively poorer since one begins to include data from the transition region also. In Fig. 2(b) we have plotted χ^2 as a function of X_{edge} along with the expected χ^2 (which is the number of bins above X_{edge} minus two, for two parameters fitted) and the 95 per cent confidence upper bound on the expected χ^2. The observed χ^2 is normal at large X_{edge} and increases rapidly at smaller values, as expected. By interpolation, we obtained the value of X_{edge} where the observed χ^2 just equals the 95 per cent confidence upper bound. At this value of X_{edge} the curve fitting is seen to definitely break down. We adopted this value of X_{edge} as S_0 Although this approach tends to underestimate S_0, it has the important merit of being an objective way of analysing the data. We obtain S_0 = 7·6 mJy, or βS_0 = 7·9 mJy, which is close to the quoted value of 8·0 mJy. We interpret this agreement as lending support to the validity of our approach. A similar exercise with Fig. 3(a) gives S_0 = 6·6 mJy.

We then computed the width of the transition region in Fig. 2(a) using the estimate

$$\sigma_{tr}^2 = \sum \{f_i (\log X_i - \log S_0)^2\} \Big/ \sum f_i \tag{11}$$

where $f_i = N_0/N_e$ is the weight in each bin. The summation in Equation (11) is taken over all bins below S_0. We obtain σ_{tr} = 0·20. For Fig. 3(a) we get σ_{tr}=0·15. Comparing the results of Figs 2 and 3 we see that (i) the width of the transition region is reduced by incorporating the period and declination dependent selection effects through Equation (8) and (ii) there are 60 pulsars below S_0 in Fig. 2(a) but only 33 in Fig. 3(a). Both these results support our contention that Equation (8) is a better representation of the selection effects in the II MS than Equation(1).

Finally, we have repeated the calculations of Table 1 using Equation (8) with S_0 = 6·6 mJy, instead of Equation (1) with S_0 = 8 mJy. The results are shown in Table 2. The values of σ quoted are not equal to the corresponding $n_e^{1/2}$ but have been computed by including the fluctuations as well as the correlations of all the variables entering in $(n_0 - n_e)$. We have computed a χ^2 using the estimate

$$\chi^2 = \sum_{i=1}^{3} \{(n_0 - n_e)^2/\sigma_i^2\} \tag{12}$$

where the summation extends over all bins. We obtain χ^2 =5·0 in Table 2(a) and χ^2=1·2 in Table 2(b) as against the expected value of 3. In both cases there is a clear improvement over the results of Table 1.

The various tests described above would appear to confirm the presence of the period-dependent and declination-dependent selection effects in the II MS. However, because of the noisy data, we believe the strongest argument is really the discussion of Section 2 which says such effects must exist.

Table 2. Each column shows (i) observed number of pulsars (n_0) with $S_{pulsar}/S_{min} < 1{\cdot}0$, (ii) all pulsars in that bin ($n_0 + m_0$), (iii) expected number (n_e) in that bin, (iv) the difference ($n_0 - n_e$), and (v) standard deviation (σ) on $n_0 - n_e$. S_{min} was derived using Equation (8).

	(a) Pulsars in bins of period (in seconds):			(b) Pulsars in bins of declination:		
	$0{\cdot}0 \leqslant P < 0{\cdot}5$	$0{\cdot}5 \leqslant P < 1{\cdot}0$	$1{\cdot}0 \leqslant P < 1{\cdot}5$	$0° \leqslant \delta < 30°$	$30° \leqslant \delta < 60°$	$60° \leqslant \delta < 90°$
n_0	6	15	5	15	11	7
$n_0 + m_0$	76	89	40	97	89	38
n_e	9·6	11·3	5·1	14·3	13·1	5·6
$n_0 - n_e$	−3·6	3·7	−0·1	0·7	−2·1	1·4
σ	2·3	2·4	1·9	2·6	2·6	2·0

4. Implications for injection

VN (1981) based their statistical study of pulsar data on the current J_p of pulsars (number of pulsars yr^{-1} galaxy^{-1} 'flowing' along the P-axis) in various bins of period (0·0 to 0·5 s, 0·5 to1·0 s, *etc.*). They computed J_p using the equation

$$J_p = \sum_i \dot{P}_i \, S(L_i) \tag{13}$$

where $\dot{P}$ are the observed period derivatives and $S(L_i)$ are derived scale factors, which account for radio-luminosity selection effects. The summation in Equation (13) is over all pulsars in a given period bin. VN showed that the current averaged between 0·0 s to 0·5 s is significantly lower than that averaged between 0·5 s to 1·0s. Since this has important implications for the understanding of pulsars, in this section we investigate whether the result is qualitatively altered when the new P-dependent and δ-dependent selection effects are included.

We have recalculated $S(L)$ using Equation (8) (by means of the Monte Carlo technique employed by VN) and obtained new scale factors $S(L, P)$, which are now a function of both luminosity and period. The ratios of the new to old scale factors are, on the average, higher by 18 per cent in the first period bin ($0 \leqslant P < 0{\cdot}5$) and by 6 per cent in the second bin ($0{\cdot}5 \leqslant P < 1{\cdot}0$), both compared to longer period bins. Obviously these changes will not affect the substantial injection noted by VN. For further confirmation, we have repeated the injection calculations for II MS pulsars alone using Equation (8) with $S_0 = 6{\cdot}6$ mJy and assuming $d = d_0$. Fig. 4 shows the mean currents we now obtain in the various bins of P. We have here included a few additional pulsars whose $\dot{P}$ values have recently been measured with improved accuracy. It will be noticed that the currents in the first two bins continue to differ significantly. In spite of the large (95 per cent confidence) error bars, it is still quite apparent that these two currents are unlikely to be equal. We thus conclude that the new period selection effect modifies the earlier injection result only marginally.

At this stage it is worth investigating if there could be any other period-dependent selection effect not yet identified. A somewhat remote possibility lies in the measurement of $\dot{P}$ values.. While the detection of a pulsar is independent of its $\dot{P}$, the later estimation of $\dot{P}$ with any significance becomes increasingly difficult at lower values of

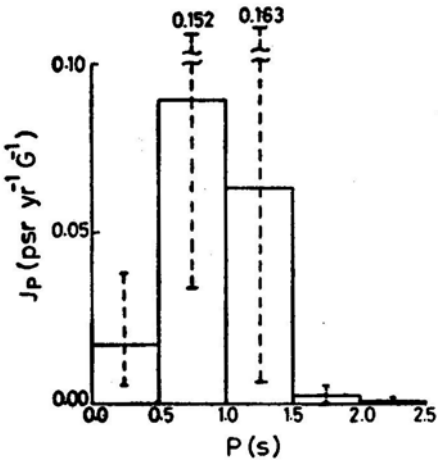

Figure 4. Mean pulsar current in bins of period for the II Molonglo Survey using Equation (8) for $S_{\min}$ (see VN for details). The current in the second bin is significantly higher than the current in the first bin, showing that injection exists in spite of the extra selection effects. The error bars represent 95 per cent confidence limits.

$\dot{P}$. Now, in the list of pulsars used for the injection calculation of Fig. 4, there are some whose $\dot{P}$ values are yet to be determined reliably. It would be interesting to know how these $\dot{P}$ values, if and when they are measured, would affect the results. We have tried to estimate this effect by binning the non-$\dot{P}$ pulsars belonging to the II MS in the same period bins as in Fig. 4. We find that the histogram of non-$\dot{P}$ pulsars is quite similar to that of the rest of the pulsars whose $\dot{P}$ are known, showing that there is no obvious period-dependence. In addition, the missing $\dot{P}$ values are more likely to be of lower magnitudes, and we have verified that the mean scales of these pulsars are approximately in the same proportions as the currents in Fig. 4. We therefore expect the effect to be marginal.

To summarize the results of this paper :

1. The period-dependent selection effect Equation (8) has been shown to exist, and the II MS data show some evidence for it. We believe the evidence is not as strong as one might like because of the small numbers we are dealing with. In addition, the II MS also shows a declination-dependent selection effect. On the other hand, there appears to be no reason to fear a period-dependent selection effect arising from the lack of measured $\dot{P}$ for some pulsars.

2. The 'injection' of pulsars pointed out by VN is affected only marginally by the additional selection effects discussed here. The qualitative result is unaltered and awaits an explanation in terms of pulsar physics.

Acknowledgements

We thank Rajaram Nityananda for many useful discussions and, in particular, for suggesting some of the tests in Section 3, and C. J. Salter for numerous suggestions to

improve the manuscript. We also thank the referee for drawing our attention to the work of Large and Vaughan (1971) who had earlier investigated one of the effects we have considered here.

References

Davies, J. G., Lyne, A. G., Seiradakis, J. H. 1972, *Nature*, **240,** 229.
Davies, J. G., Lyne, A. G., Seiradakis, J. H. 1973, *Nature*, *Phys. Sci.*, **244,** 84.
Huguenin, G. R. 1976 in *Methods of Experimental Physics.* Ed. M. L. Meek, Vol. 2, Part C, Academic Prees, New York, p. 78.
Hulse, R. A., Taylor, J. H. 1974, *Astrophys. J.*, **191,** L59.
Hulse, R. A., Taylor, J. H. 1975, *Astrophys. J.*, **201,** L55.
Krishnamohan, S. 1981, *Mon. Not. R. astr. Soc.*, **197,** 497.
Large, M I., Vaughan, A. E. 1971, *Mon. Not. R. astr. Soc.*, **151,** 277.
Manchester, R. N., Lyne, A. G., Taylor, J. H., Durdin, J. M., Large, M. I., Little, A. G. 1978, *Mon. Not. R. astr. Soc.*, **185,** 409 (II MS).
Taylor, J. H., Manchester, R. N. 1977, *Astrophys. J.*, **215,** 885.
Vivekanand, M., Narayan, R. 1981, *J. Astrophys. Astr.*, **2,** 315 (VN).

J. Astrophys. (1982) 3, 249–266

Eclipse Observations of Coronal Emission Lines. I. [Fex] 6374Å Profiles at the Eclipse of 16 February 1980

Jagdev Singh, M. K. V. Bappu* and A. K. Saxena
Indian Institute of Astrophysics, Bangalore 560034

Received 1982 May 19; accepted 1982 June 28

Abstract. Coronal spectra during the total solar eclipse of 1980 February 16, were obtained in the 6374Å [Fex] line using a multislit spectrograph. These spectra have a dispersion of 2·5 Å mm^{-1}. The observed line profiles from 1·1 to 1·7 $R_\odot$ with a spatial resolution of 10 × 22 $arcsec^2$, give half-widths that vary between 0·6 Å and 2·4Å. A large number of locations have half-widths around 1·3 Å corresponding to a temperature of 4·6 × 10^6 K. If temperature of the order of 1·3 × 10^6 K are typical of the regions that emit [Fex], then turbulent velocities of ~ 30 km s^{-1} need to be invoked for the enhanced line broadening. The line-of-sight velocities measured range between +14 km s^{-1} to –17 km s^{-1} . Most of the locations have velocities less than ±5 km s^{-1}. From these observations we conclude that corona does not show any localized differential mass motion and that it co-rotates with the photospheric layers deeper down.

Key words: Solar corona — red coronal line — turbulent velocities — rotation of solar corona

1. Introduction

Much information on the physical characteristics of the solar corona can be evaluated from the study of emission-line profiles of the forbidden lines in the coronal spectrum at a total solar eclipse. They permit us to determine the spatial dependence of kinetic temperature or the influence of turbulent velocities that contribute to the enhanced broadening of the line profile. Such studies help us attain an improved understanding of the coronal heating mechanism and the gradients of temperature that contribute to solar wind outflow. The advantage of the total eclipse lies in providing a minimum of scattered-light background and Fraunhofer-line contamination, factors that normally restrict the coronagraph in providing similar information with the aid of an artificial eclipse.

*Deceased on 1982 August 19

Line-profile measures for temperature evaluation have in the recent past been used mostly with coronagraphs. At eclipses, such measures have almost exclusively been carried out with Fabry-Perot interferometers both in the two-dimensional mode by photographic techniques and at a few specific locations by photoelectric scan methods. Such slitless evaluations pioneered by Jarrett and von Klüber (1955, 1961) have been used at subsequent eclipses by Delone and Makarova (1969), Marshall and Henderson (1973), Liebenberg, Bessey and Watson (1975) and Chandrasekhar, Desai and Angreji (1981). The Fabry-Perot instrumentation has the advantage of simultaneous registration of interference fringes over most of the corona, from which a line profile can be evaluated; the disadvantage is the uncertainty of the contribution by Doppler-shifted elements to the line profile and which is inherent in a slitless mode. Such limitations are absent in a slit survey, since the finite width of the slit samples a limited areal extent of the corona. On the other hand, the slit permits the acquisition of information only along the coronal emission regions intercepted by its length, and hence the multiplicity of spatial information collected by the Fabry-Perot technique is missing. Procedures to minimize this handicap, however, do exist and have been used for other purposes at recent solar eclipses (Livingston, Harvey and Doe 1970). The multislit technique has been used by the Kitt Peak investigators only for measures of coronal rotation. It is, however, a technique that can be used to provide a good two-dimensional coverage of the corona by judicious choice of instrumentation and spatial sequencing at the eclipse and has all the advantages to offer which standard slit spectroscopy does over its slitless counterpart.

2. Instruments

An objective of 14 cm aperture and 140 cm focal length formed an image of the sun on the multislit spectrograph. The doublet was corrected for the 6500Å region and was fed by a single mirror 45-cm coelostat with Zerodur optics, and a well-regulated stepper-motor friction drive. The multislit spectrograph functioned in the Littrow mode with a 600-line grating that gave a dispersion of 2·5 Å mm^{-1} in the fourth order red. Four entrance slits, each separated by 5 mm from its neighbour, together formed the multislit. The slits, therefore, were spaced 12·3 arcmin on the solar image. An interference filter of 9·5Å pass-band and peaked at 6374 Å was used in front of the multislit. In the Littrow focal plane, four spectra originating from the multislit each about 10 Å in width—were stacked side by side on the photocathode of a single-stage Varo image intensifier. The image intensifier has a gain of 20 and an effective aperture of 30 mm. A plate-holder magazine enabled rapid change-over of the emulsion that had to be in contact with the fibre-optic faceplate. Each spectrum has a neon comparison. Since these spectral lines were not filtered by the interference filter, there were many lines from overlapping orders available that permitted velocity measurements by comparison.

3. Observations

Two of the three plates exposed during the total phase of the eclipse have been used in this study. The third had to be discarded because of excessive tube back-

ground that had accumulated by virtue of the hot afternoon and the fact that the image tube had been turned on in readiness for the event several minutes before totality. The exposures used were both of 45 s duration and enabled emission lines to be detected to distances as far as 1·7 $R_{\odot}$. Between the first and second exposures, the solar image was shifted through 4·5 arcmin along the axis of rotation in order to sample a new set of coronal regions with the multislit. The orientation of the multislit was along position angle 89·5°. The spectra were exposed on Eastman 103a-D emulsion and developed in D-19 at 20°C for five minutes together with the step-wedge calibration obtained immediately after the eclipse with the same spectrograph. Neon spectra obtained along the entire length of the four slits permitted the evaluation of the instrumental line profiles at several points of each slit. We show in Fig. 1 the values of full width at half maximum (FWHM) of these instrumental line profiles at several points on each slit and the final mean value assigned to each for determination of coronal line widths.

Microphotometer scans of these spectra have been obtained with a projected slit size of 4·5 × 22 arcsec^2 on the plate. Successive scans have been made that were separated by 30 arcsec along the slit. This spacing had to be increased to 45 or 50 arcsec at locations where the ratio of maximum line intensity to continuum intensity was low. The transmission curve of the narrow interference filter was evaluated with the aid of the solar spectrum and the Kodaikanal 18-m spectrograph. Working at a

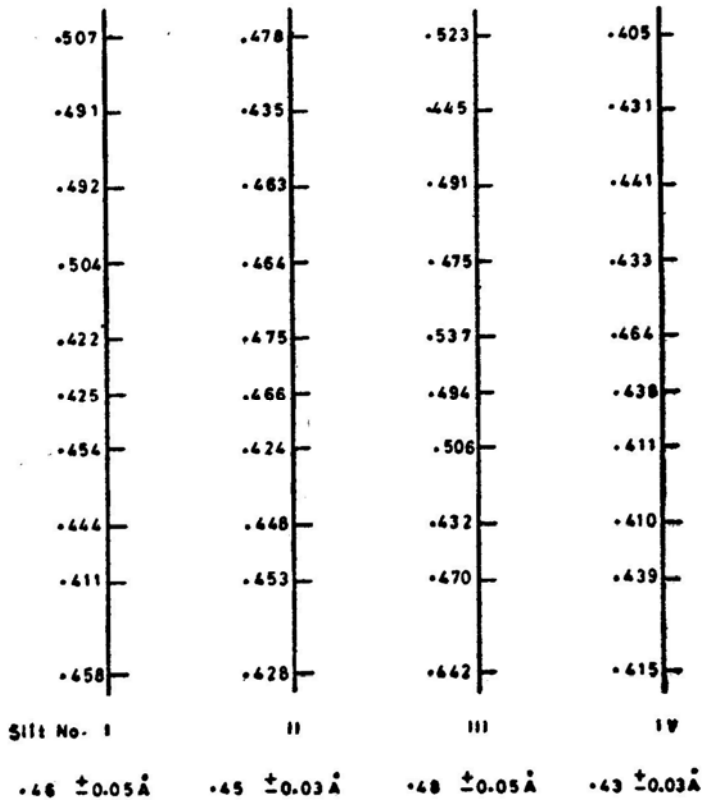

Figure 1. Full width at half maximum of instrumental line profile at various locations on the slits. Mean value is indicated below each slit.

dispersion of 9 mm $Å^{-1}$, transmission spectra through several different regions of the interference filter—each spaced 5 mm from its neighbour, have been used in the evaluation of the average filter characteristic. The normalized mean transmission curve of the filter thus obtained is used to operate on the intensity curve of the red coronal line, as evaluated at each point along the slit (Fig. 2). The procedure gives the observed profile of the coronal line. The FWHM is corrected for instrumental line-width using the data of Fig. 1 and the assumption that both profiles are gaussian.

Image-tube spectra usually call for extra precautions in radial-velocity measurements over those photographed directly, due to the pin-cushion effect of the image intensifier. We have used the full-length neon spectra and made dispersion measures at several points along the length in terms of a fiducial reference of a cross hair placed against the slits during the eclipse and the measures that followed immediately after. The 6374Å line was flanked on either side by the neon lines 8495·36Å (third order spectrum) and 6382·99Å of the normal fourth order. The Doppler displacements of the line as a whole were evaluated from microphotometer scans that included the neon comparison lines as well. The velocity measures were spaced 30 arcsec along each slit.

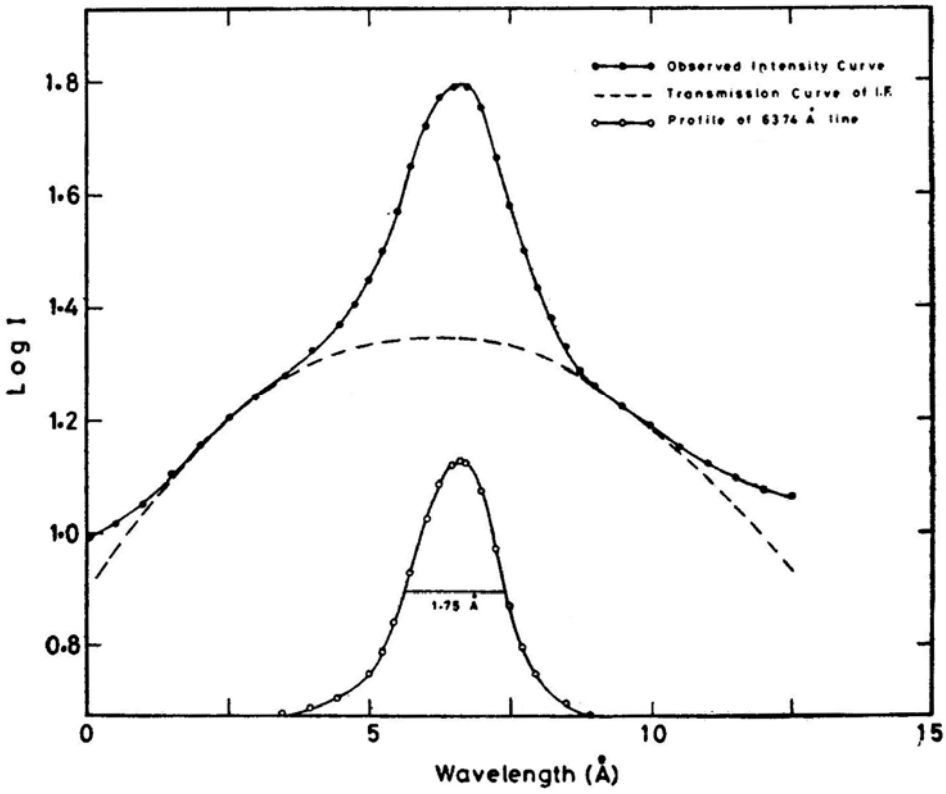

Figure 2. A typical line profile of [Fe x] 6374Åat one of the locations of .corona is shown. Full line is a plot between log *I* and wavelength whereas the dotted one is the transmission curve of the interference filter on the same scale. Shown below is the line profile plotted as intensity versus wavelength, after correction for the transmission of the interference filter.

4. Results

We have measured the widths of the red coronal line at 236 locations in the solar corona. These locations range from 1·1 $R_\odot$ to 1·7 $R_\odot$ and aim to give a satisfactory coverage all around the solar limb. The data are presented in Table 1. The position angle measured from the north point of the projected axis of solar rotation and the radial distance from the centre of the disc are given in Columns (2) and (3). The values of FWHM are in Column (4) While those in Column (5) express turbulent velocities derived by assuming the temperature of corona to be 1·3 × 10^6 K. In Columns (6) and (7) we give the peak brightness of the continuum at the line centre as well as the peak brightness of the line. This is expressed as a ratio in Column (8) and serves to portray the localized enhancements of the line emission to that of the background K corona.

Table 1. Line widths, intensities and turbulent velocities derived from the red coronal line.

No.	Position angle θ	$R/R_\odot$	FWHM Å	V_t km s^{-1}	I_c	I_{max}	$\frac{I_{max}}{I_c}$
(1)	(2)	(3)	(4)	(5)	(6)	(7)	(8)
				Slit IV (1)			
1	322·9	1·437	1·34	29	19	34	1·79
2	323·4	1·428	1·40	32	18	32	1·78
3	323·9	1·418	1·11	19	22	42	1·91
4	324·4	1·409	1·12	20	19	41	2·16
5	324·9	1·400	1·23	25	25	47	1·88
6	325·4	1·391	1·29	28	23	46	2·00
7	325·9	1·382	1·30	28	29	53	1·83
8	327·0	1·365	1·33	29	31	47	1·52
9	328·1	1·349	1·23	25	47	66	1·40
10	329·2	1·332	1·41	32	54	74	1·37
11	330·3	1·317	1·37	30	59	80	1.36
12	331·5	1·301	1·44	33	67	90	1·34
13	332·7	1·287	1·44	33	68	93	1·37
14	333·9	1·273	1·18	23	77	102	1·32
15	335·2	1·259	1·33	29	81	105	1·30
16	335·5	1·246	1·39	31	83	107	1·29
17	337·8	1·234	1·29	27	91	111	1·22
18	339·1	1·222	0·92	9	98	119	1·21
19	340·5	1·212	1·10	19	101	118	1·17
20	341·8	1·202	1·21	24	105	125	1·19
21	40·0	1·475	1·27	26	22	36	1·64
22	39·1	1·456	1·04	17	22	37	1·68
23	38·1	1·437	1·02	15	25	40	1·60
24	37·1	1·418	1·07	18	28	42	1·50
25	36·1	1·400	1·33	29	31	42	1·35
26	35·1	1·383	1·40	31	34	43	1·26
27	34·0	1·365	1·44	33	39	48	1·23
28	32·9	1·349	1·21	24	43	52	1·21
29	31·8	1·332	1·22	25	48	62	1·29
30	30·7	1·317	1·20	24	53	67	1·26
31	29·5	1·302	1·65	40	57	72	1·26
32	28·3	1·287	1·55	36	62	77	1·24
33	27·1	1·273	1·23	25	74	85	1·15
34	25·8	1·259	1·09	19	79	91	1·15
35	24·5	1·247	1·16	22	85	100	1·18

Table 1. Continued.

No.	Position angle θ	$R/R_\odot$	FWHM Å	V_t kms^{-1}	I_c	I_{max}	$\frac{I_{max}}{I_c}$
(1)	(2)	(3)	(4)	(5)	(6)	(7)	(8)
36	23·2	1·234	1·46	33	89	102	1·15
37	21·9	1·223	1·18	23	94	113	1·20
38	20·5	1·212	1·36	30	96	111	1·16
39	19·2	1·202	1·35	29	106	132	1·25
40	17·8	1·192	1·04	17	108	140	1·30
41	15·6	1·179	1·47	34	107	168	1·57
			Slit IV (2)				
42	308·4	1·403	0·98	13	21	26	1·24
43	310·0	1·355	0·76	1	30	38	1·27
44	312·6	1·285	0·96	12	43	52	1·21
45	313·5	1·263	1·28	27	32	48	1·50
46	314·5	1·240	1·39	31	35	58	1·66
47	315·5	1·218	1·34	29	41	68	1·66
48	316·5	1·197	1·45	33	47	78	1·66
49	318·2	1·165	1·23	25	65	99	1·52
50	319·9	1·134	0·67	0	90	207	2·30
51	322·4	1·096	1·10	19	116	299	2·58
52	324·3	1·068	1·67	40	148	407	2·75
53	56·8	1·553	1·33	29	10	13	1·30
54	56·2	1·528	1·43	32	12	16	1·33
55	55·5	1·502	1·27	26	12	17	1·42
56	54·8	1·477	1·31	28	16	23	1·44
57	54·1	1·452	1·26	26	19	27	1·42
58	53·4	1·428	1·17	22	22	33	1·50
59	52·6	1·403	1·29	27	20	44	2·20
60	51·8	1·379	1·59	38	26	48	1·85
61	51·0	1·355	1·33	29	28	53	1·89
62	50·2	1·332	1·31	28	35	57	1·63
63	49·3	1·308	1·18	23	41	67	1·63
64	48·4	1·285	1·26	26	50	73	1·46
65	47·5	1·263	1·35	29	57	77	1·35
66	46·5	1·240	1·34	29	71	89	1·25
67	45·5	1·218	1·27	26	77	87	1·13
68	44·5	1·197	1·25	26	86	98	1·14
69	43·4	1·176	1·23	25	96	112	1·17
70	42·3	1·155	0·72	0	108	146	1·35
71	41·1	1·135	1·02	15	125	327	2·62
72	39·9	1·115	1·42	32	137	426	3·11
			Slit III (1)				
73	283·9	1·660	2·37	62	8	11	1·38
74	284·2	1·623	1·41	32	10	13	1·30
75	284·5	1·586	1·47	34	10	13	1·30
76	285·0	1·541	1·71	42	14	20	1·43
77	285·3	1·511	1·80	45	14	21	1·50
78	285·6	1·481	1·83	46	17	24	1·41
79	285·9	1·452	1·75	43	21	31	1·48
80	286·2	1·422	1·52	35	28	43	1·54
81	286·5	1·393	1·58	37	35	51	1·46
82	286·9	1·363	1·54	36	41	65	1·59
83	287·4	1·326	1·72	42	53	81	1·53
84	287·9	1·289	1·55	36	71	104	1·46
85	288·3	1·260	1·34	29	85	140	1·65

Table 1. Continued.

No.	position angle θ	$R/R_\odot$	FWHM Å	V_t km s^{-1}	I_c	I_{max}	$\frac{I_{max}}{I_c}$
(1)	(2)	(3)	(4)	(5)	(6)	(7)	(8)
86	76·3	1·571	1·73	42	8	12	1·50
87	76·0	1·541	1·42	32	8	13	1·63
88	75·8	1·511	1·64	40	9	16	1·78
89	75·3	1·467	1·65	40	11	24	2·18
90	75·0	1·437	1·64	40	13	34	2·62
91	74·6	1·407	1·72	42	17	45	2·65
92	74·1	1·363	1·75	43	22	62	2·82
93	73·7	1·334	1·93	49	28	78	2·79
94	73·3	1·304	2·18	57	34	89	2·62
95	72·9	1·275	2·32	61	45	106	2·36
96	72·5	1·245	2·15	56	57	127	2·23
97	72·1	1·216	2·12	55	68	151	2·22
			Slit III (2)				
98	274·4	1·573	1·10	19	6	9	1·50
99	274·5	1·542	1·65	40	6	10	1·67
100	274·6	1·511	1·47	34	7	11	1·57
101	274·7	1·481	1·02	15	9	13	1·44
102	274·8	1·450	1·45	33	10	17	1·70
103	274·9	1·419	1·28	27	12	22	1·83
104	275·0	1·389	1·31	28	16	28	1·75
105	275·1	1·358	1·30	28	22	36	1·64
106	275·2	1·327	1·52	35	28	44	1·57
107	275·3	1·297	1·47	34	35	55	1·57
108	275·4	1·266	1·25	26	50	74	1·48
109	275·5	1·235	1·40	31	71	90	1·27
110	275·6	1·205	1·38	30	86	113	1·31
111	275·8	1·174	0·96	12	106	202	1·91
112	275·9	1·143	1·57	37	132	424	3·21
113	87·0	1·788	1·31	28	5	8	1·60
114	86·9	1·711	0·74	1	6	9	1·50
115	86·7	1·634	1·39	31	7	10	1·43
116	86·6	1·604	0·96	12	7	14	2·00
117	86·6	1·573	1·03	16	9	16	1·78
118	86·5	1·542	1·39	31	8	18	2·25
119	86·4	1·512	1·30	28	10	25	2·50
120	86·3	1·481	1·24	25	10	31	3·10
121	86·2	1·450	1·47	34	12	38	3·17
122	86·1	1·419	1·45	33	14	48	3·43
123	86·0	1·389	1·54	36	19	65	3·42
124	85·9	1·358	1·68	41	25	79	3·16
125	85·8	1·327	1·89	48	36	92	2·56
126	85·7	1·297	1·94	49	37	113	3·05
127	85·6	1·266	1·10	19	56	200	3·57
128	85·5	1·235	1·01	15	70	248	3·54
129	85·4	1·205	1·24	25	93	492	5·29
130	85·2	1·174	1·27	26	104	441	4·24
131	85·1	1·144	1·71	42	124	452	3·65
			Slit II (1)				
132	257·6	1·657	1·92	48	9	11	1·22
133	257·3	1·620	1·28	27	9	10	1·11
134	257·0	1·582	1·79	44	11	13	1·18
135	256·6	1·537	1·19	23	13	17	1·31
136	256·3	1·507	1·56	37	14	19	1·36

Table 1. Continued.

No.	Position angle θ	$R/R_\odot$	FWHM Å	V_t km s^{-1}	I_c	I_{max}	$\frac{I_{max}}{I_c}$
(1)	(2)	(3)	(4)	(5)	(6)	(7)	(8)
137	256·0	1·478	1·62	39	18	22	1·22
138	255·7	1·448	2·00	51	21	26	1·24
139	255·4	1·418	1·81	45	31	38	1·23
140	255·1	1·388	1·88	47	39	46	1·18
141	254·7	1·359	1·81	45	52	60	1·15
142	254·3	1·322	1·65	40	72	79	1·10
143	253·8	1·285	1·51	35	93	100	1·08
144	253·4	1·255	1·24	25	110	125	1·14
145	104·1	1·567	1·94	49	12	15	1·25
146	104·4	1·537	20·6	53	12	14	1·17
147	104·7	1·507	1·88	47	13	16	1·23
148	105·1	1·463	2·17	56	14	19	13·6
149	105·4	1·433	2·09	54	18	22	1·22
150	105·8	1·403	2·23	58	21	25	1·19
151	106·3	1·359	2·33	61	25	29	1·16
152	106·6	1·329	2·40	63	29	24	1·17
153	107·0	1·300	1·76	43	34	40	1·17
154	107·4	1·270	1·48	34	43	50	1·16
155	107·8	1·241	1·65	40	49	55	1·12
156	108·2	1·211	1·67	41	57	62	1·19
157	108·7	1·182	1·73	42	72	78	1·08
158	109·2	1·153	1·75	43	76	82	1·08
159	109·9	1·109	1·21	24	91	108	1·19
			Slit II (2)				
160	248·1	1·697	1·94	49	5	8	1·60
161	247·7	1·669	1·32	28	6	9	1·50
162	247·3	1·640	2·09	54	6	9	1·50
163	246·9	1·612	1·72	42	6	10	1·67
164	246·4	1·584	1·35	29	8	12	1·50
165	246·0	1·556	1·17	22	9	15	1·67
166	245·5	1·528	1·32	28	10	19	1·90
167	245·0	1·500	1·65	40	11	24	2·18
168	244·5	1·472	1·90	48	13	31	2·38
169	242·8	1·363	1·91	48	28	77	2·75
170	241·6	1·336	1·44	33	46	92	2·00
171	240·9	1·309	1·50	35	58	103	1·78
172	240·3	1·282	1·34	29	75	126	1·68
173	238·8	1·230	1·13	21	104	333	3·20
174	115·5	1·528	0·68	0	9	15	1·67
175	116·0	1·500	1·20	24	11	19	1·73
176	116·5	1·472	1·55	36	11	18	1·64
177	117·0	1·445	1·52	35	12	21	1·75
178	117·6	1·417	1·68	41	14	28	2·00
179	118·2	1·390	1·88	47	16	33	2·06
180	118·8	1·363	1·70	41	23	43	1·87
181	119·4	1·336	1·57	37	27	47	1·74
182	120·1	1·309	1·71	42	31	54	1·74
183	120·8	1·282	1·51	35	42	63	1·50
184	121·5	1·256	1·52	35	51	71	1·39
185	122·2	1·230	1·17	22	64	79	1·23
186	123·0	1·203	1·27	26	77	84	1·09
187	123·8	1·178	1·43	32	85	96	1·13
188	124·6	1·152	0·69	0	99	114	1·15
189	125·5	1·127	1·10	19	104	127	1·22
190	126·4	1·102	1·38	31	132	256	1·94

Table 1. Concluded.

No.	Position angle θ	$R/R_\odot$	FWHM Å	V_t km s^{-1}	I_c	I_{max}	$\frac{I_{max}}{I_c}$
(1)	(2)	(3)	(4)	(5)	(6)	(7)	(8)
				Slit I (1)			
191	218·5	1·425	2·05	53	40	46	1·15
192	217·5	1·406	2·03	52	42	48	1·14
193	216·5	1·388	1·91	48	48	55	1·15
194	215·4	1·370	2·06	53	49	55	1·12
195	214·4	1·353	1·21	24	53	58	1·09
196	213·3	1·336	1·64	40	53	58	1·09
197	212·2	1·319	2·04	52	57	61	1·07
198	209·2	1·281	1·18	23	66	68	1·03
199	146·1	1·361	1·54	36	17	21	1·24
200	148·8	1·319	2·21	58	20	25	1·25
201	151·8	1·280	2·14	55	26	30	1·15
202	154·9	1·245	2·10	54	32	41	1·28
203	158·2	1·214	2·32	61	47	54	1·15
204	161·6	1·187	1·71	42	62	68	1·10
205	168·9	1·147	1·52	35	93	100	1·08
				Slit I (2)			
206	213·9	1·677	1·35	29	12	17	1·42
207	213·0	1·660	0·72	0	12	18	1·50
208	212·1	1·644	1·23	25	12	17	1·42
209	211·2	1·628	1·61	39	12	16	1·33
210	209·8	1·605	1·44	33	13	19	1·46
211	208·3	1·583	1·42	32	15	22	1·47
212	206·3	1·555	1·45	33	16	25	1·56
213	204·8	1·535	1·28	27	19	26	1·37
214	203·2	1·517	1·56	37	21	28	1·33
215	201·0	1·495	1·31	28	24	28	1·17
216	199·3	1.479	1.10	19	26	32	1·23
217	197·6	1.465	1·32	28	29	36	1·24
218	195·3	1·448	1·74	43	30	38	1·27
219	193·5	1·437	1·25	26	34	38	1·12
220	191·7	1·427	1·54	36	34	40	1·18
221	189·3	1·416	1·72	42	35	41	1·17
222	187·4	1·410	1·20	24	38	41	1·08
223	185·5	1·405	1·03	16	42	45	1·07
224	183·0	1·401	1·10	19	43	54	1·26
225	181·1	1·400	1·28	27	42	50	1·19
226	156·3	1·536	1·13	21	9	10	1·11
227	158·9	1·506	1·33	29	10	13	1·30
228	161·1	1·484	1·72	42	12	16	1·33
229	162·8	1·469	1·23	25	15	20	1·33
230	164·6	1·456	1·68	41	18	23	1·28
231	166·9	1·440	1·36	30	24	32	1·33
232	168·7	1·430	1·45	33	28	36	1·29
233	170·5	1·421	1·93	49	31	38	1·23
234	172·4	1·414	1·23	25	31	40	1·29
235	174·2	1·408	1·52	35	31	39	1·26
236	179·2	1·400	0·96	12	38	42	1·11

4.1 *Line Widths*

The derived values of FWHM of the red coronal line varies between 0.6Å and 2.4 Å. The values at the different locations are depicted in Fig. 3. One can thus evaluate the association of any line widening with coronal form. When we plot a histogram of line-width dependence, as in Fig. 4, we find a predominance of values of FWHM

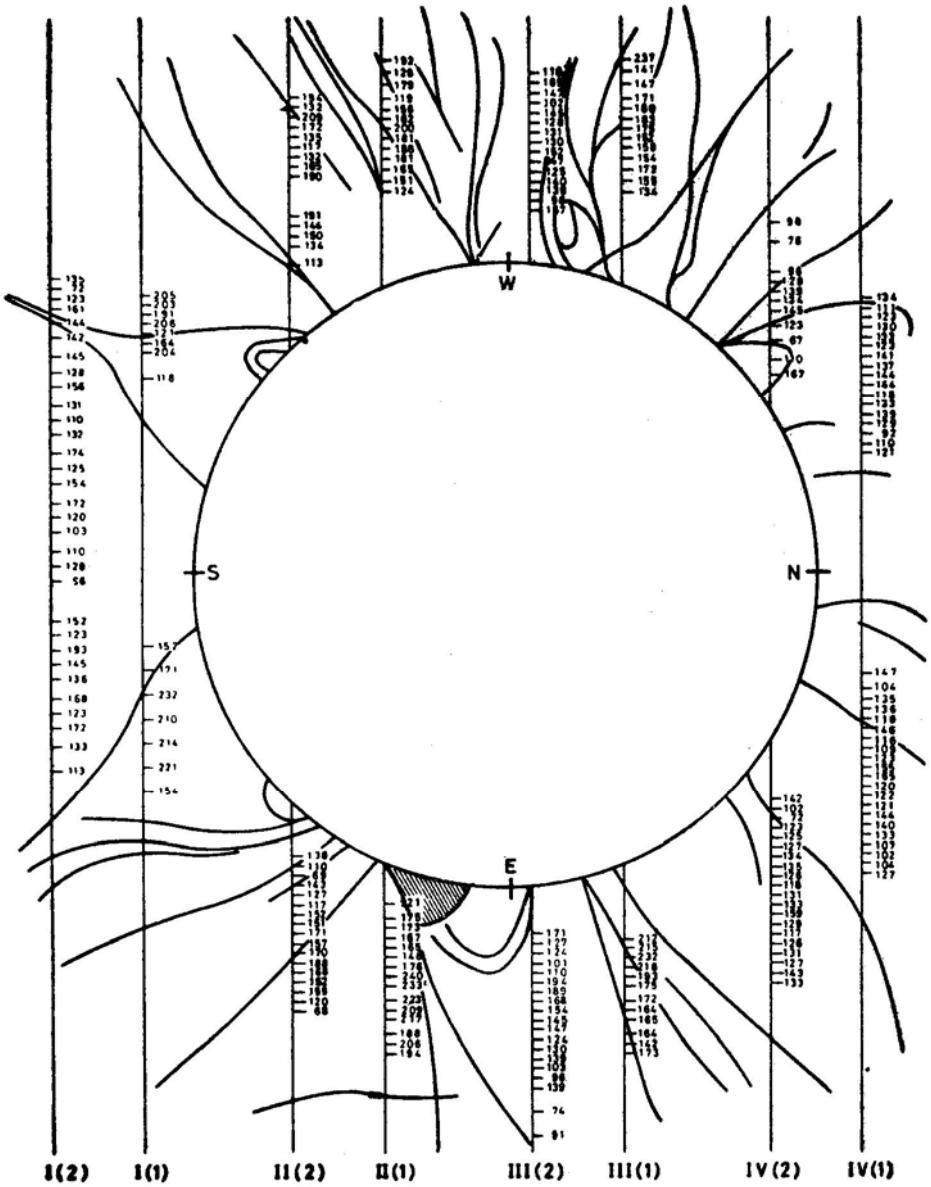

Figure 3. True line widths of [Fe x] 6374 Å line are written at various locations in Å × 10^{-2}. I(1), II(1), III(1) and IV(1) are the slit positions on solar disc with plate 1 and correspondingly with suffix 2 in bracket are due to plate 2. A sketch of white-light corona is super-imposed to compare the two. Shaded area on E-limb is an enhancement observed in white light corona and the horizontal line crossing slit positions II(2) and II(1) is the filament.

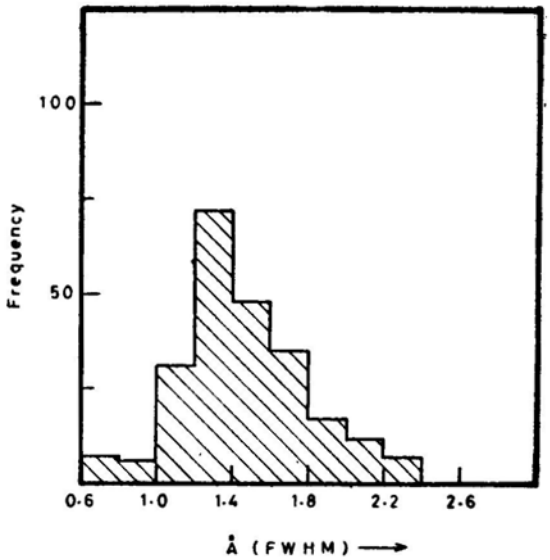

Figure 4. Frequency distribution of true line widths of [Fe x] 6374Å.

around 1·3 Å and an extended tail towards larger values. The lowest value of line width is 0·6Å If thermal broadening is the only contributor to line widths then with the aid of the standard kinetic-temperature formula one derives a temperature of $1{\cdot}2\times10^6$ K for a line width of 0·67 Å. The temperature assumes higher values, if one converts the peak of the FWHM of 1·3Å. The value is then $4{\cdot}6 \times 10^6$ K while the largest value of line width of 2·4Å represents even a higher value of temperature, if one interprets it to be so. Jordan (1969) had calculated the ionization equilibrium as a function of temperature for several of the ions commonly seen in eclipse spectra. Fe x is mostly available in the temperature zone 5×10^5–2×10^6, with a peak at $1{\cdot}3 \times10^6$K. It therefore becomes inadmissible to accept the high values of temperature inferred from line widths, especially for a relatively low temperature ion like Fe x. Therefore the need to assume an additional line-broadening agency seems necessary. Introducing a turbulence parameter in the equation, and assuming the ions of iron to be controlled by the peak value of $1{\cdot}3 \times10^6$ K (Jordan 1969), one finds turbulent velocities of 30 km s^{-1} from line broadening. The smallest values in the histogram of line widths seems to be representative of the state of ionization. The larger FWHM must necessarily signify the appreciable contribution to it by Doppler motion. An evaluation of this characteristic is extremely difficult. For, in the line of sight of an optically thin gas, we witness—besides the effects of thermal broadening—several other factors. The presence of broadening by random motions is clear. The value of 30 km s^{-1} is in good accord with that derived by Delone and Makarova (1969). The advantages of similar studies at future eclipses, based on simultaneous exposures of lines of at least two different atomic weights, are obvious.

4.2 *Line and Continuum Intensities*

Our measures of intensity, both at the peak of the line and at the underlying continuum, can be used for the study of gradients of both the emission corona and the K corona.

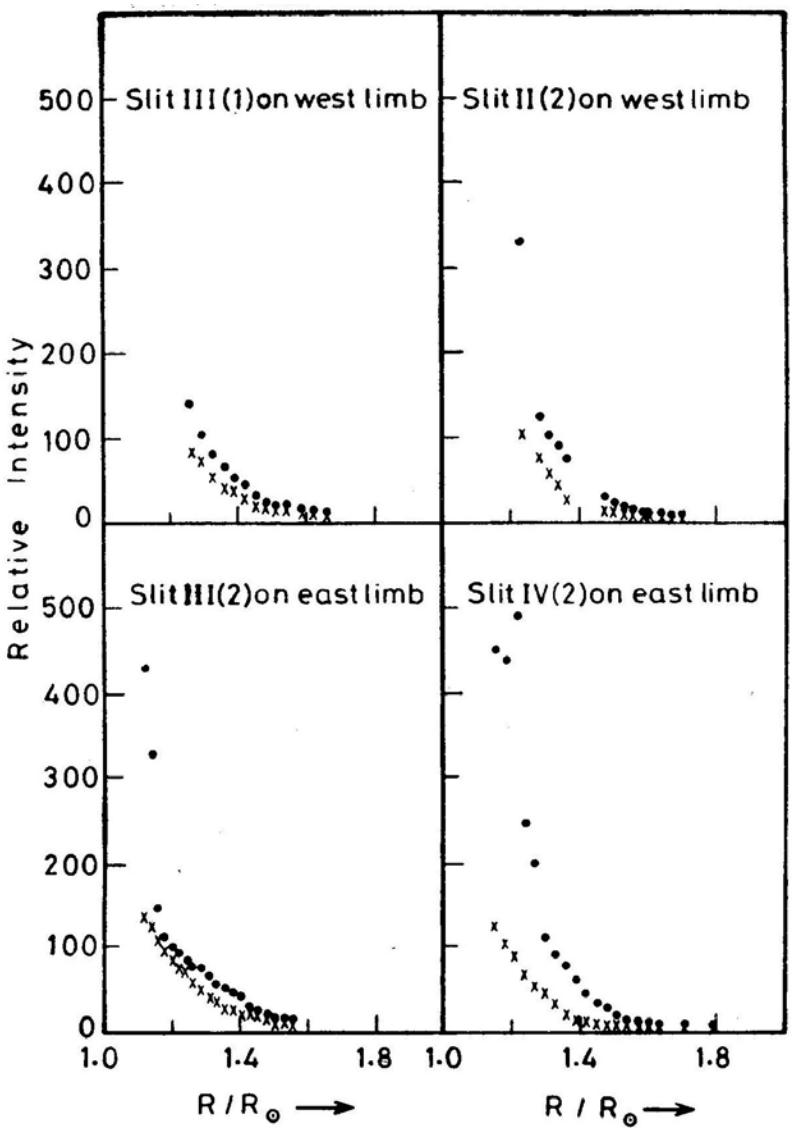

Figure 5. A plot of continuum (crosses) and the [Fe x] line (filled circles) intensity Versus radial distance.

The multislit arrangement covers several helmets and streamers and it is possible to choose those locations where the slit has an almost radial orientation. When we do this for the K corona along the locations (a) western part of slits II (2) and III (1) and (b) eastern part of slits III (2) and IV (2) as indicated in Fig. 3, we obtain gradients of intensity shown in Fig. 5 consistent with the trends known to exist in such features over a century of observing eclipses. Coronal emission-line intensities are the straight ratios of Column (8) in Table 1. These conform to the steep gradients of emission lines that we are familiar with. A logarithmic representation is seen in Fig. 6.

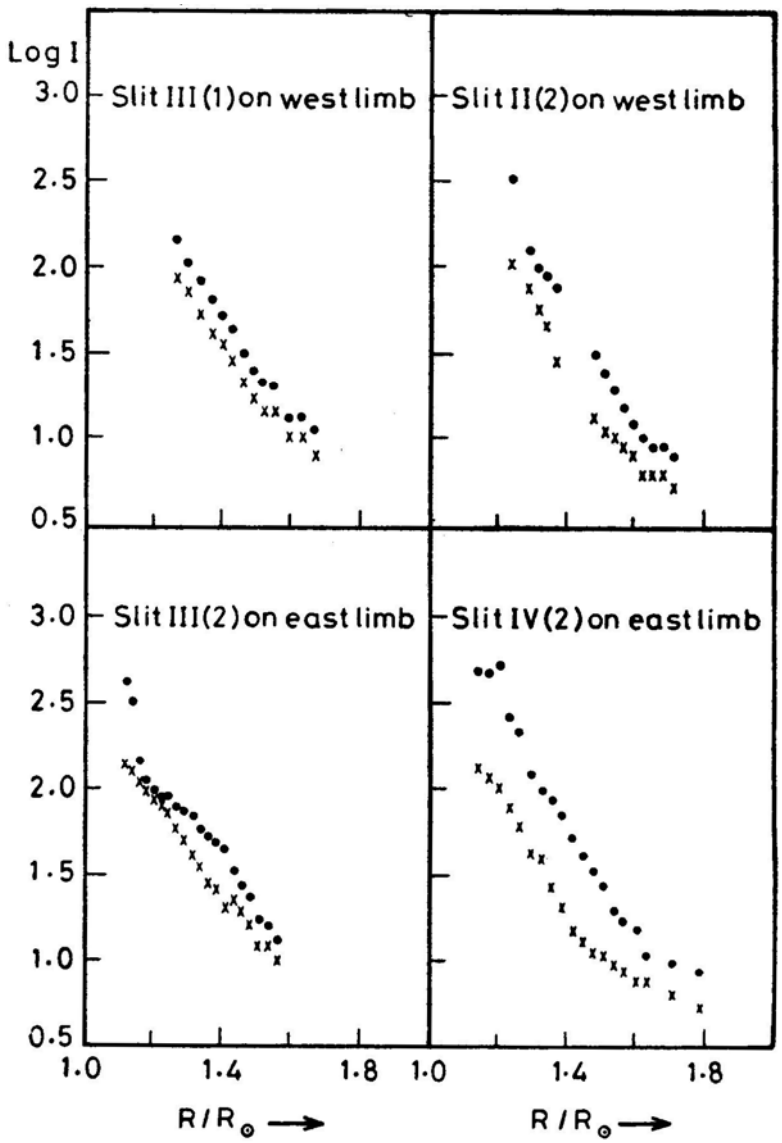

Figure 6. Logarithmic intensity of continuum (crosses) and the [Fe x] line (filled circles) versus radial distance.

4.3 *Coronal Hole and Transient*

A noticeable coronal hole near the south pole was one of the striking features of the 1980 eclipse. We have several measures that cover the position angle range 170°–190°. The tangential slit position restricts the $R/R_{\odot}$ values from 1·43 to 1·53. A noticeable characteristic of the line widths is that a majority of them have small values. We interpret this to mean that the random motions sampled in this region in the line of sight are of small magnitude, a picture consistent with the open field structure and guided radial plasma outflow over a coronal hole.

Coronal transients are normally rare events to be observed during an eclipse. Such features were observed above the west limb by Japanese observers among others located in Kenya. The region had quietened down by the time moon's shadow had reached India. There is an enhancement near the limb in the white light corona at position angle 106° seen by several teams. K. K. Scaria of Indian Institute of Astrophsics, who obtained high-resolution white-light pictures of the sun in India, reports a filament structure in the position angle range 95° to 118° and at a mean distance of 1·73 $R_{\odot}$. This filament seems to be remnant of a transient display. The region near the limb continued to be highly disturbed; the highest values of line width of the red line measured anywhere in the corona are found in this region even to large values of $R_{\odot}$.

4.4 *Line-of-Sight Velocities in the Corona and Coronal Equatorial Rotation*

We have measured radial velocities with the aid of the neon comparison lines, at several points along each slit on both the east and west corona. These values are shown in Table 2 and refer to the solar equator. In particular, slit positions II (1), III (2) and III (1) have been utilized for the rotation measures. The differences amongst the several different values of displacement of the coronal emission line lowers the accuracy of measurement; this is unlike the measures from absorption lines of photospheric origin. We have therefore grouped for each slit position, the east and west values. The mean wavelength of the line is derived from the measures near the north and south poles of the sun. The coronal rotation is thus 2·6 km s^{-1} and is comparable to the photospheric value. The limited accuracy of our measures (probable error ± 1·5 km s^{-1}) of faint broad lines only permits a confirmation of co-rotation of the corona.

A distribution of line-of-sight velocities measured all over the corona is displayed in Fig. 7. None of the regions covered by our multislit arrangement show abnormally

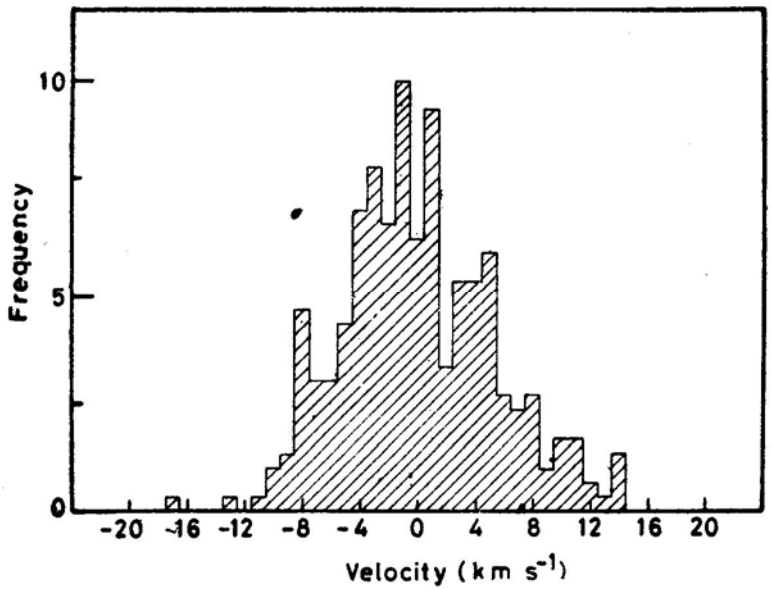

Figure 7. Frequency distribution of line-of-sight velocities as derived from [Fe x] 6374Å line.

large velocities in the corona reported earlier by Delone and Makarova (1969) and for this eclipse by Chandrasekhar, Desai and Angreji (1981). The latter find a splitting of the interference fringe pattern at position angle 256° indicating a component with a line-of-sight velocity of 70 km s^{-1}. This would imply, if confirmed, that there is a mass component with a velocity indicating expansion in perhaps a preferred direction. This region is covered by our slit position II (1), that spans the position angle 252°–257°. Not only do we not see any splitting of the emission line, but we also do not find any abnormal shift even of the line as a whole. The observed velocities are all within the range ±11 km s^{-1}. However, one should note that we have derived the line-of-sight velocities from the red coronal line sensitive to a region with temperature of $1{\cdot}3\times10^6$K whereas Chandrasekhar, Desai and Angreji (1981) have measured from the green line contributed mostly from regions with a temperature of $2{\cdot}5\times10^6$ K.

Table 2. Line-of-sight velocities derived from the red coronal line.

No.	Position angle	$R/R_\odot$	v km s^{-1}	No.	Position angle	$R/R_\odot$	v km s^{-1}
(1)	(2)	(3)	(4)	(1)	(2)	(3)	(4)
	Slit IV (1)			36	7·4	1·151	8
				37	9·0	1·156	2
1	320·1	1·495	1	38	10·0	1·162	−1
2	321·0	1·475	1	39	12·0	1·168	2
3	321·9	1·456	1	40	13·4	1·175	5
4	322·9	1·437	0				
5	323·9	1·418	−5	41	14·9	1·183	3
				42	16·3	1·192	5
6	324·9	1·400	−6	43	17·8	1·202	3
7	325·9	1·383	−1	44	19·2	1·212	−1
8	327·0	1·365	−2	45	20·5	1·223	1
9	328·1	1·348	0				
10	329·2	1·332	1	46	21·9	1·234	1
				47	23·2	1·247	−2
11	330·3	1·317	−7	48	24·5	1·259	−2
12	331·5	1·301	−3	49	25·8	1·273	−2
13	332·7	1·287	3	50	27·1	1·287	−7
14	333·9	1·273	−1				
15	335·2	1·259	0	51	28·3	1·302	−2
				52	29·5	1·317	−3
16	336·5	1·247	−1	53	30·7	1·332	−1
17	337·8	1·234	2	54	31·8	1·349	−4
18	339·1	1·223	1	55	32·9	1·365	−8
19	340·5	1·219	−1				
20	341·8	1·202	−1	56	34·0	1·383	1
				57	35·1	1·400	−6
21	343·2	1·192	0	58	36·1	1·418	−4
22	344·7	1·183	1	59	37·1	1·437	−1
23	346·1	1·175	−2	60	38·1	1·456	−1
24	349·1	1·162	4				
25	350·5	1·156	8	61	40·0	1·475	−8
				62	40·9	1·495	−5
26	352·0	1·151	5	63	41·8	1·515	−3
27	353·6	1·147	5	64	42·7	1·536	−8
28	355·1	1·144	11	65	43·5	1·557	−3
29	356·6	1·141	7				
30	358·2	1·139	4	66	44·3	1·578	−6
				67	45·1	1·599	−10
31	359·7	1·139	3	68	45·9	1·621	−3
32	1·3	1·139	2	69	46·6	1·643	−8
33	2·8	1·141	3	70	47·3	1·665	−9
34	4·4	1·143	4				
35	5·9	1·147	0				

Table 2. Continued.

No.	Position angle	$R/R_\odot$	v km s^{-1}
(1)	(2)	(3)	(4)
	Slit IV (2)		
71	312·1	1·297	0
72	313·1	1·274	−1
73	314·0	1·251	1
74	315·0	1·229	2
75	316·0	1·207	3
76	317·1	1·186	5
77	318·2	1·165	5
78	319·3	1·145	10
79	320·5	1·125	10
80	53·8	1·440	−7
81	53·0	1·415	−2
82	52·2	1·391	−2
83	51·4	1·367	−1
84	50·6	1·343	0
85	49·8	1·320	−4
86	48·9	1·297	−3
87	48·0	1·274	−1
88	47·0	1·251	−4
89	46·0	1·229	−3
90	45·0	1·208	−3
91	43·9	1·186	−5
92	42·8	1·165	0
93	41·7	1·145	−1
	Slit III (1)		
94	284·2	1·631	1
95	284·4	1·600	−4
96	284·7	1·571	−10
97	285·0	1·541	−2
98	285·3	1·511	0
99	285·6	1·482	−3
100	285·9	1·452	−4
101	286·2	1·422	−4
102	286·5	1·392	1
103	286·9	1·363	0
104	287·3	1·333	−1
105	287·7	1·304	5
106	288·1	1·275	4
107	288·5	1·245	9
108	289·0	1·216	−1
109	289·4	1·187	11
110	289·9	1·158	10
111	290·4	1·129	14
112	77·3	1·690	3
113	77·1	1·660	−4
114	76·9	1·631	−7
115	76·6	1·601	−5
116	76·3	1·571	−9
117	76·0	1·541	−6
118	75·8	1·511	−7
119	75·5	1·482	−4
120	75·1	1·452	−3
121	74·8	1·422	−6
122	74·5	1·393	−4
123	74·1	1·363	−2
124	73·7	1·334	−5
125	73·3	1·304	−4
126	72·9	1·275	−7
127	72·5	1·245	−3
128	72.1	1·216	−6
129	71·6	1·187	0
130	71·1	1·158	1
	Slit III (2)		
131	274·6	1·496	−1
132	274·7	1·465	−3
133	274·8	1·435	−2
134	274·9	1·404	0
135	275·0	1·373	−1
136	275·1	1·343	1
137	275·2	1·312	4
138	275·3	1·281	6
139	275·4	1·251	5
140	275·6	1·220	5
141	275·7	1·189	4
142	86·7	1·619	0
143	86·6	1·588	−2
144	86·5	1·557	−2
145	86·5	1·527	−5
146	86·4	1·496	−3
147	86·3	1·465	−5
148	86·2	1·435	−8
149	86·1	1·404	−8
150	86·0	1·373	−8
151	85·9	1·342	−4
152	85·8	1·312	−3
153	85·7	1·281	−2
154	85·6	1·251	−2
155	85·4	1·220	−4
156	85·3	1·189	−3
157	85·2	1·159	−4
158	85·0	1·128	−4
	Slit II (1)		
159	256·3	1·507	11
160	256·0	1·477	6
161	255·7	1·448	9
162	255·4	1·418	1
163	255·1	1·388	3
164	254·7	1·359	0
165	254·4	1·329	1
166	254·0	1·300	5
167	253·6	1·270	1
168	253·2	1·241	−9
169	252·8	1·211	−3
170	252·3	1·182	−4

Table 2. Continued.

No.	Position angle	$R/R_\odot$	v km s^{-1}	No.	Position angle	$R/R_\odot$	v km s^{-1}
(1)	(2)	(3)	(4)	(1)	(2)	(3)	(4)
171	104·1	1·567	7	221	214·4	1·353	6
172	104·4	1·537	1	222	213·3	1·335	4
173	104·7	1·507	5	223	212·2	1·319	−3
174	105·0	1·478	−4	224	211·0	1·303	−6
175	105·3	1·448	1	225	207·4	1·259	−1
176	105·6	1·418	14	226	204·8	1·232	−1
177	106·0	1·388	−7	227	202·2	1·208	12
178	106·3	1·359	−2	228	198·0	1·177	1
179	106·6	1·329	−8	229	195·1	1·160	−2
180	107·0	1·300	−3	230	190·6	1·140	1
181	107·4	1·270	−2	231	182·9	1·124	4
182	107·8	1·241	−17	232	175·0	1·128	−1
183	108·2	1·211	−11	233	167·4	1·153	−7
184	108·7	1·182	−6	234	165·9	1·160	−13
185	109·2	1·153	−3	235	164·5	1·168	−1
186	109·7	1·124	−10	236	163·0	1·177	−3
187	110·2	1·095	−8	237	161·6	1·187	−8
				238	160·2	1·197	−8
	Slit II (2)			239	158·8	1·208	−1
				240	157·5	1·220	4
188	247·1	1·626	−3				
189	246·6	1·598	−5	241	156·2	1·232	6
190	246·2	1·570	−4	242	154·9	1·245	8
				243	153·6	1·259	11
191	245·7	1·542	0	244	152·4	1·273	14
192	245·2	1·514	0	245	151·2	1·288	7
193	244·7	1·486	4				
194	244·2	1·459	7	246	150·0	1·303	7
195	242·5	1·376	8	247	148·8	1·319	13
				248	147·7	1·335	10
196	241·9	1·349	3	249	146·6	1·353	5
197	241·3	1·322	4	250	145·6	1·370	3
198	240·6	1·296	1				
199	239·9	1·269	4	251	144·5	1·387	14
200	239·2	1·242	5	252	143·5	1·406	5
				253	142·5	1·425	−1
201	238·4	1·216	0				
202	237·6	1·190	5		Slit I (2)		
203	117·3	1·431	1				
204	117·9	1·404	3	254	208·8	1·590	3
205	118·5	1·376	2	255	207·8	1·576	1
206	119·1	1·349	−1	256	206·8	1·562	8
207	119·7	1·322	1	257	205·8	1·548	3
208	120·4	1·296	0	258	204·8	1·536	3
209	121·1	1·269	1	259	203·7	1·523	6
210	121·8	1·243	−4	260	202·6	1·511	3
211	122·6	1·217	−1	261	201·5	1·500	4
212	123·4	1·190	−8	262	200·4	1·489	6
213	124·2	1·165	−8	263	199·3	1·479	4
214	125·0	1·139	−8	264	198·2	1·469	6
215	126·0	1·114	−4	265	197·0	1·460	10
216	126·9	1·089	1	266	195·9	1·452	11
				267	194·7	1·444	8
	Slit I (1)			268	193·5	1·437	5
				269	192·3	1·430	−1
217	218·5	1·425	7	270	191·1	1·424	9
218	217·5	1·406	8				
219	216·5	1·387	12	271	189·9	1·419	4
220	215·5	1·370	8	272	188·6	1·414	−7

Table 2. Concluded.

No.	Position angle	$R/R_\odot$	v km s^{-1}	No.	Position angle	$R/R_\odot$	v km s^{-1}
(1)	(2)	(3)	(4)	(1)	(2)	(3)	(4)
273	187·4	1·410	−5	287	167·5	1·437	−4
274	186·1	1·407	−3	288	166·3	1·444	−1
275	184·9	1·404	−3	289	165·1	1·452	2
				290	164·0	1·460	−3
276	183·6	1·402	1				
277	182·4	1·401	0	291	162·8	1·469	−2
278	181·1	1·400	2	292	161·7	1·479	−1
279	179·9	1·400	2	293	160·6	1·489	−2
280	178·6	1·401	5	294	159·5	1·500	−1
				295	158·4	1·511	−6
281	174·9	1·407	7				
282	173·6	1·410	6	296	157·3	1·523	−5
283	172·4	1·414	4	297	156·3	1·535	−9
284	171·1	1·419	3	298	155·2	1·548	−5
285	169·9	1·424	5	299	154·2	1·562	−5
				300	153·2	1·576	−5

Acknowledgements

We are grateful to T. P. Prabhu for much help both at the eclipse site and later in the reduction of the data. The successful operation of the instrument owes much to the fabrication skill of F. Gabriel, A. Charles and A. Samson.

References

Chandrasekhar, T., Desai, J. N., Angreji, P. D. 1981, *Appl. Opt.*, **20,** 2172.
Delone, A. B., Makarova, E. A. 1969, *Solar Phys.*, **9,** 116.
Jarrett, A. H., von Klüber, H, 1955, *Mon. Not. R. astr. Soc.*, **115,** 343.
Jarrett, A. H., von Klüber, H. 1961, *Mon. Not. R. astr. Soc.*, **122,** 223.
Jordan, C. 1969, *Mon. Not. R. astr. Soc.*, **142,** 501.
Liebenberg, D. H., Bessey, R. J. Watson, B. 1975, *Solar Phys.*, **44,** 345.
Livingston, W., Harvey, J., Doe, L. 1970, *Solar Eclipse 1970 Bulletin F*, National Science Foundation, Washington, p. 72.
Marshall, P. M., Henderson, G. 1973, *Solar Phys.*, **33,** 153.

J. Astrophys. Astr. (1982) **3,** 267–276.

HD 147010: The Ap Star in the Reflection Nebula vdB 102 in Upper Scorpius Region

N. Kameswara Rao and R. Rajamohan
Indian Institute of Astrophysics, Bangalore 560034

Received 1982 March 17; accepted 1982 July 1

Abstract. HD 147010, which is in the reflection nebula vd B 102, has been found to be a hot Ap silicon star rather than a normal A supergiant. From the *UBV and JHK* photometry of the star, colour excess $E(B - V)$ of 0·29 and the ratio of total-to-selective absorption R of 4·3 have been obtained. The high value of R implies bigger grain size and also confirms the association of the star with the nebula. The dereddened colours of the star can be fitted to a theoretical energy distribution with $T_{\rm eff} \simeq 13000 \pm 500$ K and $\log g = 3{\cdot}6 \pm 0{\cdot}2$. HD 147010 has also been found to be a spectrum variable; in particular, lines of Cr II show large intensity variations.

Key words: peculiar stars—spectrum variables

1. Introduction

Study of peculiar stars in young stellar aggregates like I Ori and Scorpio-Centaurus are thought to be particularly important because it would provide constraints on the timescales of possible mechanisms that explain both the abundance peculiarities and also the low rotational velocities (Hack 1976). Van Rensbergen, Hammerschlag-Hensberge and van den Heuvel (1978) concluded from the study of several galactic clusters that Ap and Am phenomena develop at a very early stage in the life of a star—during or before the arrival on the main sequence. Moreover, young stars embedded in nebulosities might still be in pre-main-sequence phase and thus might possess active and unstable atmospheres (*e.g.* Herbig Ae and Be stars). If one of these stars also happens to be peculiar, this might place further constraints on the mechanisms responsible for the origin of these peculiarities. Presently there seems to be mainly two hypotheses for explaining the abundance anomalies: the radiation-pressure-driven diffusion hypothesis (Michaud 1970, 1976) and the selective magnetic accretion of matter from normal interstellar medium (Havnes and Conti 1971) and its variations

such as accretion of supernova-enriched material (Rajamohan and Pati 1980), or accretion from an evolved companion (van den Heuvel 1967; Guthrie 1968). Diffusion as well as accretion hypotheses predict a gradual development of the peculiarities during the main-sequence life of a star although for diffusion the time scales are rather short (~ 10^4 yr). One attractive suggestion by van Rensbergen, Hammerschlag-Hensberge and van den Heuvel (1978) was that the peculiarities might result from the accretion of solid particles (probably made up of silicon and iron peak elements) from the proto-planetary clouds. Recently Havnes (1979) has shown that grains may in fact be more important in an accretion process than the gas and he also suggests some qualitative tests for this hypothesis. Thus, a study of peculiar stars associated with dark clouds is of particular interest. We have undertaken to study these stars to see whether any systematic trends would emerge from their properties related to abundance and/or rotation. One such star seems to be HD 147010, which is located in the nebulosity vdB 102 (van den Bergh 1966) in upper Scorpius.

HD 147010 is classified as one of the peculiar A-type stars in the upper Scorpius region by Garrison (1967). This forms a group along with HD 147009, HD 147103, HD 147104 and HD 146834, as illustrated by Garrison (1967, Fig. 8). The two pairs HD 147009, 147010 and HD 147103, 147104 are in a small complex of reflection nebulae (vdB 102) with a heavy dust lane connecting them, and a faint nebulosity extends further from these two pairs to HD 146834. HD 146834 is classified as of spectral class K5 III and probably is not part of this complex. Both HD 147009 and HD 147010 are considered to be members of Scorpio-Centaurus stream by Garrison on the basis of proper motions. These two stars form a visual binary system with a separation of 47·1 arcsec (Jeffers, van den Boss and Greenby 1963).

The spectroscopic peculiarities of HD 147010 have been described by Garrison (1967, Fig. 3). 'The lines of Si II and Fe II are sharp and very strongly enhanced as in a supergiant at about A2. Other lines present are seen at this low dispersion (86Å mm^{-1} at H_γ)to be lines of Ti II, Fe I and Cr II. However, the weak Ca II K line is so shallow and broad that it is barely visible and the hydrogen lines are considerably broader than in a supergiant.... The spectrum is definitely inconsistent with the photometry.' Further, Garrison points out also that HD 147010 could not be classified as a shell star (like Pleione) because shell stars usually show a strong K line of Ca II in the shell stage, which is absent in HD 147010. Slettebak (1968) in his study of the rotational velocities of ScorpioCentaurus stars also gave a similar description of the spectrum of HD 147010. 'The spectrum is peculiar as pointed out by Garrison (1967). Helium appears to be faintly present and the Ca II K line is weak. The Balmer lines suggest luminosity class II or IV, but the lines of Si II and Fe II indicate still higher luminosity.' Thus it was not clear whether HD 147010 is an A2 supergiant or a peculiar star. However, recently Wolff (1981) has mentioned it as an Ap Si-Cr. We have obtained a wide variety of spectroscopic and photometric observations to study the nature of this star and in particular to see whether we could gather up any evidence for accretion of matter on to the star.

2. Observations

All the spectroscopic observations have been obtained with 1-m telescope at Kavalur with the Cassegrain spectrograph. A Varo image intensifier has been used

to secure the red and near-infrared spectrograms. The journal of observations and the details of the spectrograms are given in Table 1.

All the available (published) photometric observations both in *UBV* (Hardie and Crawford 1961; Moreno and Moreno 1968) and in Strömgren system along with the β index (Glaspey 1971) are given in Table 2.

It was shown by Groote and Kaufmann (1981) that 60 per cent of the Ap and Bp stars they studied exhibit infrared excess at 4·8μm. In particular, they claim that younger stars possess more infrared excess. Thus it was felt that if HD 147010 has a circumstellar shell it might give rise to enhanced emission at infrared wavelengths in the form of either free-free emission from ionized gas envelope or thermal radiation from heated dust. So photometric observations of the star were obtained in *JHK* bands also. The *JHK* photometry of HD 147010 was done in 1981 February using a liquid-nitrogen cooled InSb detector of Physical Research Laboratory, Ahmedabad, with the 1-m telescope at Kavalur. Standard stars near HD 147010 (Whittet and van Breda 1980) have been observed along with HD 147010 to minimise extinction errors. The magnitudes are on Johnson's system and are given in Table 2. The typical errors in the magnitudes are 0·07 mag. The conversion to flux has been done using Johnson's (1966) calibration.

Table 1. Details of spectrograms obtained.

Plate no.	Date U. T.		Emulsion Central wavelength	Dispersion Å mm^{-1}	Exposure min
δ 2064	1973 March	15·897	IIa−0 4000	47	64
δ 1403	1981 February	7·915	IIa−D+Varo H_α	22	97
δ 1459	1981 February	20·928	IIa−D+Varo H_α	22	153
δ 1499	1981 February	26·917	IIa−0 λ 4000	22	172
δ 1510	1981 March	4·893	IIa−D+Varo H_α	22	171
δ 1515	1981 March	5·922	IIa−0 λ 4000	22	225
δ 1606	1981 April	9·814	IIa−D+Varo λ 7774	130	30
δ 1628	1981 April	11·834	IIa−D+Varo λ 5870	22	120
δ 1646	1981 April	23·808	IIa−D+Varo λ 5870	22	86
δ 1812	1982 February	14·929	IIa−0 λ 4000	22	155

Table 2. Colour indices of HD 147010.

V	$B-V$	$U-B$	$b-y$	m_1	c_1	B	J	H	K	Reference
			0·125	0·122	0·512					1
7·41	0·16	−0·25				2·769				2
7·38	0·162	−0·274								3
							6·67	6·63	6·69	4

References:
1. Glaspey (1971) 2. Hardie and Crawford (1961) 3. Moreno and Moreno (1968)
4. present investigation.

3. Luminosity class

One of the main uncertainties about HD 147010 is the luminosity class, *i.e.* whether it is an A supergiant as indicated from the lines such as of Si II, or an Ap star close to the main sequence (Garrison 1967). It is well known that λ7774 feature of OI is a good indicator of luminosity class for stars between spectral types B to early G (Keenan and Hynek 1950; Osmer 1972; Rao and Mallik 1978). If HD 147010 is a normal A2 supergiant, a strong absorption feature of λ7774 is to be expected. Spectrograms of the star obtained at a dispersion of 130 Å mm^{-1} do not show any absorption feature at λ 7774, whereas α Cyg—the standard A2 supergiant—shows a very strong absorption of λ 7774. Also, λ 7774 line is present on the spectrograms of HR 2618 (B6 III) obtained at the same dispersion. Thus it is seen that HD 147010 is not a normal A-type supergiant and could be of luminosity class IV or so, as already commented by Slettebak (1968).

4. Reddening, effective temperature and gravity

Based on the spectral type of A2, Garrison (1967) obtained a value of colour excess $E(B-V)$=0·12 for HD 147010, whereas Moreno and Moreno (1968) obtained a value of $E(B-V)$=0·29 based on its membership of Scorpio-Centaurus association; the latter authors also obtained a photometric spectral type of B6. It has been shown by Schild, Neugebauer and Westphal (1971) that the stars of upper Scorpius obey the interstellar extinction law characterized by the ratio of total-to-selective absorption $R \sim 3$. With this value of R and adopting Garrison's estimate of $E(B-V)$, the $(U-B)_0$ colour of HD 147010 would be much too blue for the spectral type A. A comparison with the theoretical energy distribution computed by Kurucz (1979) shows that if the spectral type is assumed as A2 corresponding to $T_{\rm eff} \simeq 9500$ K, then the observed U flux can only be satisfied if log g is lower than 1·5; *i.e.* the star has to be Ia supergiant. As already mentioned, the strength of λ 7774 feature indicates that it is not a normal supergiant. Moreover, the model normalised at 0·55 μm shows that the theoretical fluxes in the J, H and K passbands are much less than the observed ones. The same result is obtained by a comparison of the fluxes of the star with the observed fluxes of 78 Vir—another Ap star with the same $(B-V)_0$. The value of $E(B-V)$=0·29 leads us to a theoretical energy distribution corresponding to a model with $T_{\rm eff}$ = 13000 K and log $g \sim 3{\cdot}5$ [corresponding to $(B-V)_0 = -0{\cdot}13$] which can fit the reddening-corrected observed U flux, although the infrared fluxes predicted are much less than observed (see Fig. 1). The difficulty persists for every plausible value of $E(B-V)$ if R is assumed to be ~ 3. The value of $E(B-V)$=0·29 for HD 147010 seems to be consistent with the estimate of $E(B-V)$=0·33 for

Table 3. Equivalent widths.

Star	θ	log g	W_λ (mÅ) λ 4128 Si II	λ 4130 Si II	λ 4471 He I	λ 4481 Mg II
HD 14392	0·38	3·7	220	240	160	240
HD 68351	0·38	3·7	350	310	10	250
HD 147010*			190	200	120	220

* measured on plate δ 1499.

HD 147009 (based on a colour-spectral-type relation; Garrison 1967) which is only 47·1 arcsec away and appears to be embedded in the same reflection nebula.

The infrared colours (*J–H*, *H–K*) of HD 147010 do not indicate a presence of infrared excess. It was shown by Whittet and van Breda (1980) that in (*J–H*, *H–K*) plot for early type stars, the single Be stars and nebular shell stars occupy a separate region (higher $H - K$ index for a given $J - H$) whereas high-luminosity shell stars (supergiants and Of stars) and normal stars follow a blackbody line. The $J - H$ and $H - K$ colours of HD 147010 place it on the normal and shell star position. However, as shown earlier, HD 147010 is not a high-luminosity star. Thus a different value of *R* seems to be required to bring the infrared and visual photometry in agreement with the theoretical energy distribution. It is known that stars embedded in the dark clouds have a high value of *R*. Whittet (1974) has found that the stars associated with reflection nebulosities generally have R=4·2 while those not associated with nebulosities have R=3·3. Further, it was shown by Whittet, van Breda and Glass (1976) that *R* reaches a maximum of 4·3 in the central molecular cloud regions of Scorpio-Ophiuchus region. Thus it seemed that since HD 147010 is embedded in the reflection nebula $R \sim 4{\cdot}3$ is appropriate. The colours of HD 147010 have accordingly been corrected using this value of *R* also (using the relations given in Whittet and van Breda 1980) and are shown in Fig. 1 along with the theoretical energy distribution for a model with $T_{\rm eff}$ = 13000 K and log g= 3·5 (Kurucz 1979) normalised at *V*. The observations match quite well with the theoretical energy distribution. Thus the value of *R* in this region seems to be ~ 4·3.

The equivalent widths of H_γ and H_δ computed from the above theoretical model are consistent with the observed equivalent widths of H_γ and H_δ (9·8 Å and 9·0 Å respectively; Rajamohan 1976). Once $T_{\rm eff}$ is fixed (13000 ± 500 K), the observed

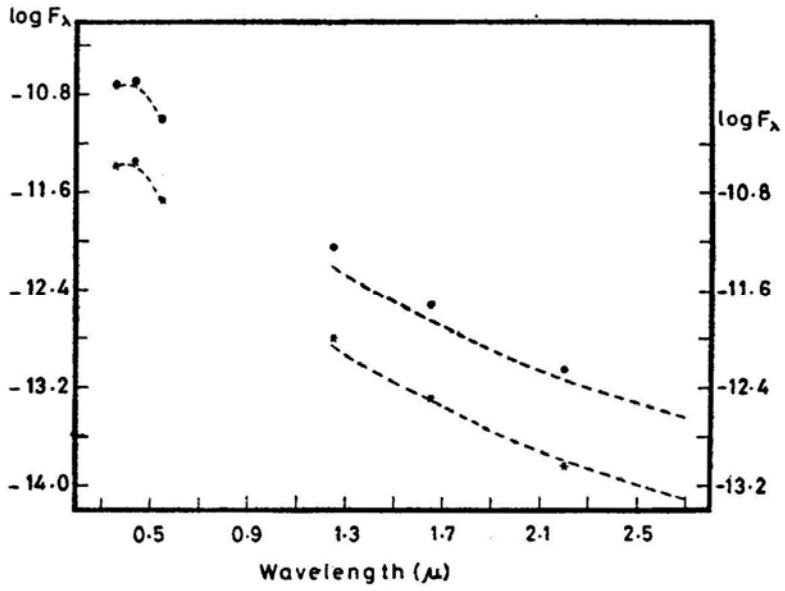

Figure 1. The energy distribution of HD 147010 corrected for different reddening values of R = 3·0 (filled circles) and 4·3 (asterisks). The dashed curve represents the theoretical energy distribution given by Kurucz (1979) for $T_{\rm eff}$ =13000 K and log g=3·5 normalised at *V* (0·55 μm). The scale for the lower curve is marked on the right-hand side.

equivalent widths of H_γ and H_δ yield log g =3·7 on a comparison with the theoretical equivalent widths of Kurucz (1979). Thus, the colours between 0·36 μm and 2·2 μm and the equivalent widths of hydrogen lines are both consistent with a theoretical model of HD 147010 with $T_{\rm eff}$ = 13000 ± 500 K and log g = 3·6 ± 0·2. In these estimates of $T_{\rm eff}$ and log g, it has been assumed that the theoretical energy distribution computed from line-blanketed models of normal stars (Kurucz 1979) is applicable to the *UBV* and *JHK* colours of HD 147010—which is apparently an Ap star. It is known that for Ap stars $T_{\rm eff}$ determined from *UBV* colours alone is an overestimate (Shallis and Blackwell 1979). However, Stepien and Muthsam (1980) have shown that the corrections needed to transform $U - B$, $B - V$ colours of Ap stars to the colours of normal stars of corresponding $T_{\rm eff}$, are usually small for hot Ap stars (not exceeding 0·07 in $U - B$ and 0·03 in $B - V$). Thus our use of these colours along with the infrared colours (which are not affected by blanketing) could cause errors of only a few hundred degrees in the estimation of $T_{\rm eff}$.

5. The line spectrum

The above estimate of $T_{\rm eff}$ and log g show that the star is a late B-type star and thus the presence of strong λλ4128, 4130 lines of Si II seen by Garrison indicates that it belongs to the class of hot Ap stars. Wolff (1981) mentions this as an Ap Si-Cr star.

One of the primary results of this study is that HD 147010 is a spectrum variable and the intensities of some of the lines vary in strength with time. Particularly, lines due to Cr II show major changes in intensity, whereas lines due to Si II and to some extent Fe II do not appear to show such variations. Also, a few other lines seem to vary in an opposite phase with respect to Cr II lines. This effect is conspicuously seen in the lines of λ4012·54 and λ 4002·90 as shown in Fig. 2.

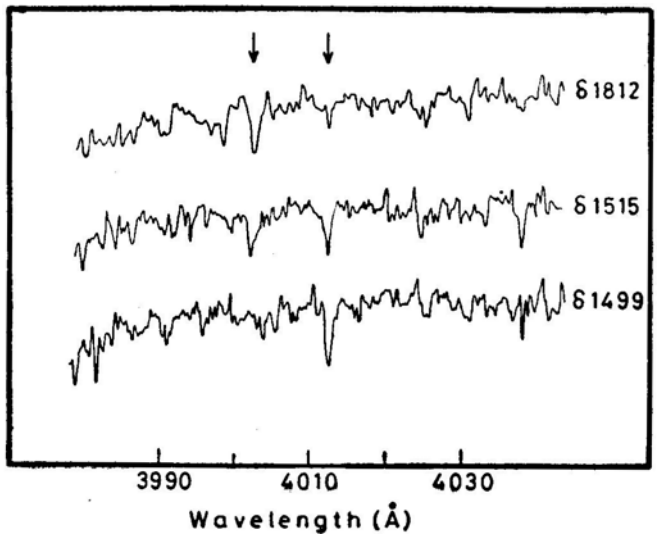

Figure 2. Density tracings of the three plates δ 1499, δ 1515 and δ 1812 in the region of λ4000. The arrows point to the two lines λ4002·9 and λ4012·5, which show changes in strength with antiphase.

λ 4012·54 is mainly due to Cr II (multiplet 183) whereas the identification of 4002·90 is not certain. λ 4012·54 is quite strong on plate δ 1499. Other lines due to Cr II are also quite strong on this plate (e.g. λ 3979 of multiplet 183, λλ 4242·38, 4261·92, 4269·28 etc.), whereas λ 4002·90 is quite weak or absent. On plate δ 1515, obtained a few days later (see Table 1), both λ 4012·54 and λ 4002·90 are of roughly equal strength and on the plate δ 1812, λ4012·54 is very weak but λ 4002·90 is very strong. Also, the other Cr II lines are very weak on δ 1812. These changes appear to be gradual. There are other lines which behave similar to λ 4002·90 feature, particularly lines of λλ 4082·2, 3998·95, 3874·7 and 3959·6. Presently, we cannot provide definite identifications for these features from the spectroscopic material available. It is known in α^2 CVn (Si-Cr-Eu star) which also shows large variations of Cr lines, that the lines which vary with opposite phase to Cr lines are mostly due to rare earths (Burbidge and Burbidge 1954). Probably such a phenomenon is also applicable in HD 147010.

The He I lines appear to be extremely weak for a star of spectral type B6. Our plate material (Table 1) shows that He I λλ 6678, 5876 may be marginally present, while λ 4026 and others are extremely weak or absent. On the blue plates, λ 4471 appears weaker than λ 4481 of Mg II, which itself is weak. The equivalent widths of Si II λλ 4128, 4130 (which do not seem to vary in strength with time), λ 4481 of Mg II and λ 4471 of He I have been measured on the plate δ 1499. These are shown in Table 2 along with the data for two other Si λ 4200 stars with the same $T_{\rm eff}$ and log g (Norris 1971, and Searle and Sargent 1964). The equivalent widths—in particular of λ4471 of He I and 4481 of Mg II—should be considered as upper limits. These are given here for a qualitative comparison. However, the equivalent width of λ 4471 He I places HD 147010 in the same place as Si λ 4200 stars and helium-weak stars in the plot between W (λ 4471) and θ_e (Norris 1971). Thus He I is quite weak in HD 147010, which is apparently a common characteristic of Ap stars. The equivalent widths of λλ 4128, 4130 of Si II also place this star in the same region occupied by Si λ4200 stars in the plots of W (λ 4481, Mg II)/W (λ 4130, Si II) and W (λ 4130) versus $B - V$ or θ_e (Norris 1971; Searle and Sargent 1964). From the relationship between equivalent width and Silicon over-abundance (Searle and Sargent 1964), one obtains a value of ~ 0·6 (±0·2) for [Si/H].

Apart from λλ4128, 4130 several other lines of Si II are also present— λ 3855, 3856, 3862, 4075,4076 and even high excitation lines of λ 3954 and λ 4200. Contrary to the description given by Garrison that K line of Ca II is a broad shallow line, we find it

Table 4. Observed radial velocities.

Date U. T.		Radial velocity km s^{-1}	p.e. km s^{-1}	Dispersion Å mm^{-1}
1920 May	12·297*	− 8·2	3·8	36
1921 April	29·359*	−14·7		36
1921 July	22·161*	− 3·5		
1973 March	15·897	− 8·1	9·8	47
1981 February	26·917	− 6·9	4·0	22
1981 March	5·922	− 6·1	4·7	22
1982 February	14·929	(− 4·6)		22

*Abt (1973)

to be a sharp line. Many moderately strong lines of Fe II are also present along with lines of Ti II. There appears to be some change in the shape of some Balmer lines. On one plate (δ 1403) H_α shows a sharp red edge.

Although the strength of several lines appear to be variable, the radial velocity of the star essentially remains constant. All the published measures of radial velocity of the star (Abt 1973; Wilson and Joy 1950) along with the measures of our four blue plates are given in Table 4. There is no significant variation in radial velocity and the mean valueis—7 km s^{-1}. This probably indicates that the star is not a spectroscopic binary.

6. Discussion

HD 147010 seems to be imbedded in the nebulosity vdB 102 and appears to be the source of illumination, although van den Bergh (1966) gives HD 147009 as the source. The $E(B - V)$ and R value estimated earlier show that HD 147010 is at least 1 mag brighter than HD 147009 and also earlier in spectral type. Use of Hubble's relation as given by Brück (1974) for the diameter, estimated to be illuminated by HD 147010 is about 305 arcsec which agrees with the diameter of the reflection nebulosity measured on the J plate of SRC sky survey.

The large value of $R = 4{\cdot}3$ derived for the grains around HD 147010 is similar to the extinction properties of grains around stars like ρ Oph, which are also imbedded in the reflection nebula. This high value of R is attributed to the particles larger than those causing the interstellar extinction. If they are approximated to be spherical dielectric grains (silicates) then the Mie scattering calculation indicates particles of radii greater than 0·2 μm. In the picture presented by Havnes (1979) for accretion of grains on chemically peculiar (CP) stars, relatively large grains approach the CP star and are heated whereas small and/or light grains are pushed away. At least around HD 147010, this requirement of large grains for accretion seems to be partly met.

Recently Wolff (1981) has discussed the rotational velocities of Ap stars in clusters. She obtained a value of $\leqslant 20$ km s^{-1} for the $V \sin i$ of HD 147010 (consistent with our spectroscopic material). In the plot between the $V \sin i$ and age (Wolff 1981, Fig. 2), HD 147010 occupies the lowest position for the stars of the same age (~2 $\times 10^7$ yr according to Wolff) and deviates appreciably from the mean relation. However, the age of upper Scorpius sub-group of the Scorpio-Centaurus association could be much less (~ 5 × 10^6 yr) and the deviation of the position of HD 147010 would be much more.

The above estimate of $V \sin i$ indicates a low rotational velocity of the star, although the sin i value is unknown. The approximate value of sin i could be estimated if the spectrum variability discussed earlier is found to be periodic and also if it is assumed to be due to rotation. An estimate (admittedly uncertain) depending on the behaviour of line strengths on our four blue plates indicates a period of 5–7 days. Further, the radius of the star estimated to be 3 $R_\odot$ from M_v and T_{eff}, leads to a rotational velocity ~27 km s^{-1}. Wolff has presented arguments in favour of mass accretion processes being responsible for the magnetic breaking resulting in the low rotational velocities for Ap silicon stars, although at which stage in the evolution (main sequence or pre-main sequence) this starts operating is far from clear. If the process is operative for

HD 147010 also, then the lower-than-normal velocity might indicate higher rate of mass accretion.

As indicated earlier, *JHK* magnitudes of HD 147010 do not show the presence of infrared excess. In contrast, Groote and Kaufmann (1981) have detected infrared excess at 4·8 μm in 60 per cent of Ap and Bp stars. At least in a few cases, infrared excess seems to be due to circumstellar grains. Further infrared observations at 4·8 μm and longer wavelengths are desirable to ascertain whether HD 147010 would also show some excess.

We have observed this star as the first of a sample of Ap stars situated in the regions of dark clouds to see whether any common trends emerge. Presently, one other peculiar star connected with dark clouds seems to be HR 6000 which is helium-weak and also shows the presence of lines due to P II (Bessell and Eggen 1972). HR 6000 is the visual companion (45 arcsec away) to one of the bright pre-main-sequence shell star HR 5999 and is associated with the dark cloud complex containing several T Tauri stars (Eggen 1975; Thé and Tjin A Djie 1981). The *UBV colours* of both HD 147010 and HR 6000 are in a very close agreement. It would be interesting to investigate the rotational velocity and any other spectroscopic anomalies common to these two systems.

Acknowledgements

We would like to express our thanks to Professor P. V. Kulkarni and N. M. Ashok for their help in obtaining the *JHK* magnitudes. We are also thankful to B. N. Ashok and K. Jayakumar for their help with the data reductions.

References

Abt, H. A. 1973, *Astrophys. J. Suppl. Ser.*, **26**, 365.
Bessell, M. S., Eggen, O. J. 1972, *Astrophys. J.*, **177,** 209.
Brück, M. T. 1974, *Mon. Not. R. astr. Soc.*, **166,** 123.
Burbidge, G. R., Burbidge, E. M. 1954, *Astrophys. J. Suppl. Ser.*, **1**, 431.
Eggen, O. J. 1975, *Publ. astr. Soc. Pacific*, **87**, 37.
Garrison, R. F. 1967, *Astrophys. J. Ser.*, **147,** 1003.
Glaspey, J. W. 1971, *Astr. J.*, **76,** 1041.
Groote, O., Kaufmann, J. P. 1981, *Astr. Astrophys.*, **94**, L 23.
Guthrie, B. N. G. 1968, *Publ. R. Obs. Edinburgh*, **6**, 145.
Hack, M. 1976, in *IAU Coll. 32: Physics of Ap stars*, Eds W. W. Weiss, H. Jenker and H. J. Wood, Universitätssternwarte, Wien, p.255.
Hardie, R. H., Crawford, D. L. 1961, *Astrophys. J.*, **133,** 843.
Havnes, O. 1979, *Astr. Astrophys.*, **75,** 197.
Havnes, O., Conti, P. S. 1971, *Astr. Astrophys.*, **14,** 1.
Jeffers, H. M., van den Boss, W. H., Greeby F. 1963, *Index Catalogue of Visual Double Stars; Publ. Lick obs.*, Eds W. W. Weiss, H. Jenker and H. J. Wood, p. 21.
Johnson, H. L. 1966, *A. Rev. Astr. Astrophys.*, **4**, 193.
Keenan, P. C., Hynek, J. A. 1950, *Astrophys. J.*, **111,** 1.
Kurucz, R. L. 1979, *Astrophys. J. Suppl. Ser.*, **40,** 1.
Michaud, G. 1970, *Astrophys. J.*, **160,** 641.
Michaud, G. 1976, in *IAU Coll.* 32: *Physics of Ap Stars*, Eds W. W. Weiss, H. Jenker and H, J. Wood, Universitätssternwarte, Wien, p.81,

Moreno, A. G., Moreno, H. 1968, *Astrophys. J. Suppl Ser.*, **15,** 459.
Norris, J. 1971, *Astrophys. J. Suppl. Ser.*, **23,** 213.
Osmer, P. S. 1972, *Astrophys. J. Suppl. Ser.*, **24,** 247.
Rajamohan, R. 1976, *Pramāna*, **7,** 160.
Rajamohan, R., Pati, A. K. 1980, *J. Astrophys. Astr.*, **1,** 155.
Rao, N. K., Mallik, S. G. V. 1978, *Mon. Not. R. astr. Soc.*, **183,** 211.
Schild, R., Neugebauer, G., Westphal, J. A. 1971, *Astr. J.*, **76,** 237.
Searle, L., Sargent, W. L. W. 1964, *Astrophys. J.*, **139,** 793.
Shallis, M. J., Blackwell, D. E. 1979, *Astr. Astrophys.*, **79,** 48.
Slettebak, A. 1968, *Astrophys. J.*, **151,** 1043.
Stepien, K., Muthsam, H. 1980, *Astr. Astrophys.*, **92,** 171.
Thé P. S., Tjin A Djie, H. R. E. 1981, *The Messenger*, No. 23, p. 25.
van den Bergh, S. 1966, *Astr. J.*, **71,** 990.
van den Heuvel, E. P. J. 1967, *Bull. astr. Soc. Netherlands*, **19,** 11.
van Rensbergen, W., Hammerschlag-Hensberge, G., van den Heuvel, E. P. J. 1978, *Astr. Astrophys.*, **64,** 131.
Whittet, D. C. B. 1974, *Mon. Not. R, astr. Soc.*, **168,** 371.
Whittet, D. C. B., van Breda, I. G. 1980, *Mon. Not. R. astr. Soc.*, **192,** 467.
Whittet, D. C. B., van Breda, I. G., Glass, I. S. 1976, *Mon. Not. R. astr. Soc.*, **177,** 625.
Wilson, R. E., Joy, A. H. 1950, *Astrophys. J.*, **111,** 221.
Wolff, S.C.1981, *Astrophys. J.*, **244,** 221.

J. Astrophys. Astr. (1982) **3,** 277–296.

Chromospheric Activity of Late-type Giants and Supergiants: Reappearance of Dynamo Activity in the Interior due to the Spin-up of the Core in Evolution

Yutaka Uchida and M. K. V. Bappu*
Tokyo Astronomical Observatory, University of Tokyo, Mitaka, Tokyo, 181 Japan

Received 1982 March 24; accepted 1982 July 5

Abstract. The renewal of chromospheric activity in red giants and supergiants is interpreted in terms of the reappearance of dynamo activity in the interior due to the spin-up of the core caused by its contraction in the course of evolution from the main sequence to the giant stage. A region of very high rotational shear (differential rotation) develops between the core, which spins up by a large factor through the drastic contraction, and the envelope, which spins down in contrast by virtue of expansion. Mechanisms of angular momentum transfer may operate to smear this large shear, and bring the inner part of the envelope into sheared rotation. A convective layer, on the other hand, develops in the envelope from the surface inwards, when the envelope expands and the temperature is lowered. A dynamo layer, or a layer in which the sheared rotation coexists with the convection (the presence of a remnant magnetic field being postulated), will thus reappear in the inner part of the envelope when the envelope-convection reaches down and invades the layer of sheared rotation. Surface chromospheric activity due to the magnetic field is thus renewed when the regenerated magnetic field is brought up to the surface by the envelope-convection. These phenomena occur as the star evolves into the giant stage and hence explain the observed characteristic of gradual revival of chromospheric activity from the subgiant to the giant stage.

Key words: stellar evolution—chromospheric activity—dynamo activity —red giants

*Visiting Scientist at the Tokyo Astronomical Observatory under the support of the Japan Society for the Promotion of Sciences. On leave from the Indian Institute of Astrophysics. Deceased on 1982 August 19

1. Introduction

Ca II H- and K-line emission is well known to be a good indicator of the chromospheric magnetic activity in the case of the Sun (Thomas and Athay 1961; Bappu and Sivaraman 1971; Bray and Loughhead 1974; Skumanich, Smythe and Frazier 1975). The Ca II K-line (Wilson and Bappu 1957; Wilson 1976), and more recently, resonance lines like Mg II h and k lines in the ultraviolet observed from space (Basri and Linsky 1979; Weiler and Oegerle 1979) have been extensively studied to investigate stellar chromospheres (Linsky 1980).

Two aspects of chromospheric behaviour have been the focus of much attention. These are the relationship between K-line widths and absolute magnitude (Wilson and Bappu 1957), and the age dependence of K-line emission intensities for stars on the main sequence (Wilson and Skumanich 1964; Skumanich 1972). The principal contributor to the integrated calcium emission spectrum that enables the Sun to follow the Wilson-Bappu relation is the bright fine mottle of size 1–2 arcsec (Bappu and Sivaraman 1971). There is little difference between the emission profile of the single bright fine mottle and the integrated spectrum of the Sun (Bappu and Sivaraman 1977). This is true at least for the quiet Sun; the localized enhancement that comes from active regions gives rise to a 'temporal' component that arises from the rotational modulation if the Sun is viewed as a star. The emission intensity has a linear dependence on surface magnetic field strengths to measurable low values in the case of the Sun (Frazier 1972), and there is enough circumstantial evidence available for the association of magnetic fields with the bright fine mottle (Bappu 1981). The decrease of chromospheric emission with age, experienced by stars on the main sequence, can well be considered to be due to a decrease in the magnetic field whose dissipation enhances chromospheric heating. Middelkoop and Zwaan (1981) have plotted Wilson's eye-estimates against $B - V$ values and find that the G giants show a large spread in H and K emission; those giants that have broadened spectral lines tend to produce enhanced emission and hence are indicative of dynamo efficiency that is correlated with the rotation characteristic.

Bappu (1981) has shown recently from the distribution on the H-R diagram of late-type stars that show K-line emission that, if traced back in time along the evolutionary track, the low-mass red giants—which today have chromospheric intensities that are strong and easily measurable—must have had periods in the late phase of their main-sequence stage during which they would have had no detectable chromospheric line emission. In a recent communication (Bappu 1982) he has used normalized Ca II chromospheric fluxes to show that it is necessary to postulate a renewal of magnetic activity in the atmosphere of the evolving star. Such renewal during the giant stage is, however, not expected from the simple application of the dynamo picture considered for main-sequence stars. The dynamo action in stars, which is an intensification of the pre-existing magnetic field by the cooperation of the sheared rotation and the convection (*e.g.* Parker 1955; Yoshimura 1975; Stix 1976), is expected to be strong in the envelope of young main-sequence stars—right after the Hayashi phase—due to the coexistence of strong convection and (sheared) rotation. Such dynamo action, however, decays through the long life in the main-sequence stage along with the decay of the stellar rotation, and the decay of the stellar rotation is more severe in going over to the giant stage due to the expansion and mass loss (Mestel 1972).

In the present paper, we propose an interpretation for the above-mentioned

unexpected re-flourishing of the chromospheric magnetic activity in low-mass red giants in the following way. After the magnetic activity has ceased in these low-mass stars in the late phase of its main-sequence stage, the stars evolve into the giant stage in which the outer part of the star expands to form an extended envelope while the central part contracts to form a compact core because the central pressure cannot be maintained otherwise after the disappearance of the heat source at the centre (Schwarzschild 1958; Iben 1967a). If the star has been rotating at all, the core will spin up by a large factor due to the angular momentum conservation in the contraction whereas the envelope will spin down in the expansion for the same reason, and a large gradient in the angular velocity developes in the boundary region. Mechanisms of the angular-momentum transfer, such as the rotational instability causing turbulent viscosity (Goldreich and Schubert 1967; Fricke 1967) or the magnetic torquing (Lüst and Schlüter 1955; Mestel 1972), will then be set in operation and the core drags the inner part of the envelope into sheared rotation. The envelope, on the other hand, becomes convective starting from outside as the temperature is lowered due to the expansion in the course of evolution (Iben 1967a), and after some time the convection zone reaches down and invades the region which has been set into sheared rotation by the drag. A dynamo layer will thus be established and restarts the process of regeneration of the magnetic field. The magnetic field may be carried out to the surface by the envelope convection itself, but there exists another possibility that the magnetic bubble produced by the ballooning instability (Parker 1966) in the overly-wound-up field in the sheared rotation directly emerges (*cf.* Layzer, Rosner and Doyle 1980). According to the time-lag between the start of the evolution of a star on the evolutionary track to the giant stage, and the spinning-up of the core and deepening of the envelope convection, the chromospheric activity in red giants will be rekindled and will flourish some time after the star evolves into the giant stage, explaining the observation.

We first summarize the observational basis of the argument in Section 2. The spin-up of the core in evolution and the mechanisms of the angular momentum transfer caused by the large difference of the rotation of the core and the envelope are discussed in Sections 3 and 4, respectively. The renewal of the dynamo action and the reappearance of the magnetic field to the stellar surface is discussed in Section 5. Overall discussion is given in Section 6.

2. The observational basis: a brief review

Wilson's catalogue (1976) is a plentiful data source of K-emission intensities in late-type main-sequence stars, giants and supergiants. Stars in this catalogue are general galactic field stars and are given eye-estimates of chromospheric emission intensity on a scale of 1–5 (5 is the most intense). Ideally, we should have available normalized flux values of the emission to eliminate all effects of background variation caused by spectral type and luminosity differences. Very few of these, however, are available at the present time, and hence we use the eye-estimates that form a homogeneous set, for indicating post-main-sequence behaviour. Since, for all these stars the K-emission line widths provide absolute magnitudes, it is possible to plot all the stars on an M_v, $B - V$ plane. Fig. 1 shows such diagrams for different chromospheric intensity values. We have superposed on each of these diagrams the colour–magnitude loci of stars of

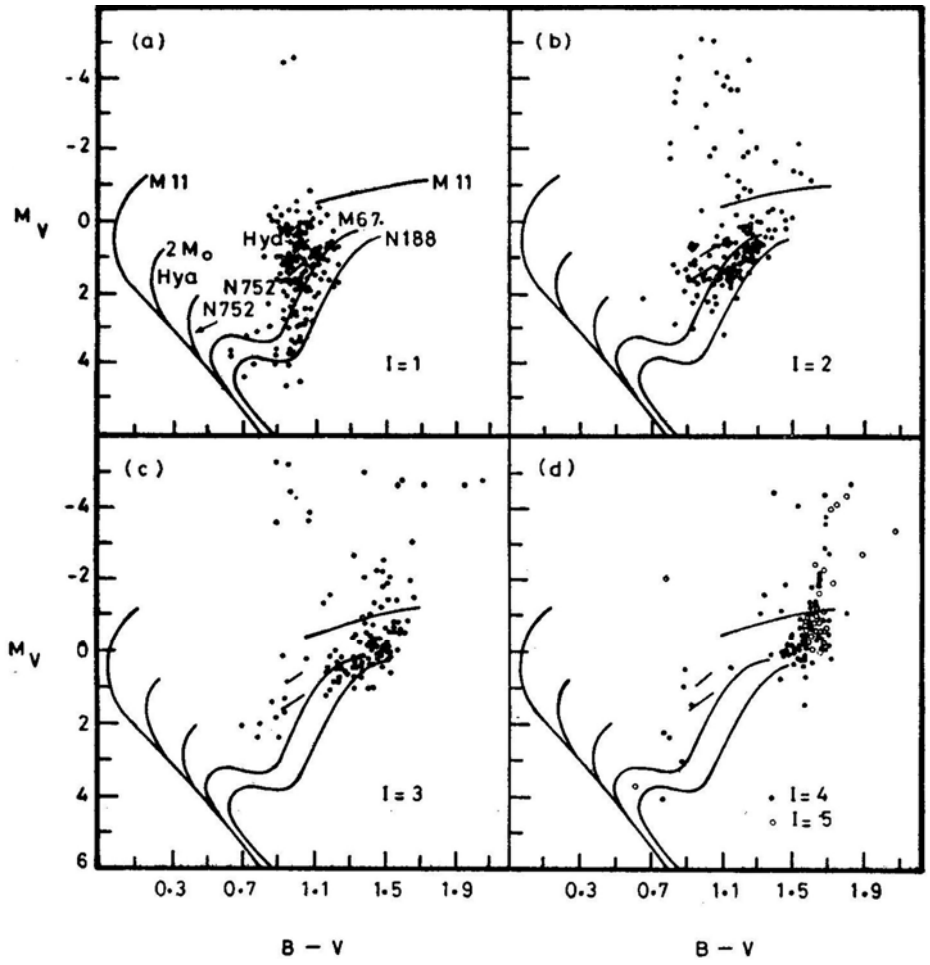

Figure 1. K-line-width absolute magnitude plotted against $B - V$ for different K-emission eye-estimates for stars of the general galactic field.

M 11, the Hyades, NGC 752, M 67 and NGC 188. The brightest stars in the Hyades have a turn-off point consistent with the Iben track of a $2M_{\odot}$ star. Hence we use these locations to indicate the ages of the stars involved in the study.

There are several salient features in this diagram that are of interest. The higher chromospheric intensities display a migration to brighter absolute magnitudes and redder colours. Part of this shift can be easily explained by the increase in apparent emission intensity as one assesses it against the weaker continuous background of later spectral types. To minimize its contribution we can make qualitative comparisons at any $B - V$ value. If we confine our attention to the narrow colour interval, $B - V$ =0·9 to 1·0, and examine the vertical spread of the points, we find that we have an appreciable density of points that cover the absolute magnitude interval from about M_v= – 0·5 to + 4·0 for stars with intensity I = 1, the number in this colour band decreasing as one goes to higher chromospheric intensity levels. The two extremes of luminosity available in this colour band in Fig. 1a are the giants younger than those in the Hyades and the subgiants comparable in age to those in M 67 or NGC 188. A

low value of chromospheric emission for the luminous giants is consistent with their age if one assumes that the decay of emission has a rate independent of stage of evolution. In other words, these stars had chromospheres that—according to the Skumanich (1972) estimate of initial values—would be much greater, while still on the main sequence, than the present value of the Sun. On the other hand those stars located between the isochrones of the two very old galactic clusters must certainly have lost all traces of chromospheric emission before they have left the main sequence; that they are detectable at intensity level 1 on 10-Å mm^{-1} dispersion spectra is suggestive of a considerable revival of the chromospheric emission in the first stages of post-main-sequence evolution. By examining the star distribution in adjacent colour bands, we also note the steady enhancement of intensity, especially in the subgiant to giant phases of evolution.

This revival of chromospheric emission becomes apparent in our plot of the ratio of chromospheric flux in the Ca II lines to the bolometric luminosity for stars where such information is available in the literature (Fig. 2). The Ca II and Mg II radiative loss rates are taken from Linsky *et al.* (1979) as well as Basri and Linsky (1979). Dwarfs, giants and supergiants are identified separately. The numbers on each point in the diagrams of both lines represent the Wilson eye-estimates of Ca II emission intensity. The insufficiency of systematically obtained observational data is an obvious characteristic with ground-based Ca II observations—the sparser of the two. We notice that the values of flux are shared by main-sequence objects, the supergiants and some of the giants. As plotted therein, on a two dimensional diagram, there is no systematic dependence of the ratio of the chromospheric flux and the total luminosity on the luminosity class. We note, however, that in general, stars of higher luminosity emit proportionally stronger K-or k-line emission at any effective temperature. In each diagram, the curve defining a limit of chromospheric emission (LCE) beyond which a normal star of luminosity class I, III or V can seldom be located, is drawn in Bappu (1982). The drawing of this curve at low effective temperatures is aided by the eye-estimates of K emission; we know from experience that brighter cases than those marked in the diagram are seldom seen amongst the large number of stars in the solar neighbourhood. Its position is particularly uncertain at the higher effective temperatures corresponding to the later classes of spectral type F. The fact that we can specify an empirically located LCE implies that, in the overall energy balance scheme, the chromospheric contribution has an upper limit that is seldom exceeded and which depends on the effective temperature. In postulating any mechanism for the generation of chromospheric emission, the magnitudes to be sought for in the energy generation are limited by the LCE. A peak in the chromospheric-flux distribution normalized to the bolometric flux has been shown some years ago by Blanco *et al.* (1974). The LCE is now used to introduce (Bappu 1982) the display of the age parameter, the evaluation of which is to be done by a measure of the deviation from it of the flux values of any star. Consider the vertical distribution of points at 5600 K that passes through the location of the quiet Sun. With intensity 4 near the LCE and the Sun located far from it, one can interpret the K-emission decay seen on the main sequence (Skumanich 1972) as measurable in terms of the deviation from the LCE. For T_e = 4300 K we have a variety of objects located over a wide range of chromospheric flux in both sections of Fig. 2. The main-sequence star in the Ca II diagram with a large deviation from the LCE is an old object despite its high eye-estimate value of emission intensity, and typifies the effect of background contrast.

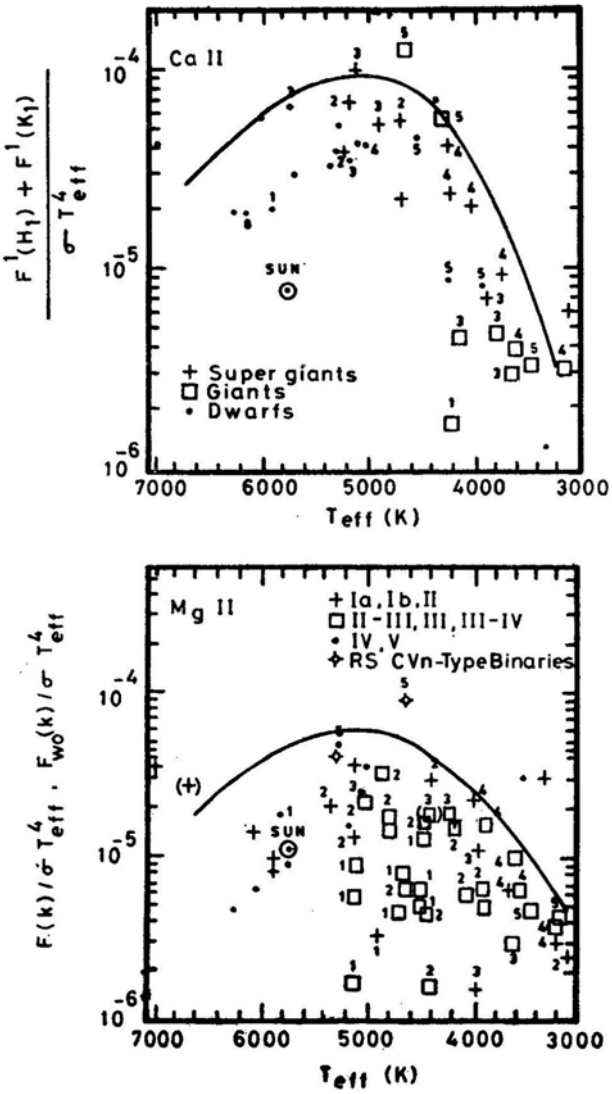

Figure 2. The ratio of chromospheric flux to bolometric luminosity for different values of T_e for the Ca II and Mg II lines (see text).

There are supergiants near the LCE and even a single giant that is an RS CVn object with enhanced contribution from plages. Notice the lone K1 IV object that is so far from the LCE and which, on the basis of the arguments presented earlier, will acquire more chromospheric emission as it evolves further. It would then drift higher up and to the right, closer to the LCE, as several other giants on the diagram have presumably done. A main-sequence star moves away from the LCE with age while a star evolving into a giant attempts to get closer to it. With the sparse data we now have, it will not be possible to indicate whether in this second phase of chromospheric renewal the star can reach the LCE. The supergiants have the best of both contributions and hence hover around the LCE.

Their present chromospheric intensities may benefit also from the original surface magnetic fields that have not had time to decay in addition to the new contributions acquired by virtue of the changes in the post-main-sequence evolution. Observations of K emission in old galactic clusters like M 67 assume a role of importance in providing evidence for such conjectures of chromospheric revival. Such observations, difficult as they are likely to be, are nevertheless within the scope of today's technology.

3. Evolution of the internal state of rotation—spin-up of the core

As mentioned in Section 1, it is well known that a compact core is formed by contraction during the course of evolution of a star into the giant stage. Our proposal here is based on the change in the distribution of the angular velocity inside a star (if it is rotating) due to such a change in the distribution of mass in the course of evolution.

In order first to estimate the upper limit of the rotational velocity of the spun-up core, we assume for the time being that there exists no mechanism of angular-momentum exchange between thin elementary rings [located at (r_0, θ_0) in the spherical coordinate whose origin is at the centre of the star and the axis coincides with the axis of the rotation], and that each ring expands or contracts to its new (r, θ) in the course of evolution without interacting with one another. The conservation of angular momentum J of a thin elementary ring,

$$\frac{dJ}{dt} = 0, \tag{1}$$

implies that

$$J = r^2 \sin^2 \theta \, \Omega \, \Delta M = \text{const} \equiv r_0^2 \sin^2 \theta_0 \, \Omega_0 \, \Delta M_0 \tag{2}$$

where ΔM is the mass of the ring, Ω is the angular velocity, and the subscript 0 denotes those quantities before the particular part of the evolution under consideration takes place. Since ΔM is conserved and θ is constant in the radial contraction or expansion, we have,

$$\frac{\Omega}{\Omega_0} = \left(\frac{r}{r_0}\right)^{-2} \tag{3}$$

We can calculate the change in the angular velocity of the ring by using this relation with the calculated model stellar evolution which gives the change with time of $r\ (m,t)$, where $m \equiv M_r/M_*$ is the mass-fraction from the centre. Fig. 3 shows the change in the distribution of the mass before and after the evolution from Iben's model calculations for the evolution of a 1 $M_\odot$ star (Iben 1967b). Using similar graphs also for 1·25 $M_\odot$ and 1·5 $M_\odot$ stars from Iben (1967b), we can obtain the expected ratios of the angular velocity before and after the evolution (normalized

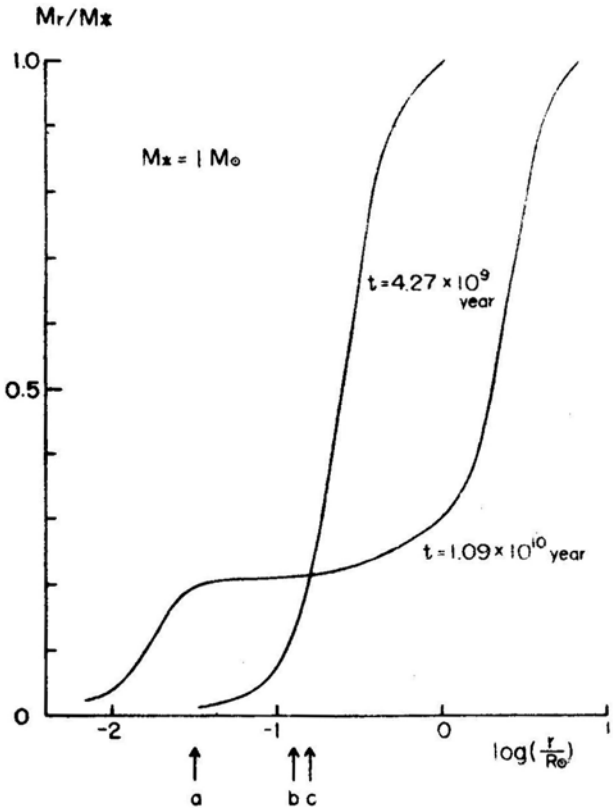

Figure 3. $(r/R_\odot)$–(M_r/M_*) diagram for 1 $M_\odot$ star at $t = 4{\cdot}27 \times 10^9$yr and $1{\cdot}09 \times 10^{10}$ yr (from Iben 1967b). This shows that the part $r > r_{ssl}$ expands roughly by one order of magnitude while $r < r_{ssl}$ contracts by about the same factor during the time interval, where r_{ssl} is the radius of the stand-still layer. The edge of the core, the bottom of the envelope convection, and the stand-still layer are indicated by arrows a, b and c, respectively, for the curve of $t = 1.09 \times 10^{10}$ yr.

to the corresponding values before the evolution) in these stars* (Fig. 4). It is seen that the core spins up by a large factor. Kippenhahn (1963) has mentioned this aspect in a different context of a possible modification of stellar evolution. A more elaborate discussion on these lines is seen in Endal and Sofia (1976). Also, a large shear in the angular velocity is seen to build up in the region surrounding the core in all these models. The region with large gradient in Ω is the region of sheared rotation, and the top of it may be defined by a radius which fulfils the equation $\Omega\ (m) = \Omega_0\ (m)$. This particular layer neither expands nor contracts (stand-still layer) and keeps its original angular velocity. The layer of sheared rotation appears due to the structural change in the star, and the latter becomes appreciable some time after the star evolves away from the main sequence. Fig. 5 shows the edge of the core and the stand-still layer in terms of the mass-fraction, and Fig. 6 shows the epoch at which the structural change

*Observed stellar properties such as rotational velocity or surface convection differ for stars with different masses along the main sequence. The ratio Ω/Ω_0, however, depends only on the change in the distribution of mass inside the star. The presence of convection near the surface, or the presence of internal differential rotation do not matter. The presence of internal rotation will affect the detailed value of Ω through Ω_0, but our conclusion of faster-rotating core will not be affected unless the profile of initial rotational velocity has a sharp decrease toward the core.

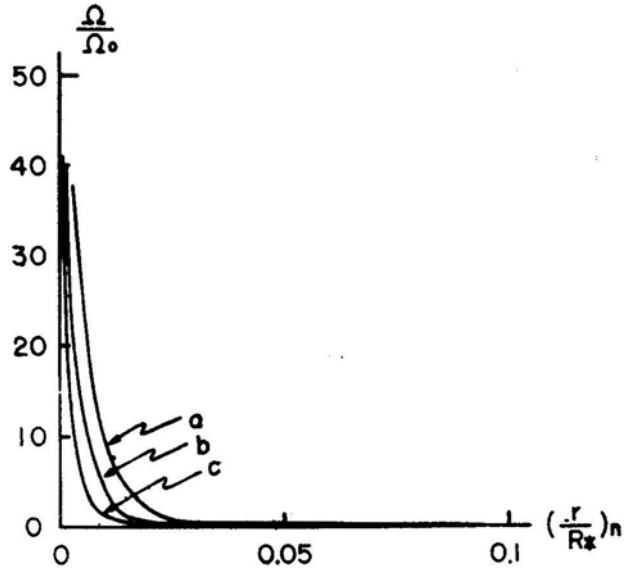

Figure 4. (r/R_*)–(Ω/Ω_0) curves a, b and c of the spin-up calculated for M = 1 $M_\odot$, 1·25 $M_\odot$ and 1·5 $M_\odot$ model stars of Iben, respectively.

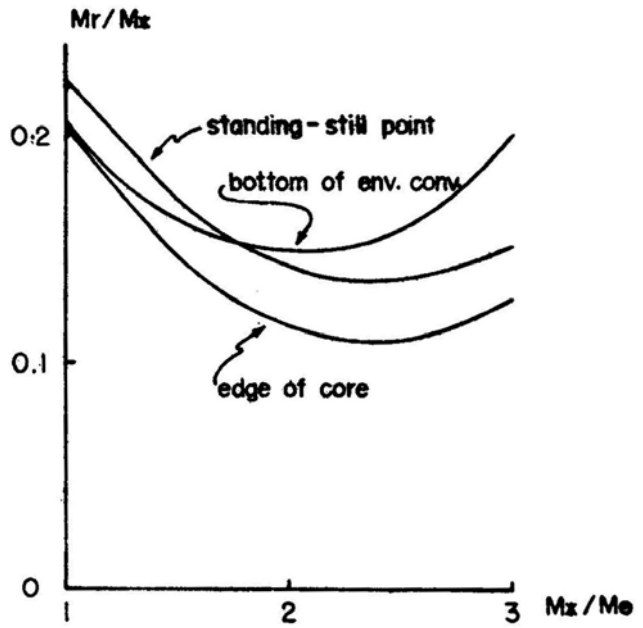

Figure 5. Mass-fractions of the edge of the core, of the stand-still layer, and of the bottom of the envelope of the model stars as functions of stellar mass, deduced from the calculations of Iben (1967a, b, c).

becomes appreciable; these are all derived from Iben's models for 1$M_\odot$, 1·25 $M_\odot$, 1·5 $M_\odot$, 2·25 $M_\odot$ and 3 $M_\odot$ stars (Iben 1965, 1967b, 1967c).

On the other hand, the convection develops from the surface inwards due to the cooling of the envelope by expansion, and finally covers most of the envelope. The greatest depth which the bottom of the envelope convection reaches and the time

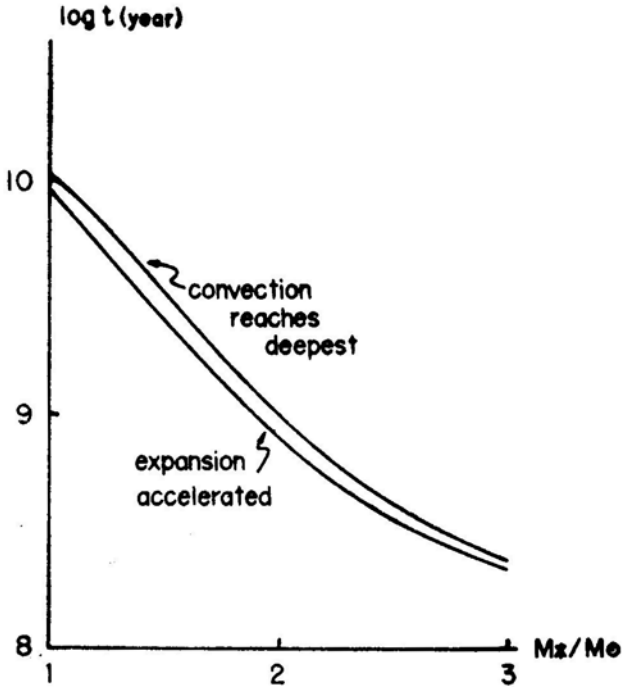

Figure 6. Epochs at which the change of the internal structure is accelerated in the course of evolution, and at which the bottom of the envelope-convection reaches its greatest depth, as functions of stellar mass (deduced from the calculations of Iben 1967a, b, c).

taken to reach this state are also plotted in Figs 5 and 6, respectively, for each of these models. The radii of the edge of the core, of the stand-still layer, and of the bottom of the envelope convection are indicated in Fig. 3 for the case of 1 $M_{\odot}$ star, as an example. It is seen from Fig. 6 that the bottom of the envelope convection is inside the region where the strong shear in the rotation exists. In the case of more massive stars, however, the bottom of the envelope convection lies outside the region of sheared rotation, but not very far away. There exist mechanisms of angular-momentum transfer which tend to relax the large gradient in Ω, or by which the fast-rotating core drags the inner part of the convective envelope and brings it into a sheared rotation. A 'dynamo-layer' which has both sheared rotation and convection in it (the presence of a remnant magnetic field being postulated) will thus appear in these heavier stars also, while it is strengthened in the case of the 1 $M_{\odot}$ star. In Section 4, we will seek mechanisms which allow such angular-momentum transfer. Finally, Fig. 7 shows the locations on the H-R diagram at which the structural changes are accelerated and the bottom of the envelope convection reaches its greatest depth, respectively, on Iben's model evolutionary tracks. These coincide with the renewed appearance of chromospheric emission after the evolution of the stars to the giant stage (Bappu 1981).

The problem of 'the rapidly rotating core of red giants and the angular momentum transfer to the envelope' reminds us of Dicke's (1964) proposal of the 'rapidly rotating core of the Sun' and the controversial debate on its spin-down (Howard, Moore and Spiegel 1967; Goldreich and Schubert 1967; Fricke 1967; Sakurai 1975). This problem and ours are directly related, but the parameters involved are very

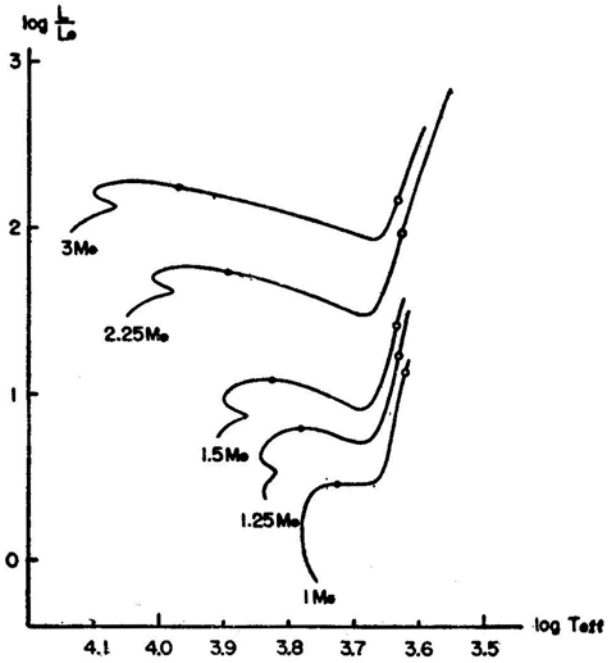

Figure 7. Locations along Iben's (1967a) evolutionary tracks on the H-R diagram of the epochs of acceleration of structural changes in evolution (dots) and of envelope-convection reaching the greatest depth (open circles).

different. For example, the radius and the central density of the core in a giant of $R_* \simeq (10–20)\ R_\odot$ in our case are of the order of $0{\cdot}03\ R_\odot \simeq (0{\cdot}003–0{\cdot}0015)\ R_*$ and 10^5 g cm^{-3}, respectively, while in Dicke's solar case ($R_* = 1\ R_\odot$) these are $0{\cdot}53\ R_\odot = 0{\cdot}53\ R^*$ and 10^2 g cm^{-3}, respectively. Therefore, most of the mechanisms of the spin-down that argued against Dicke's hypothesis by relying upon the interaction through the interface of the core and the envelope, become ineffective in our case of red giants due to the very small surface area of the core.

4. Mechanisms of angular momentum transfer from the core to the inner part of the envelope

There are some mechanisms of angular momentum transfer which may still be efficient with this small surface area of the rotating core even though the efficiency may be low. This decreased efficiency, however, is in a sense favourable, because we do not want a mechanism which is so efficient that it smears out all the differential rotation and makes the star rotate quasi-rigidly, thus destroying the merit of the differentially rotating interior. The total angular momentum of the core, if redistributed evenly, ensures only a rather slow rotation even for stars initially rotating rapidly as seen in Section 6.

4.1 *Goldreich-Schubert-Fricke Mechanism*

One possibility of a suitable mechanism is the Goldreich-Schubert-Fricke mechanism

which uses the eddy viscosity of the turbulence caused by the instability of the sheared rotation when either one or both of the conditions

$$\frac{\partial(\varpi^2\Omega)}{\partial\varpi} > 0 \tag{4}$$

and

$$\frac{\partial\Omega}{\partial z} = 0, \tag{5}$$

where $\varpi \equiv r \sin\theta$, are violated (Fricke 1967). ϖ and z are coordinates in a cylindrical coordinate system (ϖ, ϕ, z) with the axis of rotation coinciding with the z-axis. These criteria are violated in our case. According to Kippenhahn and Thomas (1981), the eddy viscosity η_t due to the destabilized axisymmetric torus is given as $\eta_t = \rho v_t\, d$, where ρ is the density, d is the cross-sectional size of the torus which is assumed to dissolve as it moves a distance of its own size, and v_t is the velocity of the element estimated by

$$v_t \simeq \frac{H_p}{H_\Omega}\frac{2\chi}{\nabla_{ad}-\nabla}\frac{d}{\tau^*}. \tag{6}$$

Here $H_P \equiv \mathcal{R}T\,\varpi^2/GM_r$ is the scaleheight, $H_\Omega \equiv \{-\partial \text{ In } (\varpi^2\Omega)/\partial\varpi\}^{-1}$ is the scale length of variation of $\varpi^2\Omega$, $\chi \equiv \varpi^3\Omega^2/GM_r$ is the ratio of centrifugal to gravitational forces, $\nabla \equiv \partial \text{ In } T/\partial \text{ In } p$, and τ^* is the timescale of the thermal adjustment, $\tau^* = 3C_p\, k\, \rho^2\zeta d^2/8acT^3$, in which C_p is the specific heat at constant pressure, k is the absorption coefficient per mass, a is the Stefan-Boltzmann constant, c is the velocity of light, and ζ is a constant factor of order unity. $\nabla_{ad} - \nabla$ and τ^* come into the expression since the element moves up because of the temperature stratification with the heat exchange by radiation. η_t is thus given by,

$$\eta_t \simeq \frac{16}{3}\frac{\chi}{\nabla_{ad}-\nabla}\frac{H_p}{H_\Omega}\frac{acT^3}{\zeta C_p\kappa\rho}. \tag{7}$$

The angular momentum transport by the turbulent viscosity caused by this mechanism may occur diffusively as

$$\frac{\partial}{\partial t}(\rho\varpi^2\Omega) = \frac{1}{\varpi}\frac{\partial}{\partial\varpi}\left(\eta_t\varpi^3\frac{\partial\Omega}{\partial\varpi}\right) \tag{8}$$

and the timescale for the diffusion may roughly be estimated as

$$\tau_{GSF} \simeq \frac{\rho(\Delta\varpi)^2}{\eta_t} \simeq \frac{\zeta C_p\kappa\rho^2}{16acT^3}\frac{\nabla_{ad}-\nabla}{\chi}\frac{H_\Omega}{H_P}(\Delta\varpi)^2 \tag{9}$$

where $\Delta\tilde{\omega}$ is the width of the region over which the transport takes place. This may be compared with Dicke's case as

$$\tau_{\mathrm{GSF}} \simeq \left(\frac{\rho}{\rho_{\mathrm{D}}}\right)^{2}\left(\frac{T}{T_{\mathrm{D}}}\right)^{-1/2}\left(\frac{M_r}{M_{r\mathrm{D}}}\right)^{2}\left(\frac{\tilde{\omega}_t}{\tilde{\omega}_{t\mathrm{D}}}\right)^{-5}\left(\frac{\Delta\tilde{\omega}}{\Delta\tilde{\omega}_{\mathrm{D}}}\right)^{2}\left(\frac{\Omega}{\Omega_{\mathrm{D}}}\right)^{2}\left(\frac{H_\Omega}{H_{\Omega\mathrm{D}}}\right)\left(\frac{(\nabla_{\mathrm{ad}}-\nabla)}{(\nabla_{\mathrm{ad}}-\nabla)_{\mathrm{D}}}\right)\tau_{\mathrm{GSF\ D}}, \quad (10)$$

Subscript D refers to the values in the boundary region in Dicke's case. Roughly estimating ratios ρ/ρ_{D} *etc.* from the model, τ_{GSF} in our case turns out to be $10^{3\sim5}$ times of $\tau_{\mathrm{GSF,\ D}}$. The estimate of $\tau_{\mathrm{GSF,\ D}}$ itself, however, was controversial as mentioned above, ranging from 10^5 yr (Goldreich and Schubert 1967) to the Kelvin-Helmholz timescale (Kippenhahn 1969) or longer due to the nonlinear suppression of the mode (James and Kahn 1970, detailed discussion may be found in Fricke and Kippenhahn 1972).

If the value of $\tau_{\mathrm{GSF,\ D}}$ falls on the smaller side in the range of the estimates, the Goldreich-Schubert-Fricke mechanism may serve in thickening the 'tail' in the distribution of the rotational shear. The mechanism is self-breeding (*i.e.* the newly produced region of sheared rotation will in turn produce turbulence which then serves in transporting angular momentum outwards) and therefore it may work even if the size of the core is small. However, the action of it may not be powerful enough to cover the entire star, since the new supply of the angular momentum from the dense core to the 'tail' cannot be too effective due to the compactness of the core, and also the expansion of the turbulent region may be suppressed by non-linear effects (James and Kahn 1970).

4.2 *Magnetic Torquing*

Another possibility is magnetic torquing (*e.g.* Lüst and Schlüter 1955). We assume that certain magnetic field remains inside the star from the earlier phase of the main-sequence stage in which the dynamo activity existed, but weakened later on. The weakening of the dynamo activity may be due to the decay of the differential rotation which in turn may be due to the damping of the rotation itself in the later phase of the main-sequence stage. Since the diffusion time of the once-generated magnetic field in the star, $\tau_{\mathrm{d}}=4\pi\sigma R_*^2/c^2$, is rather long (of the order of 10^{10} yr for Spitzer conductivity), the magnetic field may be retained even after the dynamo action has ceased.

When the redistribution of the mass takes place in the course of evolution, a redistribution of the magnetic field may also be caused due to the frozen in character of the magnetic field. The magnetic field in the outer part is expanded along with the expansion of the envelope, and that of the inner part is contracted with the contracting core. What is to be noted is the behaviour of the magnetic field in the region of sheared rotation (Section 3). The field lines having one end in the core and the other in the envelope will be wound up quickly and tightly due to the large difference in the rotational velocity of the core and the envelope.

Angular momentum transport from the rapidly-rotating core to the envelope may be due to the tension of the thus-wound-up field exerted on the inner-most part of the envelope in which the extention of the field lines is imbedded. The magnetic

torque exerted over the inner surface of the low-latitude part of the shell which lies immediately outside of the region of sheared rotation may be written as

$$I = \int_{S_b} \varpi \frac{B_\varpi B_\phi}{4\pi} dS \simeq \int_{S_b} \rho \varpi^2 \tilde{\Omega} V_{A\varpi} dS \tag{11}$$

where S_b is the low-latitude part of the inner surface of the shell immediately outside of the shearing region [for example,$(\pi/2)\ \varpi_b^2$], $V_{A\varpi} = B_\varpi (4\pi\rho)^{-\frac{1}{2}}$, $B_\phi^2/8\pi \simeq \rho\varpi^2\tilde{\Omega}^2/2$, and $\tilde{\Omega}$ is the angular velocity of the shell relative to the region of the wound-up magnetic field which is considered to be almost corotating with the core. The adopted picture is that the field is stretched by the sheared rotation to such a degree in which the weaker side of the anchoring ground (inner edge of the shell immediately outside of the shearing region) can barely stand. Since I is roughly $(\pi/2)\ \rho_b \varpi_b^4\ \tilde{\Omega}_b\ V_{A\varpi_b}$, and $J_b = \varpi_b^2\ \tilde{\Omega}_b\ \Delta\ M_b = (\pi/2)\ \rho_b\ \varpi_b^4\ \tilde{\Omega}_b\ \Delta\varpi$,the equation of the spin-up of the shell, $dJ/dt = I$, may be written as

$$\frac{\pi}{2}\rho_b\ \varpi_b^4 \Delta\varpi \frac{d\tilde{\Omega}_b}{dt} \simeq \frac{\pi}{2}\rho_b\ \varpi_b^4\ \tilde{\Omega}_b\ V_{A\varpi_b} \tag{12}$$

and therefore

$$\frac{d \ln \tilde{\Omega}_b}{dt} \simeq \frac{V_{A\varpi_b}}{\Delta\varpi}. \tag{13}$$

The timescale of the magnetic spin-up is therefore

$$\tau_{\mathrm{msu}} \simeq \frac{\Delta\varpi}{V_{A\varpi_b}} \tag{14}$$

coinciding with the expression given by Mouschovias (1981) for the magnetic braking in the star formation. τ_{msu} is rather short, of the order of 10^{10}s for $\Delta\varpi \sim 10^{11}$ cm, even with a low estimate of the order of 10^2 G for the ϖ-component of the remnant magnetic field at the bottom of the envelope. The winding-up of the field and the drag due to the tension of this field take place almost immediately compared with the Kelvin-Helmholz timescale. How, then, is it possible that the effect of this does not dominate and bring the entire star into corotation? There are many factors which can prevent such a dominance. For example, since the small spherical core is not an ideal spindle which can hold a large amount of wound-up field on it, the field will slip off poleward and the wound-up region will not continue to grow beyond a certain radius which is a small fraction of the stellar radius. This radius, however, may be larger than the radius to which the bottom of the convection zone comes down, since these radii are rather close from each other and a dynamo layer will be formed.

It is also possible that the wound-up field loaded with gravitated mass is unstable for the perturbation as in the ballooning instability argued by Parker (1966) for the

formation of the cloud in the galactic plane. Once a part of the field is raised, the mass will slide down to the lower part, and the evacuated part of the field-line will float up further. This popped up part will serve as a paddle around the rotator and enhances the angular momentum transfer to the surrounding envelope. The time-scale of the rise will again be a short dynamical timescale but again the range in radius for the angular momentum transfer is restricted in favour of our requirement, since the field strength in the bubble decreases as $[(\varpi - \varpi_b)/b]^{-3}$, where b is the horizontal scale of the perturbation on the sphere at the bottom of the envelope, and is not large. The capability of this magnetic paddle in giving angular momentum to the surrounding mass will decrease quickly as the bubble rises.

One or other of the mechanisms of angular momentum transfer discussed thus far, therefore, seem to be appropriate for our requirement since they are effective in ranges short compared with the radius of the star, R, but long enough to produce a region of sheared rotation in the convective envelope, the bottom of which comes down close to the edge of the core (Section 2) and forms the so-called dynamo layer.

5. Dynamo action and the emergence of the magnetic field to the stellar surface

Dynamo mechanism developed for the Sun refers to the regeneration process of the magnetic field in the differentially-rotating convective atmosphere. The differential rotation stretches the field and produces the toroidal component (Parker 1955; Babcock 1961), and the convection with the effect of Coriolis force serves as the back-feeder from the toroidal to the poloidal field (Parker 1955). Our situation described above in which the inner part of the convective envelope is dragged into a sheared rotation through the coupling with the rapidly rotating core, just provides us with a dynamo layer.

The equation describing this regenerative process of the magnetic field may be written in the form,

$$\frac{\partial A}{\partial t} = \alpha_{AA} A + \alpha_{AB} B \tag{15}$$

$$\frac{\partial B}{\partial t} = \alpha_{BB} B + \alpha_{BA} A \tag{16}$$

where A is the φ-component of the vector potential and B is the averaged toroidal field intensity, and represent poloidal and toroidal field, respectively. The expressions of coefficients differ from one model to another, depending upon the flow patterns and velocity amplitude considered in the model.

For example, in Yoshimura's model (1972), which is one of the most successful models introducing the notion of the global convection, these are,

$$\alpha_{AA} \equiv D_s + D_{GA}, \tag{17}$$

$$\alpha_{BB} \equiv D_s + D_{GB}, \tag{18}$$

$$\alpha_{AB} \equiv R_{GA}, \tag{19}$$

$$\alpha_{BA} \equiv R_{DR} + R_{GB}, \tag{20}$$

where

$$D_{GA} \equiv \frac{U^2}{2r_s^2 \left| \omega^{(0)} \right|} L_A(\mu, z), \tag{21}$$

$$D_{GB} \equiv \frac{U^2}{2r_s^2 \left| \omega^{(0)} \right|} L_B(\mu, z), \tag{22}$$

$$R_{GA} \equiv \frac{U^2}{2r_s^2 \left| \omega^{(0)} \right|} \frac{D}{\pi} \frac{\Omega_e}{\left| \omega^{(0)} \right|} L_A(\mu, z), \tag{23}$$

$$R_{GB} \equiv \frac{U^2}{2r_s^2 \left| \omega^{(0)} \right|} \frac{\pi}{D} \frac{\Omega_e}{\left| \omega^{(0)} \right|} L_B(\mu, z), \tag{24}$$

$$D_s \equiv \frac{\eta_m}{r_s^2} L_s(\mu, z), \tag{25}$$

$$R_{DR} \equiv \frac{a_1 \Omega_e}{D} L_{DR}(\mu, z), \tag{26}$$

in which $L_A(\mu, z)$ *etc.* are operators inherent to the assumed flow-patterns, $\omega^{(0)}$ is the angular frequency of the dynamo cycle, Ω_e and a_1 are the angular velocity and the coefficient of its $(1 - \mu^2)$ dependence at the inner radius of the dynamo layer, respectively; r_s is the inner radius, D is the thickness of the dynamo layer, U is the velocity amplitude of the convection, and η_m is the magnetic diffusivity. Coefficients D_{GA}, D_{GB} and D_s represent dissipative effects by convection and by magnetic diffusivity respectively, and R_{GA}, R_{GB} and R_{DR} represent regenerative effects by convection and by differential rotation, respectively. It is to be noted that the convection contributes to the dissipation of A and B as well as to the regeneration of A from B while the differential rotation contributes to the generation of B from A and to the regeneration of A from B,

From the discussion of Sections 3 and 4, we here assume, as a set of rough parameters, that Ω_e is greater by a factor 10, U is smaller by a factor 10, respectively, than those in the solar case, while other parameters are of the same order as those of the solar case. Then, modifying the values in Yoshimura's (1975) estimates according to their dependence on Ω_e and U, we have the estimates for the coefficients as,

$$|D_{GA}| \sim |D_{GB}| \sim 10^{-11}\ \mathrm{s^{-1}}, \quad |D_s| \sim 10^{-9}\ \mathrm{s^{-1}}$$

$$|R_{GA}| \sim 5\ \mathrm{cm\ s^{-1}}, \quad |R_{GB}| \sim 4 \times 10^{-20}\ \mathrm{cm^{-1}\ s^{-1}}$$

and

$$|R_{DR}| \sim 10^{-15}\ \mathrm{cm^{-1}\ s^{-1}}. \tag{27}$$

It is seen from this that the production of the toroidal field from the poloidal field is enhanced by one order of magnitude mainly due to the effect of the high differential rotation. The regeneration of the poloidal from the toroidal is smaller by one order of magnitude due to the enhancing effect by large Ω_e and the reducing effect by small U. Dissipation effect by convection is weaker by two orders of magnitude due to the assumed smaller velocity amplitude of the convection at the bottom of convection zone.

A very rough measure of the regeneration may be given by the ratio of B_p/B_t when A reaches an extremum ($\partial A/\partial t \simeq 0$ in Equation 15) which is

$$\frac{B_p}{B_t} \simeq \frac{\frac{1}{r}\frac{\partial (rA)}{\partial r}}{B} \sim \frac{A}{rB} \sim \frac{R_{GA}}{r_s D_s} \sim 5 \times 10^{-2}. \tag{28}$$

If B_t is a fraction of the wound-up field which is stretched by the difference in the rotation between the core and the envelope, $B_t \simeq (4\pi\rho_b)^{1/2}\, \varpi_b\, \tilde{\Omega}_b \sim 10^6$G, B_p can attain high enough a value as the regenerated source.

Marked differences between our case and the solar case are as follows. For the mechanism of the maintenance of the differential rotation in the solar case, some special mechanism of angular momentum transport to the region of higher angular velocity at low latitudes has been considered in order to explain the equatorial acceleration on the surface (Busse 1970; Durney 1970). In contrast, in our case, the differential rotation is sustained simply by the gradual transfer of the angular momentum from the spun-up core to the inner-most part of the envelope.

Also, the dynamo layer in our case is located very deep in the envelope around $R \sim 0{\cdot}1\ R_*$, while in the solar case it is in the outer convection zone of $R > 0{\cdot}85\ R_*$. The magnetic field at the upper boundary of the dynamo layer is directly observable in the solar case, but the corresponding layer is deep-lying and the magnetic field released from this deep-lying dynamo layer is carried out to the stellar surface diffusively by convection. This may make the emerging magnetic flux diffuse in an extended area in the case of giants. The detection of stellar rotation may then be possible either from the flux variation of chromospheric lines (Wilson 1978), or from the variation of the total light (*e.g.* Eaton and Hall 1979 for RS CVn case).

6. Discussion

First, it is interesting to ask whether our picture for low-mass giants is also relevant for the case of supergiants. These objects, which have evolved from massive stars, had greater rotational velocities and probably stronger fossil magnetic fields than those of low-mass giants when they were on the main sequence. It therefore seems possible that the chromospheric activity of them may be either due to the diluted fossil field itself, or due to the field regenerated in the dynamo process by the differential rotation which survived the spin-down of the convective envelope.

We may, however, argue against these possibilities. Take as an example a B5-type star ($M_* = 6M_\odot$, $R_* = 4R_\odot$, $V \sin i \lesssim 160$ km s^{-1} and, say, $B_{\rm surf} \sim 3 \times 10^3$ G). In the course of evolution, it will expand to $10^2\ R_\odot$; the fossil magnetic field of even

3×10^3 G on the average on the main sequence will be diluted to $3 \times 10^3 \times (1/25)^2 \sim 5$ G, and the angular velocity, which was $20\Omega_\odot$, will drop to $20\Omega_\odot \times (1/25)^2 \sim 0{\cdot}032\ \Omega_\odot$. We thus note in the case of supergiants that the effect of rapid initial rotation tends to be cancelled by the larger spin-down ratio due to the larger ratio of radii in the expansion. These estimates show that the diluted fossil field and the spun-down angular velocity of the envelope are too small to do much. Non-fossil, or non-potential field character is indeed required in order to explain the magnetic activity including the heating of the corona (*e.g.* Uchida 1980).

In contrast to these, the process similar to the one discussed in the present paper will inevitably take place also in supergiants. Spin-up of the core is more pronounced than in the case of low-mass giants due to the larger ratio of radii in the contraction. Also, the regenerated field in supergiants will be stronger than in the case of giants, since the density in the rapidly rotating core and in the surroundings, the anchor-ground for stretching the field in the region of sheared rotation, is higher and can wind-up the toroidal field stronger. If diffused to a similar field strength over the larger surface area of supergiants, this may explain the observation of Basri and Linsky (1979) and Weiler and Oegerle (1979) that supergiants emit one to two orders of magnitude more energy in the chromospheric lines than the giants.

It should be mentioned that the detailed values of the resulting magnetic field, for example, depend not only on the mass but also on the distribution of the initial magnetic field and initial rotation in the interior. This may explain the scatter in the observed intensities of Ca II or Mg II lines for stars with the same mass since initial magnetic field and initial rotation are the factors which also depend on the circumstantial condition at the star formation, rather than solely on the mass of the star.

Finally, we may make a comment on the relation of the rotation of a star to its magnetic activity (Ayres and Linsky 1980; Walter 1981; Vaiana 1980). It has usually been considered by applying the Standard picture of the dynamo action that, among late-type stars with surface convection, those with higher rotational velocity may be regenerating stronger magnetic field. This picture may well be true in the case of young late-type dwarfs, or in the case of synchronously-rotating binaries like RS CVn type. In the case of single giants and supergiants, however, the discussion above suggests that it may not be the surface rotational velocity inherited from the rotation in the main sequence that is responsible for the dynamo action. How, then, is the correlation of the magnetic activity with the surface rotational velocity interpreted in our picture? A possible answer to this question is that, contrary to the usual view, the latter may be due to the angular momentum transported from the interior, *e.g.* by the magnetic field effect, and thus the excess angular velocity over the value expected from the angular momentum conservation of individual shells goes parallel to the appearance of the internally-produced magnetic field to the surface. Indeed some of the chromosphere-active giants or supergiants seem to have larger rotational velocities than what is explicable by the spin-down according to the angular momentum conservation of the shell of the surface mass.

Acknowledgements

One of the authors (M. K. V. B.) acknowledges the support of his stay at the Tokyo Astronomical Observatory by the Japan Society for the Promotion of Sciences. He

also thanks Professor Y. Kozai, the director, and the staff of the Observatory for their hospitality. The authors express their gratitude to Mrs. H. Suzuki and Mr. Y. Shiomi for their help in preparing the manuscript

References

Ayres, T. R., Linsky, J. L. 1980, *Astrophys. J.*, **241,** 279.
Babcock, H. D. 1961, *Astrophys. J.*, **133,** 572.
Bappu, M. K. V. 1981, *Bok Festschrift*, Ed. R. E. White (in press).
Bappu, M. K. V. 1982, *Curr. Sci.*, **51,** 24.
Bappu, M. K. V., Sivaraman, K. R. 1971, *Solar Phys.*, **17,** 316.
Bappu, M. K. V., Sivaraman, K. R. 1977, *Mon. Not. R. astr. Soc.*, **178,** 279.
Basri, G. S., Linsky, J. L. 1979, *Astrophys. J.*, **234,** 1023.
Blanco, C., Catalano, S., Marilli, E., Rodono, M. 1974, *Astr. Astrophys.*, **33,** 257.
Bray, R. J., Loughhead, R. E. 1974, *The Solar Chromosphere*, Chapman and Hall, London.
Busse, F. H. 1970, *Astrophys. J.*, **159,** 629.
Dicke, R. H. 1964, *Nature*, **202,** 432.
Durney, B. 1970, *Astrophys. J.*, **161,**1115.
Eaton, J. A., Hall, D. S. 1979, *Astrophys. J.*, **227,** 907.
Endal, A. S., Sofia, S. 1976, *Astrophys. J.*, **210,** 184.
Frazier, E. N. 1972, *Solar Phys.*, **24,** 98.
Fricke, K. 1967, *PhD Thesis*, University of Göttingen.
Fricke, K. J., Kippenhahn, R. 1972, *A. Rev. Astr. Astrophys.*, **10,** 45.
Goldreich, P., Schubert, G. 1967, *Astrophys. J.*, **150,** 571.
Howard, L. N., Moore, D. W., Spiegel, E. A. 1967, *Nature*, **214,** 1297.
Iben, I. Jr. 1965, *Astrophys. J.*, **142,** 1447.
Iben, I. Jr. 1967a, *A. Rev. Astr. Astrophys.*, **5,** 571.
Ibea, I. Jr. 1967b, *Astrophys. J.*, **147,** 624.
Iben, I. Jr. 1967c, *Astrophys. J.*, **147,** 650.
James, R. A., Kahn, F. D. 1970, *Astr. Astrophys.*, **5,** 232.
Kippenhahn, R. 1963, in *Star Evolution*, Ed. L. Gratton, Academic Press, New York, p. 330.
Kippenhahn, R. 1969, *Astr. Astrophys.*, **2,** 309.
Kippenhahn, R., Thomas, H. C.1981, in *Proc. IAU Symp. 93*: *Fundamental Problems in the Theory of Stellar Evolution*, Eds D. Sugimoto, D. Q. Lamb and D. N. Schramm, D. Reldel, Dordrecht, p. 237.
Layzer, D., Rosner, R., Doyle, H. T. 1980, *Centre for Astrophys. Preprint* No. 1078.
Linsky, J. L. 1980, *A. Rev. Astr. Astrophys.*, **18,** 439.
Linsky, J. L., Worden, S. P., McClintock, W., Robertson, R. M. 1979, *Astrophys. J.Suppl. Ser.*, **41,** 47.
Lüst, R., Schlüter, A. 1955, *Z. Astrophys.*, **38,** 190.
Mestel, L. 1972, in *Stellar Evolution*, Eds H.-Y. Chiu and A. Muriel, MIT Press, Cambridge, p. 643.
Middelkoop, F., Zwaan, C. 1981, *Astr. Astrophys.*, **101,** 26.
Mouschovias, T. C. 1981, in *Proc. IAU Symp. 93*: *Fundamental Problems in the Theory of Stellar Evolution*, Eds D. Sugimoto, D. Q. Lamb and D. N. Schramm, D. Reidel, Dordrecht, p. 27.
Parker, E. N. 1955, *Astrophys. J.*, **122,** 293.
Parker, E. N. 1966, *Astrophys. J.*, **145,** 811.
Sakurai, T. 1975, *Mon. Not. R. astr. Soc.*, **171,** 35.
Schwarzschild, M. 1958, *Stellar Structure and Evolution*, Princeton University Press.
Skumanich, A. 1972, *Astrophys. J.*, **171,** 565.
Skumanich, A., Smythe, C., Frazier, E. N. 1975, *Astrophys. J.*, **200,** 747.
Stix, M. 1976, in *Proc. IAU Symp. 71*: *Basic Mechanisms of Solar Activity*, Eds V. Bumba and J. Kleczek, D. Reidel, Dordrecht, p. 367.
Thomas, R. N., Athay R. G. 1961, *Physics of Solar Chromosphere*, Interscience, New York.

Uchida, Y. 1980, in *Proc. Japan-France Seminar on Solar Physics*, Eds S. F. Moriyama and J.-C. Henoux, Tokyo Astronomical Observatory, p.83.
Vaiana, G. 1980, in *ISAS Symp. on Space Astrophysics*, Ed. S. Hayakawa, ISAS, p. 173.
Walter F. M. 1981, *Astrophys. J.,* **245,** 677.
Weiler, E. J., Oegerle, W. R. 1979, *Astrophys. J. Suppl. Ser.*, **39,** 537.
Wilson, O.C., 1976, *Astrophys. J.,* **205,** 823.
Wilson, O. C., Bappu, M. K. V. 1957, *Astrophys. J.*, **125,** 661.
Wilson, O. C., Skumanich, A. 1964, *Astrophys. J.*, **140,** 1401.
Yoshimura, H. 1972, *Astrophys. J.*, **178,** 863.
Yoshimura, H. 1975, *Astrophys. J. Suppl. Ser.*, **29,** 467.

J. Astrophys. Astr. (1982) **3,** 297–302

On the Balmer Progression in the Expanding Shell of Pleione

A. Peraiah *Indian Institute of Astrophysics, Bangalore 560034*

Received 1982 March 11; accepted 1982 July 7

Abstract. An attempt has been made to explain the Balmer progression in velocities seen in Pleione and other shell stars. Equations of conservation of mass and momentum are simultaneously solved with assumptions which simplify the calculations of the solution. We have considered the radiation pressure due to lines and continuum. It is found that the high-excitation lines are formed where the velocity gradients are high.

Key words: Balmer progression—velocity gradients-—shell stars

1. Introduction

One of the very interesting results of the extensive work by Merrill on shell stars is the detection of a progression in the velocities of the absorption lines of Balmer series of hydrogen atom, which occurs at a certain phase of the shell episode. This is the so-called Balmer progression. Merrill (1952) studied this behaviour over an extended interval in the case of Pleione. The displacements of the centres of gravity of all hydrogen lines from their positions of rest were the same between 1938—when the shell episode of Pleione began—and 1945. These corresponded roughly to the radial velocity of Pleione and therefore the Pleiades cluster. Around 1941, the average radial velocity was found to be + 5·5 km s^{-1} (Struve and Swings 1943), whereas the radial velocity of the entire cluster was found to be + 7 or + 8 km s^{-1}. From this difference in the radial velocities between Pleione and the Pleiades cluster, it can perhaps be interpreted that the shell of Pleione was expanding very slowly. Since 1946, the displacements of different Balmer lines changed in a systematic way. Higher the Balmer quantum number, more negative was the displacement of the line. That is, higher excitation Balmer lines showed higher radial velocities. Balmer progression had become quite large around 1950 and the lines were sharp. At the extreme of the progression in 1951, the H_β core continued to be strong and cores of lines of higher excitation potential had become weak and asymmetrical;

There was another shell outburst which started in the early seventies. Higurashi and Hirata (1978) report that until 1978, no Balmer progression has been noticed.

Balmer progression has been noticed in several shell stars by Merrill, In HD 33232, the radial velocities changed very slowly with Balmer quantum number till 1948, and thereafter, the change was as dramatic as in Pleione. However, the shell star 48 Librae showed no such Balmer progression (Merrill 1952).

In this paper, we shall make an attempt to understand the Balmer progression without undertaking the complicated calculations of non-LTE radiative transfer and hydrodynamics of the shells. We would like to show qualitatively, that the high excitation Balmer lines of hydrogen are formed in a region where the velocity gradients are high and therefore these lines show high radial velocities.

2. Velocity gradients in the shell

In this section, we shall study how radiation field affects the gas motion through the pressure due to line radiation. Our aim is, in particular, to study the varying effect that it produces on lines of different quantum numbers. There are two main aspects that we should study: the hydrodynamics of the gas flow and how this motion affects the Balmer lines.

To understand the motion of the gases in the shell, one must solve simultaneously, the equation of continuity and equations of conservation of momentum and energy. We have to take into account the radiation pressure due to continuum and lines. It is difficult to obtain a simultaneous solution (analytical or numerical) without making a few simplifying assumptions.

For a spherically-symmetric flow in steady state, the equation of momentum together with the equation of continuity is written as (Mihalas 1978, p. 562)

$$\left(1-\frac{a^2}{v^2}\right) v\,\frac{dv}{dr}=\frac{2a^2}{r}-2a\,\frac{da}{dr}-\frac{GM(1-\Gamma_e)}{r^2}+g_{r,l} \tag{1}$$

where a is the thermal velocity, v is the gas velocity, M is the mass of the central star, Γ_e is the ratio of radiative acceleration (due to a continuum dominated by electron scattering) and acceleration due to gravity given by,

$$\Gamma_e \simeq 2{\cdot}5\times 10^{-5}\left(\frac{L_*}{L_\odot}\right)\left(\frac{M_\odot}{M_*}\right) \tag{2}$$

(Mihalas 1978, p. 554). The quantity $g_{r,l}$ expressed as (Mihalas 1978, p. 558),

$$g_{r,l}=\frac{2\pi}{c\rho}\sum_l\int_0^1 d\mu\int_0^\infty dv\;\chi_l(v)\,I_v(0)\,\mu\exp(-\tau_v/\mu) \tag{3}$$

is the acceleration due to radiation force in the lines. The sum extends over all lines. The specific intensity decays exponentially and therefore we have written

$I_\nu(\tau_\nu) = I_\nu(0) \exp(-\tau_a/\mu)$, τ_ν being the optical depth at frequency ν, c the velocity of light, ρ the material density and $\chi_l(\nu)$ the absorption coefficient at frequency ν in the line l. When summed up over all the lines, Equation (3) is given by,

$$g_{r,l} = \frac{S_e L}{4\pi c r^2} M(t), \tag{4}$$

where $S = n_e \sigma_e/\rho_e$, n_e being the electron density and σ_e being Thomson scattering coefficient. The quantity $M(t)$ is called the radiation force multiplier and if we manage to obtain a suitable form of this function, we can estimate $g_{r,l}$. Castor, Abbot and Klein (1975) evaluated this function assuming a C III spectrum and taking the abundance of C^{++} equal to 10^{-3}. They have also assumed line-forming ions on the basis of LTE approximation. They fitted $M(t)$ as

$$M(t) = kt^{-\alpha} \tag{5}$$

with $k \sim 1/30$ and $\alpha = 0{\cdot}7$. The quantity t is calculated by the relation,

$$t = \sigma v_{th} \left(\frac{dv}{dr}\right)^{-1} \tag{6}$$

where v_{th} is the thermal velocity of the gas.

Let us assume that the matter in the shell of Pleione is in radiative equilibrium and the temperature can be taken to vary as

$$T(r) = T_0 \left(\frac{r_0}{r}\right)^{1/2}. \tag{7}$$

We can estimate various quantities in Equation (1) and they are given by,

$$\frac{dT(r)}{dr} = -\tfrac{1}{2} T_0 \frac{1}{r} \left(\frac{r_0}{r}\right)^{1/2},$$

$$a(r) = 1{\cdot}2842 \times 10^4 T_0^{1/2} \left(\frac{r_0}{r}\right)^{1/4},$$

$$\frac{da(r)}{dr} = -3{\cdot}2105 \times 10^3 T_0^{1/2} \frac{1}{r} \left(\frac{r_0}{r}\right)^{1/4},$$

$$\frac{2a^2(r)}{r} = -2a(r)\frac{da(r)}{dr} \simeq 8{\cdot}248 \times 10^7 x r^{-3/2}. \tag{8}$$

with

$$x = r_0^{1/2} T_0 (1 + T_0^{1/2}) \tag{9}$$

and also

$$\frac{dv(r)}{dr} = \frac{\dfrac{2a^2(r)}{r} - 2a(r)\dfrac{da(r)}{dr} - \dfrac{GM(1-\Gamma_e)}{r^2} + g_{r,l}}{v(r)\,[1 - a^2(r)/v^2(r)]}. \tag{10}$$

By substituting Equations (2)–(9) in Equation (10), we obtain

$$\frac{dv(r)}{dr} = v(r)\left[8{\cdot}2484 \times 10^{7}\, x\, r^{-3} - GMr^{-3}\left\{1 - 2{\cdot}5 \times 10^{-5}\left(\frac{L_*}{L_\odot}\right)\left(\frac{M_\odot}{M_*}\right)\right\}\right.$$

$$\left. + S_e\, L\,(4\pi c r^2)^{-1}\, M(t)\right] \Big/ \left\{v^2(r) - 1{\cdot}6492 \times 10^{8}\, T_0\left(\frac{r_0}{r}\right)^{1/2}\right\}. \qquad (11)$$

We calculate the velocity gradient from Equation (11) by using appropriate values of parameters for Pleione. Mass, luminosity, radius and temperature of a star of spectral type are obtained from Allen (1973). The shell has been divided into several sectors of equal geometrical length. The velocity gradient *dv*/*dr* in Equation (11) is calculated in each of these sectors. The calculation is started with initial velocity

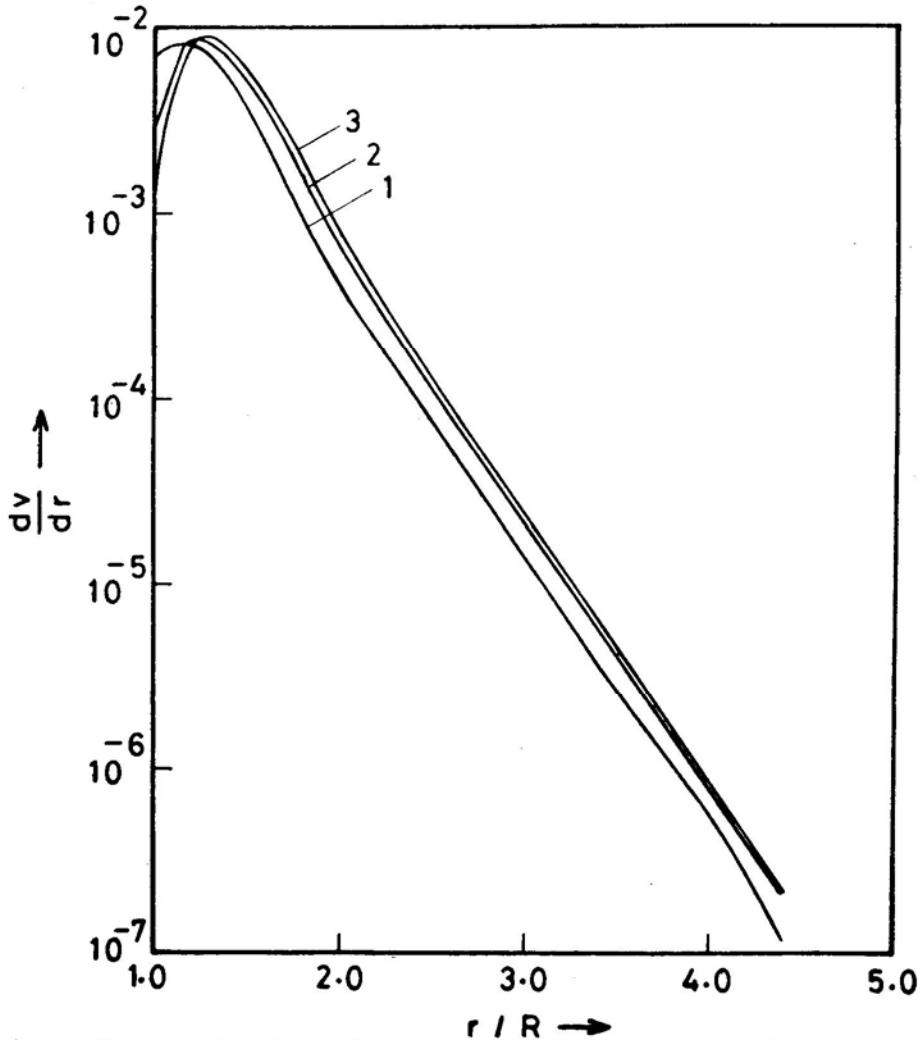

Figure 1. Velocity gradiant *dv*/*dr* is plotted against radius. The curves labelled 1, 2 and 3 refer to 2, 4 and 8 times the mean thermal values of *a* at *r*/*R* = 1, respectively.

$V_0 = pa(r_0)$ (p = 2,4,8) and t is calculated with an assumed electron density. In the subsequent sector, we utilize velocity and the new velocity gradient calculated in the previous sector. New thermal velocity and velocity gradients have been used to calculate the factor t. We normally stopped the calculation of dv/dt as soon as it becomes negative because negative t will not allow us to estimate M (t). One must remember that the values of k and α in Equation (5) are taken to be 1/30 and 0·7. These values represent a star of an early spectral type and we have calculated the function M (t)by using several different values for k and α. In all the cases, the nature of variation of the velocity gradient remains the same.

We have plotted in Fig. 1, the velocity gradient as a function of stellar radius. We notice that intitially, in the first twenty per cent of stellar radius of the shell, the velocity gradient increases sharply and then falls rapidly. At about $r/R \approx 4$, the velocity gradient becomes almost negligible and the shell moves with constant velocity. At about $r/R \approx 4{\cdot}5$, the velocity gradient becomes negative. This is because the radiation force $g_{r,\,l}$ is decreasing faster than the gravity term. Therefore, the quantity t becomes negative and hence no further calculations of dv/dr are possible. It is interesting to note that the velocity gradients are extremely large in the sector between r/R = 1 and 2. This has an important consequence, in that the atoms of higher Balmer number are more abundant in this sector.

The number of hydrogen atoms in various stages of excitation, is calculated by using the Boltzmann equation (Aller 1963)

$$\log \frac{N_i}{N_2} = -\theta \chi_{2,\,i} + 2 \log i - 0{\cdot}6021$$

where $\theta = 5040/T$ and the quantum numbers are given by i = 3, 4,... 30; $\chi_{2,\,i}$ is the excitation potential measured in electron volts. We have calculated the radial variation of the temperature (see Table 1) using Equation (7).

Utilizing the temperature distribution shown in Table 1, we have evaluated N_i/N_2 along the radius vector. These results are shown in Fig. 2. It is interesting to note that the atoms of higher Balmer quantum numbers are concentrated in the sector bounded by r/R = 1 and 2, Therefore these lines are formed in this region.

If we examine Fig. 1, we notice that the gas in this sector is moving with a very high, velocity gradient. This leads us to the conclusion that the lines of higher Balmer quantum numbers are formed where the velocity gradients are large, thus explaining the Balmer progression observed by Merill (1952). For a quantitative theoretical

Table 1. Radial distribution of temperature in the model envelope.

r/R	T(K)
1	12000
1·5	9797
2	8485
2·5	7589
3	6928
3·5	6414
4	6000
4·5	5656
5	5366

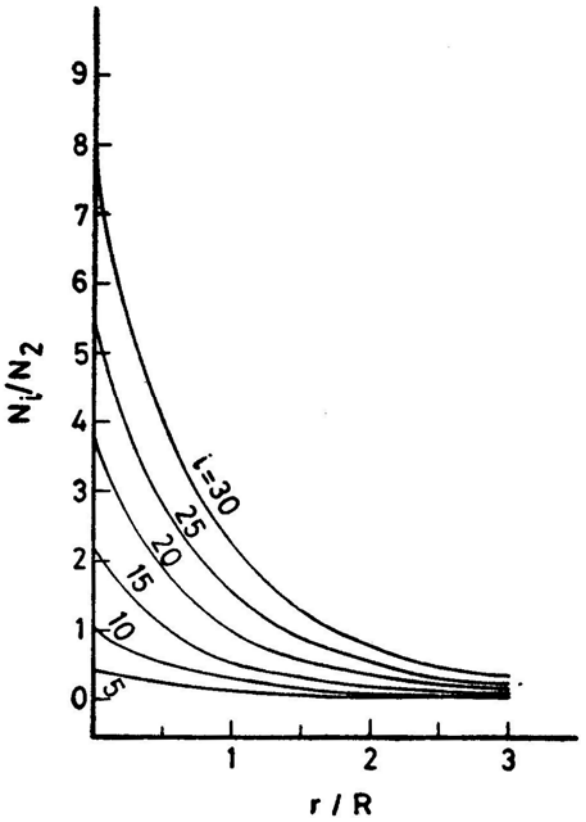

Figure 2. The radial distribution of high excitation Balmer atoms is described. *i* represents the Balmer quantum number.

estimate of the velocities, one has to obtain the simultaneous solution of the equations of gas dynamics and radiative transfer with non-LTE physics. Presently this is under investigation.

Acknowledgement

The author wishes to thank late Professor M. K. V. Bappu for directing his attention towards the problems of Pleione.

References

Allen, C. W.1973, *Astrophysical Quantities*, 3 edn, Athlone, London.
Aller, L. H. 1963, *Astrophysics: The Atmospheres of the Sun and Stars*, 2 edn, Ronald Press, New York.
Castor, J. I., Abbott, D. C., Klein, R. I.1975, *Astrophys. J.*, **195**, 157.
Higurashi, T., Hirata, R. 1978, *Publ. astr. Soc. Japan*, **30,** 615.
Merrill, P. W. 1952, *Astrophys. J.*, **115,** 145.
Mihalas, D. 1978, *Stellar Atmospheres*, 2 edn, Freeman, San Francisco.
Struve, O., Swings, P. 1943, *Astrophys. J.*, **97,** 426.

J. Astrophys. Astr. (1982) **3,** 303–324

Intensity and Polarization Line Profiles in a Semi-Infinite Rayleigh-Scattering Planetary Atmosphere. I. Integrated Flux

R. K. Bhatia and K. D. Abhyankar
Centre of Advanced Study in Astronomy, Osmania University, Hyderabad 500007

Received 1982 April 13; accepted 1982 July 12

Abstract. Absorption and polarization line profiles as well as the curves of growth in the integrated light of a planet over the whole range of phase angles have been computed assuming a semi-infinite atmosphere scattering according to Rayleigh's phase-matrix which takes polarization into account. The relative change in line depth and equivalent widths qualitatively agree with the observations of the CO_2 bands in Venus reported by Young, Schorn and Young (1980). It is pointed out that the bands might be formed in a part of the atmosphere which is different from that where continuum polarization originates.

Key words: Rayleigh scattering—line profiles—atmosphere of Venus

1. Introduction

Efforts to compute line profiles in a scattering planetary atmosphere have been directed towards their computation for the centre of the disk or for some specific points on the disk (Lenoble 1968, 1970; Fymat 1974; Michalsky *et al.* 1974; Teifel 1976; Buriez, Fouquart and Fymat 1979). Attention has also been paid to the study of the variation of equivalent widths with phase angle in the integrated light of the planet (Belton 1968; Whitehill and Hansen 1973; Young and Kattawar 1976; Sato, Kawabata and Hansen 1977). This study is important for knowing the phase function, which determines the nature of the particles, and the structure of the atmosphere (Regas *et al.* 1975; Hunt 1973; Whitehill and Hansen 1973; Kattawar and Young 1977; Anikonov 1977; Buriez and de Bergh 1980). However, there is a lack of a comprehensive coverage of all phase angles for the change in the polarization profile of an absorption line in the integrated light. A few phase angles were covered in the work of Lenoble (1970), Fymat (1974), and Buriez, Fouquart and Fymat (1979). As we shall see, at extreme phase angles, the results obtained are quite different.

We present here results of computations of line profiles and polarization profiles in the integrated light of the planet for the following phase angles: 0, 20, 40, 60, 80, 100, 120, 135, 150 and 175 degrees. We assume a plane-parallel atmosphere with a phase matrix which is realistic for molecular scattering, *viz.* Rayleigh's phase matrix. We have pointed out in a previous paper (Bhatia and Abhyankar 1981) the inadequacy of using Rayleigh's phase function. For Venus, the work of Hansen and Hovenier (1974) based on a Mie-scattering model explained the phase variation of the continuum polarization. In that model, the phase variation of the computed equivalent widths requires that the equivalent widths should show a dip at small phase angles superposed on the general trend in which they first increase with increasing phase angle up to a phase angle of about 80° and then decrease again. However, Young, Schorn and Young (1980) find that the CO_2 bands at 7820, 7883 and 8689 Å do not exhibit such a dip at small phase angles. This has rekindled interest in Rayleigh-scattering models.

2. Basic theory

2.1 *Radiative Transfer*

Let unpolarized radiation of flux $\pi \mathcal{F}$ be incident on a plane-parallel atmosphere in the direction ($\mu_0 = \cos\theta_0, \varphi_0$), θ and φ being spherical coordinates. Then $\mathcal{F}_l = \mathcal{F}_r = \frac{1}{2}\mathcal{F}$, where $\pi\mathcal{F}_l$ and $\pi\mathcal{F}_r$ are the fluxes in two mutually perpendicular directions l and r, parallel and perpendicular to the meridian plane defined by the incident ray (Chandrasekhar 1960). The three components I_l, I_r and U of the scattered radiation I in the direction (μ, φ), where l and r are now the directions parallel and perpendicular to the meridian plane defined by the scattered ray, are given by (Chandrasekhar 1960, p. 259; Lenoble 1970; Abhyankar and Fymat 1971)

$$\mathbf{I}(\mu, \varphi) = \begin{bmatrix} I_l \\ I_r \\ U \end{bmatrix} = \frac{1}{4\mu}\tilde{Q}\tilde{S}(\mu, \varphi, \mu_0, \varphi_0) \begin{bmatrix} \mathcal{F}/2 \\ \mathcal{F}/2 \\ 0 \end{bmatrix}, \tag{1}$$

where

$$\begin{aligned}\left(\frac{1}{\mu}+\frac{1}{\mu_0}\right)\tilde{S}(\mu, \varphi, \mu_0, \varphi_0) &= \tfrac{3}{4}\tilde{\omega}_0 \begin{bmatrix} L_1(\mu) & L_2(\mu) \\ L_3(\mu) & L_4(\mu) \end{bmatrix}\begin{bmatrix} L_1(\mu_0) & L_3(\mu_0) \\ L_2(\mu_0) & L_4(\mu_0) \end{bmatrix} \\ &+ \tfrac{3}{4}\tilde{\omega}_0 (1-\mu^2)^{\frac{1}{2}}(1-\mu_0^2)^{\frac{1}{2}} H^{(1)}(\mu) H^{(1)}(\mu_0) \\ &\times \begin{bmatrix} -4\mu\mu_0\cos(\varphi_0-\varphi) & 0 & 2\mu\sin(\varphi_0-\varphi) \\ 0 & 0 & 0 \\ 2\mu_0\sin(\varphi_0-\varphi) & 0 & \cos(\varphi_0-\varphi) \end{bmatrix} \\ &+ \tfrac{3}{4}\tilde{\omega}_0 H^{(2)}(\mu) H^{(2)}(\mu_0) \\ \times \begin{bmatrix} \mu^2\mu_0^2\cos 2(\varphi_0-\varphi) & -\mu^2\cos 2(\varphi_0-\varphi) & -\mu^2\mu_0\sin 2(\varphi_0-\varphi) \\ -\mu_0^2\cos 2(\varphi_0-\varphi) & \cos 2(\varphi_0-\varphi) & \mu_0\sin 2(\varphi_0-\varphi) \\ -\mu\mu_0^2\sin 2(\varphi_0-\varphi) & \mu\sin 2(\varphi_0-\varphi) & -\mu\mu_0\cos 2(\varphi_0-\varphi) \end{bmatrix}, \end{aligned} \tag{2}$$

$$\tilde{Q} = \begin{bmatrix} 1 & 0 & 0 \\ 0 & 1 & 0 \\ 0 & 0 & 2 \end{bmatrix}, \tag{3}$$

and

$$\tilde{L}(\mu) = \tilde{M}(\mu) \cdot \tilde{H}(\mu) . \tag{4}$$

Here

$$\tilde{M}(\mu) = \begin{bmatrix} \mu^2 & (1-\mu_0^2)\sqrt{2} \\ 1 & 0 \end{bmatrix} \tag{5}$$

and

$$\tilde{H}(\mu) = \begin{bmatrix} H_1 & H_2 \\ H_3 & H_4 \end{bmatrix} \tag{6}$$

is defined by

$$\tilde{H}(\mu) = \tilde{E} + \mu \tilde{H}(\mu) \int_0^1 \frac{\tilde{H}^{\mathrm{tr}}(\mu') \tilde{\Psi}(\mu') d\mu'}{\mu + \mu'}, \tag{7}$$

where E is the unit matrix, 'tr' denotes transpose, and the characteristic matrix $\tilde{\psi}(\mu)$ is given by

$$\tilde{\Psi}(\mu) = \tfrac{3}{8} \tilde{\omega}_0 \tilde{M}^{\mathrm{tr}}(\mu) \cdot \tilde{M}(\mu). \tag{8}$$

The matrix $\tilde{H}$ is related to the matrix $\tilde{N}$ defined by Abhyankar and Fymat (1971) as

$$\tilde{N}(\mu) = \tfrac{1}{2} \sqrt{3}\, \tilde{M}(\mu) \cdot \tilde{H}(\mu). \tag{9}$$

The functions $H^{(1)}(\mu)$ and $H^{(2)}(\mu)$ are obtained from

$$H^{(n)}(\mu) = 1 + \mu H^{(n)}(\mu) \int_0^1 \frac{\Psi^{(n)}(\mu') H^{(n)}(\mu') d\mu'}{\mu + \mu'}, \quad (n = 1, 2) \tag{10}$$

where the characteristic functions $\psi^{(1)}(\mu)$ and $\psi^{(2)}(\mu)$ are given by $\frac{3}{8} \tilde{\omega}_0(1 + 2\mu^2)(1 - \mu^2)$ and $\frac{3}{16} \tilde{\omega}_0(1 + \mu^2)^2$, respectively. Here $\tilde{\omega}_0 \in (0, 1)$ is the is the single scattering albedo. We have, therefore,

$$\begin{aligned} I_i(\mu, \varphi) = {} & \tfrac{3}{32} \frac{\mu_0 \tilde{\omega}_0}{\mu + \mu_0} \{ L_1(\mu) [L_1(\mu_0) + L_3(\mu_0)] + L_2(\mu) [L_2(\mu_0) + L_4(\mu_0)] \\ & - 4 \mu\mu_0 (1-\mu^2)^{\frac{1}{2}} (1-\mu_0^2)^{\frac{1}{2}} H^{(1)}(\mu) H^{(1)}(\mu_0) \cos(\varphi_0 - \varphi) \\ & + \mu^2 (\mu_0^2 - 1) H^{(2)}(\mu) H^{(2)}(\mu_0) \cos 2(\varphi_0 - \varphi) \} \mathcal{F}, \end{aligned} \tag{11}$$

$$I_r(\mu, \varphi) = \tfrac{3}{32} \frac{\mu_0 \tilde{\omega}_0}{\mu + \mu_0} \{L_3(\mu)\,[L_1(\mu_0) + L_3(\mu_0)] + L_4(\mu)\,[L_2(\mu_0) + L_4(\mu_0)]$$

$$- (\mu_0^2 - 1)\, H^{(2)}(\mu)\, H^{(2)}(\mu_0) \cos 2(\varphi_0 - \varphi)\}\, \mathcal{F}, \tag{12}$$

$$U(\mu, \varphi) = \tfrac{3}{16} \frac{\mu_0 \tilde{\omega}_0}{\mu + \mu_0} \{2\mu_0 (1 - \mu^2)^{\frac{1}{2}} (1 - \mu_0^2)^{\frac{1}{2}} \sin(\varphi_0 - \varphi)\, H^{(1)}(\mu)\, H^{(1)}(\mu_0)$$

$$- \mu (\mu_0^2 - 1) \sin 2(\varphi_0 - \varphi)\, H^{(2)}(\mu)\, H^{(2)}(\mu_0)\}\, \mathcal{F}. \tag{13}$$

$I = I_l + I_r$ gives the total intensity. Further, in terms of the Stokes parameters, the degree of linear polarization is given by

$$\sigma = \frac{[(I_l - I_r)^2 + U^2]^{\frac{1}{2}}}{I_l + I_r}. \tag{14}$$

It should be noted that one can write $\sigma = -Q/I$ if and only if $U = 0$; but in general $U \neq 0$. Also, polarization is a positive quantity (*cf.* Clarke 1974) and mention of negative polarization should be avoided. Instead, the fact can be stated as: the *l*-component becomes larger than the *r*-component. In planetary studies, the definition $\sigma = -Q/I$ is used because it is found observationally that the electric vector for the integrated flux lies either along the equator or perpendicular to it (Dollfus 1961), which implies that $U = 0$ in that case.

2.2 *The Line Profile*

We assume a Lorentz line profile for absorption in the line, which holds at high pressures. In terms of the absorption coefficient k_0 at the line centre, the absorption coefficient k at any frequency ν is given by

$$k = k_0 \{[1 + ((\nu - \nu_0)/\alpha_L)^2]\}^{-1} \tag{15}$$

where $\alpha_L = \alpha_0\, p$ is the Lorentz half-width of the line at pressure p expressed in units of the standard pressure. It is more convenient to express the line profile in terms of the albedo $\tilde{\omega}_\nu$, given by

$$\tilde{\omega}_\nu = \frac{\sigma}{\sigma + k_\nu} \tag{16}$$

where σ is the scattering coefficient assumed to be independent of frequency over the line.

If k_c is the absorption coefficient in the continuum, the monochromatic albedo will be

$$\tilde{\omega}'_\nu = \frac{\sigma}{\sigma + k_\nu + k_c}. \tag{17}$$

Then

$$\tilde{\omega}'_\nu = \left[\frac{1}{\tilde{\omega}_\nu} + \frac{1}{\tilde{\omega}_c} - 1\right]^{-1},$$

or

$$\tilde{\omega}'_\nu = \left[\frac{1-\tilde{\omega}_0}{\tilde{\omega}_0\,(1+x^2)} + \frac{1}{\tilde{\omega}_c}\right]^{-1} \tag{18}$$

where

$$x = (\nu - \nu_0)/\alpha_L. \tag{19}$$

2.3 *Equivalent Width*

Equivalent width is a measure of the radiation depletion produced by the line and is given by

$$W = \int_{\text{line}} (1 - I_\nu/I_c)\, d\nu$$

And (20)

$$W = \int_{\text{line}} (1 - F_\nu/F_c)\, d\nu$$

in terms of intensity and flux respectively. Here the subscript 'c' denotes the continuum, while I and F represent the total intensity in both states of polarization. We can similarly define the equivalent width for intensity or flux for the two components in any two perpendicular directions, separately.

2.4 *The Curve of Growth*

In a non-scattering atmosphere, the variation of the equivalent width with the number of absorbing particles gives the curve of growth. The analogue of the number of absorbing particles in a scattering atmosphere is the specific abundance. We have chosen for the abscissa of the curve of growth the quantity $[(1/\tilde{\omega}_0) - 1] = S/\pi\alpha_L\sigma$ which is proportional to the line strength, S. Here $\tilde{\omega}_0$ is the albedo at line centre without continuum absorption. This definition differs from that used by Chamberlain (1978) by a factor $\tilde{\omega}_c$, the continuum albedo, in the numerator: $S\,\tilde{\omega}_c/\pi\alpha_L\sigma$.

3. Computation of integrated flux

We use Horak's (1950) method to compute the flux. Consider any point A on the planet (see Fig. l). This point can be represented in two different coordinate systems:

(i) the usual spherical coordinates (μ = cos θ, φ), and (ii) the planetary coordinate system. In the first case a rectangular coordinate system is set up at point A with the z-axis in the radial direction and x-axis in the horizontal plane in such a way that the azimuthal angle of the incoming ray is zero. The second system is represented by the planetary longitude η and the colatitude β which are defined with respect to the intensity equator and the meridian. The direction cosine of the incident ray μ_0, the direction cosine of the scattered ray μ and its azimuthal angle φ are given in terms of the phase angle α, by

$$\mu_0 = \sin\beta \cos(\eta - \alpha), \tag{21}$$

$$\mu = \sin\beta \cos\eta, \tag{22}$$

$$\cos\varphi = \frac{\mu\mu_0 - \cos\alpha}{(1-\mu^2)^{1/2}(1-\mu_0^2)^{1/2}} \tag{23}$$

and

$$\sin\varphi = \frac{\sin\alpha\cos\beta}{(1-\mu^2)^{1/2}(1-\mu_0^2)^{1/2}}. \tag{24}$$

For a particular phase angle α , the flux at earth is given by

$$F' = \frac{1}{D^2}\int\int I(\theta, \varphi)\,\mu dA \tag{25}$$

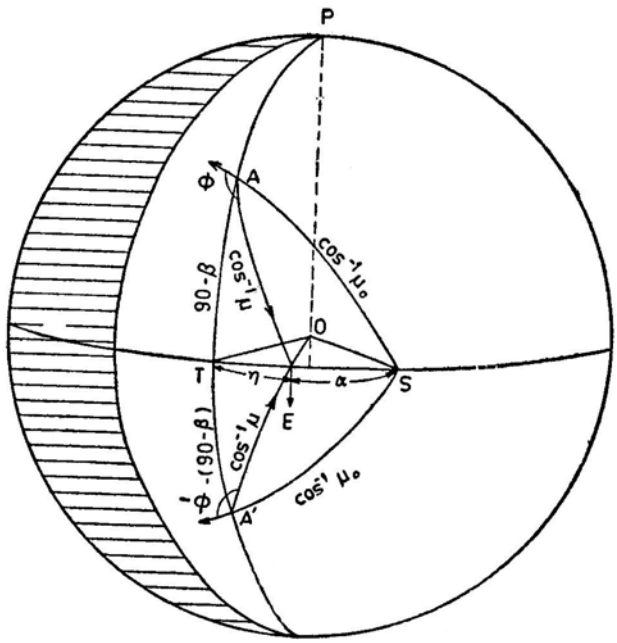

Figure 1. Geometry of scattering for a point on the disk of the planet at a phase angle α.

where D = distance of the planet from the earth and $dA = r^2 \sin\beta\, d\beta\, d\eta$ is an element of area, r being the radius of the planet. The integration is performed over the visible planetary disk. Substituting the values of μ and dA we have

$$F' = (r/D)^2 \int_0^{\pi} \int_{\alpha-\pi/2}^{\pi/2} I(\beta, \eta) \sin^2\beta d\beta \cos\eta\, d\eta. \tag{26}$$

Since (r/D) is a constant, we have

$$F = F'/(r/D)^2 = \int_0^{\pi} \int_{\alpha-\pi/2}^{\pi/2} I(\beta, \eta) \sin^2\beta d\beta \cos\eta\, d\eta. \tag{27}$$

Any one of the various numerical methods can be used to evaluate the double integral. The most efficient method is that of Chebycheff–Gauss quadrature. The necessary transformation equations and weights and divisions are given by Horak (1950). We have then

$$F = \tfrac{1}{2}(1 + \cos\alpha) \sum_i \sum_j a_i\, b_j\, I(\psi_i, \xi_j) \tag{28}$$

where a_i and b_j are the weights and ψ_i and ξ_j the divisions for β and η respectively. We have used a 36-point grid for quadrature. The integral can be evaluated for one hemisphere and the total flux can be obtained by doubling the result.

The above discussion is valid for the total intensity I which is independent of the coordinate frame chosen. However, for computing the integrated flux for the Stokes components, two additional factors have to be taken into consideration:

(i) The Stokes parameters I_l and I_r calculated from Equations (11) and (12) for a given point characterized by μ, μ_0 and φ are respectively parallel and perpendicular to the meridian plane of the scattered ray defined in the coordinate system set up at that point. In Fig. 1 the arc AE defines this meridian plane at point A. Therefore, before performing the integration over the disk, these parameters have to be referred to a common coordinate system. As is customary and convenient for observations we choose the two axes to be parallel and perpendicular to the intensity equator.

(ii) The sign of the azimuthal angle φ will be different in the two hemispheres; while this will not affect I_l and I_r, the parameter U will have opposite signs at the corresponding points in the two hemispheres (*cf.* Equations 11–13).

The new Stokes parameters, which we will differentiate from the original set by the superscript e, can be obtained by the transformation

$$\begin{bmatrix} I_l^e \\ I_r^e \\ U^e \end{bmatrix} = \begin{bmatrix} \cos^2 i & \sin^2 i & \tfrac{1}{2}\sin 2i \\ \sin^2 i & \cos^2 i & -\tfrac{1}{2}\sin 2i \\ -\sin 2i & \sin 2i & \cos 2i \end{bmatrix} \begin{bmatrix} I_l \\ I_r \\ U \end{bmatrix}, \tag{29}$$

where i, the angle between the meridian plane containing the direction (μ, φ) of the scattered ray and the equator, is given by

$$\cos i = (\sin\beta - \mu \cos\eta)/(1 - \mu^2)^{\frac{1}{2}} \sin\eta.$$

In the northern hemisphere the transformation is applied clockwise and i is positive. However, for the corresponding point in the southern hemisphere with the same μ and μ_0 the transformation matrix has to be applied counter-clockwise ; in addition although the magnitude of φ is the same, its sign is negative (*cf.* point A' in Fig. 1). One therefore obtains the following expressions for the Stokes parameters for the northern and southern hemispheres.

$$I_l(N) = (\cos^2 i)I_l + (\sin^2 i)I_r + (\tfrac{1}{2}\sin 2i)U,$$

$$I_r^e(N) = (\sin^2 i)I_l + (\cos^2 i)I_r - (\tfrac{1}{2}\sin 2i)U,$$

$$U^e(N) = \sin 2i\,(I_r - I_l) + (\cos 2i)U \tag{30}$$

and

$$I_l^e(S) = I_l^e(N),$$

$$I_r^e(S) = I_r^e(N),$$

$$U^e(S) = -U^e(N). \tag{31}$$

Adding Equations (30) and (31), we get the following expressions for the combined result for the two points:

$$I_l^e = 2[(\cos^2 i)I_l + (\sin^2 i)I_r + (\tfrac{1}{2}\sin 2i)U],$$

$$I_r^e = 2[(\sin^2 i)I_l + (\cos^2 i)I_r - (\tfrac{1}{2}\sin 2i)U],$$

$$U^e = 0. \tag{32}$$

With these expresions, after performing the integration over the disk, the degree of polarization given by Equation (13) becomes

$$\sigma = (F_r^e - F_l^e)/(F_r^e + F_l^e) \tag{33}$$

showing that we are justified in taking $\sigma = -Q/I$, as $U = 0$ for the integrated flux.

Using Equations (11), (12), (13), (32), (33) and (28) with the H-functions given by Abhyankar and Fymat (1971) the fluxes F_l^e, F_r^e, $F = F_l^e + F_r^e$ and the degree of polarization σ were calculated for various albedos at different phase angles. These results are presented and discussed below.

4. The line profiles in F_l^e, F_r^e and F

4.1 *General Behaviour*

For the total flux F, the absorption profiles for three line strengths $\tilde{\omega}_0 = 0{\cdot}2$, $0{\cdot}6$ and $0{\cdot}9$ are shown in Figs 2, 3 and 4, respectively. In all the three cases, these curves

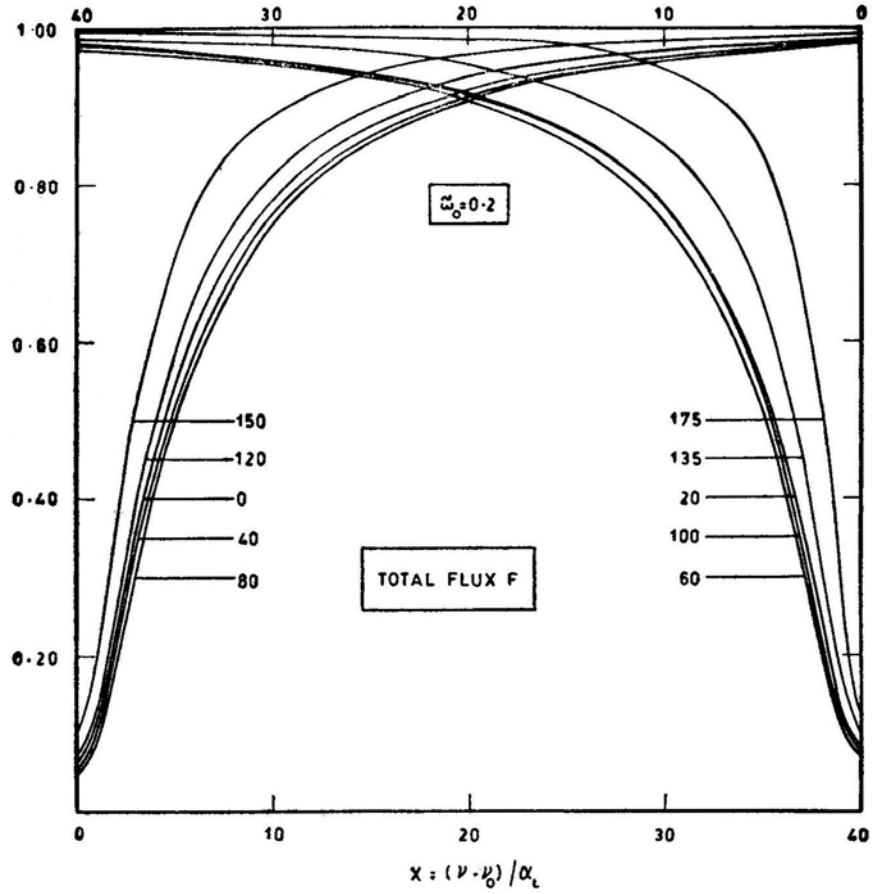

Figure 2. Line profiles for the total flux F in the case of a strong line with $\tilde{\omega}_0 = 0{\cdot}2$ at different phase angles.

point to an increase in absorption with phase angle up to about 90° and then a decrease. Further, we note that the absorption profile in the inner part of the line at phase angle 20° is slightly lower than at phase angle 100°, but in the outer part the profile is higher; there is no such crossover in other cases.

Figs 5 and 6 show the F_l^e and F_r^e profiles for $\tilde{\omega}_0 = 0{\cdot}2$. It may be noted from Fig. 6 that the F_r^e line becomes monotonically weaker with increasing phase angle. On the other hand Fig. 5 shows that the F_l^e line shows first an increase in strength and then a decrease. Further, the change in the F_l^e profile with phase angle is evidently much more pronounced than that in the F_r^e profile. This can be explained as follows. The F_r^e component, being perpendicular to the scattering plane, is scattered isotropically while the F_l^e component, being parallel to the scattering plane, has the $\cos^2 \Theta = \cos^2 \alpha$ dependence, $\Theta = 180 - \alpha$ being the scattering angle. The behaviour of the lines of other strengths ($\tilde{\omega}_0 = 0{\cdot}6$ and $0{\cdot}9$) is essentially similar, except that the changes become more pronounced as the line becomes weaker with increasing value of $\tilde{\omega}_0$. The effects of changing the continuum albedo are shown in Fig. 7 for a line of strength $\tilde{\omega}_0 = 0{\cdot}6$. It is seen that the lines become stronger for $\tilde{\omega}_c = 0{\cdot}997$

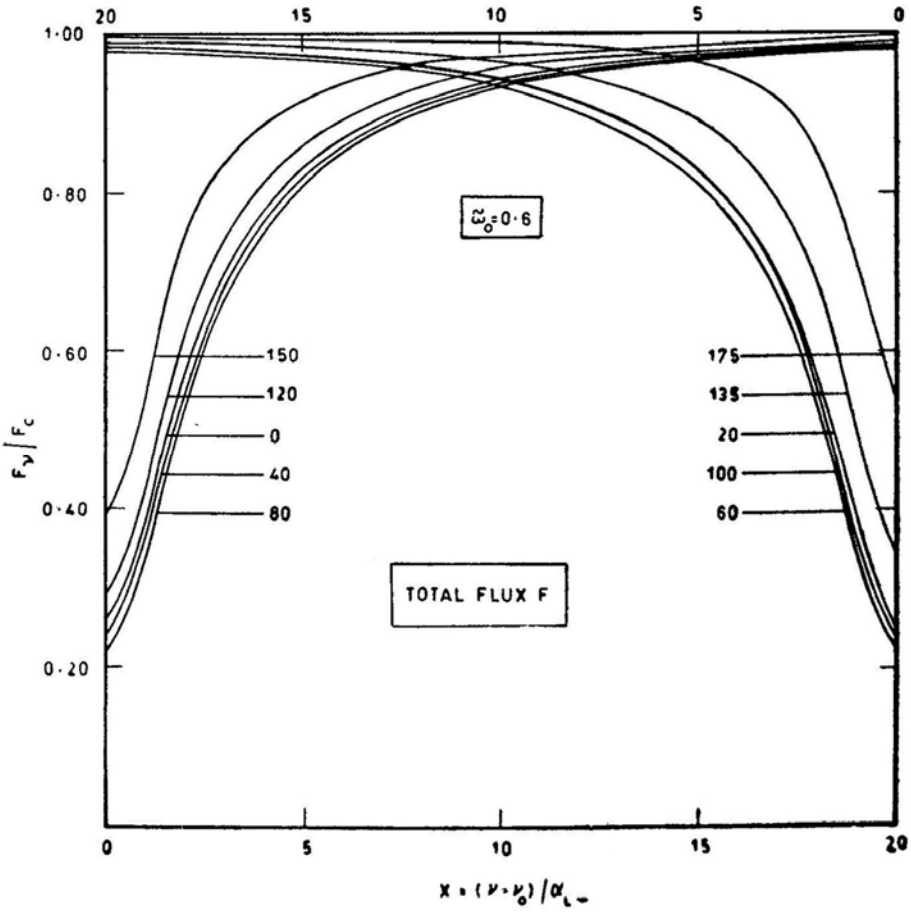

Figure 3. Line profiles for the total flux F in the case of a strong line with $\tilde{\omega}_0 = 0{\cdot}6$ at different phase angles. Note the change in the scale of the abscissa compared with Fig, 2.

as compared with $\tilde{\omega}_c = 0{\cdot}99$, both the line centre and wings being lower in the former case. This effect also becomes more pronounced for weak lines.

4.2 *Line Depth*

The change in line depth R_0 defined by $(1 - Zv_0/Z_c)$, $(Z = F, F_l^e, F_r^e)$, with phase angle is shown in Fig. 8 for $\tilde{\omega}_0 = 0{\cdot}9$. We note that for the F_r^e component there is an almost monotonic decrease while F_l^e and F first show an increase and then a decrease which has been noted above. These changes are small for a strong line and become more pronounced as the line becomes weaker. However, observations of weak lines are difficult, one of the major problems being the delineation of the continuum. Line-depth ratios can be obtained photometrically quite accurately and fast.

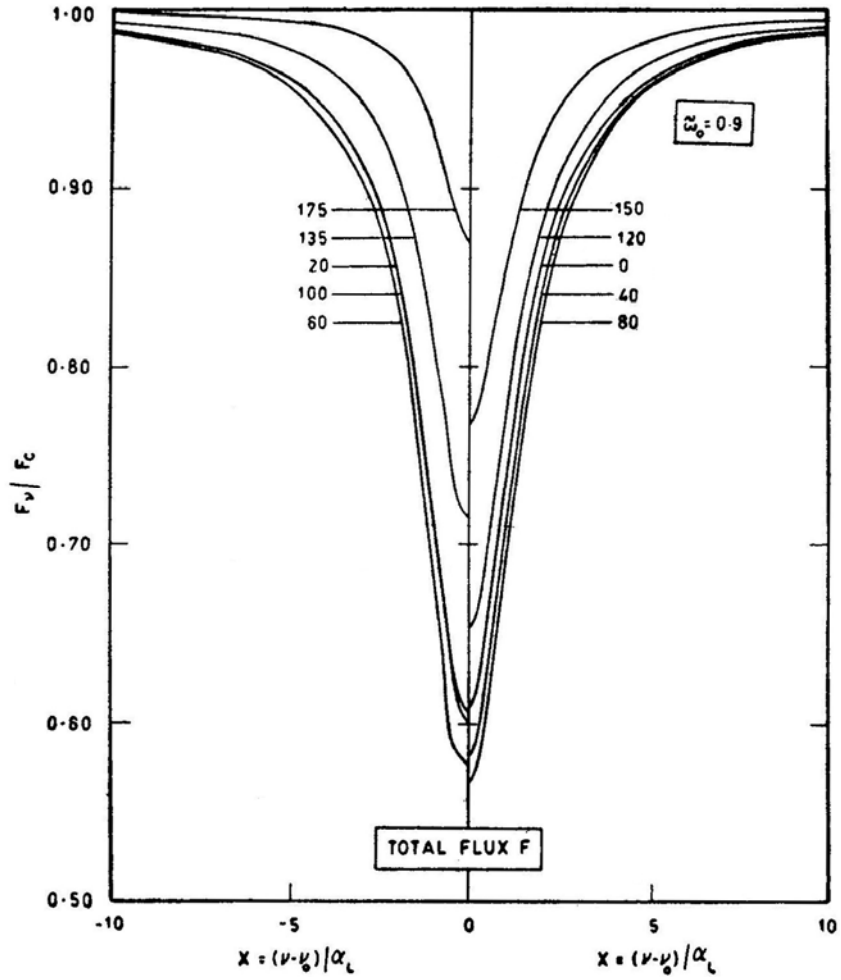

Figure 4. Line profiles for the total flux F in the case of a strong line with $\tilde{\omega}_0 = 0{\cdot}9$ at different phase angles. Note the change in the scale compared with Figs 2 and 3.

5. Equivalent widths and curves of growth

5.1 *The Equivalent Widths*

The variation of relative equivalent width with phase angle is shown in Fig. 9 for three cases: $\tilde{\omega}_0 = 0{\cdot}1$, $0{\cdot}9$, and $0{\cdot}9999$. The long-dashed curve is for the F_l^e component, the short-dashed one for the F_r^e component and the full curve for the total flux F. Two features are prominently seen in these figures: (i) The F_r^e component shows a continuous decrease with increasing phase angle while the F_l^e component shows an increase up to $\alpha = 90°$ and then a decrease. Further, the variation in equivalent width is much larger in F_l^e than in F_r^e and (ii) the change shown by all three curves is a function of line strength, the weakest line exhibiting the maximum change.

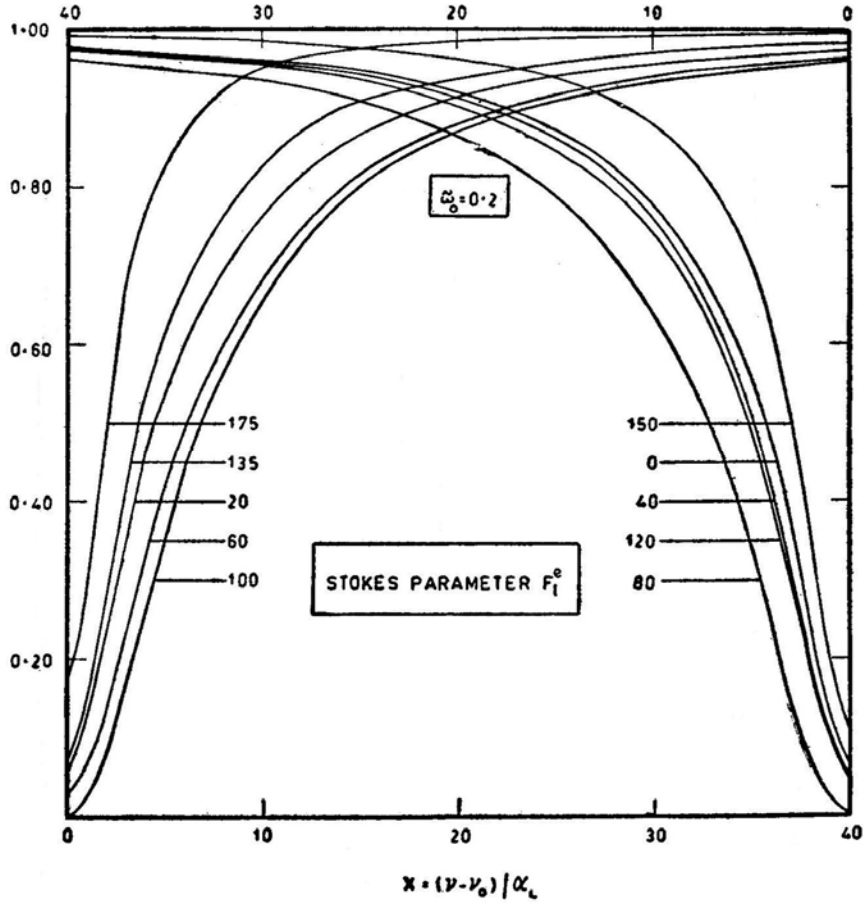

Figure 5. Line profiles for the Stokes' parameter F_l^e in the case of a strong line with $\tilde{\omega}_0 = 0{\cdot}2$ at different phase angles.

The first, fact has already been explained: the F_r^e component is scattered isotropically while the F_l^e component is Scattered according to $\cos^2 \Theta$. Thus, it is to be expected that the phase variation of the F_r^e component should agree with that computed for the total flux F for an atmosphere scattering isotropically. This indeed is the case (see *e.g.* Chamberlain 1978 p. 139; Lestrade and Chamberlain 1978).

Observations for the CO_2 bands in Venus do show that the equivalent widths first increase with phase angle and then decrease (Young 1972; Barker and Macy 1977; Macy and Trafton 1977). Consequently, a homogeneous atmosphere scattering isotropically is ruled out because as noted above, it predicts a monotonic decrease of equivalent widths with phase angle (see also Chamberlain 1970). Hunt (1972) has argued for a two-layer atmosphere to explain this effect while Regas *et al.* (1973) disagree and emphasize that a two-layer model is not necessary (see also Kattawar and Young 1977). Whitehill and Hansen (1973) and Barker and Macy (1977) have investigated this effect taking Mie scattering into account for a single-layer atmosphere. However, this requires an additional dip in equivalent widths at very small phase angles, between 0° and 10°. Schorn, Young and Young (1979) comment: 'We conclude that the 8689 Å data suggest a rather uncertain decrease of the order

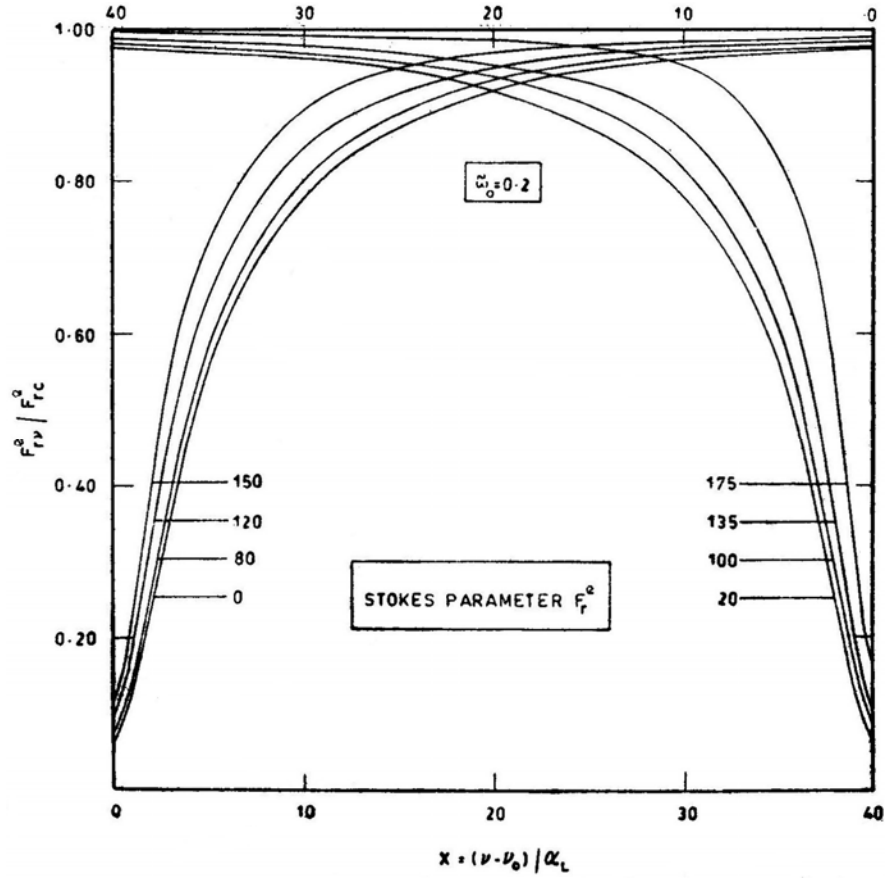

Figure 6. Line profiles for the Stokes' parameter F_r^Q in the case of a strong line with $\tilde{\omega}_0 = 0{\cdot}2$ at different phase angles. The profiles for phase angles 40° and 60° (not shown) are very close to those at 0° and 20° , respectively.

of 10 per cent in equivalent width at small phase angles'. In a later paper, Young, Schorn and Young (1980) have analysed the observations of the 7820, 7883 and 8689 A bands from 1967 to 1975 in which there was no indication of a dip at small phase angles in any of the three bands. But all of them show first an increase in equivalent width with increasing phase angle up to about 80° and then a decrease at larger phase angles. This so-called inverse phase effect becomes more pronounced as we go from stronger to weaker lines which is exactly what we see in Fig. 9 for a Rayleigh scattering atmosphere. It appears that the region where the bands are formed is different from the level in the atmosphere where continuum polarization requiring Mie scattering is produced. As discussed by us elsewhere (Bhatia and Abhyankar 1982) the total phase matrix can be represented as a sum $\tilde{P} = a\tilde{R} + (1 - a)\,\tilde{M}$ where $\tilde{R}$ and $\tilde{M}$ stand for Rayleigh and Mie phase matrices, respectively and the weight a varies from unity at the top of the atmosphere to zero as we go deeper into the atmosphere, at a rate characteristic of the relative scale heights of the aerosols and gas molecules.

The dependence of phase effect on line strength can be understood from the concept of the effective depth of line formation (Lestrade and Chamberlain 1980). As

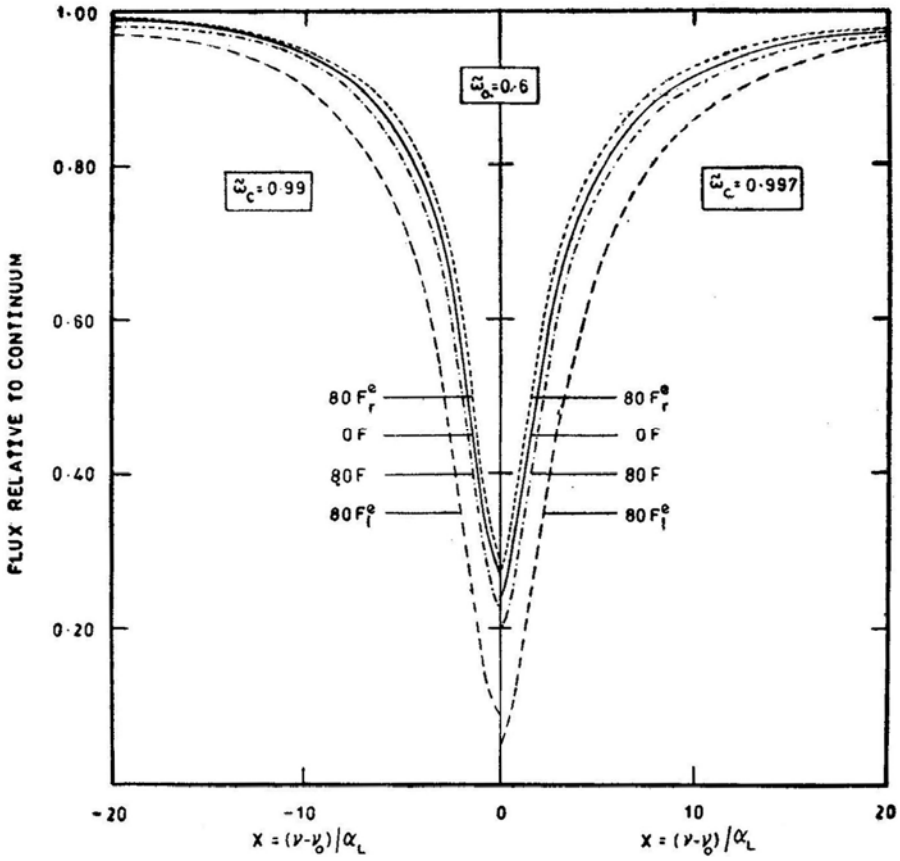

Figure 7. The effect of varying the continuum albedo on the F, F_l^e and F_r^e profiles at two phase angles of 0° and 80° ($\tilde{\omega}_0 = 0{\cdot}6$).

the line becomes weaker, more number of scatterings take place in its formation. Consequently, photons penetrate deeper into the atmosphere and therefore the weakest line shows the maximum change [Young and Kattawar (1976) found the change to be independent of line strength, when they considered a finite atmosphere with Rayleigh's phase function]. Therefore, to sample deeper layers of the atmosphere, one should use the weakest F_l^e lines, which are, however, difficult to observe.

We have repeated the calculations with $\tilde{\omega}_c = 0{\cdot}997$ and $\tilde{\omega}_c = 0{\cdot}999$; while there is not much change in the ratio in the region $0 \leqslant \alpha \leqslant 100$, the decrease in the relative equivalent widths in the remaining region becomes sharper as we go from $\tilde{\omega}_c = 0{\cdot}99$ to $\tilde{\omega}_c = 0{\cdot}999$.

5.2 *The Curves of Growth*

Fig. 10 shows the curves of growth for the total flux F for the following phase angles: 0, 80, 120, 135, 150 and 175 degrees. The transition from the linear to the square-root part is clearly visible in all the curves, the transition being sharper as we approach the phase of 90° where the absorption is maximum. As the absorption becomes

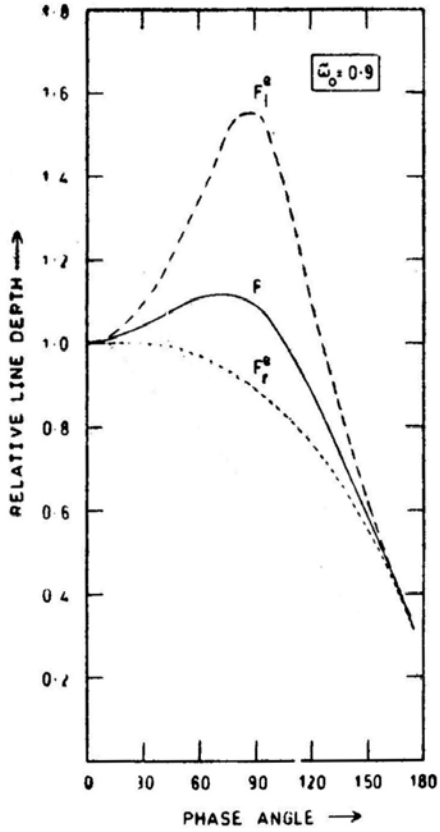

Figure 8. The variation of relative line depth with phase angle for F, F_l^e and F_r^e ($\tilde{\omega}_0 = 0.9$).

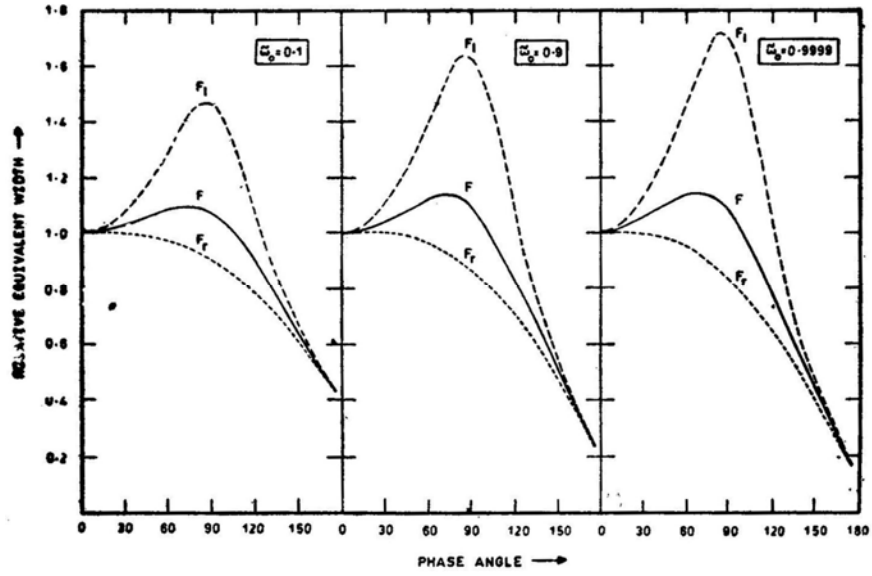

Figure 9. The variation of relative equivalent width with phase angle for F, F_l^e and F_r^e profiles ($\tilde{\omega}_0 = 0{\cdot}1$, $0{\cdot}9$ and $0{\cdot}9999$).

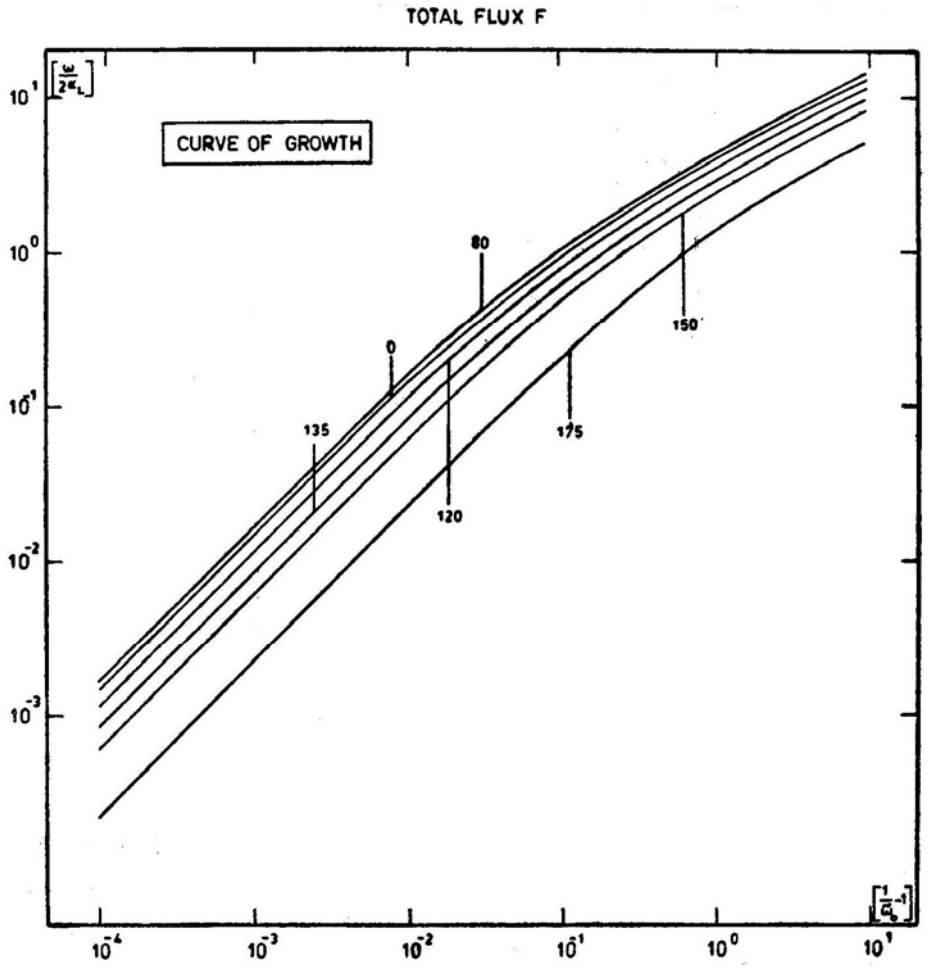

Figure 10. The curve of growth at he different phase angles.

weaker at other phase angles, the extent of the linear portion of the curve of growth increases.

6. Polarization line profiles

The polarization line profiles are shown in Figs 11 and 12 for all the three cases mentioned earlier. The profiles are shown for all the phase angles except 0° and 175° which will be discussed separately. From the two figures it is seen that maximum polarization occurs at line centre and decreases towards the wings, *i.e.* as we approach the continuum, where the values we have computed approach that of Horak (1950) for albedo $\tilde{\omega}_0 = 1{\cdot}0$. The polarization profiles at phase angles 80° and 100° match very closely at the centre but there is a discernible difference towards the wings. A similar behaviour is exhibited at angles 60° and 120° except that the curve at 60° starts above the curve at 120° and falls below as we go from the centre outwards. Thus there is a small asymmetry in the variation of polarization with

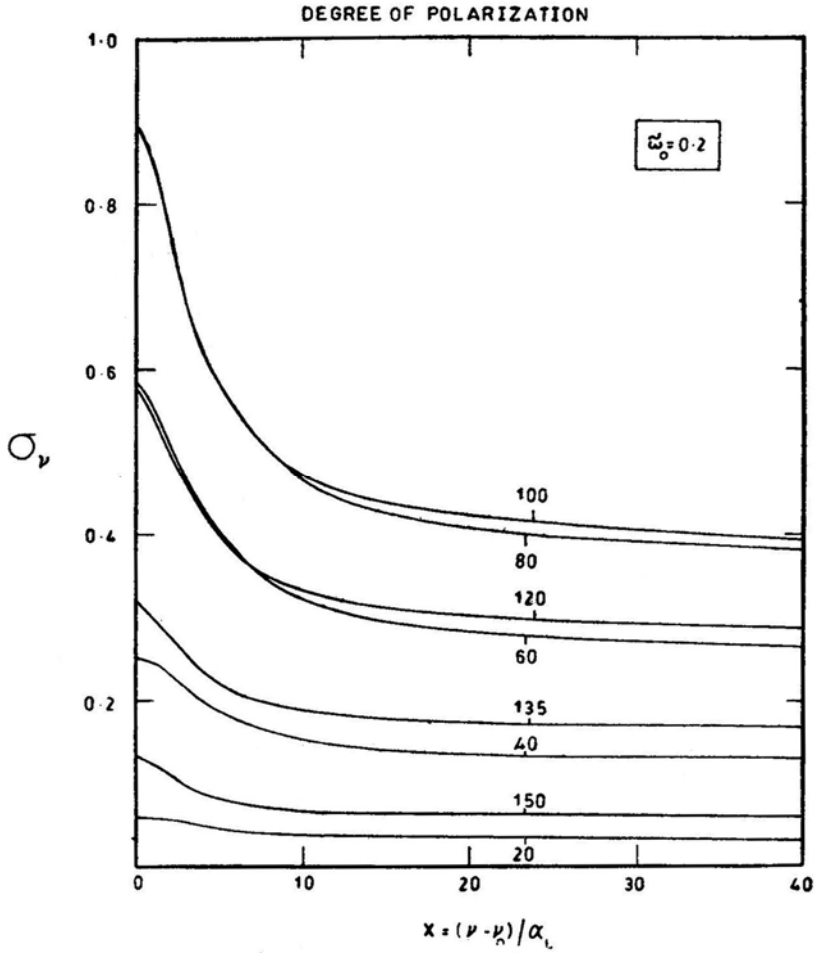

Figure 11. Polarization line profiles at different angles ($\tilde{\omega}_0 = 0.2$).

phase angle which becomes more pronounced towards the wings where the albedo is higher. Fig. 13 shows the asymmetry for three values of the albedo, in which the curve for $\tilde{\omega} = 1$ is due to Horak (1970, personal communication). This can be explained as follows: the polarization in the case of Rayleigh scattering is symmetrical around a scattering angle of 90° for single scattering; this is essentially what we observe at the line centre where the effective number of scatterings is small due to higher absorption. As we go from the line centre to the wings, the effects of multiple scattering predominate which produce increasing asymmetry. Multiple scattering can also be invoked to explain the decrease in polarization towards the wings: it 'scrambles' the initial (high) polarization carried by the lower orders of scattering.

It should also be noted that polarization increases as we go from a weaker ($\tilde{\omega}_0 = 0{\cdot}6$) to a stronger ($\tilde{\omega}_0 = 0{\cdot}2$) line. This is to be expected because the effective number of scatterings at any particular frequency in the line decreases as the line becomes stronger. We have confirmed this by performing calculations for $\tilde{\omega}_0 = 0{\cdot}1$.

Polarization profiles for phase angle 0° and 175° merit separate discussion because the situation here is more complex as shown in, Table 1. At phase angle 0°, the

Table 1. Polarization profiles for extreme phase angles.

ϖ	$X = (\nu-\nu_0)/\alpha_L$			Degree of polarization	
	$\varpi_0 = 0{\cdot}2$	$\varpi_0 = 0{\cdot}6$	$\varpi^0 = 0{\cdot}9$	$\alpha = 0°$	$\alpha = 175°$
0·1				0·6894 (−05)*	0·2079 (−02)
0·2	0·0503			0·1640 (−04)*	0·2588 (−03)
0·4	1·2980			0·3882 (−04)*	0·3675 (−02)*
0·6	2·2566	0·1240		0·6761 (−04)*	0·8112 (−02)*
0·7	2·9255	0·7701		0·8408 (−04)*	0·1057 (−01)*
0·8	3·9590	1·3338		0·1000 (−03)*	0·1323 (−01)*
0·9	6·2129	2·3664	0·3162	0·1121 (−03)*	0·1614 (−01)*
0·93	7·7705	3·0381	0·8396	0·1129 (−03)*	0·1706 (−01)*
0·95	9·6462	3·8308	1·2698	0·1123 (−03)*	0·1767 (−01)*
0·96	11·2125	4·4855	1·5875	0·1110 (−03)*	0·1797 (−01)*
0·97	13·8224	5·5669	2·0821	0·1095 (−03)*	0·1826 (−01)*
0·98	19·6743	7·9800	3·1273	0·1058 (−03)*	0·1854 (−01)*
0·99	∞	∞	∞	0·1004 (−03)*	0·1878 (−01)*

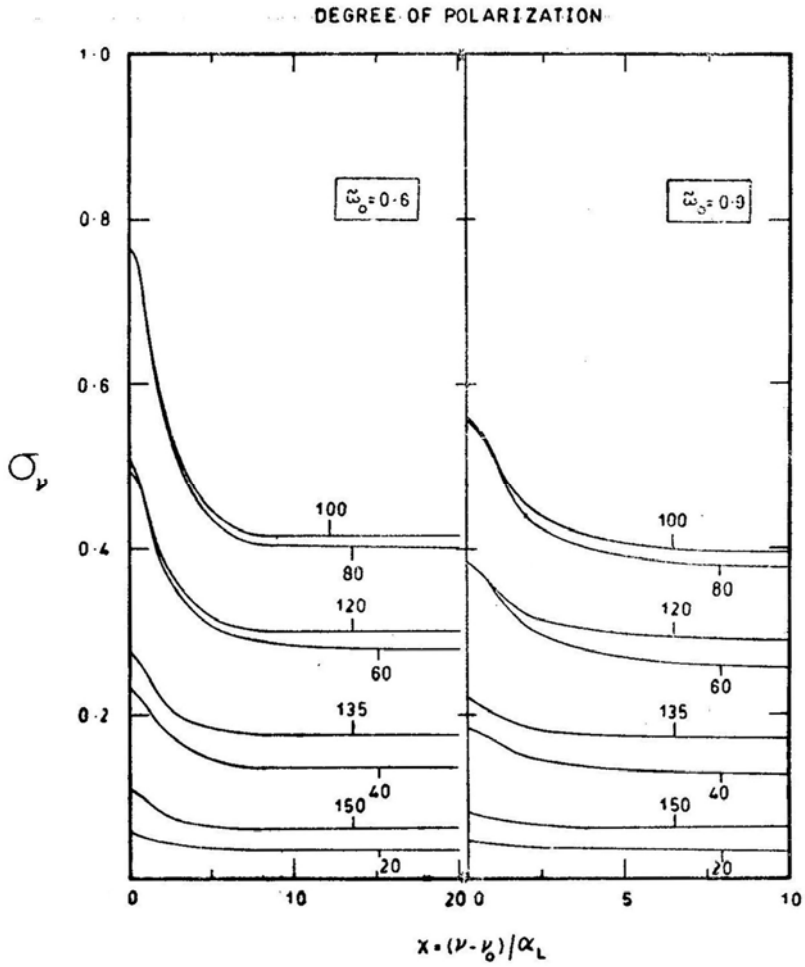

Figure 12. polarization line profiles at different phase angles ($\tilde{\omega}_0$ = 0·6 and 0·9). Note the difference in the scales of abscissa for the two cases.

polarization at line centre for the case $\tilde{\omega}_0$ = 0·2 is small with the F_r^e component less than F_l^e component, and *increases* as we go outwards till the frequency corresponding to albedo 0·93, and then decreases slightly in the extreme wings. For phase angle 175°, again confining our discussion to a line of strength $\tilde{\omega}_0$ = 0·2, we note that the F_r^e component becomes less than the F_l^e component (starred quantities) at a frequency around that corresponding to albedo 0·4. However, in this case there is no decline in polarization in the extreme wings. Further, if we were to consider a line for which $\tilde{\omega}_0$ = 0·1 we would find first a decrease and then an increase in polarization. This upsets the simple picture that multiple scattering always decreases the degree of polarization. It is noteworthy that in both these cases the degree of polarization is small. It seems that if the initial degree of polarization carried by the lower orders of scattering is low, multiple scattering might actually increase the degree of polarization. The Monte-Carlo method or computations of polarization carried by successive orders of scattering can be used to test this theoretically. Calculations to see what Mie-scattering models predict are under way. Further, the

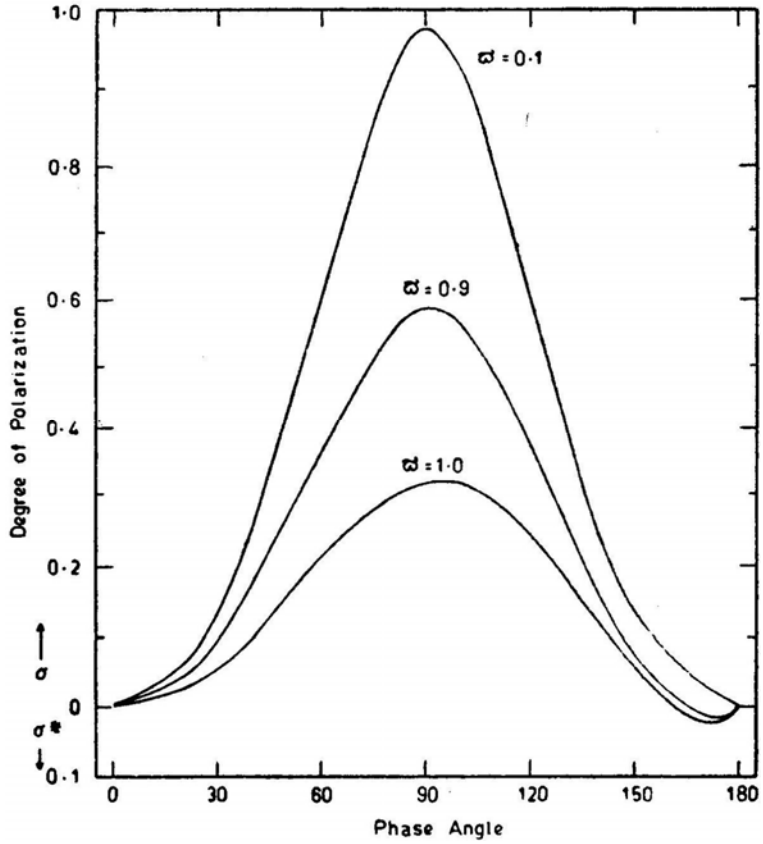

Figure 13. Variation of the degree of polarization of the phase angle for three values of the albedo.

sphericity of the atmosphere has to be taken into account for calculations near phase angle 180°.

It is interesting to note the fact that polarization can increase with albedo already existed in Fig. 8 of Abhyankar and Fymat (1970 a,b), although its significance was not recognized. That the polarization decreased in the extreme wings at $\alpha = 0$ was deduced from the above figure by van de Hulst (1980) who performed the order of scattering calculations for one case corresponding to $\mu = \mu_0 = 0{\cdot}5$ to determine the polarization carried by various orders. He found that the fourth-order scattering carried the maximum polarization.

At present there are no observations against which these results can be checked. Wolstencroft and Smith (1979) have presented some observations of polarization profiles, but they are at a low resolution. With modern detectors, it should be possible to obtain spectra at different phase angles with a polaroid in front of the slit, from which we can get polarization profiles. Alternatively, Fourier transform spectroscopy can be used.

A similar behaviour for points in the disk has been reported elsewhere (Bhatia and Abhyankar 1981). Analysis of the variations of the polarization with albedo at the points of integration for phase angle 0° shows that at some points there is an increase

of polarization with albedo and at some other points a decrease. In the integrated flux, however, there is a decrease. For the phase angle 175° all the points of integration show an increase of polarization with albedo. A detailed analysis of variation on the disk will be published in another paper of the series.

The question remains open: Is the phase effect due to an inhomogeneous atmosphere or due to the phase matrix or both? If it is due to the phase matrix what is the relative importance of Mie and Rayleigh scattering? Further observations having high spectral, spatial and temporal resolution are necessary to decide these questions.

Acknowledgement

R. K. B. would like to thank the University Grants Commission, New Delhi, for the award of a fellowship.

References

Abhyankar, K. D., Fymat, A. L. 1970a, *Astr. Astrophys.*, **4,** 101.
Abhyankar, K. D., Fymat, A. L. 1970b, *Astr. Astrophys.*, **5,** 491.
Abhyankar, K. D., Fymat, A. L. 1971, *Astrophys. J. Suppl. Ser.*, **23,** 35.
Anikonov, A. S. 1977, *Soviet Astr.*, **21,** 95.
Barker, E. S., Macy, W. W. Jr. 1977, *Icarus*, **30,** 551.
Belton, M. J. S. 1968, *J. atmos. Sci.*, **25,** 596.
Bhatia, R. K., Abhyankar, K. D. 1981, *Bull. astr. Soc. India*, **9,** 181.
Bhatia, R. K., Abhyankar, K. D. 1982, *Proc. Indo-U.S. Workshop on High Resolution Spectroscopy*, Bombay.
Buriez, J. C., de Bergh, C. 1980, *Astr. Astrophys.*, **83,** 149.
Buriez, J. C., Fouquart, Y., Fymat, A. L. 1979, *Astr. Astrophys.*, **79,** 287.
Chamberlain, J. W. 1970, *Astrophys. J.*, **159,** 137.
Chamberlain, J. W. 1978, *Theory of Planetary Atmospheres*, Academic Press, New York.
Chandrasekhar, S. 1960, *Radiative Transfer*, Dover, New York,
Clarke, D. 1974, in *Planets*, *Stars and Nebulae*, Ed. T. Gchrels, University of Arizona Press, Tucson p. 45.
Dollfus, A. 1961, in *Planets and Satellites*, Eds G. P. Kuiper and B. M. Middlehurst, University of Chicago Press, p. 343.
Fymat, A. L. 1974, in *Planets*, *Stars and Nebulae*, Ed. T. Gehrels, University of Arizona Press, Tucson, p. 617.
Hansen, J. E., Hovenier, J. W. 1974, *J. atmos. Sci.*, **31,** 1137.
Horak, H. G. 1950, *Astrophys. J.*, **112,** 445.
Hunt, G. E. 1972, *J. quantit. Spectrosc. radiat. Transfer*, **12,** 405.
Hunt, G. E. 1973, *Icarus*, **18,** 637.
Kattawar, G. W., Young, L. D. G. 1977, *Icarus*, **30,** 179.
Lenoble, J. 1968, *J. quantit. Spectrosc. radiat. Transfer*, **8,** 641.
Lenoble, J. 1970, *J. quantit. Spectrosc. radiat. Transfer*, **10,** 533.
Lestrade, J. P., Chamberlain, J. W. 1978, *Icarus*, **34,** 52.
Lestrade, J. P., Chamberlain, J. W. 1980, *Icarus*, **44,** 813.
Macy, W. Jr., Trafton, L. 1977, *Icarus*, **32,** 27.
Michalsky, J. J., Stokes, R. A., Avery, R. W., DeMarcus, W. C. 1974, *Icarus*, **21,** 55.
Regas, J. L., Boese, R. W., Giver, L. P., Miller, J. H. 1973. *J. quantit. Spectrosc. radiat. Transfer*, **13**, 461.
Regas, J. L., Giver, L. P. Boese, R. W ., Miller, J. H. 1975, *Icarus,* **24,** 11.

Sato, M., Kawabata, K., Hansen, J. E. 1977, *Astrophys. J.*, **216,** 947.
Schorn, R. A., Young, A. T., Young, L. D. G. 1979, *Icarus*, **38,** 411.
Teifel, V. G. 1976, in *Jupiter*, Ed. T. Gehrels, University of Arizona Press, Tucson, p. 441.
van de Hulst, H. C. 1980, *Multiple Light Scattering*, Academic Press, New York..
Whitehill, L. P., Hansen, J. E. 1973, *Icarus*, **20,** 146.
Wolstencroft, R. D., Smith, R. J. 1979, *Icarus*, **38,** 155.
Young, L. D. G. 1972, *Icarus*, **17,** 632.
Young, L. D. G., Kattawar, G. W. 1976, *Icarus*, **29,** 483.
Young, L. D. G., Schorn, R. A. J., Young, A. T. 1980, *Icarus*, **41,** 309.

J. Astrophys. Astr. (1982) **3,** 325–334

Exact Relativistic Model for a Superdense Star

P. C. Vaidya *Department of Mathematics, Gujarat University, Ahmedabad 380009*
Ramesh Tikekar *Department of Mathematics, Sardar Patel University, Vallabh Vidyanagar 388120*

Received 1982 May 26; accepted 1982 July 12

Abstract. Assuming that the physical 3-space t = const in a superdense star is spheroidal, a static spherically symmetric model based on an exact solution of Einstein's equations is given which will permit densities of the order of 2×10^{14} gm cm^{-3}, radii of the order of a few kilometers and masses up to about four times the solar mass.

Key words: neutron stars—general relativity

1. Introduction

General relativity establishes a correspondence between matter-energy and the geometry of the physical 3-space, the presence of the former inducing curvatures in the latter. The space-times associated with Schwarzschild's interior metric representing the gravitational field within a sphere containing homogeneous fluid at rest, or with Einstein's metric representing a static model of the universe, or de Sitter's and Robertson-Walker metrics representing models of the expanding universe, contain enough matter-energy to curve up the physical 3-space t= const into 3-spheres. The radius R of the 3-sphere is related to the density of matter in each of the above cases.

This suggests that it would be worthwhile investigating the gravitational situations described by space-times which give physical spaces t=const as simple closed 3-spaces. We have explored here the gravitational significance of space-times which have hypersurfaces t=const as 3-spheroids. It is shown that these space-times can be used to develop static models describing the gravitational field in the interior of superdense condensations of matter like white dwarfs and neutron stars. The astrophysical significance of this result is apparent in the light of the fact that only a few out of a large number of static solutions of Einstein's field equations for spherical matter-distributions entertain these possibilities.

In the next section, the metric on the 3-spheroid is deduced from the metric of the four-dimensional flat space in which it is immersed. It is observed that spheroidal 3-space exhibits central symmetry. The spherically symmetric form of the space-time metric for which the hypersurface t = const will be the given spheroidal 3-space, can be easily written down. The geometry of the space-time is governed by two parameters denoted by R and K.

Following Tolman's (1939) approach, Einstein's field equations for spherical distributions of matter in the form of a perfect fluid at rest are written out explicitly. The relationship between the matter-density and the geometry of the associated physical 3-space governed by the parameters R and K is critically examined in the next section. If λ denotes the ratio of the matter-density at the boundary of the star to the density at its centre, then it is possible to estimate the size of the configuration for different values of λ and K, if the order of magnitude of the density on the boundary is known. The gravitational field in the exterior region is uniquely described by Schwarzschild's exterior solution. The continuity of metric potentials across the boundary enables one to estimate the total mass inside the configuration.

An exact solution of the field equations is derived in Section 4 corresponding to the particular value $K = -2$ and this solution is used to develop the model for a superdense star. Assuming the matter-density on the boundary surface of the configuration to be $\rho_a \simeq 2 \times 10^{14}$ gm cm^{-3} *i.e.* of the order of the average matter density in a neutron star (Rees, Ruffini and Wheeler 1975), the size and the total mass of the configuration is computed by the scheme outlined in the previous section.

For different values of density-variation parameter λ, the respective relevant quantities are displayed in a tabular form in Section 6. These estimates clearly indicate that the solution gives physically viable static models for superdense stars. If we apply these results to describe a neutron star, we find that a maximum mass $3{\cdot}575\ M_\odot$ is obtained with a radius of 18 ·371 km when λ attains the minimum permissible value 0·4598. This maximum permissible mass is higher than the maximum upper limit 3.2 $M_\odot$ obtained by Rhoades and Ruffini (1974) without any recourse to nuclear theory. The consequences of relaxing the requirement $\rho - 3p/c^2 \geqslant 0$ to $\rho - p/c^2 \geqslant 0$ are also examined and it is found that the mass limit can be raised even further. This is an interesting feature of this model because raising the mass limit of a neutron star is of significance in deciding whether the unseen component of a binary star system is a black hole or a neutron star.

2. The field equations

Consider a 4-dimensionaI Euclidean flat space with the metric

$$do^2 = dx^2 + dy^2 + dz^2 + dw^2.$$

A 3-spheroid immersed in this 4-dimensional flat space will have the 'Cartesian' equation

$$(w^2/b^2) + (x^2 + y^2 + z^2)/R^2 = 1.$$

The sections w=const of the 3-spheroid are concentric spheres while sections x=const y=const or z=const represent systems of confocal ellipsoids. The parametrization

$x=R \sin \lambda \sin \alpha \cos \beta$,

$y=R \sin \lambda \sin \alpha \sin \beta$,

$z=R \sin \lambda \cos \alpha$,

$w=b \cos \lambda$,

of the 3-spheroid leads to the metric on the 3-space as

$$d\sigma^2=(R^2 \cos^2 \lambda + b^2 \sin^2 \lambda)\, d\lambda^2 + R^2 \sin^2 \lambda\, (d\alpha^2 + \sin^2 \alpha d\beta^2). \tag{1}$$

On introducing the space variable r through

$r = R \sin \lambda$,

metric (1) transforms to

$$d\sigma^2 = [1 - K(r^2/R^2)]\, [1 - (r^2/R^2)]^{-1}\, dr^2 + r^2\, (d\alpha^2 + \sin^2 \alpha d\beta^2) \tag{2}$$

where

$$K = 1 - (b^2/R^2). \tag{3}$$

For $K < 1$, the metric (2) is regular and positive definite at all points $r^2 < R^2$. In the case K=1, the spheroidal 3-space degenerates into flat 3-space and in the case K=0 (*i.e.* b=R) the spheroidal 3-space becomes spherical.

We shall study the space-time with the metric

$$ds^2 = e_\nu\, dt^2 - d\sigma^2$$

$$= e^\nu\, dt^2 - [1 - K(r^2/R^2)]\, [1 - (r^2/R^2)]^{-1}\, dr^2 - r^2\, (d\alpha^2 + \sin^2 \alpha d\beta^2) \tag{4}$$

where

$$\nu = \nu(r);\ x^1 = r,\ x^2 = \alpha,\ x^3 = \beta,\ x^4 = t.$$

It is clear that when K=0, the physical 3-space t = const becomes spherical and so

(i) when $e^\nu = \{A + B\, [1 - (r^2/R^2)]^{1/2}\}^2$, K= 0, metric (4) gives the metric of Schwarzschild's interior solution;

(ii) when $\nu = 0$, $K = 0$, metric (4) gives the metric of Einstein's Universe and

(iii) when $e^\nu = 1 - (r^2/R^2)$, $K = 0$, metric (4) gives the metric of de Sitter Universe.

Our aim is to consider the perfect fluid distribution represented by metric (4) when $K < 1$, $K \neq 0$ *i.e.* when in metric (4) the physical 3-space t=const is spheroidal and not spherical. For a perfect fluid the energy-momentum tensor is given by

$$T_{ik} = \left(\rho + \frac{p}{c^2}\right) u_i\, u_k - \frac{p}{c^2} g_{ik}$$

where ρ and p denote the density and pressure respectively of the fluid and u^i stands for the four-velocity, $u^i u_i = 1$. For an equilibrium situation with the metric (4) we can take

$$u^i = (0, 0, 0, e^{-\nu/2}).$$

The field equations of Einstein,

$$R_{ik} - \frac{1}{2} g_{ik} R = -\frac{8\pi G}{c^2} T_{ik}$$

will now give, for the space-time metric (4)

$$(8\pi G/c^2)\,\rho = \frac{3\,(1-K)}{R^2} \frac{\left(1 - K\frac{r^2}{3R^2}\right)}{\left(1 - K\frac{r^2}{R^2}\right)^2}, \tag{5}$$

$$(8\pi G/c^2)\,\frac{p}{c^2} = \frac{\left(1 - \frac{r^2}{R^2}\right)}{\left(1 - K\frac{r^2}{R^2}\right)}\left[\frac{\nu'}{r} + \frac{1}{r^2}\right] - \frac{1}{r^2} \tag{6}$$

together with the consistency condition ($T_1^1 = T_2^2$) which reads as

$$\left(1 - \frac{r^2}{R^2}\right)\left(1 - K\frac{r^2}{R^2}\right)\left(\nu'' + \frac{1}{2}\nu'^2 - \frac{\nu'}{r}\right) - \frac{2\,(1-K)\,r}{R^2}\left(\frac{1}{2}\nu' + \frac{1}{r}\right)$$
$$+ \frac{2\,(1-K)}{R^2}\left(1 - K\frac{r^2}{R^2}\right) = 0. \tag{7}$$

Here and in what follows an overhead prime implies differentiation with respect to r($\nu' \equiv d\nu/dr$ *etc*).

Equation (5) shows that the density of the fluid is determined by the curvature of the physical 3-space. Thus, in our approach we have replaced the usual equation of state of matter by the geometrical requirement that the physical 3-space be spheroidal which predetermines the law of variation of density with r. The field equation (6) gives the variation of pressure with r when ν is chosen to satisfy Equation (7). In the next section we shall see how the law of variation of the density given by Equation (5) enables us to estimate the mass and the radius of the configuration.

3. Law of variation of density

Expression (5) for the matter density implies that at $r = 0$,

$$(8\pi G/c^2)\,\rho_0 = 3\,(1 - K)/R^2. \tag{8}$$

As $K < 1$, the central density ρ_0 is positive. From Equation (5) we see that if $0 < K < 1$, ρ remains positive in the spherical region $r^2 < 3R^2/K$ which imposes a restriction on the size of the configuration. However, if $K < 0$, there is no such restriction and ρ remains positive throughout the configuration. It can be verified that ρ' is negative so that as r increases, the density decreases from the maximum value ρ_0 at the centre. On the boundary $r = a$, it attains the value

$$(8\pi G/c^2)\,\rho_a = 3\,(1 - K)\left(1 - K\frac{a^2}{3R^2}\right)\left(1 - K\frac{a^2}{R^2}\right)^{-2}R^{-2}. \tag{9}$$

We find that the ratio ρ_α to ρ_0 is given by

$$\lambda = \rho_a/\rho_0 = \left(1 - K\frac{a^2}{3R^2}\right)\Big/\left(1 - K\frac{a^2}{R^2}\right)^2 < 1. \tag{10}$$

The field in the exterior region $r \geqslant a$ is described by the Schwarzschild's exterior metric

$$ds^2 = (1 - 2m/r)\,dt^2 - (1 - 2m/r)^{-1}\,dr^2 - r^2\,(d\alpha^2 + \sin^2\alpha d\beta^2). \tag{11}$$

Hence the metric (4) should be continuous with the metric (11) as we cross the boundary $r = a$. This is achieved by stipulating the continuity of the metric coefficients g_{11} and g_{44} as also the continuity of the fluid pressure p across the boundary. The continuity of g_{11} at $r = a$ implies that

$$m/a = [(1 - K)\,a^2/2R^2]/(1 - Ka^2/R^2). \tag{12}$$

Equation (10) determines a^2/R^2 in terms of K and λ as

$$a^2/R^2 = [6\lambda - 1 - \sqrt{(1 + 24\lambda)}]/6K\lambda \tag{13}$$

and subsequently Equation (12) determines m/a in terms of K and λ.

Given ρ_α, λ and K, the parameter R can be calculated from Equation (8). The radius a and the total mass m of the configuration can subsequently be calculated from Equations (13) and (12). It is thus seen that the. knowledge of the curvature of the physical 3-space is sufficient to form estimates about the size and the mass of the star-model. However it is necessary to solve the field Equations (6) and (7) in order to see that the physical conditions like $p \geqslant 0$, $\rho - 3p/c^2 \geqslant 0$ are satisfied throughout the configuration. We now go to study these conditions after solving the field equations in the next section.

4. Solutions of field equations

To solve the linear differential Equation (7) for v, we make the following changes in the variables v and r.

$$\psi^2 = e^{\nu},$$

$$u^2 = K(1 - r^2/R^2)/(K - 1) \quad \text{if} \qquad K < 0$$

or

$$u^2 = K(1 - r^2/R^2)/(1 - K) \quad \text{if} \quad 0 < K < 1.$$

Then Equation (7) reduces to the convenient form

$$(1 - u^2)\frac{d^2\psi}{du^2} + u\frac{d\psi}{du} + (1 - K)\psi = 0.$$

The points $u = \pm 1$ are regular singular points and all other points are regular points for this linear equation. If we seek a series solution of this equation in the form $\psi = \Sigma A_k u^k$, one gets the following recurrence relation for the coefficients A_k.

$$(n + 1)(n + 2) A_{n+2} = [n^2 - 2n + K - 1] A_n.$$

If the parameter K has value such that the equation

$$n^2 - 2n + K - 1 = 0$$

admits integral values of n as solutions, either of the two sets (A_0, A_2, A_4, ...), (A_1, A_3, A_5....) contains finite number of elements and the corresponding terms in the solution-series constitute a finite polynomial. It can be verified that if K is to be in the range $K < 1$, the simplest value of K is -2 which corresponds to $n = 3$. With $K = -2$ one obtains the following solution

$$\psi = A_0\left(1 - \frac{3}{2}u^2 + \frac{3}{8}u^4 + \frac{1}{16}u^6 + \ldots\right) + A_1 u\left(1 - \frac{2}{3}u^2\right)$$

It will be observed that the infinite series with A_0 as the coefficient is the expansion of $(1 - u^2)^{3/2}$. Hence we find the closed-form solution of Equation (7) with $K = -2$ as

$$\exp(\nu/2) = \psi = Az\left(1 - \frac{4}{9}z^2\right) + B\left(1 - \frac{2}{3}z^2\right)^{3/2}$$

where $z^2 = 1 - r^2/R^2$, and A and B are undetermined constants of integration.

Closed-form solutions of Equation (7) have also been obtained for $K = -7$, $K = -14$ *etc.* but are not reported here.

5. Particular solution $K = -2$

We shall now write down the solution of the field equations corresponding to $K = -2$ in explicit form and verify that the fluid content satisfies all the relevant physical restrictions. The metric describing this solution explicitly is

$$ds^2 = \left[B\left(1-\frac{2}{3}z^2\right)^{3/2} + Az\left(1-\frac{4}{9}z^2\right)\right]^2 dt^2 - \frac{3-2z^2}{z^2}dr^2 - r^2(d\alpha^2 + \sin^2\alpha d\beta^2) \tag{14}$$

where

$$z^2 = 1 - r^2/R^2.$$

The matter density and the fluid pressure are found to be

$$(8\pi G/c^2)\,\rho = \frac{3}{R^2}\frac{(5-2z^2)}{(3-2z^2)^2}, \tag{15}$$

$$(8\pi G/c^2)\frac{p}{c^2} = \frac{3}{R^2}\frac{B(2z^2-1)(1-\frac{2}{3}z^2)^{1/2} - \frac{1}{3}Az(5-4z^2)}{(3-2z^2)[B(1-\frac{2}{3}z^2)^{3/2} + Az(1-\frac{4}{9}z^2)]}. \tag{16}$$

The density ρ and the pressures p at the centre ($r = 0$) attain the values

$$(8\pi G/c^2)\,\rho_0 = \frac{9}{R^2}, \tag{17}$$

$$(8\pi G/c^2)\frac{p_0}{c^2} = \frac{9}{R^2}\frac{B\sqrt{3}-A}{B\sqrt{3}+A}. \tag{18}$$

If the fluid sphere is of radius a, for $r \geqslant a$ the field is described by Schwarzschild's exterior solution (11). Making the metric (14) continuous with metric (11) at $r=a$, one gets

$$(1 - a^2/R^2)(1 + 2a^2/R^2)^{-1} = 1 - 2m/a, \tag{19}$$

$$B\sqrt{3}(1 + 2a^2/R^2)^{3/2} + A(1 - a^2/R^2)^{1/2}(5 + 4a^2/R^2) = 9(1 - 2m/a)^{1/2}. \tag{20}$$

A further boundary condition is that the fluid pressure must vanish at $r = a$. This leads to

$$B\sqrt{3}(1 - 2a^2/R^2)(1 + 2a^2/R^2)^{1/2} - A(1 - a^2/R^2)(1 + 4a^2/R^2) = 0. \tag{21}$$

Equations (19), (20) and (21) give A, B and m as

$$A = \frac{3}{2}(1 - 2a^2/R^2)(1 - a^2/R^2)^{-1/2}(1 - 2m/a)^{1/2}, \tag{22}$$

$$B = \frac{\sqrt{3}}{2}(1 + 4a^2/R^2)(1 + 2a^2/R^2)^{-1/2}(1 - 2m/a)^{1/2}, \tag{23}$$

$$m = \frac{3}{2}(a^2/R^2)(1 + 2a^2/R^2)^{-1}\, a. \tag{24}$$

It is clear that the constants B and m are always positive. However if $a^2/R^2 > \frac{1}{2}$, A will be negative. But it can be verified that $A < 0$ would imply $\rho_0 < p_0/c^2$, an unphysical situation. So A is also positive and we have the restriction $a^2/R^2 < \frac{1}{2}$, as a restriction on the boundary radius a.

In order to ensure that at the centre $\rho_0 \geqslant 3p_0/c^2$, it is easy to see that we should further restrict the boundary radius a by

$$a^2/R^2 \leqslant 0{\cdot}31$$

or

$$a/R \leqslant 0{\cdot}5567. \tag{25}$$

As a matter of fact, with the restriction (25) on the boundary, we ensure that at the centre

$$\rho_0 > 0, \quad p_0 > 0, \quad \rho_0 - 3p_0/c^2 \geqslant 0.$$

In order to ensure that ρ and p are well behaved throughout the configuration we impose the restriction $dp/d\rho < c^2$. (This will also ensure that the velocity of sound in the fluid is smaller than c). The calculations leading to this restriction are rather stiff but straight-forward and we have found that for $A/B \geqslant 0{\cdot}26$ the condition $dp/dp < c^2$ will be satisfied for all r such that $0 < r \leqslant a$.

A physically viable model can be constructed to satisfy all the restrictions and we give in the concluding section a model for a neutron star based on this particular solution.

6. Discussion: superdense stars

When thermonuclear sources of energy in the interior of a star are exhausted, the star undergoes gravitational contraction. As it contracts, its mass density goes on increasing and it ultimately ends up as a white dwarf or a neutron star or a black hole. It is this last stage of stellar evolution which leads to the formation of superdense condensations of matter. The model that we have presented here can describe the hydrostatic equilibrium conditions in such a superdense star with densities in the range of $10^{14} - 10^{16}$ gm cm^{-3}.

Using the scheme outlined in Section 3, we take the matter density on the boundary $r=a$ of the star as $\rho_a = 2 \times 10^{14}$ gm cm^{-3}. Again, we choose different values for the ratio $\lambda = \rho_a/\rho_0$ and for each chosen value of λ and the assumed value, ρ_a we calculate ρ_0. Equation (8) is then used to calculate R^2. Equation (13) then gives us an

Table 1. Masses and equilibrium radii of superdense-star models corresponding to $K = -2$ and $\rho_a = 2 \times 10^{14}$ gm cm^{-3}

No.	λ	a/R	m/a	R km	a km	m km	$m/M_\odot$	A	B	A/B
1	0·9	0·181	0·046	46·63	8·44	0·39	0·2644	1·3581	0·9043	1·5018
2	0·8	0·269	0·095	43·96	11·82	1·12	0·7593	1·1987	0·8780	1·3653
3	0·7	0·348	0·146	41·12	14·32	2·10	1·4237	1·0202	0·9705	1·0512
4	0·6	0·429	0·202	38·07	16·33	3·29	2·2305	0·8101	0·9924	0·8163
5	0·5	0·517	0·261	34·75	17·98	4·70	3·1864	0·5639	1·0001	0·5638
6	0·4598	0·5567	0·287	33·33	18·37	5·273	3·575	0·4481	0·9946	0·4506
7	0·4	0·622	0·327	31·08	19·33	6·32	4·2847	0·2526	0·975	0·2616
8	0·3384	0·70	0·3712	28·58	20·00	7·426	5·005	0·0213	0·9253	0·023
9	0·3	0·757	0·401	26·92	20·38	8·16	5·5322			
10	0·2	0·959	0·486	21·98	21·08	10·25	6·9492			
11	0·1	1·367	0·592	15·54	21·25	12·58	8·53			

Note:
The mass 'm' recorded in the table is measured in km. The corresponding value in gm is $M = mc^2/G$. $1\ M_\odot = 1{\cdot}475$ km.

estimate of a, the radius of the star and finally Equation (12) gives the mass of the star. The value of m as given by Equation (12) will be in km. The mass M of the star in gm is obtained by $MG/c^2 = m$ or $M = mc^2/G$. It is easier to express the mass of the star as a multiple of one solar mass $M_\odot$. The results of the calculations for various values of λ are given in Table 1.

It will be seen from Table 1 that a/R is a decreasing function of λ. Now the physical requirement that ρ, p and $\rho - 3p/c^2$ be all $\geqslant 0$ restricts a/R to the condition (25) *viz.* $a/R \leqslant 0{\cdot}5567$.

Therefore the corresponding restriction on λ is $\lambda \geqslant 0{\cdot}4598$. Thus the first six values of λ in the table give a series of physically viable star-models. The equilibrium radius of each of these models is of the order of the radius of a neutron star. The maximum mass for the configuration is $3{\cdot}573\ M_\odot$ and is obtained at the radius of 18·37 km. Both m and a are decreasing functions of λ.

If however we relax the physical requirement to $\rho > 0$, $p \geqslant 0$, $\rho - p/c^2 \geqslant 0$, the restriction on a/R is $a^2/R^2 < \frac{1}{2}$ or $a/R \leqslant 0{\cdot}7$ and we can go as far as the first eight values of λ in the table. The models will admit higher values of masses and radii, the maximum mass being $5{\cdot}037\ M_\odot$ occurring for a radius of 20 km.

Thus the space-time with metric (14) with space-sections t=const as spheroids (of eccentricity $\sqrt{2/3}$) gives us a series of equilibrium configurations each having surface density, mass and radius of the same order as in a neutron star. Without recourse to any equation of state, but using purely geometrical properties, we have been able to derive these models. One good feature of these models is that they permit higher values of maximum mass of a neutron star than the values permitted by a similar non-nuclear analysis by Rhoades and Ruffini (1974).

Though numerical calculations have been carried out for the exact solution corresponding to $K = -2$, the method is quite general and can be used for a whole series of models with $K < 1$.

Acknowledgement

One of us (PCV) would like to thank the Sardar Patel University for the hospitality during the period when the major part of this work was done.

References

Rees, M., Ruffini, R., Wheeler, J. A. 1975, *Black Holes*, *Gravitational Waves and Cosmology*, Gordon and Breach, New York, p. 8.

Rhoades, C. E., Ruffini, R. 1974, *Phys. Rev. Lett.*, **32,** 324.

Tolman, R. C. 1939, *Phys. Rev.*, **55,** 365.

J. Astrophys. Astr. (1982) **3,** 335–350

Further Observations of Radio Sources from the BG Survey. II. Mainly Extragalactic

F. Mantovani and M. Nanni *Istituto di Radioastronomia del C. N. R.*, *Istituto di Fisica* '*A. Righi*', *via Irnerio 46*, *40126 Bologna*, *Italy*

C J. Salter *Radio Astronomy Centre*, *Tata Institute of Fundamental Research, Indian Institute of Science Campus*, *PO Box 1234*, *Bangalore 560012*

P. Tomasi *Istituto di Radioastronomia del C.N.R., Istituto di Fisica* '*A. Right*', *via Irnerio 46*, *40126 Bologna, Italy*

Received 1982 April 27; accepted 1982 July 22

Abstract. New observations of six fields from the low galactic latitude BG survey are presented. The radio sources within each of these fields appear to be of a predominantly extragalactic nature. However, one object is in close positional proximity to the pulsar 1922 + 20 and the possibility of their association is considered. The extended source BGE 0323 + 65 is shown to be unlikely to exist.

Key words: extragalactic radio sources—pulsar-radio source association

1. Introduction

The present paper is the second in a series presenting new data on a number of fields containing objects from the low galactic latitude, BG and BGE Surveys (Fanti *et al.* 1974; Felli *et al.* 1977). The first article in the series, Mantovani *et al.* (1982), will be referred to below as Paper 1.

In their statistical study of the BG catalogue, Fanti *et al.* (1975) demonstrated that for the more compact sources in the survey the following conclusions can be drawn,

1. At least 85 per cent of sources with deconvolved angular diameter (θ) less than 2 arcmin are of extragalactic origin.
2. At least 70 per cent of sources with $2 < \theta$ (arcmin) < 7, and flux density (S) between 1·2 Jy and 2·4 Jy are of extragalactic origin.
3. Sources of $2 < \theta$ (arcmin) < 7 and $S > 2{\cdot}4$ Jy are mostly galactic.

It was thus to be expected that a number of the objects of smaller angular size and lower flux density studied in the present series of observations would prove to be extragalactic.

The present paper deals with those BG sources in our sample whose fields possess an exclusively, or predominantly, extragalactic nature. In one case (BGE 0323 + 65) an extended source from the BGE catalogue is shown, in all probability, to be spurious.

2. Observations and analysis

Observations made at 1·4 GHz with the Westerbork Synthesis Radio Telescope, at 1·7 GHz and 10·7 GHz with the Effelsberg 100-m Telescope and at 408 MHz with the full Bologna Cross Telescope have been described in detail in Fanti, Mantovani and Tomasi (1981, referred to below as FMT) and in Paper 1.

Further observations with the 100-m telescope were made at 4·75 GHz in 1981 August from the telescope secondary focus. These used the new 5-GHz three-channel, cooled parametric-amplifier system; the essential parameters of the observations are summarised in Table 1. The system operates both as a correlation Polarimeter measuring values of the Stokes parameters Q and U and as a correlation radiometer in which the left-hand circularly-polarized component of the total radiation is measured relative to a reference signal from a cooled load.

The fields studied at 4·75 GHz were observed twice, one coverage being made by scanning in right ascension and the other in declination. During the analysis, the values at the intersections of the orthogonally scanned sets were used to set the scans on to a consistent base-level. The observations were reduced with the NOD2 programme package (Haslam 1974) to produce maps of the Stokes parameters I, Q and U. All maps were given base-levels such that areas containing no discrete emission were level and had no average offset about zero. The maps of Q and U were combined as described in Paper 1 to give I', the most probable value of polarized intensity.

The observations were calibrated by mapping the Standard sources shown in Table 1. Flux densities for the sources were obtained from Baars *et al.* (1977). Polarization percentages and position angles of 4·8 per cent at 105° for 3C 48 and 11·2 per cent, at 33° for 3C 286 were derived from the tables of Tabara and Inoue (1980). To obtain the beam solid angle necessary to convert flux density into bright-

Table 1. Observational parameters at 4·75 GHz.

Frequency	4·75 GHz
Date of observations	1981 August
Scan separation	1 arcmin
Bandwidth	500 MHz
System temperature	70 K
Half-power beamwidth	2·4 arcmin
Point source response	2·43 K Jy^{-1}
(Full-beam brightness temperature per Jy)	
Calibration sources	3C 48, 3C 286, 3C 295*

* Unpolarized calibration source.

ness temperature, a 14 × 14 arcmin^2 area was mapped around point source calibrators. Observation of unpolarized calibrators indicated that spurious polarization responses to an unpolarized point source were everywhere less than 1 per cent.

3. Results

The results for the individual fields are presented below. The positions, flux densities and—where measureable—polarization characteristics of sources are presented in Tables 2 and 3 for the various new observations. Also included in these tables are the root-mean-square (rms) noises on the total power and linear polarization maps. The Effelsberg maps presented display total intensity contours overlayed with vectors representing the linearly polarized intensity. The maps made with the Bologna 'Northern Cross' display only total intensity contours.

3.1 *BG 1916 + 19* (*4C 19·67*)

The 1·4 GHz observations of FMT showed the BG object to be a combination of four relatively compact sources. Following their notation, we refer to these sources as A–D in Tables 2 and 3. At 408 MHz (Fig. la) the three sources B, C and D appear mutually confused. However, the sources are clearly separated on both the 4·75 GHz and 10·7 GHz maps (Figs 1b and lc), none of the sources being significantly resolved at either frequency.

The published measurements of the BG survey represent the sum of the four sources. Combining their fluxes from Table 3 and from FMT gives a spectral index ($S \propto \nu^{-a}$) of 0·95 ± 0·04 between 1·4 GHz and 4·75 GHz. Using the FMT-combined flux density and that from the new 408 MHz measurements, together with fluxes from Ehman *et al.* (1974), Hoglund (1967) and Fanti *et al.* (1974), we obtain a spectral index of 0·60 ± 0·05 between 408 MHz and 1·4 GHz. (All flux densities used in this article have been brought on to the flux scale of Baars *et al.* 1977). Thus, it appears that the combined spectrum of the four sources flattens significantly below 1·4 GHz.

The separate flux density measurements of Table 3 together with those of FMT lead to the high-frequency spectral indices for the four individual sources given in Table 4. Using the data of Table 2, spectral indices have been computed for the components B + C and D between 408 MHz and 1415 MHz. The component B + C shows a spectral index of 0·36 ± 0·07 indicating considerable spectral flattening below 1415 MHz. Component D has a spectral index over the same range of 0·79 ± 0·06, also suggesting some flattening at lower frequencies. This spectral flattening for 1916 + 19D seems to be confirmed by the 408 MHz flux density of 2·1 ± 0·2 Jy measured by Munro (1972) with the Molonglo Cross.

In view of the high linear-polarization percentage measured at 4·75 GHz on 1916 + 19D, it is somewhat surprising that no significant polarization was detected at 10·7 GHz, a 2σ upper limit of about 10 per cent being set for the source. A more sensitive 10-GHz measure would clearly be of interest. The rather high polarization percentage at 4·75 GHz for a small diameter, low-latitude source measured on 1916 + 19D (16·5 ± 2·6 per cent) makes it relevant to consider if this source could

Table 2. Discrete sources within the BG fields (Bologna data).

Field	Field centre h m s ° ′ ″	Field size deg²	Frequency MHz	rms noise mJy (beam area)$^{-1}$	Source name	R.A. (1950) h m s s	Dec. (1950) ° ′ ″ ″	Flux Jy
BG 1916+19	19 16 18 19 38 45	1·0×0·63	408	30	1916 + 19 (B+C)	19 16 12·7 ± 0·9	19 39 04 ± 17	0·59 ± ·06
					1916 + 19 D	19 16 28·3 ± 0·9	19 38 35 ± 15	2·4 ± ·2
BG 1922+20	19 21 48 20 39 32	1·0×0·63	408	20	1921 + 20	19 21 24·9 ± 0·9	20 34 45 ± 16	0·44 ± ·04
					1922 + 20 A	19 22 07·0 ± 1·0	20 37 41 ± 16	0·34 ± ·03
					1922 + 20 B	19 22 24·4 ± 0·9	20 41 45 ± 15	0·59 ± ·06
					1922 + 20 C	19 22 27·0 ± 0·8	20 29 04 ± 13	1·8 ± ·2
					1923 + 20	19 23 29·8 ± 0·9	20 34 53 ± 16	0·57 ± ·06
BG 2056+42	20 56 49 42 39 12	1·5×0·63	408	30	2056 + 42 A	20 56 11·6 ± 0·8	42 43 16 ± 15	2·1 ± ·2
BG 0428+44	4 27 57·5 44 42 25	1·0×0·63	408	22	0428 + 44 B	04 28 10·3 ± 1·0	44 35 38 ± 17	3·1 ± ·3

Table 3. Discrete sources within the BG fields (Effelsberg data).

Field	Field centre h m s ° ′	Field size arcmin²	Frequency GHz	rms noise mK T_b total intensity	rms noise mK T_b linear polarization	Source name	R.A. (1950) h m s s	Dec. (1950) ° ′ ″ ″	Flux (mJy) mJy	Linear polarization per cent	Position angle deg
BG 1916+19	19 16 20 19 40	40×40	4·75	18	16	1916 + 19 A	19 16 09·8 ± 0·8	19 52 20 ± 12	50 ± 5		
						1916 + 19 B	19 16 10·9 ± 0·8	19 38 15 ± 10	108 ± 9		
						1916 + 19 C	19 16 17·3 ± 0·9	19 42 45 ± 16	35 ± 6		
						1916 + 19 D	19 16 27·8 ± 0·7	19 38 38 ± 10	259 ± 19	16·5 ± 2·6	76 ± 5
BG 1916+19	19 16 20 19 38	22×16	10·7	8	11	1916 + 19 B	19 16 11·5 ± 0·7	19 38 16 ± 10	45 ± 3		
						1916 + 19 C	19 16 18·1 ± 0·8	19 42 26 ± 12	13 ± 2		
						1916 + 19 D	19 16 28·3 ± 0·7	19 38 39 ± 10	118 ± 6		
BG 1922+20	19 22 32 20 29	21×20	10·7	19	14	1920+ 22 C	19 22 27·9 ± 0·7	20 29 05 ± 10	[291 ± 22]		
BG 2056+42	20 56 14 42 43	22×20	10·7	7	9	2056 + 42 A	20 56 14·7 ± 0·9	42 43 20 ± 10	[87 ± 10]		
BG 0052+68	00 58 00 67 45	120×60	4·75	24	15	0050 + 675	00 50 20·9 ± 3·0	67 30 51 ± 18	24 ± 5		
						0051 + 679	00 51 05·9 ± 1·8	67 55 00 ± 10	154 ± 10		
						0052 + 681	00 52 46·6 ± 1·8	68 06 07 ± 10	[2448 ± 132]	5·0 ± 0·4	164 ± [3
						0055 + 675	00 55 07·1 ± 1·8	67 32 51 ± 10	310 ± 17		
						0056 + 674	00 56 04·6 ± 2·1	67 24 26 ± 12	61 ± 8		
						0056 + 677	00 56 33·5 ± 2·1	67 47 36 ± 12	75 ± 8		
						0057 + 678	00 57 36·4 ± 1·8	67 52 13 ± 10	1290 ± 67		
						0100 + 677	01 00 21·5 ± 1·8	67 45 28 ± 11	92 ± 8		
						0101 + 675	01 01 59·3 ± 1·8	67 35 09 ± 10	135 ± 8		
						0103 + 673	01 03 00·6 ± 1·8	67 23 46 ± 10	240 ± 13	7·0 ± 1·9	5 ± 9
						0105 + 674	01 05 34·4 ± 3·5	67 29 10 ± 12	32 ± 6		
						0106 + 678	01 06 53·6 ± 1·8	67 49 58 ± 10	819 ± 43		
BGE 0323+65	3 23 00 65 18	72×69	1·72	38	30	0317 + 654	03 17 18·4 ± 2·8	65 27 52 ± 12	221 ± 14		
						0320 + 650	03 20 48·9 ± 3·7	65 00 19 ± 32	78 ± 10		
						0323 + 657	03 23 41·1 ± 3·4	65 42 50 ± 21	170 ± 18		
						0326 + 657	03 26 59·2 ± 4·4	65 45 59 ± 22	95 ± 12		
BG 0428+44	4 28 15 44 36	20×22	10·7	8	12	0428 + 44 B	04 28 15·8 ± 1·0	44 36 09 ± 10	[204 ± 12]		
						N–E Compt.	04 28 12·8 ± 1·0	44 35 28 ± 10	86 ± 9		
						S–W Compt.	04 28 18·8 ± 1·0	44 36 51 ± 10	80 ± 8		

Note: Flux densities are peak values except for those enclosed in square brackets which are integrated values.

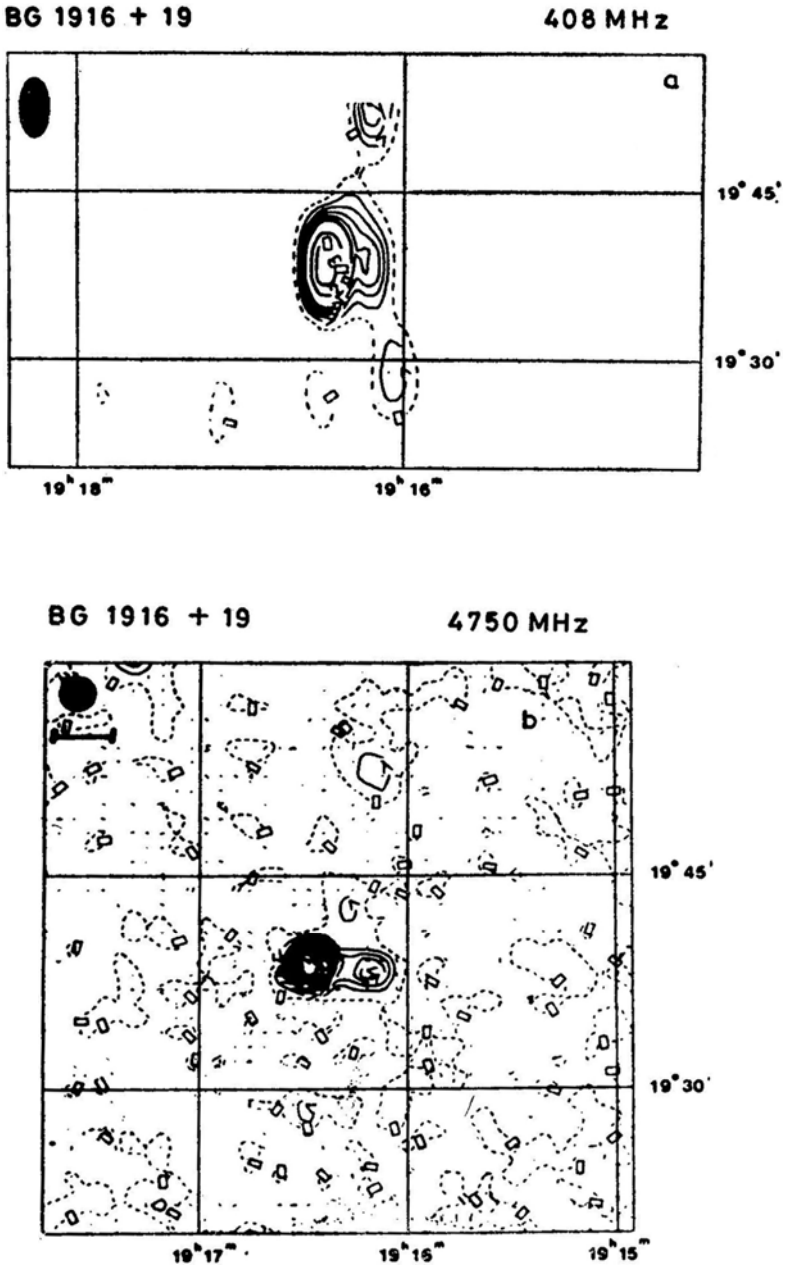

Figure 1. (a) BG 1916 + 19 at 408 MHz. The contours represent the total continuum intensity; the contour interval is 50 mJy (beam area)$^{-1}$. The dashed contour shows the assumed local zero level for the Source. Up to the contour labelled '10', *i.e.* 500 mJy (beam area)$^{-1}$, only alternate contours are drawn. Above this, only every tenth contour is given. The arrows on the contour lines point in an anticlockwise direction around peaks and in a clockwise direction around minima. (b) BG 1916 + 19 at 4·75 GHz. The contours represent the total continuum intensity; the contour interval is 50 mK. The vectors present the linearly polarized component of the radiation. The length of the vector is proportional to the intensity of the linearly polarized component; the scale shown at the top left-hand corner represents 400 mK. The orientation of the vector gives the position angle of the electric vector of the polarized radiation.

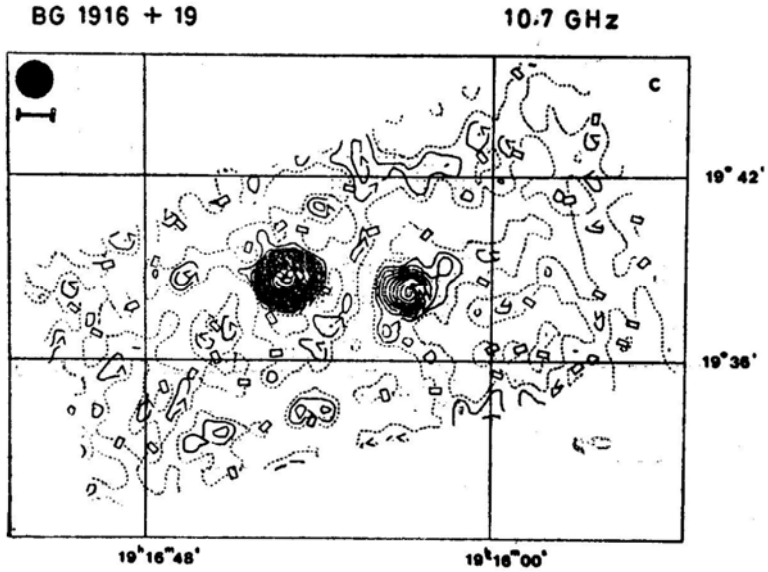

Figure 1.(c) BG 1916 + 19 at 10·7 GHz. The contour interval is 10 mK. Above 150 mK (*i.e.* the contour line labelled '10') only alternate contours are drawn. The vector scale is as in Fig. 1(b).

Table 4. Spectral indices ($S \propto \nu^{-\alpha}$) of sources in the field of BG 1916 + 19.

Source	Frequency range GHz	α
1916 + 19A	1·4– 4·75	0·95 ± 0·09
1916 + 19B	1·4–10·7	0·87 ± 0·07
1916 + 19C	1·4–10·7	0·98 ± 0·10
1916 + 19D	1·4–10·7	1·00 ± 0·02

represent a distant, young supernova remnant (SNR) within the galaxy. Its spectral index is considerably steeper than the mean of 0·45, with standard deviation of 0·15, expected for an SNR (Clark and Caswell 1976). In addition, a spectral break at around 1 GHz has only been suggested for three rather old remnants, the Cygnus Loop HB 9 and S 147 (Kundu and Becker 1972; Willis 1973; Kundu *et al.* 1980) and the reality of the break for HB 9 has recently been questioned (Dwarakanath, Shevgaonkar and Sastry 1982). In view of these spectral properties it would thus seem more probable that 1916 + 19D represents a background extragalactic object.

3.2 *BG 1922 + 20* (*4C 20·48*)

FMT have shown this BG source to consist of three separate components and following their notation we refer to them as A–C. The.408 MHz map of the area is shown in Fig 2(a) Two fields were observed at 10·7 GHz. The northern field was centred on 1922 + 20B, which is the H II region S 83 and will be dealt with in a subsequent paper of this series. The southern field was centred near 1922 + 20 C and is shown in Fig. 2(b).

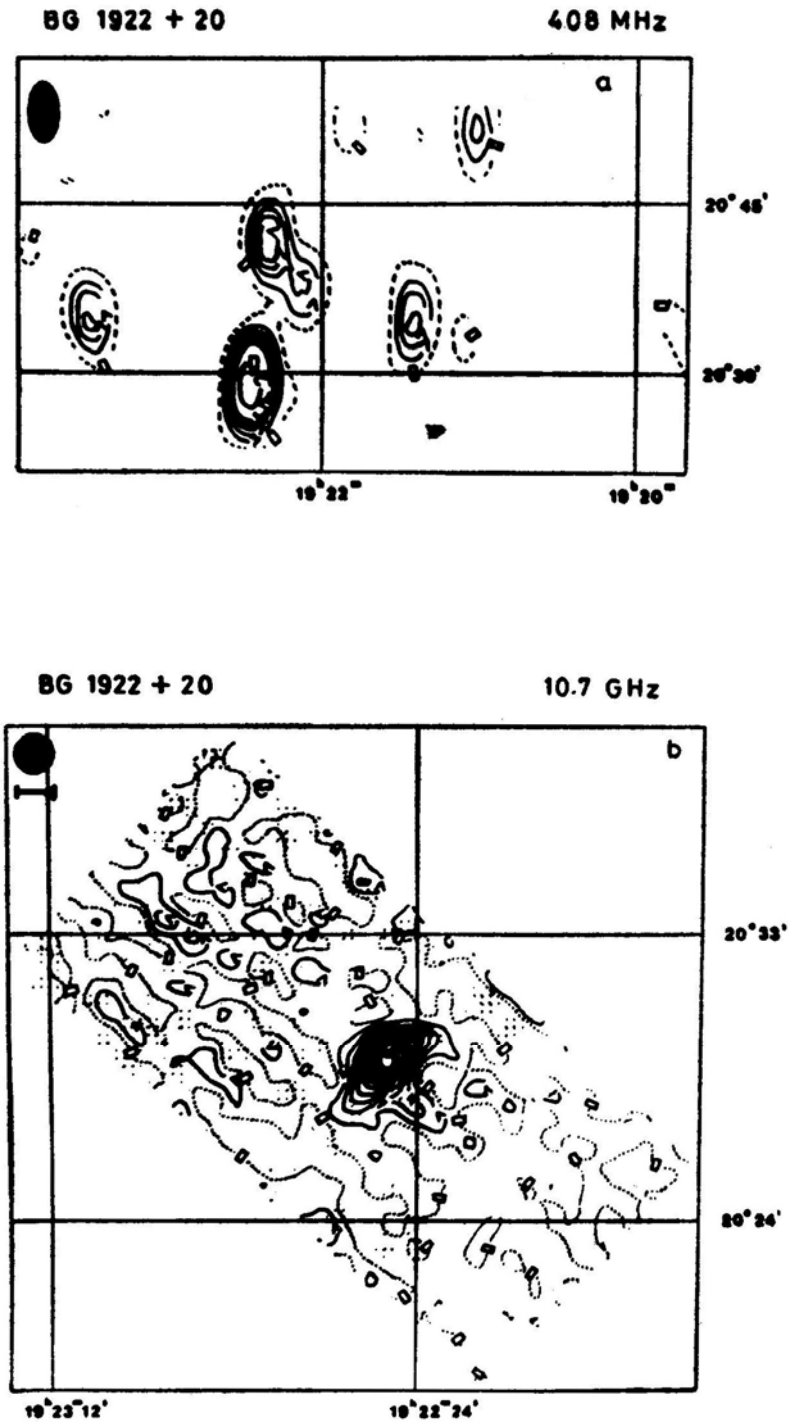

Figure 2. (a) BG 1922 + 20 at 408 MHz. Contour intervals are as in Fig. l(a). (b) BG 1922 + 20 C at 10·7 GHz. Contour interval is 30 mK. The vector scale is as in Fig. l(b).

Three weak sources catalogued by FMT at 1415 MHz were also detected at 408 MHz; between these two frequencies they have the following spectral indices; 1921 + 20 (α = 1·12 ± 0·10), 1922+ 20 A (α = 1·24 ± 0·10) and 1923 + 20 (α = 1·30 ± 0·15). The steep, non-thermal spectrum of 1922 + 20A is confirmed by its non-detection at 10·7 GHz. All the three sources are believed to be extragalactic in origin. The continuum spectrum of 1922 + 20 C has been investigated using measurements at 80 MHz (Slee and Higgins 1973), 160 MHz (Slee 1977), 1·4 GHz (FMT), 2·65 GHz (Ekers 1969) and 2·7 GHz (Day, Caswell and Cooke 1972) together with the present 408 MHz and 10·7 GHz flux densities. The spectrum of the source is straight between 80 MHz and 10·7 GHz with a spectral index of 0·55 ± 0·02.

By far the most intriguing feature of 1922 + 20 C is its positional coincidence with the faint pulsar PSR 1922 + 20 (Hulse and Taylor 1975). The pulsar has a position (Epoch 1950·0) of R.A. = $19^h\ 22^m\ 30^s \pm 20^s$, Dec. = 20°30' ± 5'. It should be noted, however, that the positional errors of the pulsar are considerably larger than the extent of the continuum source as measured by FMT. Despite this, it is still of interest to consider whether this extended continuum source might represent the remnant of the supernova in which PSR 1922 + 20 was formed. The 1·4 GHz map of FMT, although having the highest resolution available, does not possess sufficient resolution to reveal the detailed structure of 1922 + 20 C. Nevertheless, the observed distribution of emission has a morphology which is not incompatible with that expected from a partial shell. The structure could also be compatible with the 'bent double' configuration found for certain extragalactic objects. The straight continuum spectrum and the value derived for the spectral index could also be appropriate for an SNR origin (Clark and Caswell 1976), although again they are not incompatible with that expected for an extragalactic source.

We have applied the surface brightness–linear diameter (Σ–D) relations for SNR (Caswell and Lerche 1979; Milne 1979) to predict the parameters of 1922 + 20 C, if it is an SNR. These derived parameters can then be directly compared with those of the pulsar. In the Σ–D analysis, we have adopted the largest angular size measured by FMT (1·3 arcmin) as the smallest possible angular diameter for the hypothetical remnant, while a nominal maximum diameter of 5 arcmin is felt to be representative, should the structure represent a partial shell. The Z-independent Σ–D relations of Caswell and Lerche (1979) and Milne (1979) yield a linear diameter of ~ 17·0 pc (~38 pc) and a distance of ~44 kpc (~26 kpc), where the solution for a diameter of 5 arcmin are given in parentheses. Such distances would place an SNR at least as far out in the galaxy as the solar radius and possibly far outside the galaxy. The Z-dependent versions of the Σ–D relation give a diameter of ~ 5 pc (~ 14 pc), a distance of ~ 12·5 kpc (~ 10 kpc) and a Z of ~ 500 pc (~ 400 pc). These distances are reasonably compatible with the distance of 8·4 kpc derived for the pulsar from its dispersion measure by Manchester and Taylor (1977). A major difficulty exists, however, if one wishes to associate the radio source and the pulsar. The derived parameters from Σ–D–Z relations for the hypothetical SNR would suggest that this should be a rather young SNR. In contrast, the derived spin-down age of the pulsar, using the recent period derivative measurement of Ashworth and Lyne (1981), gives an age of 2×10^6 yr which would seem compatible with only an extremely old remnant.

A higher resolution continuum map of 1922+20 C may be expected to settle the problem of the nature of the object, while an improved position for PSR 1922+20 is also clearly desirable. On the present evidence, an extragalactic origin for 1922+20 C would perhaps seem the more likely.

3.3 *BG 2056 + 42* (*4C42·49*)

This small diameter source lies near the edge of the extensive H II region W 80, the North America Nebula (Matthews and Goss 1980). However, its morphology at 1·4 GHz (FMT) is completely consistent with that of an extragalactic double source. The 408 MHz map of the source is shown in Fig. 3(a) and the 10·7 GHz map in Fig. 3(b).

To study the continuum spectrum of the object, the present integrated flux densities at 408 MHz and 10·7 GHz have been combined with those at 178 MHz (Gower, Scott and Wills 1967), 1·4 GHz (FMT) and a 1·72 GHz measurement of the present authors (593 ± 65 mJy) from a map of W 80 which will be published separately. The 610 MHz flux density of Matthews and Goss (1980) has not been used, as the source will have been considerably resolved by their beam. A spectral index of 0·91 ± 0·06 is derived, consistent with that expected for a normal steep-spectrum extragalactic source.

Weak, extended emission is seen to the west of BG 2056+42 in the map at 408 MHz, coinciding with the southern edge of the North America Nebula visible on the Palomar Sky Survey. Although the field observed at 10·7 GHz covers only part of the area of extended emission at 408 MHz, low brightness emission to the west of the compact source is again clearly present. After smoothing the 10·7-GHz data to the 408-MHz resolution, we can roughly estimate the spectral index of the part of the extended filament nearest to the compact source. The emission from the compact source was subtracted at both frequencies before performing this operation. A spectral index of 0·2 ± 0·1 is derived, consistent with a thermal nature for the filament. It is not believed that the feature is associated with the compact object BG 2056+42 and most probably it represents weak thermal emission associated with the North America Nebula.

3.4 *BG 0052 + 68* (*3C 27*)

The area around 3C 27 has been studied by Salter and Haslam (1980), referred to below as SH. These authors demonstrated that a statistically significant excess of point sources exists around 3C 27. From their small angular sizes and a study of their continuum spectra, it was concluded that most, and perhaps all, of these sources are of extragalactic origin and the possibility was suggested that the grouping could represent a cluster of galaxies as yet unidentified due to the high galactic obscuration in the area. A 2° × 1° area, representing the western half of the field mapped by SH, has been observed at 4·75 GHz (Fig. 4). The aims of this exercise were to extend the spectral data on this unusual grouping and to make an initial search for measurable linear polarization to the radio radiation of the sources.

Table 3 contains the parameters of the sources in the field. The table is believed to be essentially complete down to a level of 30 mJy (~ 3σ). One weaker source, 0050+675, is included as its reality is strongly suggested by the 2·7 GHz map of SH. All

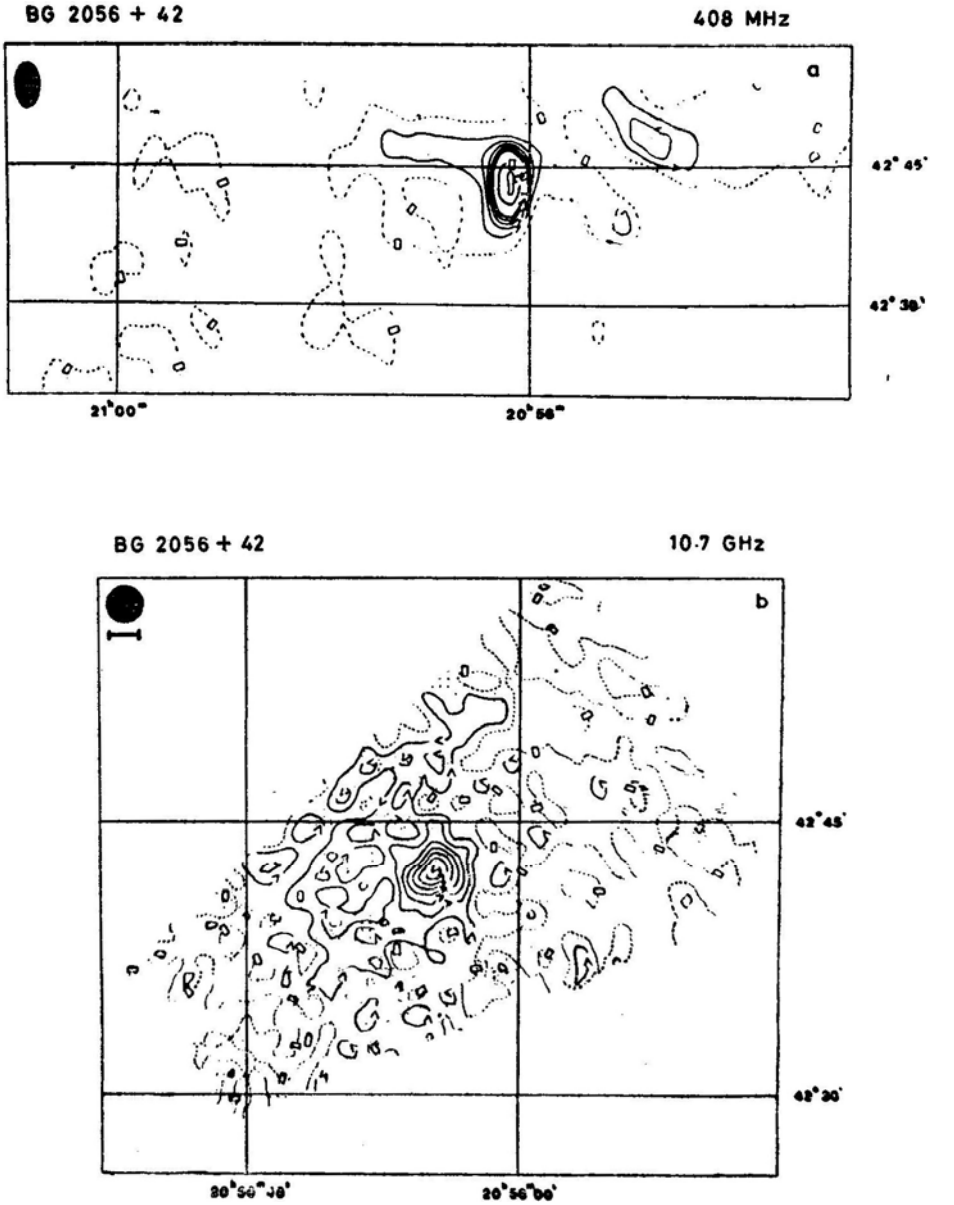

Figure 3. (a) BG 2056 + 42 at 408 MHz. Contour intervals are as in Fig. l(a). (b) BG 2056 + 42 at 10·7 GHz. Contour intervals are as in Fig. l(c); vector scale (top left-hand corner) is 400 mK.

flux densities in the table are peak flux densities except in the case of 3C 27 itself where a small correction for resolution has been made. All sources listed by SH which lie in the area of Fig. 4 are detected by the present measurements.

The flux density of 3C 27 from Table 3 is in close accord with the 4·75 GHz value of 2470 mJy derived from the best-fit spectrum of SH. Table 5 gives the spectral indices of the sources between 2·7 and 4·75 GHz. The sources 0056+674 and 0101 + 675 appear to have rather steep spectra over this frequency range although their

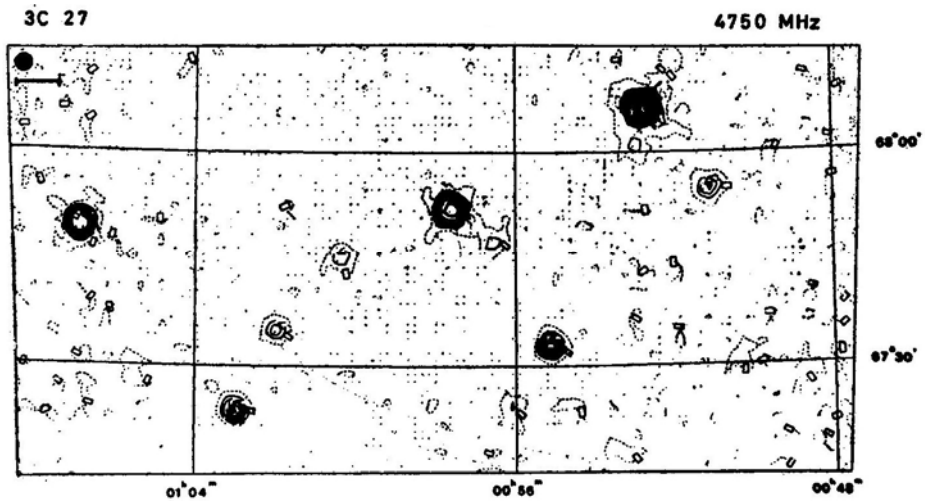

Figure 4. 3C 27 at 4·75 GHz. Contour interval is 100 mK; vector scale (top left-hand corner) is 600 mK.

Table 5. Spectral indices of sources in the field of 3C27 for frequency range 2·7–4·75 GHz.

Source	Spectral index (α)
0050 + 675	...
0051 + 679	0·24 ± 0·24
0052 + 681	0·89 ± 0·13
0055 + 675	0·95 ± 0·14
0056 + 674	0·14 ± 0·43
0056 + 677	1·54 ± 0·30
0057 + 678	0·35 ± 0·13
0100 + 677	1·26 ± 0·20
0101 + 675	1·30 ± 0·15
0103 + 673	0·86 ± 0·14
0105 + 674	1·17 ± 0·52
0106 + 678	0·60 ± 0·14

indices between 408 MHz and 2·7 GHz are not abnormally steep (see SH). While these sources may show some spectral steepening at higher frequencies, it should be noted that small-resolution effects at 4·75 GHz might contribute significantly to steepening the apparent spectra in view of the closeness of the two frequencies. 0051+679, the source only 14 arcmin from 3C 27, has a significantly flatter spectrum than the 3C source and this would suggest that the two sources are not related to the same parent object. This would not, of course, preclude their being objects physically nearby to each other. The strong spectral curvature of 0057+678 appears to be confirmed by the 4·75 GHz measurement and the spectrum of this source is shown in Fig. 5.

A comparison of the 2·7 and 4·75 GHz positional data gives an average right-ascension difference (4·75 GHz—2·7 GHz) of 8·6 ± 2·2 arcsec, with a Standard deviation of 6·9 arcsec on a typical measurement. The corresponding values in declination are 0·7 ± 2·6 and 8·1 arcsec. The position of the centroid of the emission from 3C 27 using the high resolution 1·4 GHz observations of Högbom and Carlsson (1974), differs from the 4·75 GHz position by 2 arcsec in right ascension and – 1

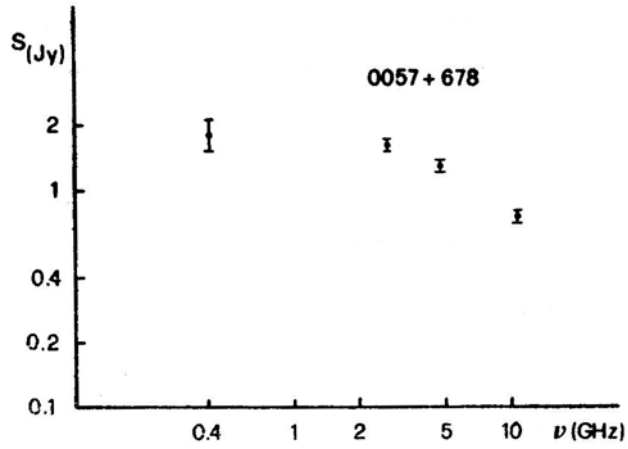

Figure 5. The continuum spectrum of the source 0057 + 678.

arcsec in declination (in the sense of 4·75 GHz–1·4 GHz) and this can be taken as demonstrating only very small systematic offsets in the present measurements.

The measured linear polarization of 3C 27 is consistent with the 5-GHz value of Sastry, Pauliny-Toth and Kellermann (1967) of 3·3 ± 1·8 per cent at 167° ± 16° (a position angle of 165° at 4·75 GHz assuming the rotation measure of—90·7 rad m^{-2} derived by Tabara and Inoue 1980). Polarization was only detected on one other source, 0103+673, and a detailed polarization study of the field will clearly require considerable sensitivity and dynamic range.

3.5 *BGE 0323 + 65*

BGE, the catalogue of the more extended sources from the BG survey (Felli *et al.* 1977), contains an entry for the position (epoch 1950·0) R.A. $03^h\ 23^m\ 00^s$, Dec. 65°·3. The source was assigned a peak flux density of 1·4 Jy, making it one of the faintest objects in the survey. A diameter of 16·3 arcmin and an integrated flux density of 5·5 Jy were given. No source had been previously catalogued at this position.

The area of BGE 0323 + 65 has been mapped at 1·72 GHz (Fig.6). The parameters of four point sources within the field are given in Table 3. Of these, only 0323+657 might have appeared within the BGE source area in the 408-MHz fan-beam observations but the flux density of this object at 408 MHz is expected to be only some 10 per cent of the catalogued flux of the extended source. No evidence is found at all for an extended source within the mapped region at 1·72 GHz, although the BGE positional errors are such that the source should fall within the presently-observed area. After subtraction of the point sources of Table 2, the map of Fig. 6 was smoothed to a resolution of 12 arcmin to give maximum signal-to-noise ratio for the hypothetical extended structure. Still no extended source was visible and an rms brightness temperature of 17 mK was measured on the resultant map. If the extended source were to exist at a level of $\leqslant 3\sigma$, its integrated flux density would be $\leqslant 81$ mJy, assuming the BGE angular diameter and a circular-disc brightness distribution. Combining this with the 408 MHz flux density, a flux spectral index of $\alpha \geqslant 2{\cdot}9$ is implied. Such a spectrum would seem impossibly steep and we believe that the extended source BGE 0323+65 should be considered as unlikely to exist.

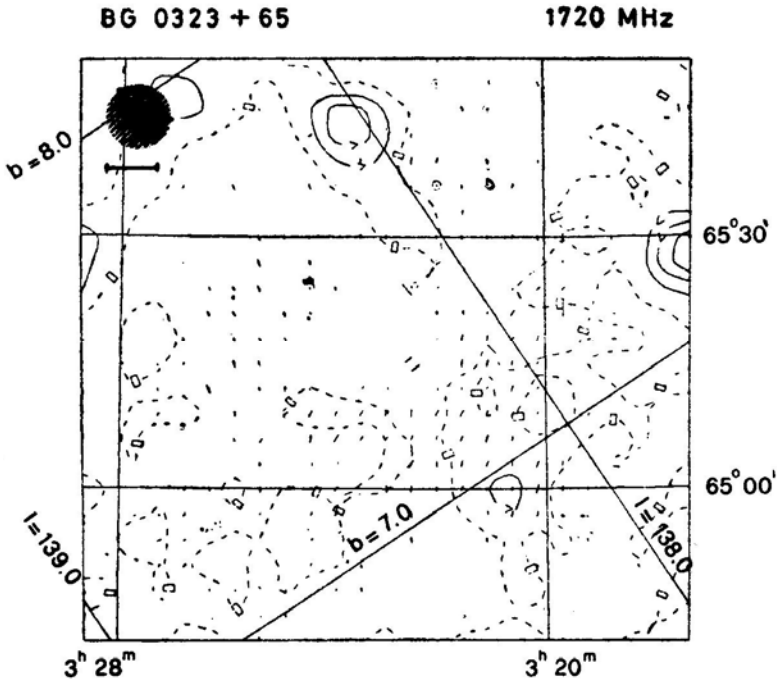

Figure 6. BG 0323 + 65 at 1720 MHz. Contour interval is 100 mK; vector scale (top left-hand corner) is 400 mK.

3.6 *BG 0428 + 44* (*4C 44·11*)

The principal object contributing to BG 0428+44 is the radio source 4C 44·11, designated 0428+44B by FMT. The source has been mapped at 408 MHz (Fig. 7a) and at 10·7 GHz (Fig. 7b) and the integrated properties of the object, as well as the parameters of its compact components, are given in Tables 2 and 3. Allowing for the somewhat lower resolution at 10·7 GHz, the source shows similar structure in Fig. 7(b) to the 1·4 GHz map of FMT. Its morphology marks it clearly as an extragalactic double source. At 1·4 GHz, the south-preceding hotspot is seen to be located well interior to the maximum extension of the source in this direction.

Combination of the present total flux densities with values at 38 MHz (Williams, Kenderdine and Baldwin 1966), and at 1·4 GHz (FMT and Dixon, Merg and Kraus 1965) yields a straight spectrum of spectral index 0·83±0·02.

4. Conclusions

New continuum maps have been presented for six fields from the BG survey. Consideration of the sources contained within these fields suggests that most of these discrete objects have, an extragalactic nature. However, one of the sources, 1922+20 C, is found to be in close positional proximity to the pulsar, PSR 1922+20. While it seems, most probable that the two objects are not physically associated, further observations are desirable for both of these sources. Finally, an extended

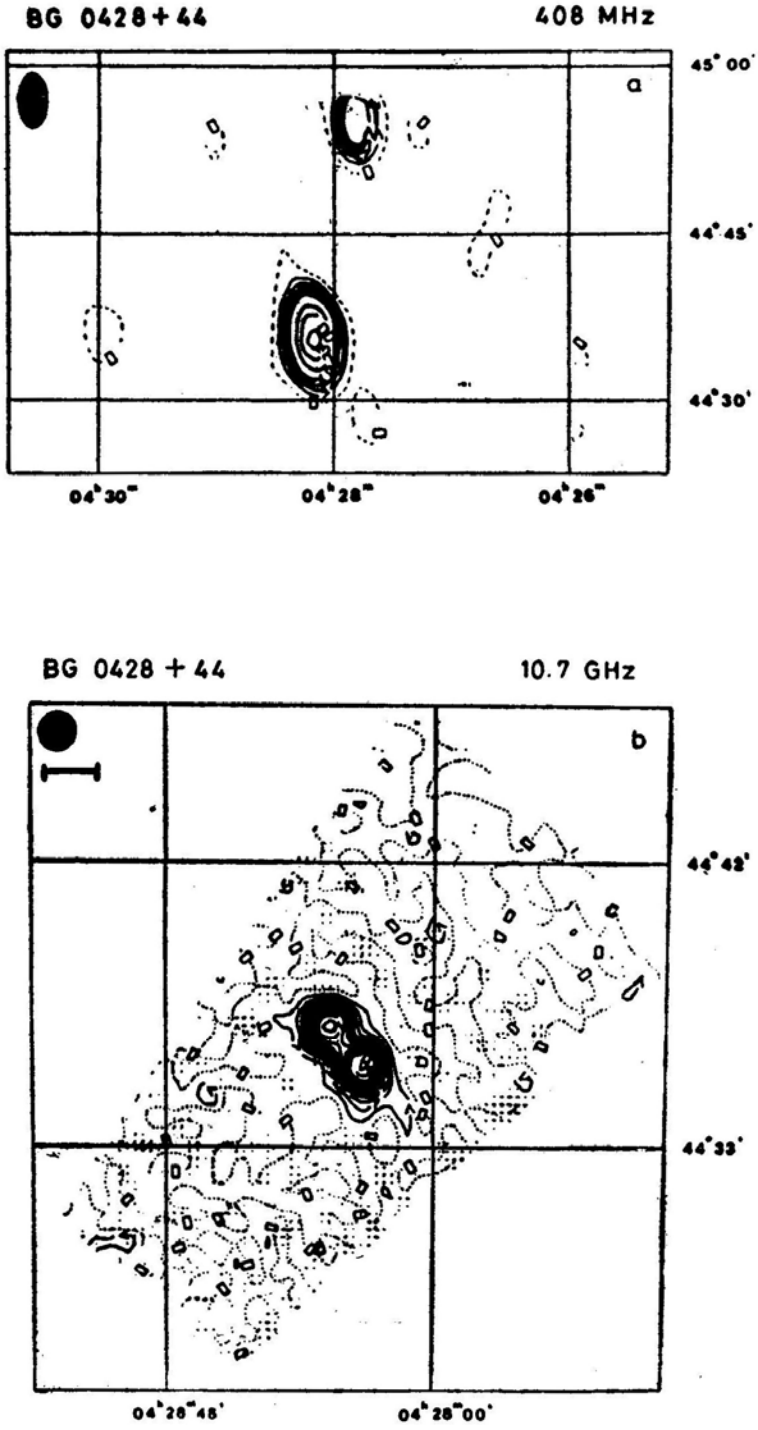

Figure 7. (a) BG 0428 + 44 at 408 MHz. Contour intervals are as in Fig. l(a). (b) BG 0428 + 44 at 10·7 GHz. Contour intervals are as in Fig. l(c); vector scale (top left-hand corner) is 400 mK.

filamentary feature, which probably represents weak thermal emission associated with the nearby North America Nebula, has been detected in the field of the extragalactic source BG 2056+42.

Acknowledgements

The authors wish to thank Antonio Ficarra for the pre-reduction of the 408 MHz observations, Luciano Baldeschi and Reginaldo Primavera for their skill in producing the drawings and photographs reproduced in this article and P. P. Gopalakrishnan for typing the manuscript.

References

Ashworth, M., Lyne, A. G. 1981, *Mon. Not. R. astr. Soc.*, **195,** 517.
Baars, J. W. M., Genzel, R., Pauliny Toth, I. I. K., Witzel, A. 1977, *Astr. Astrophys.*, **61,** 99.
Caswell, J. L., Lerche, I. 1979, *Mon. Not. R. astr. Soc.*, **187,** 201.
Clark, D. H., Caswell, J. L. 1976, *Mon. Not. R. Astr. Soc.*, **174,** 267.
Day, G. A., Caswell, J. L., Cooke, D. J. 1972, *Austr. J. Phys. Astrophys. Suppl.*, No. **25,**1.
Dixon, R. S., Meng, S. Y., Kraus, J. D. 1965, *Nature*, **205,** 755.
Dwarakanath, K. S., Shevgaonkar, R. K., Sastry, Ch. V. 1982, *J. Astrophys. Astr.*, **3,** 207.
Ehman, J. R., Dixon, R. S., Ramakrishna, C. M., Kraus, J. D., 1974, *Astr. J.* **79,** 144.
Ekers, J. A. 1969 *Austr. J. Phys. Astrophys. Suppl.*, No. 7, 1.
Fanti, C., Felli, M., Ficarra, A., Salter, C. J., Tofani, G., Tomasi, P. 1974, *Astr. Astrophys. Suppl Ser.*, **16,** 43.
Fanti, C., Felli, M., Panagia, N., Tofani, G., Tomasi, P. 1975, *Astr. Astrophys.*, **45,** 277.
Fanti, C., Mantovani, F., Tomasi, P. 1981, *Astr. Astrophys. Suppl. Ser.*, **43,** 1 (FMT).
Felli, M., Tofani, G., Fanti. C., Tomasi,. P. 1977, *Astr. Astrophys. Suppl. Ser.*, **27,** 181.
Gower, J. F. R., Scott, P. F., Wills, D. 1967, *Mem. R. astr. Soc.*, **71,** 49.
Haslam, C. G. T. 1974, *Astr. Astrophys. Suppl. Ser.*, **15,** 333.
Högbom, J. A., Carlsson, I. 1974, *Astr. Astrophys.*, **34,** 341.
Hoglund, B. 1967, *Astrophys. J. Suppl. Ser.*, **15,** 61.
Hulse, R. A., Taylor, J. H. 1975, *Astrophys. J.*, **201,** L55.
Kundu, M. R., Becker, R. H. 1972, *Astr. J.*, **77,** 459.
Kundu, M. R., Angerhofer, P. E., Furst, E., Hirth, W, 1980, *Astr. Astrophys.* **92,** 225.
Manchester, R. N., Taylor, J. H. 1977, *Pulsars*, W. H. Freeman, San Francisco.
Mantovani, F., Nanni, M., Salter, C. J., Tomasi, P. 1982, *Astr. Astrophys.*, **105,** 176 (Paper 1).
Matthews, H. E., Goss, W. M. 1980, *Astr. Astrophys.*, **88,** 267.
Milne, D. K. 1979, *Austr. J. Phys.*, **32,** 83.
Munro, R. E. B. 1972, *Austr. J. Phys. Astrophys. Suppl.*, No.22, 1.
Pilkington, J. D. H., Scott, P. F. 1965, *Mem. R. astr. Soc.*, **69,** 183.
Salter, C. J., Haslam, C. G. T. 1980, *Astr. Astrophys.*, **81,** 240 (SH).
Sastry, Ch. V., Pauliny-Toth, I. I. K., Kellermann, K. I. 1967, *Astr. J.*, **72,** 230.
Slee, O. B. 1977, *Austt. J. Phys. Astrophys. Suppl.*, No. 43, 1.
Slee, O. B., Higgins, C. S. 1973, *Austr. J. Phys. Astrophys. Suppl.*, No. 27, 1.
Tabara, H., Inoue, M 1980, *Astr. Astrophys. Suppl. Ser.*, **39,** 379.
Williams, P. J. S., Kenderdine.S., Baldwin, J. E. 1966, *Mem. R. astr. Soc.*, **70,** 53.
Willis, A. G. 1973, *Astr. Astrophys.*, **26,** 237.

J. Astrophys. Astr. (1982) **3,** 351–361

A New Look at the Birthrate of Supernova Remnan

G. Srinivasan and K. S. Dwarakanath *Raman Research Institute, Bangalore 560080*

Received 1981 August 12; accepted 1982 July 29

Abstract. We have reanalysed a homogeneous catalogue of shell-type supernova remnants and we find that the radio data are consistent with a birthrate of one in 22±3 yr. Our approach is based on the secular decrease of surface brightness of the historical remnants whose ages are precisely known. The abovementioned birthrate is significantly higher than most previous estimates which range from one in 50–150 yr, and is consistent with the supernova rate in our galaxy derived from historical observations, as well as with recent estimates of the pulsar birthrate.

Key words: supernova remnants, birthrates

1. Introduction

The rate of Supernovae (SN) in our galaxy has been variously estimated to be one in every 11 yr to one in 30 yr (Clark and Stephenson 1977a; Katgert and Oort 1967; Tammann 1977). These numbers were arrived at in two different ways. One way was to determine the observed SN rate in external galaxies of similar morphology to our own. The other method was to estimate the rate of SN in our galaxy from historical records. Katgert and Oort, using the latter approach have suggested a rate of one in 25 yr. and Clark and Stephenson suggested one in 30 yr or less. It may be recalled that only 7 SN were recorded in the last 2 millennia. The failure to detect the other 70 or so SN which must have gone off in the last 2000 yr (as suggested by the above rates) is explained by the above authors as due to obscuration, horizon limitations *etc.*

It is generally accepted that SN explosions are associated with the formation of neutron stars as originally suggested by Baade and Zwicky (1934). According to this picture, the birthrate of neutron stars must match the SN rate. It is also generally believed that all neutron stars function as pulsars. Therefore it is natural to try to relate the birthrate of pulsars to the SN rate. The pulsar birthrate estimates in the literature vary from one every 7–40 yr (Taylor and Manchester 1977; Phinney and

Blandford 1981). Recently, Vivekanand and Narayan (1981) have arrived at a rate of one in 21^{+6}_{-4} yr; since this is the first calculation to incorporate luminosity selection effects, it is probably the most reliable number to date. Thus it would appear that the pulsar birthrate and SN rate are reasonably consistent, though there are inherent errors in each of these estimates.

The third number which must agree with the above two rates is the birthrate of supernova remnants (SNRs), There have been numerous attempts in the literature to estimate this in various ways. We mention a few of the methods and the results obtained.

1. One assumes that all SNRs with surface brightness Σ greater than that of a given age calibrator are younger. Using this method Caswell (1970) arrived at $\tau = 55^{+25}_{-15}$ yr (where τ is the mean interval between births of SNRs).

2. A variant of the above method is to assume that all SNRs with a linear diameter D less than that of an SNR with known age are younger. Ilovaisky and Lequeux (1972) obtained $\tau = 50 \pm 25$ yr, using this approach.

3. Clark and Caswell (1976) have argued that the cumulative counts of SNRs [$N(<D)$ and $N(>\Sigma)$ plots] suggest that all SNRs with diameter $\leqslant 32$ pc evolve according to the self-similar solution given by Sedov. Using consistency arguments, they relate τ to E_0/n, where E_0 is the energy of the explosion and n is the density of the interstellar medium. Using a value of $E_0/n = 5 \times 10^{51}$ erg cm^3, as suggested by X-ray observations of four remnants, they arrive at $\tau \sim 150$ yr.

The above methods have some inherent drawbacks. For example, it need not be true that a remnant with Σ greater than a given one is necessarily younger. The brightness of the remnant may be intimately connected with the initial parameters of the explosion, as well as the density of the ISM (Gull 1973). The same criticism would apply to the $N(<D)$ approach. Again, it may not be true that all remnants with $D<32$ pc are evolving according to the Sedov solution. It is well known that the exploding shell will evolve in a self-similar manner only when the mass swept up far exceeds the mass ejected. This may not be true for a remnant of a given diameter, if it is expanding in a region of very low density or the mass ejected is very high.

In this paper, we wish to reexamine this question. Our method, a variant of the one used by Caswell (1970), is based on the secular decrease of the surface brightness of historical shell SNRs. In a recent paper, Higdon and Lingenfelter (1980) have derived a birthrate for SNRs using a similar approach, though there are important differences in detail. We shall return to this in later sections. In Section II, we shall outline our procedure and derive a birthrate for shell SNRs. In Section III, we attempt to incorporate the possible effect of the density of the interstellar medium on the radio brightness of the remnants.

2. Surface brightness–age relation

The radio surface brightness of a remnant is a function of its age. Basically, two kinds of mechanisms for radio emission have been proposed in the literature for shell remnants. In the first it is assumed that the magnetic field in the shell is the compressed interstellar field, and that the particles responsible for the synchrotron radiation are either the interstellar cosmic rays or the particles produced in the

original explosion (van der Laan 1962). The alternative is to say that the magnetic field and/or the relativistic particles are generated within the shell itself. Gull (1973) has advanced a model where both the magnetic field and the particle energy are amplified by turbulent motions in the convective interface between the ejecta and the interstellar gas. He has argued that this will continue till equipartition is reached between the turbulent energy, the particle energy and the field energy. In this paper we shall assume that this is the operative mechanism for young remnants. According to this model, the radio emission will reach a maximum at a time $t = t_0$ when the mass swept up is of the order of 0·1–0·3 times the mass ejected, and then will decay with time. Thus, for $t \geqslant t_0$ one may write

$$\Sigma = \Sigma_{\max} (t_0/t)^{\alpha} \tag{1}$$

where $\Sigma_{\max}$ is the brightness at time t_0. Gull's theory does not give any specific value for α. In what follows we shall write

$$\Sigma = At^{-\alpha} \tag{2}$$

and treat α as a parameter. It should be emphasized here that this equation is general in character and is not necessarily tied to Gull's theory, though consistent with it. For any given value of α, one can determine the constant A for a specific age calibrator. This combination of A and α can then be used to calculate the 'ages' of all the known remnants, and thus a birthrate can be obtained. This assumes that α is constant in time. We shall impose the following criteria for the choice of α.

1. If one restricts oneself to a time interval which is small compared to the mean lifetime of remnants, then one must have $N(< t) \propto t$, where t is the age of the remnant. This will be true as long as 'deaths' of remnants have not yet set in.

2. More than one age calibrator is available (see below) for determining the constant A, for a given α. The most appropriate value of α must satisfy the criterion that it give reasonably good ages for all the other age calibrators.

As was mentioned in the Introduction, there were seven definite recordings of SN in historical times. They were recorded in AD 185, AD 393, AD 1006, AD 1054, AD 1181, AD 1572 (Tycho), and AD 1604 (Kepler). Clark and Stephenson (1977b) have discussed in detail the association of radio SNRs with these historically-observed explosions. They come to the conclusion that—with the exception of the supernova of AD 393—a reasonably certain identification can be made in every other case. Recently, it has been suggested (Ashworth 1980; Brecher and Wasserman 1980) that the SN that produced the radio remnant Cas A may have been seen by the astronomer Flamstead in AD 1680, but we shall not use this remnant as an age calibrator. The Crab nebula and 3C 58 (probably associated with the SN of AD 1181) have a morphology quite different from the other historical remnants, which are of the shell type. There are reasons to believe (see for example Weiler and Panagia 1980; Radhakrishnan and Srinivasan 1980a) that the evolution of these objects is different from those of shell SNRs. In what follows, we shall therefore restrict ourselves to shell SNRs. One is thus left with four shell remnants whose ages are accurately known, *viz*. SNR185, SNR 1006, SNR1572 and SNR1604, with which one can calculate the ages of all the known SNRs. We have used the catalogue of SNRs compiled by Clark and Caswell (1976). They list 120 SNRs out of which Σ (the surface brightness at 408 MHz) is quoted for all but four. From this list of 116,

we delete the Crab, 3C 58, MSH 15–56 and Vela X because of their filled-in appearance, and apply our analysis to the remaining 112.

In Figs 1–3, we show $N(<t)$ *vs.* t plots for $\alpha = 1{\cdot}2, 2{\cdot}5, 3{\cdot}5$ respectively. $\alpha = 1{\cdot}2$ corresponds to evolution according to the Sedov solution if $\beta = 3$(where, $\Sigma \propto D^{-\beta}$). For a given α, each one of the curves corresponds to the constant A in Equation (2) determined through one of the age calibrators.

There are three striking features in these plots:

1. Beyond 300 years or so, the $N(< t)$ curves are remarkably linear (till about 2000 years), indicating a uniform birthrate. Since, as we have already mentioned, it takes a time t_0 (which depends on the density of the medium *etc.*) for the radio brightness to build up, the behaviour of the curves for the first few hundred years can be understood.

2. As α increases, the $N(< t)$ curves calculated from SNR 185, SNR1572 and SNR 1604 approach each other; but the curves are insensitive to an increase in α beyond $2{\cdot}5$. It may be noted that when SNR 1006 is used as a calibrator, one obtains a much higher birthrate, irrespective of α. We shall discuss the possible reasons for this in some detail in the next section.

3. Most of the SNRs appear to be less than 2000 years old.

An examination of Figs 1–3 shows that it is difficult to choose the optimum value of α on this basis. In order to do this we have computed the residual R defined by

$$R = \left[\frac{1}{4}\sum_{i=1}^{4} \ln^2\left(\frac{t_{\mathrm{cal},\,i}}{t_{\mathrm{true},\,i}}\right)\right]^{1/2} \tag{3}$$

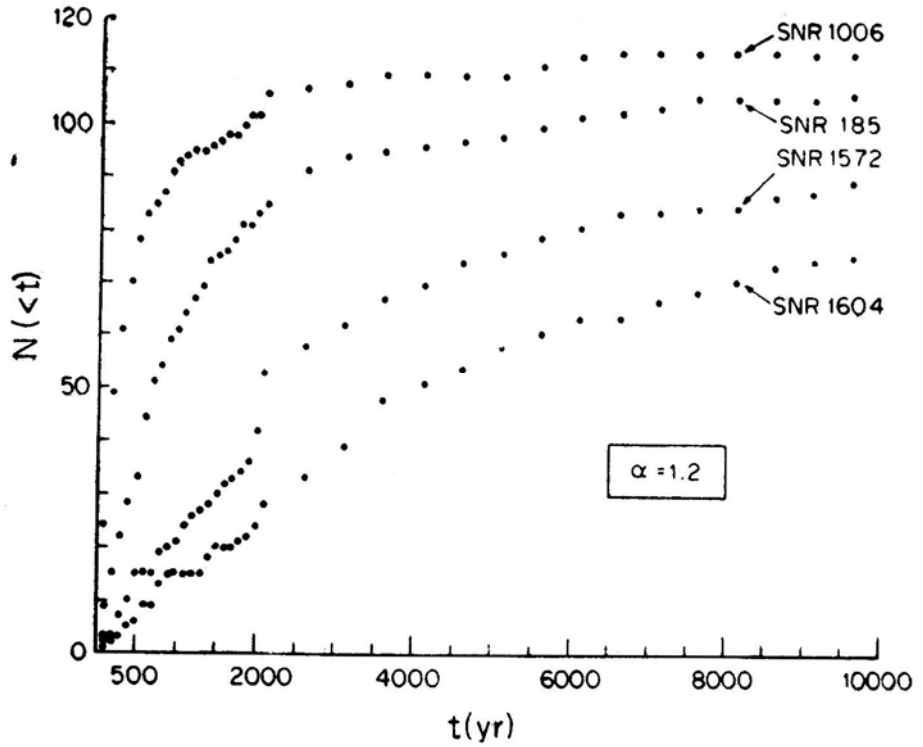

Figure 1. The number of shell SNRs with ages less than a given age, for $\alpha = 1{\cdot}2$. The labels refer to the calibrator used to determine the constant A in Equation (2).

where $t_{cal,i}$ is the age of one of the above-mentioned calibrators, derived from Equation (2) and $t_{true,\ i}$ is its actual age. It was found that R is minimum for $\alpha = 3{\cdot}5$ and $A = 4{\cdot}4 \times 10^{-10}$. Since the number of calibrators are only four, one cannot obtain a meaningful statistical error for R. So we have adopted the following approach to estimate the scatter in α and A. There are reasons to suspect that SNR 1006 may be subluminous for its age (possible reasons are discussed in the next section). If so, it will strongly bias the above procedure towards a larger value of α. To get a feeling for this we left out SNR 1006 as a calibrator and repeated the above procedure. The minimum value of R now corresponded to $\alpha = 2{\cdot}5$ and $A = 1{\cdot}1 \times 10^{-12}$. In what follows we shall assume that α lies in the range 2·5–3·5.

In Fig. 4 we show the number of SNRs whose ages are less than 2000 years, as a function of α. The curves are labelled by the calibrator used. The flatness of the curve labelled SNR 185 is an artifact because SNR 185 itself is ~ 2000 years old. The dashed curve is a ' least-squares fit' using all the four calibrators. For $\alpha = 3{\cdot}5$, this gives for the mean interval τ between SN that produce shell remnants, a value of 19 yr.

A similar procedure, but leaving out SNR 1006 this time, gives $\tau = 25$ yr (for the appropriate value of $\alpha = 2{\cdot}5$). Since the true value of α can lie anywhere in the range 2·5–3·5, we obtain $\tau = 22 \pm 3$ yr. In this context it is worth mentioning that the *measured* value of α for Tycho is $2{\cdot}0 \pm 0{\cdot}8$ (Strom, Goss and Shaver· 1982), consistent with our range for α. There is one other remnant, *viz.* Cas A, for which α has been measured. In this case $\alpha \sim 3$ (Stankevich 1979).

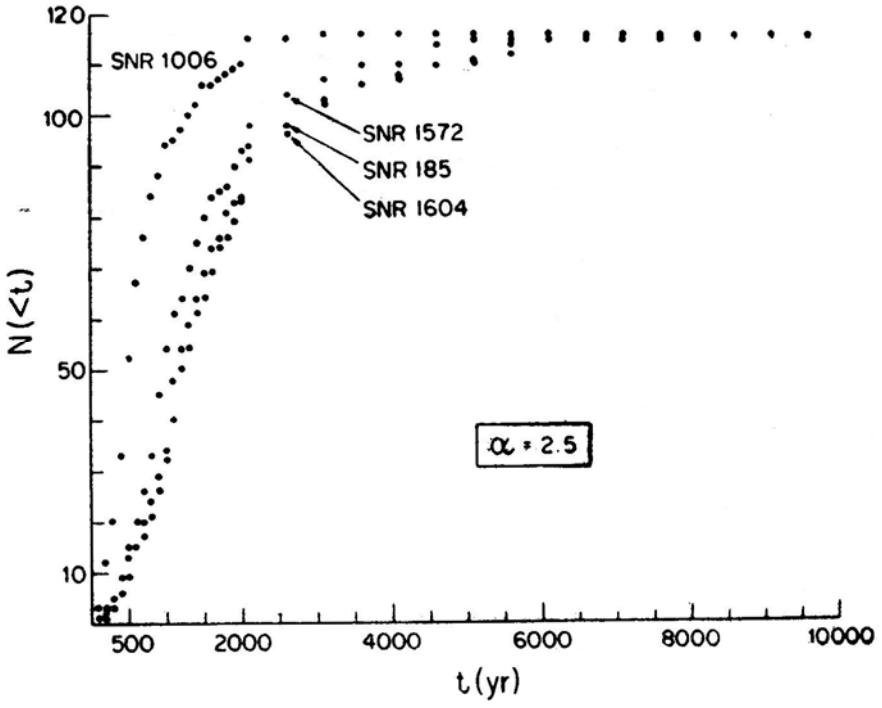

Figure 2. $N(< t)$ versus t plot for $\alpha = 2{\cdot}5$.

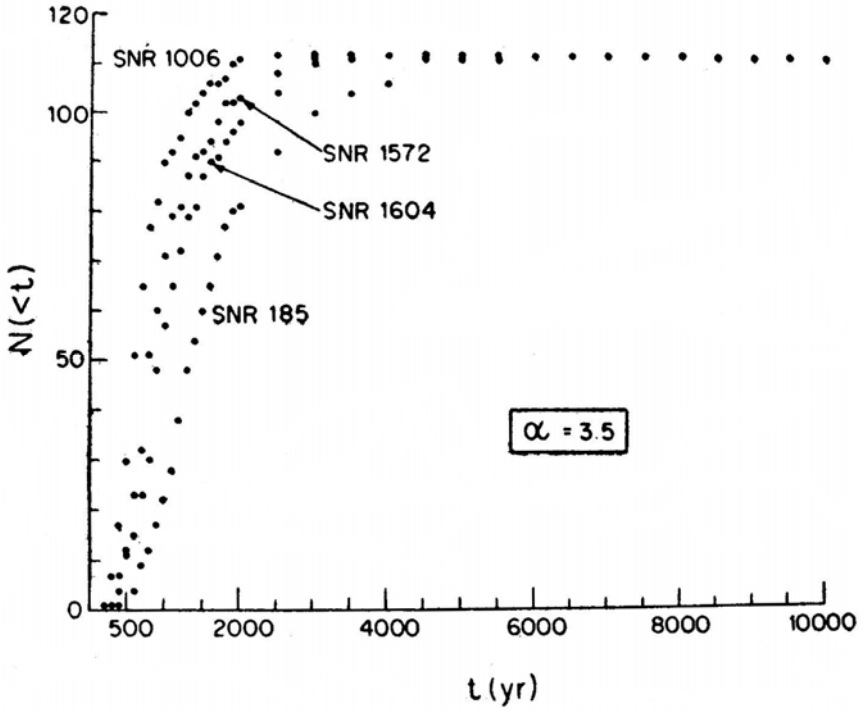

Figure 3. $N(< t)$ versus t plot for $\alpha = 3{\cdot}5$.

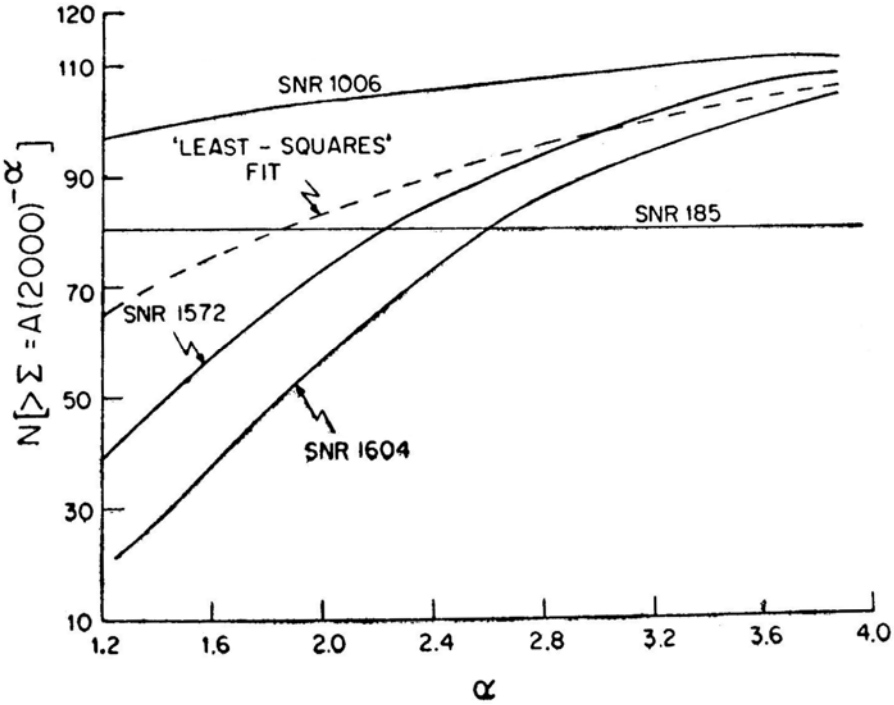

Figure 4. The number of SNRs whose ages are less than 2000 years as a function of α. The labels refer to the calibrator used. For each value of α we have also determined this number with an A which minimises the residual R (Equation 3); this curve is labelled 'leastsquares' fit

At this stage it is perhaps worth emphasizing the salient differences between the method outlined above and that adopted by Higdon and Lingenfelter (1980). The starting point is the secular decrease in the surface brightness (Equations 1 and 2). However, we determine both A and α by ' fitting' the historical remnants; Higdon and Lingenfelter *assume* $\alpha = 2{\cdot}3$, which they say is given by Gull's theory (though we cannot find such an explicit statement in Gull 1973). They then normalise Equation (1) by assuming that Kepler is at its maximum brightness and that Kepler, Tycho, SNR 1006 and SNR 185 are all expanding in regions of similar density.

3. Dependence of the surface brightness on the density of the interstellar medium

The method outlined above assumes that all remnants brighter than a given one are younger. This need not be true. For example, the remnant SNR 1006 may be very subluminous since its surface brightness is somewhat smaller than that of Vela XYZ. If the Vela pulsar is associated with the latter remnant its age would be $\sim 10^4$ yr (Clark and Caswell 1976). Thus if one uses SNR 1006 as an age calibrator one would grossly underestimate the ages of other remnants. This is precisely what we found in Figs 1–3. One possible reason why SNR 1006 is subluminous is that it is at a height of 325 pc above the galactic plane, where the hydrogen density is expected to be smaller than in the plane. For a given initial energy of the explosion (E_0), a remnant expanding in a region of low ambient density will attain a larger diameter in a given time than one expanding in a higher-density medium and will, therefore, have a lower surface brightness. In addition to this, two remnants of the same diameter may have different Σs if the density of the medium determines the radio flux in some way. Combining these two effects Caswell and Lerche (1979) have argued that the Σs of two SNRs of the same age but at different z (distance from the galactic plane) may be related as follows:

$$\Sigma(z, t) = \Sigma(z = 0, t) \exp(-|z|/z_{\Sigma}) \tag{4}$$

Where z_{Σ} is the ' scale height for the surface brightness '. They have suggested that z_{Σ} ~110 pc. If one pursued similar arguments put forward by Milne (1979), one would get $z_{\Sigma} = 50$ pc. It must be remembered that Equation (4) merely takes into account the variation of density as a function of z and does not take into account local fluctuations of density in the interstellar medium (ISM). We shall come back to this point later.

Let us now return to the SNR 1006 and its anomalously low surface brightness. If one ignores the fluctuations in density in the plane, one can use Equation (4) to normalize the Σs of all the remnants and thus convert a catalogue complete down to a limiting surface brightness (Clark and Caswell 1976) to one complete to a limiting age (Caswell and Lerche 1979; Milne 1979). One can then repeat the procedure adopted in Section 2 and obtain a new birthrate for SNRs. The results of the calculations using $z_{\Sigma} = 100$ pc are shown in Fig. 5; the labels have the same meaning as in Fig 4. We have not included the results obtained with Kepler as a calibrator; the reasons for this will be discussed below. Again, it will be seen that the mean birthrate is fairly insensitive to α. Using the same criteria mentioned in the previous

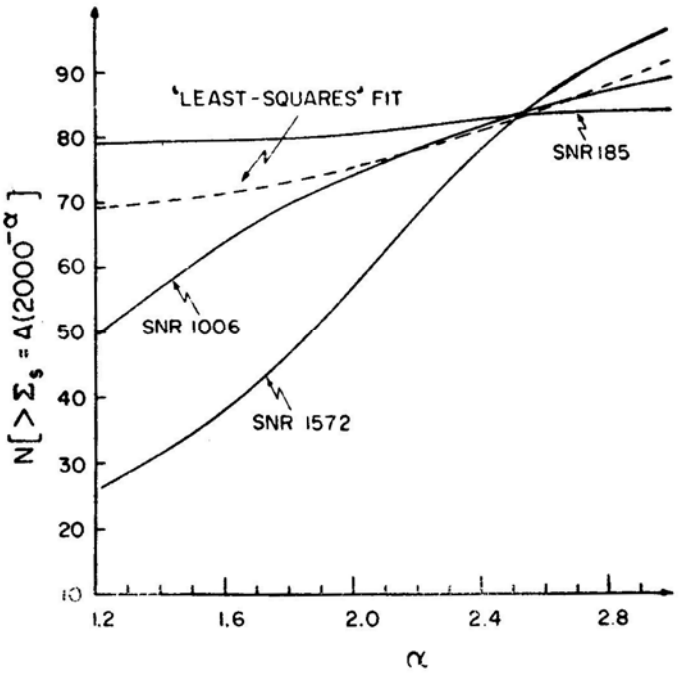

Figure 5. The curves have the same meaning as in Fig. 4, but the surface brightness of all the remnants were scaled up using Equation (4) and z_Σ = 100 pc; this is denoted by Σ_S.

section, we would like to suggest that for z_Σ= 100 pc, the evolution of the surface brightness is best described by $\alpha = 2{\cdot}5 \pm 0{\cdot}1$ yielding $\tau = 25 \pm 1$ yr. For z_Σ =150 pc,we find $\tau = 22 \pm 3$ yr for the same range of α.

An examination of Figs 4 and 5 reveals that the birthrate obtained through SNR 185 and SNR 1572 are not affected much by the z_Σ used to normalize the Σ_S (Fig. 4 corresponds to $z_\Sigma = \infty$, *i.e.* no scaling). This is because most of the SNRs are at fairly small z (z_{185} = 100 pc, z_{1572} = 150 pc *etc*); and hence their Σs are not scaled up very much (Clark and Caswell 1976, give a scale height of 60 pc for the distribution of SNRs).

SNR 1604 (Kepler) poses a problem, however. There are no reliable measurements of the distance to Kepler and therefore its height above the galactic plane is uncertain. Assuming that it was a typical Type I SN one can place it at a distance of between 6·5 to 10 kpc (Clark and Stephenson 1977b); this would correspond to a z-distance of 770 to 1180 pc above the plane. Yet, its diameter (9 pc at d = 10 kpc) and surface brightness (twice that of Tycho) suggest that it is expanding into a region of density similar to that in the plane. Clark and Stephenson (1977b) have suggested that if one adopted a distance of 10 kpc, it would place the remnant in the nuclear bulge of the galaxy; perhaps the scale height of the gas in the bulge is much higher than in the disk. At any rate, it would be meaningless to scale up the surface brightness of Kepler with a $z_\Sigma \sim 100$ pc;it would make it more than 100 times brighter than Tycho! Recently, Danziger and Goss (1980) have suggested a distance of 3·2 kpc to Kepler. This would place the remnant at 380 pc above the plane, but would make its linear diameter a mere 3 pc, Given its age, such a small diameter would imply a very low

value for $E_0 / n \sim 10^{49}$ erg cm ^{3}, where E_0 is the energy of the explosion and n the density of the medium. It is because of these gross uncertainties that we have not used Kepler as a calibrator in the analysis given in this section.

As was mentioned above, we have so far ignored possible variations in the density of the ISM at any given z. This may be at least as important as the variation in density with z. According to the emerging picture of the large-scale structure of the ISM there are two kinds of intercloud medium; one with $n_w \sim$ 0·2-0·3 cm^{-3}, $T \sim 8000$ K and the other with $n_H \sim 10^{-2\,5}$ cm^{-3}, $T \sim 10^6$ K (McKee and Ostriker 1977; Radhakrishnan and Srinivasan 1980b). The precise filling factors of these two components of the ISM are not known, but it is clear that if the above picture is true then some of the remnants must be expanding in the tenuous medium and the rest in the dense medium.

According to Gull (1973) the maximum surface brightness and the time t_0 when this is reached will scale as $\Sigma_m \propto n^{1\,42}$, $t_0 \propto n^{-1/3}$. These scaling laws when combined with Equation (1) tell us how the ages of two remnants, with a given Σ, scale with the density of the ISM into which they are expanding. One can formally write

$$N(>\Sigma) = \frac{t_H}{\tau} f_H + \frac{t_W}{\tau} f_W \tag{5}$$

where f_H and f_W, are the filling factors of the hot and warm medium respectively. If all the calibrators were expanding in the same component of the ISM, and if we knew the densities and filling factors of both the components, one could in principle use Equation (5) to correct the birthrate obtained in Section 2. Since these are not known, we shall not attempt to do this in this paper. Higdon and Lingenfelter (1980) have assumed that Kepler, Tycho and SNR 185 are expanding in the hot, low-density medium and deduced an effective birthrate for SNRs by treating the filling factor as a parameter. However, recent observation of the expansion of Tycho suggests that it was decelerated significantly implying that it may not be expanding in the coronal gas (Strom, Goss and Shaver 1982).

4. Discussion and summary

There has been a longstanding discrepancy between estimates of the SN rate in our galaxy and the SNR birthrate which ranged from one in 50 yr to one in 150 yr (Ilovaisky and Lequeux 1972; Clark and Caswell 1976; Caswell and Lerche 1979). Clark and Stephenson (1977a) suggested that the above discrepancy could be reconciled if only ~ 20 per cent of SNRs are ‘ long lived’. This is acceptable only if SNRs do not turn on till they are’ middle aged’. Bright young remnants such as Cas A, Kepler and Tycho militate against this. Alternatively, one can say that not all Supernovae leave behind radio remnants. This possibility has to be rejected because all the recorded SN in historical times have produced a remnant of one kind or another. It has also been suggested (Lozinskaya 1979; Tomisaka, Habe and Ikeuchi 1980) that most of interstellar space is filled with a hot, very low-density gas (as suggested by McKee and Ostriker 1977) and that remnants expanding in this gas will not be detected. The difficulty with this argument is that it would require all the

historical SN to have occurred in the dense medium with a very low filling factor. All these force one to the conclusion that the SNR birthrate must match the SN rate.

This was our motivation to have a fresh look at the SNR birthrate using the secular decrease in the surface brightness of the historical remnants as the starting point. The distinct advantage of this method over many of the previous ones is that it uses only the surface brightness which is independent of the distance to the source. Age calculations in the 'standard model' explicitly or implicitly involve the linear diameter, to determine which a distance estimate is needed. This is possible only for a fraction of SNRs. The disadvantage of our method is that there are very few historical remnants and one has to assume they are typical of the whole sample.

We now summarise our important conclusions and their implications:

1. The secular decrease of the surface brightness of the calibrators used is best described by $\Sigma \propto t^{-\alpha}$, where α is between 2·5 and 3·5. This is consistent with the measured slope of 2·0 ± 0·8 for Tycho and ~3 for Cas A.

2. This rate of decrease, if taken as typical of all SNRs, implies a birthrate for shell remnants of 1 in 22 ± 3 yr. This is in reasonable agreement with the supernova rate deduced from historical observations.

3. A majority of SNRs are relatively young with ages of a few thousand years. This is to be contrasted with the typical SNR lifetime of $\gtrsim 10^4$ yr as derived from the 'standard' model. *

4. Since only ~ 6 out of 120 SNRs resemble the Crab nebula and the mean lifetime of a shell remnant as derived by us is comparable to the expected lifetime of the Crab nebula (Weiler 1978; Weiler and Panagia 1980) it becomes unimportant to correct the birthrate of shell SNRs to obtain the total birthrate of all SNRs.

Acknowledgements

We wish to thank R. Nityananda for suggesting the method outlined in Section 2 and for many illuminating comments. Critical comments on an earlier version of the manuscript by V. Radhakrishnan, Ramesh Narayan,W. M. Goss, C. J, Salter, P. A. Shaver, K. W. Weiler and two anonymous referees are also gratefully acknowledged.

References

Ashworth, W. B. 1980, *J. Hist. Astr*., **11,** 1.
Baade, W., Zwicky, F. 1934, *Phys. Rev*., **45**,138.
Brecher, K., Wasserman, I. 1980, *Astrophys. J*., **240,** L 105.
Caswell, J. L. 1970, *Astr. Astrophys*., **7,** 59.
Caswell, J. L,, Lerche, I.1979, *Mon. Not. R. astr. Soc.*, **187,** 201.
Clark, D. H., Caswell, J. L. 1976, *Mon. Not. R. astr. Soc.*, **174,** 267.
Clark, D. H., Stephenson, F. R. 1977a, *Mon. Not. R. astr. Soc.*, **179**, 87p.
Clark, D. H., Stephenson, F. R. 1977b, *The Historical Supernovae*, Pergamon Press, Oxford.
Danziger, I. J., Goss, W. M. 1980, *Mon. Not. R. astr. Soc.*, **190,** 47p.

*The recent discovery of a pulsar with a characteristic age of 1677 yr, in the shell remnant MSH 15–52, clearly shows that the SNR cannot be older than ~ 1600 yr. The age calculated from the 'standard model' is, however, ~ 10^4 yr. This lends support to our viewpoint that the standard ages are often gross overestimates. Our age for MSH 15–52 is ~ 1200 yr, consistent with the maximum age of 1677 yr as implied by the pulsar (Srinivasan; Dwarakanath and Radhakrishnan 1982).

Gull, S. F. 1973, *Mon. Not. R. astr. Soc.*, **161**, 47.
Higdon, J. C., Lingenfelter, R. E. 1980, *Astrophys. J.*, **239,** 867.
IIovaisky, S. A., Lequeux, J. 1972, *Astr. Astrophys*., **20**, 347.
Katgert, P., Oort, J. H. 1967, *Bull. astr. Inst. Netherl*., **19,** 239.
Lozinskaya, T. A. 1979, *Soviet Astr*., **23,** 506.
McKee, C. F., Ostriker, J. P.1977, *Astrophys. J*., **218,** 148.
Milne, D. K. 1979, *Austr. J. Phys.,* **32,** 83.
Phinney, E. S., Blandford, R. D. 1981, *Mon. Not. R. astr. Soc.*, **194,** 137.
Radhakrishnan, V., Srinivasan, G. 1980a, *J. Astrophys. Astr*., **1,** 25.
Radhakrishnan, V., Srinivasan, G. 1980b, *J. Astrophys. Astr*., **1,** 47.
Srinivasan, G., Dwarakanath, K. S., Radhakrishnan, V. 1982, *Curr. Sci*., **51,** 596.
Stankevich, K. S. 1979, *Austr. J. Phys*., **32,** 95.
Strom, R. G., Goss, W. M., Shaver, P. A. 1982, *Mon. Not. R. astr. Soc.*, **200,** 473.
Tammann, G. A. 1977, *Ann. N. Y. Acad. Sci*., **302,** 61.
Taylor, J. H., Manchester, R. N. 1977, *Astrophys. J*., **215,** 885.
Tomisaka, K., Habe, A., Ikeuchi, S. 1980, *Progress theor. Phys*., **64,** 1587.
van der Laan, H. 1962, *Mon. Not. R. astr. Soc.*, **124***,* 125.
Vivekanand, M., Narayan, R. 1981, *J. Astrophys. Astr*., **2,** 315.
Weiler, K. W. 1978, *Mem. Soc. astr. Ital*., **49**, 545.
Weiler, K. W., Panagia, N. 1980, *Astr. Astrophys*., **90,** 269.

Astrophys. Astr. (1982) **3,** 363–378

Posterior Probability of the Deceleration Parameter q_0 from Quasars provided with a Luminosity Indicator

T. Kiang and F.-h. Cheng* *Dunsink Observatory, Castleknock, County Dublin, Ireland*

Received 1982 June 4; accepted 1982 July 20

Abstract. We have worked out a 'statistical algorithm' for obtaining the posterior probability density of the deceleration parameter q_0 from quasars where there is a luminosity indicator available. We point out that the role of the luminosity indicator is to provide a *second* estimate of individual luminosities after a first estimate has been obtained from measured brightness and redshift together with an assumed q_0. Discrimination of q_0 is to be sought in the statistical properties of the set of differences between the two estimates (the residuals). We show that the variance of the residuals and their correlation with redshifts (further refined to luminosity distances) are two independent test-statistics for q_0, whose known distributions then lead to the probability density sought.

We have applied the above algorithm to a sample of flat-spectrum radio quasars with measured CIV, MgII and Ly α lines. A combined Baldwin's relation was used for all 3 lines. Our result is that log q_0 is normally distributed with a mean value of + 0·270± 0·135 (s.d.), or, q_0 = + 1·86 ± 0·135 dex. This result, we believe, is the sharpest result so far published on q_0.

Key words: deceleration parameter—quasi-stellar objects (QSOs)—luminosity indicators—Baldwin's relation

1. Introduction

1.1 *Our Aim*

The present work was prompted by recent identifications of *luminosity indicators* of quasars. In one case, it is the equivalent width of certain emission lines in the quasar spectrum (Baldwin 1977; Baldwin *et al.* 1978, hereafter BBGW); in another, it is

*Permanent Address: Astrophysics Research Division, University of Science and Technology of China, Hefei, Anhui Province, China

the linear separation between the radio components in double and multiple systems (Fang *et al.* 1976; Zhou *et al.* 1977; Fang *et al.* 1979). When a luminosity indicator is available, a direct and effective determination of the posterior probability density (in the Bayesian sense) of the deceleration parameter q_0 should be possible, but this does not seem to have been done. We therefore set ourselves the task of constructing, from first principles and with full logical rigour, an algorithm or machine to do that. Into this machine we put the measured values of apparent magnitude, redshift, and the quantity identified with the luminosity indicator; out will come the complete probability density of q_0 based on the information fed. The construction of this machine is described in Section 2 and forms the main thrust of this paper. This machine is a 'general-purpose' one in that it can be applied to any luminosity indicator. A specific application using Baldwin's identification is made in Section 3. Further applications are being considered.

In our construction of the machine, we assumed that typical quasar luminosities have not changed significantly in time and we did this for methodological reasons. We are aware that there is a body of opinion inclined to the contrary view, but we cannot find in the literature any independently derived result on the evolution of quasar luminosities that can be usefully incorporated into our scheme at the start. Rather, we have the impression that the main cause for this opinion is the *a posteriori* discrepancy between the formal value of q_0 derived on assuming zero evolution and the value implied by the amount of recognized forms of matter in the universe. If so, then there is all the more reason for us to provide a general and rigorously derived method which will give a correct assessment of the formal value and its error-bounds in particular instances. As a matter of interest, there is a possibility at present of resolving this discrepancy without invoking luminosity evolution anyway. About this, more is said in Section 4.

1.2 *Our Approach*

The machine or algorithm we worked out applies also to *luminosity classifiers.* Formal definitions of luminosity classifiers as well as of luminosity indicators will be more conveniently given after we have stated our basic idea that underlies our construction. In our view, the role of a luminosity indicator or classifier is to provide a *second* estimate of the individual luminosities, after a first estimate has been obtained from measured brightness and redshift together with an assumed q_0. Let the first estimate be represented by absolute magnitude M, and the second, by M^*. Then it is in the statistical properties of the set of differences (or 'residuals'), $\Delta M = M - M^*$, that we find the means to distinguish the more probable from the less probable values of q_0. More specifically, we shall show in Sections 2.2 and 2.3 that the variance of the residuals and their correlation with redshift (further refined to luminosity distance) are two independent test-statistics for q_0, and their known likelihood functions then effectively determines the posterior probability density of q_0.

Now the formal definitions: By a luminosity *indicator* we mean an observable quantity P which is found to be correlated with M. In this case, M^* is to be read off the mean P–M relation. By a luminosity *classifier* we mean an observable attribute, the possession of which qualifies the object to be a member of a set with a restricted luminosity range. In this case, we simply set all the M^* as equal to the group mean $\langle M \rangle$. We have already referred to two examples of indicators. As

to classifiers, the steep radio spectrum of Setti and Woltjer (1973), the flat spectrum of Stannard (1973), the strong radio scintillation of Qu *et al.* (1979) and the small optical variation of Yang *et al.* (1980) may be instanced.

A classifier may be regarded as a degenerate indicator whose correlation with M over certain range of its value is vanishingly small. Hence, as remarked above, our statistical algorithm also applies to classifiers. In practice, of course, there will be some difference in the quality of the results obtained because indicators generally involve smaller dispersions than classifiers do. Also, in the present terminology, the more recent form of Baldwin's relation (BBGW), namely, a relation between line width and M, restricted to quasars with flat radio spectra, is a logical product of an indicator with a classifier. It is this more recent form that we shall be using in our specific application in Section 3.

2. How to find the probability density of q_0 when there is a luminosity indicator available

2.1 *The Basic Functional Relation*

By definition, the relation between luminosity distance D_L in Mpc, the absolute and apparent magnitudes, M_{tot} and m_{tot}, measuring the total emitted and received fluxes, is

$$M_{\text{tot}} = M_{\text{tot}} + 5 \log D_L + 25. \tag{1}$$

For a pressureless Friedmanii universe, Mattig (1958) gave the exact expression of D_L as a function of the redshift z with H_0 and q_0 as adjustable constants. We shall write Mattig's expression in the form

$$D_L = (c / H_0)\, f(z; q_0), \tag{2}$$

with

$$f(z; q_0) = q_0^{-2} \{q_0 z + (q_0 - 1)\,[(2q_0 z + 1)^{1/2} - 1]\}, \tag{3}$$

c being the velocity of light. We shall be using published monochromatic (per unit frequency interval) magnitudes $m_{\nu'}$, at the redshifted frequency ν' of some emission line; if M_ν is the absolute magnitude at the emitted frequency ν, then we have

$$m_{\text{tot}} - M_{\text{tot}} = m_{\nu'} + 2{\cdot}5 \log (1 + z) - M_{\nu}. \tag{4}$$

It is convenient to use a redshift-corrected apparent magnitude m defined by

$$m = m_{\nu'} + 2{\cdot}5 \log (1 + z) \tag{5}$$

and a zero-adjusted absolute magnitude M defined by

$$M = M_\nu + 5 \log (c/H_0) + 25. \tag{6}$$

(For example, if H_0 = 100 km s^{-1} Mpc^{-1}, the adjustment amounts to + 42·38). Using this zero-adjusted absolute magnitude frees us from further dealings with H_0. From Equations (l)–(6), we then obtain the basic functional relation in a form stripped of all nonessentials:

$$m - M = 5 \log f(z; q_0). \tag{7}$$

This equation contains 2 observables m, z, and 2 unknowns M, q_0, and a known function (3)—with the present observed values of quasar redshifts and the values of q_0 of possible interest, it is advisable that the full form of (3) be retained.

2.2 *Search for Test Statistics*

Our aim is to find out something about q_0, but since M is unknown, we resort to the following procedure. We first assume a value of q_0 and use Equation (7) to get a *first* luminosity estimate M_i for each individual. Of course, these individual M_i-values can never tell us anything about the probability of the assumed value of q_0; but if the objects were selected by a *classifier*, then by hyopthesis they belong to a class of limited luminosity dispersion σ_M and then we should be able to find discriminators of q_0 in some group properties of the whole set of M_i-values. Consider the residuals from the group mean,

$$\Delta M_i = M_i - \langle M \rangle, \tag{8}$$

and let us denote their rms value by $s_{\Delta M}$. This $s\Delta M$ depends, of course, both on σ_M and on the assumed q_0. If the latter happens to be the true value, then $s_{\Delta M}$ is equal to σ_M up to the sampling error; on the other hand, a false value of q_0 would in all likelihood cause some increase in $s_{\Delta M}$. Hence we can identify the particular value of q_0 that gives the least $s_{\Delta M}$ as the most probable one.

Again, since we do not know enough about cosmological evolution of quasar luminosity, we have to assume that σ_M is independent of z; then, the most probable q_0 should be that which gives zero correlation between ΔM and z. Thus, the correlation between ΔM, calculated on some assumed value of q_0, and z (or any monotonic function of z) serves as another measure of the probability of that assumed value. These two statistics will be further discussed and refined in the next subsection.

Now, suppose, in addition to a classifier, we also have an *indicator*. This means that we now have, in addition to m and z, a third observable P whose observed values P_i are found to correlate with M_i. Let us suppose this correlation to be represented by a linear regression line,

$$M = \langle M \rangle + b_0 (P - \langle P \rangle). \tag{9}$$

It is well known that, in this case, the variance about the regression line is $(1 - r_0^2)$

times the original variance in M. So, if we define a *second* luminosity estimate for the i-th object, , M_i^*, by

$$M_{*i} = \langle M \rangle + b_0 \ (p - \langle p \rangle), \tag{10}$$

so that the residual is

$$\Delta M_i = M_i - M_i^* = (M_i - \langle M \rangle) + b_0 (P_i - \langle P \rangle), \tag{11}$$

then we have

$$\sigma^2_{\Delta M} = (1 - r_0^2)\, \sigma^2_M. \tag{12}$$

This shows that an indicator is the more useful, the tighter it correlates with M; in the limit of a perfect correlation ($r_0 = 1$), a single observed value will suffice to determine q_0 within measuring errors. The argument for the two test stastistics remains the same, after generalizing Equations (8) to (11). Alternatively, we can say that a classifier is a special case of an indicator where $r_0 = 0$ and $b_0 = 0$, and all the second luminosity estimates are the same:

$$M_i^* = \langle M \rangle, \text{ for all } i. \tag{13}$$

2.3 *Hubble Diagram and Distance-Modulus-Redshift Diagram*

A description of what actually happens when we compare observations with theoretical expectations will clarify and refine the foregoing points. We note first that while the observations are naturally plotted in the (m, log z) diagram or the Hubble diagram, the theoretical curves, *i.e.* the Mattig curves given by Equations (7) and (3) are appropriately placed in the ($m - M$, log z) plot, or the distance-modulus-redshift diagram. We shall plot log z as abscissa in both diagrams and shall place the former above the latter, as in Fig. 1. Again, consider first the case where the data is selected by a classifier. To confront a chosen $q_0$curve with the observed points, we must move the curve bodily up by $\langle M \rangle$ so as to place it in the position of the best fit in the sense of least squares; in other words, the curve must pass through the mean observation. The residualsr ΔM_i of Equation (8) are then just the vertical distances of the observed points from the curve. To make an impartial choice of q_0, all the candidate curves must be made to pass through the mean observation. Their curvature over the observed z-range being generally negligible, we can identify the most probable q_0 with that for which the theoretical gradient is equal to the observed, 'least-squares' gradient; it then follows that for any other $q_0$curve, the mean residual $s_{\Delta M}$ will be larger; and also there will be a nonlinear correlation between ΔM and log z. If, as a refinement, we take the curvature into account, then a linear correlation is to be expected between ΔM and log $f(z;q_0)$. We therefore take, as our two test statistics, $s^2_{\Delta M}$ (simply s^2 hereafter) and the linear correla tion coefficient r between ΔM and log f (z; q_0).

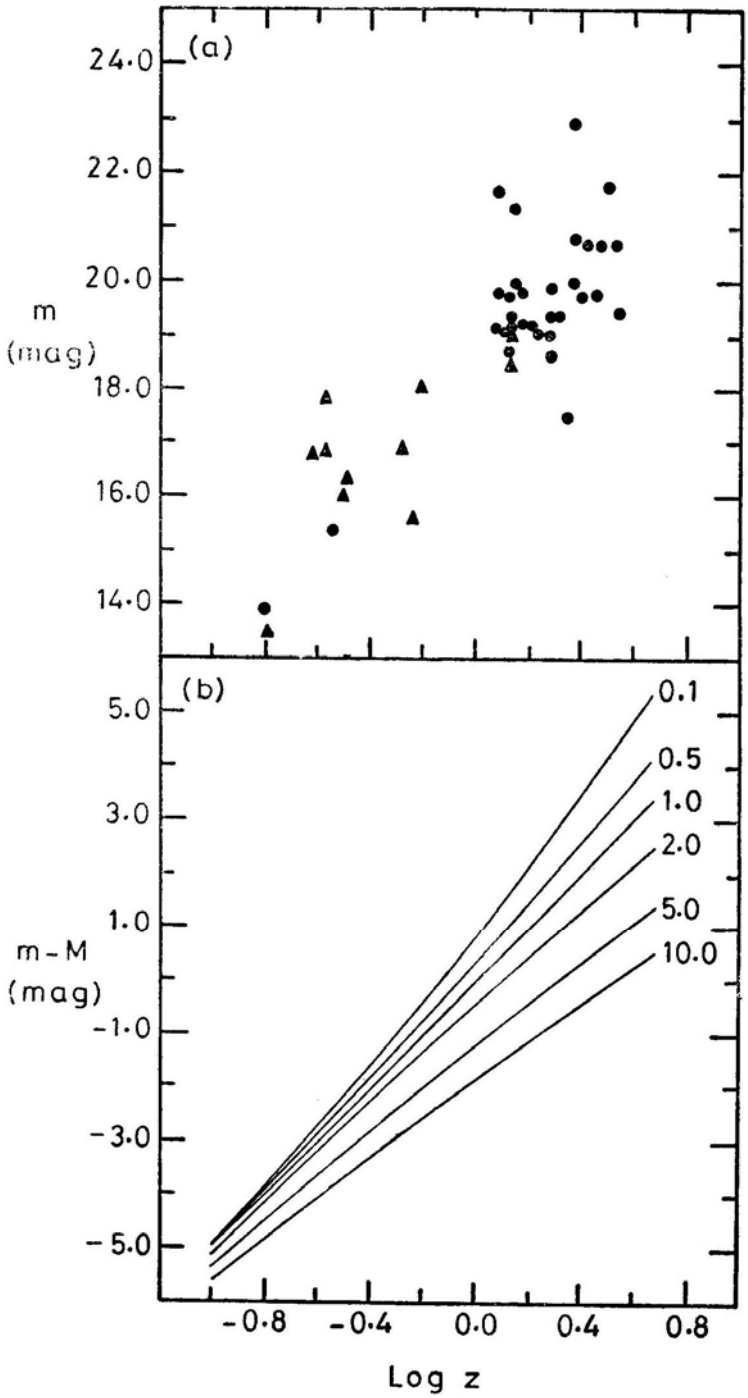

Figure 1. (a) The observed Hubble diagram of 43 flat-spectrum radio quasars. The various symbols are explained in Fig. 2. The regression line of m on $\log z$ (not show) has a slope of 4·21 and the rms scatter about the line is 1·08 mag. (b) The theoretical distance-modulus-redshift curves for selected values of the deceleration parameter q_0

When there is a luminosity *indicator* available, comparison between the observed points and the theoretical curve can no longer be made in the (m, log z) diagram, because each point requires a different shift M_i^* of the curve. Instead, we move each point down by the appropriate amount shown by Equation (10) and make our comparison in the (m — M, log z) diagram. Using the indicator illustrated in Fig. 2, Fig. 3 results from Fig. 1(a) by such a process. The ordinate of the shifted point is, apart from a difference in zero, the 'compensated magnitude' of BBGW. Here, again, the vertical distances of the points from the curve are none other than the residuals ΔM_i (now defined by Equation 11), and our argument for using s^2 and r as test statistics can be repeated. Note, in this case, that the comparison between observation and theory should be made for values of q_0 one at a time–it can be shown that, only if the indicator is completely uncorrelated with the redshift, can we compare without bias a q_0-curve with observed points shifted by amounts that were calculated on another assumed value of q_0.

2.4 *Bayesian Probability*

We shall adopt the Bayesian approach in probability theory and use Jeffreys' (1948) notation and terminology. Accordingly, we write

$$P(dq_0 \mid r\, s^2\, H) \propto P(dq_0 \mid H) \cdot P(dr\, ds^2 \mid q_0\, H). \tag{14}$$

That is, the *posterior* probability of q_0 is proportional to the product of its *prior* probability and the *likelihood* of the two test statistics r and s^2. The letter H stands for all relevant knowledge and assumptions and serves as a reminder as to what sample space the random variates (placed before the bar) refer to. Following Jeffreys'

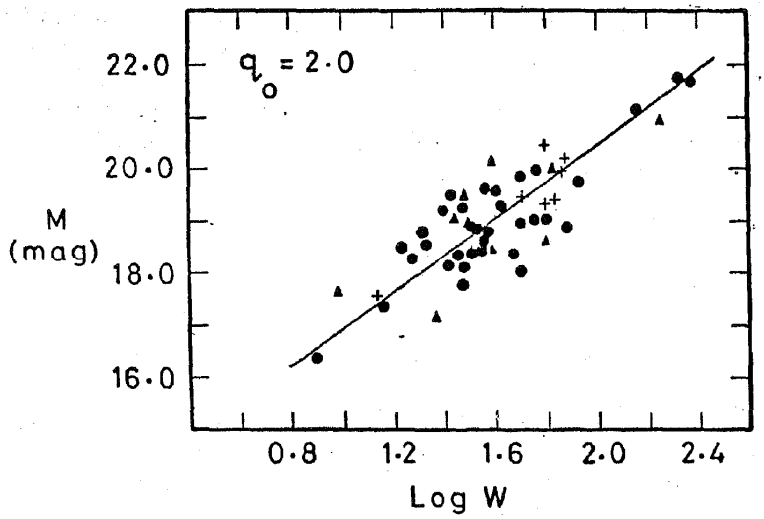

Figure 2. A combined log W–M relation for CIV (circles), Mg II (triangles) and Ly α (crosses) emission lines. W is the equivalent width reduced to the rest frame. M is the zero-adjusted absolute magnitude defined by Equation (6) calculated here with q_0 = + 2. The triangles and crosses have been given systematic corrections of +0·1 mag and + 1·2 mag in M respectively. The mean relation has a slope of 3·61 mag dex^{-1} and the rms scatter about the line is 0·63 mag.

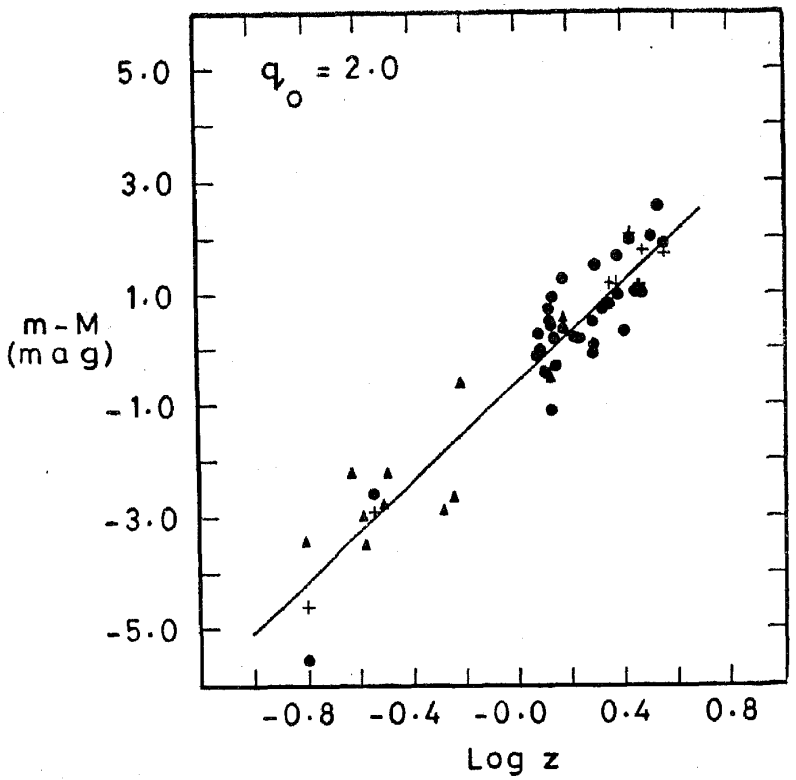

Figure 3. Illustration of the confrontation between theory and observation in the case of $q_0 = +2$. The individual residuals are identical with those in Fig. 2, but are plotted here against log z, rather than log W.

recommendation, we shall take the prior probability to be the one that is uniform in log q_0, since q_0 is essentially positive. We can further restrict its range within some safe limits. The ratio of galaxian density to the critical density can be put at not less than 0·02 (Allen 1973) and this means a lower limit of 0·01 for q_0. The age of the Earth is reliably determined at $4{\cdot}5 \times 10^9$ yr (*cf.* Lang 1980, p. 509); this, together with a 'safe' lower bound of 30 km s^{-1} Mpc^{-1} for H_0, gives a safe upper limit for q_0 at about 50. Accordingly, writing

$$Q = \log q_0, \tag{15}$$

we put

$$P(dQ \mid H) \propto dQ, \quad (-2{\cdot}0 \leqslant Q \leqslant +1{\cdot}7). \tag{16}$$

Now consider the likelihood $P(dr\ ds^2 \mid QH)$. From the last subsection we may have gained the impression that r and s^2 are correlated, so that we cannot equate their joint likelihood to the product of their separate likelihoods; but that would be a misconception. What happened there was that, for a fixed set of m and z measurements, r and s^2 are correlated on *varying* q_0; this correlation arises because of their parametric dependence on q_0 and not because of any *random* variation. But when considering the likelihoods, we keep q_0 *fixed* and ask what happens if, instead of the

actual sample of measurements, we have other samples from the same statistical population or sample space—and this is implicit in the letter *H*. It is then easy to see that, as s^2 is a property of the *unordered* set of ΔM_i while r is a property of the *ordered* set, ordered along z, they must be statistically independent. So we have

$$P(dr\ ds^2 \mid QH) \propto P(dr \mid QH) \cdot P(ds^2 \mid QH). \tag{17}$$

The likelihood of r can be identified with the well-known sampling distribution (sample size n) of the correlation coefficient from an uncorrelated bivariate normal population (Kendall and Stuart 1969, hereafter KS1, p. 387):

$$P(dr \mid QH) \propto (1 - r^2)^{(n-4)/2}\, dr. \tag{18}$$

As for the likelihood of s^2, we can regard $ns^2 = \Sigma\ (\Delta M_i)^2$ as the sum of squares of n normal variates with mean 0 and variance σ^2, which is to be estimated by $s^2_{\min}$, the least s^2 obtained as q_0 is varied. According to a well-known formula (Kendall and Stuart 1972, hereafter KS2, p. 5), we equate then σ^2 to $[(n - 1)/n]\ s^2_{\min}$, and hence, using the sampling distribution of sums of squares of n normala variates (KS1 p. 247), we obtain

$$P(ds^2 \mid QH) \propto (s/s_{\min})^{n-2} \exp\ [-(n-1)\ (s/s_{\min})^2/2]\ ds^2. \tag{19}$$

We shall denote the densities given by Equations (18) and (19), regarded as functions *of Q,* by $F_1\ (Q)$ *and* $F_2(Q)$:

$$F_1(Q) = [1 - r^2(Q)]^{(n-4)/2}, \tag{20}$$

$$F_2(Q) = [s(Q)/s_{\min}]^{n-2}\ \exp\ [-(n-1)\ (s(Q)/s_{\min})^2/2]. \tag{21}$$

We shall denote the prior and posterior probability densities by $F_0\ (Q)$ and $F\ (Q)$; then the Bayesian formula (14) assumes the explicit form

$$F(Q) \propto F_0(Q)\ F_1(Q)\ F_2(Q), \tag{22}$$

where, corresponding to formula (16), we take

$$F_0(Q) = 1/3{\cdot}7, \quad -2{\cdot}0 < Q < +1{\cdot}7,$$
$$= 0 \quad , \quad \text{otherwise} \tag{23}$$

We may observe that formula (22) can be regarded as representing *two* Bayesian processes in tandem: in the first, F_0 is the prior probability and F_1 the likelihood; in the second, F_0F_1 is the prior probability and F_2 the likelihood. This exemplifies the Bayesian position that the prior probability is actually the instrument by which we incorporate our previous experience in our search for statements of ever greater probability.

2.5 *A Statistical Algorithm*

To the question posed at the head of this section, we now give our answer in the form of a set of precepts. We assume that we start with a set of n objects with known values of redshifts z_i, of the redshift-corrected apparent magnitude m_i and of the luminosity indicator P_i. Then,

1. Assume a value of Q, that is, $\log q_0$.
2. Find M_i by Equation (7).
3. Find the b_0 in Equation (9). Where random errors in P_i are thought to be comparable to those in M_i, b_0 should be identified with the gradient of the 'line of best normal fit' (see Section 3·2).
4. Find ΔM_i according to Equation (11).
5. Calculate the linear correlation coefficient r between ΔM_i and logarithm of $f(z_i; q_0)$ defined by Equation (3), and hence the value of $F_1(Q)$ according to Equation (20).
6. Calculate the variance s^2 of ΔM_i and find the minimum $s^2_{\min}$ with respect to q by varying the assumed q_0; hence find the value of $F_2(Q)$ according to Equation (21).
7. Adopt an $F_0(Q)$. For a 'first' determination, we suggest the form (23). For a subsequent determination based on independent data, the result $F(Q)$ obtained in a previous determination can be used.
8. Calculate $F(Q)$ according to formula (22).

3. A specific application using line width as luminosity indicator

3.1 *The Line-Width Data*

In this Section, a specific application of the statistical algorithm derived above will be made. We shall use as luminosity indicator the recent form of Baldwin's relation and so confine ourselves to flat radio-spectrum quasars with published equivalent widths of the CIV (1549 Å), Mg II (2800 Å), or Ly α (1216 Å) emission lines. The equivalent widths come mainly from BBGW (23 CIV widths and 11 Mg II widths) and Baldwin (1977) (8 CIV and 7 Ly α). From Green *et al.* (1980) we took the CIV and Ly α widths of the quasar 1302 — 102, and from Boksenberg *et al.* (1978) and Davidsen, Hartig and Fastie (1977) we took respectively the CIV and Ly α widths of 3C 273. Altogether, we have 33 CIV, 11 Mg II and 9 Ly α values. These 53 line widths belong to 43 different objects, whose Hubble Diagram is shown in Fig. 1 (a).

3.2 *A Combined Log W-M Relation*

Previous works on the log W–M relation have invariably treated the CIV, Mg II and Ly α lines separately. One reason could be the feeling that, should the relation be caused by selection, then a separate treatment would be informative. At present, there is, however, a. general agreement (Wampler 1980; Jones and Jones 1980; Baldwin *et al* 1980) that the complete sample used in BBGW is free from selection effects. To this consensus we would add the results of some of our own calculations. We argue that, since selection effects are generally taken to depend on the raw apparent

magnitude above all else, we should take a careful look at the *partial* correlation between log W and M at constant $m_{v'}$. Results of our calculation are shown in row (5) of Table 1. Referring to the 5 per cent and 1 per cent values given in rows (2) and (3), we see that the correlation coefficients, on passing from 'total' to 'partial', have remained 'highly significant' (two asterisks) or at least 'significant' (single asterisk). We should point out that 10 out of the 33 CIV lines in Table 1 and all the 9 Ly α lines come from data other than BBGW, and so it seems that not only is the BBGW sample selection-free, but so is our slightly enlarged sample. For interest, we give in row (6) the partial correlation coefficients at constant log z. These quantitatively corroborate the statement (Wampler 1980; Baldwin *et al.* 1980) that the log W-M relation is independent of z, and also extend that statement in the same sense.

We now ask: 'Are the (total) correlations in the 3 sets statistically different?' To the correlation coefficients given in row (4) we now add the regression coefficients b_0 of M on log W and the rms scatter s in rows (7) and (8). By Fisher's F-test (KS1, p. 377), we find the variance ratio between CIV and Ly α to be not significant at 5 per cent and that between CIV and MgII, only marginally so. Tests of the MgII and Ly α values of r_0 and b_0 (KS1, pp. 390, 393), taking the CIV values as parent values, show none of them to be significant at 5 per cent. Thus, as judged purely from the statistic-cal angle, the 3relations are not significantly different and we shall combine them into one single relation. We should add that, should there be any observational or theo-retical reason to insist on separate treatment, nothing prevents us from doing so in future applications of our algorithm. In this particular instance, we are going to use the combined relation for the sake of definiteness.

When making the combination, we should, of course, allow for possible differences in the zero-point. We therefore wrote the equations of conditions in the form

$$\alpha + b \log W = M + \delta \tag{24}$$

and found the systematic corrections by least squares to be

$$\begin{aligned} \delta = \;& 0{\cdot}00 \text{ mag for C IV (assumed)}, \\ & + 0{\cdot}10 \text{ mag for Mg II}, \\ & + 1{\cdot}20 \text{ mag for Ly } \alpha. \end{aligned} \tag{25}$$

These corrections were based on values calculated with $q_0 = +1$.

Table 1. Parameters of the log W-M correlation in various data sets.

	Correlation parameter	Data set C IV	Mg II	Ly α	Combined
(1)	sample size	33	11	9	53
(2)	r (5 per cent)	0·34	0·60	0·67	0·27
(3)	r (1 per cent)	0·44	0·73	0·80	0·35
(4)	r (total)	+0·85**	+0·75**	+0·93**	+0·83**
(5)	r (constant $m_{v'}$)	+0·76**	+0·63*	+0·92**	+0·79**
(6)	r (constant log z)	+0·85**	+0·80**	+0·93**	+0·84**
(7)	b_0 (mag dex^{-1})	+3·04	+2.68	+3·56	+3·01
(8)	s_0 (mag)	±0·58	±0·81	±0·37	±0·60
(9)	b_1 (mag dex^{-1})	+3·56	+3·61	+3·84	+3·61
(10)	s_1 (mag)	±0·60	±0·87	±0·38	±0·63

A regression line presumes all the random errors to be in one of the two coordinates, which is certainly unreasonable in the present case. Theoretically, one should be able to uncover the underlying 'structural relationship' (KS2 Chapter 29) between M and log W, but our attempt to do so resulted in an unacceptable solution which implied much larger measuring errors than stated in BBGW. We therefore propose the use of the 'line of best normal fit'. This is the line with the least squares of deviations in the direction normal to it, after the variables have been 'standardized' to unit variances (Kendall 1965, p. 11). In the 'standardized' coordinates, the line has gradient unity (Kendall 1965, p. 15 for $p = 2$), hence in the original coordinates, the gradient is equal to the ratio of the standard deviations:

$$b_1 = s_M / s_{\log W}. \tag{26}$$

This shows that the 'line of best normal fit' is the geometric mean of the two regression lines, M on log W, and log W on M. Our proposal means that the b_0 in Equations (9)–(11) is to be replaced by the b_1 defined by Equation (26). The parameters corresponding to the 'normal fit' are given in the last two rows of Table 1. We may note that the 3 'normal fit' gradients b_1 for the 3 separate data sets agree with one another much better than do the 3 regression coefficients b_0—the correlations in the 3 cases become more alike when some account is taken of the random errors in log W as well as in M.

Our combined relation is illustrated for the case $q_0 = +2$ in Fig. 2. The line shown in the 'line of the best normal fit' with a gradient of + 3·61 mag dex^{-1}. The regres sion line of M on log W with a gradient of + 3·01 mag dex^{-1} would give visibly systematic residuals.

3.3 *Results of the Specific Application*

For our combined data of 53 entries, the variations of r and of s^2 with Q are shown in Figs 5(a) and (b), while Fig. 4 illustrates the scatter diagram that produces r in three selected instances. From these, the $F_1(Q)$ and $F_2(Q)$ curves of Fig. 5(c) follow readily from Equations (20) and (21). Note, with the form (23) assumed for $F_0(Q)$, either curve would also be the posterior density derived on using that statistic alone. Both statistics proved effective in reducing our ignorance about q_0, r being especially so. Before either, we assumed a total range of uncertainty of 3·7 dex, after applying the s^2-test alone, it is reduced to 1·1 dex, and after applying the r-test alone, to 0·6 dex. Moreover, the two statistics act in phase, so that the combined effect—the curve $F(Q)$—is a further sharpening of the result. Both $F_1(Q)$ and $F(Q)$ are in fact close to the normal form and $F(Q)$ has mean + 0·270 and standard deviation 0·135:

$$Q = +0{\cdot}270 \pm 0{\cdot}135. \tag{27}$$

The corresponding result in q_0 may be written

$$q_0 = +1{\cdot}86 \pm 0{\cdot}135 \text{ dex}, \tag{28}$$

but we should keep in mind that the ditribution of q_0 is not normal, so that the value

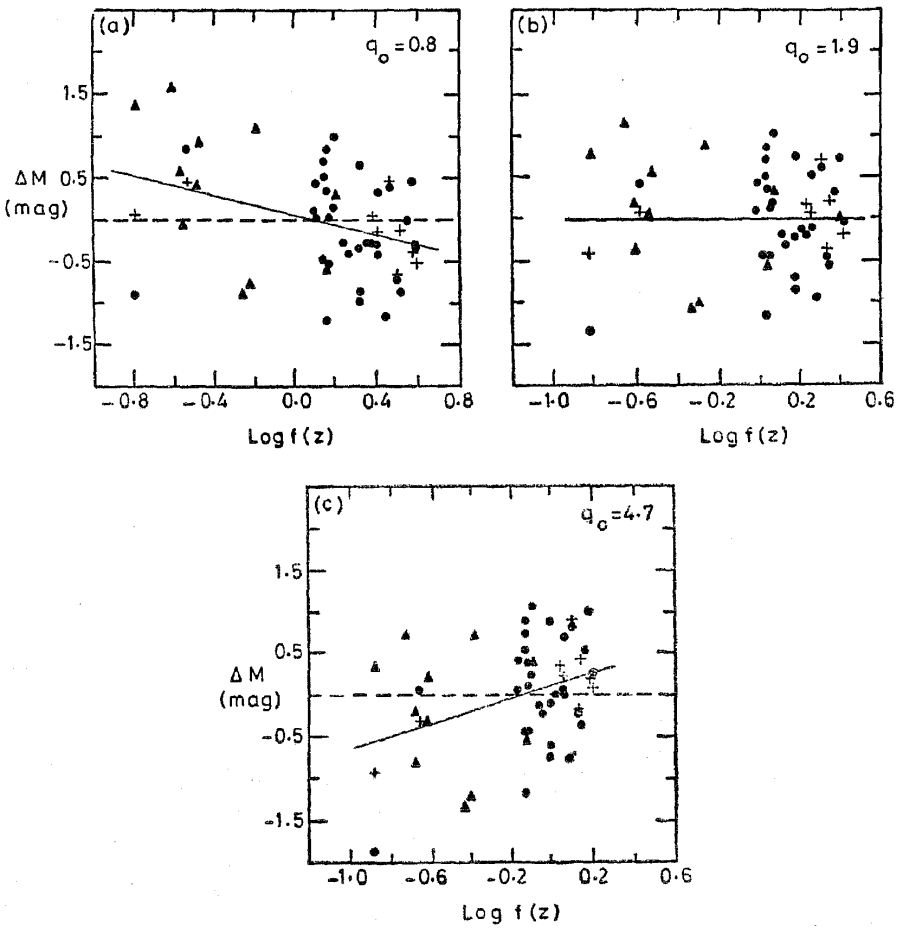

Figure 4. Correlation diagram between residual ΔM and log f (z; q_0) for 3 values of q_0. Freedom from correlation distinguishes the more probable from the less probable values of q_0.

+ 1·86 represents the median rather than the mean of the distribution. We can replace the '±0·135 dex' by a 'multiplicative' 1·36, which we propose to be preceded by the composite sign '$\overset{\times}{\div}$' and write Equation (28) as

$$q_0 = +\,1{\cdot}86\,\overset{\times}{\div}\,1{\cdot}36. \tag{29}$$

With these understandings, any of the three expressions (27), (28) and (29) adequately summarizes the result of this particular application.

It is of interest to know how the result depended on (a) the statistics used and (b) the data used. For this, we give in Table 2 the median q_0 resulting in different cases and the '4σ end-ratio' values (ratio of the values at the upper and lower 2·28 per cent points). Reading down the 4σ end ratios confirms what was mentioned above: the r-test is more resolving than the s^2-test and the combined test is a little better still. This is also reflected in the variations in the median q_0 values: the combined test values differ from the r-test values by only small amounts in the direction of the s^2-test values.

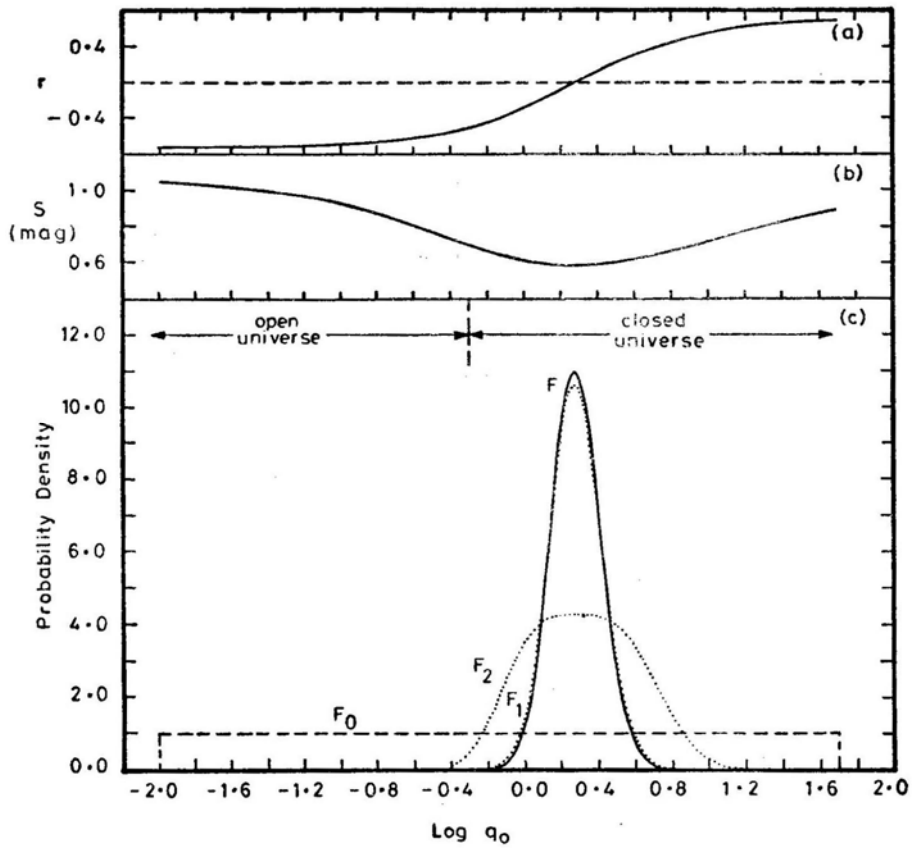

Figure 5. (a) Variation of the test statistic r with log q_0. (b) Variation of the rms scatter s with log q_0 (The test statistic is s^2). (c) Probability density curves of the deceleration parameter q_0. F_0 is the assumed prior density, F_1 the posterior density using the test statistic r alone, F_2 that using s^2 alone, and F that using both. F is very nearly normal in log q_0, with mean +0·270 and s.d. 0·135.

Table 2. Results by various tests in 3 nested sets.

C33 = 33 C IV; CM44 = 33 C IV + 11 Mg II; CML53 = 33 C IV + 11 Mg II + 9 Ly α.

Test	C33	CM44	CML53
		median q_0	
r-test	1·04	2·07	1·84
s^2-test	1·34	2·30	1·96
rs^2-test	1·10	2·07	1·86
		4σ end-ratio	
r-test	27·	5·9	3·9
s^2-test	136·	25·	13·
rs^2-test	11·4	5·0	3·5

Now read across and we are struck by the improvement in resolution as we add a mere 11 MgII lines to the data of 33 CIV lines: the 4σrange decreases by a factor between 2·3 and 5·4. Adding the 9 Ly α lines improves further, bringing the improvement factor to between 3·2 and 10·5. Our use of the combined data seems to be justifiable *a posteriori.*

4. Final remarks

The improvement brought about by the Mg II objects is no doubt due to their being located in the low-redshift range (*cf.* Fig. la). The possibility was foreseen in BBGW, but the authors preferred not to use the Mg II data in that paper. Their result was not stated directly in terms of q_0. According to their Equation (11), (BBGW, p. 434), their result would correspond to $q_0 = + 2{\cdot}4 \pm 1{\cdot}4$. Compared to our result, the formal uncertainty is much greater—the standard deviation corresponds to a 4σ end-ratio of at least $(3{\cdot}8/1{\cdot}0)^2 = 14$, which is more than 4 times our value for the combined data. The qualitative difference between the BBGW and our results can be highlighted as follows: their result, while favouring a closed universe, does not exclude the possibility of an open universe ($q_0 < 0{\cdot}5$) with a high probability, whereas ours does, for in our case, the critical value is more than 4σ below the mean value.

Our value of $q_0 = + 1{\cdot}86$ requires the universe to contain some 100 times more mass than in the form of galaxies. It also implies that the age of the universe is $9{\cdot}4 \times 10^9$ yr (assuming $H_0 = 50$ km S^{-1} Mpc^{-1}), which is exceeded by some of the estimated ages of globular clusters (Lang 1980 p. 512), though still decidedly longer than the radioactivity age of the Earth of $4{\cdot}5 \times 10^9$ yr. Because of these apperent contradictions and of the strong constraint imposed by the cosmic abundance of He on the amount of matter in the universe (we owe this remark to a referee of this paper), many astronomers hold the view that the universe is open and that such a large value of q_0 as we obtained is due to the neglect of cosmological evolution of quasar luminosity in the derivation. On the other hand, following the report of a finite mass of neutrino, an alternative interpretation is emerging (*cf.* Waldrop 1981, Qing *et al.* 1981). This says, that the universe is in fact closed and the missing mass is to be found in neutrinos.

It is not our intention here to discuss the pros and cons of these two interpretations. The basic conflict is between the determinations of the mean mass density of the universe on the one hand and those of q_0 on the other, and this question has been discussed in some detail in a recent review paper (Fang *et al.* 1982). The aim of the present paper, we recall, was to work out a rigorous procedure which will give the posterior probability density of q_0 whenever there is a luminosity indicator or classifier available. This we did in Section 2, culminating in the set of precepts of Section 2.5. These form the main result of the present paper. What we did in Section 3 can be regarded as an illustration of our method, though it seems to have brought into a sharper focus than before the age-old question whether the universe is open or closed.

References

Allen, C. W. 1973, *Astrophysical Quantities*, 3 edn, Athlone Press, London, p. 293.

Baldwin, J. A. 1977, *Astrophys. J.*, **214,** 679.

Baldwin, J. A., Burke, W. L., Gaskell, C. M., Wampler, E. J. 1978, *Nature*, **273,** 431 (BBGW).

Baldwin, J. A., Burke, W. L., Gaskell, C. M., Wampler, E. J. 1980, *Bull. am. astr. Soc.*, **12,** 537.

Boksenberg, A., Snijders, M. A. J., Wilson, R., Benvenuti, P., Clavell, J., Macchetto, F., Penston, M., Boggess, A., Gull, T. R., Gondhalekar, P., Lane, A. L., Turnrose, B., Wu, C. C., Burton, W. M., Smith, A., Bertola, F.,Capaccioli, M., Elvius, A. M., Fosbury, R., Tarenghi, M., Ulrich, M. H., Hackney, R. L., Jordan, C, Perola, C. G., Roeder, R. C, Schmidt, M. 1978, *Nature*, **275,** 404.

Davidsen, A.F., Hartig, G.F., Fastie, W.G.1977, *Nature*, **269,** 203.

Fang, L. -z., Zhou, Y. -y., Cheng, F. -*z*., Chu, Y. -q. 1976, *Acta. astr. Sin.*, **17,** 134: 1977, *Chinese Astr.*,**1,** 278.
Fang, L. -z., Zhou, Y. -y., Cheng, F. -z., Chu, Y. -q., Cheng, F. -h. 1979, *Scientia Sin.*, **22,** 1292.
Fang, L. -z., Kiang, T., Cheng, F. -h., Hu, F. -x., 1982, *Q. J. R. astr. Soc*, **23,** 363.
Green, R. F., Pier, J. R., Schmidt, M., Estabrook, F. B., Lane, A. L., Wahlquist, H. D. 1980, *Astrophys. J*., **239,** 483.
Jeffreys, H. 1948, *Theory of Probability*, 2 edn, Clarendon Press, Oxford.
Jones, B. J. T., Jones, J. E. 1980, *Mon. Not. R. astr. Soc.*, **193,** 537.
Kendall, M. G. 1965, *A Course in Multivariate Analysis,* Griffin, London.
Kendall, M. G., Stuart, A. 1969, *The Advanced Theory of Statistics,* Vol. 1, 3 edn, Griffin, London (KS 1).
Kendall, M. G., Stuart, A. 1972, *The Advanced Theory of Statistics,* Vol. 2, 3 edn, Griffin, London (KS 2).
Lang, K. R. 1980, *Astrophysical Formulae,* Springer-Verlag, Berlin.
Mattig, W. 1958, *Astr. Nachr.*, **284,** 109.
Qing, C. -r., Wu, Y. -s., He, Z. -x., Zhang, Z. -x., Zou, Z. -1. 1981, *Acta Astrophys. Sin.*, **1,9:** 1981, *Chinese Astr. Astrophys*., **5,** 17.
Qu, Q. -y., Qin, Z. -h., Han, C. -s., Zhou, F. -a. 1979, *Acta. astr. Sin.*, **20,** 98: 1980 *Chinese Astr.*, **4,** 97.
Setti, G., Woltjer, L. 1973, *Astrophys. J.*, **181,** L61.
Stannard, D. 1973, *Nature,* 246,295. Waldrop, M. M. 1981, *Science*, **211,** 470.
Wampler, E. J. 1980, *in IAU Symp.92: Objects of High Redshift*, Eds, G.O. Abell and P. J. E. Peebles, D. Reidel, Dordrecht, p. 119.
Yang, L. -t., Xiao, X.-h., Cao, C. -1., Ao, X. -b., Bian, Y. -1., Tang, X. -y. 1980, *Acta astr. Sin.*, **21,** 208.
Zhou, Y. -y., Cheng, F.-z., Chu, Y. -q., Fang, I. -z. 1977, *Acta astr. Sin*., **18,** 113: 1978, *Chinese Astr.*, **2,** 147.

J. Astrophys. Astr. (1982) **3,** 379–382

Morphology of H-Alpha Filaments and Filament Channel Systems

V. I. Makarov and M. N. Stoyanova *The Kislovodsk Station of the Pulkovo Observatory, 357741 Kislovodsk, USSR*

K. R. Sivaraman *Indian Insitute of Astrophysics, Bangalore 560034*

Received 1982 March 8; accepted 1982 August 10

Abstract. Ring-like filaments have been detected on the spectroheliograms in the H-alpha line. Inside these filaments the magnetic field flux has a predominant polarity. Some of the dark filaments are connected by filament channels which can be seen at the limb either as (a) weak prominences or (b) dense low chromospheric features or (c) multi-channel system of matter flow between two prominences or (d) common quiescent prominences. The filament and the filament channel together form a continuous closed contour and outline the region of the f polarity particularly at the beginning of the solar cycle. The change in sign of the polar field of the Sun is associated with the drift of the filament band to high latitudes.

Key words: Sun—magnetic fields—filaments—filament channel

1. Introduction

Quiescent filaments and prominences, most clearly seen in the H-alpha line, have a distribution far from random on the solar surface. Their location is intimately associated with the distribution of solar magnetic fields which is characterised by an inhomogeneous structure and varying coverage over the disc (Babcock and Babcock 1955; Mclntosh 1972a).

The smallest scale of magnetic fields at the photospheric level is located mostly in structures of the order of granulation or less (Stenflo 1976; Krat 1977). On the cells comparable with an active region, a noticeable predominance of the field of one polarity is observed. Filaments are formed along the dividing line of opposite polarities of this large-scale magnetic field (Mclntosh 1975). On the basis of an analysis of the filament-band motion, Makarov and Fatianov (1980) have studied the process of the sign-change of the polar magnetic field of the Sun in the 20th

solar cycle, and have also given a forecast for the 21st cycle. We report here the results of a study on the morphology of the large-scale filament structures and their relations with the distribution of the large-scale magnetic field on the solar surface.

2. Data

The Kodaikanal Observatory plate collection has an extensive series of spectroheliograms in the H-alpha and K line of Ca II since 1904. Our present study is based on these spectroheliograms for the period 19051979 and the H-alpha filtergrams of the Kislovodsk station during 1969-1980.

3. Structures formed by single filament

A very interesting feature which we have detected on the spectroheliograms of the Kodaikanal Observatory and on the Kislovodsk filtergrams is a continuous filament which forms a closed circular contour. A few examples of such structures are presented in Fig. 1. We use the term 'ring filament' to designate these structures. The filament intensity on the contour is not uniform. Such structures can be detected particularly during the maximum phase of the solar cycle. Their mean size seldom exceeds 10°. Their lifetimes occasionally span over several days. For instance, a ring filament could be traced from 1979 March 4 to 8 in the H-alpha spectroheliograms, but as a rule part of the ring filament becomes invisible in a day. Identification of the location of several such ring filaments with reference to magnetic fields using the Mount Wilson and Kitt Peak magnetograms show that the circular filament outlines an island of opposite polarity magnetic field with respect to its surroundings. In Fig. 3, we illustrate one example of the ring filament-magnetogram pair.

A single dark filament in the centre of the H-alpha line gives an impression of a system of elements which build up the common structure, each element forming a coil of the helix. On the disc, the filament is formed by the piling of several arches (Fig. 2), which show up as a spiral and sometimes as a helical structure at a certain projection to the limb. Such a structure is suggestive of a prominence with rotational motion (Öhman 1969). The matter of the filament is concentrated in the helical coil and has no apparent direct connection with the photospheric layers. The matter in the denser elements flows down, forming arch-like feet on the disk or the footpoints of the prominence.

4. The filament channel

In the core of the H-alpha line, single filaments are seen connected with one another by a regular structure of dark chromospheric elements of several tens of degrees in extent or at times by a conglomeration of absorption grains of 1° to 3° in length (Mclntosh 1972a, b; Makarov and Stoyanova 1979). Such chromospheric structures with floccular corridor termed in the literature as filament channels are known to be

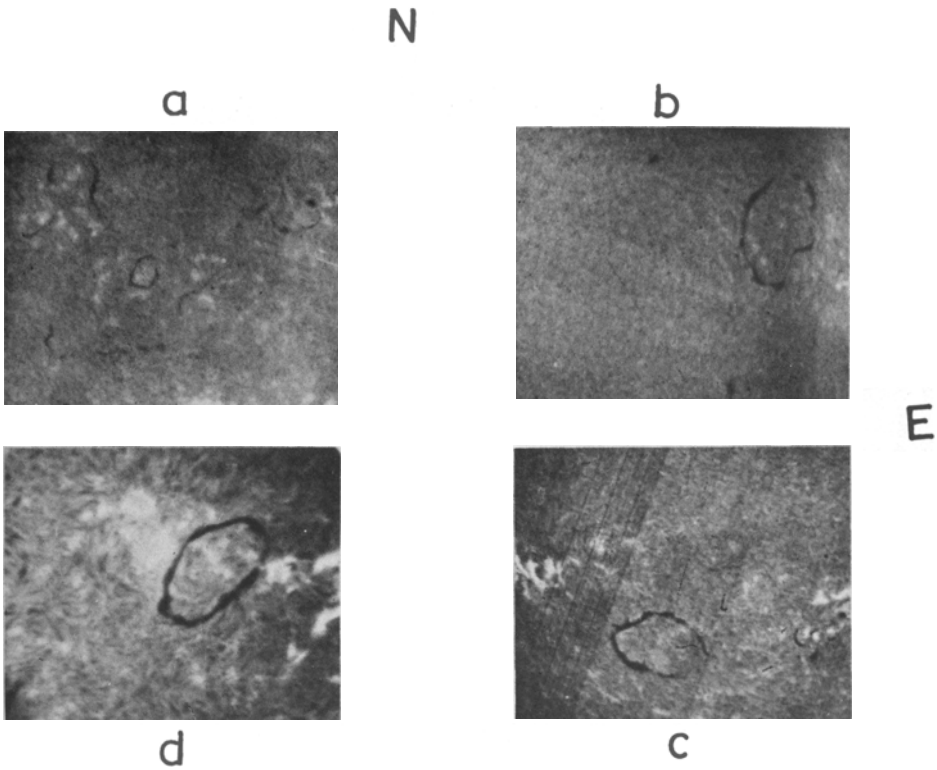

Figure 1. Portions of H-alpha pictures showing 'Ring filaments'. (a) 1918 August 13, (b) 1921 Number 14, (c) 1978 December 17, (d) 1980 June 7, (a), (b) and (c) are Kodaikanal spectroheliograms; scale : 1 cm = 10^5 km on the Sun. (d) is Kislovodsk station filtergram; scale: 2 cm = 10^5 km on the Sun.

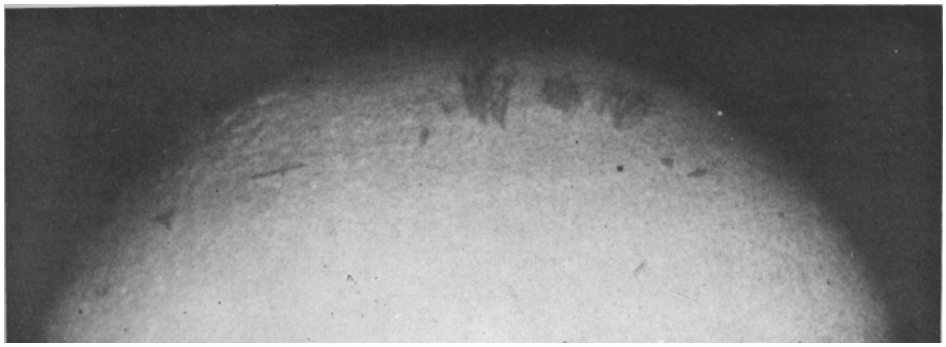

Figure 2. H-alpha spectroheliogram of 1938 February 13 showing the arch-like structures within the filament (Kodaikanal Observatory).

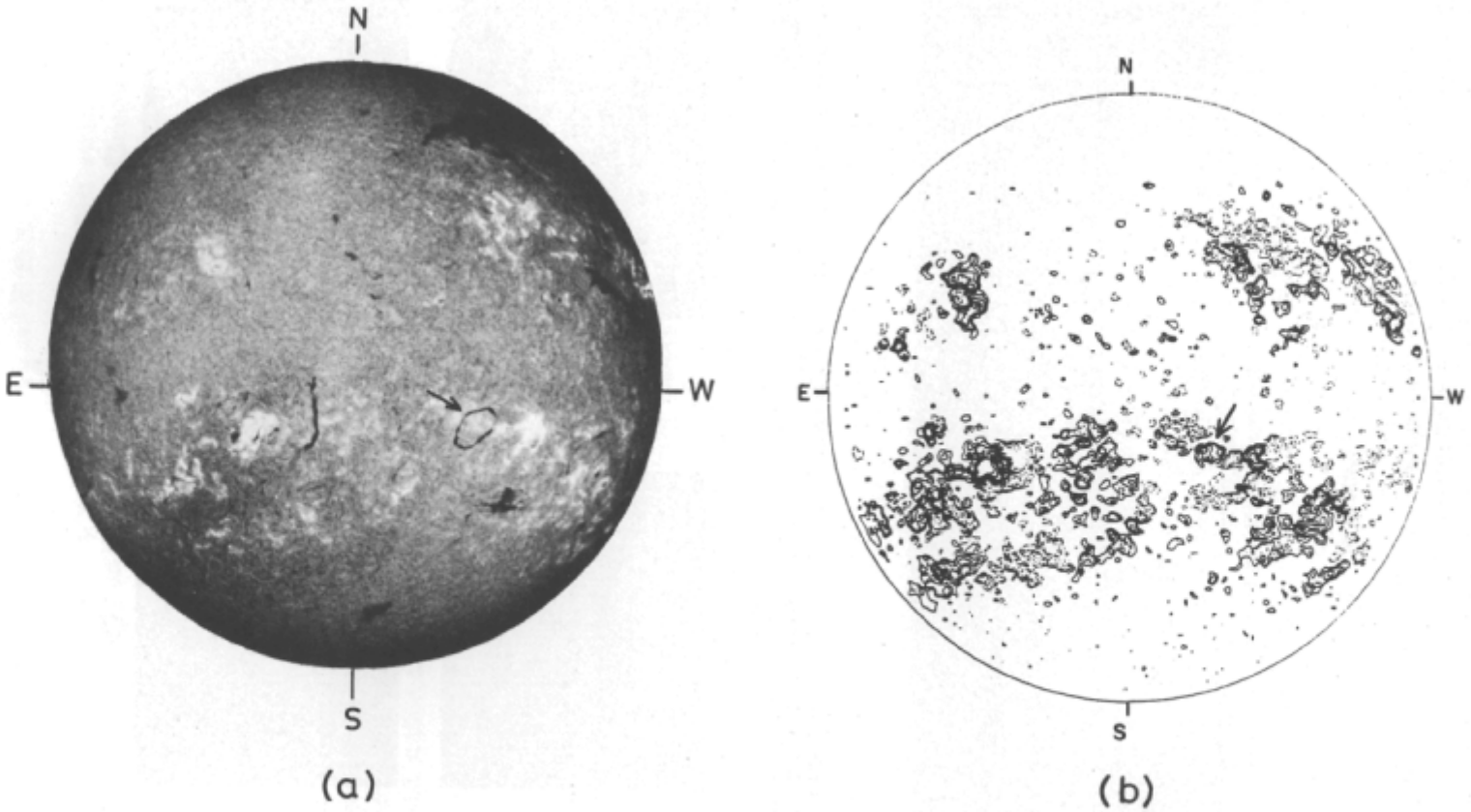

Figure 3. Filtergram-magnetogram pair, (a) Kislovodsk H-alpha filtergram at 0495 UT of 1980 June 7. The arrow indicates the ring filament. (b) Mt. Wilson magnetogram at 1652-1775 UT of 1980 June 6 (from Solar Geophysical Data, Prompt Reports). The arrow shows the location corresponding to the filament on the magnetogram. Notice that within the filament ring the magnetic field is of one polarity.

located on the polarity-inversion line of the large-scale magnetic field. On the limb the filament channel can show up either as weak prominences, or dense chromospheric features extending to small heights, or as multichannel flows connecting two prominences or as quiescent prominences. They are invisible on the solar disc as dark filaments, because the optical depths along the line of sight is much less than unity.

Occasionally, prominences can be detected which are located above filament channels. In this case, an elongation of some arches of the filament channel may take place with an associated local increase in intensity in the corona. Such prominences do not show up on the solar disk as *a* visible filament. However, continuous long-term observations of such prominences enable us to realize that they form a continuous contour in the chromosphere as depicted in synoptic charts (Fig. 4b). This prominence property can best be seen in polar regions at the maximum epoch of the cycle (Fig. 4a). The polar ring filament separates the old background magnetic field from the new one in the middle latitudes, which formed during the subsequent period of solar activity. Subsequently, the disappearance of the filament is observed, but the polarity-dividing line remains and shows up as a filament channel. The existence of the filament channel is confirmed by the presence of continuous prominences on the east and west limbs (Fig. 4b). The filament channel is a more stable and long-lived feature than the filament itself.

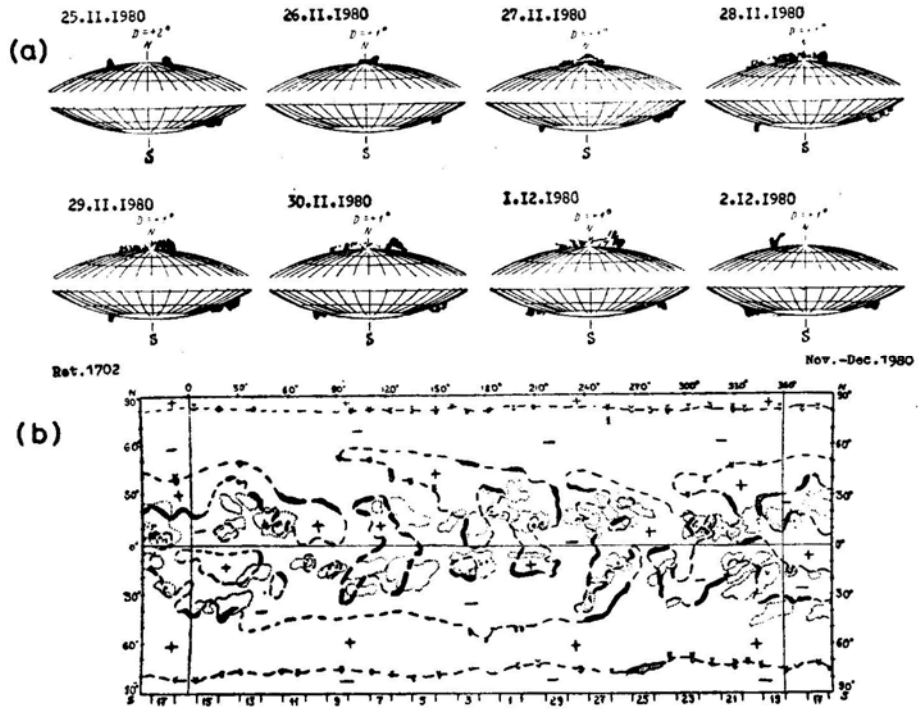

Figure 4. (a) Day-to-day solar maps from 1980 November 25 through December 2. (b) Sample synoptic chart. Prominences are observed in north and south polar regions and filaments are invisible on the east and west limbs. On the synoptic chart, prominences are marked thus ∨. They form a polar band of filament channels (Kislovodsk).

The number and area of filaments and prominences are parameters closely associated with solar cycle changes on the sun. The evolution of filaments and filament channels portray the evolution of large-scale magnetic fields and hence can be used as tracers to study their motion on the solar surface. Such a detailed study extending over a few solar cycles is in progress and the results will be reported in a subsequent paper.

Acknowledgements

We wish to thank Dr M. K. V. Bappu, Director, Indian Institute of Astrophysics for his kind encouragement. Two of us (V. I. M. S.) are thankful to Dr M. N. Gnevyshev, Director, Kislovodsk solar station for the help in planning the obserarvations related to this work at the Kislovodsk station and to Dr M. K. V. Bappu, for his kind hospitality during our stay at the Indian Institute of Astrophysics

References

Babcock, H. W., Babcock, H. D. 1955, *Astrophys. J.*, **121,** 349.
Krat, V. A. 1977, *Radiofizika J.*, **20,** 1302.
Makarov, V. I., Fatianov, M. N. 1980, *Soln. Dann. Bjull.*, Moskva, No. 10, 96.
Makarov, V. I., Stoyanov, M. N. 1980, *Soln. Dann. Bjull.*, Moskva, No. 8, 89.
McIntosh, P. S. 1972a, *Rev. Geophys. Space Phys.*, **10,** 837.
McIntosh, P. S. 1972b, in *Solar Activity Observations and Prediction*, Eds P. McIntosh and M. Dryer, MIT press, Cambridge, p. 65.
McIntosh, P. S. 1975, *World Data Center A for solar Terrestrial Physics Report UAG-40.*
Öhman, Y. 1969, *solar phys.*, **9,** 427.
Stenflo, J. O. 1976, in *IAU Symp. 71: Basic Mechanisms of solar Activity*, Eds Y. Bumba and J. Kleczek, D. Reidel, Dordecht, p. 69.

J. Astrophys. Astr. (1982) **3,** 383–392

Spectroscopic Binaries near the North Galactic Pole Paper 6: BD 33° 2206

R. F. Griffin *The Observatories, Madingley Road, Cambridge, England, CB3 OHA*

Received 1982 July 27; accepted 1982 August 18

Abstract. Photoelectric radial-velocity measurements have confirmed O. C. Wilson's finding that BD 33° 2206, the secondary star in the wide visual binary ADS 8470, is a spectroscopic binary. It has an eccentric orbit with a period of 100 days. Its γ-velocity is close to the constant radial velocity of the visual primary, confirming the physical association of the stars.

Key words: radial velocities—spectroscopic binaries—stars, individual

1. Introduction–The multiple system ADS 8470

HD 106365 (BD 33° 2205) is a seventh-magnitude late-type giant, the primary star of the wide visual binary ADS 8470 (Aitken 1932), which was first catalogued by F. G. W. Struve (1827) as Σ1615. The secondary star, a ninth-magnitude solar-type object 27 arcsec following the primary, is the spectroscopic system whose orbit is presented now. The separation and position angle of the two visual components have remained virtually unchanged over the century and a half covered by measurements, although the system as a whole has been carried by proper motion across an angular distance of more than 15 arcsec over the same interval. Such relative fixity is a strong indication of the physical association of the stars; indeed the uncertainty arising from the smallness of the relative motion led Stephenson and Sanwal (1979) to infer the improbably high mass of 19·22 $M_{\odot}$ for the system.

Aitken (1910) discovered a third visual component, a very faint star almost on the line joining the primary and secondary but much closer to the latter. The pair formed by Σ 1615 B and the faint star is designated A 2058 or ADS 8470 BC. The few available positional measurements suggest that the faint star, too, shares the proper motion of the wide pair and is therefore a physical member of the system. In what follows, we shall for convenience refer to ADS 8470 simply as 'the system' and to its individual components simply as A, B and C.

O. C. Wilson is reported by Olsen (1971) as finding that B is a spectroscopic binary. It is the principal purpose of the present paper to corroborate and amplify

that finding. The system therefore consists of not fewer than four components, probably in an arrangement of hierarchy (Evans 1968) three. Bakos (1974) considers A too to be 'probably' a spectroscopic binary, but we shall show below that the evidence for such a conclusion is weak.

2. Space motion; photometry

The proper motion of the system is about 0·11arcsec yr^{-1} (*e.g.* Boss 1937; Heckmann and Dieckvoss 1975), and indicates an appreciable space motion transverse to the line of sight. This led Miczaika (1940) to include it in his catalogue of high-velocity stars, defined as those with space motions greater than 63 km s^{-1} relative to the centroid of the motions of stars near the Sun. Miczaika's catalogue was one of the sources used by Miss Roman in compiling her own list of high-velocity stars (Roman 1955), where she presented photoelectric magnitudes and MK spectral types for the first time for both A and B; it is rather ironic that she also concluded that the space motion of the system was not, after all, as high as 63 km s^{-1}.

The system features in a number of papers by Eggen on photometry and stellar dynamics. At first Eggen (1962) used Miss Roman's magnitudes, but later he gave his own measurements (Eggen 1963,1968)—it would appear that the 1968 magnitudes are merely repeated from the 1963 paper but with a misprint corrected–and later still (Eggen 1969,1971a, b) he gave another set. Photometry of the system has also been reported by Tolbert (1964). The various sets of photometry are collected for ease of reference in Table 1, together with the 'homogenized' mean values catalogued by Nicolet (1978).

In an early paper, Eggen (1958) claimed that the system is a member of the 'ζ Herculis group'. The distance which membership of the group would necessitate (to obtain the correct space velocity from the known proper motion) required that M_V (A) = 1·25 mag. Subsequently he (Eggen 1963) claimed instead that it is a member of the '61 Cygni group', entailing M_V (A) = 0·3 mag, a value close to the 0·5 mag that he quoted as having been derived by Adams *et al.* (1935) from the spectroscopic parallax. [Adams *et al.* (1935) actually appear to give a value of 0·7 mag.] The assignment to the 61 Cygni group has since been reaffirmed a number of times (Eggen 1969, 1971a, b); in the last of these papers the system appears in a table of 'certain' members of the group.

Table 1. Published photoelectric magnitudes for ADS 8470 A and B, with Nicolet's 'homogenized' mean values.

Source	A			B		
	V	$(B-V)$	$(U-B)$	V	$(B-V)$	$(U-B)$
Roman (1955)	6·87	1·13	1·07	8·77	0·59	0·06
Eggen (1963)	6·80	1·17	1·05	9·77	0·61	0·08
Eggen (1968)	6·80	1·17	1·05	8·77	0·61	0·08
Eggen (1969)	6·84	1·15	1·06	8·77	0·60	0·07
Tolbert (1964)	6·89	1·13	1·07	8·78	0·57	0·05
Nicolet (1978)	6·88	1·13	1·07	8·77	0·58	0·06

3. Spectral types and luminosities

Roman (1955) gave the MK types of A and B as K2 III and F9 V, and those remain the generally accepted spectral types. Tolbert (1964), Schild (1973) and Bakos (1974) agreed with Roman's K2 III for A, while Upgren (1962) found K1 III. Tolbert (1964) gave a type of F8 IV, Bakos (1974) F8 V, for B.

Tabular values interpolated from Allen (1973) for the absolute visual magnitudes of stars of types K2 III and F9 V are + 0·2 mag and + 4·2 mag. They differ by very considerably more than the 1·9 mag difference in the observed V magnitudes of A and B. It would be easy to argue that the tabular M_V (A) is the one more likely to be correct–especially as it agrees with the value required if the system is to be a member of Eggen's 61 Cygni group—and that the M_V (B) of + 2·1 mag that follows from it is evidence in favour of Tolbert's (1964) subgiant classification for B. Moreover, since we now know B to be itself a binary, B could well have a composite spectrum not yet recognized as such; in that case any luminosity assigned on spectroscopic or spectrophotometric premises would be liable to error. Unfortunately for such a line of argument, the several modern spectroscopic luminosity estimates in the literature (summarized in Table 2) are unanimous in finding that *the primary is somewhat under-luminous for its type*, leaving no discrepancy to be explained between the luminosity of the secondary and its main-sequence type. We shall probably not be far wrong in adopting a distance modulus of 5·0 mag, corresponding to a distance of 100 pc, for the system. It will be difficult to reconcile such a distance with membership of the system in the 61 Cygni group.

4. Radial velocities; discussion

4.1 *Component A*

The radial velocity of A was first determined by Adams *et al.* (1929), who reported a mean value of – 10·3 km s^{-1} from three plates. Wilson and Joy (1950) gave a mean of – 9·8 km s^{-1} from four plates, noting that theirs was a revision of the earlier value on the basis of additional plates or measurements. In his *Radial Velocity Catalogue* Wilson (1953) listed A with the Adams *et al.* (1929) velocity of – 10·3 km s^{-1} but gave the number of plates as four. Subsequently Abt (1973), who published from the card files at Mount Wilson Observatory the individual details of all plates from which the radial velocities had previously been printed merely as mean values,

Table 2. Published absolute-magnitude estimates for ADS 8470 A and B.

Source	M_V(A)	M_V(B)	Method
Adams *et al.* (1935)	0·7		Line-strength ratios
Stephenson (1960)*	1·6	3·5	Spectral classification
Hansen and Kjærgaard (1971)	1·5		Copenhagen photometry
Olsen (1971)	2·01	4·12	*uvbyβ* photometry
Boyle and McClure (1975)	1·20		DDO photometry
Wilson (1976)	1·8		K-line width

*Values for A and B are not independent.

only found details of three plates. They are evidently the three used by Adams *et al.* (1929), because (a) they are all pre1929 and (b) their mean of – 9·4 km s^{-1} agrees exactly with the mean published by Adams *et al.* when account is taken of the systematic correction of – 0·9 km s^{-1} referred to by those authors. However, the systematic correction used in the *Radial Velocity Catalogue* for Mount Wilson observations of K-type stars was – 0·5 km s^{-1}, so the *Catalogue* entry of – 10·3 km S^{-1} for A should probably be understood as the Wilson and Joy (1950) value thus corrected, rather than as a citation of the Adams *et al.* (1929) value whose agreement with it is then fortuitous. Why the card files at Mount Wilson apparently do not contain details of the fourth plate utilized by Wilson and Joy is a question which unfortunately cannot be resolved here. By working backwards from the published mean velocity and the known individual results of the other three plates, we can infer that the velocity given by the missing plate was – 11·1 km s^{-1}.

Bakos (1974) published two measurements of the radial velocity of A, and concluded that it was 'probably variable'. His own two observations were in tolerable mutual agreement, so Bakos's conclusion must have been based upon the discrepancy between his weighted mean value of – 19·1 km s^{-1} and the Mount Wilson mean.

The star has been observed, in the course of the North Galactic Pole survey (Griffin 1981), a total of six times in six different years with the photoelectric radial-velocity spectrometers at Cambridge (Griffin 1967) and Palomar (Griffin and Gunn 1974). The photoelectric measurements are shown in Table 3 along with the historical photographic ones. Table 3 appears to warrant the conclusion that the velocity of A is constant. The only velocities that possibly deviate significantly from the photoelectric ones are those taken from the paper by Bakos (1974); it may be appropriate to recall here that there has been difficulty (Griffin 1975, 1978) in confirming other instances of velocity variations reported in that paper.

For present purposes, then, the photoelectric mean value of – 11·0 ± 0·4 km s^{-1} will be adopted as the constant radial velocity of A.

Table 3. Radial-velocity measurements of HD 106365 (ADS 8470 A).

Date	Velocity km s^{-1}	Note	Date	Velocity km s^{-1}	Note
1924 Feb 22·39	−6·9	1	1974 Mar 1·98	−11·1	4
1926 Jan 26·47	−8·2	1	1975 May 22·16	−10·8	5
1926 Jan 27·44	−13·0	1	1977 Apr 2·00	−10·2	6
	−11·1	2	1978 May 23·19	−10·5	5
1955 Mar 30·26	−19·4	3	1979 June 6·16	−10·6	5
1955 Apr 8·23	−16·2	3	1982 May 25·91	−12·6	6

Notes:
1. Published by Abt (1973) from the data by Adams *et al.* (1935).
2. Velocity inferred from literature (see text), but date unknown.
3. Published by Bakos (1974).
4. Observed by Dr G. A. Radford with the Cambridge photoelectric spectrometer (Griffin 1967).
5. Observed by the author in collaboration with Dr J. E. Gunn with the Palomar photoelectric spectrometer (Griffin and Gunn 1974).
6. Observed by the author with the Cambridge spectrometer.

4.2 *Component B*

A mean velocity of – 44 km s^{-1}, based on four observations, was published by Wilson and Joy (1950). Abt (1973) gives details of *five* plates, all pre-1950; they are listed as the first five entries in Table 4. By a comparison of the published mean with the five individual velocities, it can be deduced that the one that Wilson and Joy did not include in the mean was that of 1947 February 1. There is no means of knowing now whether it was deliberately rejected or merely overlooked; it does not give an especially large residual, either from a straight mean or from the orbit derived below.

Bakos (1974) has one velocity, of – 8·4 km s^{-1}, for B. He notes that the velocity of B is 'probably variable'; that conclusion is presumably based on the range of the Mount Wilson measurements (Abt 1973).

The observational basis of O. C. Wilson's discovery of velocity variations (Olsen 1971) has not been published. Dr Wilson has kindly informed me that unfortunately the details of that work are no longer extant, and that the plates themselves cannot at present be located.

Although B, owing to its early spectral type (which causes it to be observable only with some inefficiency with the photoelectric spectrometer), is not formally eligible for inclusion in the photoelectric survey of Galactic, Pole radial velocities (Griffin 1981), it was observed simply out of the interest attaching to its proximity to A, which *is* on the survey programme. The velocity of B has been determined 44 times, with the results given in Table 4. All entries not otherwise noted in Table 4 are photoelectric measures made at Cambridge (Griffin 1967).

The orbit derived from the photoelectric observations is plotted in Fig. 1 and has the following elements:

$P = 100{\cdot}260 \pm 0{\cdot}021$ days	$(T)_{151} = \text{MJD } 44489{\cdot}72 \pm 0{\cdot}28$
$\gamma = -9{\cdot}94 \pm 0{\cdot}15$ km s^{-1}	$a_1 \sin i = 24{\cdot}9 \pm 0{\cdot}4$ Gm
$K = 20{\cdot}26 \pm 0{\cdot}26$ km s^{-1}	$f(m) = 0{\cdot}061 \pm 0{\cdot}003\ M_\odot$.
$e = 0{\cdot}454 \pm 0{\cdot}011$	
$\omega = 257{\cdot}7 \pm 1{\cdot}7$ degrees	rms residual = 0·9 km s^{-1}

Although the published photographic observations were not included in the orbital solution, they may be seen from Fig. 1 to be in reasonable accord with the orbit found from the photoelectric measurements alone. In particular, they do not strongly suggest that the period needs adjustment. However, the uncertainty of the phases of the Mount Wilson observations, which were made about 140 cycles before the photoelectric ones, is about 140 ϵ $(P)/P$ or 0·03 cycles; this quantity is too small in relation to the accuracy of the Mount Wilson results for the latter to be very helpful in reducing it further.

The γ-velocity of B differs from the constant radial velocity of A by 1·1 ± 0·4 km s^{-1}, a probably significant quantity. The projected separation of A and B, 27 arcsec at 100 pc, is 2700 AU. Let us suppose, first, that the actual distance between A and B is similar to the projected distance–equivalent to assuming that the line joining A and B lies in the 'plane of the sky'–and, secondly, that the total mass of

Table 4. Radial-velocity measurements of BD 33° 2206 (ADS 8470 B).

Date			MJD	Velocity km s^{-1}	Phase	$(O-C)$ km s^{-1}
1939	May	2·27*	29385·27	−6·2	0·348	−6·4
1943	Mar	13·39*	30796·39	−11·4	14·422	−7·8
	May	22·18*	866·18	+4·3	15·118	−3·8
1947	Feb	1·49*	32217·49	−11·1	28·596	+1·7
		7·50*	223·50	−4·3	·656	+12·0
1957	Mar	10·74†	35907·74	−8·4	65·403	−5·8
1975	May	22·16‡	42554·16	−19·3	131·695	−0·6
1977	Apr	1·99	43234·99	−6·1	138·485	+0·7
1978	Mar	26·01	43593·01	+1·5:	142·056	−0·3
	May	23·20‡	651·20	−14·7	·637	+0·4
1979	Jan	13·18	43886·18	−22·7	144·980	+0·3
	Feb	25·14	929·14	−4·0	145·409	−1·1
	Mar	8·07	940·07	−9·9	·518	−1·4
	Apr	29·01	992·01	−3·8	146·036	−0·3
	May	13·94	44006·94	+7·8	·185	+0·3
	June	6·15‡	030·15	−4·3	·416	−1·0
	Dec	4·23	211·23	+6·9	148·222	+0·8
1980	Jan	2·20	44240·20	−9·0	148·511	−0·8
	May	5·95	364·95	−22·3	149·756	+0·5
		9·91	368·91	−24·8	·795	+0·8
		11·90	370·90	−27·4	·815	−0·4
		12·98	371·98	−27·8	·826	0·0
		13·89	372·89	−28·2	·835	+0·3
		14·90	373·90	−27·7	·845	+1·5
		15·89	374·89	−29·5	·855	+0·3
		16·89	375·89	−31·5	·865	−1·1
		17·91	376·91	−31·9	·875	−0·9
		18·90	377·90	−31·0	·885	+0·5
1981	Mar	1·11	44664·11	−20·5	152·739	+1·2
		13·09	676·09	−31·1	·859	−1·0
	Apr	14·98	708·98	+6·0	153·187	−1·4
		18·00	712·00	+5·6	·217	−0·7
		27·96	721·96	+2·9	·316	+1·2
	May	2·95	726·95	0·0	·366	+0·8
		17·34‡	741·34	−6·8	·510	+1·3
		24·96	748·96	−12·0	·586	+0·2
		31·92	755·92	−16·3	·655	0·0
	June	21·93	776·93	−30·3	·865	+0·1
	July	4·91	789·91	−19·4	·994	−1·0
		16·91	801·91	+9·6	154·114	+1·6
	Dec	3·58‡	941·58	−8·1	155·507	−0·2
1982	Jan	10·17	44979·17	−32·6	155·882	−1·2
		21·15	990·15	−17·1	·991	+2·3
	Mar	4·07	45032·07	−3·1	156·409	−0·2
	May	4·01	093·01	−11·1	157·017	−1·3
		5·00	094·00	−6·0	·027	+0·3
		7·00	096·00	−0·6	·047	−0·3
		13·98	102·98	+8·6	·117	+0·5
		23·93	112·93	+6·5	·216	+0·2
		25·90	114·90	+4·4	·236	−1·1

*Mount Wilson Observatory photographic observation (Abt 1973); not utilized in orbital solution, but plotted in Fig. 1.

†David Dunlap Observatory photographic observation (Bakos 1974); not utilized in orbital solution, but plotted in Fig. 1.

‡Observed, in collaboration with Dr J. E. Gunn, with the 200inch telescope (Griffin and Gunn 1974).

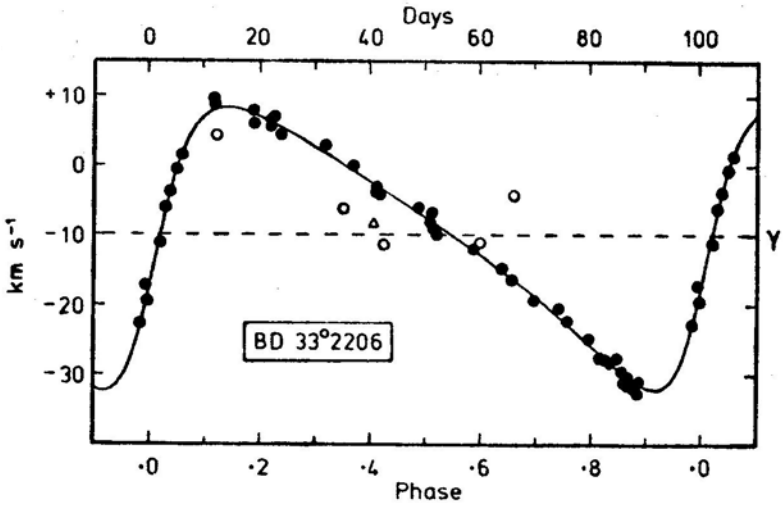

Figure I. The computed radial-velocity curve for BD 33° 2206, with the measured radial velocities plotted. photoelectric observations are represented by filled circles. The earlier photographic observations, which were not used in solving the orbit, are represented by open symbols circles for Mount Wilson Observatory (Abt 1973) and a triangle for David Dunlap Observatory (Bakos 1974).

the three stars in the A B system is $3M_{\odot}$ .Then, working in solar-system units of distance, mass and orbital velocity (d = 1 AU, M =1$M_{\odot}$, $V \simeq 30$ km s^{-1}) and recalling that, from Kepler's third law, V^2 is proportional to M/d, we find that a relative velocity of 1 km S^{-1} is to be expected between A and B. Thus the observed difference of radial velocity is entirely consistent with membership of A and B in a physical system, even if the difference is accepted at face value, without the need to invoke the presence of C or of other, invisible, companions to explain it.

4.3 *The Gravitational Redshift—A Digression*

Notwithstanding the above argument which shows that there is no difficulty in reconciling the true association of A and B with the observed difference in their radial velocities, there is a good reason why that observed difference should *not* be taken at face value: the gravitational red-shifts of the two stars are different. The gravitational redshift of the Sun, which is typical of that of main-sequence stars in general and is similar to the value to be expected in the particular case of ADS 8470 B, is 0.637 km s^{-1}. It is proportional to the gravitational potential at the stellar surface, and therefore scales directly as the mass and inversely as the radius. Since giant stars are many times as big as dwarfs but are at most a few times the mass, their redshifts are much less than the solar redshift. Thus any comparison of radial velocities between dwarf stars and giants in binary systems or star clusters is likely to involve a systematic bias—the velocities measured for dwarfs will be too positive in relation to those found for giants. The approximate magnitude of the differential effect is 0·5 km s^{-1}—a quantity that is by no means negligible at the level of accuracy of the best modem radial-velocity measurements. If we allow for such an effect in the case of present interest, the difference in the centre-of-mass velocities of A and B is reduced from 1.1 to 0,6 ± 0·4 km s^{-1}, *i.e.* to insignificance,

Because this matter seems not to have been discussed explicitly before in its application to normal stars as opposed to white dwarfs, it seems useful to present a brief tabulation (Table 5) of the gravitational redshifts expected from stars of different types. The entries in the table follow directly from the values of mass and radius quoted by Allen (1973). The entries for late-type giants must be regarded as upper limits, since Allen gives masses for such stars in the range 3 $M_{\odot}$(G5 III)to 6$M_{\odot}$ (M0 III).There is (not universally accepted) dynamical and spectroscopic evidence for the existence of giant stars of sub-solar mass (*cf.* Wilson 1967; Mäckle *et al.* 1975), as well as the seemingly incontrovertible fact that in globular and old galactic star clusters with main-sequence turn-off points near to solar type the giants can hardly be much more massive than the Sun. Thus in individual cases the redshifts from giant stars may be only a fraction of the values derived from Allen (1973) and listed in Table 5. On the other hand, the values tabulated for main-sequence stars should be fairly reliable.

It would not require an observational accuracy much higher than that obtained in the present work before a realistic comparison of giant and dwarf radial velocities would necessitate a full discussion—not attempted here—of the relationship between the measured velocities and the true velocities of the centres of mass. Such a discussion would need to take into account not only the gravitational redshift but also the complex effects of mass motions and of variations of brightness and spectral-line strengths—on both large and small scales—over the complete hemisphere whose integrated light is observed.

4.4 *Spectroscopic Companion of B*

The mass function of B, together with the mass of 1·1–1·2 $M_{\odot}$ inferred from the spectral type of the spectroscopic primary (Allen 1973) points to a minimum mass of about 0·55$M_{\odot}$ for the secondary in the 100-day orbit. If the secondary is a main-sequence star, its type can be no later than late K and its luminosity in the blue must be within four magnitudes of that of its primary. Its presence has not been noticed on the radial-velocity traces, so it must be considerably fainter than the F9 V primary: it is more likely to be a K star than a G.

Table 5. Gravitational redshift (km s^{-1}) as a function of spectral classification.

Type	Luminosity class I	III	V
B0	1·60	0·71	1·53
B5	0·51	0·41	1·08
A0	0·25	0·33	0·82
A5	0·16		0·77
F0	0·13		0·80
F5	0·08	0·21	0·68
G0	0·06	0·25	0·67
G5	0·06	0·20	0·64
K0	0·04	0·16	0·58
K5	0·03	0·13	0·59
M0	0·02		0·47
M5			0·43

4.5 *Component C*

ADS 8470 C, whose magnitude was estimated by Aitken (1932) to be 14·0, must have an absolute magnitude of about 9·0 if it is physically related to A and B. It may therefore be expected to have a spectral type close to MO V. On 1979 June 6.16 a brief attempt was made at Palomar to determine its radial velocity, and a result of –6 ± 2 km s^{-1} was obtained—a difference of 4 ± 2 km s^{-1} from the γ-velocity of its putative primary, B. This result tends to support the association of C with AB. Unfortunately the velocity of B (5 magnitudes brighter than C and only 2·7 arcsec distant) was found on the same occasion to be –4.3 km s^{-1}. Although—or perhaps because—there was no doubt at the time that the velocity of C had been measured, no test integrations were recorded to provide complete conviction in retrospect that the feature seen in the radial-velocity trace of C was not partly (or even wholly) due to scattered light from B. It would be reassuring to make a further measurement at a time when the radial velocity of B is well removed from the γ-velocity, but no opportunity to do so has yet arisen.

Acknowledgements

It is a pleasure to thank Dr J. E. Gunn for his collaboration in radial-velocity observations made with the Palomar 200-in telescope, and Dr O. C. Wilson for helpful correspondence.

References

Abt, H. A. 1973, *Astrophys. J. Suppl. Ser.*, **26,** 365.
Adams, W. S., Joy, A. H., Humason, M. L., Brayton, A. M. 1935, *Astrophys. J.*, **81,** 187.
Adams, W. S., Joy, A. H., Sanford, R. F., Strömberg, G. 1929, *Astrophys. J.*, **70**, 207.
Aitken, R. G. 1910, *Lick. Obs. Bull.*, **5,** 166.
Aitken, R. G. 1932, *New General Catalogue of Double Stars within 120° of the North Pole,* Carnegie Institution of Washington.
Allen, C. W. 1973, *Astrophysical Quantities,* Athlone Press, London, pp. 206, 209.
Bakos, G. A. 1974, *Astr. J.* **79,** 866.
Boss, B. 1937, *General Catalogue of 33342 Stars for the Epoch 1950*, Carnegie Institution of Washington, **4,** 12.
Boyle, R. J., McClure, R. D. 1975, *Publ astr. Soc. Pacific,* **87**, 17.
Eggen, O. J. 1958, *Observatory*, **78**, 21.
Eggen, O. J. 1962, *R. Obs. Bull.*, No. 51.
Eggen, O. J. 1963, *Astr. J.*, **68,** 483.
Eggen, O. J. 1968, *R. Obs. Bull.,* No. 137.
Eggen, O. J. 1969, *Publ. astr. Soc. Pacific*, **81,** 553.
Eggen, O. J. 1971a, *Astrophys. J.*, **165,** 317.
Eggen, O. J. 1971b, *Astrophys. J. Suppl. Ser.*, **22**, 389.
Evans, D. S. 1968, *Q. J. R. astr. Soc.*, **9**, 388.
Griffin, R. F. 1967, *Astrophys. J.*, **148,** 465.
Griffin, R. F. 1975, *Astr. J.*, **80,** 245.
Griffin, R. F. 1978, *Astr. J.*, **83,** 1650.
Griffin, R. F. 1981, *J. Astrophys. Astr.*, **2**, 115.
Griffin, R. F., Gunn, J. E. 1974, *Astrophys. J.*, **191,** 545.
Hansen, L., Kjaergaard, P. 1971, *Astr. Astrophys.*, **15,** 123.

Heckmann, O., Dieckvoss, W. 1975, *AGK 3*, Hamburger Sternwarte, Hamburg-Bergedorf, **4,** 245.
Mäckle, R., Holweger, H., Griffin, R., Griffin, R. 1975, *Astr. Astrophys.*, **38,** 239.
Miczaika, G. 1940, *Astr, Nachr.*, **270,** 249.
Nicolet, B. 1978, *Astr. Astrophys. Suppl. Ser.*, **34,** 1.
Olsen, E. H. 1971, *Astr. Astrophys*., **15,** 161.
Roman, N. G. 1955, *Astrophys. J. Suppl. Ser.*, **2,** 195.
Schild, R. E. 1973, *Astr. J*., **78,** 37.
Stephenson, C. B. 1960, *Astr. J.*, **65,** 60.
Stephenson, C. B., Sanwal, N. B. 1969, *Astr. J*., **74,** 689.
Struve, F. G. W. 1827, *Catalogus Novus Stellarum Dupliciuim et Multiplicium*, Senatus Universitatis Dorpatensis, Dorpat, p. 41.
Tolbert, C. R. 1964, *Astrophys. J*., **139,** 1105.
Upgren, A. R. 1962, *Astr. J*., **67,** 37.
Wilson, O. C. 1967, in *Modern Astrophysics, A Memorial to Otto Struve*, Ed. M. Hack, Gauthier-Villars, Paris, p. 241.
Wilson, O. C. 1976, *Astrophys. J.*, **205,** 823.
Wilson, R. E. 1953, *General Catalogue of Stellar Radial Velocities,* Carnegie Institution of Washington, p. 147.
Wilson, R. E., Joy, A. H. 1950, *Astrophys. J*., **111,** 221.

J. Astrophys. Astr. (1982) **3,** 393–398

On a Nonlinear and Lorentz-Invariant Verson of Newtonian Gravitation

J. J. Rawal *Nehru Planetarium, Nehru Centre, Dr. Annie Besant Road, Bombay 400018*
J. V. Narlikar *Tata Institute of Fundamental Research, Homi Bhabha Road, Bombay 400005*

Received 1982 August 2; accepted 1982 August 27

Abstract. The Newtonian theory of gravitation is modified to include the gravitational energy as a source of gravitational potential, thus making the theory self-coupled and nonlinear. The modified theory can be derived from a Lorentz-invariant action principle. The Kepler problem is discussed in this theory and it is shown that the perihelion of the orbit steadily precesses. The rate of precession is, however, insufficient to account for the observed precession of the perihelion of Mercury. The differences from the Newtonian theory for the bending of light and the gravitational redshift of spectral lines are shown to be marginal.

Key words: Newtonian gravitation—Lorentz-invariant generalization

1. Introduction

In the language of field theory the Newtonian law of gravitation is described by Poissons' equation

$$\nabla^2\phi = -4\pi G\rho \tag{1.1}$$

where ϕ is the potential and ρ the matter density. The gravitational force per unit mass is given by

$$\mathbf{F} = \nabla\phi \tag{1.2}$$

If we wish to reconcile Newtonian gravitation with special relativity we have to make Equation (1.1) Lorentz invariant. Thus ∇^2 on the left-hand side is replaced by the wave operator

$$\nabla^2 - \frac{1}{c^2}\frac{\partial^2}{\partial t^2}, \tag{1.3}$$

What should we replace the right-hand side by? There are two choices open to us, both dictated by the equivalence of mass and energy in special relativity.

The first choice is to recognize ρc^2 as the time-time component of the energy momentum tensor T_{ik}. In this case, we cannot restrict the theory to a scalar form. The function ϕ must be replaced by a tensor ϕ_{ik} whose time-time component satisfies

$$\frac{1}{c^2}\frac{\partial^2 \phi_{00}}{\partial t^2} - \nabla^2 \phi_{00} = \frac{4\pi G}{c^2} T_{00}. \tag{1.4}$$

We feel that a modification along these lines would change the Newtonian character of the theory in the sense that a simple scalar potential has been replaced by a second-rank tensor.

The second alternative preserves ϕ as a scalar and replaces ρ by the scalar T obtained by taking the trace of T_{ik}. Thus Equation (1.1) is changed to

$$\frac{1}{c^2}\frac{\partial^2 \phi}{\partial t^2} - \nabla^2 \phi = \frac{4\pi GT}{c^2}. \tag{1.5}$$

We will start with Equation (1.5) as the first step in our modification of Newtonian theory.

The next step will bring the theory closer in spirit to general relativity. In this step we introduce the notion that T includes all sources of energy. Thus T_{ik} may include electromagnetic energy tensor and any other energy tensor that happens to be relevant. This raises the question: 'What about gravitational energy?'

A little consideration shows that the inclusion of gravitational energy on the right-hand side of Equation (1.5) will make the theory nonlinear. Naive Newtonian considerations show that the gravitational energy density is given by

$$\rho_g c^2 = -\frac{1}{8\pi G} |\nabla \phi|^2. \tag{1.6}$$

Thus, inclusion of (1.6) on the right-hand side makes the potential equation non-linear.

Apart from conceptual considerations, another reason for investigating such a theory is to see if the resulting equations give a better agreement with the solar system tests than the original Newtonian theory. Before considering these applications, it is desirable to place the heuristic considerations above on a more formal footing. We therefore approach the problem with an action principle.

2. The action principle

Consider first the action principle which gives rise to Equation (1.5). We will use the Minkowski line element

$$ds^2 = \eta_{ik} dx^i\, dx^k \tag{2.1}$$

with η_{ik} = diag (+1, – 1, –1, –1). The coordinates x^1, x^2, x^3 are the Cartesian space coordinates while, $x^0 = ct$ is the time coordinate. Denote $\partial\phi/\partial x^i$ by ϕ_i, and use the summation convention. Then the action is given by

$$J = \frac{1}{16\pi Gc}\int \phi_i \phi^i \, d^4x + \int \frac{T\phi}{c^3} d^4x. \tag{2.2}$$

The energy tensor for ϕ is given by

$$T_{ik}(\phi) = -\frac{1}{8\pi G}[\phi_i \phi_k - \tfrac{1}{2}\eta_{ik}\phi^l \phi_l], \tag{2.3}$$

so that

$$T(\phi) = \frac{1}{8\pi G}\phi^l \phi_l. \tag{2.4}$$

If we now imagine T in the second term to include $T(\phi)$, we have to write

$$T = T_m + T(\phi), \tag{2.5}$$

T_m being the contribution from matter alone.

If we do not take note of ϕ dependence in Equation (2.5) and perform a variation of ϕ, $\delta J = 0$ gives us

$$\Box\phi = \frac{4\pi GT}{c^2}, \tag{2.6}$$

which is the same as Equation (1.5). However, this procedure is obviously incorrect. We should vary ϕ in $T(\phi)$ also, thus writing

$$J = \frac{1}{8\pi Gc}\int \left(1 + \frac{\phi}{c^2}\right)\phi_i \phi^i \, d^4x + \frac{1}{c^3}\int T_{\mathrm{m}}\phi \, d^4x, \tag{2.7}$$

which gives, from $\delta J/\delta\phi = 0$, the following source equation for ϕ:

$$\left(1 + \frac{\phi}{c^2}\right)\Box\phi - \frac{1}{2c^2}\phi_i \phi^i = 4\pi G T_{\mathrm{m}}/c^2. \tag{2.8}$$

These equations are different from those derived by Nordstrom (1913) from other considerations.

In static case, this reduces to the modified Poisson equation

$$\left(1 + \frac{\phi}{c^2}\right)\nabla^2\phi - \frac{1}{2c^2}(\nabla\phi)^2 = -4\pi G\rho_{\mathrm{m}}. \tag{2.9}$$

We will now consider the solution of Equation (2.9) outside a spherical mass M.

3. Gravitational field outside a spherical mass

Since outside a spherical mass M, $\rho_m = 0$, Equation (2.9), with the assumption of spherical symmetry and with ϕ as a function of the radial coordinate r only, becomes

$$\left(1+\frac{\phi}{c^2}\right)\left[\frac{d^2\phi}{dr^2}+\frac{2}{r}\frac{d\phi}{dr}\right]-\frac{1}{2c^2}\left[\frac{d\phi}{dr}\right]^2=0. \tag{3.1}$$

This non-linear equation can be solved with the substitution $\mu = \ln\left(1+\frac{\phi}{c^2}\right)$. A simple calculation gives

$$e^{\mu/2}=\left(A+\frac{B}{r}\right), \tag{3.2}$$

A, B beingc onstants. Assuming that $\phi \sim GM/r$ as $r \to \infty$, we get $A = 1$ and $B = \mathrm{GM}/2c^2$ so that

$$\phi=\frac{GM}{r}+\frac{G^2M^2}{4c^2r^2}. \tag{3.3}$$

Thus, in addition to the inverse square force, we also have an inverse cube force which varies as $G^2M^2\,2r^3/c^2$.

With this force we can work out the precession of the perihelion of a planetary orbit. In polar coordinates the equations of motion are

$$\ddot{r}-r\dot{\theta}^2=-\frac{GM}{r^2}-\frac{G^2M^2}{2c^2r^3}, \tag{3.4}$$

$$\dot{r}^2\dot{\theta}=\dot{\mathrm{h}}\ (=\text{constant}). \tag{3.5}$$

To solve these, substitute $u = 1/r$ and $R_0 = 2GM/c^2$. Then Equations (3.4) and (3.5) give

$$\frac{d^2u}{d\theta^2}+\left[1-\frac{R_0^2c^2}{8h^2}\right]u=\frac{R_0c^2}{2h^2}. \tag{3.6}$$

Define a new angular coordinate $\bar{\theta}$ by

$$\bar{\theta}^2=\left[1-\frac{R_0^2c^2}{8h^2}\right]\theta^2. \tag{3.7}$$

When the orbit is completed once from perihelion to perihelion, $\bar{\theta}$ increases by 2π. But θ increases by

$$\frac{2\pi}{\left[1-\frac{R_0^2c^2}{8h^2}\right]^{1/2}}\simeq 2\pi+\frac{\pi R_0^2c^2}{8h^2}. \tag{3.8}$$

For an orbit of semi-latus rectum l and eccentricity e, we have in the Newtonian case

$$h^2 = GMl \tag{3.9}$$

and the orbital period

$$T = \frac{2\pi l^2}{(1-e^2)^{3/2}\,h}. \tag{3.10}$$

From Equation (3.8) we get the rate of perihelion precession as

$$\varpi = \frac{\pi R_0^2 c^2}{8h^2 T} = \frac{\pi GM}{2lTc^2}. \tag{3.11}$$

This is 1/12 of the general-relativistic value

$$\varpi_{GR} = \frac{6\pi\, GM}{lTc^2}. \tag{3.12}$$

In the above analysis, we did not include the effect of special-relativistic terms. It is well known (see Stephenson and Kilmister 1958) that the special-relativistic terms give–in the usual linear Newtonian theory–a precession rate

$$\varpi_{SR} = \tfrac{1}{6}\,\varpi_{GR}. \tag{3.13}$$

A similar analysis carried out in our non-linear theory gives the total effect as the sum of (3.11) and (3.13) in the case of Mercury. That is, the total effect is $\tilde{\omega}_{GR}/4$. The calculation of bending of light in the present theory yields a bending angle

$$\theta = \frac{2GM}{Rc^2}\left[1 + \frac{\pi GM}{8Rc^2}\right], \tag{3.14}$$

where R is the radius of the gravitating object. Although the bending is marginally greater than the Newtonian angle, it falls far short of the actual bending observed for microwaves grazing the solar surface. The gravitational redshift formula also gives a correction of the order GM/Rc^2 to the Newtonian value.

4. Conclusion

Our calculations show that the logical modification of Newtonian gravitation as a Lorentz-invariant self-coupled scalar field theory fails to satisfy the solar system tests, although it gives a better agreement with observations than the original Newtonian theory.

References

Nordstrom, G. 1913, *Ann. Phys.*, Paris, **42**, 533.
Stephenson, G., Kilmister, C. W. 1958, in *Special Relativity for Physicists*, Longmans, Green and Co. p. 77.

J. Astrophys. Astr. (1982) **3,** 399–412

Interstellar Electron Density

M. Vivekanand and R. Narayan *Raman Research Institute, Bangalore 560080*

Received 1982 June 21; accepted 1982 September 6

Abstract. We impose the requirement that the spatial distribution of pulsars deduced from their dispersion measures using a model of the galactic electron density (n_e) should be consistent with cylindrical symmetry around the galactic centre (assumed to be 10 kpc from the Sun). Using a carefully selected subsample of the pulsars detected by the II Molonglo Survey (II MS), we test a number of simple models and conclude that (i) the effective mean $\langle n_e \rangle$ for the whole galaxy is $0.037^{+0\,020}_{-0\,012}$ cm^{-3}, (ii) the scale height of electrons is greater than 300 pc and probably about 1 kpc or more, and (iii) there is little evidence for variation of n_e with galactic radius R_{GC} for $R_{GC} \gtrsim 5$ kpc. Further, we make a detailed analysis of the contribution to n_e from H II regions. Combining the results of a number of relatively independent calculations, we propose a model for the galactic electron density of the form

$$n_e\ (z) = 0{\cdot}030 + 0{\cdot}020\ \exp\ (-\ |z|/70)\ \text{cm}^{-3}$$

where z(pc) is the height above the galactic plane and the second term describes the contribution from H II regions. We believe the statistical uncertainties in the parameters of this model are quite small.

Key words: pulsars, dispersion measure–interstellar electron density—H II regions

1. Introduction

The interstellar electron density n_e (cm^{-3}) is an important parameter in pulsar studies since it is used to determine pulsar distances d(pc) from their observed dispersion measures D(pc cmr^{-3}). Hall (1980) has summarized in detail the various previous attempts to estimate n_e. Although there have been discussions based on free-free absorption, hydrogen radio recombination lines, Faraday rotation and interstellar scattering, these usually require some assumptions regarding temperature, magnetic field or degree of clumping of the electrons. The most reliable studies of the galactic

electron distribution have used the dispersion measures of the few pulsars for which independent distances have been obtained through 21 cm H I absorption measurements. However, mean ne values for these pulsars obtained using the relation

$$n_e = D/d \tag{1}$$

range all the way from 0·01 cm^{-3} to 0·2 cm^{-3}, with an average value $\langle n_e \rangle$ of 0·03 cm^{-3}. Obviously one needs other independent studies to fix confidence limits on $\langle n_e \rangle$ more accurately. To our knowledge, the only pulsar dispersion study not depending upon estimates of distances to individual pulsars is that by del Romero and Gomez-Gonzalez (1981), who estimated $\langle n_e \rangle$ to be 0·03 cm^{-3} on the *a priori* assumption that pulsars are predominantly a spiral-arm population. In this paper, we make a further independent study of n_e by assuming that the galactic pulsar population is cylindrically symmetric about the galactic center. We estimate the mean value of electron density $\langle n_e \rangle$ to be $0.037\ ^{+0\cdot022}_{+0\cdot010}\ cm^{-3}$.

The galactic electron density has often been modelled in the exponential form

$$n_e(z) = n_e\ (0)\ \exp(\ —\ |z|/z_0) \tag{2}$$

where z is the height above the galactic plane. The scale height z_0 has been estimated to be 264 pc by Hall (1980) and 1000 pc by Taylor and Manchester (1977), while Lyne (1980) concluded that it is essentially infinite, barring a component due to H II regions with $z_0 = 70$ pc. One reason for the disparity in these estimates is that $\langle\ |\ z\ |\ \rangle$for the pulsars with reliable independent distances (as against distance limits) is only of the order of 100 pc (Table 1); these pulsars are therefore not sensitive probes of large z. The pulsars we use in this paper have a mean $|z|$ of about 350 pc and hence our test has more sensitivity in estimating z_0. On the basis of our results, we rule out low z_0, say below 300 pc, and favour $z_0 = 1000$ pc or more.

We have also tested the suggestion that the mean electron density is enhanced in the inner regions of the Galaxy (Ables and Manchester 1976; del Romero and Gomez-Gonzalez 1981, Harding and Harding 1982). We find that such an enhancement is not as large as indicated by earlier studies. We favour a model with $\langle n_e \rangle$ = 0·04 cm^{-3} within a cylindrical region of galactic radius $R_{GC} \sim 7$ kpc around the galactic centre, and $\langle n_e \rangle$ = 0·03 cm^{-3} for $R_{GC} > 7$ kpc, though a constant electron density independent of R_{GC} would be nearly as good.

Finally, we have studied the contribution to $\langle n_e \rangle$ from H II regions in the Galaxy. Prentice and ter Haar (1969) have given a procedure to estimate this contribution for known H II regions within 1 kpc of the Sun. At larger distances one can only estimate a statistical contribution. We separate n_e into a uniform component plus a contribution from H II regions of scale height 70 pc as done by Lyne (1980), and estimate the magnitudes of the two components by means of a number of different approaches. Combining all the evidence, we propose the following galactic electron density model (for all R_{GC} except possibly $R_{GC} < 5$ kpc where our sensitivity is poor)

$$n_e\ (z) = 0\cdot030 + 0\cdot020\ \exp\ (-|z|/70). \tag{3}$$

From the close agreement of the various independent calculations that we have made, we believe Equation (3) to be a simple formula which probably models the actual

Table 1. Dispersion measures of pulsars with independently measured distances (taken from Manchester and Taylor 1981). The last column shows if the line of sight to the pulsar intersects any known H II region within 1 kpc from the Sun.

Pulsar	Distance d (kpc)	$\lvert z \rvert$ (pc)	Dispersion measure D(pc cm^{-3})	H II regions
0318 + 59	3·0	110	34·8	no
0329 + 54	2·3	50	26·776	no
0355 + 54	1·6	20	57·03	no
0525 + 21	2·0	240	50·955	no
0531 + 21	2·0	200	56·791	no
0736 − 40	2·5	400	160·8	yes
0740 − 28	1·5	60	73·77	no
0833 − 45	0·5	20	69·08	yes
0835 − 41	2·4	10	147·6	yes
1054 − 62	6·0	310	323·4	yes
1154 − 62	7·0	20	325·2	yes
1240 − 64	12·0	320	297·4	yes
1323 − 62	7·9	30	318·4	no
1356 − 50	8·8	170	295·0	yes
1557 − 50	7·8	220	270·0	no
1558 − 50	2·5	60	169·5	no
1641 − 45	5·3	20	475·0	yes
1859 + 03	11·0	120	402·9	no
1900 + 01	5·0	170	243·4	no
1929 + 10	0·08	5	3·176	no
2002 + 31	8·0	0	233·0	no
2111 + 46	4·3	100	141·5	yes
2319 + 60	2·8	30	96·0	yes

situation rather closely. We do not agree with Arnett and Lerche (1981) who claim that $\langle n_e \rangle$ cannot be known with an accuracy better than a factor of two.

2. Method

All our calculations are based on the assumption of azimuthal symmetry for the galactic pulsar population. The Sun is taken to be situated 10 kpc from the galactic centre. We describe here the basic method employed to determine a uniform mean electron density $\langle n_e \rangle$ for the whole Galaxy. We then proceed to discuss the modifications made in order to study more complicated models of n_e.

It is clear that the observed pulsar distribution will be consistent with cylindrical symmetry about the galactic centre for only a limited range of values of $\langle n_e \rangle$ Distance estimates of pulsars obtained using Equation (1) with overlarge values of $\langle n_e \rangle$ would appear to move the centre of gravity of the pulsar distribution away from the galactic centre towards the Sun (after allowing for selection effects), while the converse would be true for too small values of $\langle n_e \rangle$ In our calculations we assume a value of $\langle n_e \rangle$ and compute the corresponding positions of all pulsars in the galaxy. For each pulsar we consider a circle passing through it, centred on the galactic centre and parallel to the galactic plane (Fig. 1 shows the circle projected on

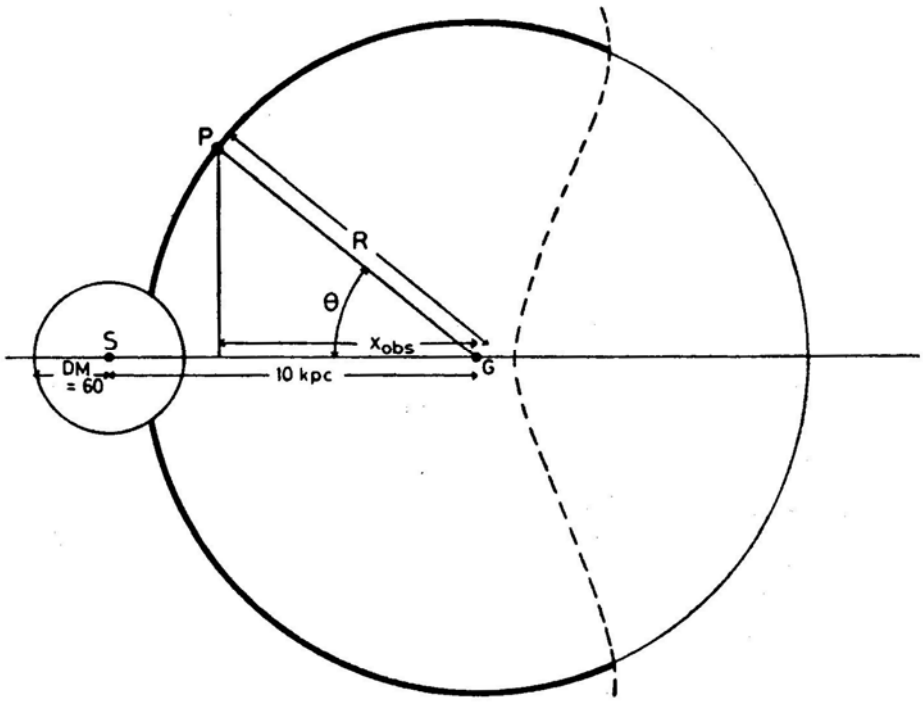

Figure 1. Schematic illustration of a typical pulsar P and its corresponding galactocentric circle, both projected onto the galactic plane. G is the centre of the Galaxy. Around the Sun S an approximately spherical volume of radius corresponding to a dispersion measure of 60 pc cm^{-3} is removed in our calculations for reasons discussed in the text. The dashed curve represents a typical viewing limit for the II Molonglo Survey. For our calculations, we require (i) $x_{\mathrm{obc},\,i}$, the projection of the radius PG onto the line SG, (ii) $x_{\mathrm{exp},\,i}$, the mean value of the projection averaged over the visible portion of the pulsar circle (thick line), and (iii)σ_i^2, the variance of the projection, obtained by averaging the deviation $(x–x_{\mathrm{exp},\,i})^2$ over the visible portion of the circle. These quantities are obtained for each pulsar for a given model of the galactic electron density and used in Equation (4) to compute X. Note that $|\theta|$ could have been used in place of x; however, the sensitivity of the test is then found to decrease.

to the plane of the Galaxy). We then compute x_{obs}, the projection of the derived radius vector from the galactic centre to the pulsar on to the line joining the Sun and the galactic centre. We also compute x_{exp}, the expected value of x for the circle, considering all selection effects and assuming a uniform probability of pulsar occurrence around the circle. Since for a given pulsar period and luminosity only a portion of each circle is visible to the pulsar surveys on Earth due to the various selection effects in pulsar searches (Taylor and Manchester 1977; Vivekanand, Narayan and Radhakrishnan 1982), x_{exp} is generally different from zero. Finally we compute the following mean deviation

$$X(\langle n_e \rangle) = \sum_{i=1}^{N} w_i \{x_{\mathrm{obs},\,i} - x_{\mathrm{exp},\,i}\}/\sigma_i \tag{4}$$

where σ_i is the calculated variance on $x_{\mathrm{obs},\,i}$. The summation is over all the pulsars included in our calculations and w_i is a weight given to the contribution

from the ith pulsar. w_i is estimated on the basis of the effective contribution of the pulsar to our test, which in turn depends upon its radio luminosity. Pulsars with high luminosity can be potentially detected far away from the Sun and are therefore best suited to test for a cylindrical distribution on a galactic scale. The lower luminosity pulsars are closer to the Sun, and so are of lesser importance for our calculations. We have investigated the sensitivity of our estimator $(x_{\rm obs} - x_{\rm exp})/\sigma$ to changes in $\langle n_{\rm e}\rangle$ and have derived a simple weighting scheme in which pulsars with radio luminosity (at 400 MHz and assuming $\langle n_{\rm e}\rangle = 0{\cdot}03$ cm^{-3}) greater than 10 mJy kpc^2 are each given a weight 1·5, those with luminosity less than 10 mJy kpc^2 but greater than 4 mJy kpc^2 are each given a weight 1·0 and pulsars with still lower luminosities are eliminated altogether. These last pulsars are very close to the Sun and only add 'noise' to the estimate of $X(\langle n_{\rm e}\rangle)$ in Equation (4). The particular choice of the projected distance x in Equation (4) was found to be more sensitive than other choices such as $|\theta|$ and was therefore used in all calculations.

Since for the best value of $\langle n_{\rm e}\rangle$ each of the terms $(x_{{\rm obs},\,i} - x_{{\rm exp},\,i})\sigma_i$ in Equation (4) has an expected mean of 0·0 and a standard deviation of 1·0, the mean value of X is 0·0 while its variance σ_X is given by

$$\sigma_X^2 = \sum_{i=1}^{N} w_i^2. \tag{5}$$

In our calculations, we therefore accept those values of $\langle n_{\rm e}\rangle$ which lead to $(X/\sigma_X)^2 \leqslant 1$ and reject the rest.

The above procedure needs to be modified when testing more complicated electron density models. For example, in testing a model having the form of Equation (2), we need to determine two parameters, $n_{\rm e}$ (0) and z_0. We do this by testing the cylindrical symmetry of pulsars separately in low-z and high-z regions of the galaxy. We choose to divide the pulsars into two classes such that the dividing value of $|z|$ represents the median $|z|$ for the sample. For each choice of $n_{\rm e}$ (0) and z_0, we obtain X_1, σ_{X1}, X_2, σ_{X2} for the two regions separately. Then the criterion for the acceptability of the model is that

$$\Sigma = \left(\frac{X_1^2}{\sigma_{X_1}^2} + \frac{X_2^2}{\sigma_{X_2}^2}\right) \leqslant 1. \tag{6}$$

We restricted our test to the 224 pulsars discovered by the II Molonglo Survey (II MS; Manchester *et al.* 1978) since it is the most extensive survey, and its selection effects are well understood. We have taken the minimum sensitivity S_0 to be 8·0 mJy (Manchester *et. al.* 1978), and used the modified model of the selection effects suggested by Vivekanand, Narayan and Radhakrishnan (1982). We employed three criteria to select a subsample of II MS pulsars. Firstly, all low-luminosity pulsars (<. 4 mJy kpc^2) are given weights $w_i = 0$ as discussed earlier. Secondly, nearby pulsars are unreliable for our purposes since the dispersion measure contribution from H II regions can have large fluctuations; this effect is expected to be less significant for more distant pulsars. Consequently, we have removed all pulsars

with $D < 60{\cdot}0$ pc cm^{-3}. To be consistent, while computing $x_{\mathrm{exp},\,i}$ and σ_i we deleted the appropriate segments of those circles which intersect this volume. Thirdly; we have deleted all pulsars whose mean flux densities are below the detection threshold of II MS. This is necessary since we compute $x_{\mathrm{exp},\,i}$ on the basis of the assumed detection threshold. After this selection process, we were finally left with a working sample of 52 pulsars. Fig. 2 shows the distribution of these 52 pulsars projected on the galactic plane. The distances have been computed using the optimized electron density model of Equation (3). It should be noted that very few of the pulsars lie beyond the galactic centre. Therefore our tests may be expected to have rather limited sensitivity.

3. Some simple models

We have tested a number of simple electron density models that are currently popular. Since ours is an independent test, it gives new bounds on the parameters of these models.

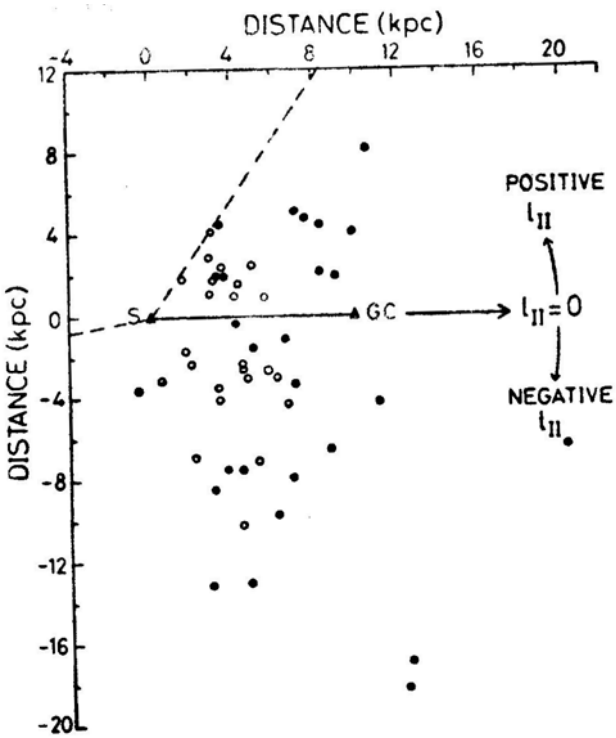

Figure 2. Positions of the 52 pulsars used in our calculations computed using Equation (3) and projected on to the galactic plane. The triangles S and GC mark the positions of the Sun and the galactic centre respectively. The dashed lines represent the longitude limits of the II Molonglo Survey in the galactic plane (corresponding to declination + 20°. Filled circles represent more luminous pulsars which are given a higher weightage (weight = 1·5) in our calculations, as compared to the medium luminosity pulsars which are represented by open circles (weight = 1·0). Note that very few pulsars lie beyond the galactic centre, which might lead to a reduction in our sensitivity

3.1 *Uniform Electron Density Model*

Using the method described in Section 2, we estimate the effective mean electron density in the Galaxy to be $\langle n_e \rangle = 0{\cdot}037^{+0\,020}_{-0\,012}$ cm^{-3}, where the quoted errors represent satistical fluctuations at the 1σ level. Fig. 3 shows the variation of X/σ_x as a function of the assumed $\langle n_e \rangle$ and illustrates our method of estimating the confidence limits on $\langle n_e \rangle$ Note that the lower bound is rather tight, suggesting that values below 0·025 are unlikely. This is of interest because lower values $\langle n_e \rangle$ have been commonly invoked to resolve the problem of high pulsar birthrates. We now find this improbable.

3.2 *Exponential Model*

We have studied an exponential model of the form of Equation (2) by testing the pulsar distribution separately in high-z and low-z regions (boundary chosen to divide the pulsars equally in the two regions), as described in the previous section. We obtain bounds on n_e (0) at each value of scale height z_0, based on the criterion of Equation (6). The results are shown as the two solid lines in Fig. 4. For very low z_0 values (< 250 pc), the electron density decreases very rapidly with increasing z, and it is impossible to account for the high D of certain pulsars even by placing them at infinity. The dashed line in Fig. 4 is the locus of points at which about 20 per cent of our 52 pulsars run into this problem. In our view, models lying below this line can definitely be rejected. Hall's (1980) model, marked in Fig. 4, is seen

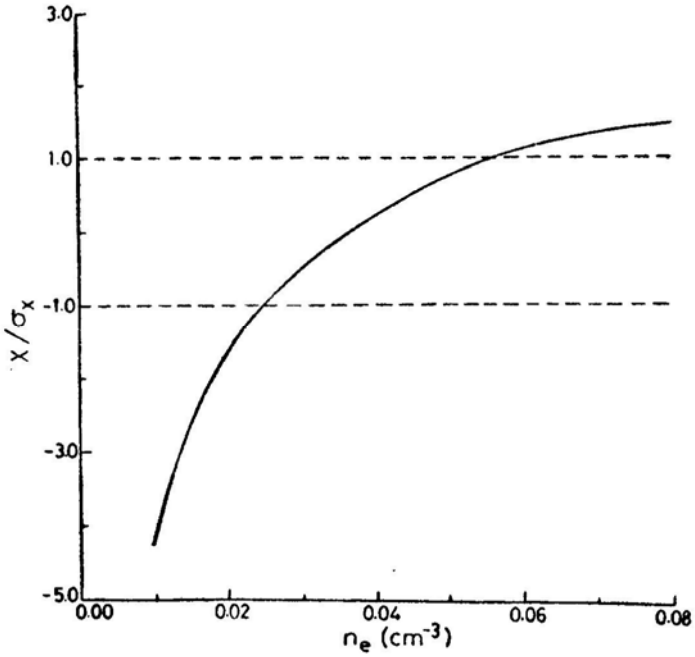

Figure 3. Computed variation of X/σ_x as a function of the assumed $\langle n_e \rangle$. Allowed values of $\langle n_e \rangle$, for which $|X/\sigma_x| \leqslant 1.0$, lie within the dashed line. The curve is very steep at low $\langle n_e \rangle$, allowing us to set confident lower limits on $\langle n_e \rangle$.

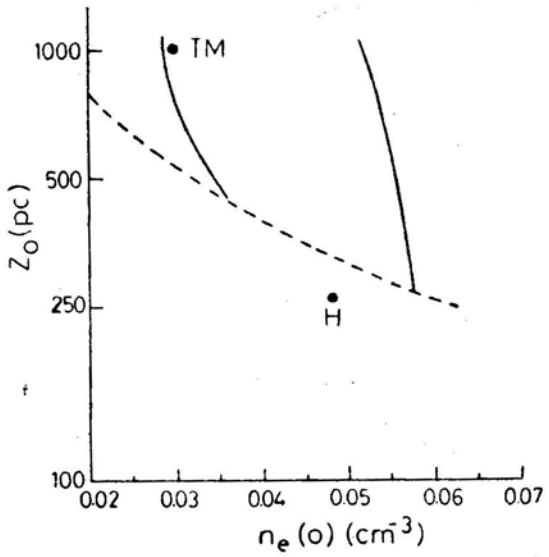

Figure 4. Results for the exponential model of n_e (Equation 2). The solid lines mark the 1σ limits of $n_e(0)$ at each z_0. The dashed line represents points at which the model is unable to explain the observed high dispersion measures of 11 of our 52 pulsars. Models corresponding to points below this line can definitely be rejected. The models proposed by Hall (1980), and Taylor and Manchester (1977) are marked by H and TM.

outside the 'allowed region'. The widely used model proposed by Taylor and Manchester (1977) is acceptable.

Our test rejects low values of z_0. This might have some relevance to the applicability of the McKee and Ostriker (1977) model for the interstellar medium (ISM) where the ionized component (H II) of the ISM is mostly associated with the neutral (H_I) clouds. Since H_I clouds have a scale height $\simeq$ 170 pc (Crovisier 1978), the same value is implied for H II and hence for n_e. Our test, however, shows that this is unlikely.

3.3 *Variation of Electron Density with Galactic Radius*

We have also studied an electron density model of the form

$$\langle n_e \rangle = n_e<, \quad R_{GC} < R_0,$$
$$= n_e>, \quad R_{GC} \geqslant R_0. \tag{7}$$

As before, we divide the Galaxy into two regions, an inner one ($R_{GC} < R'$) and an outer one ($R_{GC} > R'$), where R' (kpc) is chosen such that each region has approximately the same number of pulsars. We accept only those combinations of $n_{e<}$ and $n_{e>}$ for which Equation (6) is satisfied. Fig. 5 shows the allowed combinations of $n_e<$ and $n_e>$ for R_0 = 7 kpc. There seems to be no reason to suspect significantly different values for $n_e<$ and $n_e>$, contrary to some recent suggestions. On the basis of Fig. 4 and keeping in mind the evidence of earlier studies (Ables and Manchester 1976; del Romero and Gomez-Gonzalez 1981; Harding and Harding 1982) we sug-

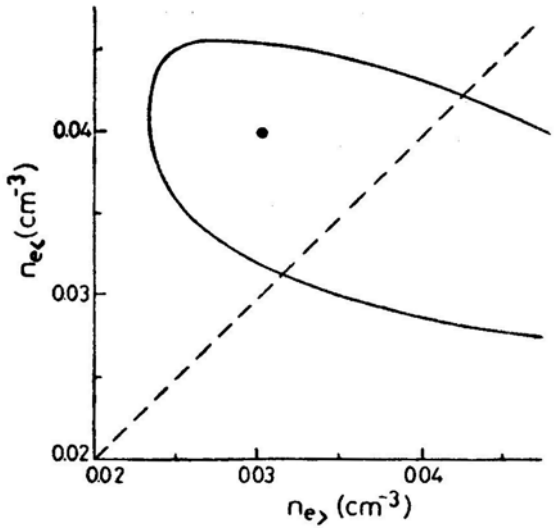

Figure 5. Allowed combinations of $\langle n_e \rangle$ (in the inner regions of the Galaxy, $R_{GC} < 7$ kpc) and $n_{e>}$ (in the outer regions, $R_{GC} > 7$ kpc) lie within the solid curve, which represents the 1σ limits on these parameters. The allowed region is nearly equally distributed on either side of the $n_{e<} = n_{e>}$ line (dashed line in the figure). Therefore a uniform electron density model for the whole Galaxy is quite adequate. If at all, $n_{e>}$ appears to be larger than $n_{e<}$. However, since other studies seem to show that $n_{e<} > n_{e>}$, we suggest the model corresponding to the dot may be close to the truth.

gest that $n_{e<} = 0{\cdot}04$ cm^{-3} and $n_{e>} == 0{\cdot}03$ cm^{-3} ($R_0 = 7$ kpc) may be a reasonable model. In fact, for pulsar studies, an $\langle n_e \rangle$ independent of R_{GC} is quite adequate. We note that our test is quite insensitive to the value of n_e in the very inner portion of the galaxy (R_{GC} below say 5 kpc) since very few of our pulsar lines of sight intersect this region. We cannot therefore rule out significantly higher n_e in this region.

4. H II regions

The results of Section 3 show that

(a) the scale height of thermal electrons is most probably quite large;

(b) there is negligible variation of electron density with galactic radius (barring the region $R_{GC} < 5$ kpc which is not very important for pulsar studies).

A constant electron density would therefore appear to be a good model for many purposes. However, we have so far neglected the effect of H II regions. If we include this contribution, a reasonable model for the electron density in the Galaxy would be (Lyne 1980)

$$n_e(z) = n_{e1} + n_{e2} \exp(-|z|/70) \quad (8)$$

where the second term is due to H II regions which are known to have a scaleheight of about 70 pc. In this section we combine a number of different techniques in order to estimate optimum values of n_{e1} and n_{e2}.

(i) The methods of Sections 2 and 3 can be applied to a model of the type of Equation (8) by dividing pulsars into high and low z categories as before and require-

ing that Equation (6) be satisfied. The curve labelled A in Fig. 6 shows our results. All points within this curve in the n_{e1}–n_{e2} space are 'allowed' and those outside are unlikely.

(ii) Table 1 shows 23 pulsars for which reliable independent distances are available (Manchester and Taylor 1981). 13 other pulsars for which only distance limits are known have been omitted. For a pulsar at distance d and galactic latitude b (hence $z = d \sin b$), Equation (8) leads to the following expression for the dispersion measure

$$D = n_{e1}\, d + n_{e2}\, d', \tag{9}$$

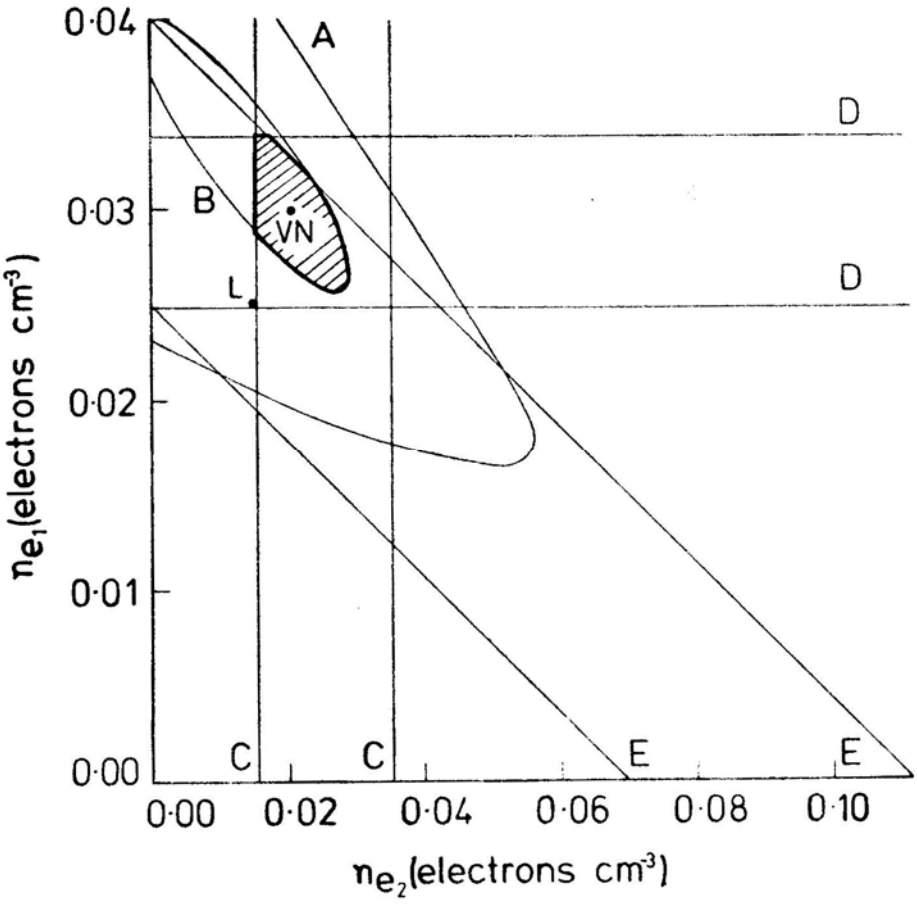

Figure 6. Optimization of the parameters n_{e1} and n_{e2} in an electron density model of the form of Equation (8). Curves labelled from A through E show the respective allowed regions. in the n_{e1}–n_{e2} space based on five relatively independent arguments: (a) cylindrical symmetry of the pulsar distribution in the Galaxy, (b) independent pulsar distances, of Table 1, (c) calculation of H II region contribution to the dispersion measures as evaluated by Prentice and ter Haar (1969), (D) independent distances of pulsars whose lines of sight do not intersect a known H II region, (e) results of del Romero and Gomez-Gonzalez (1981). The allowed region common to all the five arguments is shown hatched in the figure. The dot in the centre of this region represents our model (Equation 3). Lyne's (1980) model is marked L.

where

$$d' = \frac{70}{|\sin b|}\,[1 - \exp(-|z|/70)]. \tag{10}$$

Here d' is an effective path length through the H II regions zone of the Galaxy (of electron density n_{e2}). Using the data in Table1onecandetermine n_{e1} and n_{e2} by minimising

$$R = \sum_{i=1}^{18} (n_{e1}\, d_i + n_{e2}\, d_i' - D_i)^2/d_i'. \tag{11}$$

This leads to n_{e1} = 0·0327 cm^{-3}, n_{e2} = 0·0138 cm.^{3}. The 1σ permitted region is marked by the curve B in Fig. 6. It is gratifying that curves A and B, obtained by quite independent means, are consistent with each other. Substituting the above values of n_{e1} and n_{e2} into Equation (11) one obtains a value of R which corresponds to a dispersion measure fluctuation of 54·7 pc cm^{-3} per kpc path length. Since the mean D per kpc is itself only of the order of 35 pc cm^{-3}, this shows that the H II regions, if not treated properly, can completely mask the proportionality between D and d at small distances.

(iii) For distances within 1 kpc from the Sun, Prentice and ter Haar (1969) have developed a scheme to treat the known H II regions individually. We have used their scheme to analyse 217 pulsars with computed distances greater than 1 kpc [out of 302 pulsars listed by Manchester and Taylor (1977) and Manchester *et al.* (1978)]. Considering only the lines of sight of these 217 pulsars within 1 kpc of the Sun, we find they have a cumulative d' (Equation 10) of 1369 kpc and a cumulative D from H II regions of 3225·4 pc cm^{-3}. This corresponds to

$$n_{e2} = 0{\cdot}0236 \text{ cm}^{-3}. \tag{12}$$

Making liberal allowance for errors, we can safely expect

$$n_{e2} > 0{\cdot}0236/1{\cdot}5 = 0{\cdot}0157 \text{ cm}^{-3}; \quad n_{e2} < 1{\cdot}5 \times 0{\cdot}0236 = 00353 \text{ cm}^{-3}. \tag{13}$$

These limits have been plotted as the vertical lines marked C in Fig. 6. It is significant that the range of n_{e2} in Equation (13) is in reasonable agreement with that obtained by the method in (ii). Also, the fluctuation in D calculated by the Prentice ter-Haar formula is 43·3 pc cm^{-3} per kpc path length which agrees well with 54·7 pc cm^{-3} per kpc estimated in (ii). All these suggest that the Prentice ter-Haar correction is quite reliable in an average sense, though, in individual cases, it might be significantly in error.

(iv) We have tried to approximately estimate ne1 as follows. 13 pulsars in Table 1 do not intersect any of the Prentice ter-Haar H II regions within 1 kpc of the Sun. If we leave out PSR 1323 + 62 and PSR 2002 + 31, the cumulative d' of the others, outside the 1 kpc sphere, is only 10·3 kpc while their cumulative d (in cluding the 1 kpc sphere) is 38·8 kpc. These numbers suggest that these 11 pulsars

mostly sample n_{e1} and interact very little with n_{e2}. We can therefore estimate n_{e1} by means of

$$n_{e1} = \Big(\sum_{i=1}^{11} D_i - n_{e2} \sum_{i=1}^{11} d_i' \Big) \Big/ \Big(\sum_{i=1}^{11} d_i \Big) \tag{14}$$

where any reasonable value of n_{e2} may be used. Using the limits on n_{e2} given in Equation (13) and also allowing for the fluctuations in D due to H II regions, we obtain the following limits on n_{e1}

$$0{\cdot}0248 \text{ cm}^{-3} < n_{e1} < 0{\cdot}0337 \text{ cm}^{-3}. \tag{15}$$

These are plotted as the horizontal lines D in Fig. 6.

(v) Del Romero and Gomez-Gonzalez (1981) have estimated that the effective $\langle n_e \rangle$ for regions out to about 5 kpc from the Sun is about 0·03 electrons cm^{-3}. By Appendix 1, this implies for the model in Equation (8),

$$\langle n_e \rangle = n_{e1} + 0{\cdot}358\ n_{e2} = 0{\cdot}03 \text{ cm}^{-3}. \tag{16}$$

Del Romero and Gomez-Gonzalez (1981) have not given confidence limits for their estimate of $\langle n_e \rangle$. However, a study of their Fig. 2 suggests that the following are very safe bounds

$$0{\cdot}025 \text{ cm}^{-3} < \langle n_e \rangle \ (= n_{e1} + 0{\cdot}358\ n_{e2}) < 0{\cdot}04 \text{ cm}^{-3}. \tag{17}$$

These lines (marked E) have also been drawn in Fig. 6.

Combining all the above results we see in Fig. 6 that the parameters of Equation (8) are rather well determined. The hatched region shows the (n_{e1} — n_{e2} parameter space that is common to all the different approaches. Our choice for a good model is marked VN near the centre of this region and corresponds to Equation (3). This formula should be used only beyond 1 kpc from the Sun. Within the 1 kpc sphere, we suggest using n_{e2} = 0·030 along with the Prentice and ter Haar (1969) correction for H II regions.

The model of Lyne (1980) is marked L in Fig. 6. While it is by no means impossible, we believe our choice (Equation 3) is probably a better approximation to reality. In any case, the results of Fig. 6 show that our knowledge of the galactic electron density is by no means as limited as it has been claimed. The model given by Equation (3) can be used in future pulsar studies with good confidence. We do not expect more than about ~ 20 per cent error on the average (Fig. 6) though, in individual cases, the error may be somewhat larger.

5. Discussion

We have ignored some effects which could possibly affect the validity of our results.

(i) Although it is known that pulsars are found preferably along the spiral arms in the Galaxy (del Romero and Gomez-Gonzalez 1981), we have assumed that the

pulsar distribution is cylindrically symmetric around the galactic centre. We believe that, in an average sense, the spiral arm structure can be treated as a cylindrically symmetric system. For example, the distribution of pulsar galactocentric longitudes would be essentially uniform, in spite of the spiral structure. Therefore our simplifying assumption is unlikely to introduce any large systematic error in our results.

(ii) In our calculations, we have treated the H II regions in terms of an equivalent uniform electron density medium. However, the calculations in the previous Section 4 (ii and iii) show that for small distances (< 2 kpc) the D contribution from H II regions can fluctuate considerably. Thus, at such small distances, the proportionality between D and d (Equation 1) which is fundamental to all our calculations may not be valid. We have been cautious in this matter by deleting from our calculations a volume around the Sun of radius approximately 2 kpc ($D \leqslant 60$ pc cm^{-3}). However, even at large distances, some fluctuations in $\langle n_e \rangle$ will be present, which we have ignored. Therefore the statistical errors we have quoted may be underestimated.

(iii) We have not incorporated any selection effects due to interstellar scattering (ISS) of pulsar radiation. ISS increases with increasing D; hence we might miss high D pulsars. This is believed to be strongest in the inner regions of the Galaxy (say, $| l^{II} | < 30°$; Rao 1982, personal communication). However, since the number of pulsars involved in this effect is small, we believe our results will not be significantly affected.

(iv) We have assumed the distance to the galactic centre to be 10 kpc. If the true distance is d, say 8·7 kpc (Oort 1977), then our electron density estimates will need to be multiplied by a factor $(10/d) = 1{\cdot}15$.

None of the above effects is very serious. We therefore believe Equation (3) can be used with confidence in pulsar studies as a reasonable approximation to the galactic electron distribution.

Acknowledgements

We thank Rajaram Nityananda for many helpful discussions. We also thank V. Radhakrishnan and C. J. Salter who kindly went through the manuscript and suggested many improvements.

Appendix 1

Let the scale height of electrons be z_e

$$i.e. \quad n_e(z) = n_e(0) \exp(-|z|/z_e). \tag{A1}$$

Consider a pulsar at height z and galactic latitude b (hence distance $d = |z| / \sin b$). Its dispersion measure is given by

$$D = \frac{n_e(0)\, z_e}{|\sin b|} [1 - \exp(-|z|/z_e)]. \tag{A2}$$

The 'mean' electron density for this pulsar is

$$\langle n_{\rm eff}(z)\rangle = \frac{n_{\rm e}(0)\, z_{\rm e}}{|z|}\left[1 - \exp\left(-|z|/z_{\rm e}\right)\right]. \tag{A3}$$

Let pulsars also be distributed exponentially with scale height $z_{\rm p}$. Then the effective electron density for the whole pulsar population is

$$\langle n_{\rm e}\rangle = \frac{n_{\rm e}(0)\, z_{\rm e}}{z_{\rm p}} \int_0^\infty \frac{1}{z}\left\{1 - \exp\left(-z/z_{\rm e}\right)\right\} \exp\left(-z/z_{\rm p}\right) dz$$

$$= \frac{n_{\rm e}(0)\, z_{\rm e}}{z_{\rm p}} \ln\left(1 + z_{\rm p}/z_{\rm e}\right). \tag{A4}$$

Taking $z_{\rm e}$ = 70 pc (as for H II regions) and $z_{\rm p}$ = 350 pc, we obtain

$$\langle n_{\rm e}\rangle = 0{\cdot}358\, n_{\rm e}(0). \tag{A5}$$

References

Ables, J. G., Manchester, R. N. 1976, *Astr. Astrophys*., **50,** 177.
Arnett, W. D., Lerche, I. 1981, *Astr. Astrophys*., **95,** 308.
Crovisier, J. 1978, *Astro*, *Astrophys*., **70,** 43.
del Romero, A., Gomez-Gonzalez, J. 1981, *Astr. Astrophys*., **104,** 83.
Hall, A. N. 1980, *Mon. Not. Rastr. Soc.*, **191,** 751.
Harding, D. S., Harding, A. K. 1982, *Astrophys. J*., **257,** 603.
Lyne, A. G. 1980, in *IAU Symp. 95: Pulsars*, Eds W. Sieber and R. Weilebinski, D. Reidel, Dordrecht, p. 413.
Mancheser, R. N., Lyne, A G., Taylor, J. H., Durdin, J. M., Large, M. I., Little, A. G. 1978, *Mon. Not. R. astr. Soc.*, **185,** 409.
Manchester, R. N., Taylor, J. H. 1977, *Pulsars,* Freeman, San Francisco.
Manchester, R. N., Taylor, J. H. 1981, *Astr. J*., **86,** 1953.
McKee, C. F., Ostriker, J. P. 1977, *Astrophys. J*., **218,** 148.
Oort, J. H. 1977, *A. Rev. Astr. Astrophys.*, **15,** 295.
Prentice, A. J. R., ter Haar, D. 1969, *Mon. Not. R. astr. Soc*., **146,** 423.
Taylor, J. H., Manchester, R. N. 1977, *Astrophys. J*., **215,** 885.
Vivekanand, M., Narayan, R., Radhakrishnan, V. 1982, *J. Astrophys. Astr*., **3,** 237.

J. Astrophys. Astr. (1982) **3,** 413–418

The Role of Proton Cyclotron Emission near Acereting Magnetic Neutron Stars

K. M. V. Apparao and S. M. Chitre
Tata Institute of Fundamental Research, Homi Bhabha Road, Bombay 400005
M. J. Rees *Institute of Astronomy, Cambridge, England*

Received 1982 August 13; accepted 1982 September 22

Abstract . The process of coherent and incoherent protonn cyyclotron emission occurring near the polar regions of a strongly magnetic accreting neutron star is considered. The soft X-ray flux resulting from the incoherent emission process is calculated for application to Her X-1 and also to gamma ray bursts, a consequence of which is that gamma ray bursts will be accompanied by soft X-ray bursts.

Key words: neutron stars—X-ray bursts—*y*-ray bursts

1. Introduction

The X-radiation from strong X-ray sources is generally believed to be due to accretion onto a neutron star from a binary companion star. The occurrence of pulsation in some X-ray sources is attributed to a strong magnetic field associated with the neutron star which channels the captured matter onto the polar regions of the star. A strong magnetic field of the order of 5×10^{12} G is believed to be the cause of line emission observed in the case of X-ray source Her X-l (Trümper *et al.* 1978) which is attributed to the electron cyclotron process. The strong magnetic fields present near the polar region of a neutron star will also make the accreting protons to radiate by the cyclotron process and here we consider the nature of coherent and incoherent radiation emerging from the polar regions.

2. Proton cyclotron emission mechanism

2.1 *Coherent Emission*

The observation of infrared flux from some X-ray sources by Glass (1979), has prompted us (Gnedin *et al.* 1981), to consider proton cyclotron emission from the

polar region of an accreting neutron star. The observed flux at infrared wavelengths implies a large brightness temperature which led us to examine the possibility of a coherent cyclotron process. The conditions obtained near the poles of an accreting neutron star with a magnetic field of about 10^{11} G are found to be appropriate for the emission of such radiation. The incoming protons, when they impinge on the plasma at the poles, acquire a transverse momentum due to Coulomb scattering (Pavlov and Yakovlev 1976; Kirk and Galloway 1981). It is found that in the process a sufficient anisotropy in the pitch-angle distribution can develop resulting in the coherent cyclotron emission by protons with an intensity of the coherent radiation about a few per cent of the X-ray emission. Recently Kirk and Stoneham (1982) have explicitly calculated the transverse energy acquired by the accreting protons in the deceleration zone, and their analysis with the Fokker-Planck equation has given a firm basis to the coherent cyclotron emission process. It is suggested by them that as a result of such coherent proton-emission process operating in the presence of a magnetic field of~10^{12} G, ultraviolet radiation with an intensity of a few per cent of the X-radiation should be emitted by X-ray sources.

2.2 *Incoherent Emission*

The possibility of generation of proton cyclotron emission near the poles of accreting neutro n stars was briefly mentioned by Gnedin and Sunyaev (1974). It was also considered by Kirk and Stoneham(1982), who however assumed very low temperatures For the plasma and as a result found considerably lower incoherent proton cyclotron emission. In our consideration, we take into account the occurrence of a shock near the neutron star surface which results in protons attaining very high temperatures. The higher temperatures lead to appreciable incoherent cyclotron emission by the protons.

The accreting protons—guided by the magnetic field—stream towards the neutron star surface and acquire an energy E_p~160 ($M/M_\odot$) (l0 km/R) MeV. In the resulting stand-off shock, the incoming protons are thermalised and reacha temperature in the rang e 10^{11}–10^{12} K (Yahel 1982; Shapiro and Salpeter 1975). The production of such a, shock above the neutron star surface has been considered by Shapiro and Salpeter (1975), Inoue (1975), Basko and Sunyaev (1976), Wang and Frank (1981), Langer and Rappaport (1982) and Yahel (1982). The standoff distance of the shock has been placed by these authors between 10^s cm and 10^6 cm above the surface under different circumstances of accretion flow. The temperature profile of the protons in the sinking column below the shock, as a function of the distance from the shock, has also been calculated by these authors. Yahel (1982) has computed the thermal profile of protons in accretion columns with magnetic fields in excess of 10^{12} G a n d high luminosities. The protons are found to retain their high temperature (~5 × 10^{11} K) for a large fraction of the height of the sinking column. The thermalised protons are able to emit incoherent cyclotron radiation in the column.

The fundamental proton cyclotron frequency is given by $\omega_{ic} \sim 10^4 B$ s^{-1}. The emission however may not occur at the fundamental frequency because of self absorption. The harmonic m^* at which the medium becomes transparent, is determined by (Bekefi 1966),

$$A\,\phi \simeq 1, \qquad (1)$$

with

$$\Lambda = \frac{\omega_{ip}^2 L}{\omega_{ic} c}. \tag{2}$$

Here ω_{ip} is the proton plasma frequency, ω_{ic} is the proton gyrofrequency, L is the thickness of the plasma slab and c is the velocity of the light. The functional form of ϕ which depends on the harmonic number m, and the temperature of the protons T and ω_{ic} is given by Bekefi (1966). The self-absorbed cyclotron harmonics form a Rayleigh-Jeans spectrum up to the critical frequency $m^*\omega_{ic}$, where the optical depth for cyclotron absorption becomes of the order of unity. The total amount of radiation is given by,

$$F = \frac{(m^* \omega_{ic})^3 kT}{12\pi^2 c^2} \text{ erg cm}^{-2} \text{ s}^{-1}. \tag{3}$$

As mentioned earlier, the temperature of the protons is in the range 10^{11}–10^{12} K and a luminosity L corresponding to a brightness temperature of the same order can be attained. It is interesting to note that the electrons in the plasma will not be able to drag down the brightness temperature by synchrotron absorption. In order that the electrons be effective as absorbers, their Lorentz factor γ_e has to satisfy the condition (see Rees 1968)

$$\gamma_e > (m_p/m_e)m^{-1}, \tag{4}$$

Here m_p and m_e are respectively the proton and electron masses. In the case of X-ray sources like Her X-l, $m \sim 10$ (see Section 3) so that $\gamma_e \geqslant 100$, which is unlikely to obtain in the accreting column since the strong energy losses due to inverse Compton and synchrotron processes will prevent γ_e from becoming much larger than unity.

3. Applications

We now examine two situations, that of Her X-l and gamma-ray bursts, where incoherent cyclotron emission process might operate.

3.1 *Her X–1*

The optical behaviour of ΄HZ Her, the companion of the neutron star, has necessitated the postulation of soft X-ray flux from the X-ray star (Avni *et al.* 1973; Pringle 1973) The soft X-ray flux in the region, 0·16–0·28 keV was later detected from Her X-l (Shulman *et al.* 1975; Catura and Acton 1975) with the energy output of about 3×10^{36}erg s^{-1} in this energy band. This is less than the hard X-ray luminosity in the range 1–60 keV, We now examine the question if the soft X-ray flux can arise from the process of incoherent proton cyclotron emission.

The magnetic field at the poles of the neutron star in Her X-l is inferred to be about 5×10^{12} G (Trümper *et al.* 1978) corresponding to which the proton gyrofrequency $\omega_{ic} = 5 \times 10^{16}$ s^{-1}. If we assume the proton number density as 10^{21} cm^{-3} and L as 10^5 cm, then using Equations (1) and (2) we get $m^* \sim 9$. The harmonic, $m^* \omega_{ic}$ which escapes from the plasma slab corresponds to an energy of about 0·25 keV which is in the soft X-ray region. We have adopted an emitting area of 6×10^{10} cm^2 and $T \sim 5 \times 10^{11}$ K and find the soft X-ray emission due to incoherent proton cyclotron process, using Equation (6) to be about 3×10^{36} erg S^{-1} as observed.

3.2 *Gamma-Ray Bursts* (*GRB*)

Recently, spectral features have been detected in gamma-ray bursts which are interpreted as cyclotron emission (or absorption) lines (Mazets *et al.* 1981). The periodic variations of the flux from the gamma-ray burst FXP 0520-66 and the observed cyclotron features from some GRB suggest that a rotating neutron star with a strong magnetic field (5×10^{12} to 10^{13} G) is probably the underlying object for gamma-ray bursts. If such a picture is indeed correct and if there is sporadic accretion onto the neutron star surface which results in gamma ray bursts, there should occur proton cyclotron emission from these objects. In a magnetic field of 5×10^{12} G, soft X-ray emission (~ 0·25 keV) with an intensity comparable to the total emission would then be expected to accompany the gamma-ray bursts.

In some thermonuclear flash models for GRB (Woosley 1982), it has been suggested that–following the thermonuclear detonation—there should occur X-ray reradiation from the neutron star surface in the region $\geqslant 2$ keV but with an energy flux considerably lower than that of GRB. This reradiation is expected to be of long duration (tens of minutes to an hour), unlike the proton cyclotron radiation which will resemble the profile of the GRB. The proton cyclotron X-rays are also much softer and the flux much higher than the reradiated X-rays.

It should be possible to detect the soft X-ray emission accompanying GRB. However, the soft X-ray instrumentation used so far in satellites have collimators which restrict the field of view to a few tens of square degrees. Let us take as an example the HEAO1 soft X-ray detectors with an opening angle of nearly ten square degrees. If we take the effective operation time of HEAO-1 as about one year, then with the assumption of isotropic distribution of GRB's of all energies occurring at the rate of 10^3 yr^{-1}, the number of soft X-ray bursts from GRB, observed by HEAO-1 will be less than one. Further, in some satellites with several different detectors, the soft X-ray detector is in anticoincidence with others and since GRB trigger all the detectors, the soft X-ray bursts accompanying GRB are not recorded. It seems that the detectors flown so far may not have detected or identified the soft X-ray bursts.

4. Discussion

The importance of incoherent proton cyclotron emission near accreting neutron stars associated with high luminosity X-ray sources has not been widely recognized hitherto. We have demonstrated here that such a process makes a significant contri-

bution to the total radiation emanating from the polar regions. In the case of Her X-l endowed with a strong magnetic field (~5 × 10^{12} G) the emission is in the soft X-ray region. For other powerful X-ray sources with magnetic fields ~ 10^{12} G we expect the corresponding flux in the extreme ultraviolet region with somewhat lower intensity.

The incoherent proton cyclotron process provides a valuable diagnostic for the gamma-ray burst sources. Should the soft X-ray bursts be observed to accompany the gamma-ray bursts, this will enable us to distinguish between theories of GRB based on thermonulcear flash models and those based on sporadic accretion onto magnetic neutron stars. We suggest that an uncollimated soft X-ray detector of small area along with a shielded detector placed in a satellite can possibly detect several soft X-ray bursts associated with GRB in a time period of a few months.

Finally, we wish to point out that the energy in the proton cyclotron emission from magnetized neutron stars is less than the bulk of the energy emitted which is from electron cyclotron and bremsstrahlung processes.

Acknowledgements

We should like to thank Professor J. Trümper for valuable discussions.

References

Avni, Y., Bahcall, J. N., Joss, P. C., Bahcall, N. A., Lamb, F. K., Pethick, C. J., Pines, D. 1973, *Nature Phys. Sci.*, **246,** 36.

Basko, M. M., Sunyaev, R. A. 1976, *Mon. Not. R. astr. Soc.*, **175,** 395.

Bekefi, G. 1966, *Radiation Processes in Plasmas,* John Wiley, New York.

Catura, R. C., Acton, L. W. 1975, *Astrophys. J.*, **202,** L5.

Glass, I. S. 1979, *Mon. Not. R. astr. Soc.*, **187,** 807.

Gnedin, Yu. N., Sunyaev, R. A. 1974, *Astr. Astrophys.* **36,** 379.

Gnedin, Yu. N., Pavlov, G. G., Apparao, K. M. V., Chitre, S. M. 1981, *Astrophys. Space Sci.*, **76,** 105.

Inoue, H, 1975, *Publ. astr. Soc. Japan*, **27,** 311.

Kirk, J. G., Galloway, D. J. 1981, *Mon. Not. R. astr. Soc.*, **195,** 45P.

Kirk, J. G., Stoneham, R. J. 1982, *Mon. Not. R. astr. Soc.*, **201,** 1183.

Langer, S. H., Rappaport, S. 1982, *Astrophys. J.*, **257,** 733.

Mazets, E. P., Golentskii, S. V., Aptekar', R. L., Gur'yan, Yu. A., Il'inski, V. N. 1981, *Nature*, **290,** 378.

Pavlov, G. G., Yakovlev., D. G. 1976, *Soviet Phys., JETP*, **43,** 389.

Pringle, J. E. 1973, *Nature Phys. Sci.*, **243,** 90.

Rees, M. J. 1968, *Astrophys. Lett.*, **2,** 1.

Shapiro, S. L., Salpeter, E. E. 1975, *Astrophys. J.*, **198,** 671.

Shulman, S., Friedman, H., Fritz, G., Henry, R. C., Yentis, D. J. 1975, *Astrophys. J.*, **199,** L101.

Spitzer, L.Jr. 1956, *Physics of Fully Ionised Gases*, Interscience, New York.

Trümper, J., Pietsch, W., Reppin, C., Voges, W., Staubert, R., Kendziorra, E. 1978, *Astrophys. J.*, **219,** L105.

Wang, Y. -M., Frank, J. 1981, *Astr. Astrophys.*, **93,** 255.

Woosley, S. 1982, in *Proc. Workshop on Accreting Neutron Stars*, Eds W. Brinkmann and J. Trümper, MPE, Garching bei München, p. 189.

Yahel, R. 1982, in *Proc. Workshop on Accreting Neutron Stars,* Eds W. Brinkmann and J. Trümper, MPE, Garching bei München, p. 289.

Note added in proof

The soft X-ray observations of McCray *et al.* (1982, *Astrophys. J.*, **262,** 301,) agree very well with our suggestion. The soft X-ray spectrum in the range 0.10.8 keV is a blackbody type with a maximum approximately in the range predicted by us. Most importantly, peak of the soft X-ray pulse occurs at the minimum of the hard X-ray (greater than than 1 keV) pulse in agreement with our picture. The hard X-ray pulse is a pencil beam (W. Voges, 1982, in *Proc. Workshop on Accreting Neutron Stars*, Eds, W. Brinkmann and J. Trümper, MPE, München, P. 125) while the proton cyclotron emission will be a fan beam as it emerges preferentially perpendicular to the magnetic field. Thus the soft X-rays and hard X-rays will be in antiphase as is observed. The calculated flux of soft X-rays also agrees with observation.

J. Astrophys. Astr. (1982) **3,**. 419–450

Maximum Entropy Image Reconstruction–A Practical Non-Information-Theoretic Approach

Rajaram Nityananda and Ramesh Narayan
Raman Research Institute, Bangalore 560080

Received 1982 April 28; accepted 1982 September 27

Abstract. The maximum entropy method (MEM) of image reconstruction is discussed in the context of incomplete Fourier information (as in aperture synthesis). Several current viewpoints on the conceptual foundation of the method are analysed and found to be unsatisfactory. It is concluded that the MEM is a form of model-fitting, the model being a non-linear transform of a band-limited function. A whole family of 'entropies' can be constructed to give reconstructions which (a) are individually unique, (b) have sharpened peaks and (c) have flattened baselines. The widely discussed $1nB$ and $-B1nB$ forms of the entropy are particular cases and lead to Lorentzian and Gaussian shaped peaks respectively. However, they hardly exhaust the possibilities–for example, $B^{1/2}$ is equally good.

The two essential features of peak sharpening and baseline flattening are shown to depend on a parameter which can be controlled by adding a suitable constant to the zero spacing correlation ρ_{00}. This process, called FLOATing, effectively tames much of the unphysical behaviour noted in earlier studies of the MEM. A numerical scheme for obtaining the MEM reconstruction is described. This incorporates the FLOAT feature and uses the fast Fourier transform (FFT), requiring about a hundred FFTs for convergence. Using a model brightness distribution, the MEM reconstructions obtained for different entropies and different values of the resolution parameter are compared. The results substantiate the theoretically deduced properties of the MEM.

To allow for noise in the data, the least-squares approach has been widely used. It is shown that this method is biased since it leads to deterministic residuals which do not have a Gaussian distribution. It is suggested that fitting the noisy data exactly has the advantage of being unbiased even though the noise appears in the final map. A comparison of the strengths and weaknesses of the MEM and CLEAN suggests that the MEM already has a useful role to play in image reconstruction.

Key words: image reconstruction—maximum entropy method

1. Introduction

In a pioneering paper, Ables (1974) drew the attention of astronomers to the maximum entropy method (MEM) of restoring a spectrum from partial knowledge of its Fourier components (autocorrelations) and exhibited examples showing that (i) artifacts such as sidelobes could be suppressed and (ii) resolution could be increased. Since many fields *e.g.* aperture synthesis, very-long baseline interferometry (VLBI), speckle interferometry, share the common problem of incomplete Fourier information, it is natural that the MEM should have received a great deal of attention (see for example the conference proceedings edited by van Schooneveld 1979). In X-ray astronomy, some use on real data has begun (Willingale 1981; Pye *et al.* 1981) but it seems fair to say that the method has not lived up to its initial promise. We attribute this to two factors: (i) There has been a continuing and inconclusive discussion of the merits of different 'entropies' such as $\ln B$ and $-B\ln B$ (B being the surface brightness), each backed by statistical/thermodynamic/information-theoretic/combinatorial reasoning; (ii) A clear picture of the properties of MEM restorations is lacking and a method of controlling the resolution and sensitivity to noise is not available. Numerical implementation has also been a problem, although the scheme of Gull and Daniell (1978) has been found satisfactory by later workers (Willingale 1981). In this paper we attempt to give the MEM an alternative motivation and discuss its practical implementation. Section 2 discusses the need for nonlinear restoration methods in general, thus arguing in favour of 'non-classical' techniques such as the MEM. In Section 3 we summarise earlier work on the MEM and introduce our basic approach. In Section 4 we discuss the whole family of restoration methods based on maximising the integral of some function $f(B)$ of the brightness. The popular $\ln B$ and $-B\ln B$ entropies are members of this family. Criteria for the choice of f and the properties of different choices are given. A parameter R, which is a measure of the resolution in the restored map, is identified and a scheme for controlling R by adding a constant to the zero-spacing correlation ('FLOATing') is introduced. Section 5 discusses numerical schemes for implementing the MEM and Section 6 compares and contrasts the restorations obtained with various choices of f as well as with the CLEAN algorithm. Section 7 is devoted to the effect of noise in the data and shows that the Standard least-squares approach leads to a bias in the restoration. It is argued that our methods, though fitting the data exactly, have desirable properties in the presence of noise. In Section 8 we summarise our conclusions. The MEM is compared with CLEAN, bringing out the strengths and weaknesses of both the methods. We conclude that the MEM is now sufficiently well understood to be applied in certain practical situations. Some problematic areas calling for further work are identified. Appendix A discusses the uniqueness of the MEM solution, Appendix B considers the appearance of delta functions in MEM restorations and Appendix C discusses a multidimensional restoration scheme proposed by Newman (1977, 1978) which is shown to be incorrect.

2. The need for nonlinearity in restoration methods

Let us, for simplicity, consider a function in the range $0 \leqslant (x, y) \leqslant 1$. It is specified completely by its Fourier coefficients $\rho_{m,n}$ where

$$B(x,y) = \sum_{m,n=-\infty}^{+\infty} \rho_{m,n} \exp\,[2\pi i(mx+ny)]\,;$$

$$\rho_{m,n} = \int\int B(x,y) \exp\,[-2\pi i\,(mx+ny)]dx\,dy. \tag{1}$$

If we are given measurements of $\rho_{m,n}$ for some specified values M, N belonging to the set K(for known.), we can form the so-called principal solution $B_p(x, y)$ by restricting the summation in Equations (1) to this range

$$B_p(x,y) = \sum_{M,N\in K} \rho_{M,N} \exp\,[2\pi i\,(Mx+Ny)]. \tag{2}$$

$B_p(x, y)$, as is well known, is the convolution of $B(x, y)$ with the so called 'dirty beam' $d(x, y)$ which is. a function with Fourier coefficients 1 for $(M, N) \in K$ and zero otherwise.

Any attempt to improve on $B_p(x, y)$ without modifying the measurements would need to make some nonzero choice for the unmeasured autocorrelations *viz.* $\rho_{m,n}$ for $(m, n) \in U$ (U for unknown). One might at first think that the standard methods of interpolation and extrapolation would suffice for this. These methods are linear. Let us therefore restrict ourselves to restored maps $B_r(x, y)$ resulting from *linear* operations on $B_p(x, y)$. Let us also require that the operation should be *translation invariant*, *i.e.* that a given source should be restored in the same way regardless of its position. These two requirements restrict our linear operation to a convolution

$$B_r(x, y) = \int\int dx'\,dy'\,B_p\,(x', y')\,K(x-x', y-y'). \tag{3}$$

This means that the non-vanishing Fourier coefficients $\rho_{M,N}$ are multiplied by $K_{M,N}$ [the transform of $K(x, y)$] and $\rho_{m,n}$ for $(m, n) \in U$ continue to remain zero. Of course, this is what the classical weighting schemes achieve at the cost of modifying the measurements. We therefore conclude that (a) to leave the measured $\rho_{M,N}$ unaltered, (b) to retain translation invariance and (c) to give nonzero values to the unmeasured $\rho_{m,n}$, we need to make $B_r(x, y)$ a *nonlinear* function of $B_p(x, y)$. This generates new spatial frequencies in a manner that is well known in the time domain. Another way of appreciating the need for nonlinearity is to consider model-fitting procedures. For example, if we have to fit a given data set to the sum of three gaussian peaks, adding the fits obtained with two data sets would give six peaks whereas fitting the sum of the data would give us three. Thus we again have a non-linear operation being performed on the data.

The MEM is a non-linear technique as discussed below. The above arguments show that this is inevitable. However, the nonlinearity leads to some peculiar properties which one should thoroughly understand before applying the technique. This is further discussed in the rest of the paper.

3. Prevailing views on the MEM

The ME methods of restoration are all based on choosing the unmeasured Fourier coefficients to maximise a quantity which is the integral of a function $f(B)$ of the brightness; *i.e.*, maximise

$$E\{B(x,\ y)\} = \int\int f(B)\ dx\ dy. \tag{4}$$

Since $B(x,\ y)$ should satisfy the measurements,

$$\int\int B(x,\ y)\ \exp\ [\ -2\pi i(Mx + Ny)]\ dx\ dy = \rho_{MN}\ ,\ (M,\ N) \in K. \tag{5}$$

Equations (5) represent constraints to be obeyed in maximising Equation (4). It is clear from the form of Equation (4) that the restoration is translation invariant.

Before discussing our interpretation of Equations (4) and (5), we summarise some of the views prevalent in the literature on the nature of the MEM. If one is given only the integral of the brightness *viz.* ρ_{00}, it is clear that a uniform brightness distribution maximises E in Equation (4) for the usual choices $f = \ln B$, $-B\ln B$. This has perhaps led to the view that the MEM would like to produce as featureless a map as is consistent with the data (Ponsonby 1973), and that it is maximally noncommittal with regard to the unmeasured data (Ables 1974). A related point of view (Gull and Daniell 1978, 1979) is to define the 'most probable' map consistent with the data. The difficult step in this approach is assigning an *a priori* probability distribution for brightness maps in general. Gull and Daniell (1978, 1979) have adopted a combinatorial approach, based on building up a map by random distribution of 'quanta', to estimate the *a priori* distribution.* Others (*e.g.* Kikuchi and Soffer 1977; Ponsonby 1979) have invoked the Bose-Einstein distribution for photons over available modes. Another approach to the MEM has been through time series. Parzen (1968) and van den Bos (1971) have pointed out the relationship between the MEM and the autoregressive model for a time series. However, attempts to generalise this to two dimensions (Newman 1977, 1978) have not been successful (see Appendix C). Yet another very interesting approach is that of Komesaroff and Lerche (1979) in which the positivity constraint confines the first unmeasured Fourier coefficient (in one dimension) to a circle in the complex plane, and the MEM is shown to be equivalent to choosing sequentially the centre of each such, circle. In fact, this approach was used by Komesaroff and the present authors (Komesaroff, Narayan and Nityananda 1981) to study the properties of one-dimensional MEM restorations in some detail. However, our attempts to generalise this approach to two or more dimensions have not been successful. Meanwhile, Högbom (1979) and Subrahmanya (1979, 1980) have suggested that the successes of the MEM are simply because of the 'penalty' which functions like $\ln B$ and $-B\ln B$ impose on the undesirable baseline ripples in the brightness distribution. In their view, the choice of an entropy function is just a means of incorporating *a priori* information into the reconstruction.

*The referee has drawn our attention to a recent preprint by Gull and Skilling (1982) giving a new information-theoretic derivation of the $-B\ln B$ form and a criticism of other forms. This does not affect our subsequent discussion, which is concerned with the influence of different 'entropies' on the reconstructed image.

In this paper, we adopt and extend the last-mentioned approach. We find it difficult to assign, in any reasonable way, an *a priori* probability distribution for the brightness levels in a map. The argument from statistical mechanics (Kikuchi and Soffer 1977; Ponsonby 1979) is surely inappropriate since the photons from different parts of the source, corresponding to different cells in the map, have hardly been in thermal contact with one another. The combinatorial argument (Gull and Daniell, 1978, 1979) again seems to have in mind a specific model for how the ensemble of sources which we observe was generated. It appears to us that seeking a universal *a priori* probability distribution for map brightness levels is too rigid an approach. We have therefore explored the implications of a whole family of restorations, not in terms of underlying statistical principles (which may not exist), but in terms of their impact on specific features of the restored map, *viz.* peak width, peak shape, baseline and sensitivity to noise. It turns out that this family of ME restorations has two parameters which influence the degree of peak sharpening and baseline flattening in the restoration process, as well as the sensitivity to noise. In fact, Subrahmanya (1979, 1980) has emphasized that useful reconstruction schemes contain one or more parameters to be set by the user.

4. The family of maximum entropy restorations

We return to the problem of maximising the 'entropy' (4) subject to the constraints (5). Differentiating Equation (4) with respect to an unknown Fourier coefficient ρ_{mn}, we get

$$\frac{\partial E}{\partial \rho_{mn}} = 0 = \int\int f'(B) \exp\left[2\pi i\,(mx + ny)\right]\, dx\, dy;\ \ (m, n) \in U. \tag{6}$$

This implies that the Fourier coefficients of $f'(B)$, which we denote by σ_{mn}, vanish outside the set $(m, n) \in K$. We call such a function band limited [the principal solution $B_{\mathrm{p}}(x, y)$ is an example]. We thus have

$$\sigma(x, y) \equiv f'(B(x, y)) = \sum_{(M, N) \in K} \sigma_{MN} \exp\left[2\pi i\,(Mx + Ny)\right]. \tag{7}$$

Denoting the inverse of the function f' by g, we have from Equation (7)

$$B(x, y) = g\left[\sigma(x, y)\right] = g\left[\sum_{(M, N) \in K} \sigma_{MN} \exp\left[2\pi i\,(Mx + Ny)\right]\right]. \tag{8}$$

Equations (7) and (8) also follow from maximising Equation (4) subject to the constraints (6) by the method of Lagrange multipliers, whose role is played by the σ_{MN}.

It is important to ensure that there is only one function maximising the entropy expression (4). For a set of nonlinear equations such as (5) and (6), there is no general way of determining whether the solution is unique. However, it is shown in Appendix A that $f''(B) < 0$ is a sufficient condition for unique solutions and we therefore consider only such functions in this paper. Another natural question is whether a solution of the form (8) can be found at all. This again places restrictions

on the choice of the function f depending on the dimension d of the space over which the map B is defined. This problem is discussed in Appendix B which shows that with the familiar ln$B$ entropy, for instance, one may sometimes find no solution of the form (8) in three and higher dimensions.

Equations (7) and (8) state that the restored brightness distribution $B_r(x, y)$, after undergoing the nonlinear transformation $f'(B_r)$, becomes a band-limited function. We can use this fact to identify the particular features of f' that are important for obtaining 'good' restorations. To do this, we introduce *a priori* knowledge about $B_r(x, y)$, namely that it has a *flat baseline* and *sharp peaks*.* In contrast, the band-limited function $f'(B_r)$ has a rippled baseline and rounded peaks. The schematic argument in Fig. 1 shows that the two required characteristics (of flat baseline and sharp peaks) can be achieved if the 'amplification factor' $f''(B)$ is large for small B and small for large B. We thus see that in addition to $f''(B) < 0$ (required for uniqueness), we also need $f'''(B) > 0$. When these requirements are met, the transformation g defined in Equation (8) constructs $B(x, y)$ by sharpening the peaks and suppressing the baseline ripple in the band-limited function $\sigma(x, y)$ (Fig. 1). From the above arguments, it is also clear that there are no sign restrictions on either $f(B)$ or $f'(B)$.

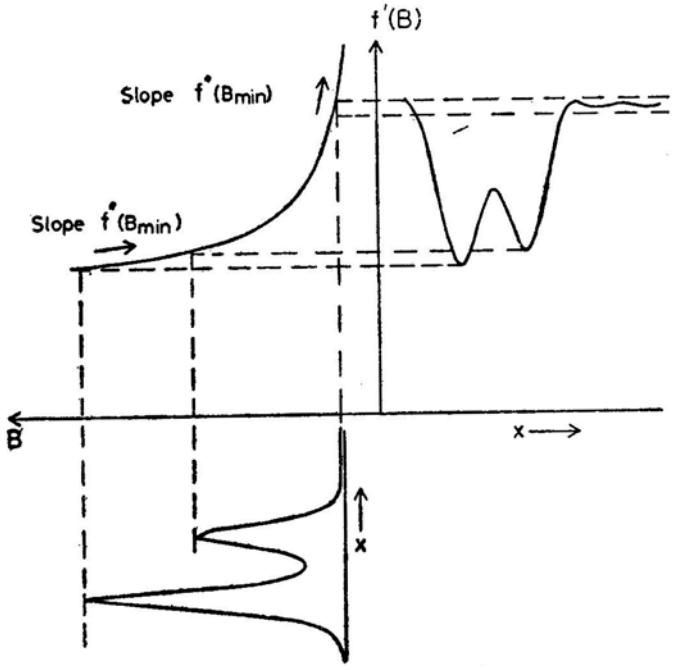

Figure 1. Illustration of the peak-sharpening and baseline-flattening properties of the MEM. The case shown is $f(B) = \ln B$. According to Equation (7) $f'(B) = 1/B$ is a band-limited function, shown to the right of the vertical axis. The function shown below is B. It is clear that the large slope [$f''(B)$] of the curve of $f'(B)$ *vs.* B at small B ensures a flat baseline, and the small slope at large B ensures sharp peaks.

*It is noteworthy that this is similar to the assumptions made in the CLEAN algorithm (Högbom 1974) though the information is used in a different way.

To lowest order, one expects the restoration to be determined by the two extreme values $f''(B_{\min})$ and $f''(B_{\max})$. Since the absolute scale of f is immaterial, we define the following ratio.

$$R = f''(B_{\min}) / f''(B_{\max}) \tag{9}$$

which decides how nonlinear the transformation in Equation (8) is. R thus measures the extent of peak sharpening and baseline flattening compared to a band-limited function such as the principal solution. Alternatively, we can think of R as a measure of how far we are extrapolating the measured Fourier coefficients. Surely, such an important characteristic of the restoration process should be chosen by the user, whereas in most present realisations of the MEM, the ratio R would be decided by the value of ρ_{00} (the average of the map) and therefore predetermined by the data. Bhandari (1978) had suggested that ρ_{00}, should be varied to achieve useful results and had illustrated this in one dimension. There is a very simple technique by which the value of R can be set by the user. In our implementation of the MEM, a suitable constant C is added to the map so that $f''(B_{\min}) / f''(B_{\max})$ equals the preassigned number R. We refer to this process as 'FLOATing' the map. Those who regard ρ_{00} as a sacred part of the data not to be modified could instead imagine that we are maximising $f(B+C)$ instead of $f(B)$. As pointed out by R. D. Ekers (personal communication), the true value of ρ_{00} in many aperture-synthesis observations at high frequencies would be dominated by the 3 K background which most practitioners of the MEM would regard as irrelevant! We note in this context that CLEAN makes no use of ρ_{00}.

Having chosen a suitable value for R (examples are given in Section 6), we can next classify the different functions f as 'soft' or 'hard' depending on whether the transition from the high value of f'' at small B to the small value at large B is rapid or slow. We expect that the soft functions will only affect the low-level features of the map leaving the peaks relatively unsharpened, while the hard functions will sharpen the peaks significantly with correspondingly lower efficiency in flattening the baseline. Let us consider a family of functions f with f'' being negative and varying as an inverse power of B (hence $f''>0$). In this family, the cases $f'' \propto -1/B^2$ and $-1/B$ correspond to the $\ln B$ and $-B\ln B$ entropies. For brightness distributions B varying from 0 to 1 and a given value of R, the normalised form of f'' is

$$f_n''(B) = -\frac{1}{[1 + B(R^{1/n} - 1)]^n}. \tag{10}$$

Fig. 2 shows the shape of $f_n''(B)$ at R=10 for typical values of n. For large n, Equation (10) asymptotically tends to the form $-\exp(-B\ln R)$, which is the hardest entropy in the above family. At the other end, we notice that as $n \to 0$, $f_n''(B)$ is a constant over most of the range, rising (in absolute value) from $1/R$ to 1 only for B very close to zero. Since the amplification factor f'' tends to a constant, the restoration tends to a band-limited function. More directly, n=0 corresponds to $f(B)=\frac{1}{2}B^2$ which implies that $f'(B) = B$ is a band-limited function. A band-limited restoration which fits the data is of course nothing but the principal solution. Another limit in which we obtain the principal solution is as $R \to 1$, since $f_n''(B)$ then

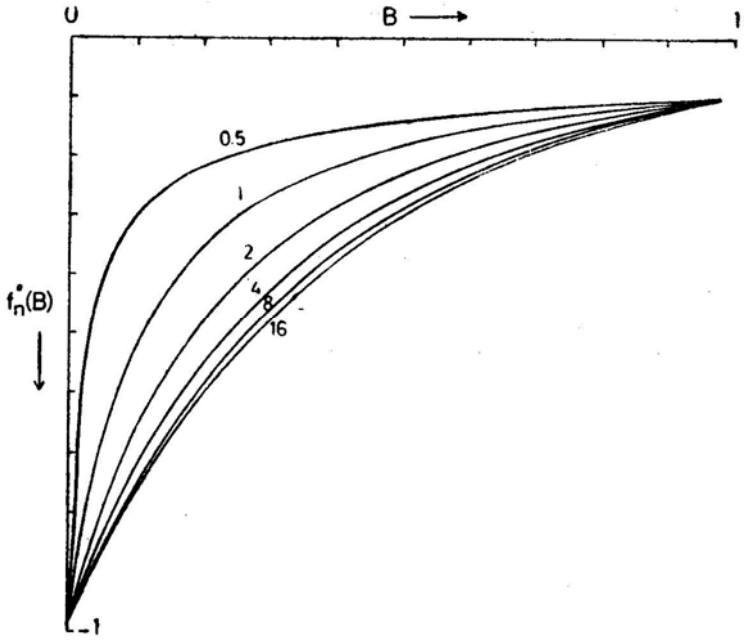

Figure 2. Variation of $f''(B)$ *vs. B* for various entropies characterised by $f'' = 1/(B + C)^n$. f'' varies from –10 to – 1 as B varies from 0 to 1. The values of n go from 0·5 to 16 and are indicated against the corresponding curves. Note that all the entropies with large n tend to a single curve (corresponding to the exponential entropy $f = -e^{-\alpha\beta}$). The 'softer' entropies with smaller values of n produce a flatter baseline and blunter peaks than the 'hard' entropies with large n.

tends to a constant as shown in Equation (10). This case is realised when we add a large constant C to ρ_{00}. Since $B_{\min}/B_{\max}$ tends to 1, so does R. Bhandari (1978) noted that for large ρ_{00} the ME restoration tends to the principal solution and proved it analytically in the one dimensional, $f = 1nB$ case. We now see that the result is completely general.

From the above arguments we see that there is a two-dimensional family of ME reconstructions described by two parameters R and n. R gives a measure of the compression of the baseline relative to the peaks when compared to a band-limited function. The parameter n in the expression $f''(B) \propto -1/B^n$ is a measure of how far this flattening effect extends upwards from the baseline. As $n \to 0$, the 'soft' limit, only the very lowest features in the map undergo the nonlinear transformation and we tend to the principal solution. The common form $-B\ln B$ is near this end. Restorations with this entropy would have flat baselines but relatively wide peaks (though the peaks could be sharpened by increasing R). As n increases, we obtain 'harder' entropies which are less efficient at baseline flattening but are better at sharpening peaks (*i.e.* increasing the resolution). The $\ln B$ entropy is 'harder' than $-B\ln B$ while $-\exp(-B\ln R)$ is the hardest in the whole family. However, we should point out that R and n can only be semiquantitative measures of the above tendencies, since even at a fixed value of R, the properties of the restoration obviously depend on the data as well. We have chosen $B_{\min}$ and B_{max} as representing the baseline and peak regions but it could happen for example that B_{min} is only an isolated fluctuation and much of the baseline lies above it. Similarly a single large peak may get

sharpened relative to lower-level peaks. This latter tendency was noted by Komesaroff, Narayan and Nityananda (1981).

We now show that the parameter n can also be interpreted as introducing *a priori* information on the *shapes* of peaks. Let us expand the band-limited function $\sigma(x, y)$ in Equation (7) about any minimum:

$$\sigma\,(x, y) = \sigma_0 + ax^2 + by^2. \tag{11}$$

For convenience, the minimum has been chosen as the origin of x and y and the axes have been chosen to make the second-order term a sum of squares. For the two entropies $f_1 = \ln B$ and $f_2 = -B\ln B$, $f_1' = 1/B$ and $f_2' = -1 - \ln B$. The shape of the peak thus becomes (from Equations 7 and 8),

$$\begin{aligned} B\,(x, y) &\simeq [\sigma_0 + ax_2 + by_2]_{-1} \qquad \text{for } f_1, \\ &\simeq \exp\,(-1 - \sigma_0 - ax^2 - by^2) \qquad \text{for } f_2 \end{aligned} \tag{12}$$

We thus have a generalised Lorentzian peak for f_1 and a gaussian peak for f_2. Each choice of $f(B)$ similarly leads to a corresponding peak shape. These results are valid when the width of the peak in B is much less than the width of the minimum in $\sigma(x, y)$, so that the Taylor expansion in Equation (11) is accurate. This will be true for high values of R, as discussed earlier. Apart from the earlier arguments regarding baseline flattening and peak sharpening, the required peak shapes in the restored map could also be used as a criterion to select the form of entropy $f(B)$. The question of peak shapes is discussed further in Appendix B.

5. Numerical procedures for obtaining the MEM reconstruction

We now describe the numerical procedures that we have used to implement the MEM. We are given a set of Fourier coefficients ρ_{MN}, $(M, N) \in K$ and are required to find values for ρ_{mn}, $(m, n) \in U$ satisfying Equation (6), which is the condition that the entropy be maximised. A Standard approach to maximisation of any function E is to start from a trial solution and evaluate the gradient of E there. In this case the components of the gradient are given by $\sigma_{\_m,\ \_n}$, the Fourier coefficients of $f'(B)$. We have

$$\frac{\partial E}{\partial \rho_{mn}} = \int\int f'(B) \exp\,[2\pi i\,(mx + ny)]\; dx\, dy \equiv \sigma_{-m,\,-n}. \tag{13}$$

In practice, the integrals in Equations (1) and (4) and hence also in Equation (13) are replaced by discrete sums with x and y varying on an $N\times N$ grid, where N is usually a power of 2 in order to implement the Fast Fourier Transform (FFT) conveniently. Correspondingly, m and n also vary on an $N\times N$ grid. The number of unknown Fourier coefficients to be determined is therefore finite. A more convenient form of Equation (13) is obtained by introducing the real and imaginary parts (denoted by single and double primes) of ρ, $\delta\sigma$, and σ. We have

$$\delta E = 2\,\sigma''_{mn}\,\delta\rho''_{mn} + 2\,\sigma'_{mn}\,\delta\rho_{mn}'. \tag{14}$$

From Equation (14), we identify the derivatives of E with respect to ρ'_{mn} and ρ''_{mn} to be $2\ \sigma'_{mn}$ and $2\ \sigma''_{mn}$. In the gradient method of implementing the MEM, one increments the unknowns by a multiple μ of the gradient

$$\rho'^{(k+1)}_{mn} = \rho'^{(k)}_{mn} + \mu\ \sigma'^{(k)}_{mn}, \quad \rho''^{(k+1)}_{mn} = \rho''^{(k)}_{mn} + \mu\ \sigma''^{(k)}_{mn}. \tag{15}$$

The coefficient μ is chosen so as to reach the highest value of E on the line defined by Equation (15). In practice, this is achieved by making a small shift in the ρ_{mn} proportional to $\delta\mu$ and computing the gradient at the new point. By linear extrapolation, one can find the value of μ at which the component of the gradient vector parallel to the search direction is zero. Starting with the new values of ρ_{mn}, one again computes the gradient and repeats the process iteratively.

An essential part of the gradient scheme as we implement it is the choice of ρ_{00} In each Iteration the ratio of the highest and lowest values of if is computed. It is then possible to add a suitable constant C to all values in the map such that $f''(B_{\min} + C)/f''(B_{\max} + C)$ is equal to the preassigned value of the ratio R. Such a 'FLOAT' step may be introduced at every cycle, or every few cycles, but is mandatory whenever $B_{\min}$ is negative at any stage.

A well-known improvement to the gradient method is the conjugate gradient method (Fletcher and Reeves 1964). In this method, each search direction is a weighted sum of the previous search direction and the present gradient, with the weights involving squared gradients. Without going into details, we point out that all the quantities required for this scheme are readily computable via the FFT, as shown by Equation (13). We have implemented the conjugate gradient method, with each cycle requiring four FFT's. At a value of R=100, for a 32×32 map, we need typically about 40 iterations for convergence. Much of the improvement in the map really takes place within the first 10 iterations. Execution time on a minicomputer system (PDP 11/34) is about 15 min for the above example. The time required for convergence increases with R, which is to be expected since R measures the degree of extrapolation of the data.

We have also explored the so-called fixed-point iteration scheme which exploits the fact that $f'(B)$ is a band-limited function. For concreteness, we describe the case f=ln$B$, f' =1/B. The stages are: (i) One starts from the principal solution, (ii) The reciprocal of the map is taken after FLOATing. (iii) The Fourier transform is then computed. In general, it will not vanish outside the known set *i.e.* $\sigma_{mn} \neq 0$, $(m, n) \in U$. (iv) These values are set equal to zero and $\sigma(x, y)$ is computed from $\sigma_{M,N}$ using Equation (7). (v) After a FLOAT step, the reciprocal is taken to obtain a map which is then transformed to give a new set ρ_{mn}. (vi) This will not agree with the measured ρ_{MN} which are therefore reset to their true values. However, we have now extrapolated ρ_{MN} outside the measured region. The new map is computed and the entire cycle from (ii) to (vi) is repeated until convergence is obtained.

Our experience is that the straightforward scheme described above converges only for small R. For the large values of R which are of interest, it is necessary to improve upon step (iv). Setting the σ_{mn} for $m, n \in U$ equal to zero is not the best strategy since, in any case, they become nonzero after one iteration. The following alternative approaches have proved to be quite successful. In the first iteration, the σ_{mn} are set

equal to zero. At the next iteration, one now finds new nonzero values $\sigma_{mn}^{(1)}$. We can express these in the form

$$\sigma_{mn}^{(1)} = \alpha\, \sigma_{mn}^{(0)} + \tau_{mn}, \tag{16}$$

where the vector τ_{mn} is orthogonal to $\sigma_{mn}^{(0)}$. The motive behind Equation (16) is to find a pattern in the as which, after one iteration, repeats with a constant multiple α. The τ_{mn} represent the error or noise in this simplified picture. Setting $\sigma_{mn}^{(0)}$ to zero gives $\sigma_{mn}^{(1)}$ in the next iteration. Instead we set $\sigma_{mn}^{(0)}$ equal to $\beta\sigma_{mn}^{(0)}$ where β is given by

$$\beta\, \sigma_{mn}^{(0)} = -\left(\frac{\alpha}{1-\alpha}\right) \sigma_{mn}^{(0)}. \tag{17}$$

One can check by linear interpolation that this choice will give $\sigma_{mn}= 0$ in the next iteration. The argument is illustrated in Fig. 3. In practice, the presence of the τ_{mn} term leads to a non zero residual and the process has to be repeated.

The following refinement of the above technique has proved quite effective. Using a simplified linear picture, we may consider $(1 - \alpha)$ to be the 'eigenvalue' of the approximate eigenvector $\sigma_{mn}^{(N)}$ for the transformation corresponding to one cycle of the fixed point algorithm. At each iteration, one can obtain the 'eigenvalue' of the previous set of σ_{mn}. By keeping track of the largest and smallest eigenvalues, one can optimize β in Equation (17) for maximum convergence in the residuals. We have had good results with this approach. This scheme is related to the one described by Willingale (1981) but has a more flexible procedure of averaging successive iterations to achieve fast convergence.

6. Illustrative examples of MEM reconstructions

In this section we present some examples of two-dimensional reconstructions with different choices of the function $f(B)$ to illustrate the general ideas put forward in

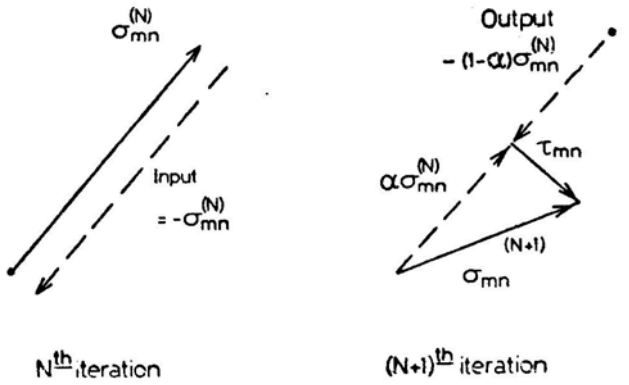

Figure 3. Illustrating the fixed-point iterative scheme for numerical computation of the MEM solution. The space of the Fourier coefficients of the reciprocal (for the ln$B$ entropy) of the brightness, is shown. It is desired to reach the origin, σ_{mn} = 0(ρ_{mn} not measured). In the simplest scheme, $\sigma_{mn}^{(N)}$, the values at the Nth iteration, are set equal to zero and after one cycle they take the values $\sigma_{mn}^{(N+1)}$, which are decomposed into $\alpha\sigma_{mn}^{(N)}$ plus 'noise' τ_{mn}. The dashed vectors labeled 'input' and 'output' show the shifts from the original position before and after one iteration. It is possible to improve the scheme to make the 'output' vector terminate near the origin (Equation 17)

Section 4. These results were all computed by the conjugate gradient method described in the previous section. We also compare our results with those obtained with the widely used CLEAN algorithm (Högbom 1974).

The model source is represented in Fig. 4 and consists of two strong unequal anisotropic gaussian peaks near each other and a broader low-level feature further off. The values of brightness were sampled on a 32×32 grid and Fourier transformed to produce the visibility function ρ_{mn}. The values of ρ_{mn} for $|m|$, $|n|$ greater than 3 were then set equal to zero. The response to a point source is now the 'dirty beam' shown in Fig. 5. The 'dirty map' obtained by transforming the truncated data back to the map plane is shown in Fig. 6. The two strong features have merged and their sidelobes drown the weak feature. The contours in the figures have been chosen to highlight the low-level features in the map since the improvement obtained by using the MEM or CLEAN is most apparent there.

Figure 4. A model source consisting of two strong anisotropic overlapping gaussian peaks with a weaker circular peak some distance away. The three peaks are at (13, 9), (11, 17) and (27, 21) on a 32 × 32 grid with peak heights 1, 1 and 0·1. Their major axes are located at position angles 135 , 100 and 90 and the pairs of rms values in the two principal directions are (3, l·5), (3, 2) and (2, 2) respectively. In all the following figures the x axis runs downwards and the y axis from left to right. The contour levels are 0·01, 0·03, 0·05, 0·1, 0·2, 0·3, 0·5, 0·7, 1·0, 1·5 in all the 'maps shown in this paper except those in Fig. 12.

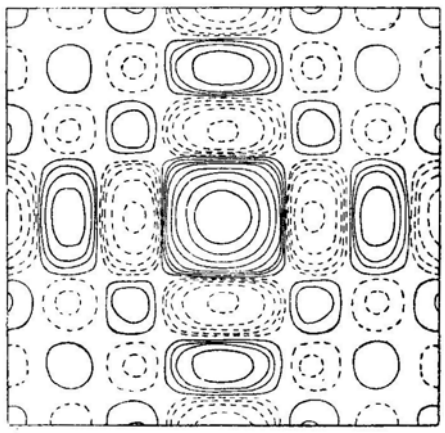

Figure 5. The reconstruction of a point source using only Fourier coefficients ρ_{mn} with $|m|$, $|n| \leqslant 3$. This is the so-called dirty beam. Negative contours are shown by broken lines.

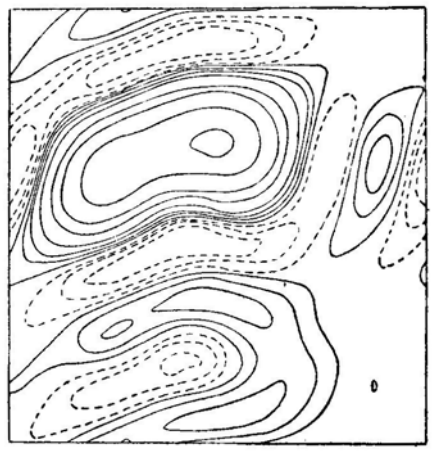

Figure 6. The dirty map made with the Fourier coefficients ρ_{mn} of the model in Fig. 4 ($|m|, |n| \leqslant 3$). This is the convolution of Fig. 4 with Fig. 5.

For comparison with the MEM solutions given later, Fig. 7 shows the result of applying the CLEAN algorithm with a gain factor of 0·25 to the dirty map of Fig. 6. Figs 7a, b and c are the results for CLEAN restoring beams of decreasing half width. Clearly the resolution in Fig. 7c is too large and false detail appears while Fig. 7a has degraded the resolution of the original map (Fig. 3). The suppression of the ripple, revealing the weak component, is excellent in the CLEAN restorations.

Now we look at the restorations performed with the ln$B$ MEM with R values of 25 and 100 respectively. These are given in Figs 8a and b. The enhanced peak sharpening and baseline suppression for R=100 relative to R=25 are readily apparent. One can also see that in this case, the restoration with R=100 is probably more faithful to the original than any of the CLEAN restorations in Fig. 6. Of course, we only take this to mean that the *a priori* information introduced by the MEM was more appropriate *for this map.* Figs 9a and b give the restorations with $f = -B\ln B$ and R=25 and 100. Note the approximate correspondence with Figs 8a and b, showing that R is a good measure of resolution, approximately independent of the form of entropy. We find that Fig. 9b is very close to the original. This can be understood since the starting model has gaussian peaks, which are naturally produced by the $-B\ln B$ entropy (Section 4).

Figs 10a and b show reconstructions from the dirty map of Fig. 5 using an un conventional form of 'entropy', $B^{1/2}$. It is notable that this form, with nothing in it to suggest the name 'entropy', is as good as either of the other two shown in Figs 8 and 9. In terms of our one-parameter classification of entropies, $B^{1/2}$ is midway between $-B\ln B$ and $\ln B$. Table 1 clearly illustrates the gradation in properties from $-B\ln B$ to $B^{1/2}$ to $\ln B$. At a constant R, peak height as well as ripple (maximum negative value) both increase down the sequence. For a given entropy, increasing R leads to an increase in peak height and decrease in ripple. Using the two parameters R and n one should be able to achieve independently the desired degree of peak sharpening and ripple suppression.

Figs 11b and 11a illustrate reconstructions with the same data as before with two choices $-e^{-aB}$, R=25 and $B^{3/2}$, R=100 which represent very 'hard' and very 'soft' functions respectively, as explained in Section 4. As expected, the peak sharpening in

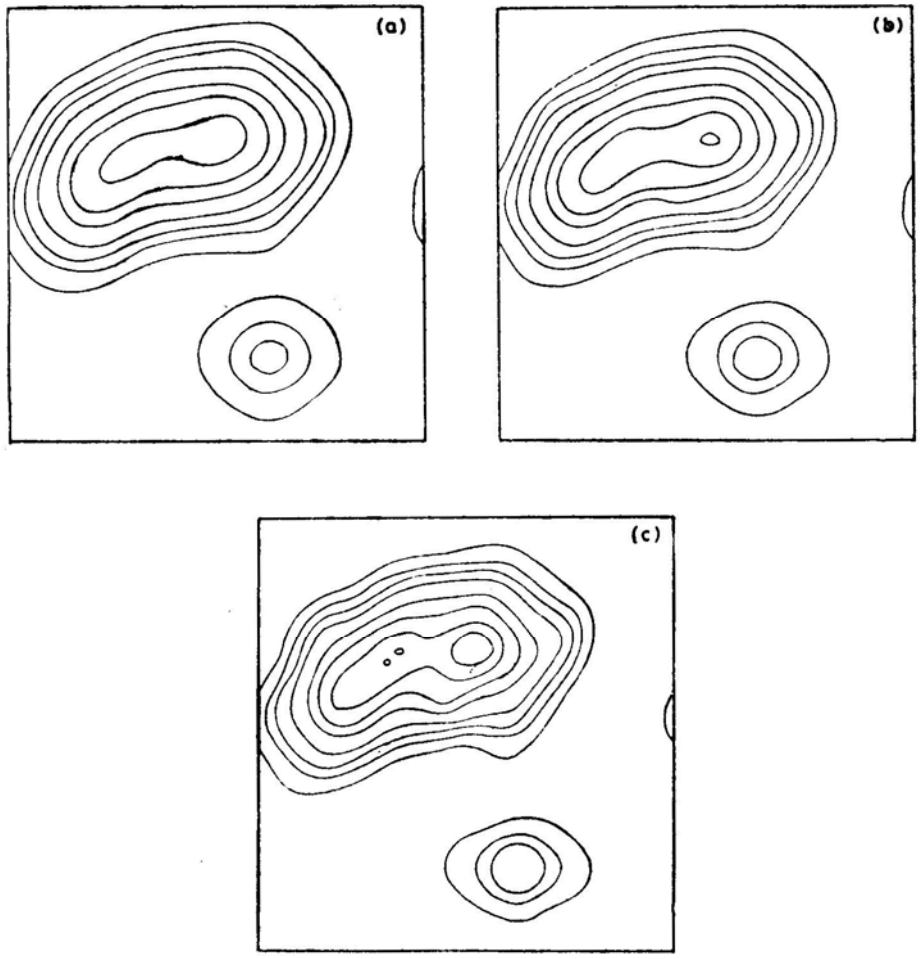

Figure 7. Restored brightness distribution obtained by applying to Fig. 6 Högbom's CLEAN algorithm with gain factor 0·25. (a), (b) and (c) correspond to gaussian restoring beams of σ = 2, 1·75 and 1·5. Note the false detail in (c) and the lowering of the peak height in (a).

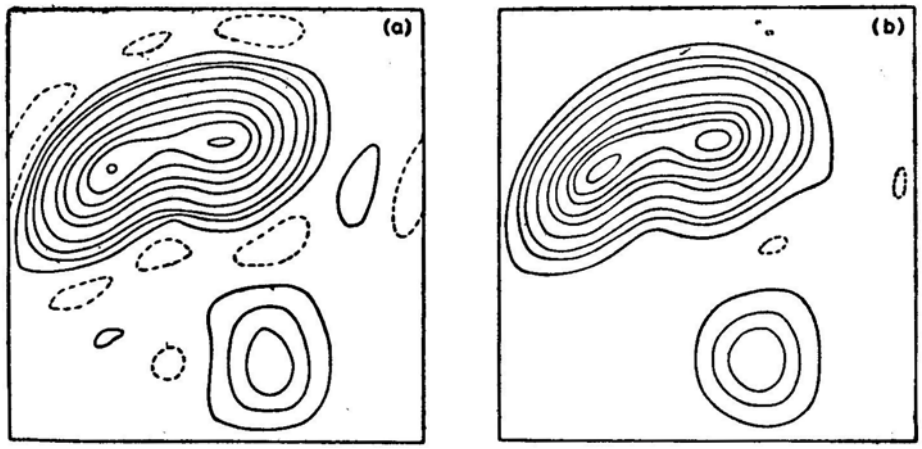

Figure 8. MEM restoration starting from the data of Fig. 6 with the ln$B$ entropy; resolution darameter R = 25 (a), and R= 100 (b).

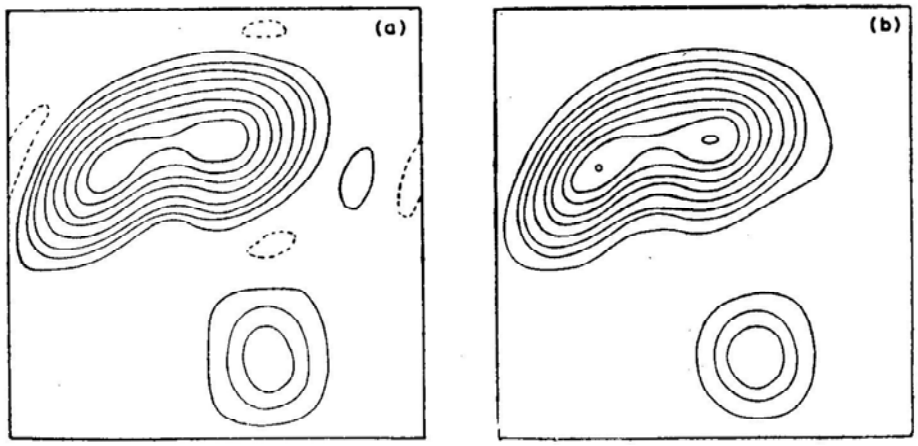

Figure 9. MEM restoration starting from the data of Fig. 6 with the $-B\ln B$ form of entropy; (a) $R = 25$, (b) $R = 100$.

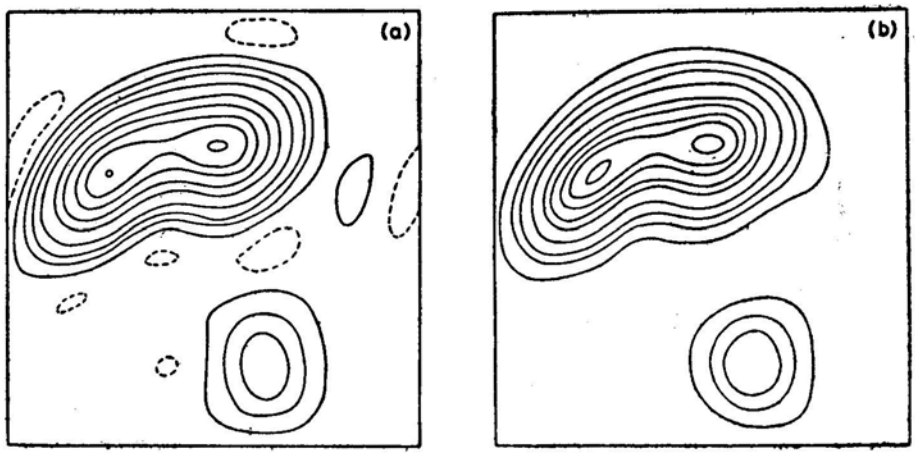

Figure 10. MEM restoration starting from the data of Fig. 6 with the $B_{1/2}$ form of entropy; (a)$R = 25$, (b)$R = 100$.

Table 1. Gaussian map of Fig. 4 restored with different forms of the MEM and with CLEAN.

Entropy	Maximum peak height		Maximum negative value	
	$R = 25$	$R = 100$	$R = 25$	$R = 100$
$B^{3/2}$		0·8800		−0·0174
$-B \ln B$	0·9808	1·0180	−0·0145	−0·0059
$B^{1/2}$	1·0420	1·1469	−0·0167	−0·0080
$\ln B$	1·0711	1·2484	−0·0189	−0·0111
$-1/B^2$	1·1072	1·3571	−0·0242	−0·0185
$-e^{-B \ln R}$	1·1890		−0·0280	

True map	1·0	0·0
Dirty map	0·7483	−0·0783
CLEAN (High resolution)	0·8619	−0·0036
CLEAN (Medium resolution)	0·7314	−0·0027
CLEAN (Low resolution)	0·6393	−0·0017

Fig. 1 la is tremendous with very little ripple suppression. In fact at R = 100, this form of entropy is so active that it begins to split peaks. This form is obviously not recommended for radio astronomy applications though it could have its uses elsewhere. The reconstruction with $B^{3/2}$ has flatter peaks than any of the earlier figures as expected but surprisingly has more ripple than some of the harder forms. The reason is that the series of entropies going from $B^{1+\epsilon}$ to $B^{2-\epsilon}$ (i.e. n going from $-1+\epsilon$ to $-\epsilon$) are in a separate class. These forms do not have an infinite barrier at B=0 and positivity can be maintained only by FLOATing. By this argument, $-B\ln B$ is the last of the positivity-enforcing entropies. The form $B^{3/2}$ is interesting for another reason. Since reconstructions with this entropy have $B^{1/2}$ band limited, this means Fourier extrapolation does not exceed twice the measured range (this, in fact, explains why the baseline cannot be flattened beyond a point).

Figs 12ad show an interesting example of a case where the MEM as well as CLEAN fail. The true map (Fig. 12a) is an elliptic plateau. When the 'measured' range is restricted to $|m|, |n| \leqslant 3$, one obtains the dirty map in Fig. 12b. The MEM reconstruction with the $-B\ln B$ entropy at R=100 is shown in Fig. 12d. The ripple at the base has been largely removed but the ripple at the top of the plateau has actually increased. This is a two-dimensional analogue of an effect first discussed by Komesaroff, Narayan and Nityananda (1981) for one-dimensional plateaus. As a matter of interest we show in Fig. 12c the CLEAN reconstruction with gain=0·5. CLEAN, being peak seeking (as is the MEM), has fitted peaks on the plateau. Moreover, being a sequential technique (which the MEM is not), it has broken the symmetry of the map. Fig. 12e is discussed in Section 8.

The $-B\ln B$ MEM (for example) has introduced sharp ripple whose wavelength is related to the cutoff in the data. Since this method has been interpreted as maximising a certain *α priori* probability for brightness distributions (Gull and Daniell 1978, 1979), we conclude that this *α priori* distribution does not agree with usual ideas on which features in a map are reasonable and which ones are artefacts. In our way of looking at the MEM, it is clear that the assumption of sharp peaks at high B and a flat baseline at low B (Section 4) has been violated. The ripples on top of the plateau

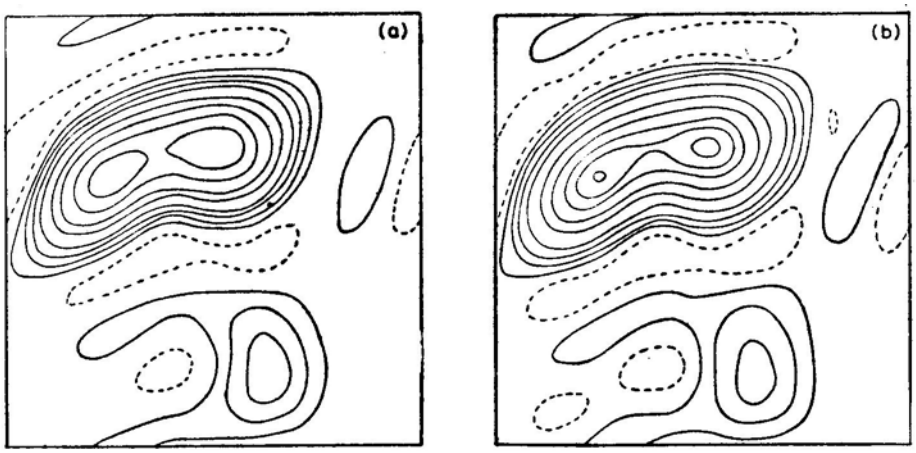

Figure 11. Reconstruction from the data of fig. 6 using (a) a very 'soft' entropy $-B^{3/2}$ with R = 100 (note the ripple in the baseline and rounded peak), (b) a very hard entropy $-\exp(-\alpha B)$ with R = 25; note the very sharp peaks and rippled baseline.

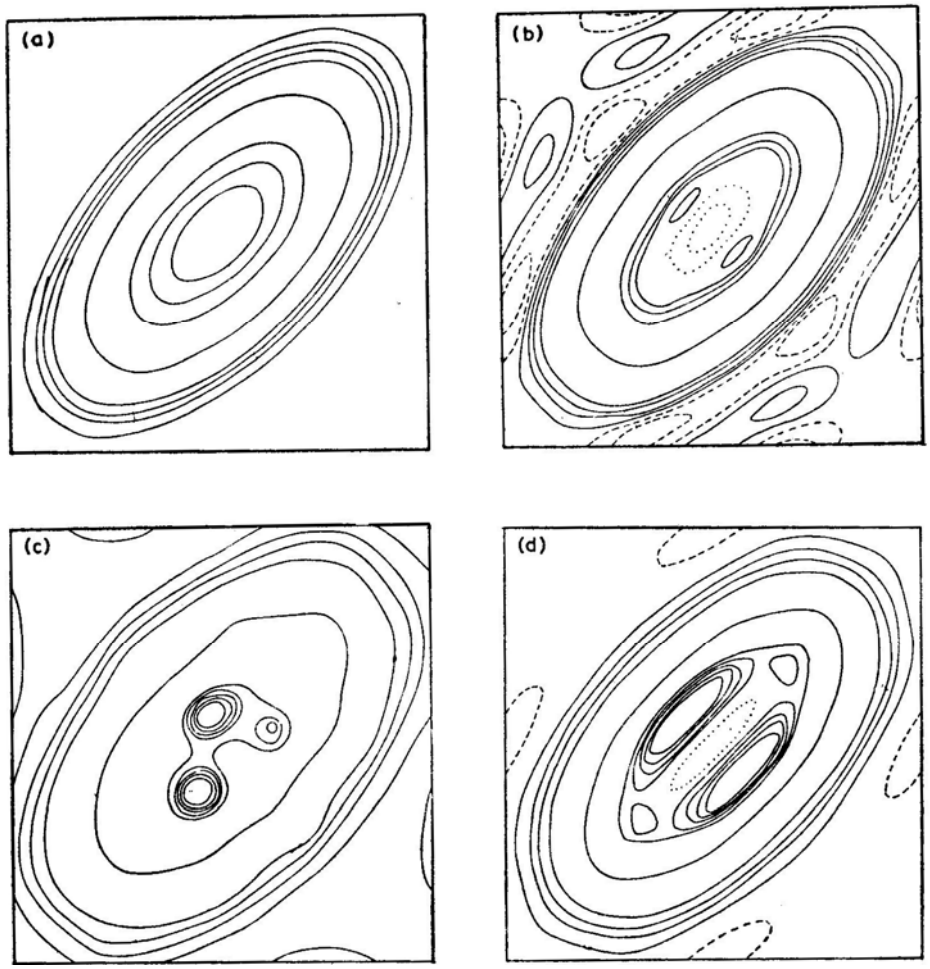

Figure 12. (a) Model source consisting of an elliptic plateau. The contour levels are 0.01, 0.03, 0.05, 0.1, 0.5, 0.9, 0.95, 0.97, 0.99, 1.01, 1.03, 1.05, 1 1. the contour levels have been chosen so as to bring out the low-level ripple as well as the ripple on the plateau, whose parameters are give in. Table 3. (b) Dirty map obtained from (a) by retaining only Fourier components ρ_{mn} with $|m|$, $|n| \leqslant 3$. Dashed contours represent negative values while dotted contours indicate depressions in which the height decreases inwards. (c) Restoration by CLEAN starting from (b). The gain factor used is 0·5 and the rms of the restoring gaussian beam is $\sigma = 2$. Note the effective suppression of low-level ripple accompanied by spurious, symmetry-breaking peaks on top of the plateau. (d) Restoration by $-B\ln B$ MEM with $R = 100$. Note that low-level ripple is suppressed. However, the spurious features on the plateau are similar to and even stronger than those in the dirty map.

have been treated as peaks to be sharpened. Clearly, CLEAN also fails because its underlying *α priori* assumptions about the map are not true in this case.

7. Treatment of noise in the measurements

In any real problem the measured Fourier coefficients $\rho_{mn}^{(m)}$ will have errors which we take, for simplicity, to be gaussian with rms σ (please note that σ_{mn} and σ are different objects!). The superscript (m) stands for 'measured' and we continue to use ρ_{mn} for

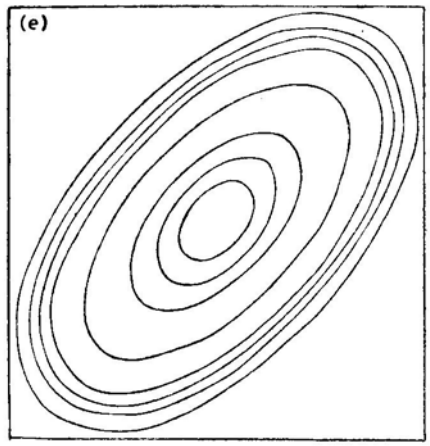

Figure 12. (e) Restoration with a modified entropy in $(B + C_1) + \ln (C_2 - B)$ with C_1 and C_2 FLOATing constants determined by $(B_{\max} + C_1)^2/ (B_{\min} + C_1)^2 = 100$, $B_{\min} + C_1 = C_2 - B_{\max}$. with this entropy the ripple has disappeared both from the low-lying region and the plateau.

the Fourier coefficients of the reconstructed brightness distribution (which need not agree with the measured values). Ables (1974) suggested that in the presence of noise one should satisfy the condition

$$\sum_{(m,\, n)\in K} | (\rho_{mn} - \rho_{mn}^{(\mathrm{m})}) |^2 = 2N\sigma^2 \tag{18}$$

where N equals the number of (complex) correlations measured. We refer to this approach as least-squares MEM. Ables' suggestion was implemented by Gull and Daniell (1978). Willingale (1981) has given the appropriate generalisation for the deconvolution problem in X-ray astronomy where the errors (σ) vary over the map. The condition (18) would appear to be reasonable since it gives deviations of the right overall size between the model and the measurements. However, we show below that these deviations ($\rho_{MN} - \rho_{MN}^{(\mathrm{m})}$) are far from randomly distributed and indeed introduce a systematic bias into the reconstruction.

We introduce a Lagrange multiplier λ for the single constraint (18) (which replaces the set of constraints (4) in the noise-free case). We thus have

$$\frac{\partial}{\partial \rho_{mn}} \left\{ \int\int f(B)\, dx\, dy - \lambda \sum_{(M,\, N)\in K} \left[(\rho'_{MN} - \rho'^{(\mathrm{m})}_{MN})^2 + (\rho''_{MN} - \rho''^{(\mathrm{m})}_{MN})^2 - 2\sigma^2 \right] \right\} = 0 \tag{19}$$

where we again use the real and imaginary parts ρ' and ρ'' of the Fourier coefficients. For clarity, we discuss the $f = \ln B$ case though the argument is general. Differentiating with respect to an unmeasured Fourier coefficient gives the same result as before *viz.* B is the reciprocal of a band-limited function $\sigma(x, y)$. Differentiating with respect to a measured coefficient ρ_{MN} in Equation (19) gives

$$\rho_{MN} = \rho_{MN}^{(m)} + \frac{1}{\lambda}\int\int f'(B)\,\exp\,[-2\pi i\,(Mx+Ny)]\,dx\,dy$$

i.e.

$$\rho_{MN} = \rho_{MN}^{(m)} + \frac{1}{\lambda}\sigma_{MN}. \tag{20}$$

Equation (20) immediately suggests an iterative scheme for implementing Equation (19). We can find the MEM solution with zero noise ($\lambda=\infty$), which has $\rho_{MN}=\rho_{MN}^{(m)}$, by any of the methods already described in Section 5. We then have available a good first approximation to the coefficients σ_{MN} in Equation (20). It is now easy to choose λ to satisfy Equation (18). Equation (20) would then give modified values of ρ_{MN} in the measured range. Since–in practical cases–the shifts are expected to be small, the process can be iterated and convergence is quite rapid.

The important lesson of the iterative scheme described by Equation (20) is that the residuals ($\rho_{MN} - \rho_{MN}^{(m)}$) are just proportional to the Fourier coefficients of the reciprocal of the MEM brightness distribution(!) and have no relation to the true errors in the measurements. Fig. 13 illustrates the nature of the bias which least-squares MEM can introduce. Schematically, we have a 2*N*dimensional space of data in which the coordinates of a point are the 2*N* measured Fourier coefficients. P_0 represents the true values of ρ_{MN} and a sphere of radius $\sigma\sqrt{2N}$ around P_0 represents the data sets obtained with various realisations of the noise. Given any point P_1 on this sphere, the least-squares MEM method modifies the measurements by the same residuals

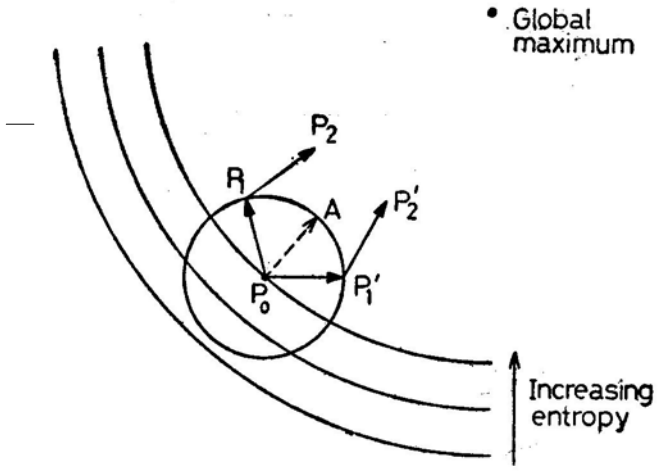

Figure 13. The space of measured Fourier coefficients. P_0 represents the true values, while P_1, P_1' etc. represent the values that would be obtained in measurements with different realisations of the noise. P_1, P_1' *etc.* lie on a sphere of radius $\sigma\sqrt{2N}$ where 2*N* is the number of (real) measurements and σ the rms of each. Starting from the noisy data, P_1, P_1' *etc;* the least-squares approach moves a distance $\sigma\sqrt{2N}$ to P_2, P_2' *etc.* The average over all realisations of the MEM solutions P_2, P'_2 *etc.* is the point A which has a systematic and predictable bias P_0A from the true data. The vectors P_1P_2, P_1' P'_2 represent the residuals and, for small σ , are independent of position on the sphere, pointing in the direction of increasing entropy, perpendicular to the constant entropy contours. At the centre of these contours is the unconstrained maximum entropy solution *viz.* a flat map (ρ_{00} is assumed fixed).

since, by Equation (20), these are dominated by the zero-order values of σ_{MN} (*i.e.* those corresponding to the noise-free case). The average of the solutions obtained with different realisations of the noise is *not* the same as the noise-free solution but differs from it to *first order* in σ(Fig.13). We can treat the two vectors P_0P_1 and P_1P_2 in Fig. 13 as orthogonal since there is no correlation between the noise, represented by P_0P_l, and the residuals introduced by the MEM, represented by P_1P_2. Therefore $P_0P_2 \simeq \sqrt{2}\ P_0P_1$, showing that the MEM has really taken us further from the true data.

An alternative approach is to fit the noisy data exactly, using the methods described in Section 5. The noise will propagate to the unmeasured correlations as well. However, there is the advantage that the measurements are not further degraded or biased. Fig. 14 illustrates the two approaches to noise. Fig. 14a shows the result of

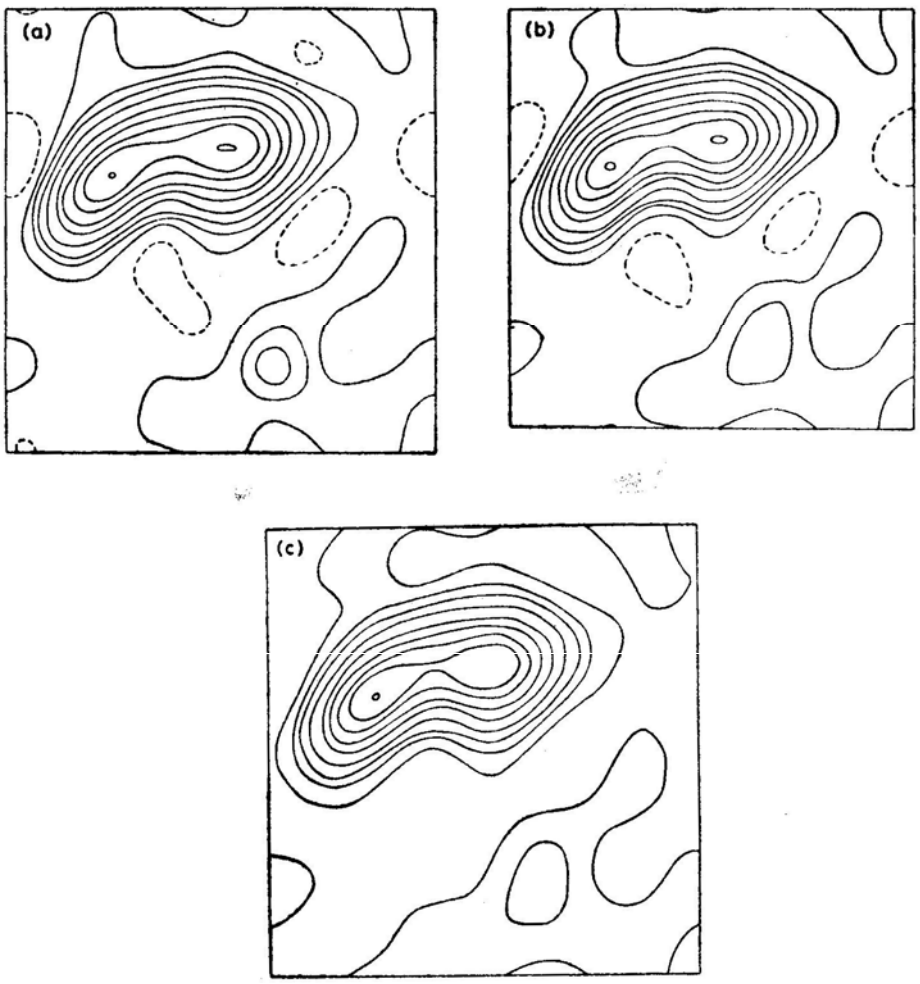

Figure 14. Illustration of the different ways of treating nosy data with the MEN. (a) R = 100, $-B\ln B$ MEM map of Fig. 9b with gaussian noise of rms = 1 added to the Fourier coefficients ρ_{mn} $|m|, |n| \leqslant 3$; (b) $-B\ln B$ MEM restoration from the noisy data in (a) with R = 100 fitting the data exactly; (c) $-B\ln B$ MEM restoration fitting the data in (a) by the least-squares method with σ = 1. Note that the result is not less noisy than (b) but has rounded off the peaks and distorted the ripple so that it no longer goes negative.

adding random noise with, a gaussian distribution of standard deviation 1 to the known coefficients $\rho_{mn}(|m|, |n| \leqslant 3)$ of the MEM map of Fig. 9b. Fig. 14b shows a reconstruction ($-B\ln B$ entropy, R=100) which fits the noisy data exactly. It is seen that the spurious features are not identical to those in Fig. 14a, since the noise has also affected the values of extrapolated coefficients. Fig. 14c shows the result of using the least-squares MEM scheme (Equations 1820). It can be seen that the spurious features have been modified more than in Fig. 14b. The peak and baseline values given in Table 2 confirm this. The reason is that now not only unknown but even measured coefficients have been changed. It is clear that this change has not reduced the effects of noise. In fact, the rms deviation of the $\rho_{mn}(|m|, |n| \leqslant 3)$ from the true values is 1 for the reconstruction in Fig. 14b but 1·32 for Fig. 14c, showing that the least-squares approach is taking us further from the noise-free MEM solution by approximately the $\sqrt{2}$ factor expected.

The unphysical nature of the residuals in conventional least-squares MEM has been pointed out by Bryan and Skilling (1980). They have proposed a new algorithm which forces the residuals to have a gaussian distribution. This indeed represents the use of additional *a priori* information, though with added computational complexity. The bias discussed above is not basically surprising. When the measurements are inaccurate, the *a priori* distribution of brightness levels can make its presence felt and pull the solution towards the global maximum–a flat distribution. This is illustrated by the constant entropy contours in Fig. 13, which enforce a specific choice of the error vector normal to them (Bryan and Skilling 1980). The net effect on the map is to flatten and raise the baseline and lower the peaks.

We illustrate this in Fig. 15. Fig. 15a shows the result of adding uncorrelated gaussian noise of rms 0·25 to *all* the correlations of Fig. 9b. The result of the least-squares MEM procedure treating all the correlations as measured is shown in Fig. 15b. Here, there is no question of extrapolation and we see quite clearly that the least-squares approach has not suppressed the noise but only modified it by removing the negative parts. Table 2 gives the peak and baseline values for the two maps in Fig, 15.

We conclude that using *a priori* information to solve for the noise is likely to lead to bias. This bias should always be kept in mind in interpreting maps made by the least-squares method. In many situations the alternative approach of fitting the noisy data may be preferable.

Table 2. Peak and minimum values of restorations from noisy data with the $-B\ln B$ MEM.

Figure	Description	Peak	Minimum
14a	Map of Fig. 9b with noise added to ρ_{mn} ($\|m\|, \|n\| < 3$) (R = 100, rms = 1)	1·0187	−0·0229
14b	Reconstruction fitting the noisy data exactly	1·0334	−0·0178
14c	Reconstruction fitting the noisy data by least squares with σ = 1	1·0020	−0·0080
15a	Fig. 9b with noise of rms = 0·25	1·0223	−0·0355
15b	Fig. 15a fitted by least squares with σ = 0·25	0·9832	−0·0088

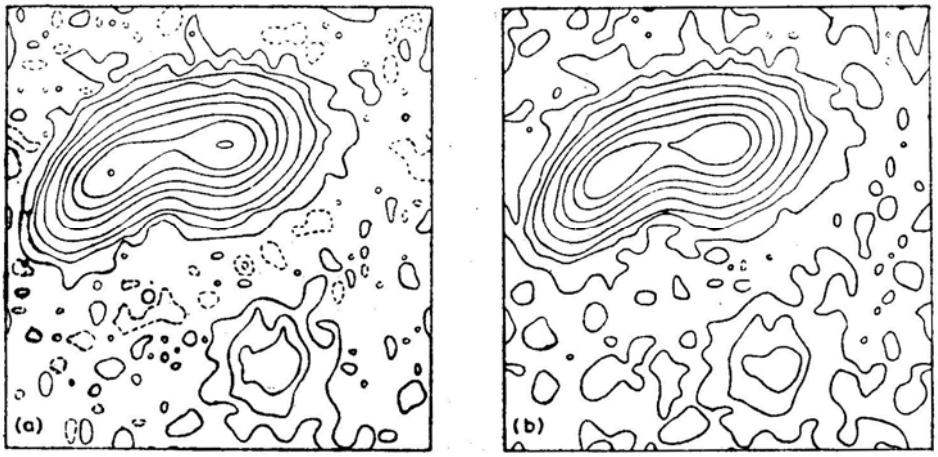

Figure 15. (a) A map obtained by adding gaussian noise with rms = 0.25 to all the Fourier coefficents of Fig. 9b. (b) Result of applying the least-squares method with σ =0.25 to the map in (a). There is no extrapolation of the data involved here. Comparing (b) to (a) show off the last-squares method distorts (and increases) the noise already present in (a) so as to round off the peaks and remove negative regions.

8. Summary and discussion

The major conclusions of our study are the following:

(a) The MEM is basically a model-fitting procedure which works well if the reconstruction is required to be peaky with a flat baseline. We do not agree that it is 'maximally noncommittal' with respect to the missing data. In fact, the unknown correlation values are 'committed' to developing peaks and a baseline in conformity with the model. Nor is it right to say that the reconstruction is as featureless as possible. Given the wrong problem, such as the plateau in Fig. 12, MEM produces spurious features stronger than even those in the dirty map! Regarding peak strengths and widths, it should be noted that higher peaks are likely to be sharper and stronger than lower ones. This result was pointed out by Komesaroff, Narayan and Nityananda (1981) for the one-dimensional ln$B$ entropy. We have been able to generalise it to all entropies and all dimensions in this paper. Moreover, the reconstructed peaks could sometimes have very curious properties, as discussed in Appendix B. All these peculiarities should be kept in mind in practical applications of the MEM.

(b) We have shown that the common—Bln$B$ and ln$B$ forms of entropy are members of a continuous family of functions characterised by a parameter n (see Equation 10). All these functions satisfy the important restrictions $f''(B) < 0$, $f'''(B) > 0$, which are necessary for acceptable reconstructions. The character of the reconstructions changes gradually from one end of this family to the other. For any particular application, depending on the requirements, a restricted range of n would be suitable [see (c) below]. What we would like to emphasize, however, is that no single form of 'entropy' can be considered fundamental and better than all others. This has been a source of considerable controversy, with two schools backing the — Bln$B$ and ln$B$ entropies respectively. Arguments and analogies from statistics, thermodynamics and information theory have all been applied in order to identify the best entropy. However, the results of Fig. 12 (which can be obtained with any

form of entropy) show that any 'ideal' entropy would fail badly if the conditions are not right.

To settle the controversy we recommend widespread use of the $B^{1/2}$ entropy. This is midway between $-B\ln B$ and $B\ln B$ and gives equally good reconstructions. As a major benefit, there is no temptation to associate any information-theoretic or thermodynamic concept with it. We also believe the misleading name of 'Maximum Entropy Method' should be changed to something more appropriate such as 'Variational Method'.

(c) If fundamental arguments are not appropriate, how should one select the form of f ? We suggest the following criteria, discussed in Section 4.

(i) Soft functions (small but positive values of n in Equation 10) generate fairly broad peaks but extremely flat baselines. On the other hand, hard functions (large n) reconstruct sharp peaks and leave a lot of residual ripple. For radio astronomy applications, soft functions are probably more appropriate.

(ii) The shapes of peaks reconstructed by any $f(B)$ can be predicted approximately. For gaussian peaks one should use $-B\ln B$ entropy, for Lorentzian peaks $\ln B$, *etc.* It should, of course, be kept in mind that all the functions considered are geared towards sharp peaks and flat baselines. If this is not an appropriate model in a particular case, then the results can be poor. Thus, in the case of the plateau (Fig. 12), if one knew in advance about the flat top, then a more appropriate function to maximise would be $\ln (C_1 + B) + \ln (C_2 - B)$ where C_1 and C_2 are FLOATing constants. Fig. 12e shows the remarkable improvement that this can make.

(d) There are two basic symmetries in all forms of the MEM.

(i) The reconstructions are translationally invariant in the sense that if the data are modified to correspond to a shift in the origin of (x, y), the reconstructed map also displays the same shift, but does not otherwise change.

(ii) If the data are scaled by a constant, so is the reconstruction. However, an important symmetry is missing in MEM reconstructions.

(iii) If one trivially modifies the dirty map by adding a constant to $B(x, y)$ at all x, y, the MEM reconstruction shows non-trivial changes.

One way of understanding this is to note that all the forms of the MEM with $n \geqslant 0$ in Equation (10) impose positivity. If one adds a large constant to the map, positivity becomes a weak or irrelevant consideration, while if one subtracts a constant, one may even end up with no positive solution at all. Thus, the form of the reconstruction is apparently at the mercy of the experimental value of ρ_{00} (the zero Fourier coefficient). If one had a large value of ρ_{00}, the MEM would give back the principal solution, a lower value would give a 'good' reconstruction, a still lower value would give a highly spiky function, *etc.* (Bhandari 1978; Komesaroff, Narayan and Nityananda 1981).

The modification of the MEM which we call FLOAT avoids this undesirable feature and has the added advantage that the user, can control the resolution of the restored map. In our scheme, we maximise the integral of $f(B + C)$ where C is a number which is set as follows. We have identified the ratio $R = f''(B_{\min} + C)/$

f'' (B_{max} + C) (see Equation 9) as a measure of the resolution in the restoration. C is chosen so that R attains a preset value. As R increases, the resolution also increases. We have found that R = 100 gives good maps. The results are however not significantly changed for a fairly large range of R.

When the FLOAT feature is incorporated, the results are insensitive to ρ_{00} and MEM becomes identical to the classical methods of restoration as far as symmetries are concerned. Another point to be noted is that one is no longer strictly enforcing positivity. It is $B + C$ which is positive. In fact most of the restorations displayed in this paper go negative at some point.

(e) Komesaroff, Narayan and Nityananda (1981) showed that, for fixed ρ_0, as the noise in the measured data increases, MEM restorations in one dimension with the ln$B$ entropy become progressively more peaky until, at a given noise level, there are no positive functions which fit the data. This is no doubt a feature of all entropies and all dimensions. However, with the FLOAT modification, this is not a problem. Since R is specified, a larger constant will be automatically added when the data are noisy, and the resolution of the restoration is not affected. If necessary one could even empirically reduce the value of R with increasing noise.

An alternative approach to noise is the least-squares approach (Ables 1974; Gull and Daniell 1978, 1979) which allows the map to deviate from the measured data, thus ensuring positivity. In this scheme, the resolution is apparently automatically reduced with increasing noise level. The main criticism we have of this apprroach is that the residuals between the fitted and measured data are *biased* (see Section 7). We believe it is betterto fit the data exactly.

(f) Although the method CLEAN (Högbom 1974) was proposed at about the same time as MEM, it has found far wider acceptance in radio astronomy. Most observations are CLEANed while MEM maps are a rarity. Based on the results of this and earlier papers, we make a comparison of the two methods.

(i) Both CLEAN and MEM are ideally suited to a map with well-separated point sources and an extensive fiat background. As the sources become extended, both methods become relatively less effective, but it appears that MEM may be marginally superior (see Figs 7–10 which correspond to a model with fairly extended sources).

(ii) CLEAN is excellent at ripple suppression even when the dirty beam has very large sidelobes. In the examples discussed so far in this paper, the sidelobe level is not very high because the uv coverage is compact ($|u|$, $|v| \leqslant 3$ in all cases). Fig. 16 shows a more diflicult case where the data are missing in two sectors (as could happen in a practical case when the source 'sets').* The CLEAN restoration is excellent. However the MEM restoration with $-B\ln B$ (the results are the same for other forms) is rather bad, with ripple suppression being relatively poor. The reason is not difficult to see. Equation (8) shows that the logarithm of the reconstructed brightness is band-limited with nonzero Fourier coefficients corresponding only to measured points. The large sidelobes of this function cannot be adequately removed by taking the exponential unless very high values of R are used. An alternative explanation is to note that the MEM generates the unmeasured ρ_{mn} by non-linear operations on the

*Table 3 gives details of the missing data in the u-v plane.

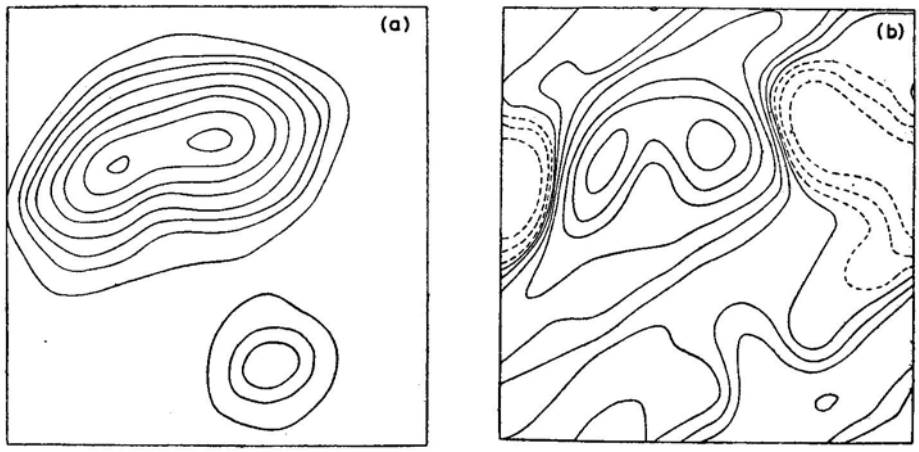

Figure 16. (a) Result of a CLEAN restoration with the model of Fig. 4 When a sector of data in the u –v plane is missing. Details of the missing sector are given in Table 3. (b) Result of the $-B\ln B$ MEN restoration with R = 100 on the same 'sectored' data as in (a). The method is now unable to suppress the sidelobes.

Table 3. Particulars of Figs. 12 and 16.

The plateau in Fig. 12 has the form

$$B(x, y) = 1/[1 + (\text{gaussian function})^{-1}]$$

When the parameters of the gaussian are

strength = e^4 = 54.598
position angle of major axis = 135
rms along major axis = 4.5
rms along minor axis = 2.25

The data in the uv plane used for Fig. 16: for each value of u the range of positive v s is given (of course u, v is accompanied by – u, –v). The points (approximately) form a sector in the u–v plane.

u	$v_{\min}$	$v_{\max}$	u	$v_{\min}$	$v_{\max}$
−4	1	3	0	1	7
−3	1	5	1	1	7
−2	1	6	2	2	6
−1	1	7	3	3	5

Band-limited function $\sigma(x, y)$. In all earlier examples, the extrapolated values of ρ_{mn} were relatively small. However, in Fig. 16, some of the unmeasured ρ_{mn} have large values. To produce these by interpolation needs large non-linearity *i.e.* large R. At very large R, the numerical schemes converge very slowly.

(iii) One of the problems that prevents a deeper understanding of CLEAN is the sequential nature of the method. Schwarz (1979) has shown that the position and strength of each point source identified by CLEAN (with unit gain) can be understood as a least-squares fit to the current map. However, there is no least-squares interpretation of the entire collection of point sources. Because of this we believe one can at most expect to have only an empirical under standing of CLEAN. On the other hand, the MEM is a well-posed mathematical formulation and therefore in principle one should be able to appreciate its properties better. We hope the present paper has made a beginning in this direction.

Acknowledgements

It is a pleasure to thank M. M. Komesaroff for introducing us to the field and R. D. Ekers for discussions about CLEAN and related matters. We are grateful to R. K. Lakshmi and Nambu Ramam for coping cheerfully with the long and much revised manuscript and the numerous drawings.

Appendix A

Uniqueness of the MEM Reconstruction

Burg (1975) has shown that the problem of maximising the entropy $\int f(B(x))\, dx$ (where x is a position vector in a d-dimensional space) keeping certain Fourier co efficients of B fixed has a unique solution if $f''(B)$ is negative. We give here a simplified rederivation of this result.

Let $B_1(x)$ and $B_2(x)$ be two brightness distributions which fit the same set of measurements. We can interpolate between them using a parameter p which goes from 0 to 1, and calculate the entropy $E(p)$ corresponding to the interpolated function

$$B(p) = (1 - P)\, B_1(x) + P\, B_2(x), \tag{A1}$$

$$E(P) = \int f[(1 - P)\, B_1 + P\, B_2]\, dx. \tag{A2}$$

Differentiating Equation (A2) twice with respect to p

$$\frac{d^2}{dp^2} E(p) = \int f''(B(p))\, (B_1 - B_2)^2\, dx \leqslant 0 \text{ if } f''(B) \leqslant 0. \tag{A3}$$

The brightness distribution for each value of p satisfies the measured data since these are linear in B (Equation A1). As we interpolate between two brightness distributions, Equation (A3) shows that the graph of entropy versus p is convex upwards. If we now suppose that there are two maxima of E, we could interpolate between them and there would clearly have to be a minimum in between. Since this contradicts the convexity property just proved, the brightness distribution maximising the entropy is unique.

Appendix B

Limiting Behaviour of the MEM Restoration at High Resolution

Komesaroff, Narayan and Nityananda (1981) showed that one-dimensional MEM reconstructions with $f = \ln B$ approach a sum of δ functions as ρ_0 is lowered (which is equivalent to increasing the resolution parameter R defined in Equation 9). In fact, the limiting map (as $R \to \infty$) is uniquely fixed by the data and positivity, and is independent of the entropy form used. The behaviour in two and higher dimensions can be more complicated as shown by the following example.

Take $\rho_{01} = 1$, $\rho_{11} = 0{\cdot}8$, $\rho_{10} = 0{\cdot}8$. Clearly, the lowest possible value for ρ_{00} is 1. However, even after putting $\rho_{00} = 1$, we can fit the above data with a map of the form $\delta(y)\ b(x)$ where the function $b(x)$ only has to fit one number (*viz.* 0·8). Thus even in the $R \to \infty$ limit, there are many solutions consistent with the data, out of which each entropy selects one.

In this appendix, we draw attention to another unexpected property of many of the forms of MEM in certain dimensions *viz.* the appearance of δ functions in the restorations, over a *range* of values of ρ_0. Although the argument is general, it is convenient to treat the $f = \ln B$ form of MEM in three dimensions and consider a specific example *viz.* $\rho_{100} = \rho_{010} = \rho_{001} = 1$. Clearly, the lowest possible value of ρ_{000} is 1 and for any higher values, it is easy to find nonsingular maps–for example a gaussian like $A \exp [-\alpha(x^2 + y^2 + z^2)]$–which fit the data. The ln B MEM solution for this data set is the reciprocal of a band-limited function (Equation 8).

$$B(x, y, z) = \left(\sigma_0 - \frac{\sigma_1}{3}(\cos 2\pi x + \cos 2\pi y + \cos 2\pi z)\right)^{-1} \tag{B1}$$

where σ_0 and σ_1 are determined by the constraint equations

$$\rho_{000} = \int_0^1\int_0^1\int_0^1 \sigma_0 \frac{dx\,dy\,dz}{\left[1 - \frac{\sigma_1}{3\sigma_0}(\cos 2\pi x + \cos 2\pi y + \cos 2\pi z)\right]}$$

$$\equiv \frac{1}{\sigma_0} I_0\left(\frac{\sigma_1}{\sigma_0}\right), \tag{B2}$$

$$\rho_{100} = 1 = \int_0^1\int_0^1\int_0^1 \frac{\cos 2\pi x\,dx\,dy\,dz}{\sigma_0\left[1 - \frac{\sigma_1}{3\sigma_0}(\cos 2\pi x + \cos 2\pi y + \cos 2\pi z)\right]}$$

$$\equiv \frac{1}{\sigma_0} I_1\left(\frac{\sigma_1}{\sigma_0}\right). \tag{B3}$$

The crucial new feature in 3 dimensions is that the integrals in Equations (B2) and (B3) converge even when $\sigma_1 = \sigma_0$. This is because the denominator behaves as r^2, r being the distance from the point where it vanishes. In 'd' dimensions, we thus have $\int r^{d-1}\,dr/r^2$ which converges for $d \geqslant 3$. At the same time, it is impossible (because of positivity) to make σ_0 less than σ_1. Thus the ratio of ρ_{000} to ρ_{100} is restricted to the range over which the ratio of the two definite integrals defined in Equations (B2) and (B3) can vary. The ratio $(I_1/I_0) = 0$ at $\sigma_1/\sigma_0 = 0$ and increases monotonically to $(0{\cdot}516/1{\cdot}516) = 0{\cdot}34$ at $\sigma_1/\sigma_0 = 1$. Thus, when ρ_{000}/ρ_{00} becomes less than 2·94, there is no solution to the pair of equations (B2) and (B3). Put differently, this example shows that in three (or higher) dimensions, the reciprocal of a band-limited function is not able to fit a set of data with sufficiently low ρ_0, even though these data are perfectly consistent with smooth positive maps. It is easy to

see that the entropy $1/B^n$ will encounter similar problems in d and higher dimensions if $2/(n+1) < d$. Thus, the $(1/B)$ entropy is in trouble in two and higher dimensions, while this can happen for harder entropies even in one dimension.

The question now arises–what is the nature of the solution when ρ_{000} becomes less than the critical value? A deeper study shows that we can still find generalized solutions which consist (for the $f = \ln B$ case) of the reciprocal of a band-limited function plus δ-functions located at the places where the band-limited function vanishes. In the example considered earlier, when $\rho_{000} < 2{\cdot}94$ we seek a solution of the form

$$B(x, y, z) = \frac{1}{\left[\sigma_0 - \frac{\sigma_1}{3}(\cos 2\pi x + \cos 2\pi y + \cos 2\pi z)\right]} + a\,\delta(x)\,\delta(y)\,\delta(z). \tag{B4}$$

We give a non-rigorous justification of Equation (B4). The δ-function makes no contribution to the reciprocal* of (B4), which is therefore still a band-limited function, thus fulfilling the condition for a maximum (Equation 6 of the main text) with respect to variation of the individual Fourier coefficients. We further have to verify that we have a maximum of the entropy with respect to variations in the strength and position of the δ-function. Consider the equations

$$E = \int d\mathbf{x} \ln\left[\frac{1}{\sigma(\mathbf{x})} + \sum a_i\,\delta(\mathbf{x} - \mathbf{x}_i)\right] = \text{maximum}, \tag{B5}$$

$$\rho_{\mathbf{N}} = \int \left[\frac{1}{\sigma(\mathbf{x})} + \sum a_i\,\delta(\mathbf{x} - \mathbf{x}_i)\right] \exp(-2\pi i\,\mathbf{N}\cdot\mathbf{x})\,d\mathbf{x}, \tag{B6}$$

where N is a vector with integer components labelling the Fourier coefficients. Equations (B5) and (B6) represent the quantity E being maximized and the constraints respectively. Again, using one of the standard representations of the δ-function, we can check that the value of E in Equation (B5) is independent of the a_i and x_i. Introducing a Lagrange multiplier for each constraint, we have to investigate the variation of $E + \Sigma\,\lambda_{\mathrm{N}}\mathrm{x}_{\mathrm{N}}$ as we change the function σ (x) by $\delta\sigma$ (x) and the positions and strengths of the δ-functions by $\delta\mathrm{x}_i$ and δa_i respectively. The result is

$$\begin{aligned}\delta\left(E + \mathcal{W}\,\lambda_{\mathbf{N}}\,\mathbf{x}_{\mathbf{N}}\right) = &-\int d\mathbf{x}\,[\delta\sigma(\mathbf{x})/\sigma(\mathbf{x})] \\ &+ \sum_{\mathbf{N}} \lambda_{\mathbf{N}} \left\{\int d\mathbf{x} \exp(-2\pi i\,\mathbf{N}\cdot\mathbf{x})\left(-\frac{\delta\sigma}{\sigma^2} + \sum_i [\delta a_i\,\delta(x - \mathbf{x}_i)\right.\right. \\ &\left.\left. - a_i\,\delta\mathbf{x}_i\cdot\nabla_{\mathbf{x}}\,\delta(\mathbf{x} - \mathbf{x}_i)]\right)\right\} = 0\end{aligned} \tag{B7}$$

*A general nonlinear function of the delta function is not defined, but in the case of the reciprocal we can justify putting it equal to zero by using any one of the sequences (*e.g.* gaussians) which tend to the δ-function.

where the differentiation with respect to x_i has been transferred to x in the last term. Note that Equation (B5) is insensitive to a_i and x_i which appear only in the variation of Equation (B6). The variation with respect to $\delta\sigma$ gives

$$\sigma(\mathbf{x}) = -\sum \lambda_{\mathbf{N}} \exp(-2\pi i\, \mathbf{N}\cdot\mathbf{x}) \tag{B8}$$

implying that σ(x) is a band-limited function as before. Varying with respect to x_i in Equation (B7) gives

$$\nabla\left(\sum_{\mathbf{N}} \lambda_{\mathbf{N}} \exp(-2\pi i\, \mathbf{N}\cdot\mathbf{x})\right)_{\mathbf{x}=\mathbf{x}_i} = \nabla\sigma(\mathbf{x}_i) = 0. \tag{B9}$$

According to Equation (B9), the δfunctions can only be located at stationary points of σ(x). The variation of Equation (B7) with respect to a_i gives

$$\sum_{\mathbf{N}} \lambda_{\mathbf{N}} \exp(-2\pi i\, \mathbf{N}\cdot\mathbf{x}_i) = \sigma(\mathbf{x}_i) = 0. \tag{B10}$$

Equation (B10) restricts the locations still further to the zeros of σ(x) [at these places Equation (B9) is automatically fulfilled since σ(x) is a nonnegative function].

As an example, we consider the problem $\rho_{100} = \rho_{010} = \rho_{001} = 1$, $\rho_{000} = 2$. The required solution is of the form (B4). To fit the data we require that

$$\frac{1}{\sigma_0} I_0(1) + a = 2, \tag{B11}$$

$$\frac{1}{\sigma_0} I_1(1) + a = 1, \tag{B12}$$

where a is the strength of the δ-function, located at the origin by the symmetry of the data. I_0 and I_1 defined in Equations (B2) and (B3), have the values 1·516 and 0·516. Equations (B11) and (B12) then give $\sigma_0 = \sigma_1 = 1$, a =0·484.

The appearance of δ-functions in the solution of a variational problem as a parameter is varied, has a well-known physical counterpart in Bose condensation (see, for example, the text by Landau and Lifshitz 1969), where the number of particles with momentum p, is given by

$$n(P) = \{\exp[(P^2/2m - \mu)/k_B T] - 1\}^{-1}$$

For temperature T above a value T_0, the normalisation of $n(p)$ is maintained by adjusting μ. At T_0, μ becomes zero, but the integral of $n(p)$ still converges in three dimensions. For T less than T_0 we can no longer vary μ to obtain the correct number of particles, since it remains fixed at zero. The excess particles are accommodated in a δ-function at p=0. The quantity being maximised in this problem is the (thermodynamic) entropy, with the total energy and number of particles as constraints.

The arguments discussed above are true for the problem in which x, y,... are continuous variables. In any computational scheme, we are dealing with a discrete

set of points and a summation. Unlike an integral, a sum diverges if the value at any given point approaches infinity, however weakly. Thus, such a discrete computational scheme would be equivalent, in the example considered, to solving the equations (B13) and (B14) below instead of (B2) and (B3).

$$\rho_{000} = \frac{1}{N^3} \sum_{p,q,r=0}^{N-1} \frac{1}{\left[\sigma_0 - \frac{\sigma_1}{3}\left(\cos\frac{2\pi p}{N} + \cos\frac{2\pi q}{N} + \cos\frac{2\pi r}{N}\right)\right]}, \tag{B13}$$

$$\rho_{100} = \frac{1}{N^3} \sum_{p,q,r=0}^{N-1} \frac{\cos(2\pi p/N)}{\left[\sigma_0 - \frac{\sigma_1}{3}\left(\cos\frac{2\pi p}{N} + \cos\frac{2\pi q}{N} + \cos\frac{2\pi r}{N}\right)\right]}. \tag{B14}$$

We now see that the ratio ρ_{000}/ρ_{100}can vary from ∞ to 1 as (σ_1/σ_0) varies from 0 to 1, and there is no lower limit for ρ_{000} other than that set by positivity. However, one expects, even in the *discrete* case, that when r_{000} becomes less than the critical value below which there is no solution in the *continuous* case, there should be some qualitative differences in the reconstructed distribution. We conjecture that there will be an anomalous sensitivity to the grid size since the discrete analogue of the δ-function has a height varying inversely with the grid size.

Appendix C

An apparently straightforward generalization of the ln$B$ form of the MEM to two or more dimensions was given by Newman (1977, 1978). His starting point was the elegant one-dimensional form due to Burg (1967) in which B is expressed as the reciprocal of a band-limited function (as in Equation 8). This band-limited, positive, function is in turn factorised into two complex conjugate terms, one with positive and the other with negative frequencies. That is

$$B(x) = \frac{1}{\sum_{n=-N}^{N} \sigma_n \exp(2\pi i n x)} = \frac{1}{\left|\sum_{n=0}^{N} \alpha_n \exp(2\pi i n x)\right|^2}. \tag{C1}$$

In the one-dimensional case, given $\rho_0, \rho_1 \ldots \rho_N$, the nonlinear equations (5 and 6) for σ_n ($2N + 1$ real unknowns) reduce to a system *of linear* equations for the quantities α_n in the factorised form (C1) (N complex plus one real unknown).

In two dimensions, Newman (1977) writes by analogy

$$B(x,y) = \frac{1}{\sum_{m,n=-N}^{+N} \sigma_{mn} \exp[2\pi i(mx + ny)]} = \frac{1}{\left|\sum_{m,n=0}^{N} \alpha_{mn} \exp[2\pi i(mx + ny)]\right|^2}. \tag{C2}$$

He presents a system of linear equations to solve for α_{mn} in terms of ρ_{mn} ($-N \leqslant m,n \leqslant N$). There are now $(2N+1)^2$ real data in the ρ_{mn}. However, since the α_{mn} are restricted to positive frequencies, there are only $2[(N+1)^2 - 1] + 1$ real free parameters in the factorised form (C2). Therefore, a general band-limited function of x and y cannot be factorised and the solution (C2) cannot fit a general data set (of ρ_{mn}'s). The failure of factorisation in two dimensions has been noted by Burg (quoted by Woods 1972) but apparently ignored in later discussions (Newman 1978, van Schooneveld 1979).

The difficulty with Newman's solution to the multidimensional MEM problem can also be realised by considering the following alternative distinct factorised form

$$B(x,y) = \frac{1}{\left| \sum_{n=0}^{-N} \sum_{m=0}^{N} \beta_{mn} \exp\left[2\pi i(mx+ny)\right] \right|^2}. \qquad \text{(C3)}$$

Here, the allowed frequencies mn occupy the fourth quadrant of the m,n plane instead of the first (as in Equation C2). By symmetry, we must be able to find a general solution of the type (C3) if there is one of the type (C2). However, the true MEM solution is unique and is thus not of the form (C2) or (C3).

We present below a simple example illustrating the failure of Newman's solution to fit the data. Table A1 gives a two dimensional autocorrelation measured at the points (0,0), (0,1) (1,0), (1,1) and (1, –1). The α and β coefficients corresponding to these ρ's were computed using the method described by Newman (1977) and the corresponding brightness distributions were transformed to obtain the autocorrelations shown in Table A1. As expected, these do not agree with the original data. Newman (1978) has suggested that except for 'pathological' cases, his method will give the MEM solution. The simple arguments and example given above show that just the opposite is true.

Table Al. A test of the two-dimensional MEM scheme proposed by Newman (1977). The α and β Solutions represent two variants of his method described by Equations (C2) and (C3).

True	α solution	β solution
1·0	1·079	0·995
0·3	0·417	0·291
0·2	0·338	0·186
0·1	0·181	0·055
−0·2	0·131	−0·205

References

Ables, J. G. 1974, *Astr. Astrophys. Suppl. Ser.*, **15,** 383.

Bhandari, R. 1978, *Astr. Astrophys.*, **70,** 331.

Bryan, R. K., Skilling, J. 1980, *Mon. Not. R. astr. Soc*, **191,** 69.

Burg, J. P. 1967, in *Annual Meeting of the International Society of Exploration Geophysicists*, Reprinted in *Modern Spectrum Analysis*, Ed. D. G. Childers, IEEE Press, New York (1978) p. 34.

Burg, J. P. 1975, *Ph D thesis,* Stanford University.

Fletcher, R., Reeves, C. M. 1964, *Comput. J.*, **7,** 149.

Gull, S. F., Daniell, G. J. 1978, *Nature*, **272,** 686.

Gull, S. F., Daniell, G. J. 1979, in *Image Formation from Coherence Functions in Astronomy*, Ed. C. van Schooneveld, D. Reidel, Dordrecht, p. 219.

Gull, S. F., Skilling, J.1982, *Preprint.*
Högbom, J. A. 1974, *Astr. Astrophys. Suppl. Ser.*, **15,** 417.
Högbom, J. A. 1979, in *Image Formation from Coherence Functions in Astronomy*, Ed. C. van Schooneveld, D. Reidel, Dordrecht, p. 237.
Kikuchi, R., Soffer, B. H. 1977, *J. Opt. Soc. Am.*, **67,** 1656.
Komesaroff, M. M., Lerche, I. 1979, in *Image Formation from Coherence Functions in Astronomy.* Ed. C. van Schooneveld, D. Reidel, Dordrecht, p. 241.
Komesaroff, M. M., Narayan, R., Nityananda, R.1981, *Astr. Astrophys.*, **93,** 269.
Landau, L. D., Lifshitz, E. M. 1969, *Statistical Physics*, 2 edn Pergamon Press, Oxford, p. 159.
Newman, W. I. 1977, *Astr. Astrophys.*, **54,** 369.
Newman, W. I. 1978, *Astr. Astrophys.*, **70,** 409.
Parzen, E. 1968, in *Multivariate Analysis*, Vol. 2, Academic Press, New York.
Ponsonby, J. E. B. 1973, *Mon. Not. R. astr. Soc.*, **163,** 369.
Ponsonby, J. E, B. 1979, in *Image Formation from Coherence Functions in Astronomy*, Ed. C. van Schooneveld, D. Reidel, Dordrecht, p. 235.
Pye, J. P., Pounds, K. A., Rolf, D. P., Seward, F. D., Smith, A., Willingale, R. 1981, *Mon. Not. R, astr. Soc.*, **194,** 569.
Schwarz, U. J. 1979, in *Image Formation from Coherence Functions in Astronomy*, Ed. C. van Schooneveld, D. Reidel, Dordrecht, p. 261.
Subrahmanya, C. R. 1979, in *Image Formation from Coherence Functions in Astronomy*, Ed. C. van Schooneveld, D. Reidel, Dordrecht, p. 287.
Subrahmanya, C. R.1980, *Bull. astr. Soc. India*, **8,** 5.
van den Bos, A. 1971, *IEEE Trans. Inf. Theory*, **17,** 493.
van Schooneveld, C. 1979, in *Image Formation from Coherence Functions in Astronomy,* Ed. C. van Schooneveld, D. Reidel, Dordrecht, p. 197.
Willingale, R. 1981, *Mon. Not. R. astr. Soc.*, **194,** 359.
Woods, J. W. 1972, *IEEE Trans. Inf. Theory*, **18,** 232.

J. Astrophys. Astr. (1982) **3,** 451–463

Near Infrared Observations of some of the IRC Sources*

K. V. K. Iyengar *Tata Institute of Fundamental Research*, *HomiBhabha Road*, *Bombay 400005*
F. Strafella *Istituto di Fisica, Universita*, *I-73100, Lecce*, *Italy*
D. Lorenzetti *Istituto Plasma Spazio*, *CNR*, 00044, *Frascati*, *Italy*
C. B. Cosmovici *Space Research Group* (*AWF*), *DFVLR D-8031*, *Wessling*, *F.R. Germany*

Received 1982 April 12; accepted 1982 September 29

Abstract. Using an Infrared photometer with InSb photovoltaic detector at the 182cm Copernicus telescope of the Asiago Observatory, Italy, we have measured the *JHKL' M* magnitudes of 12 IRC sources 7 of which are very late type stars with $[I_{CIT} - K]$ greater than 5 magnitudes. These data have been fitted to blackbody distributions to obtain their effective temperatures. The present data, in combination with other available photometric data at longer wavelengths seems to indicate excess emission at 11 μm from sources 10066, 10510 and 10234, and at 19·8 μm from source 20052. The source 60098 shows extreme infrared colours.

Key words: IRCCIT sources–broadband infrared photometry–infrared excess

1. Introduction

We have measured the *JHKL'M* magnitudes of 12starsfromthe IRC-CIT two-micron sky survey (Neugebauer and Leighton 1969). Seven of these have $[I_{CIT} - K] > 5$ magnitudes. The photometric data on these extremely red objects in the near-infrared bands are rather scanty. Our interest was to determine the effective temperatures of these sources corresponding to their photometric magnitudes and also to use these photometric data with similar data at longer wavelengths from the AFGL Sky Survey of Price and Walker (1976), from Dyck, Lockwood and Capps (1974) and from Strecker and Ney (1974) to derive information on infrared excess (if any) from these sources.

*Work carried out when the first author was a guest scientist at Max Planck-Institut für Extraterrestrische Physik, *Garching* FRG.

2. Observations

We used an Infrared photometer with InSb photovoltaic detector from SBRC Inc., cooled by liquid nitrogen at the Cassegrain focus of the 182-cm, f/9 Copernicus telescope of the Asiago Observatory at Italy. The preamplifier used a cooled FET mounted on the cold work surface of the dewar. The NEP of the detector was 1×10^{-15} W $(\mathrm{Hz})^{-1/2}$ at 5 μm. Interference filters from Optical Coating Laboratories Inc., were used to define the *JHKL'M* photometric bands. Our L' and M bands correspond to effective wavelengths of 3·85 and 4·70 μm, respectively. The observations were carried out on the nights of 1980 November 1923, using a field of view of 10 arcsec. The beam was chopped in declination at 20 Hz and the throw was set at 18 arcsec. α Ceti, α CMa, α Tau, β And and β CMa were used for calibration of the infrared fluxes. The fluxes of these stars in our photometric bands were obtained from the data of Strecker, Erickson and Witteborn (1979). To keep the corrections due to differences in the air mass corresponding to the observation of the calibration star and the programme stars small, the observations were all carried out at an air mass of 1·2 ± 0·2.

3. Nature of the programme sources

We describe briefly in this section the nature of the programme sources (listed in Table 1) before we proceed to discuss analysis of their photometric data in Section 4, as the nature of these sources has a close bearing on the method chosen for the analysis of the data.

3.1 *Spectral Type and Variability*

3.1.1 *Sources with* $[I_{\mathrm{CIT}} - K] > 5$

Sources 10061,10066 and 10234 are Mira variables of Type M with periods ~ 350 days and spectral types ranging from M 5·0e–M 9·0e as a function of their phase. 10061 appears to be variable in the K band (Neugebauer and Leighton 1969). Source 10510 is identified with the variable SVS 102147 in the AFGL Sky Survey (Price and Walker 1976). The 4·2μm and 11·00 μm observations of 10510 from this survey seem to indicate slight variability even at these wavelengths. The CIT Sky Survey of Neugebauer and Leighton (1969) showed it to be variable in the K band. Source 20052 is classified as a star of spectral type M 8·1 (Dyck, Lockwood and Capps 1974). No information is available on the spectral type of the sources 10120 and 30091. All these sources have galactic latitude $|\ b^{\mathrm{II}}| > 10°$ save 10120 which is in the galactic plane with $b^{\mathrm{II}} = 0°.6$.

3.1.2 *Sources with* $[I_{\mathrm{CIT}} - K] < 5$

Of these five sources only 60098 is a variable. It is identified as V499 Cas by Price and Walker (1976). No information is available on its spectral type. The spectral types of the other four sources are known.

Table 1. Infrared magnitudes of programme sources.

IRC No. GL No.	Present observations	IRC catalogue	GL catalogue	Strecker and Ney	Spectral type and luminosity class
	[J] [H] [K] [L'] [M]	[I_{CIT}] [I_J] [K] [$I_{CIT}-K$]	[4·2] [11·0] [19·8]	[2·3] [3·5] [4·8] [8·6] [10·7]	
(1)	(2)	(3)	(4)	(5)	(6)
10061	4·04	8·47 ± 0·30			M5 ·0e–M8 · 0e[a]
	3·12	6·92 ± 0·34			M
	2·66	3·04 ± 0·11$_V$			
	1·9	5·43 ± 0·32			
	2·0				
10066	3·04	7·10 ± 0·14	0·6 ± 0·3		M6·5e –M8·5e[a]
608	2·11	5·49 ± 0·16	−1·4 ± 0·4		M
	1·50	1·45 ± 0·06			
	0·6	5·65 ± 0·15			
	0·3				
10120	4·08	7·83 ± 0·15		2·6 ± 0·1	
	3·00	6·35 ± 0·17		2·2 ± 0·1	
	2·55	2·69 ± 0·06		2·2 ± 0·1	
	2·0	5·14 ± 0·16		(1·3)	
	2·4			(1·4)	
10234	3·72	8·35 ± 0·24	1·0 ± 0·3		M7·5e–M9·0e[a]
1441	2·74	6·71 ± 0·26	−0·9 ± 0·4		M
	2·29	2·59 ± 0·08			
	1·2	5·76 ± 0·25			
	1·3				
10510	2·76	8·15 ± 0·75	1·0 ± 0·3		M7[b]
2851	1·70	6·39 ± 0·75	−1·3 ± 0·4		
	1·11	1·92 ± 0·06$_V$			
	0·3	6·23 ± 0·75			
20052	2·75	6·68 ± 0·09	0·8 ± 0·3	1·3 ± 0·1	M8·1[c]
414	1·67	5·18 ± 0·16		0·9 ± 0·1	
	1·25	1·44 ± 0·09	−3·1 ± 0·4	0·9 ± 0·1	
	0·9	5·24 ± 0·13		(0·8)	
	0·8			−0·4 ± 0·2	
30091	3·59	6·99 ± 0·13			
	2·39	5·52 ± 0·15			
	1·77	1·86 ± 0·06			
	1·3	5·13 ± 0·14			
30180	3·83	5·67 ± 0·09	1·4 ± 0·3		Mb[d]
4071	2·76	4·62 ± 0·13			
	2·72	2·18 ± 0·07			
	2·4	3·49 ± 0·11			
	2·2				

Table 1. Continued.

IRC No. GL No.	Present observations	IRC catalogue	GL catalogue	Strecker and Ney	Spectral type and luminosity class
	[J]	[I_{CIT}]	[4·2]	[2·3]	
	[H]	[I]	[11·0]	[3·5]	
	[K]	[K]	[19·8]	[4·8]	
	[L']	[$I_{CIT}-K$]		[8·6]	
	[M]			[10·7]	
(1)	(2)	(3)	(4)	(5)	(6)
50060	1·95	3·37 ± 0·05	0·8 ± 0·3		K4 III[d]
4022	1·26	2·65 ± 0·18			
	1·03	1·13 ± 0·05			
	0·8	2·24 ± 0·07			
	0·6				
60098	2·47	7·16 ± 0·11	1·8 ± 0·5		
4022	2·97	5·84 ± 0·15			
	2·50	2·63 ± 0·07			
	2·1	4·53 ± 0·13			
	2·8				
60133	2·42	5·24 ± 0·06	1·2 ± 0·3		M2[d]
531	1·75	4·14 ± 0·10			
	1·45	1·56 ± 0·06			
	1·3	3·68 ± 0·08			
	1·7				
70073	3·79	5·11 ± 0·07	1·6 ± 0·3		K0[d]
4067	2·94	4·34 ± 0·14			
	2·82	2·67 ± 0·09			
	2·7	2·44 ± 0·11			
	3·2				

Notes:
1. All the IRC sources referred to in this study are positive declination objects from the CIT-IRC Catalogue of Neugebauer and Leighton (1969).
2. Spectral types:
   [a]Lockwood (1972).
   [b]Wilson and Barett (1972).
   [c]Dyck, Lockwood and Capps (1974).
   [d]Neugebauer and Leighton. (1969).
3. Figures in parenthesis indicate 3σ upper limits from Strecker and Ney (1974).
4. Letter *V*, with the colour in a particular band from IRCCIT Survey, indicates variability in that band (Neugebauer and Leighton 1969).

3.2 *Luminosity Class of the Sources*

The Mira variables are late-type giants. The observed *JHKL' M* magnitudes of the other sources (whose spectral type is known) are untenably high to arise from main-sequence stars. They are likely to be giants or supergiants.

3.3 *Distance to the Sources*

The distances to these sources are not known. The knowledge of their spectral types combined with the constraint on their luminosity class, however, enables us to set upper limits to their distances from the solar neighbourhood. They are in general within a few kiloparsecs from the Sun.

4. Analysis of data and results

In Table 1 are presented the IRC number of the source and GL number (where such Identification exists), photometric data from (i) the present observation, (ii) the IRC Catalogue of Neugebauer and Leighton (1969), along with I_Js obtained from the colour transformation discussed below, (iii) the GL Catalogue of Price and Walker (1976), (iv) Strecker and Ney (1974), and spectral type. Errors on the *J*, *H* and *K* magnitudes from this observation are $\lesssim \pm 0{\cdot}05$ and on *L′* and *M* magnitudes $\lesssim \pm 0{\cdot}2$.

The I_{CIT} magnitude of the CIT survey (Neugebauer and Leighton 1969) is different from the I_J magnitude of Johnson (1966), although the *K* magnitude of the CIT survey is the same as that of Johnson. We have derived the colour transformation relation

$$[I_J - K] = 0{\cdot}74\ [I_{CIT} - K] - 0{\cdot}14 \tag{1}$$

from the data presented in Fig. 8 of Neugebauer and Leighton (1969) and used it to determine the I_J's corresponding to the I_{CIT}'s of Neugebauer and Leighton (1969).

IRC stars with $[I_{CIT} - K] > 5$, are in general cool giant stars. Their atmospheres are extended and contain molecules. Models of atmospheres of cool stars have been published by Johnson (1974). For a realistic comparison of these model predictions with observations, one needs photometric data with a resolution of 2 per cent or better in the 1–5 μm region (obtained above most of the earth's atmosphere). As our data is limited to observations from ground in the five broad photometric bands *JHKL'M*, we have not tried to compare them with predictions of model atmospheres from Johnson (1974).

We have fitted the photometric data in the *JHKL'M* bands (obtained at the same epoch) to blackbody distributions using effective temperature and interstellar extinction (which is a function of the distance to the sources) as parameters.

The interstellar extinction A_λ at wavelength λ in the direction of the source was estimated using the relation

$$A_\lambda (r) = a_{0\lambda}\, z_0\, \mathrm{cosec}\,|b|\, [1 - \exp(-r \sin|b|/z_0)]. \tag{2}$$

Here, $a_{0\,\lambda}$ is the interstellar extinction coefficient in the galactic plane at wavelength λ, z_0 is the scale height of the obscuring matter, *r* is the distance to the source from the Sun (both in parsecs) and *b* is the galactic latitude. We assumed $z_0 = 140$ pc and $\alpha_{0\lambda} = 0{\cdot}8 \times 10^{-3}$ mag pc^{-1} in the *V* band in accordance with Allen (1973). We used the theoretical curve No. 15 of Van de Hulst (quoted by Johnson 1968) to evaluate $\alpha_{0\lambda}$ as a function of λ. It should be noted that the value assumed for $a_{0\lambda}$ is a statistical mean value for extinction in the galactic plane and is likely to differ from this value as a function of direction.

The temperatures obtained from this fitting procedure are the best fit values within ± 50 K for these sources.

In Table 2 are listed the source number, their celestial and galactic coordinates, the variable name and other relevant parameters and the best fit values of distance and temperature. These fits appear extremely insensitive to distance.

Table 2. Temperature from fits of blackbody distributions to photometric data obtained in the present investigation.

IRC No. GL No.	RA. (1950) l^{II}	Dec. (1950) b^{II}	Variable name Period (d) ⟨Max⟩ ⟨Min⟩	Parameters obtained from blackbody fits to data Distance (pc)	Temperature (°K)
(1)	(2)		(3)	(4)	
10061	$04^h\ 26^m\ 29^s$	$+09°\ 50'·6$	S Tau[a]	600	2575
	185°·6	−22°·5	373·3		
			10·2		
			15·3		
10066	04 35 30	+08 13·6	RX Tau[b]	100	2300
608	188·5	−24·7	335·1		
			9·6		
			14·0		
10120	06 21 24	+14 15·2		1900	2700
	197·2	0·6			
10234	10 50 58	+13 59·1	W Leo[b]	200	2475
1441	233·0	59·4	385·5		
			9·8		
			14·2		
10510	22 04 52	+11 39·3	SVS 102147	25	2225
2851	71·9	−34·3			
20052	02 58 43	+21 36·1		200	2450
414	158·9	−31·8			
30091	04 34 28	+32 31·5		25	2075
	168·4	− 9·6			
30180	07 17 04	+31 27·1		25	2975
4071	186·9	19·4			
50060	02 22 15	+50 30·8		25	3350
4022	137·8	−9·4			
60098	02 47 00	+60 32·8	V499 Cas[b]	25	5775
4026	137·0	1·2			
			13·4†		
			14·7†		
60133	03 51 43	+57 31·6		1900	3850
	145·6	3·2			
70073	07 00 14	+70 48·9		550	3600
	144·6	26·7			

Notes:

⟨Max⟩ and ⟨Min⟩ in column 3 correspond to mean maximum and minimum magnitudes in the visual band as given in

[a]Kukarkin *et al.* (1969),

[b]Kukarkin *et al.* (1974).

†maximum and minimum photographic magnitudes as given in Kukarkin *et al.* (1974).

Photometric data from this study, along with data from other observers (corrected for extinction on the basis of the best fit distances) are presented in Fig. 1 for sources

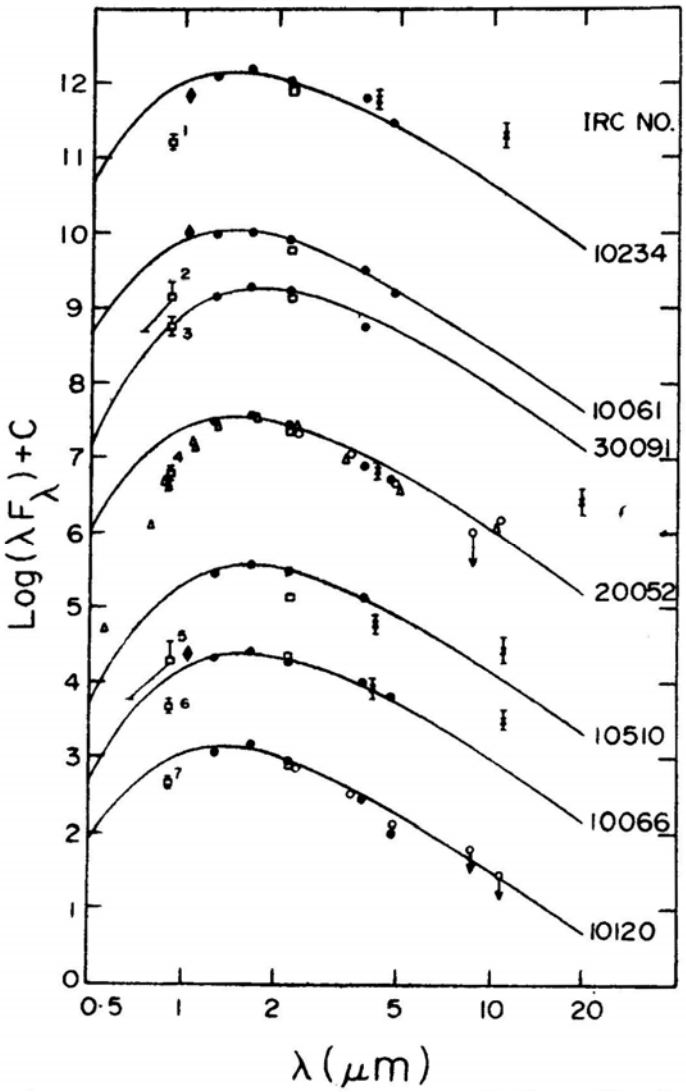

Figure 1. Flux distributions (W cm^{-2}) of programme sources with $[I_{CIT} - K] > 5$. The constant C, added to the ordinate to separate the spectra of the sources has the values 17, 18, 19, 21, 23, 24 and 26 for the sources 10120, 10066, 10510, 20052, 30091, 10061 and 10234 respectively.

● Present observations.

□ at 0·9 μm (obtained from transformation of I_{CIT} to I_J) and 2·2 mm from Neugebauer and Leighton (1969). The numbers 1, 2...7, on the 0·9 μm data points refer to sources 10234, 10061, 30091, 20052, 10510, 10066, and 10120 respectively.

× at 4·2, 11·0 and 19·8 μm from the AFGL Sky Survey (Price and Walker 1976).

○ at 2·3, 3·5, 4·8, 8·6 and 10·7 μm from Strecker and Ney (1974).

Δ at 0·55, 0·78, 0·87, 0·88, 1·04, 1·05, 1·25, 1·65, 2·2, 3·4, 5·0 and 10·2 μm from Dyck, Lockwood and Capps (1974).

ϕ at 1·035 μm are from the narrow band photometric data (Lockwood 1972) of the Mira variable sources for the phase corresponding to the time of our observation. The line through the data points of each source is the blackbody fit to the data. The flux predicted by the blackbody distribution at 2·2 μm has been normalised in each case to the observational data at that wave length. All the data points have been corrected for extinction as discussed in the text.

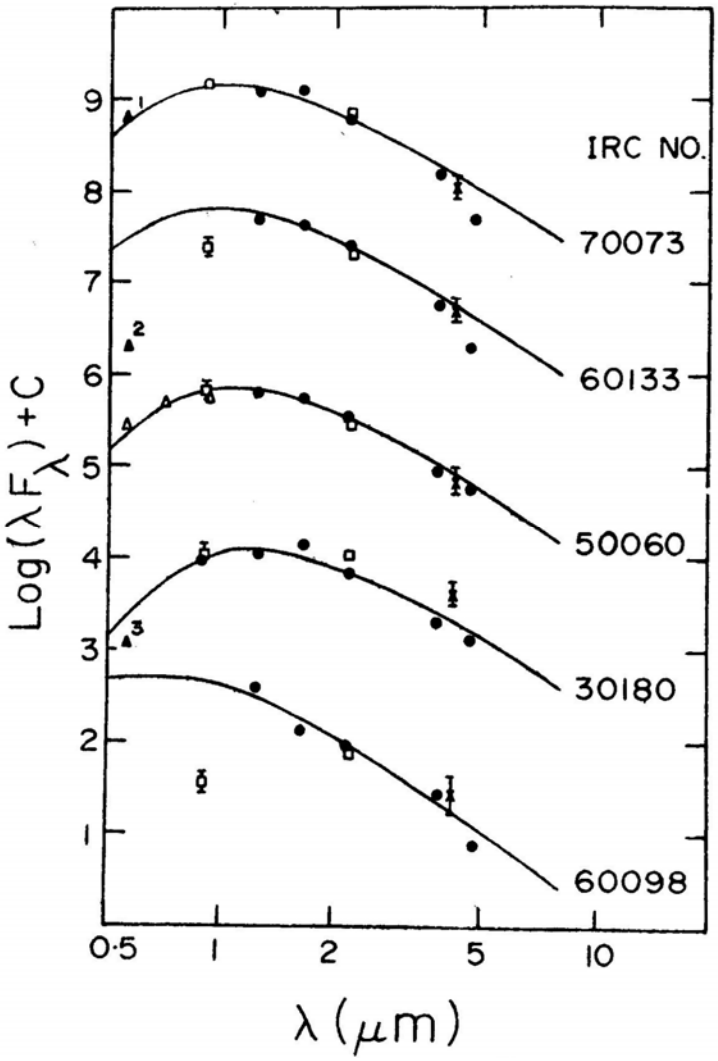

Figure 2. Flux distributions (W cm^{-2}) of programme sources with $[I_{CIT} - K] < 5$. The constant C (referred to in caption to Fig. 1) has the values 16, 18, 19, 21 and 23 for the sources 60098, 30180, 50060, 60133 and 70073 respectively. The data points Δ refer to 0·55, 0·70 and 0·90 μm magnitudes of IRC 50060 (BS 699) from Johnson *et al.* (1966). The symbols ▲^{1}, ▲^{2}, and ▲^{3} refer to the data points derived from the V magnitudes quoted by Neugebauer and Leighton (1969), for the sources 70073, 60133 and 30180, respectively. The symbols ●, □ and × along with the rest of the details are.the same as in Fig. 1.

with $[I_{CIT} - K] > 5$ and in Fig. 2 for sources with $[I_{CIT} - K] < 5$. The solid lines through the data points are the best fit blackbody distributions to the observational data from this work only. Data from other observers were not included for effecting blackbody fits, as some of the sources of this study are Mira type variables and their spectral types and magnitudes, depend sensitively on their phases at the epoch of observation.

It is seen from Fig. 1 that the observed photometric magnitudes, in the 1·25–4·7 μrn range are in. general well accounted for by blackbody distributions. A slight excess

of emission is observed at 11·0 μm from sources 10066,10510 and 10234. However, these 3 sources are Mira variables. As the data under comparison are from different authors obtained at different epochs using different techniques, one cannot exclude the possibility that the observed excess over the blackbody fits to the present data is not due to either time variation of these sources or systematic differences in the observation techniques. Excess emission from source 20052 is observed at 19·8 μm without any corresponding excess at 11·0 μm. It is a late-type M giant but not a Mira variable. The lack of excess at 11·0 μm is rather intriguing.

The flux at 0·9 μm (I_J, or I band of Johnson) for the variable as well as the nonvariable sources is generally lower than the blackbody distribution except in the case of source 30091. The mean visual flux (corrected for interstellar extinction) at the maximum brightness of the Mira variable sources is also found to be 1·3 ±0·1 mag fainter than the flux predicted by the blackbody fit to their infrared photometric data. These differences owe their origin to the line and band absorption that dominates the visual spectrum of late-type giants and which departs significantly from a blackbody curve.

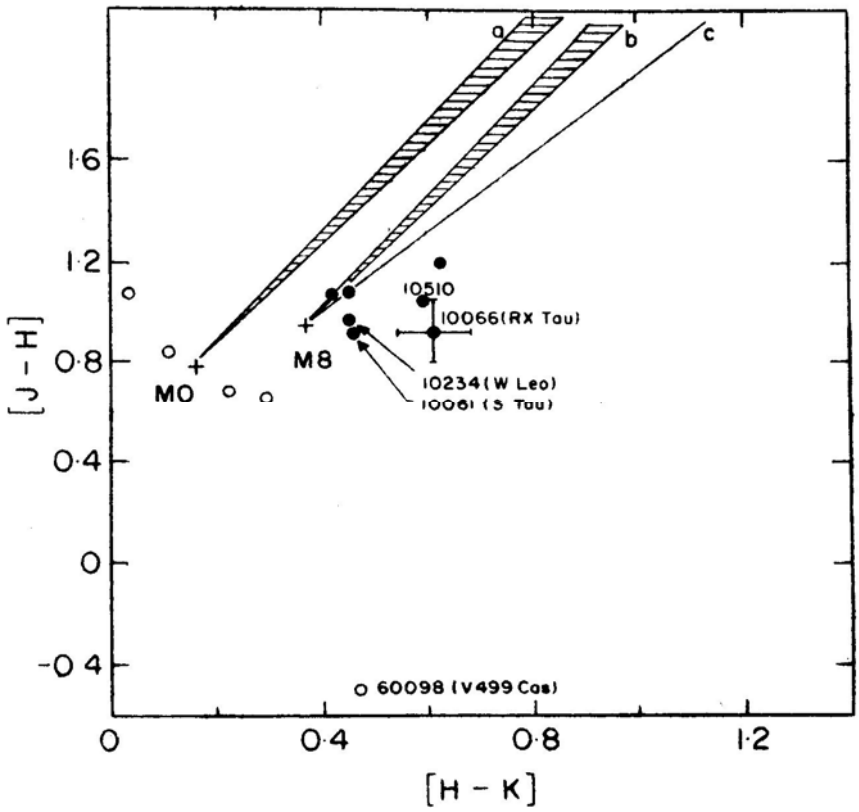

Figure 3. [$H - K$] versus [$J - H$] colour-colour diagram. The filled points and the open circles refer to sources for which [$I_{CIT} - K$] is greater than 5 and less than 5 respectively. The hatched, regions 'a' and 'b' are the interstellar reddening trajectories (for M0 and M8 giants) with slope $E(J - H)/E(H - K)$ = 2·09 ± 0·10 (Jones and Hyland 1980). Line 'c' is the reddening line with slope $E(J - H)/E(H - K)$ = 1·6, from Van de Hulst (Tapia 1981) for M8 giants. The error bars shown for IRC 10066 indicates the typical errors on the data points.

4.1 *Colour-Colour Diagrams*

A colour-colour plot of [$J - H$] versus [$H - K$] for the programme sources is presented in Fig. 3. The value for the colour excess ratio $E(J - H)/E(H - K)$ appears to be highly uncertain. The present situation in this regard is detailed below.

Becklin *et al.* (1978) obtain a value of 1 50 ± 0·10 for galactic centre objects. Elias (1978a) obtains a value of 1 56 ± 0 05 for field stars in Taurus dark cloud and Elias (1978b) obtains a value of 1 60 ± 0 04 for objects in Ophiuchus dark cloud. Jones and Hyland (1980) obtain a value of 2·09 ± 0 10 for some selected group of objects covering a wide range of colour values extending up to 4 81 in [$J - H$] and 2·18 in [$H - K$]. Jones *et al.* (1980) obtain a value of 2·12 ± 0 04 for objects in Coalsack.

Frogel *et al.* (1978) adopt for giants of spectral type MO and M8, mean values of 0 74 and 0 89 for the [$J - H$] colour and 0 16 and 0 37 for the [$H - K$] colour, respectively. Their J band is different from that of Johnson. On transformation to the Johnson's system these result in ($J - H$) values of 0 81 and 0·97 for MO and M8, respectively. The hatched regions (a) and (b) in Fig. 3 are the interstellar reddening trajectories corresponding to $E(J - H)/E(H - K)$ value from Jones and Hyland (1980) for MO and M8 type giants, respectively. The line (c)corresponds to $E(J - H)/E(H - K)$ 1-6 from curve No. 15 of Van de Hulst, (quoted by Tapia 1981). The [$J - H$] and [$H - K$] values of our programme stars are limited to a narrow range of ∼1·2 and ∼1·6 respectively. The points corresponding to sources 10066, 10510 and 60098 fall outside the reddening line. Sources 10066 and 10510 seem to have excess emission at 11·0 μm. It is likely that their excess in [$H - K$] relative to [$J - H$] is due to infrared emission that might be arising from circumstellar material around them.

The blackbody fit to the *JHKL'M* photometric data of IRC 60098 (V 499 Cas) yields a temperature of 5775 K, which corresponds to that of a giant star of spectral type GO – G5. The observed 0·9 [cm flux is lower than that predicted by its effective temperature by about 3 magnitudes. The amplitude of its variability in the photographic band is ∼1·3 mag and is much less than that of Mira-type variables. Its unusual colours appear to be due to its early spectral type, variability, and high degree of extinction at short wavelengths.

In Fig. 4 is presented the colour-colour plot of [$H - K$] versus [$K - L'$] for the programme sources. The value of the colour excess ratio $E(H - K)/E(K - L)$ is again highly uncertain and covers a wide range of values from 0·9 ± 0· 4 to 2·08 ± 0·13, as summarised by Tapia (1981).

Lee (1970) gives [$H - K$] and [$K - L$] values for an M6 III star as 0·33 and 0·30 mag respectively. From a linear extrapolation of his data for M0 III – M6 III stars one finds for an M7 III star [$H - K$] 0·36 and [K – L] = 0·35 and for an M8 III star [$H - K$] = 0·39 and [$K - L$] = 0·40. Jones and Hyland (1980) obtained a value for the colour excess ratio $E(H - K)/E(K - L)$ = 1·47 ± 0·10 for a few selected objects in close agreement with the value 1·5 from Becklin *et al.* (1978). The interstellar reddening trajectory corresponding to the slope $E(H - K)/E(K - L')$ = 1·47 ± 0·10 passing through the data points for M and K type giants is the hatched region shown as (a) in Fig. 4. Line (b) corresponds to $E(H - K)/E(K - L')$ = 1·3 from curve No. 15 of Van de Hulst (as quoted by Tapia 1981). This reddening trajectory seems to account fairly well for the observed colours of the programme

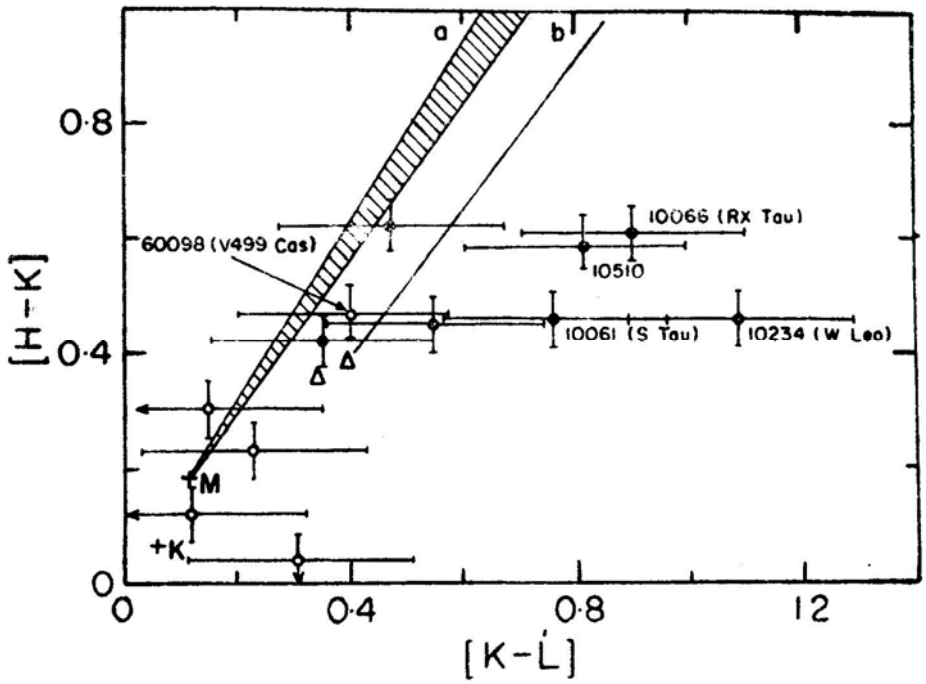

Figure 4. [$H - K$] versus [$K - L$] colourcolour diagram. The symbols referring to the data points are the same as in Fig. 3. The hatched zone 'a' and the line 'b' are the interstellar reddening trajectories with slope $E(H - K)/E(K - L') = 1{\cdot}47 \pm 0{\cdot}10$, (Jones and Hyland 1980) and $E(H - K)/E(K - L') = 1{\cdot}3$ from Van de Hulst (Tapia 1981). The points corresponding to K and M giants (from Fig. 2 of Jones and Hyland 1980) are indicated by the symbol + and the points corresponding to M7 and M8 giants (obtained from Lee (1970), as explained in the text) are indicated by the symbol Δ.

sources, save those of S Tau, RX Tau, W Leo and SVS 102147. The phase and spectral type at the time of our observation of S Tau, RX Tau, and W Leo, deduced from the time of zero phase and mean period as tabulated by Lockwood (1972) are 0·11 and M5·0,0·72 and M8·5 and 0·63 and M9·0, respectively. Similar data is not available for SVS 102147.

The late spectral types of RX Tau and W Leo at the time of our observation and possible emission from circumstellar material around them are likely to be responsible for their anomalous colours.

5. Discussion

The sources 10061 and 10234 are Mira variables of type M, and are identified as S Tau and W Leo, respectively. They were seen to be brighter in the K band during our observation by about 0·4 and 0·3 mag respectively, than during the observation of Neugebauer and Leighton (1969). Source 10061 was noted to be variable by Neugebauer and Leighton (1969). The observed magnitude differences are likely to be due to the differences in the phase at the times of observation.

Source 10066 is a Mira variable of type M and is identified as RX Tau. Its magnitude in the K band during our observation agrees well with that obtained by Neuge-

bauer and Leighton (1969). The latter authors did not find any variability in the I and/or K bands during their survey.

Source 10510 was seen to be highly variable in the K band by Neugebauer and Leighton (1969), with its magnitude varying over the range 1·5 to 2·1 during an observing period covering 836 days. It was found to be brighter by 0·8 mag during our observation compared to its mean brightness during the observation of Neugebauer and Leighton (1969). It is identified as SVS 102147 and appears to indicate variability even at 4·2 and 11·0 μm (Price and Walker 1976). It would be of interest to obtain the amplitude of its variation in different wavelength bands and the period of its variability in order to classify it.

Engels (1979), lists the distance to source 10234 (W Leo) as 1224 pc. The value of 200 pc derived for its distance by blackbody fit to our photometric data differs significantly from that of Engels (1979). The discrepancy seems to be due to the insensitivity of our fits to distance. However, the distance to the source can be estimated by using the period-luminosity relation for Mira variables. Wood (1981), gives $M_{\rm bol}$ = – 5·82 for Mira variables of average period 375 days. The apparent bolometric magnitude $m_{\rm bol}$ ~5·5 estimated from our photometric data then yields a distance of ~ 1·7 kpc in fair agreement with that of Engels (1979).

Source 20052 is well outside the galactic plane with $b^{\rm II}$ = –31°·8. Photometric data on this source are available from Dyck, Lockwood and Capps (1974) and from Strecker and Ney (1974). No significant difference is seen between the K band magnitude from this work and that from either Dyck, Lockwood and Capps or from Strecker and Ney. Dyck, Lockwood and Capps derived a colour temperature of 2290 K for this source from the flux ratio $F_{1\cdot04\mu m}/F_{3\cdot4\mu m}$. The fit of the blackbody distribution to the *JHKL'M* magnitudes from this work yields a temperature of 2450 K for this source, which does not differ significantly from its colour temperature.

All the sources discussed above have $[I_{\rm CIT} - K] > 5$. Among them, sources 10066, 10510 and 10234 show excess emission at 11·0 μm and source 20052 shows excess emission at 19·8 μm.

Among the sources with $[I_{\rm CIT} - K] < 5$, source 30180 was seen to be fainter in the K band by about 0·5 mag during our observation than during the time of survey by Neugebauer and Leighton (1969). It is also seen to be fainter in the M band than at 4·2 μm during the AFGL Sky Survey (Price and Walker 1976). It is likely that it is a variable star. Extended observations would help to verify this.

It should be remarked that the temperature derived from blackbody fit to our photometric data turns out to be too high for 60133 and too low for 70073 for their spectral type M2 and K0, respectively. Our M band magnitudes of sources 60098, 60133 and 70073 are fainter than the 4·2 jam magnitudes from the AFGL Sky Survey (Price and Walker 1976), by amounts in excess of the estimated errors on these magnitudes. The reasons for these discrepancies are, however, not obvious. Source 60098 (V499 Cas) is an irregular variable; its spectral type and period of variability are not known.

None of the sources with $[I_{\rm CIT} — K] < 5$, show any excess emission up to 4·7 μm.

Acknowledgements

We thank Professor L. Rosino for his kind hospitality at the Asiago Observatory, Italy and Professor J. Trümper, Dr G. Haerendel and Dr S. Drapatz, Max-Planck-Institut für Extraterrestrische Physik, Garching bei München, for their hospitality when one of us (KVKI) was a guest scientist there. We thank Drs T. N. Rengarajan and R. P. Verma of the Infrared Astronomy Group, Tata Institute of Fundamental Research, Bombay, for useful discussions and helpful comments.

References

Allen, C. W. 1973, *Astrophysical Quantities*, 3 edn, Athlone Press, London.
Becklin, E. E., Matthews, K., Neugebauer, G., Willner, S. P. 1978, *Astrophys. J.*, **220,** 831.
Dyck, H. M., Lockwood, G. W., Capps, R. W. 1974, *Astrophys. J.*, **189,** 89.
Elias, J. H. 1978a, *Astrophys. J.*, **224,** 857.
Elias, J. H. 1978b, *Astrophys. J.*, **224,** 453.
Engels, D. 1979, *Astr. Astrophys. Suppl. Ser.*, **36,** 337.
Frogel, J. A., Persson, S. E., Aaronson, M., Matthews, K. 1978, *Astrophys. J.*, **220,** 75.
Johnson, H. L. 1966, *A. Rev. Astr. Astrophys.*, **4,** 193.
Johnson, H. L. 1968, in *Nebulae and Interstellar Matter,* Eds B. M. Middlehurst and L. H. Aller, University of Chicago Press, p. 167.
Johnson, H. L., Mitchell, R. I., Iriarte, B., Wisniewski, W. Z. 1966, *Commun. Lunar and Planet. Lab.*, **4,** 99.
Johnson, H. R. 1974, *NCAR Tech. Note,* No. STR-95.
Jones, T. J., Hyland, A. R. 1980, *Mon. Not. R. astr. Soc.*, **192,** 359.
Jones, T. J., Hyland, A. R., Robinson, G., Smith, R., Thomas, J. 1980, *Astrophys. J.*, **242,** 132.
Kukarkin, B. V., Kholopov, P. N., Efremov, Yu. N., Kukarkina, N. P., Kurochkin, N. E., Medvedeva, G. I., Perova, N. B., Fedorovich, V. P., Frolov, M. S. 1970, *General Catalogue of Variable Stars,* 3 edn, vol. 2, Astronomical Council of the Academy of Sciences, Moscow.
Kukarkin, B. V., Kholopov, P. N., Efremov, Yu. N., Kukarkina, N. P., Kurochkin, N. E., Medvedeva, G. I., Perova, N. B., Pskovsky, Yu. P., Fedorovich, V. P., Frolov, M. S. 1974, *General Catalogue of Variable Stars,* 3 edn, 2 Suppl., Astronomical Council of the Academy of Sciences, moscow.
Lee, T.A.1970, *Astrophys. J.*, **162,** 217.
Lockwood, G. W. 1972, *Astrophys. J. Suppl. Ser.*, **24,** 375.
Neugebauer, G., Leighton, R. B. 1969, *Two-Micron Sky Survey: A Preliminary Catalog NASA SP-3047.*
Price, S. D., Walker, R. G. 1976, *The AFGL Four Colour Infrared Sky Survey. Catalog of Observations at 4·2, 11·0, 19·8 and 27·4* μm.
Strecker, D. W., Ney, E. P. 1974, *Astr. J.*, **79,** 797.
Strecker, D. W., Erickson, E. F., Witteborn, F. C. 1979, *Astrophys. J. Suppl. Ser.*, **41,** 501.
Tapia, M. 1981, *Mon. Not. R. astr. Soc.*, **197,** 949.
Wilson, W. J., Barett, A. H. 1972, *Astrophys. J.*, **17,** 385.
Wood, P. R. 1981, *Physical Processes in Red Giants,* Eds I. Iben, Jr., and A. D. Renzini, Reidel Dordrecht, Holland.

J. Astrophys, Astr. (1982) **3**, 465-483

Relativistic Beaming in the Central Components of Double Radio Quasars

V. K. Kapahi and D. J. Saikia *Radio Astronomy Centre, Tata Institute of Fundamental Research, PO Box 1234, Bangalore 560012*

Received 1982 July 22; accepted 1982 October 1

Abstract. Using a large sample of 78 well-observed double quasars, we have investigated several consequences of the relativistic beaming model. In this model the ratio of the strengths of the central component and outer lobes of a double source depends on whether the jet axis lies close to or away from the line of sight, If this is the actual situation, the fraction of emission from the core, f_c, may be used as a statistical measure of the orientation of the source and should be correlated with other source parameters which also depend on the inclination of the jet axis to the line of sight.

We find f_c to be anticorrelated with the overall projected linear size of the extended emission but to exhibit a positive correlation with both the observed degree of misalignment from a collinear double structure, and the ratio of separations of the outer hotspots from the central component. As might be expected from these relationships, we also find sources of smaller projected linear sizes to appear more misaligned and the degree of misalignment to be correlated with the ratio of separations of the outer hotspots. All these correlations are consistent with the predictions of the relativistic beaming model.

Key words: quasars–relativistic beaming–active galactic nuclei—extragalactic radio sources

1. Introduction

In the relativistic twin-jet models of Scheuer and Readhead (1979) and of Blandford and Königl (1979), both compact and extended double radio sources are believed to be intrinsically similar, only appearing to be different due to the different inclinations of their jet axes to the line of sight. When viewed from a direction close to the jet axis the radio emission from the core is strongly enhanced due to relativistic beaming and tends to mask the emission from the extended lobes which radiate

quasi-isotropically. In contrast, the jet axis of a normal double source lies well away from the line of sight and the core appears weak in comparison with the outer lobes.

It has recently been shown (Browne and Orr 1982; Orr and Browne 1982) that some observed statistical properties of quasars, such as the proportion of those with flat radio spectrum in flux-limited samples selected at different frequencies and the flux density counts of flat spectrum quasars, are quite consistent with the predictions of beaming models. In the present paper, we have attempted to verify some other statistical predictions of these models. If beaming is indeed strong in the cores of radio quasars, the fraction of the total emission coming from the core should be a statistical measure of the orientation of the source axis. This parameter should therefore be related to other observable source properties which also depend on the inclination of the jet axis to the line of sight. Three such parameters that are fairly readily measurable are (i) the projected maximum linear separation between the outer lobes, (ii) the apparent misalignment of the hotspots from collinearity with the core and (iii) the ratio of the angular displacements of the hotspots from the radio core. We have investigated these relationships using a large sample of well-observed double quasars and find the results to be consistent with the relativistic beaming hypothesis.

2. The sample of double quasars

Although compact central components (hereafter referred to as CCs) are found in radio galaxies and quasars, we consider here only quasars as in these the occurrence of CCs is known to be much more common (*e.g.* Riley and Jenkins 1977) and also because several samples of quasars have been mapped with good angular resolution in the past few years. Ideally, a complete sample observed to well-defined resolution and sensitivity limits should be used. However, the number of quasars in any such available sample is too small to make statistically significant tests and as a first step we have collected together structural information on all classical double QSOs with known redshift that have been reported in the literature (mainly from Jenkins, Pooley and Riley 1977 and references therein; Miley and Hartsuijker 1978; Potash and Wardle 1979; Owen, Porcas and Neff 1978; Wills 1979; Fanti *et al.* 1977, 1979). Nearly all these quasars have been mapped by aperture synthesis techniques at frequencies between 2·7 and 8 GHz, but with a considerable range in instrumental sensitivity and angular resolution. Therefore in order to keep the final sample fairly homogeneous and free from serious selection effects, we have imposed the following additional restrictions.

(a) We exclude quasars for which the angular separation of the outer lobes (LAS) is < 8 arcsec and those that have been mapped with less than 3 resolution elements along their main axes, where one resolution element is equal to the half-power beamwidth. The requirement of at least 3 resolution elements is necessary if a reasonably reliable estimate of the flux-density in the CC is to be made. Although few sources with LAS < 8 arcsec would satisfy the resolution criterion, several larger sources (particularly at low declinations) had also to be excluded on this criterion. This is unlikely to have introduced any serious bias into the data.

(b) We require that the total flux density of a quasar at 178 MHz be $S_{178} \geqslant 2$Jy, the limit of the 4C catalogue. This condition excludes a few weak quasars that have been mapped with poor sensitivity at high frequencies. A few quasars with $\delta < -7°$,

for which flux densities at 178 MHz have not been directly measured have, however, been included because they appear in the Parkes radio catalogue and are all known to have flux densities of greater than ~ 8 Jy at 160 MHz (Slee 1977).

(c) We have disregarded the observations of Wills (1979) as these appear to have been intended only for estimating the overall angular sizes and not for determining reliable flux densities of the CCs. Although the observations were made using the same instrument and frequencies as those reported by Potash and Wardle (1979) for samples selected at comparable flux densities at 178 MHz, there is a marked difference in the reported detection of CCs in the two sets of observations. Wills detected CCs in only 4 of the 26 quasars found to be double, while Potash and Wardle report detections in 27 of the 35 such quasars.

(d) We do not include quasars with one-sided asymmetric radio structure, often referred to in the literature as D2 type (*cf.* Miley 1971; Kapahi 1981). We shall comment on such sources in Section 3.

Our final sample consists of 78 quasars, 66 of which have detected CCs. As the positions of the outer radio components and of the optical quasars are generally known with an accuracy of ~ 1 arcsec there is little difficulty in identifying the CCs. The sources in our sample are listed in Table 1 which is arranged as follows.

Columns 1 and 2 give the coordinate designation and an alternative catalogue number of the quasar. The redshift is given in column 3 and the estimated total radio luminosity at 5 GHz in column 4. The LAS and the corresponding linear size are entered in columns 5 and 6 respectively. The next three columns give an estimate of the fractional flux density in the core (f_c), the misalignment angle (Δ), and the ratio of separations of the hotspots from the core (Q), respectively. The estimation of these parameters is explained in the subsequent sections of the paper. The last column gives coded references (explained at the end of the Table) to the best available maps of the quasars from which the observed parameters have been estimated.

3. The $f_c - l$ relation

In the relativistic beaming model, sources inclined at small angles to the line of sight should appear smaller due to projection and have more prominent cores. The fraction of radio emission from the core should therefore be anticorrelated with observed linear size. For each quasar in our sample we have calculated,

(a) the projected linear size, l, of the quasar from its measured LAS, in an Einstein -de Sitter world model ($q_0 = 0{\cdot}5$) with $H_0 = 50$ km s^{-1} Mpc^{-1}, and

(b) the ratio, f_c, of the observed flux density of the CC (or an upper limit to it) to the total flux density of the source at a fixed frequency of 8 GHz in the rest frame of the quasar. The rest frame was used because the central and outer components generally have quite different spectral indices. The transformation was made using the observed spectral indices of the central (α_c) and extended (α_e) components, when available, otherwise assuming $\alpha_c = 0{\cdot}2$ and $\alpha_e = 0{\cdot}9$ (α defined as $S \propto \nu^{-\alpha}$), the median values for quasars in the sample that have good spectral information. For quasars in which no CCs have been detected, we estimate that such components are unlikely to account for more than 10 per cent of the total flux density.

Table 1. The sample of double radio quasars.

Source	Alternative name	Redshift	log P 5GHz	LAS arcsec	Linear size kpc	f_c	Δ deg	Q	Reference
(1)	(2)	(3)	(4)	(5)	(6)	(7)	(8)	(9)	(10)
0003 + 15	4C 15·01	0·450	25·48	31·5	214	0·37			MH
0007 + 33	4C 33·01	0·750	25·48	77	625	0·05	3	1·16	PW
0017 + 25	4C 25·01	0·280	25·13	46·2	244	0·78	46	1·07	PW
0110 + 29	4C 29·02	0·363	25·11	76·6	469	0·24	12	1·11	PW
0118 + 03	4C 03·02	0·765	25·90	43	351	0·07	24	1·10	MH
0130 + 24	4C 24·02	0·453	25·36	53·4	364	0·32	9	1·23	PW
0133 + 20	3C 47	0·425	25·89	69	457	0·08	6	1·23	PH
0214 + 10	4C 10·06	0·408	25·49	119	773	0·21	10	1·18	MH
0229 + 34	3C 68·1	1·238	26·76	46	396	<	5	1·18	JPR, L81
0232 − 04	4C -04·06	1·436	26·74	13	111	0·40	13	3·26	S82
0313 + 34	4C 34·13	1·156	26·01	26·5	228	0·03	2	1·39	PW
0349 − 14	PKS	0·614	25·96	114	875	0·03	3	1·06	MH
0350 − 07	PKS	0·962	26·34	41·5	352	<0·03	0	1·52	MH
0610 + 26	3C 154	0·580	26·44	50	376	0·26	9	1·96	RP1
0704 + 38	4C 38·20	0·579	25·56	21·8	164	0·20			PW
0710 + 11	3C 175	0·768	26·21	48	392	0·06	6	1·32	JPR
0723 + 67	4C 67·14	0·846	26·49	13·6	113	0·42			OPN
0742 + 31	4C 31·30	0·462	25·92	115	792	0·78	3	1·13	F77
0814 + 22	4C 22·20	0·980	26·29	25	213	0·08			PW
0833 + 65	3C 204	1·112	26·33	31·1	267	0·12	0	1·07	PH, OPN
0835 + 58	3C 205	1·534	26·90	15·9	136	0·03	0	1·17	PH, OPN, L81
0837 − 12	PKS	0·200	25·09	169	714	0·23	6	2·13	MH
0838 + 13	3C 207	0·684	26·38	8·4	67	0·40			PH
0839 + 61	4C 61·19	0·862	25·85	25·8	215	0·09	13	1·69	OPN
0846 + 10	4C 09·31	0·366	24·99	54	332	<0·23			MH
0850 + 14	3C 208	1·110	26·47	11	94	0·08	8	1·29	JPR, L81
0855 + 14	3C 212	1·048	26·68	9	77	0·30	1	1·13	JPR, L81
0903 + 16	3C 215	0·411	25·33	28·5	186	0·07			PH
0937 + 39	4C 39·27	0·618	25·53	51·8	398	0·12	3	1·28	PW
0952 + 35	4C 35·21	1·241	26·04	18·9	163	<			PW
1001 + 22	4C 22·26	0·974	25·93	66	561	0·11	5	1·24	PW
1004 + 13	4C 13·41	0·240	25·10	115	550	0·02	8	1·56	MH
1007 + 41	4C 41·21	0·613	25·93	31·2	239	0·29	7	1·76	OPN, S82
1011 + 28	4C 28·25	0·899	25·90	14·8	124	0·46			PW
1012 + 48	4C 48·28	0·385	24·96	109	688	<0·02	6	1·01	MH
1047 + 09	4C 09·37	0·786	25·61	70	574	0·10			MH, S82
1048 − 09	PKS	0·344	25·36	83	494	0·07	6	1·30	MH
1048 + 24	4C 24·23	1·270	26·03	15·6	134	0·10			PW
1058 + 11	4C 10·30	0·420	25·23	31	204	0·41			MH
1100 + 77	3C 249·1	0·311	25·40	23	129	0·18	9	2·07	PH
1111 + 40	3C 254	0·734	26·25	13·2	107	<	15	6·3	PH, SKN
1137 + 66	3C 263	0·652	26·26	45	352	0·11	0	1·81	PH, OPN
1150 + 49	4C 49·22	0·334	25·66	13	76	0·75			OPN
1206 + 43	3C 268·4	1·400	26·82	10·2	88	0·05	14	1·13	PH, SKN
1218 + 33	3C 270·1	1·519	27·11	9	77	0·20	37	1·24	RP2, PW

Table 1. Continued.

Source	Alternative name	Redshift	log P 5GHz	LAS arcsec	Linear size kpc	f_c	Δ deg	Q	Reference
(1)	(2)	(3)	(4)	(5)	(6)	(7)	(8)	(9)	(10)
1221 + 18	4C 18·34	1·401	26·07	23	198	0·10			MH
1223 + 25	4C 25·40	0·265	24·49	67	342	0·06	1	1·01	MH
1232 − 24	PKS	0·355	25·47	86	520	0·02	4	1·04	MH
1241 + 16	3C 275·1	0·557	26·07	14	104	0·29	24	1·53	JPR, RP2
1244 + 32	4C 32·41	0·949	25·85	23·1	196	0·41	14	1·31	PW
1248 + 30	4C 30·25	1·061	25·76	28·9	248	<	2	1·18	PW
1253 − 05	3C 279	0·538	27·02	17	125	0·75			J81
1258 + 40	3C 280·1	1·659	26·67	23·1	195	0·05	20	1·06	JPR, SSS
1317 + 52	4C 52·27	1·060	26·49	28·2	242	0·59	30	1·87	OPN
1327 − 21	PKS	0·528	25·96	36	262	0·31			MH
1332 + 55	4C 55·27	1·210	25·86	76	655	0·04	4	1·13	MH
1354 + 19	4C 19·44	0·720	26·41	43	345	0·82	7	1·76	S82
1356 + 58	4C 58·29	0·321	24·67	43·8	251	<	3	1·17	OPN
1400 + 16	4C 16·39	0·244	24·97	25	121	0·46	52	1·23	B77, HO
1423 + 24	4C 24·31	0·649	25·92	20·2	158	0·20	32	1·33	PW
1451 + 09	4C 09·52	0·627	25·53	23	178	0·26			MH
1512 + 37	4C 37·43	0·371	25·28	50·9	315	0·11	1	1·28	PW
1545 + 21	3C 323·1	0·264	25·23	68·2	347	0·09	0	1·39	PH
1548 + 11	4C 11·50	0·436	25·51	50	335	0·57			A74
1606 + 28	4C 28·40	1·989	26·53	30·6	251	<			PW
1618 + 17	3C 334	0·555	25·93	48	356	0·25	20	1·35	JPR
1622 + 23	3C 336	0·927	26·45	21·7	183	0·03	0	2·75	PH
1628 + 36	4C 36·28	1·254	26·10	16·1	139	0·25			PW
1634 + 26	4C 26·49	0·561	25·74	39·3	292	<	2	1·26	PW
1704 + 60	3C 351	0·371	25·66	85·2	528	<	4	1·31	OPN, L81
1721 + 34	4C 34·47	0·206	25·02	220	949	0·59	1	1·03	CBV, J82
1732 + 65	4C 65·21	0·856	25·90	17·4	145	0·21			OPN
1857 + 56	4C 56·28	1·595	26·59	27·5	234	0·65	5	1·73	OPN
2120 + 16	3C 432	1·805	26·37	13	109	<			JPR
2135 − 14	PKS	0·200	25·23	150	634	0·10	4	1·25	MH
2308 + 09	4C 09·72	0·432	25·36	101	674	0·21	16	1·67	MH
2325 + 29	4C 29·68	1·015	26·31	50·4	430	0·07	1	1·19	PW
2349 + 32	4C 32·69	0·670	25·67	66	520	0·09	15	1·35	PW, PW80

References to radio structure:

A74	Argue *et al.* (1974)	OPN	Owen, Porcas and Neff (1978)
B77	Baldwin *et al.* (1977)	PH	Pooley and Henbest (1974)
CBV	Conway, Burn and Vallee (1977)	PW	Potash and Wardle (1979)
F77	Fanti *et al.* (1977)	PW80	Potash and Wardle (1980)
HO	Hintzen and Owen (1981)	RP1	Riley and Pooley (1976)
J81	Joshi (1981)	RP2	Riley and Pooley (1978)
J82	Jägers *et al.* (1982)	S82	Salter *et al.* (1982)
JPR	Jenkins, Pooley and Riley (1977)	SKN	Schilizzi, Kapahi and Neff (1982)
L81	Laing (1981)	SSS	Swarup, Sinha and Saikia (1982)
MH	Miley and Hartsuijker (1978)		

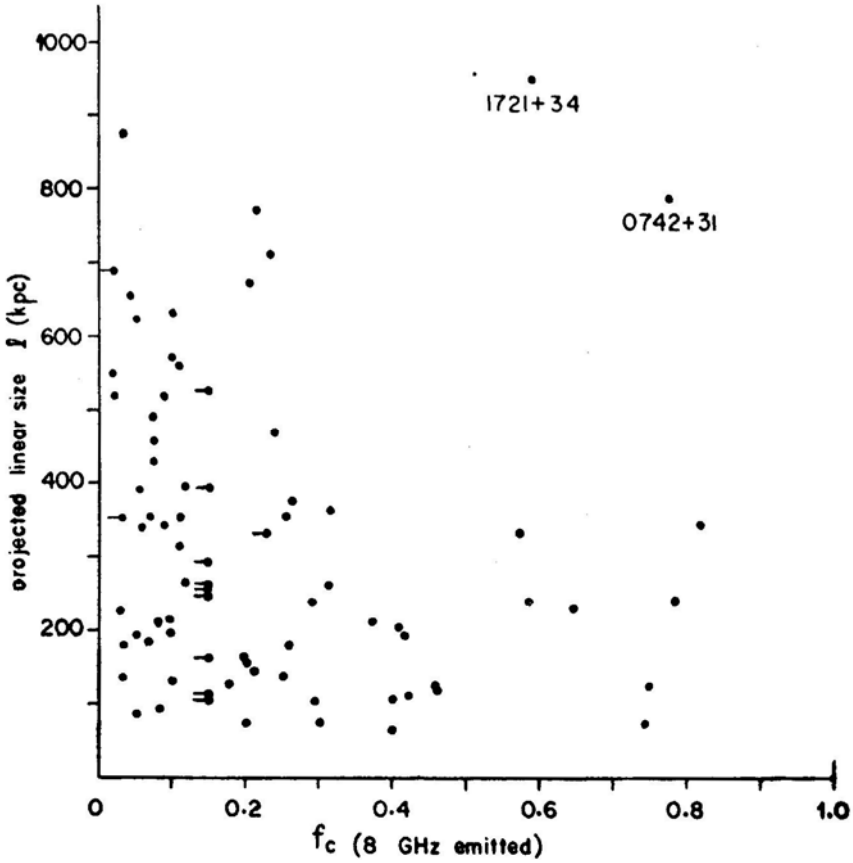

Figure 1. Plot of the projected linear size *vs.* the core fraction. Horizontal bars indicate upper limits to f_c .

A plot of the values of f_c and l for the 78 quasars is shown in Fig. 1. Except for the two large quasars with strong central components (that are separately identified in the figure and discussed in Section 7) there appears to be a tendency for quasars with larger values of f_c to have smaller projected linear sizes. The apparent deficiency of points in the region $f_c > 0{\cdot}25$ and $l > 400$ kpc is unlikely to arise from observational difficulties. The components of a source with $l = 500$ kpc in this region of the diagram would have a separation of 55 to 90 arcsec for $z > 0{\cdot}3$ and should be readily detectable by existing aperture synthesis telescopes, particularly as the individual components of QSOs are generally found to be much smaller in extent than their separations (Kapahi 1978).

The significance of the apparent anticorrelation between f_c and l may be tested by applying the Kolmogoroy-Smirnov two sample test. If the data are divided into two roughly equal groups at a linear size of $l = 250$ kpc the possibility that the two samples are drawn from the same population can be rejected at the 95 per cent confidence level if the two apparently discrepant quasars are excluded and at the 90 per cent level if they are included. Although the level of significance may not be sufficient to establish an anticorrelation beyond doubt, the data must be considered to be con-

sistent with such an anticorrelation. It is also worth noting that possible selection effects present in the data could only have led to a weakening of any true anticorrelation. The limited angular resolution and dynamic range of the observations can discriminate against sources of small size that have strong CCs because when the size of the source is not much larger than the angular resolution, it is easier to recognize the double structure in a source with low f_c than in one with large f_c . Furthermore, limiting the sample to sources larger than a certain angular size implies that at any redshift only quasars above a certain minimum projected size can come into the sample.

Since quasars in the present sample have been selected largely from radio surveys at low frequencies (< 1 GHz) there are relatively few with strong CCs. The sample may be enlarged by including quasars selected at high frequencies and by mapping the quasars that are presently unresolved in low-frequency surveys, with high angular resolution. Recent investigations on both these lines appear to provide some additional support for an anticorrelation between f_c and l. Maps of high dynamic range, made with the VLA at λ 6 cm , of many, flat-spectrum quasars selected from 5 GHz surveys indicate (Perley, Fomalont and Johnston 1980,1982) that several of them have a double or asymmetric extended structure accounting typically for $\lesssim$ 10 per cent of the total flux density and having projected angular sizes $\lesssim$ 10 arcsec. These sources would thus fall in the bottom right-hand portion of Fig. 1. Gopal-Krishna, Preuss and Schilizzi (1980) have carried out VLBI observations of unresolved sources (angular size $\lesssim$ 4 arcsec and mostly associated with empty fields) taken from an Ooty occultation survey at 327 MHz. They find at least half the sources to have compact cores accounting for $\gtrsim$ 25 per cent of the total flux density at 5 GHz. As these sources have normal spectra ($a > 0{\cdot}5$) between 327 MHz and 5 GHz, they are quite likely to have extended structure of size $\lesssim$4 arcsec.

In view of the possible selection effects in the data at small values of l we have not attempted to extract an average or median value as a function of f_c in order to check with the prediction of the beaming model. We restrict ourselves to a prediction of the expected upper envelope to the f_c–l relation by considering a standard quasar of intrinsic linear size L = 1 Mpc, typical of the largest known quasars, and estimating the values of f_c and l as the quasar is viewed from different angles.

We assume that the core emission comes from a quasi-continuous stream of material travelling at speed $\beta = v/c$ (Lorentz factor γ) in oppositely directed jets and the outer lobes to be at rest and radiating isotropically. If θ is the angle between the jet axis and the line of sight, the observed values of f_c and l are given by,

$$f_c(\theta) = \left[1 + \frac{2}{B(\theta)}\left\{\frac{1}{F_c} - 1\right\}\right]^{-1}$$

and

$$l(\theta) = L \sin\theta,$$

were

$$B(\theta) = (1 - \beta\cos\theta)^{-(2+\alpha)} + (1 + \beta\cos\theta)^{-(2+\alpha)},$$

and $F_c = f_c$ (90°), the fractional flux density in the core that would have been observed if the jet axis were transverse to the line of sight.

The relation between f_c and l thus depends on the values of F_c and the Lorentz factor γ. From the observed distribution of the parameter R [defined as the ratio of the flux density of the CC to the flux density of the outer lobes, $f_c = R/(1 + R)$], for quasars in the 3CR catalogue, Orr and Browne (1982) suggest a typical value of $R(90°) = 0{\cdot}024$ at an emitted frequency of 5 GHz, which corresponds in our case to F_c (8 GHz) = 0·033. Further, from the observed spread in the R-distribution of extended 3CR quasars, Scheuer and Readhead (1979) concluded that typically $\gamma \lesssim 2$. Orr and Browne (1982) have however argued that this result is likely to be incorrect because the core-dominated sources were excluded from the distribution. Inclusion of such sources implies typical values of $\gamma \sim 5$. Using $F_c = 0{\cdot}033$ the predicted upper envelopes to the f_c–l points for values of $\gamma = 2$ and 5 are shown in Fig. 2. While a value of $\gamma = 2$ appears to provide a satisfactory upper envelope to most of the data points, an extension of the γ distribution to larger values is required to explain the small number of sources with very strong cores ($f_c > 0{\cdot}5$).

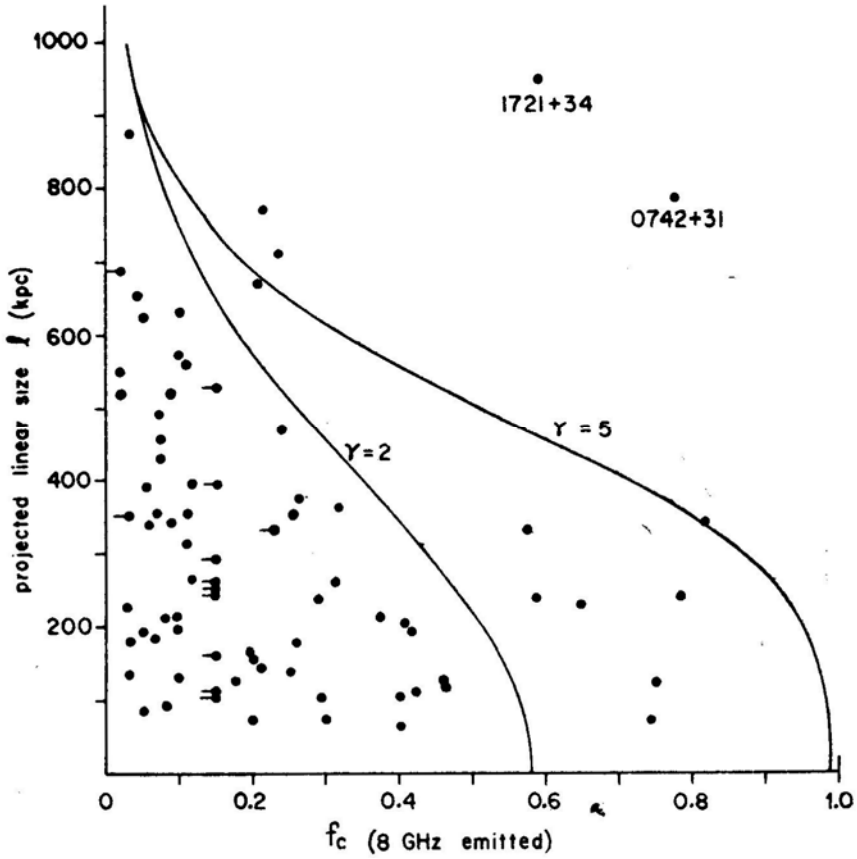

Figure 2. Upper envelopes to the f_c–l relation for values of $\gamma = 2$ and 5. estimated as explained in the text.

It is of interest to note here that the observed properties of the asymmetric D2 type quasars also seem to be consistent with the anticorrelation between f_c and l of Fig. 1. VLBI observations of a few such quasars suggest that their jet axes may indeed be oriented close to our line of sight (*e.g.* Readhead *et al.* 1978). Recently it has been pointed out by Kapahi (1981) that D2 quasars have significantly more prominent cores than the normal double quasars. Apart from 3C 186 (in which the outer lobe appears to be separated by ~ 900 kpc from the core although the reality of the physical association of the lobe with the quasar is uncertain) nearly all the other D2 quasars with known redshift and LAS > 5 arcsec have $l < 100$ kpc and $f_c > 0{\cdot}5$. They therefore fit in well with the f_c–l relation (even if their observed linear sizes are doubled to take account of the hypothetical missing weaker lobes) but suggest values of γ considerably larger than 2.

Although the observed relation between f_c and l finds a natural explanation in the relativistic beaming hypothesis, it is important to examine other possible explanations. If the CCs were on average stronger at earlier epochs or in sources of higher total luminosity, an anticorrelation between f_c and l could result from the possible decrease in linear sizes of quasars with increasing redshift or luminosity inferred from the angular-size–redshift tests (*e.g.* Wardle and Miley 1974; Masson 1980). Plots of f_c against redshift and against total radio luminosity are shown in Figs 3

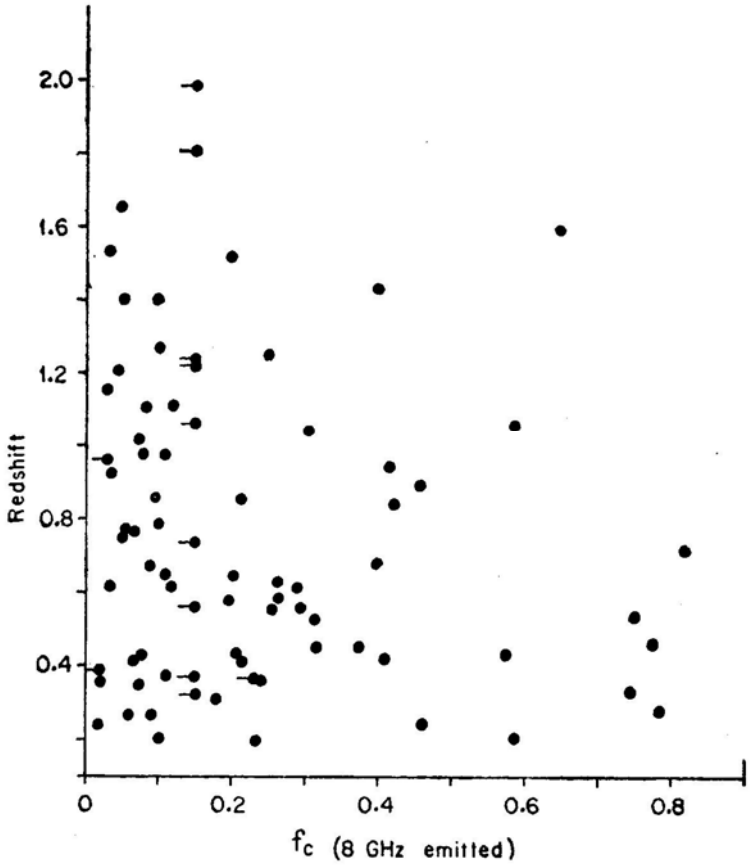

Figure 3. Plot of redshift *vs*. core fraction.

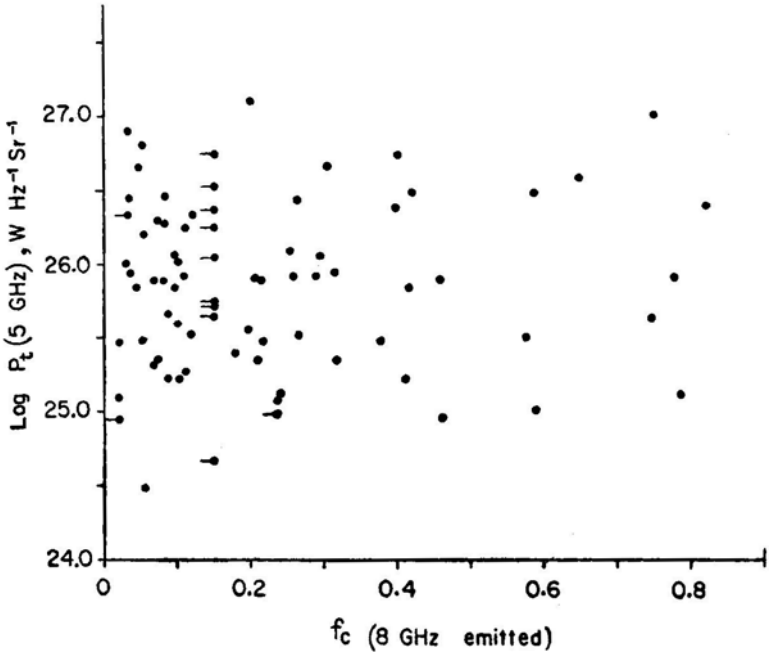

Figure 4. Plot of total radio luminosity at 5 GHz *vs.* the core fraction.

and 4 respectively. Visually, there is a possible suggestion in Fig. 3 of an inverse correlation, but opposite in sense to that required to explain the f_c–l relationship Statistical tests do not however show any significant correlations in Figs 3 and 4.

Another possibility is that quasars with strong CCs are seen at younger ages and are therefore smaller in overall size. This does not however explain the presence of a large number of sources, many of which are possibly young that have small linear sizes and weak CCs, unless most young quasars have CCs of low intrinsic luminosity. There does not also appear to be any significant difference in the spectral indices of the outer lobes of quasars with and without strong CCs that could be attributed to age differences.

4. The $f_c - \Delta$ relation

For a source in which the two outer lobes are not perfectly collinear with the CC, the intrinsic misalignment may appear amplified or diminished depending on the orientation of the source with respect to the observer. However, for sources inclined at small angles to the line of sight, the misalignment angle appears amplified for most directions of view. On the beaming interpretation, one may therefore expect a statistical relationship between f_c and the observed misalignment angle, Δ(defined to be the complement of the apparent angle formed at the CC or the optical quasar by the two outer hotspots), such that sources with larger values of f_c should, on average, appear more misaligned.

Ideally, the misalignment angles Δ should be estimated from the positions of the hotspots as these are believed to be the ends of the beams supplying energy to the

radio lobes. But since many of the quasars in the present sample have not been mapped with sufficient angular resolution to locate the hotspots, we had often to use the positions of the peaks of emission or of centroids of the outer lobes. In order to minimise such errors we have used a subsample of quasars comprising of only those sources that have been observed with at least six resolution elements along their major axes. Of the 58 quasars that satisfy this criterion, two (namely 1047 + 09 and and 1111 +40) were excluded as Δ is very poorly determined for them. It is clear from the $f_c - \Delta$ diagram for the remaining 56 quasars, shown in Fig. 5, that there is indeed a tendency for sources with stronger CCs to appear more misaligned than those with weaker CCs. In Fig. 6 we show the distributions of Δ for sources with $f_c \leqslant 15$ per cent and $f_c > 15$ per cent. A Kolmogorov-Smirnov test shows the two distributions to be different at a significance level of 99 per cent. Fig. 5 also suggests, that intrinsicially the misalignment is likely to be $< 10°$ in most cases.

Hintzen and Owen (1981) have suggested that the apparent distortion from a collinear structure seen in 1400 + 162, which is known to be in a group of galaxies

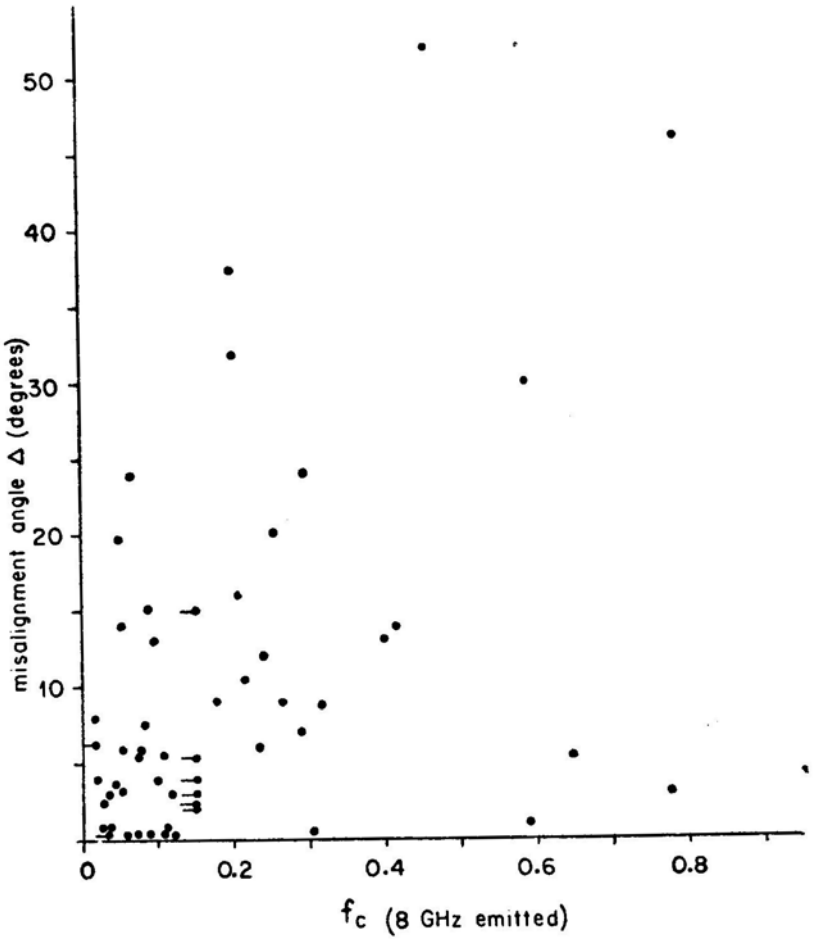

Figure 5. Plot of misalignment angle *vs.* the core fraction.

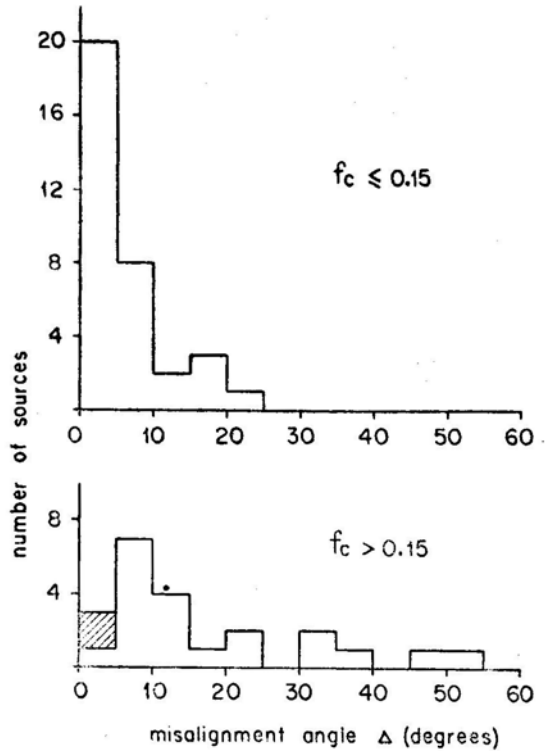

Figure 6. Distributions of the misalignment angle for sources with $f_c \leqslant 0{\cdot}15$ and $f_c > 0\,15$. In this and subsequent histograms the shaded portion refers to the two discrepant quasars identified in Fig. 1.

(Baldwin *et al.* 1977), is due to the interaction of the radiating material in the lobes with the intracluster medium. Further, Riley and Pooley (1978) have speculated that the 'bent' structures seen in 3C 270·1 and 3C 275·1 are possibly due to the motion of the parent quasar through the intergalactic medium. Although such effects can certainly give rise to structures lacking collinearity, it must be stressed that any small intrinsic misalignment will appear amplified when the source is inclined at a small angle to the line of sight. The fact that the three above-mentioned quasars all have prominent cores suggests that the intrinsic misalignment in these sources may be lower than that observed. Deep optical and X-ray studies of the fields of at least the relatively nearby quasars would be useful in studying the environments of these sources and may help in deciding between the two possibilities.

Since sources with prominent CCs have smaller linear sizes and also appear more misaligned, it is to be expected that l and Δ may also be correlated in the sense that the smallest sources appear most misaligned. We have plotted in Fig. 7 the l–Δ relationship for the subsample of 56 quasars and find good evidence for such a correlation. A somewhat similar correlation was noted earlier by Macklin (1981) who examined the symmetry parameters of a sample of 76 well-observed 3CR double sources, including both radio galaxies and quasars.

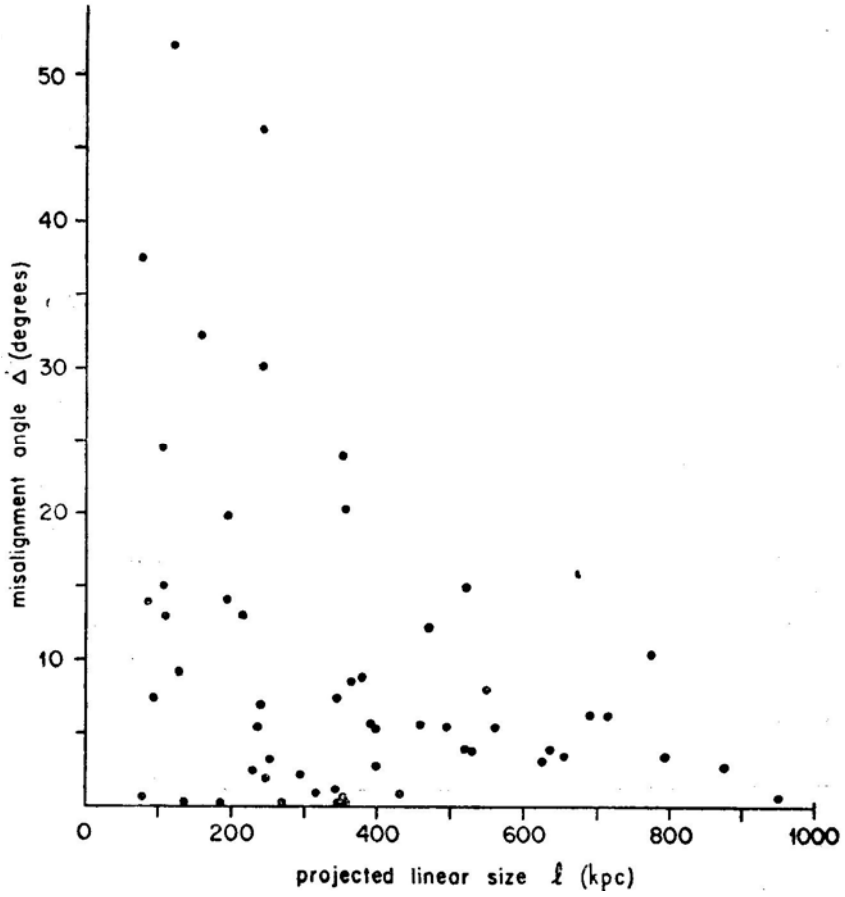

Figure 7. Plot of misalignment angle *vs.* the projected linear size.

5. The $f_c - Q$ relation and the velocity of advancement of the hotspots

If the initial ejection and the kinematic evolution of the two outer lobes are assumed to be intrinsically symmetric, then the ratio, Q of the angular separations of the outer hotspots from the CC can be expressed as

$$Q = (1 + \beta_0 \cos \theta) / (1 - \beta_0 \cos\theta)$$

where $v_0 = \beta_0 c$ is the velocity of advancement of the hotspots. Several authors have attempted to estimate v_0 from the observed distribution of Q, assuming the sources to be intrinsically symmetric and to be oriented randomly in the sky. It is clear from the above equation that the measured value of Q should tend to be closer to unity for sources inclined at larger angles to the line of sight. In the relativistic beaming model, these sources would also have less prominent CCs and thus there should be a positive correlation between f_c and Q. In estimating the values of Q, it is important that the separations be measured with respect to the hotspots or fairly large errors can result, particularly for sources with small overall sizes. There-

fore, here too we have confined ourselves to the same subsample of 56 quasars which have been observed with at least six resolution elements along their major axes.

The relationship between f_c and Q for this sample is shown in Fig. 8. Although there is a large spread in Q at all f_c there does appear to be a significant tendency for values of Q close to unity (symmetrically placed lobes) to occur more frequently among quasars with weak CCs. This can also be seen in the histograms of Q shown separately in Fig. 9 for quasars with $f_c \leqslant 0{\cdot}15$ and $f_c > 0{\cdot}15$. The distribution for quasars with weak CCs is quite similar to that for the sample of well observed 3CR double sources (both quasars and radio galaxies) considered by Longair and Riley (1979) who estimated the velocities of hotspots to be in general $\lesssim 0{\cdot}2c$. The Q distribution for quasars with strong CCs is subject to larger statistical uncertainty due to the smaller number of sources. However, it is worth noting that the distribution is relatively flat with a more pronounced tail in the region $Q > 1{\cdot}4$, suggesting that the distribution of v_0 may extend upto ~0·3c in a significant number of quasars. This is broadly in agreement with the conclusions based on an analysis of Q for sources in general (Banhatti 1980; Katgert-Merkelijn, Lari and Padrielli 1980; Swarup and Banhatti 1981; Macklin 1981). If the distributions shown in the figure are confirmed by observations of higher resolution for a larger sample of quasars with strong CCs, it would provide possibly the best available evidence for component velocities upto $\sim 0{\cdot}3c$.

Rudnick (1982) has pointed out recently that the distribution of Q in a sample of 47 double quasars shows a significant dip at values of Q close to unity. This has led him to suggest that the ejection from the nuclear engine occurs in only one direc-

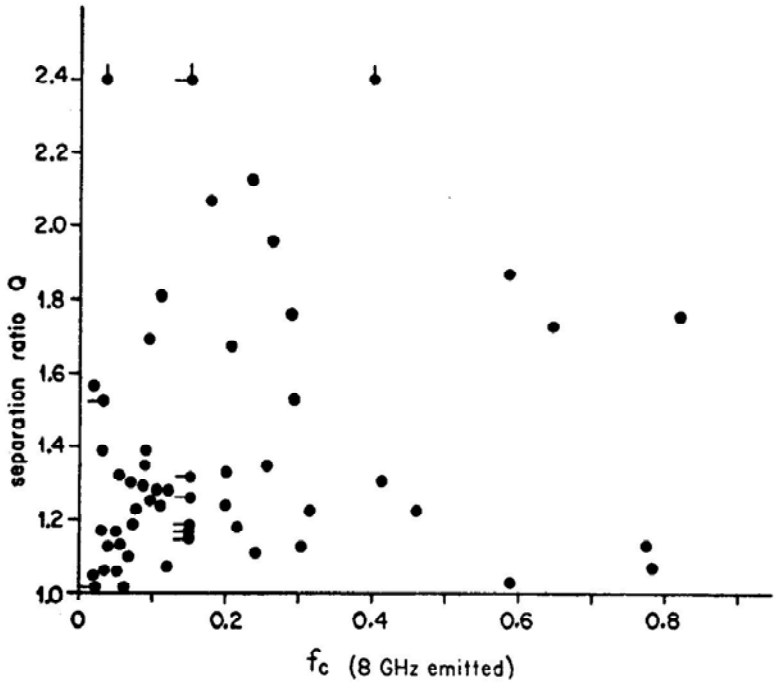

Figure 8. Plot of separation ratio *vs.* the core fraction.

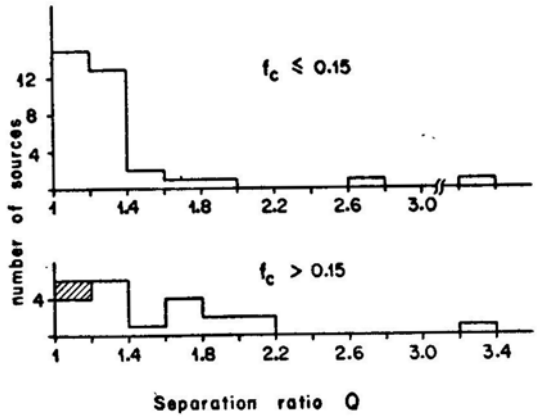

Figure 9. Distributions of the separation ratio for sources with $f_c \leqslant 0{\cdot}15$ and $f_c > 0{\cdot}15$.

tion at a time but there is a switching of the direction back and forth. For comparison with Rudnick's data, we show in Fig. 10 the Q distribution for all the 56 quasars taken together. The dip in the distribution near $Q = 1$ is seen to be much less pronounced than in Rudnick's data and is not statistically significant. It should be noted that Rudnick included only those quasars in his sample that are known to have CCs. This can introduce a bias against values of Q near 1 since sources seen transverse to the line of sight are more likely to appear symmetric and on the beaming hypothesis such sources would have the weakest CCs. Measurement errors can also contribute to an apparent dip near Q= 1 because such errors can only move sources in the first bin to larger values of β whereas those at larger Q values can move either way.

6. The Δ – Q relation

Since both Δ and Q are expected to be larger for sources inclined at small angles to the line of sight, one might expect a statistical relationship between these two parameters. Despite the large scatter, Fig. 11, which shows the Δ–Q diagram for the sample of 56 quasars, provides evidence supporting such a relationship. This can be seen more clearly in the distributions of Q for sources, with $\Delta \leqslant 5°$ and with $\Delta > 5°$ shown in Fig. 12. The most noticeable features are a possible shift in

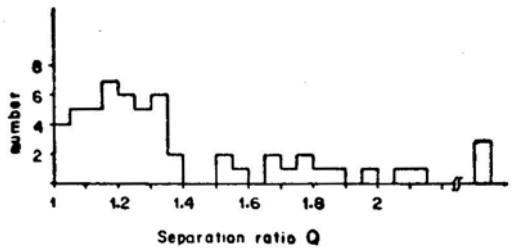

Figure 10. Distribution of the separation ratio for the sample of 56 quasars.

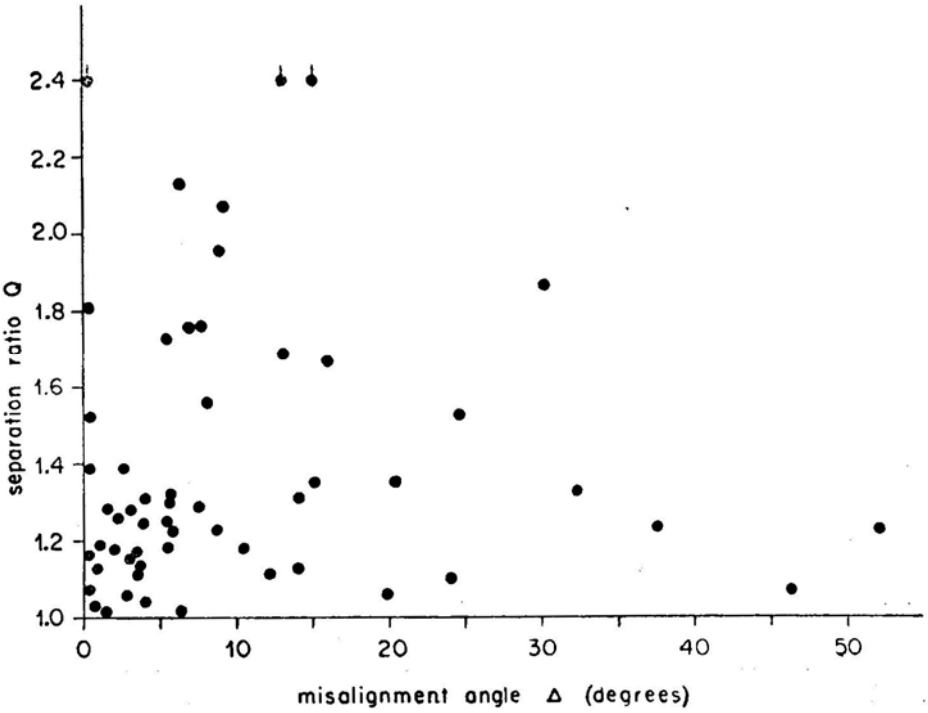

Figure 11. Plot of the separation ratio *vs.* misalignment angle.

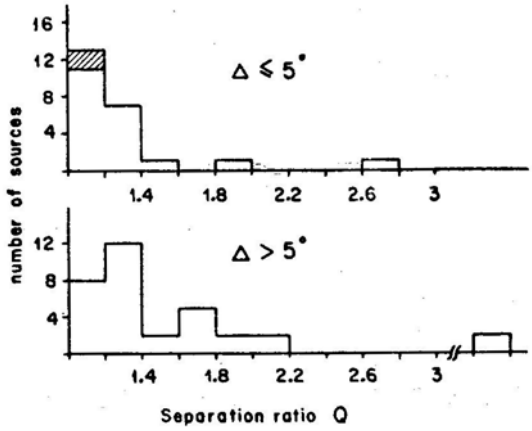

Figure 12. Distribution of the separation ratio for different values of the misalignment angle.

the peak and a more pronounced tail in the distribution of Q for sources with $\Delta > 5°$. The Kolmogorov-Smirnov test shows the two distributions to be different at a significance level of about 95 per cent.

Recently it has been reported by Macklin (1981) that in his sample of 76 3CR double sources, which includes both radio galaxies and quasars, those with the largest values of Q appear most misaligned. Macklin suggested that his correlation is best explained if the major contribution to the Q distribution is independent of orienta-

tion and is correlated with the intrinsic misalignment. However, it can be seen from his calculations that the correlation coefficient obtained by assuming a random orientation of sources in the sky and adopting values for the intrinsic misalignment parameter and the velocity of the hotspots which best fit the observed data, is also consistent with the observed coefficient. Our present analysis suggests that the observed $\Delta - Q$ correlation arises largely from the effects of orientation.

7. Discussion and conclusions

We have examined several simple statistical consequences of the relativistic beaming model using a large sample of double quasars and find the results to be consistent with this model. Using the fractional emission from the core, f_c, as a statistical measure of the orientation of the source, we find that f_c is anticorrelated with the observed linear size l, but shows a positive correlation with both Δ, the complement of the apparent angle formed at the CC or the optical object by the hotspots in the outer lobes, and Q, the ratio of separations of the hotspots from the CC or the quasar. All these correlations are in the sense predicted by the relativistic beaming model. Furthermore, in conformity with the above correlations, we also find quasars with smaller projected linear sizes to appear more misaligned and Δ to be correlated with Q.

Although the present data in the $f_c - l$ diagram do not permit an accurate determination of the Lorentz factor γ, of the radiating material *in* the nuclear jets, a typical value of $\gamma = 5$, as suggested by Orr and Browne (1982), appears to be consistent with the data.

The correlation between f_c and Q suggests that the distribution of the velocity of advancement of hotspots in the outer lobes may extend up to $\sim 0{\cdot}3c$ in a signifycant number of sources. Even larger velocities are in fact required if the asymmetry in the extended emission of D2 quasars arises from the Doppler boosting of the emission from the approaching component. One should then expect to see a correlation between f_c and the ratio of flux densities of the two outer lobes. No significant correlation can however be found in the present sample of quasars which show a fairly large spread in the flux density ratio independent of f_c. The reason is at present unclear. Possible complicating factors that may be important are (i) in general only a fraction of the emission that arises from the hotspots within the lobes is subject to Doppler boosting due to relativistic velocities; (ii) the evolution of luminosity with age must be considered since the two lobes are seen at different ages (Ryle and Longair 1967; Swarup and Banhatti 1981); (iii) it is difficult to detect weak radio lobes in the presence of strong nuclear components; (iv) the extended components of D2 sources may be counterparts of relativistic jets linking the lobes to the nuclei rather than being the lobes themselves (*e.g.* Moore *et al.* 1981; Browne *et al.* 1982). Observations with high angular resolution and large dynamic range that are now becoming available may help in understanding the importance of these factors.

In the $f_c - l$ diagram, the two discrepant quasars (*viz.* 0742 + 31 and 1721 + 34) with dominant CCs and large linear sizes do not appear to fit in with the beaming model. The reason for this is unknown. While no spectral information is available

for the different components of 0742 + 31 (Fanti *et al.* 1977), the outer lobes of 1721 + 34 appear to have normal spectral indices of about 0·75. VLBI observations of its core (Jägers *et al.* 1982) indicate that the CC is elongated in the same direction as the axis defined by the outer lobes. It is, however, of interest to note that both these quasars appear to be well aligned (Δ = 3° and 1° respectively) and symmetric (Q = 1·13 and 1·03 respectively), suggesting that they might indeed be inclined at large angles to the line of sight but have intrinsically strong radio cores, perhaps due to a recent burst of nuclear activity.

Acknowledgement

We wish to thank C. J. Salter for a critical reading of the manuscript.

References

Argue, A. N., Ekers, R. D., Fanaroff, B. L., Hazard, C, Ryle, M., Shakeshaft, J. R., Stockton, A., Webster, A. S. 1974, *Mon. Not. R. astr. Soc*., **168,** 1P.

Baldwin, J. A., Wampler, E. J., Burbidge, E. M., O'Dell, S. L., Smith, H. E., Hazard, C, Nordsieck, K. H., Pooley, G., Stein, W. A. 1977, *Astrophys. J.*, **215,** 408.

Banhatti, D. G. 1980, *Astr. Astrophys.*, **84,** 112.

Blandford, R. D., Königl, A. 1979, *Astrophys. J.*, **232,** 34.

Browne, I. W. A., Orr, M. J. L. 1982, *in IAU Symp. 97: Extragalactic Radio Sources,* Eds D. S. Heeschen and C. M. Wade, D. Reidel, Dordrecht, p. 169.

Browne, I. W. A., Orr, M. J. L., Davis, R. J., Foley, A., Muxlow, T. W. B., Thomasson, P. 1982, *Mon. Not. R. astr. Soc*., **198,** 673.

Conway, R. G., Burn, B. J., Vallee, J. P.61977, *Astr. Astrophys. Suppl. Ser.*, **27,** 155.

Fanti, C., Fanti, R., Formiggini, L., Lari, C, Padrielli, L. 1977, *Astr. Astrophys. Suppl. Ser*., **28,** 351.

Fanti, R., Feretti, L., Giovannini, G., Padrielli, L. 1979, *Astr. Astrophys. Suppl. Ser.*, **35,**169.

Gopal-Krishna, Preuss, E., Schilizzi, R. T. 1980, *Nature*, **288,** 344.

Hintzen, P., Owen, F. N. 1981, *Astr. J*., **8,** 1577.

Jägers, W. J., van Breugel, W. J. M., Miley, G. K., Schilizzi, R. T., Conway, R. G. 1982, *Astr. Astrophys*., **105,** 278.

Jenkins, C. J., Pooley, G. G., Riley, J. M. 1977, *Mem. R. astr. Soc.*, **84,** 61.

Joshi, M. N. 1981, *Mon. Not. R. astr. Soc.*, **197,** 7.

Kapahi, V. K. 1978, *Astr. Astrophys.*, **67,** 157.

Kapahi, V. K. 1981, *J. Astrophys. Astr.*, **2,** 43.

Katgert-Merkelijn, J., Lari, C, Padrielli, L. 1980, *Astr. Astrophys. Suppl. Ser*., **40,** 91.

Laing, R. A. 1981, *Mon. Not. R. astr. Soc.*, **195,** 261.

Longair, M. S., Riley, J. M. 1979, *Mon. Not. R. astr. Soc.*, **188,** 625.

Macklin, J. T. 1981, *Mon. Not. R. astr. Soc.*, **196,** 967.

Masson, C. R. 1980, *Astrophys. J*., **242,** 8.

Miley, G. K. 1971, *Mon. Not. R. astr. Soc.*, **152,** 477.

Miley, G. K., Hartsuijker, A. P. 1978, *Astr. Astrophys. Suppl. Ser*., **34,** 129.

Moore, P. K., Browne, I. W. A., Daintree, E. J., Noble, R. G., Walsh, D. 1981, *Mon. Not. R. astr. Soc*., **197,** 325.

Orr, M. I. L., Browne, I. W. A. 1982, *Mon. Not. R. astr. Soc.*, **200,** 1067.

Owen, F. N., Porcas, R. W., Neff, S. G. 1978, *Astr. J*., **83,** 1009.

Perley, R. A., Fomalont, E. B., Johnston, K. J. 1980, *Astr. J.*, **85,** 649.

Perley, R. A., Fomalont, E. B., Johnston, K. J. 1982, *Astrophys. J.*, **255,** L93.

Pooley, G. G., Henbest, S. N. 1974, *Mon. Not. R. astr. Soc*., **169,** 477.

Potash, R. I., Wardle, J. F. C.1979, *Astr. J.*, **84,** 707.
Potash, R. L, Wardle, J. F. C. 1980, *Astrophys. J.*, **239,** 42.
Readhead, A. C. S., Cohen, M. H., Pearson, T. J., Wilkinson, P. N. 1978, *Nature*, **276,** 768.
Riley, J. M., Jenkins, C. J. 1977, *in IAU Symp. 74: Radio Astronomy and Cosmology,* Ed. D. L. Jauncey, D. Reidel, Dordrecht, p. 237.
Riley, J. M., Pooley, G. G. 1976, *Mem. R. astr. Soc*., **80,** 105.
Riley, J. M., Pooley, G. G. 1978, *Mon. Not. R, astr. Soc.*, **184,** 769.
Rudnick, L. 1982, in *IAU Symp. 97: Extragalactic Radio Sources,* EdsD. S. Heeschen and C. M. Wade, D. Reidel, Dordrecht, p. 47
Ryle, M., Longair, M. S. 1967, *Mon. Not. R. astr. Soc*., **136,** 123.
Salter, C. J., Kapahi, V. K., Swarup, G., Sinha, R. P. 1982, *in preparation.*
Scheuer, P. A. G., Readhead, A. C. S. 1979, *Nature*, **277,** 182.
Schilizzi, R. T., Kapahi, V. K., Neff, S. G. 1982, *J. Astrophys. Astr.*, **2,** 173.
Slee, O. B. 1977, *Aust. J. Phys. Astrophys. Suppl.,* No. 43.
Swarup, G., Banhatti, D. G. 1981, *Mon. Not. R. astr. Soc.*, **194,** 1025.
Swarup, G., Sinha, R. P., Saikia, D. J. 1982, *Mon. Not. R. astr. Soc.,* **201,** 393.
Wardle, J. F. C, Miley, G. K. 1974, *Astr. Astrophys*., **30,** 305.
Wills, D. 1979, *Astrophys. J. Suppl. Ser.,* **39**, 291.

J. Astrophys. Astr. (1982) **3,** 485–497

Reflection Effect in Close Binaries. I. Distribution of Radiation from a Point Source

A. Peraiah *Indian Institute of Astrophysics, Bangalore 560034*

Received 1982 June 4; accepted 1982 October 25

Abstract. The radiation field along an irradiated surface of a component in a binary system is calculated. The source of irradiation is assumed to be a point source. This is done primarily to understand easily how the incident radiation will get changed after it is being scattered by the atmosphere. It is noticed that the maximum radiation comes from intermediate points of the atmosphere, the reason being that here we have the combined radiation due to the star and incident radiation from the point source outside the star although both are diluted.

Key words. radiative transfer–rod model–close binaries

1. Introduction

In radiative transfer theory, we solve the equation of transfer by assuming a certain geometrical configuration such as plane-parallel or spherically symmetric stratification of the media. These geometrical configurations assume symmetric boundary conditions and whenever we have asymmetric incident radiation, the solutions developed in the context of symmetrical geometries as mentioned above, will have to be modified. Such problems are encountered in the evaluation of radiation from the irradiated component of a binary system. The problem of incidence of radiation from a point source is termed the Searchlight problem. Chandrasekhar (1958) has calculated the diffuse scattering function in a plane-parallel medium when a pencil of beam of radiation from a point source is incident. There have been several attempts at calculating the diffuse field in such simple geometries (Rybicki 1971).

However, the calculation of the radiation field during eclipses in close binaries is of different complexity. There are two important aspects one should take into account: (1) the physical processes that take place inside the atmosphere and (2) the geometrical shape of the illuminated surface which reflects the light. Generally, if the atmosphere of the component under consideration is extended or fills its Roche

lobe, then the problem of determining the emergent radiation from such surfaces become very difficult. The process of estimating the radiation field from such surfaces becomes more complicated when the various competing physical processes are included in the calculations. Geometrical considerations alone would make it quite difficult because of the deformed shape due to tidal effects from the neighbour and due to self-rotation. The resultant shape would be an ellipsoid and the problem requires a special treatment. Solution of radiative transfer equation either in spherical symmetry or in cylindrical symmetry cannot describe appropriately the radiation field emanating from such surfaces. This requires a careful study from fundamental aspects. The problems of planetary atmospheres involve this type of radiation field but plane-parallel approximation has been employed by several authors in the past (Chandrasekhar 1960). Buerger (1969). employed plane-parallel approximation in computing the continuum and line radiation emitted by a rotationally and tidally distorted star which is irradiated by the light of the secondary component. This approach is obviously simplified to avoid the difficulties arising out of correct treatment of radiative transfer in such a situation, but is totally inadequate if we require realistic results. Although the thickness of the planetary atmosphere is quite small compared to the radius of the planet itself, the curvature of the atmosphere on which the parallel beam from the Sun is incident, would scatter and absorb this radiation differently at different points on its surface. Therefore, one must calculate the radiation from planetary atmospheres on lines similar to those described in this paper.

The aim of this series of papers is to estimate the reflected radiation (both in continuum and lines) that is incident on a binary component. Further, we would like to estimate the changes caused by the reflection effect on the light curves that are observed. In this paper, we present a method of calculating the emergent radiation from the surface irradiated by the radiation from the second component assumed as a point source.

2. Method of obtaining solution

We shall assume that the stars are spherical (the method can be extended easily to nonspherical shapes) and divide the atmosphere into several shells. In Fig. 1, we have described the model for calculating the distribution of radiation. We have assumed the albedo of single scattering to be unity, *i.e.* a pure scattering medium.

O is the centre of the component whose atmosphere is divided in spherical shells. Radiation from a point S outside the star (assuming that the radiation is coming from point source) is incident at points such as P_1, P_2 etc. These rays travel through the medium intersecting the shells at given radial points. We choose a radius vector corresponding to a given θ (the colatitude) and calculate the source functions where this radius vector meets the shell boundaries at points such as Q_l, Q_2 *etc.* The calculation of the source function is done by employing the 'rod' model of one-dimensional radiative transfer (see Sobolev 1963; Wing 1962) along the ray path inside the medium. This means we calculate the source functions at points Q_l, Q_2 *etc.* For readers who are not familiar with this approach, we shall briefly describe the method following Grant (1968). In Fig. 2, we describe the model. We assume a steady state, monochromatic ray with or without internal sources. Notice that the

optical depth is measured in the opposite direction to that of the geometrical depth. The optical depth is calculated by the relation

$$\tau = \tau(\xi) = \int_0^l \sigma(\xi')\, d\xi', \quad \tau(l) = T. \tag{1}$$

In this model, we assume that the transfer takes place along $0l$ in Fig. 2 (or P_1Q_1, P_2 Q_2 *etc.* in Fig. 1) with isotropic scattering ($\mu = \pm 1$ and $p(\tau)$ = phase matrix elements = ½). The quantities $I^+(\tau)$ and $I^-(\tau)$ represent the specific intensities in the opposite directions. The two equations for oppositely directed rays are written as

$$\frac{dI^+}{d\tau} + I^+ = S^+, \tag{2}$$

$$\frac{dI^-}{d\tau} + I^- = S^-, \tag{3}$$

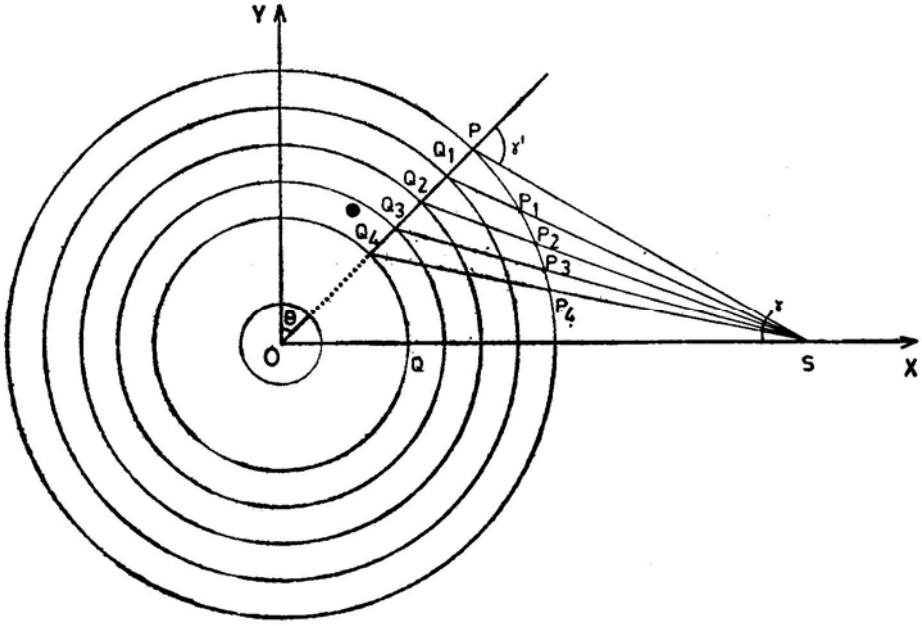

Figure 1. Model diagram showing how the radiation is calculated.

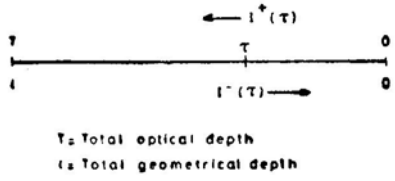

Figure 2. Rod model.

where

$$S^+ = \tilde{\omega}(\tau)\,[p(\tau)\,I^+(\tau) + (1 - p(\tau))\,I^-(\tau)], \tag{2a}$$

$$S^- = \tilde{\omega}(\tau)\,[(1 - p(\tau))\,I^+(\tau) + p(\tau)\,I^-(\tau)]. \tag{3a}$$

The boundary conditions at $\tau = 0$ and $\tau = T$ are given by

$I^+(0) = I_1$

and

$$I^-(T) = I_2, \tag{4}$$

where I_1 shall be specified later. The total source function that includes the diffuse radiation field can be written as,

$$S_d^+(\tau) = S^+(\tau) + \tilde{\omega}(\tau)\,[p(\tau)\,I_1 \exp(-\tau) + (1 - p(\tau))\,I_2 \exp\{-(T - \tau)\}]$$

$$S_d^-(\tau) = S^-(\tau) + \tilde{\omega}(\tau)\,[(1 - p(\tau))\,I_1 \exp(-\tau) + p(\tau)\,I_2 \exp\{-(T - \tau)\}]. \tag{5}$$

In this case the boundary conditions are

$I^+(0) = I^-(T) = 0.$

The mathematical aspects of the problem have been fully discussed in Grant (1968) and we shall simply quote his results. When $\tilde{\omega} = 1$, we have

$$I^+(\tau) = I_1 \frac{1 + (T - \tau)(1 - p)}{1 + T(1 - p)},$$

and

$$I^-(\tau) = I_1 \frac{(T - \tau)(1 - p)}{1 + T(1 - p)}. \tag{6}$$

From Equations (6) one can write

$$I^+(\tau = T) = I_1 \frac{1}{1 + T(1 - p)},$$

$$I^-(\tau = 0) = I_1 \frac{T(1 - p)}{1 + T(1 - p)}. \tag{7}$$

Notice that

$$r(T) = \frac{T(1 - p)}{1 + T(1 - p)} \to 1 \text{ as } T \to \infty$$

and

$$t(T) = \frac{1}{1 + T(1-p)} \to 0 \text{ as } T \to \infty, \tag{8}$$

where r (T) and t (T) are the reflection and transmission co-efficients. Therefore in the limit when $T \to \infty$ we have

$$r(T) + t(T) = 1 \tag{9}$$

which is nothing but conservation of energy.

Using the results of the above analysis we can calculate the source functions according to one-dimensional rod model at points where the radii corresponding to each θ meet the shell boundaries.

Our aim is, therefore, to obtain the source functions described in Equations (5). Here, we calculate the optical depth along the ray path *e.g.* P_1Q_2, P_2Q_2 *etc.* and employ this optical depth to estimate the specific intensities and source functions at these points.

In addition to the incident radiation, we have the radiation of the star itself. This radiation can be calculated easily by employing the spherically-symmetric approximation of the radiative transfer equation. This is done by solving the equation in spherical symmetry in discrete space theory as described in Peraiah and Grant (1973). The total source function S, at each radial point Q_1, Q_2 *etc.* is given by the sum of the source functions due to star and irradiation from the point S. That is

$$S(r, \theta) = S_1(r, \theta) + S_2(r) \tag{10}$$

where S_1 (r, θ) is due to irradiation from outside and S_2 (r) is due to self radiation field.

Next step is to calculate the distribution of intensities at the internal points like Q_1, Q_2 *etc.* along the radius and find out the distribution of the emergent radiation field at points like P_1, P_2 *etc.* The radiation field is given by the formal solution of radiative transfer equation in plane-parallel approximation, (See Chandrasekhar 1960, Equations 64 and 65 on p. 12, and Fig. 3 here),

$$I(\tau, +\mu) = I(\tau_1, \mu) \exp\left[-(\tau_1 - \tau)/\mu\right] + \int_{\tau}^{\tau_1} S(t) \exp\left[-(t-\tau)/\mu\right] dt/\mu \tag{11}$$

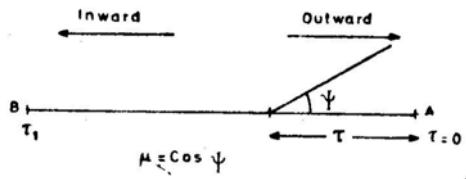

Figure 3. Plane-parallel model.

for outward intensities, and

$$I(\tau, -\mu) = I(0, -\mu) \exp(-\tau/\mu) + \int_0^{\tau} S(t) \exp[-(\tau - t)/\mu]\, dt/\mu \qquad (12)$$

for the intensities directed inwards. In Equations (11) and (12), the optical depths are always measured from A to B, and $1 \geqslant \mu > 0$ where $\cos^{-1} \mu$ is the angle made by the ray with AB. Equations (11) and (12) describe the radiation field emerging from the irradiated surface which receives the incident radiation coming from the point S.

3. Results and discussion

We have considered a component whose radius is 10^{11} cm with half the radius as its atmosphere, and assume that the incident radiation is coming from a point S at a distance of $4{\cdot}5 \times 10^{11}$ cm from the centre of the component O. We also assume the point S is on the axis OX and the axis OY is perpendicular to OX. We calculte the source functions at points Q_1, Q_2 *etc.* on a radius vector with co-latitude θ. This is done by employing the rod model described in Equations (2a), (3a), (5) and (6). We have assumed isotropic scattering and the albedo for single scattering is set equal to unity. We calculte the line segments P_1Q_2, P_2Q_2 *etc.* and estimate the optical depths according to the law that the density varies as $1/r$. While calculating the source functions due to self radiation, we have used the spherically symmetric approximations.

Let I_Q be the intensity of radiation incident spherically symmetrically at Q inside

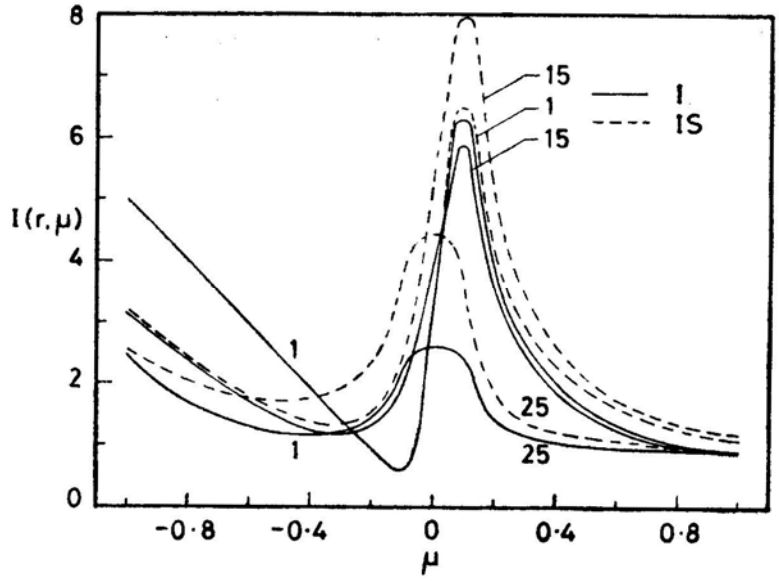

Figure 4. Distribution of radiation field at $\theta = 0°$, Case 1, for the shell numbers shown in the figures. I stands for the irradiation, and IS stands for irradiation plus selfradiation.

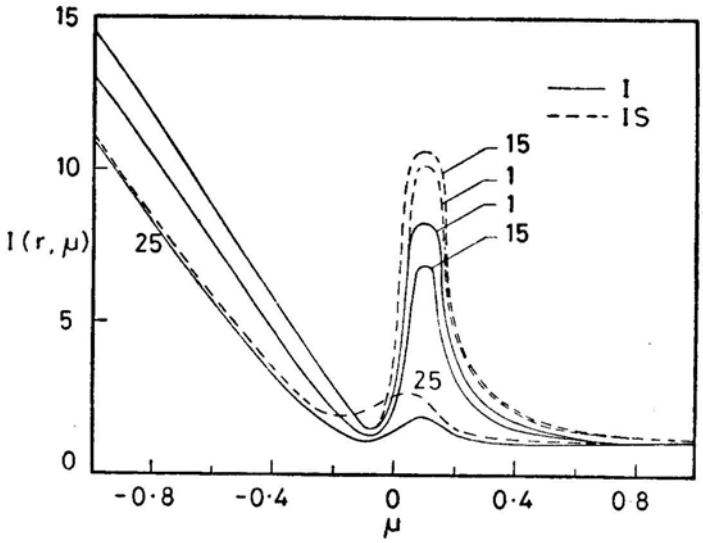

Figure 5. Distribution of radiation field at $\theta = 60°$, Case 1.

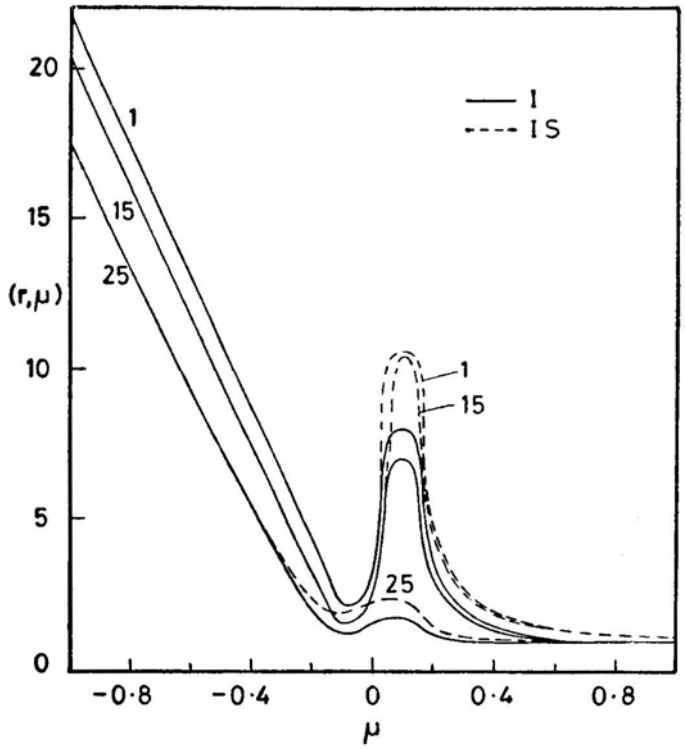

Figure 6. Distribution of radiation field at $\theta = 90°$, Case 1.

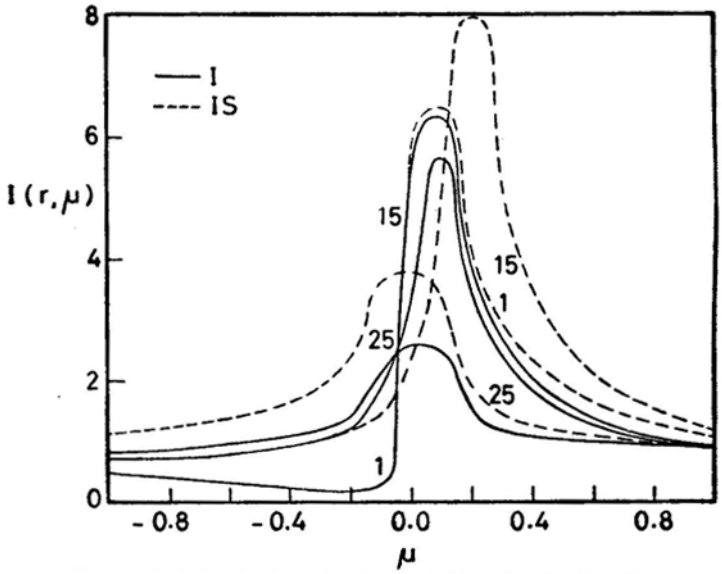

Figure 7. Distribution of radiation field at $\theta = 0°$, Case 2.

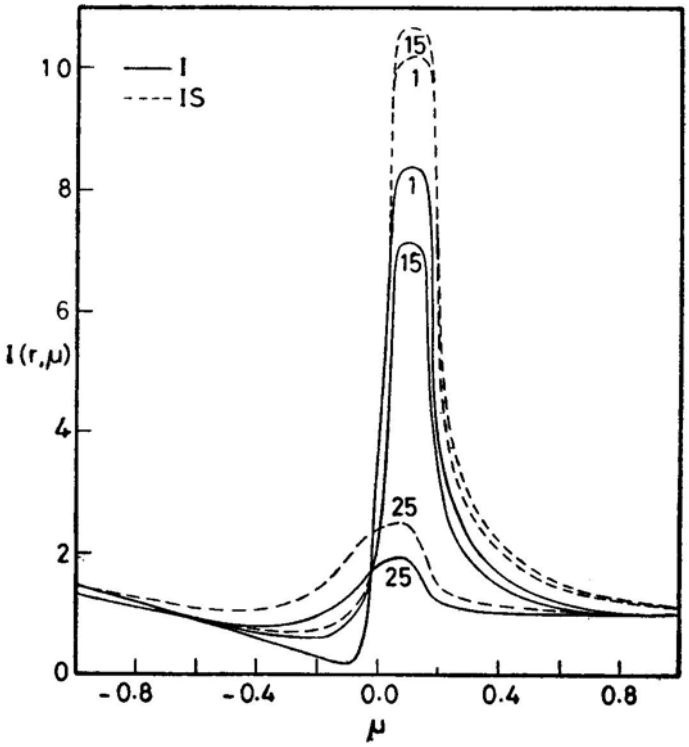

Figure 8. Distribution of radiation field at $\theta = 60°$, Case 2.

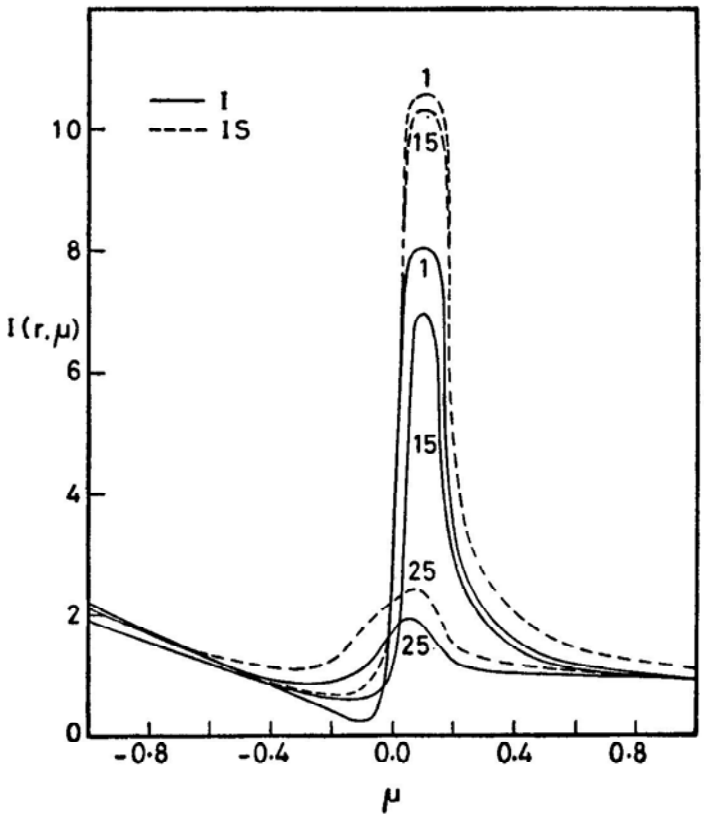

Figure 9. Distribution of radiation field at $\theta = 90°$, Case 2.

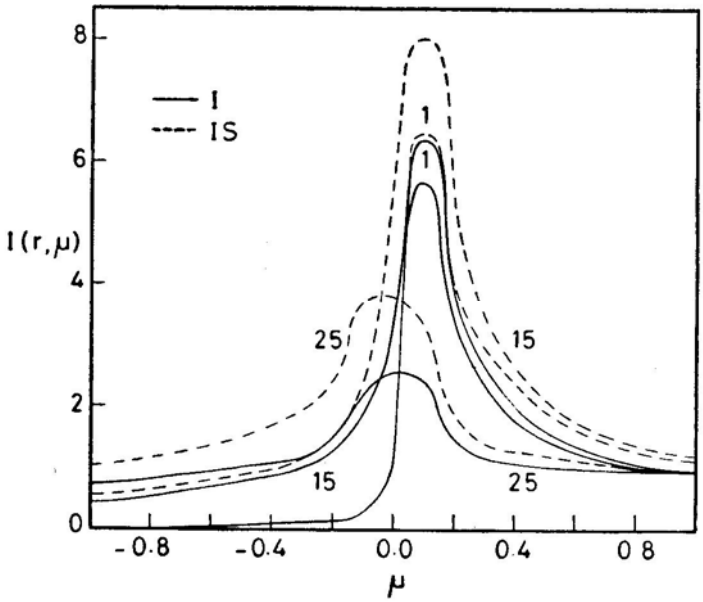

Figure 10. Distribution of radiation field at $\theta = 0°$, Case 3.

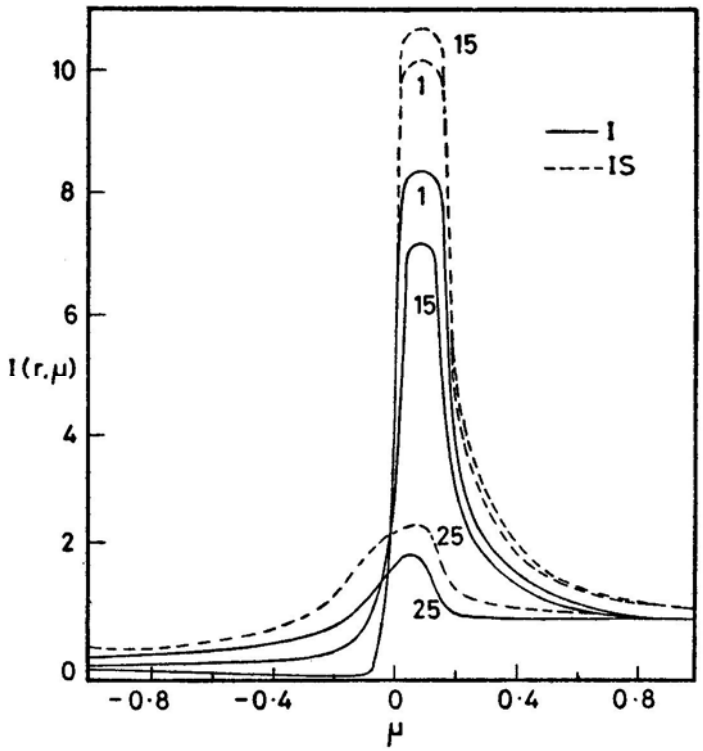

Figure 11. Distribution of radiation field at $\theta = 60°$, Case 3.

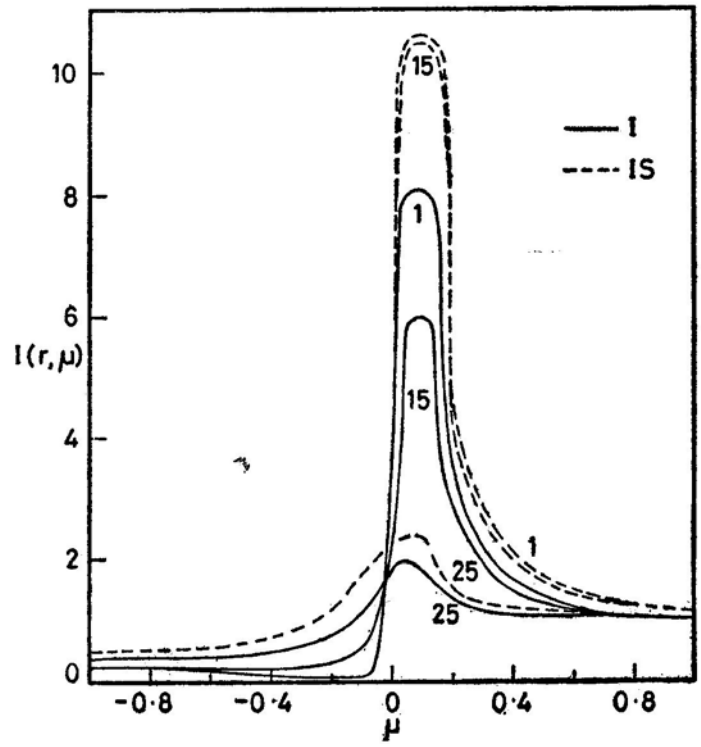

Figure 12. Distribution of radiation field at $\theta = 90°$, Case 3.

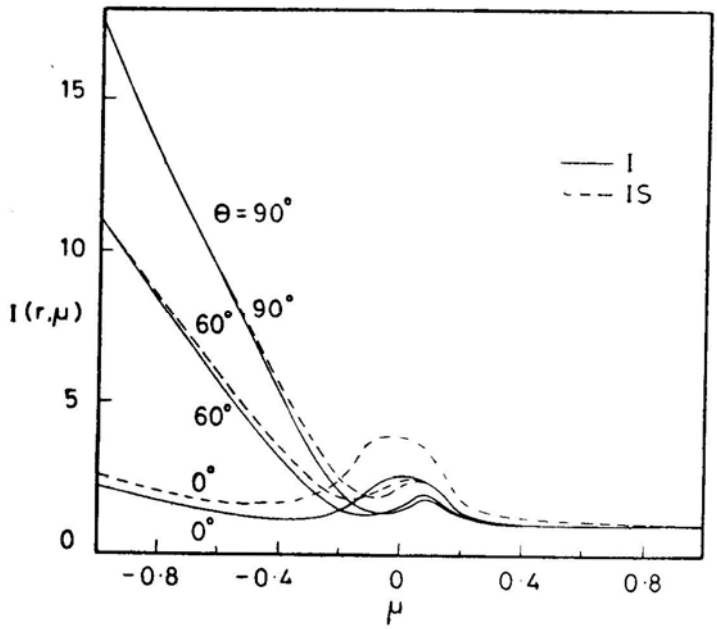

Figure 13. Distribution of the emergent radiation field at $\theta = 0°$, 60° and 90°, Case 1.

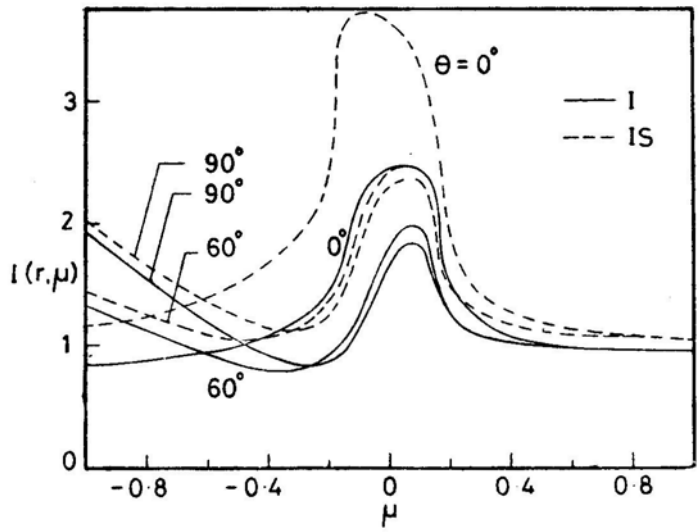

Figure 14. Distribution of the emergent radiation field at $\theta = 0°$, 60° and 90°, Case 2.

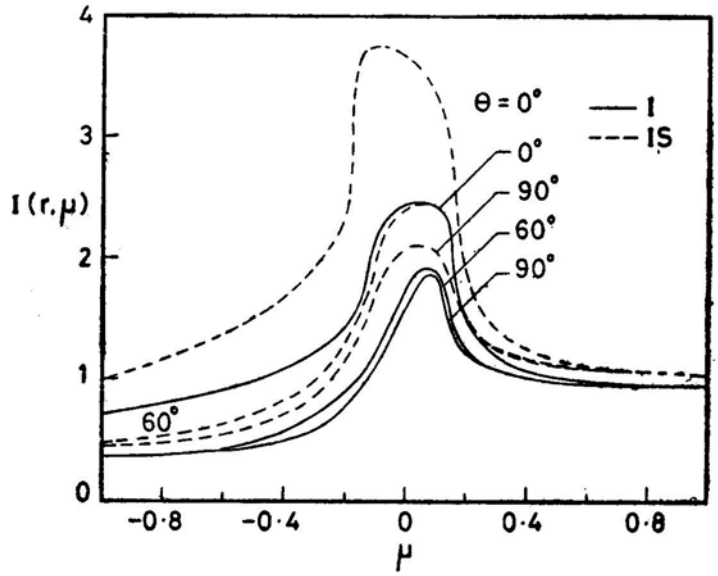

Figure 15. Distribution of the emergent radiation field at $\theta = 0°$, 60° and 90°, Case 3.

the star and the intensity coming from point S be I_S. The incident radiation at P will be $I_S\ \mu\ \cos\ \gamma$. We have considered three cases.

Case 1; $I_Q/I_S = 0{\cdot}1$

Case 2; $I_Q/I_S = 1$

Case 3; $I_Q/I_S = 10$

We have assumed scattering due to electrons in the atmosphere of the component. Calculations Have been done with several electron densities N_e(at $r = r_{in}$). N_e is set equal to 10^{12} cm^{-3} to 10^{15} cm^{-3}. We have presented results for $N_e = 10^{14}$ cm^{-3}. With this density, the radial optical depth becomes 1.1. The results are given in the form of distribution of radiation at different points along the radii such as Q_1 , Q_2 *etc.* by solving the Equations (11) and (12). These are presented in Figs 4–12 for the three cases. We have divided the medium into 25 shells. The radiation field I (θ, r, μ) are plotted against μ for a specified θ and r (in terms of the shell number where the shell numbers are counted from outside to inside, *i.e.* n =1 at $r = r_{out}$ and n =25 at $r = r_{in}$) . In Figs 46 we have plotted $I(r, \mu)$ at θ =0°, 60° and 90° respectively for Case 1. The continuous curves denote the external radiation and the dotted curves indicate the resultant radiation field due to both external and self radiation. In Fig. 4, the co-latitude $\theta = 0$, corresponds to the radiation along OY. At the bottom of the atmosphere (n=25 or $r = r_{in}$) the effect of external radiation is not much but increases when the self radiation is added to it. At the shell n =15, we see that the combined radiation field is maximum while at the outermost layer (n=1) it is not as large as that at n=15. This is not difficult to understand on physical grounds. At n=1

we have the diluted self radiation and at $n = 25$, the external radiation becomes weak. In the middle we have the combined radiation field of both, although partly diluted. In Fig. 5, we have plotted $I(r, \mu)$ for $\theta = 60°$. We can see that the same effects seen in Fig. 4, are also there in this figure, although the radiation going towards the centre of the star is enhanced. In Fig. 6, $I(r, \mu)$ is given for $\theta = 90°$. The distribution of radiation resembles that given in Fig. 5; again the radiation towards the star (along OX) increases rapidly.

The results of Case 2 are given in Figs 7, 8 and 9 for $\theta = 0°$, 60° and 90° respectively. Generally, the radiation field in Case 2, shows characteristics which are similar to those in Case 1. The main difference between these two cases is that more radiation comes out in Case 2 than in Case 1. The amount of radiation that is coming out remains almost the same whether $\theta = 0°$, 60° or 90°. Figs 10–12 describe the radiation field for Case 3. At $\theta = 0°$, $I(r, \mu)$ is similar to those given in Fig. 4. In this case also, we see more radiation coming out than going inside.

In Figs 1315, we have plotted $I(n = 1, \mu)$ for Cases 1, 2 and 3 respectively. From Fig. 13, one can see that the intensities at $\theta = 0$ are quite small and increase considerably at $\theta = 90°$. In case 2, we have again the same phenomenon (Fig. 14) although at $\theta = 90°$ (along OS) more radiation goes into the star than comes out. $I(n = 1, \mu)$ for Case 3 (Fig. 15) shows again the same features of Fig. 14, with much less radiation going into the star both at $\theta = 0°$ and 90°.

4. Conclusions

We have developed a method of obtaining radiation field along the spherical surface irradiated by an external point source of radiation, as a preliminary step towards full understanding of reflection effect in close binary systems. Here, we have assumed electron scattering and we need to investigate the temperature changes in the atmosphere due to the irradiation. Furthermore, when the components are very close, one should calculate the effects of irradiation from an extended non-spherical surface.

References

Buerger, P. 1969, *Astrophys. J.* **158,** 1151.
Chandrasekhar, S. 1958, *Proc. nat. Acad*, *Sci. Am.*, **44,** 933.
Chandrasekhar, S. 1960, *Radiative Transfer*, Dover, New York.
Grant, I. P. 1968, *Lecture Notes on New Methods in Radiative Transfer.*
Peraiah, A., Grant, I. P. 1973, *J. Inst. Math. Appl.* **12,** 75.
Rybicki, G. B. 1971, *J. quantit. Spectrosc. radiat. Transfer,* **11**, 827.
Sobolev, V. V. 1963, *A Treatise on Radiative Transfer,* Van Nostrand, New York.
Wing, G. M. 1962, *An Introduction to Transfer Theory,* John Wiley, New York.